Understanding the Role of Transporters and Ion Channels in Lysosomal Homeostasis

Sacha Salphati

Department of Biochemistry

University of Oxford

Supervisors: *Prof. Simon Newstead and Prof. Stephen Tucker*

September 26, 2024

A thesis submitted for the partial fulfilment of

the degree of Doctor of Philosophy.

St Hugh's College

Abstract

Cellular activity is regulated based on a range of cues to maintain homeostasis. The lysosome is a key regulator of cellular activity as it acts as a signaling hub for metabolic regulation and is the main site of biomolecule degradation. Following the degradation of biomolecules, including proteins, glycans, nucleic acids and lipids, nutrients are exported out of the lysosome by efflux transporters, which provide nutrients for cellular anabolic activity. Efflux transporters maintain lysosomal homeostasis by preventing the deleterious accumulation of nutrients within the lumen. Here, the mechanism of cystine transport at the lysosomal membrane by cystinosin is characterized using two-electrode voltage clamp. This work provides novel insights into the mechanisms that maintain nutrient homeostasis in lysosomes, and how they are disrupted in the lysosomal storage disorder cystinosis. Lysosomal homeostasis is also preserved by protein signaling, which regulates lysosome biogenesis, trafficking, fusion, and activity. A key regulator of cell signaling at the lysosomal membrane is the ion channel TRPML1. Numerous functions have been associated with TRPML1 activity, but its mechanisms of action remain poorly understood. This is in part due to the lack of specific tools to investigate its functions (modulators) and localization (antibodies). Nanobodies have previously been used as tools to investigate the mechanisms and localization of membrane proteins in cells. Here, high-affinity TRPML1 synthetic nanobodies (sybodies) were generated and characterized biophysically and structurally. A TRPML1-specific bivalent construct was engineered and applied to STochastic Optical Reconstruction Microscopy (STORM) imaging and immunoprecipitation of endogenous TRPML1. Future work will aim to use these binders and protocols to investigate the role of TRPML1 in neurodegeneration, which can result from the loss of lysosomal homeostasis. Moreover, the protocols described here will enable to engineer sybodies against additional lysosomal targets to investigate their role in lysosomal homeostasis.

Acknowledgments and Contributions

The work presented here would not have been possible without the tremendous support and guidance that I have received during my PhD journey. Firstly, I would like to thank my supervisors, Prof. Simon Newstead and Prof. Stephen Tucker, who have mentored me during the course of my PhD. I appreciate the tremendous amount of time and feedback provided by my supervisors during the past four years, which has been instrumental in shaping me into a better scientist and individual. I am profoundly grateful for all the phenomenal opportunities they have provided, including the opportunities to work on fascinating projects and for the opportunity to work at the University of Pennsylvania. I would also like to thank Dr. Joanne Parker for her tremendous support throughout the course of my PhD. My heartfelt appreciation extends to the wonderful colleagues in the Newstead and Tucker labs, whose mentorship and camaraderie have equipped me with many of the skills I possess today. I would also like to thank members of the Wade-Martins (Dr. Maria Claudia Caiazza and Johanna Hoffmann) and Becker (Dr. Bethan Cole) labs for their significant contributions to some of the work presented in this thesis. I would also like to thank my supervisors at the University of Pennsylvania, Prof. Melike Lakadamyali and Prof. Vera Moiseenkova-Bell, and their lab members for their tremendous technical support and dedication to the project. I am fortunate to have made wonderful friends during my time in Oxford, whose companionship has been invaluable. Most importantly, I am profoundly grateful to my family for their unwavering support and guidance throughout this journey.

Chapter 3: The Molecular Basis of Proton-Coupled Cystine Transport by Human Cystinosin

The work presented in this chapter was carried out under the supervision and guidance of Prof. Simon Newstead, Dr. Joanne Parker and Prof. Stephen Tucker. I conducted all the electrophysiology and confocal microscopy experiments in oocytes described in this chapter. The plant cystinosin work mentioned or displayed in this chapter, including the structural characterization, transporter assays and ligand binding assays were carried out by Dr. Mark Löbel. The human

cystinosin sybody selection and characterization was carried out by Dr. Mark Löbel, and the structural characterization of the sybody-cystinosin complex was carried out by Dr. Kato Takafumi. I conducted the immunofluorescence experiments using the human cystinosin sybodies. The proposed cystinosin mechanism was developed by Prof. Simon Newstead and Dr. Joanne Parker.

Chapter 4: Generation of a Synthetic Nanobody Toolkit to Investigate TRPML1 Localization, Function and Structure

The work presented in this chapter was carried out under the supervision of Prof. Simon Newstead, Dr. Joanne Parker, Dr. Oliver Adams and the support and guidance of the Newstead lab members. I performed all the experiments for the results presented in this chapter. Dr. Oliver Adams kindly provided the negative control sybody (SybBC10).

Chapter 5: Structural Characterization of TRPML1-Sybody Complexes

The work presented in this chapter was made possible by the contributions and supervision of Prof. Simon Newstead, Dr. Joanne Parker, Prof. Vera Moiseenkova-Bell, Dr. Esther Becker, Prof. Stephen Tucker and Prof. Richard Wade-Martins, and the members of their labs. For the FURA-2 assays, I prepared and transfected the cells and the assay was carried out by Johanna Hoffmann with the technical guidance of Dr. Maria Claudia Caiazza from the Wade-Martins lab. All whole-cell patch-clamp recordings included in the chapter were carried out by Dr. Bethan Cole in the lab of Prof. Esther Becker. For the cryo-EM characterization of the Syb94-TRPML1 complex, I carried out the sample preparation and the grids were prepared and screened by Dr. Ruth Pumroy from the Moiseenkova-Bell lab. For the cryo-EM characterization of the Syb57-TRPML1 complex, I carried out the sample and grid preparation. Data collection was carried out at the Beckman Center for Cryo-Electron Microscopy (UPenn) by Dr. Stefan Steimle and Dr. Prerana Gogoi. I carried out the data processing and some of the model building, which was

finalized by Dr. Ruth Pumroy. I performed all the structural analysis.

Chapter 6: Structural Characterization of TRPML1-Sybody Complexes

The work in this chapter was made possible by the supervision provided by Prof. Melike Lakadamyali and Prof. Vera Moiseenkova-Bell, and the members of their labs. Additional technical guidance was also provided by the Micron facility staff, the Seiradake lab and Dr. Andreas Gerondopoulos. I performed all the experiments in this chapter except those presented in figure 77, which were performed by Dr. Bridget McVeigh (Panel A-C), Dr. Prerana Gogoi (Panel D) and Dr. Ruth Pumroy (Panel E). The super-resolution protocol used for the immunostaining experiments was adapted from a protocol kindly provided by Dr. Charlie Bond. TMEM-175, SLC45A4 and SLC66A2 (SybBC10) constructs and sybodies were kindly provided by Sigurbjörn Markússon and Dr. Oliver Adams.

Table of Contents

1 Introduction **1**

1.1 Role of the Lysosome in the Cell 1

1.1.1 Roles of Lysosomes in Maintaining Cellular Homeostasis 1

1.1.2 Lysosomal Life Cycle 2

1.1.2.1 Vesicle and Endosome Formation 2

1.1.2.2 Endosome Maturation 4

1.1.2.3 Lysosome Life Cycle 5

1.1.3 Lysosome Composition and Homeostasis 6

1.1.4 Regulation of Cell Signaling at the Lysosomal Membrane 6

1.2 The Roles of Ion Channels and Transporters in Lysosomes 9

1.2.1 Lysosomal Membrane Proteins 9

1.2.2 Lysosomal Ion Channels and Ion Homeostasis 10

1.2.3 Lysosomal Transporters and Nutrient Homeostasis 11

1.2.4 Lysosomal Membrane Proteins in Diseases 13

1.3 TRPML1 Function and Structure 13

1.3.1 Lysosomal Calcium 13

1.3.2 TRPML1 Functions 16

1.3.3 TRPML1 Structure 17

1.3.4 Structural Basis for TRPML1 Activation 19

1.3.5 TRPML1 Dysregulation in Neurodegenerative Diseases 23

1.4 Cystinosin: Structure and Function 24

1.4.1 Cystine in Lysosomal and Cellular Homeostasis 24

1.4.2 Cystinosin is the Lysosomal Proton-Coupled Cystine Transporter . . . 26

1.4.3 Mutations in Cystinosin Cause the Lysosomal Storage Disorder Cystinosis 28

1.5 Nanobodies 30

1.5.1 Generation and Structure of Nanobodies 30

1.5.2 Synthetic Nanobodies (Sybodies) . . . 31
1.5.3 Application of Nanobodies to Structural Studies . . . 33
1.5.4 Nanobodies to Investigate Protein Localization in Cells . . . 34
1.5.5 Nanobodies to Modulate and Investigate Protein Functions in Cells . . . 35
1.6 Aims . . . 36

2 Materials and Methods **38**
2.1 Characterization of the Human Cystine Transporter Cystinosin Using Two-Electrode Voltage Clamp. . . . 38
2.1.1 Two-Electrode Voltage Clamp . . . 38
2.1.2 Oocyte Confocal Microscopy . . . 39
2.2 Generation of a Synthetic Nanobody Toolkit to Investigate TRPML1 Localization, Function and Structure . . . 39
2.2.1 TRPML1 Expression and Purification . . . 39
2.2.1.1 Full-Length TRPML1 . . . 39
2.2.1.2 TRPML1 Luminal-Domain . . . 41
2.2.1.3 Protein Biotinylation . . . 41
2.2.2 Western Blot . . . 41
2.2.3 Differential Scanning Fluorimetry . . . 42
2.2.4 Circular Dichroism . . . 42
2.2.5 Sybody Selection . . . 42
2.2.5.1 Ribosome Display . . . 43
2.2.5.2 Phage Display . . . 43
2.2.6 Sybody Expression, Purification and Labelling . . . 45
2.2.6.1 Sybody Expression and Purification . . . 45
2.2.6.2 Sybody Labelling . . . 45
2.2.7 Sybody Pull-Down . . . 46
2.2.8 Bio-layer Interferometry . . . 46
2.3 Structural and Functional Characterization of TRPML1-Sybody Complexes . . . 47

2.3.1 Cryo-EM Sample Preparation and Data Collection 47
2.3.1.1 Complex Preparation 47
2.3.1.2 Grid Preparation 47
2.3.1.3 Data Collection 48
2.3.2 Cryo-EM Data Processing: TRPML1-Syb57 48
2.3.3 Cryo-EM Data Processing: TRPML1-Syb94 50
2.3.4 Model Building 50
2.3.5 TRPML1 Activity Assays 51
2.3.5.1 FURA-2 Assay 51
2.3.5.2 Whole-Cell Patch Clamp 51
2.4 Engineering Synthetic Nanobodies to Investigate TRPML1 Localization 52
2.4.1 Sybody Fluorescence Microscopy 52
2.4.2 Sybody Fusions Expression and Purification 53
2.4.3 Sybody Dimer Expression and Purification 54
2.4.4 Cryo-Electron Microscopy with Gold-Labelled Sybodies 54
2.4.5 STORM 55
2.4.6 Immunoprecipitation with Sybodies 56
2.4.6.1 Immunoprecipitation with Directly Conjugated Sybodies . . 56
2.4.6.2 Immunoprecipitation with Avi-Tagged Sybodies 57
2.4.6.3 Immunoprecipitation with 1D4-Tagged Sybodies 58
2.5 Data Presentation and Visualization 58

3 The Molecular Basis of Proton-Coupled Cystine Transport by Human Cystinosin 60
3.1 Investigating Cystinosin Proton-Coupled Transport Using Two-Electrode Voltage Clamp 60
3.2 The Luminal Domain of Human Cystinosin is Not Required for Proton-Coupled Transport 64
3.3 Identification of a Cystine Binding Site 66
3.4 A Salt Bridge Stabilising the Inward-Open State Acts as a Luminal Gate 68

3.5 The Second PQ-Loop Motif of Cystinosin is Essential for Proton-Coupled Transport . . . 70
3.6 Interactions Formed by the Proton-Coupling Residue May Couple Substrate Release with Conformational Changes . . . 71
3.7 Mechanism of Proton-Coupled Transport . . . 72
3.8 Interpretation of Cystinosis-Causing Mutations . . . 76
3.9 Sybodies to Investigate Cystinosin Functions and Localization . . . 77
3.10 Conclusions and Future Perspectives . . . 77

4 Generation of a Synthetic Nanobody Toolkit to Investigate TRPML1 Localization, Function and Structure 80

4.1 Tools to Investigate TRPML1 Functions . . . 80
4.2 TRPML1 Sybody Pipeline . . . 81
4.3 Sybody Selection Outcome . . . 84
4.4 Characterization of Sybody Hits . . . 87
4.4.1 Sybody Purifications . . . 87
4.4.2 Characterization of Sybody Binding . . . 89
4.5 Epitope Mapping of TRPML1 Sybodies . . . 93
4.5.1 Purification of TRPML1 Luminal Domain . . . 93
4.5.2 Luminal Domain Sybody Binding Characterization . . . 95
4.5.3 Epitope Binning . . . 98
4.5.4 Validation of Cytosolic Sybody - Intrabody Application . . . 100
4.6 Binding of TRPML1 Sybodies at Lysosomal pH . . . 102
4.6.1 Stability at Lysosomal pH . . . 102
4.6.2 Binding at Lysosomal pH . . . 102
4.7 TRPML1 Sybody Selection Summary . . . 106

5 Structural Characterization of TRPML1-Sybody Complexes 108

5.1 Structural Characterization of Nanobody Complexes . . . 108
5.2 Screening of TRPML1 Sybody Modulators . . . 109

5.2.1 FURA-2 Screen . . . 109
5.2.2 Whole-Cell Patch Clamp . . . 110
5.3 Sample Preparation and Data Processing . . . 112
5.4 Structure of TRPML1-Syb94 Complex . . . 114
5.4.1 Complex Architecture . . . 114
5.4.2 TRPML1-Syb94 Interface . . . 120
5.5 Structure of TRPML1-Syb57 Complex . . . 123
5.5.1 Complex Architecture . . . 123
5.5.2 TRPML1-Syb57 Interface . . . 132
5.6 States of the Complexes . . . 134
5.7 Mechanism of Modulation . . . 138
5.7.1 Sybody Modulation of Selectivity Filter State . . . 138
5.7.2 Potential Functions of the Luminal Loop . . . 143
5.7.3 Suggested Mechanism of Modulation . . . 145
5.8 *In Silico* Predictions of Interfaces . . . 147
5.9 Outlook . . . 155

6 Engineering Synthetic Nanobodies to Investigate TRPML1 Localization 157
6.1 Lysosomal Membrane Protein Imaging . . . 157
6.2 Determining Sybody Specificity and Binding in Cells . . . 158
6.3 Sybody Engineering for Fluorescence Microscopy . . . 164
6.3.1 Sybody Fusions . . . 164
6.3.2 Direct Sybody Labeling . . . 172
6.3.3 Cryo-Correlative Light-Electron Microscopy (CLEM) . . . 181
6.4 Super-Resolution Imaging with TRPML1 Sybodies . . . 184
6.4.1 Sybody Lysosomal Imaging Protocol for Super-Resolution Microscopy 184
6.4.2 Generation and Characterization of TRPML1 Super-Binders . . . 187
6.4.3 STORM Imaging . . . 191
6.5 Validation of Sybody Specificity by Immunoprecipitation . . . 194

6.5.1 TRPML1 Immunoprecipitation Optimizations 194
6.5.2 Validation of Sybody specificity 198
6.6 Outlook 200

7 Conclusions **202**

8 Appendix **207**
8.1 Supplementary Figures and Data 207

List of Abbreviations

Ab	Antibody
AF	AlphaFold 3
ATP	Adenosine Triphosphate
AU	Arbitrary or Absorbance Units
BirA	*E. coli* Biotin Ligase
BLI	Bio-Layer Interferometry
CD	Circular Dichroism
cDNA	Complementary DNA
CDR	Complementarity-Determining Region
cryo-EM	cryogenic Electron Microscopy
cryo-ET	cryogenic Electron Tomography
CLEM	Correlative Light-Electron Microscopy
CTF	Contrast Transfer Function
CV	Column Volume
CTNS	Cystinosin
DDM	n-Dodecyl-β-D-Maltoside
DMEM	Dulbecco's Modified Eagle Medium
DNA	Deoxyribonucleic acid
ELISA	Enzyme-Linked Immunosorbent Assay
FSEC	Fluorescence-Detection Size-Exclusion Chromatography
FT	Flow-Through
GDN	Glyco-Diosgenin
GFP	Green Fluorescent Protein
GSH	Glutathione
HBS	Hepes-Buffered Saline
HEK	Human Embryonic Kidney
HRP	Horseradish Peroxidase

IgG	Immunoglobulin-γ
IP	Immunoprecipitation
IPTG	Isopropyl-β-D-thiogalactopyranoside
KD	Knockdown
KO	Knockout
qPCR	quantitative Polymerase Chain Reaction
LMNG	Lauryl Maltose Neopentyl Glycol
LD or LumD	Luminal Domain
mRNA	messenger Ribonucleic Acid
mTOR	mammalian Target of Rapamycin
nano-DSF	Nano Differential Scanning Fluorimetry
NHS	N-hydroxysuccinimide
Ni-NTA	Nickel Nitrilotriacetic Acid
Nb	Nanobody
NHS	N-Hydroxysuccinimide
PBS	Phosphate-Buffered Saline
PCR	Polymerase Chain Reaction
PDB	Protein Data Bank
PEI	Polyethylenimine
PFA	Paraformaldehyde
PIP	Phosphatidylinositol
PPI	Protease and Phosphatase Inhibitors
PVDF	Polyvinylidene Fluoride
RMSD	Root-Mean-Square Deviation
RT	Room Temperature
SA	Streptavidin
SD	Standard Deviation
SDS-PAGE	Sodium Dodecyl Sulfate-Polyacrylamide Gel Electrophoresis
SEC	Size-Exclusion Chromatography

SEM	Standard Error of the Mean
SF	Selectivity Filter
SIM	Structured Illumination Microscopy
SLC	Solute Carrier
STED	Stimulated Emission Depletion
STORM	Stochastic Optical Reconstruction Microscopy
Syb	Synthetic Nanobody
TB	Terrific Broth
TEVC	Two-Electrode Voltage Clamp
TFEB	Transcription Factor EB
$\mathbf{T}_m$	Melting Temperature
TMH	Transmembrane Helices
TMD	Transmembrane Domain
TRP	Transient Receptor Potential
TRPML1	Transient Receptor Potential Mucolipin 1
WT	Wild-type

1 | Introduction

1.1 Role of the Lysosome in the Cell

1.1.1 Roles of Lysosomes in Maintaining Cellular Homeostasis

Cells maintain a constant internal environment to survive. This is known as cellular homeostasis, which depends on the regulation of signaling pathways and nutrient levels. Lysosomes are membrane-bound organelles that act as the main site for biomolecule recycling (Figure 1). As a result, they have evolved to become a sensor and regulator of nutrient and energy levels in the cell to preserve cellular homeostasis. Biomolecule recycling in lysosomes is undertaken by more than 60 hydrolases, which digest proteins, peptides, nucleotides, polysaccharides, and lipids (Xu and Ren, 2015). Signaling proteins and membrane proteins at the lysosomal membrane act at the interface of the lysosome and cytosolic environment. They regulate: nutrient levels through nutrient transport (e.g. CTNS), key ionic gradients through ion permeability (e.g. TRPML1), cellular signaling by mediating the release of second messengers (e.g. TRPML1) and complex assembly, and gene expression (e.g. TFEB) based on the state of these two environments, shifting the cell between anabolic and catabolic states to maintain homeostasis (Xu and Ren, 2015). The mechanisms of many lysosomal membrane proteins remain poorly characterized.

Cellular homeostasis is disrupted under changing conditions and stress, for example during starvation or in diseases. Lysosomes play a key role in enabling the cell to adapt to starvation and pathological states. If lysosomes are damaged in pathological states (e.g. infections), cathepsins are released and cleave proapoptotic proteins, triggering lysosome-dependent cell death (de Castro et al., 2016). Therefore, lysosomes may also act to induce cell death if homeostasis cannot be maintained (Aits and Jäättelä, 2013; Repnik et al., 2012; Berghe et al., 2010). In Lysosomal Storage Disorders (LSDs), the functions of a lysosomal protein are disrupted and lysosomal homeostasis is lost, causing severe phenotypes (Platt et al., 2018). For example, cystinosin, the lysosomal cystine transporter, is mutated in the LSD cystinosis (Town et al., 1998). In this

thesis, I aimed to investigate its mechanism of transport to understand how cystinosis-causing mutations disrupt it. LSDs demonstrate the essential role of lysosomes in preserving cellular homeostasis. Loss of lysosomal homeostasis has been implicated in a range of other diseases, including neurodegeneration and cancer (Cao et al., 2021). Fundamental questions remain to be answered in lysosomal biology to understand how lysosomes are implicated in these diseases. Advances in this research field have been hampered by the lack of specific tools. Therefore, in this thesis, I set out to generate versatile synthetic nanobody tools to investigate the mechanisms and localization of the lysosomal ion channel TRPML1, and its potential role in diseases. My work focused on the ion channel TRPML1 due to its essential role in preserving lysosomal homeostasis and because it is being widely investigated for the treatment of neurodegenerative diseases (Santoni et al., 2020).

Both cystinosin (transporter) and TRPML1 (ion channel) play an essential role in lysosome formation and function as illustrated below.

1.1.2 Lysosomal Life Cycle

1.1.2.1 Vesicle and Endosome Formation

Substrates for the lysosomal enzymes are provided through two main pathways: endo/phagocytosis starting at the cell membrane or autophagy of molecules within the cell (Figure 1) (Saftig and Klumperman, 2009). Autophagy is a process in which double-membrane structures called autophagosomes sequester damaged organelles or protein aggregates, and fuse with endosomes and lysosomes to form autolysosomes that digest the sequestered biomolecules (Liou et al., 1997; Mizushima et al., 2001; Yamamoto et al., 1998). Endo/phagocytosis is a process that begins at the cell membrane, where primary endocytic vesicles are formed and fuse to form early endosomes that mature to become late endosomes (Futter et al., 1996; Rink et al., 2005; Stoorvogel et al., 1991). Vesicles are formed through intracellular signaling, triggering AP2-clathrin-dependent and independent pathways (Schmid et al., 2014). TRPML1 is involved in both processes as it regulates protein recruitment for autophagic vesicle biogenesis and it mediates lipid delivery to the plasma membrane for the formation of phagosomes

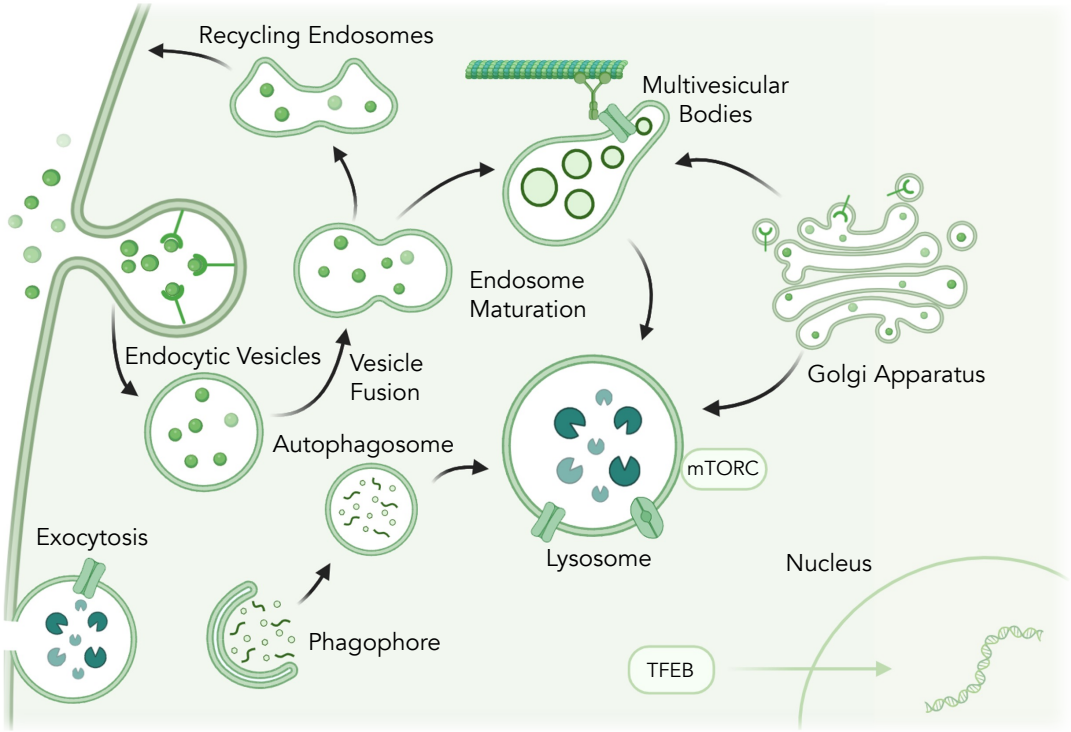

Figure 1: Lysosome functions and biogenesis in cells. Substrates are delivered to lysosomes through two main pathways: endocytosis that results from internalization of substrates at the plasma membrane and phagocytosis which occurs when intracellular substrates targeted for degradation are engulfed by autophagosomes. Endocytic vesicles fuse to form early endosomes, which mature into late endosomes that fuse with lysosomes to deliver their cargo. Late endosome maturation requires TRPML1 calcium currents, regulating the assembly of trafficking and membrane fusion complexes, and the sequestering of lysosomal substrates into multivesicular bodies. Autophagosome biogenesis and maturation are also TRPML1 regulated processes. TRPML1 is involved in phosphatidylinositol 3-phosphate production for the recruitment of proteins at the phagophores which enable autophagosome formation. Once the substrates are delivered to the lysosomes, they are degraded by hydrolytic enzymes and the ions and nutrients that are produced are released into the cytosol by ion channels like TRPML1 and transporters like cystinosin. Digested substrates can also be released through lysosomal exocytosis, which results from TRPML1 calcium release in lysosomes localized to the plasma membrane. The lysosome has a range of other functions, including the regulation of cell signaling through mTORC1 and transcriptional regulation through TFEB, which are both regulated by TRPML1. The Golgi apparatus delivers lysosomal proteins to lysosomes, enabling them to preserve their molecular compositions.

(Samie et al., 2013; Rosato et al., 2019). Following their formation, endosomes will fuse to form Rab5-containing sorting endosomes, which can mature into lysosomes or target substrates to Rab11-containing recycling endosomes (Campa et al., 2018; Stoorvogel et al., 1991; Ullrich et al., 1996). Rabs are GTP-binding proteins involved in membrane transport throughout endosomal maturation (Zerial and McBride, 2001).

1.1.2.2 Endosome Maturation

Once cargo reaches the endosomal membrane, it can return to the plasma membrane (recycling endosomes) or it can be trafficked to late endosomes (Figure 1) (Grant and Donaldson, 2009; Luzio et al., 2009). Endosomes are composed of tubular regions and vesicular regions, which are targeted for endosomal degradation (Driskell et al., 2007; Huotari and Helenius, 2011; Mellman, 1996; Sönnichsen et al., 2000). Early endosomes can fuse with late endosomes to deliver protein targeted for degradation (Gruenberg and Stenmark, 2004).

Endosome maturation is a process that requires Rab conversion, with a switch from Rab5 to Rab7 activity at the membrane (Poteryaev et al., 2010; Rink et al., 2005; Russell et al., 2012). Endosome maturation also occurs through the trafficking of hydrolases by the mannose-6-phosphate receptors, and the trafficking of proteins involved in endosomal acidification (V-ATPase) and functions from the golgi apparatus by trafficking receptors like cystinosin (Lafourcade et al., 2008; Lie et al., 2021; Pillay et al., 2002; Rink et al., 2005; Zhang et al., 2017). Biochemical maturation is typically coupled with endosomal trafficking and fusion (Rink et al., 2005). For example in neurons, TRPML1 calcium release regulates the trafficking of maturing late endosomes across axons (Lie et al., 2022; Maday et al., 2012). Late endosomes are characterized by the organization of substrates into multivesicular bodies that enable the sorting of cargo for degradation in lysosomes (Futter et al., 1996).

Substrates from the late endosomes are delivered to lysosomal enzymes through 'kiss-and-run' late-endosome-lysosome interactions or through a late-endosome-lysosome fusion to form an endolysosome (Bright et al., 2005; Futter et al., 1996; Mullock et al., 1998). Fusion is driven by multi-protein complexes bridged by the HOPS tethering complex (Schleinitz et al., 2023).

1.1.2.3 Lysosome Life Cycle

Lysosomal functions and homeostasis require positioning through trafficking (Matteoni and Kreis, 1987). Lysosomes are trafficked on microtubules through kinesins (anterograde) and dynein (retrograde) motors (Harada et al., 1998; Hofmann and Munro 2006; Pu et al., 2016; Rosa-Ferreira and Munro, 2011). Dynein recruitment at the lysosomal membrane is TRPML1-regulated through the lysosomal calcium sensor ALG-2 (Li et al., 2016).

Most lysosomal functions are undertaken through fusion events. Fusion events can be homotypic, the fusion of lysosomes, or heterotypic, which are fusions with late endosomes, autophagosomes, phagosomes and macropinosomes delivering their substrates to lysosomal enzymes (Antonin et al., 2000; Luzio et al., 2007; Hesketh et al., 2018). Lysosome fusions are regulated by calcium-mediated SNARE complex assembly, including proteins of the syntaxin, VAMP and SNAP families, small GTPases, tethering factors and autophagosome docking proteins (Luzio et al., 2007). Lysosomal substrates are delivered through late endosome-lysosome and autophagosome-lysosome fusions (Zhao and Zhang, 2019). Autolysosome formation has been suggested to be regulated by TRPML1, but the mechanism remains to be determined (Venkatachalam et al., 2015; Vergarajauregui et al., 2008).

Once substrates have been delivered and digested, transporters, like cystinosin, are essential for nutrient efflux to the cytosol (Rudnik and Damme, 2020). Degradation products can also be released by calcium-regulated (TRPML1) lysosome-plasma membrane fusions, a process called lysosomal exocytosis (Medina et al., 2011; Tsunemi et al., 2019). Following substrate digestion, lysosomes can reform from existing lysosomes by fission (Saffi and Botelho, 2019; Krajcovic et al., 2013). This can occur through a poorly understood process called lysosomal tubulation, which is also be regulated by TRPML1 (Levin-Konigsberg et al., 2019; Li et al., 2016; Saffi and Botelho, 2019).

1.1.3 Lysosome Composition and Homeostasis

Each mammalian cell can have approximately 50 to 1,000 lysosomes with a diameter of 100-500 nm (Mellman, 1989; Valm et al., 2017; Ballabio and Bonifacino, 2020). The composition and resulting functions of these lysosomes are dependent on cell type, localization, and conditions, but the key components are conserved across different lysosomal populations (Figure 2) (Akter et al., 2023; Bond et al., 2024; Yu et al., 2024). The lysosomal lumen has an acidic pH (pH $\approx$ 4.6) that is maintained by V-ATPase (Mellman, 1989). The acidic pH is required for the activity of the 60 hydrolases (proteases, lipases, phosphatases, nucleases, glycosidases and sulfatases) in the lysosomal lumen, and the proton-coupled transporters at the membrane, including cystinosin (Xu and Ren, 2015). Sodium (20-140 mM), calcium (0.5 mM), chloride (70-120 mM), iron and zinc concentrations are higher in the lysosomal lumen than in the cytosol, while potassium concentration (2-50 mM) is lower in the lysosomal lumen than in the cytosol (Xu and Ren, 2015). These concentration gradients, along with the -20 to -40 mV membrane potential, drive TRPML1 cation efflux out of the lysosome (Xu and Ren, 2015). This activity is regulated by the lipids of the lysosomal membrane, composed notably of sphingomyelin, bis(monoacylglycero)phosphate and PI(3,5)P_2 (Akgoc et al., 2015; Kobayashi et al., 1998; Lees et al., 2020). Proteins and lipids are shielded from hydrolases by their glycans (Kosicek et al., 2018). The lysosomal glycocalyx layer arises from proteoglycans, notably lamp-1 and 2 which account for 50% of the lysosomal membrane protein content (Eskelinen, 2006).

1.1.4 Regulation of Cell Signaling at the Lysosomal Membrane

Cell signaling is the transmission of messages between and within cells. Lysosomes act as important regulators of cell signaling (Figure 3).

Lysosomes are a key site for the regulation of mTORC1 activity, which regulates cellular growth and metabolic state based on nutrient levels (Saxton and Sabatini, 2017). Specifically, it promotes growth and anabolism in the cell, and inhibits catabolism at the lysosomal membrane in response to elevated amino acid or cholesterol concentrations (Castellano et al., 2017; Kim and

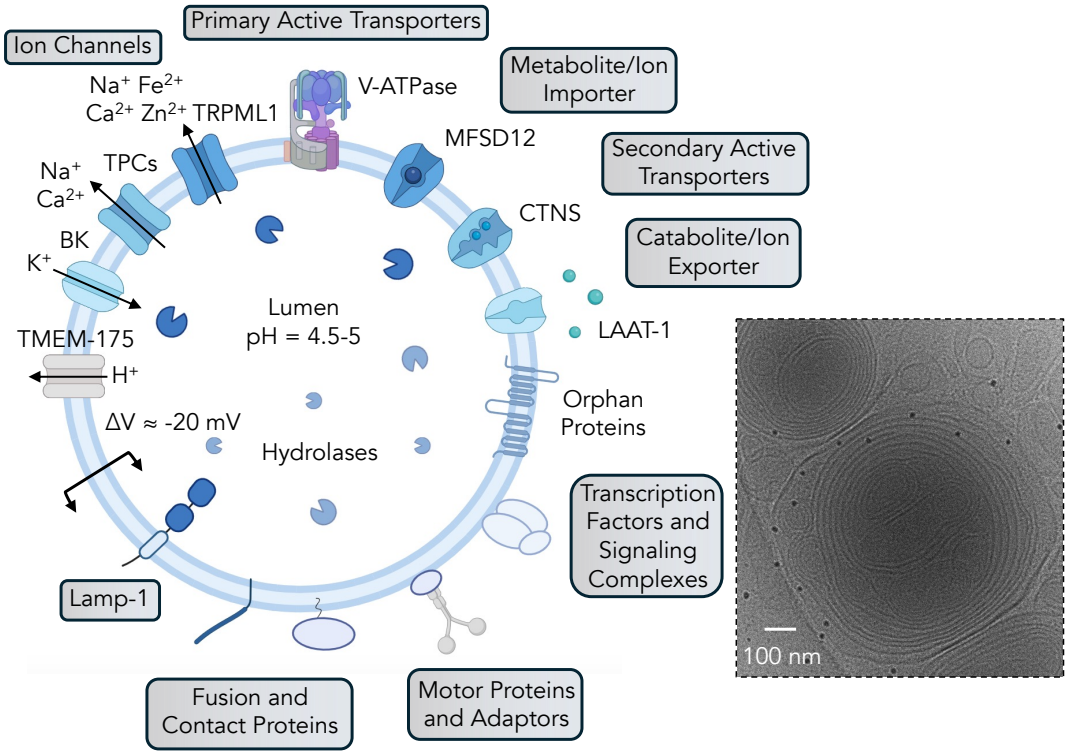

Figure 2: Composition of the lysosomal lumen and membrane. The lysosomal lumen is composed of more than 60 different hydrolases, which are specifically active in the acidic environment of the lysosome that is maintained by V-ATPases. The degradative products produced as a result of enzyme degradation are released by transporters that transport their substrates to the cytosol along the concentration gradient or potentially couple the transport process to an ion gradient (secondary active transporters). Some transporters act in the reverse direction to import ions (e.g. TMEM-165) into the lysosome, preserving the concentration gradients that are essential for lysosomal function. The lysosomal membrane potential is kept constant at approximately -20 mV by lysosomal ion channels. These ion channels display variable selectivity, and this selectivity can be altered by the environment in the lysosome. LAMP-1 is the most abundant protein at the lysosomal membrane and it forms the lysosomal glycocalyx. Additional membrane proteins or membrane-associated proteins are involved in membrane fusion, transport or cell signaling and transcriptional regulation. Many membrane proteins at the lysosomal membrane have no know function. On the right is displayed a micrograph of a lysosome, which illustrates the complexity of a real lysosome (multi-membrane layers). Micrograph kindly provided by Dr. José Juan de Jesús-Pérez.

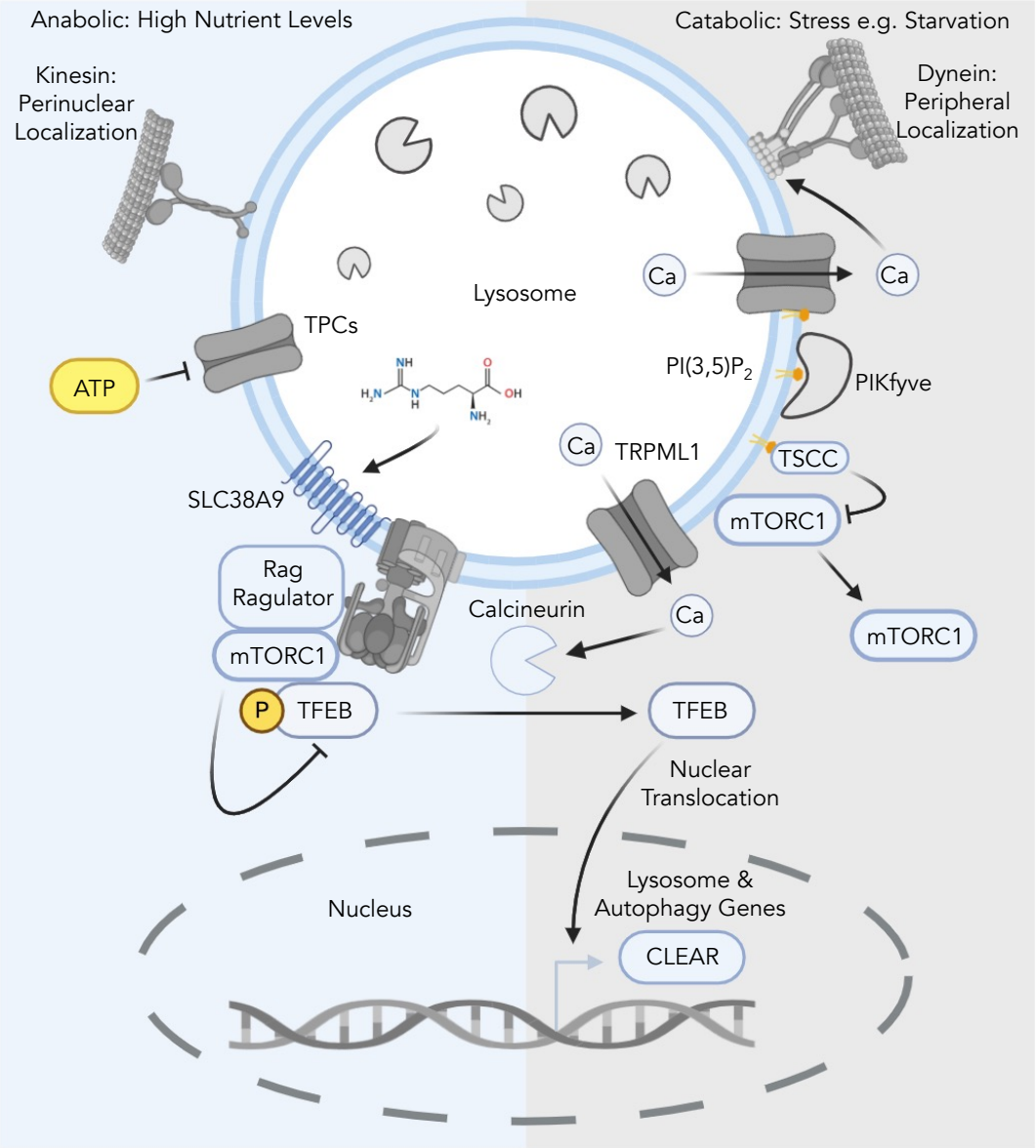

Figure 3: Signaling at the lysosomal membrane. Lysosomal signaling is regulated by nutrient levels in the cell and in the lysosomal lumen as it is one of the main sites of nutrient storage in cells. When nutrient levels are high, the cell is in an anabolic state, and high levels of ATP and amino acids inhibit lysosomal regulation of signaling. For example, high levels of ATP inhibit TPCs via mTORC1 which regulate a range of cellular processes such as cell differentiation (Webb et al., 2020). High arginine levels in the lysosomal lumen activate SLC38A9 which transports lysosomal amino acids to the cytosol, resulting in the activation of mTORC1 (Wyant et al., 2018). mTORC1 inhibits TFEB, which regulates expression of genes required for autophagy and lysosomal biogenesis, and upregulates cellular metabolism and growth. However, when nutrient levels are low, the cell transitions to a catabolic state in which high lysosomal activity is favored. TRPML1 mediated calcium efflux activates TFEB through calcineurin, leading to the expression of lysosomal genes, and the recruitment of dynein for the trafficking of lysosomal. mTORC1 is activity is downregulated by TSCC, which is recruited to the lysosomal membrane by $PI(3,5)P_2$.

Guan, 2015; Sancak et al., 2010). mTORC1 and TFEB have antagonizing functions in the regulation of autophagy and lysosome biogenesis. TFEB is a transcription factor that acts as a master regulator of lysosome and autophagosome biogenesis (Peña-Llopis et al., 2011; Sardiello et al., 2009; Settembre et al., 2011), while mTORC1 inhibits lysosome formation and autophagy (Kim et al., 2011; Martina et al., 2012; Yu et al., 2010). mTORC1 and TFEB form a supercomplex at the lysosomal membrane with the rag-ragulator-V-ATPase complex (Cui et al., 2023; Petit et al., 2013; Zoncu et al., 2011).

As a response to increases in lysosomal amino acid levels, mTORC1 is activated at the lysosomal membrane and phosphorylates TFEB, favoring its association with the 14-3-3 protein and retention in the cytosol (Napolitano et al., 2018; Roczniak-Ferguson et al., 2012; Settembre et al., 2012). Upon starvation or stress, mTORC1 is inhibited and TFEB is dephosphorylated by TRPML1-activated calcineurin, resulting in its translocation to the nucleus to induce the expression genes with the CLEAR regulatory motif (Medina et al., 2015; Napolitano et al., 2018; Palmieri et al., 2011; Papadopoulos et al., 2017; Sardiello et al., 2009; Settembre et al., 2012). This leads to the expression of genes involved in autophagosome biogenesis and fusion, and lysosomal activity (ion concentration, pH, localization and exocytosis) (Medina et al., 2011; Settembre et al., 2011; Palmieri et al., 2011; Willett et al., 2017).

1.2 The Roles of Ion Channels and Transporters in Lysosomes

1.2.1 Lysosomal Membrane Proteins

More than 700 lysosomal membrane proteins have been identified (Akter et al., 2023; Chapel et al., 2013; Rudnik and Damme, 2021). Many have no known function or remain poorly characterized (Akter et al., 2023; Chapel et al., 2013). Functions have previously been identified based on the phenotype observed in lysosomal storage disorders (Attard et al., 1999; Dong et al., 2008). In recent years, functions have been assigned based on genetic screens (Pechincha

et al., 2022; Zajac et al., 2024). The lack of tools to study these proteins remains a barrier to determining their functions (Nelson et al., 2017).

Despite these challenges, some key lysosomal membrane proteins have been identified and their functions have been characterized. These proteins act as ion channels, transporters, pumps, chaperones, enzymes, and signaling proteins/receptors (Figure 2) (Chapel et al., 2013; Rudnik and Damme, 2021).

1.2.2 Lysosomal Ion Channels and Ion Homeostasis

Ion homeostasis at the lysosomal membrane is maintained by endo-lysosomal channels. Their activity is regulated by modulators (e.g. lipids and protons) present specifically at the lysosomal membrane, which ensures that they are only active once they have reached the lysosome (Dong et al., 2010). Some channels have also been found to change selectivity depending on the modulators they are bound to (Yuan et al., 2022). It remains challenging to study the properties of lysosomal channels in their native environment. Most channels have been characterized by lyso-patch in which lysosomes are enlarged and isolated from the cell for recordings (Chen et al., 2017; Festa et al., 2022). Activity can be measured in intact lysosomes using ion reporters (Minckley et al., 2019; Shen et al., 2012; Zajac et al., 2024). Some key lysosomal channels and transporters have identified and characterized using these methods.

The membrane potential ($\approx$ -20 mV) at the lysosomal membrane is generated mostly by the potassium, proton, chloride, sodium, calcium, iron and zinc gradients (Xu and Ren, 2015). Calcium release from the lysosome has been extensively shown to be mostly mediated by TRPML1 using a combination of techniques (Dong et al., 2010; Shen et al., 2012). TPCs maintain sodium homeostasis (Wang et al., 2012). Potassium homeostasis is maintained by BK and potentially TMEM-175, which also preserves proton homeostasis in lysosomes (Cang et al., 2015; Hu et al., 2022; Zhang et al., 2023). Chloride and anion homeostasis is preserved by LRRC8 (Li et al., 2020). Pumps and transporters also preserve ion homeostasis at the lysosomal membrane. For example, the proton gradient across the membrane is mostly maintained by the V-ATPase pump and chloride homeostasis is maintained by the exchangers of the CLC family (Graves et

al., 2008; Mellman, 1989; Zhang et al., 2023).

1.2.3 Lysosomal Transporters and Nutrient Homeostasis

Lysosomal transporters are required to export the nutrients that are generated from biomolecule degradation in lysosomes. These transporters frequently couple nutrient and ion movement (secondary active transporters), making their characterization possible using electrophysiology (Jézégou et al., 2012; Jungnickel et al., 2024; Ruivo et al., 2012). However, many lysosomal transporters have been de-orphanised in the last decade as the identification of their substrates has required novel methods (Jungnickel et al., 2024; Laqtom et al., 2022; Scharenberg et al., 2023; Zajac et al., 2024).

Sugar, lipid, cofactor, amino acid and peptide transporters have been identified (Rudnik and Damme, 2021). Cystinosin (cystine), PQLC2 (cationic amino acids), PAT1 (small neutral amino acids), SNAT7 (uncharged polar amino acids) PHT1 (histidine), SLC38A9 (glutamine and arginine), and peptide transporters (MFSD1 and PHTs) have all been found to localize at the lysosomal membrane (Bhardwaj et al., 2006; Boytsov et al., 2024; Pisoni et al., 1985; Sagné et al., 2001; Scalise et al., 2019; Thamotharan et al., 1997; Verdon et al., 2017; Yamashita et al., 1997; Zhou et al., 2000). The anionic monosaccharide transporter sialin and hexose transporter GLUT8 have been identified for sugar transport, NPC1-2 for unesterified cholesterol transport, ENT3 for nucleoside transport and ABCD4 for vitamin B12 transport (Diril et al., 2009; Havelaar et al., 1998; Infante et al., 2008; Kashiwayama et al., 2009; Xu et al., 2019). These transporters are typically involved in the export of the substrates out of the lysosome into the cytosol but some transporters, such as TAPL, transport substrates to the lysosomal lumen for degradation (Park et al., 2022; Saint-Pol et al., 1999). To avoid the build-up of substrates within the lysosome, lysosomal transporters couple nutrient and ion movement (secondary active transport). Sodium and proton ions form key gradients utilized by lysosomal transporters (Lei et al., 2018; Ruivo et al., 2012). While most identified transporters are involved in nutrient export, some solely act to preserve ion homeostasis, such as the CLCs and TMEM-165 (Schrecker et al., 2020; Zajac et al., 2024).

	Protein	Function	Disorder	References
Transporter	CLC7	$2Cl^-$ / $1H^+$ antiporter	Malignant infantile osteopetrosis	Kornak et al 2001
	CLN3	Unknown	Juvenile neuronal ceroid lipofuscinosis	Lerner et al 1995
	CTNS	H^+ / Cystine symporter	Cystinosis	Town et al 1998
	ENT3	Nucleosides	Histiocytosis	Hsu et al 2011
	HGSNAT	Acetyl transfer to heparan sulfate	Mucopolysaccharidosis type IIIC	Fan et al 2006
	LAAT-1	Export of cationic amino acids	Target for cystinosis cysteamine treatment	Liu et al 2012
	LMBRD1	Export of cobalamin	Cobalamin F-type disease	Rutsch et al 2009
	NPC1	Cholesterol transport	Niemann-Pick type C	Carstea et al 1997
	Sialin	Export of sialic acid	Salla disease	Verheijen et al 1999
Ion Channel	BK	K^+	Neurological disorders	Dong et al 2022
	CLN7	Cl^-	Late infantile neuronal ceroid lipofuscinosis	Wang et al 2021
	P2X4	Na^+, Ca^{2+}	Inflammatory disorders	Peikert et al 2022
	TMEM-175	K^+, H^+	Parkinson's disease	Hu et al 2022
	TPC1-2	Na^+, Ca^{2+}	Viral infection and cancer	Nguyen et al 2017; Sakurai et al 2015
	TRPML1	Ca^{2+}, Fe^{2+}, Zn^{2+}, Na^+	Mucolipidosis Type IV	Sun et al 2000

Table 1: Summary of key lyososomal transporters and ion channels implicated in diseases. Inofrmation from Schwake et al (2013) and Li et al (2018): see for references.

The mechanisms and the effects of disease mutations in many lysosomal transporters remain to be characterized. In recent years, mechanistic information about these transporters has been obtained by combining cryo-EM, and biophysical and biochemical methods (Park et al., 2022; Schmiege et al., 2024). Here, the mechanism of the human cystine transporter, cystinosin, is characterized using electrophysiology.

1.2.4 Lysosomal Membrane Proteins in Diseases

The importance of ion and nutrient movement in preserving lysosomal and cellular homeostasis is demonstrated by the different lysosomal storage disorders that can arise from mutations in the lysosomal transporters (Table 1). Disruptions in nutrient transport can cause cystinosis, free sialic acid storage disease, H syndrome, Niemann-Pick Disease type C1, Cobalamin F Disease and ceroid lipofuscinosis neuronal diseases (Huizing and Gahl, 2020). Loss of ion homeostasis causes mucolipidosis type IV and osteopetrosis (Huizing and Gahl, 2020). Gene therapy has been the main therapy trialed for the treatment of these diseases (Sevin and Deiva, 2021). Many identified transporters and ion channels have not been involved in lysosomal storage disorders, potentially due to redundancy (compensation) or lack of it (lethal).

Lysosomal proteins are therapeutic targets of interest because lysosomes can be involved in the early stages of diseases, such as neurodegeneration. Both TRPML1 and TMEM-175 modulators are being investigated for the treatment of neurodegenerative diseases (Merck) (Hu et al., 2022; Somogyi et al., 2023). TRPML1 has also been implicated in cancer due to its role in cell migration, ferroptosis and cell signaling (Fan et al., 2024; Frey et al., 2024; Jung et al., 2019).

1.3 TRPML1 Function and Structure

1.3.1 Lysosomal Calcium

Knocking-out the main lysosomal calcium channel, TRPML1, is lethal in mice and biomolecule accumulation in lysosomes caused by lysosomal gene mutations can typically be corrected by

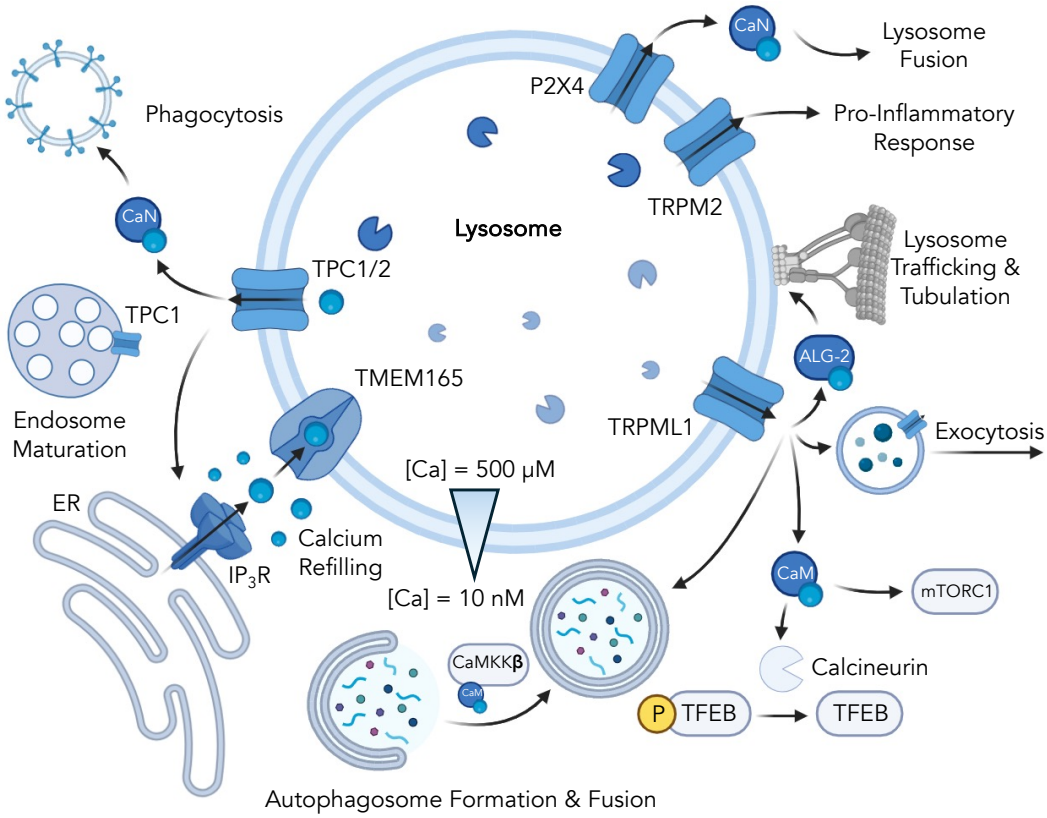

Figure 4: Functions of TRPML1 and other lysosomal calcium channels. Lysosomes are a key site for the storage of cellular calcium, with a concentration 5000-fold greater than in the cytosol. Lysosomal calcium is replenished by ER calcium stores, potentially through the transporter TMEM-165. There are very few known effectors for lysosomal calcium functions. The three main effectors are calmodulin (CaM), calcineurin (CaN) and Apoptosis-linked gene 2 (ALG-2) calcium binding protein. At the lysosomal membrane, TRPML1 calcium regulates lysosomal trafficking through ALG-2-dynein, and stimulates: phagophore formation directly or through calmodulin, TFEB activity through CaN, mTORC1 activity and lysosomal exocytosis. Other calcium-permeable channels have important functions at the lysosomal membrane, including P2X4 that promotes lysosomal membrane fusion through calmodulin, TRPM2 which is involved in regulating inflammation and TPC which regulates phagocytosis through CaN.

TFEB overexpression, except upon the loss of lysosomal calcium homeostasis (TRPML1 mutations) (Medina et al., 2011; Venugopal et al., 2007). These results demonstrate the essential role of lysosomal calcium in maintaining lysosomal and cellular homeostasis (Figure 4).

Lysosomes are a key site of calcium storage in the cell. Calcium concentration is 500 μM in the lysosomal lumen compared to 100 nM in the cytosol, generating an electrochemical gradient across the lysosomal membrane (Christensen et al., 2002). Stores are replenished from calcium in the endoplasmic reticulum, where concentrations are up to 1 mM, and through the transport of calcium into the lysosome by transporters, including TMEM-165 (Berridge et al., 2003; Garrity et al., 2016; Zajac et al., 2024).

Multiple lysosomal calcium channels have been identified to regulate calcium efflux, including TRPML1, P2X4, TPC1, TPC2, TRPA1, TRPM2, P/Q Type Voltage-Gated Ca2+ Channels (VGCCs) and TMEM-63 (Calcraft et al., 2009; Huang et al., 2014; Lange et al., 2009; Li et al., 2024; Shang et al., 2016; Tian et al., 2015). TRPML1 is the main inward rectifying calcium channel at the lysosomal membrane and is ubiquitously expressed (Dong et al., 2010). Therefore, it is involved in most functions associated with lysosomal calcium (Di Paola et al., 2018). Other lysosomal calcium channels have been identified to function in specific organelles (EE, LE and/or lysosomes), cell types or conditions (Cao et al., 2015; Gerndt et al., 2020; Huang et al., 2014; Lange et al., 2009; Sumoza-Toledo et al., 2011; Yuan et al., 2022). Upon release of calcium, these channels form segregated nanodomains within a confined radius that enable activation of distinct effectors within their vicinity (Davis et al., 2023). Some of these effectors include calmodulin, synaptotagmin VII, ALG-2, and calcineurin (Czibener et al., 2006; Li et al., 2016 Medina et al., 2015; Vergarajauregui et al., 2009).

Lysosomal calcium is involved in the regulation of most of the processes essential to maintain lysosomal homeostasis, including lysosomal biogenesis, activity, trafficking, fusion, repair, fission, exocytosis, repair and signaling (Di Paola et al., 2018; Li et al., 2013; Lloyd-Evans and Waller-Evans, 2020; Luzio et al., 2007; Reddy et al., 2001; Skowyra et al., 2018). These processes are involved in muscle repair, vascular muscle contraction, and cell migration (Frey et al., 2024; Sun et al., 2022; Thakore et al., 2020; Yu et al., 2020).

1.3.2 TRPML1 Functions

TRPML1, also known as mucolipin-1, was initially discovered as the gene that causes the lysosomal storage disorder mucolipidosis type IV (Slaugenhaupt et al., 1999; Sun et al., 2000). This autosomal recessive disorder is commonly caused by loss of function mutations (Bargal et al., 2000; Bassi et al., 2000). Mucolipidosis type IV is characterized by kidney failure, achlorhydria, retinal degeneration, motor deficits, intellectual disabilities, and a shortened lifespan (Berman et al., 1974; Boudewyn and Walkley, 2019). Mucolipidosis type IV patients display enlarged lysosomes due to the accumulation of lipids, which suggested that TRPML1 has a role in lipid trafficking or membrane fusions in lysosomes (Chen et al., 1998). TRPML1 was confirmed to localize to the lysosomal membrane and was identified to function as an ion channel by lysopatching (Dong et al., 2008; Dong et al., 2009; Miedel et al., 2006). Dong et al (2010) showed that TRPML1 conducts calcium ions at the lysosomal membrane, where it acts as an inward-rectifying non-selective calcium-permeable cation channel regulated by PIP lipids (Shen et al., 2012). PI(3,5)P_2 at the lysosomal membrane activates TRPML1, while PI(4,5)P_2 at the plasma membrane inhibits it (Dong et al., 2010). TRPML1 has also been shown to conduct other ions, such as zinc (Du et al., 2021; Minckley et al., 2019).

The TRPML subfamily of the TRP family of channels is also comprised of TRPML2 and 3, which share high sequence identity with TRPML1 (TRPML1 and 2: 48.56%; TRPML1 and 3: 56.08%) (Venkatachalam et al., 2015). TRPML2 is found throughout the endo-lysosomal pathway of immune cells and TRPML3 localizes to autophagosomes and the endo-lysosomal pathway in the urinary tract and respiratory system (Fine et al., 2018; Kondratskyi et al., 2018; Miao et al., 2015; Plesch et al., 2018; Spix et al., 2022; Sun et al., 2015).

Calcium efflux by TRPML1 is important in the regulation of cell signaling, lysosome formation, trafficking, exocytosis, tubulation and fusion, which together promote autophagy and lysosome activity as detailed above (Figure 4) (Li et al., 2016a; Li et al. 2016b; Medina et al., 2011; Medina et al., 2015; Samie et al., 2013; Rosato et al., 2019; Shen et al., 2012; Vergarajauregui et al., 2008; Wang et al., 2015).

Most of these functions have only been recently identified and the mechanisms of action of TRPML1 remain to be determined. Moreover, while most lysosomal calcium functions have been attributed to TRPML1, the role of the different lysosomal calcium channels remains to be determined (Davis et al., 2023; Morgan et al., 2021). To develop our understanding of TRPML1 function in the cell, novel tools are required.

1.3.3 TRPML1 Structure

Multiple structures of TRPML1 have been obtained by cryo-EM in the open and closed states (Schmiege et al., 2017). These structures have been obtained in different conditions (pH), in the presence of different ligands (PIP lipids, and activators and inhibitors), detergents/nanodiscs, or were obtained with different homologs (Chen et al., 2017; Fine et al., 2018; Gan et al., 2022; Schmiege et al., 2017; Schmiege et al., 2021; Zhang et al., 2017).

In these structures, TRPML1 tetramers are composed of subunits with 6-TM helices (S1-S6), two pore helices, a large luminal linker domain between S1 and S2, and cytosolic N and C-terminal regions with lysosomal targeting motifs (Figure 5A-C) (Schmiege et al., 2017). Pore Helices 1 and 2 (PH1 and 2), which include the conserved sequence GDD, make up the selectivity filter (Schmiege et al., 2017). The lower gate constriction is generated by the side chains of I514 and T518 on the S6 helix (Figure 5D) (Schmiege et al., 2017). This permeation pathway enables the movement monovalent and divalent cations (Dong et al., 2008). S1-S4 helices from one subunit form a bundle that supports the luminal domain and forms contacts with the S5-S6 helices and PHs of the neighbouring subunit (domain swapping) (Figure 5B).

The luminal domain is connected to the transmembrane helices through the S1 and S2 helices. It is composed of 7 β-strands and an alpha helix (α3) (Figure 5E). These secondary structure elements are connected through a series of loop that form interactions with the loops of the neighbouring luminal domains (Figure 5E). It enables this region to accommodate conformational changes upon channel activation (Gan et al., 2022). These loops are not always observed and have elements of secondary structure in only some of the structures (e.g. β2 and β3) (Figure 5E). Two loops have been suggested to have a functional role, the luminal pore loop and

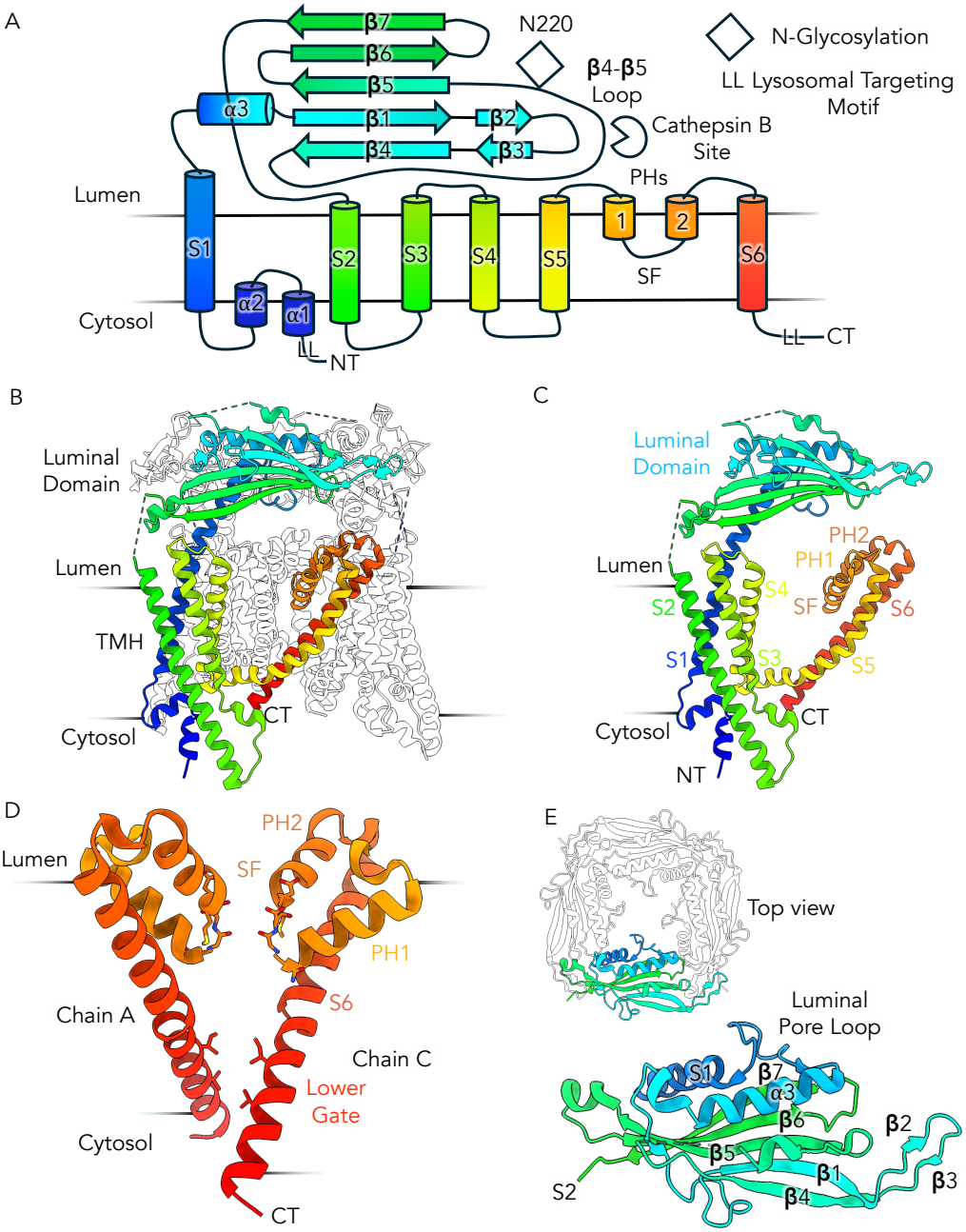

Figure 5: TRPML1 structure overview. A) Secondary structure of TRPML1. Cylinders represent α-helices and arrows represent **β**-strands. PHs: Pore Helices and SF: Selectivity Filter. Rainbow color coding is shared with the other panels. B and C) Structure of the tetrameric channel TRPML1 which contains two main regions, the TransMembrane Helices (TMHs) (S1-S6) and the Luminal Domains (LD). The S5-S6 region is domain swapped and interacts with the neighboring subunit. D) The pore helices, selectivity filter and S6 lower gate of TRPML1. Key constrictions points and selectivity filter side chains are shown. E) Luminal domain of TRPML1 from top view, which is located between S1 and S2 and contains, and contains the luminal pore loop. PDB 7SQ7.

the β4-β5 loop (Figure 5E). The luminal pore loop contains aspartate residues that have been suggested to be involved in the gating of the channel and the β4-β5 loop is cleaved for channel regulation (Kiselyov et al., 2005; Li et al., 2017). The luminal domains form contacts with the transmembrane regions through the S1 helix and the connecting loops of the transmembrane helices. These contacts couple conformational changes in the transmembrane regions to the luminal domain conformation (Gan et al., 2022).

1.3.4 Structural Basis for TRPML1 Activation

A range of TRPML1 agonists, inhibitors and endogenous modulators have been identified, including PIP lipids, ML-SA compounds (activators) and ML-SI compounds (inhibitors), and additional synthetic agonists (Dong et al., 2010; Schmiege et al., 2021; Shen et al., 2012). These modulators were identified using calcium reporters or electrophysiology (Dong et al., 2010; Shen et al., 2012). In the whole-cell patch configuration, TRPML1 is overexpressed and mislocalized to the plasma membrane, with its luminal domain facing the bath solution, by introducing mutations in the lysosomal targeting motif (Schmiege et al., 2017). This enables control of the luminal/bath solution and facilitates measurements. In these assays, TRPML1 displays an inward rectifying current at negative membrane potentials (Figure 6A-B). These inward rectifying currents are strongly enhanced by acidic pH, PI(3,5)P_2 lipids and synthetic agonist compounds (Figure 6A-B) (Fine et al., 2018).

PIP lipids are well-characterized modulators of TRPML1 activity (Dong et al., 2010). PI(3,5)P_2 and PI(4,5)P_2 bind to a positively charged patch on the cytosolic side of the extended helices of S1-S3 of TRPML1 (Figure 7A and D) (Fine et al., 2018). PI(4,5)P_2 inhibits TRPML1 while PI(3,5)P_2 activates it, but PI(3,5)P_2 binding alone does not lead to an open state of the channel (Fine et al., 2018; Gan et al., 2022). PI(3,5)P_2 has been suggested to favor channel activation through movements in the S4-S5 linker that were suggested not to occur in the PI(4,5)P_2-bound state (Fine et al., 2018). The suggested interaction driving this change was not observed in the higher-resolution structure of PI(3,5)P_2-bound mouse TRPML1 (Gan et al., 2022). Nevertheless, movement of the S4 helix and S4-S5 linker upon PI(3,5)P_2 binding is thought to allosterically ac-

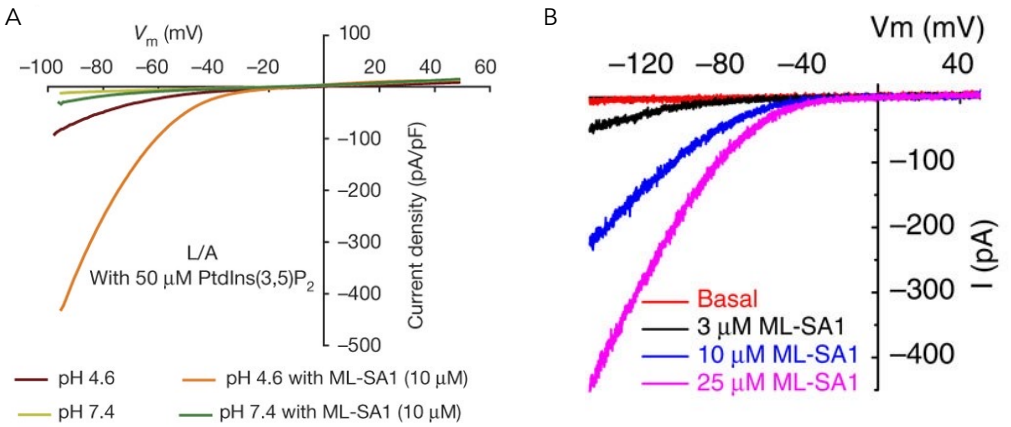

Figure 6: TRPML1 I-V curves. A) I-V curve from whole-cell patch clamp experiments on HEK293T cells transfected with the plasma-membrane mutant of TRPML1, TRPML1$^{LL/AA}$, with a mutation in the lysosomal targeting motif. Inward currents are enhanced by acidic pH, PI(3,5)P_2 binding and the addition of agonist (ML-SA1). Figure from Schmiege et al. 2017. B) Whole-endolysosome patch-clamp recordings on vacuoles from human fibroblasts. Inward-rectifying TRPML currents are measured upon the addition of ML-SA1 on the cytosolic side. Figure from Shen et al., 2012.

tivate the channel through the contact they form with the S6 helix. Additionally, binding induces small conformational changes in S1-S4, which propagate to neighbouring helices, favouring the opening of the lower gate (Fine et al., 2018; Gan et al., 2022). PI(4,5)P_2 inhibits the channel by competing with PI(3,5)P_2 binding and stabilizing the channel in a closed state by adopting a different binding pose, in which it stably binds at the entrance of the PIP-binding cavity (Gan et al., 2024). Sphingolipids have also been found to regulate channel activity by interacting at the ML-SA pocket and inhibiting activator binding (Gan et al., 2024). Lipids and synthetic agonists can display cooperative activation of TRPML1 because they bind to different sites of the channel and promote channel activation through different mechanisms (Fine et al., 2018; Gan et al., 2022).

Agonist-bound structures of TRPML1 have provided information on the mechanism of activation of the channel. ML-SA1-bound structures have shown that it activate the channel by binding to hydrophobic and aromatic residues in the pore helices, the S5 and S6 helix, and the S6 helix of a neighbouring monomer (Figure 7C) (Schmiege et al., 2017). The binding pocket is strongly conserved across the TRPML subfamily and ML-SA1-bound TRPML3 structures have also been obtained (Figure 7C) (Zhou et al., 2017). The binding of ML-SA1 induces confor-

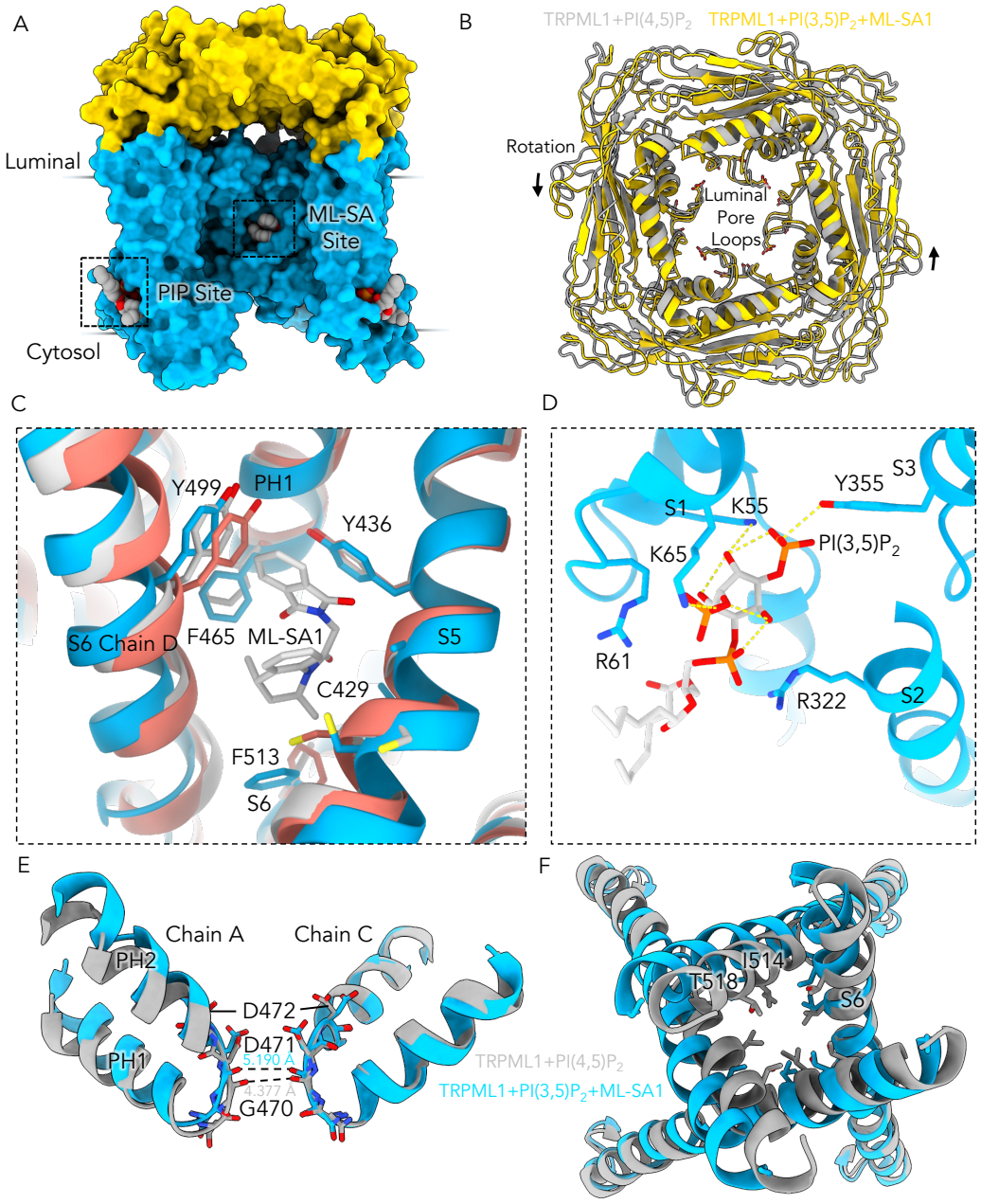

Figure 7: TRPML1 agonist and PIP binding site. Surface structure is 6E7Z, rotation is 6e7y and z. A) Surface representation of ML-SA1 and PI(3,5)P_2-bound TRPML1 structure (yellow: luminal domain; blue: transmembrane regions). PDB: 6E7Z. B) The luminal domain of TRPML1 rotates upon activation of the channel due to agonist binding. PDB: 6E7Y for PI(4,5)P_2-bound. C) The ML-SA1 (agonist) binding site is strongly conserved across TRPMLs (TRPML1 sky blue: 5WJ9; TRPML2 salmon: 7DYS; TRPML3 grey: 5W3S). D) The PIP binding site in TRPML1 is located in a positively charged patch on the cytosolic side of the transmembrane region. TRPML1 forms extensive contacts with PI(3,5)P2 through N-terminal helices and S1-S3. E) Pore Helices (PHs) and Selectivity Filter (SF), and F) lower gate state (S6 helices) in the PI(4,5)P_2 and agonist-bound structures.

mational changes that dilate the lower gate of the channel, while it only has a small effect on the conformation of the selectivity filter (Figure 7E and F) (Fine et al., 2018; Schmiege et al., 2017). Opening of the lower gate results from the outward movement of the S6 helix, which contains the highly conserved π-helix (Schmiege et al., 2017). The constriction point is formed by I514 and T518, which move outward in the agonist-bound state (Figure 7F) (Schmiege et al., 2017). Overall, these conformational changes are driven by changes in the contacts within the transmembrane regions as binding of TRPML1 to the agonist (e.g. F505 and F513) disrupts existing contacts that stabilize the closed state (Schmiege et al., 2017). Other agonists have been described to act through a similar mechanism (Gan et al., 2022). Despite the lack of large changes in the selectivity filter, electrophysiology experiments showed that small alterations in the contacts between the PHs and the surrounding S5-S6 helix can significantly affect channel activity, which is observed in disease mutations (Schmiege et al. 2017). This suggests that one of the mechanisms through which the channel activity is regulated is through the modulation of the contacts formed between the PHs, selectivity filter, and the neighboring helices, altering the dynamics of the selectivity filter.

The luminal domain is the main region of TRPML1 that is in direct contact with the lysosomal environment. Therefore, it has been suggested to be involved in pH regulation of the channel through conserved anionic residues forming a charged belt over the pore (Figure 7B) (Li et al., 2017). Large conformational changes in the luminal pore loop are observed upon pH change in TRPML3 (Zhou et al., 2017). In TRPML3, pH-induced conformational changes in the pore loop propagate to the S1 helix, which forms contacts with the S2-S4 helices that in turn alter the conformation of the S5-S6 and PHs regions from the neighbouring subunit due to domain swapping (Zhou et al., 2017). This suggests the presence of allosteric coupling between the luminal domain and transmembrane region. The conformation of the luminal pore loop is not affected by pH in TRPML1, which suggests that there is an alternative mechanism of pH regulation (Li et al., 2017). There is known to be allosteric coupling between the luminal domains and the transmembrane domains as agonist binding (ML-SA1 or temsirolimus) causes rotation of the luminal domain through its binding (Gan et al., 2022). As noted in TRPML3, it was suggested that the S1 helix, which interacts extensively with the luminal domain and the transmembrane regions,

acts to propagate conformational changes between the luminal domains and the transmembrane regions (Gan et al., 2022). The S1 helix acts cooperatively with S2-S4, which act to support the luminal domain. In these structures, the modulation of the luminal domain conformation is induced by transmembrane domain ligand binding. However, the luminal domain acts to sense the lysosomal environment, and is likely itself a modulator of the transmembrane region through interactions with endogenous modulators (e.g. pH or protein interactions). Cathepsin B and protease cleavage of the luminal domain have been identified as regulators of TRPML1 activity (Kiselyov et al., 2005; Qi et al., 2016). It has been suggested that cleavage reduces activity by reducing channel stability, and most TRPML1 is thought to be in this cleaved state (Kiselyov et al., 2005). The cleavage occurs at R200, which is located in the loop connecting β-strands 4 and 5 (Kiselyov et al., 2005). However, this region is glycosylated and partially disordered and has therefore not been previously resolved structurally. Characterization of this region and the identification of additional luminal modulators will likely enable to elucidate the mechanisms through which the luminal domains and their cleavage modulate channel activity.

Therefore, despite this wealth of TRPML1 structures, there are still fundamental gaps in our understanding of TRPML1 regulation, including the roles of the luminal domain in the regulation of channel activity and the effects of pH on channel structure.

1.3.5 TRPML1 Dysregulation in Neurodegenerative Diseases

Loss of lysosomal function and disruption of autophagy have been implicated in neurodegeneration (Nixon 2013; Udayar et al., 2022). Recently, TRPML1 has been investigated for its role in Parkinson's and Alzheimer's diseases, and as a potential target for the treatment of these diseases.

TRPML1 has been suggested to be dysregulated in neurodegeneration due to lysosomal acidification deficits (Lee et al., 2015). This can result from mutations in disease-associated or causing genes, such as presenilin-1 (Lee et al., 2015; Somogyi et al., 2020). TRPML1 hyperactivation can disrupt endosomal retrograde transport by dynein in axons, and lead to axonal dystrophy (Lie et al., 2022). Lysosomal exocytosis has also been found to be a key TRPML1 function dys-

regulated in neurodegeneration. TRPML1 activation has been shown to rescue alpha-synuclein exocytosis in dopaminergic neurons with loss-of-function mutations in ATP13A2 (Parkinson's mouse model) (Tsunemi et al., 2019). Stimulation of lysosomal exocytosis has also been shown to reduce cytotoxic iron accumulation, which is observed in Parkinson's patients (Fernández et al., 2022). TRPML1 is a key regulator of TFEB (Medina et al., 2015). Overexpression of TFEB rescues some of the phenotypes associated with neurodegenerative diseases through the regulation of autophagy and by upregulating clearance of toxic misfolded proteins (Chauhan et al., 2015; Decressac et al., 2013; Polito et al., 2014; Xiao et al., 2015; Pastore et al., 2013). Therefore, stimulation of TRPML1 has been suggested as a strategy to enhance misfolded protein clearance through TFEB activation. Merck has recently acquired Caraway Therapeutics and Calporta, which are two companies developing TRPML1 agonists for the treatment of neurodegenerative diseases. Activation of TRPML1 in neurodegeneration cell models has been shown to enhance clearance of misfolded proteins, potentially by promoting autophagosome maturation (Pollmanns et al., 2022; Somogyi et al., 2023). Despite this wide interest in targeting TRPML1, a key challenge has been modulate it specifically.

1.4 Cystinosin: Structure and Function

1.4.1 Cystine in Lysosomal and Cellular Homeostasis

L-cystine is the oxidized form of L-cysteine. At the acidic lysosomal pH (≈4.6), cystine is a zwitterion. Cystine is rapidly reduced into cysteine once it is exported into the cytosol, making the lysosome a major cysteine reservoir (Abu-Remaileh et al., 2017). Lysosomal cystine stores are generated as a result of protein degradation in the lysosomal lumen (Figure 8). Lysosomal cystine and cysteine levels are tightly regulated by a cysteine importer (MFSD12) and cystine exporter (cystinosin) (Figure 8) (Adelmann et al., 2020; Gahl et al., 1982). Loss of cystine homeostasis can result from altered activity or expression of these transporters, causing cystine accumulation in cystinosis and potentially in cancer (Figure 8) (Town et al., 1998; He et al., 2023).

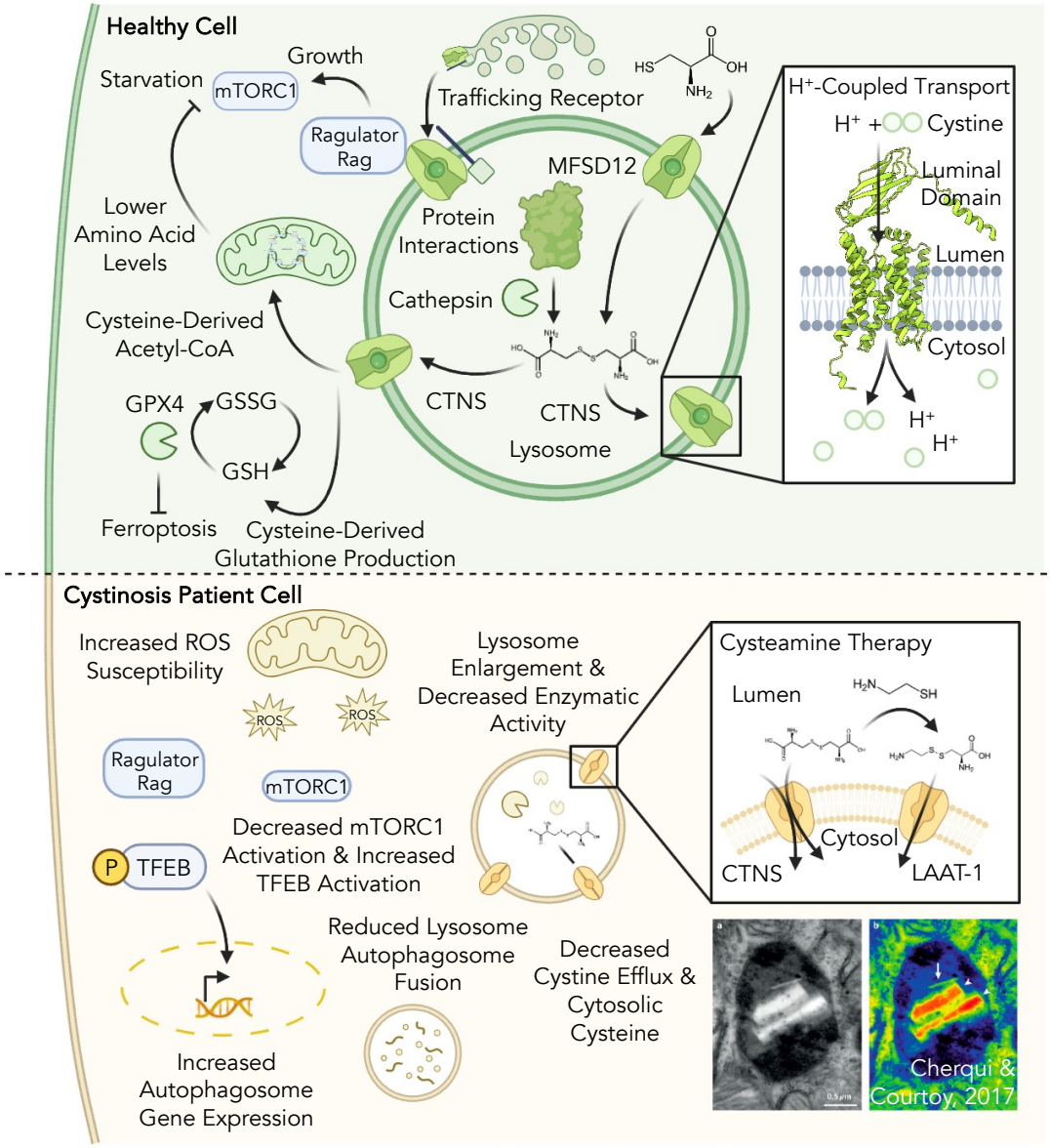

Figure 8: Cystine and cystinosin functions and their disruption in cystinosis. In healthy cells, cystinosin is involved in proton-coupled transport of cystine out of the lysosomal lumen into the cytosol. Cystine levels in the lysosomal lumen are also regulated by MFSD12, which imports cysteine into the lysosomal lumen. Cystinosin has additional cellular functions, including a potential function as a trafficking receptor and a regulator of mTORC1 signaling. Cytosolic cysteine derived from lysosomal cystine stores are used in the production of glutathione for the preservation of the redox balance in the cell. Acetyl-CoA derived from cysteine is use for the production of TCA intermediates, reducing cytosolic amino acid levels and mTORC1 activation. The disruption of lysosomal cystine transport in cystinosis patients causes the accumulation of cystine in the lumen, resulting in the formation of crystals (see images) that disrupt enzymatic function and lysosome fusion. Cellular redox balance is disrupted, leading to an increased ROS production, and the activation of TFEB. Cystinosis can be treated through cysteamine treatment, which reacts with cystine to form cysteine-cysteamine that is exported out of the lysosome by LAAT1.

Lysosomal cystine and cysteine derived from lysosomal cystine are key regulators of lysosomal homeostasis and cellular state (Figure 8) (Berquez et al., 2023; Jouandin et al., 2022; Sumayao et al., 2016; Swanda et al., 2023). Increases in lysosomal cystine storage activate mTORC1 through the Ragulator-Rag complex, stimulating cell growth and anabolic activity (Andrzejewska et al., 2016; Berquez et al., 2023; Guo et al., 2022). Lysosomal cystine also regulates ferroptosis through integrated pathways (mTORC1, GSH synthesis, ATF4 transcription) (Armenta et al., 2022; Swanda et al., 2023; Zhang et al., 2021). Upon export, lysosomal cystine becomes a source of cysteine for the generation of cytosolic glutathione, which acts as a regulator of cellular redox balance (He et al., 2023; Sumayao et al., 2016). Lysosomes also act as a source of cysteine to regulate cellular metabolism during starvation (Jouandin et al., 2022). In this mechanism, cysteine is converted to acetyl-CoA for the production of tricarboxylic acid cycle intermediates in the mitochondria, reducing amino acid levels in the cell, and inhibiting TORC1 activation and cellular growth (Jouandin et al., 2022). Regulation of lysosomal cystine levels is therefore required to preserve lysosomal and cellular homeostasis.

1.4.2 Cystinosin is the Lysosomal Proton-Coupled Cystine Transporter

The lysosomal cystine transporter was identified from cystinosis patient cells, in which lysosomal cystine transport is disrupted (Gahl et al., 1982; Jonas et al., 1982). The activity of this transporter was determined to require the proton-gradient generated by v-ATPase (Gahl et al., 1982; Jonas et al., 1982). This transporter was later found to be expressed by the CTNS gene, expressing the proton-coupled cystine transporter cystinosin (Attard et al., 1999; Cherqui et al., 2002; Kalatzis et al., 2001; Town et al., 1998). Cystinosin was suggested to be comprised of 7 transmembrane helices with a folded and glycosylated N-terminal domain on the luminal side and a C-terminal lysosomal targeting motif on the cytosolic side (Figure 9A and B) (Cherqui et al., 2001; Nevo et al., 2017).

Further studies were carried out on a mis-localized plasma membrane mutant of cystinosin (CTNSΔGYDQL or CTNSΔ) (Cherqui et al., 2001). CTNSΔ was used in cellular uptake

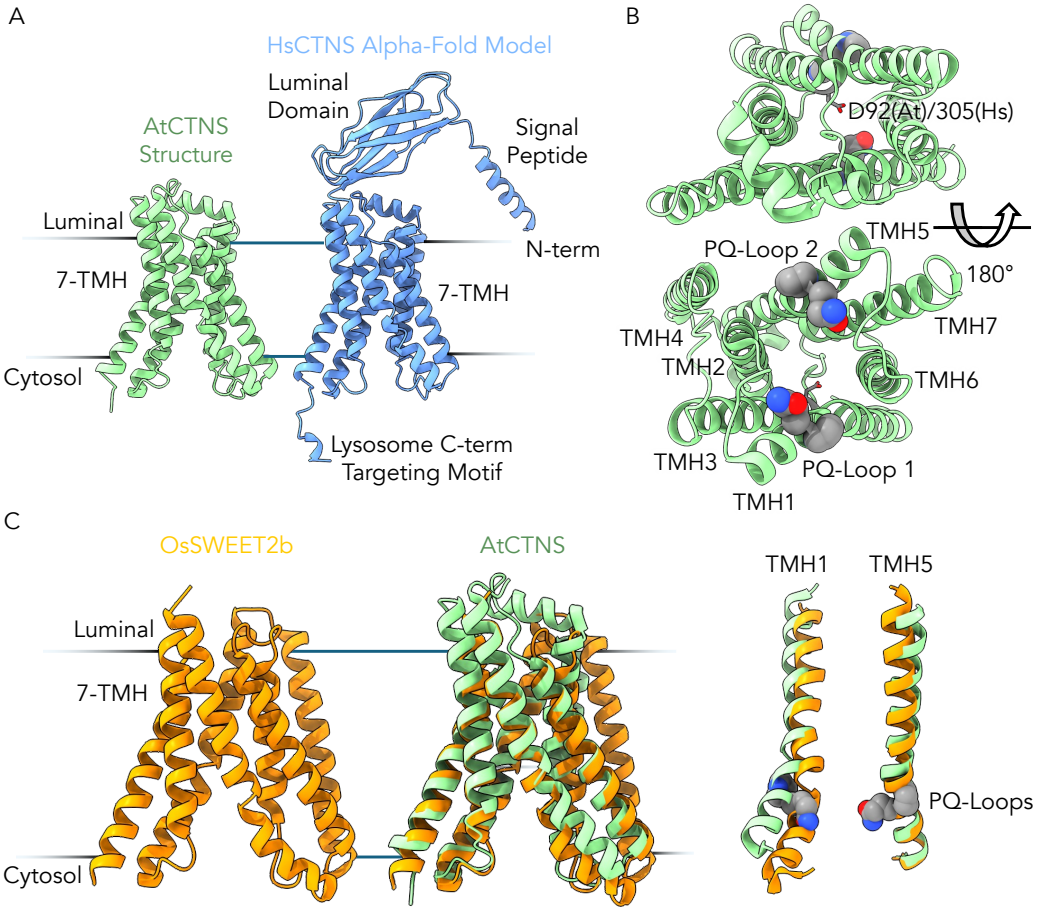

Figure 9: Cystinosin and PQ-loop family protein structures and model. A) The plant cystinosin structure in green (obtained by Mark Löbel; PDB: 7ZK1) that was used to formulate the mechanism tested in this work contains 7 TMH like the human AlphaFold model (blue). In addition, the human protein also contains a soluble luminal domain with an Ig-like fold. B) The two key sets of residues that had been identified in the literature were the PQ loop motifs, P144 (TMH1) and P283 (TMH5), and the proton-coupling residue, D305. C) Structure of *Oryza sativa* SWEET transporter (orange; PDB: 5CTG) from the PQ-loop family, which shows structural similarity with cystinosin (RMSD = 7.646 Å (210)) and is composed of a PQ-loop motif that induces kinks in the TMHs that are involved in facilitating conformational changes during the transport cycle.

assays to demonstrate that cystinosin is an L-cystine-specific transporter that has activity at acidic pH, and enabled to test the effects of cystinosis patient mutations on transporter activity (Kalatzis et al., 2001; Kalatzis et al., 2004). Using this mutant in *Xenopus laevis* oocytes, Ruivo et al (2012) demonstrated using Two-Electrode Voltage Clamp (TEVC) that cystinosin undertakes proton-coupled transport of cystine in a 1:1 ratio. The authors identified cystinosin to be a member of the PQ-loop family of membrane proteins. Members of this family contain a conserved proline-glutamine dipeptide within transmembrane helices that are involved in their mechanisms of action (Bräuer et al., 2019; Ruivo et al., 2012). It generates kinks that facilitate conformational as a result of substrate binding (Figure 9C) (Lee et al., 2015). This initial electrophysiological characterization of cystinosin enabled the authors to suggest that D305 is the proton-coupling residue of cystinosin. The protonation of this residue and cystine binding were suggested to be tightly coupled.

Apart from these early mechanistic details, the mechanism of transport of cystinosin remained uncharacterized. Therefore, we set out to investigate the structure and mechanism of cystinosin to understand how cystinosin transports cystine to maintain lysosomal amino acid homeostasis and how the transport mechanism is disrupted by cystinosis mutations.

A crystal structure of plant CTNS (AtCTNS) with and without cystine was obtained by Mark Löbel (Figure 9A)(Löbel et al., 2022). Based on this structure, a mechanism was suggested for proton-coupled cystine transport. A set of mutants were designed to test whether the findings from the plant protein are also applicable to human cystinosin (hCTNS) to understand the mechanism of the human protein and how disease mutations affect it. This process was guided by the AlphaFold model of human cystinosin that was available when undertaking these experiment.

1.4.3 Mutations in Cystinosin Cause the Lysosomal Storage Disorder Cystinosis

Cystinosin was first described by Abderhalden (1903) and Lignac (1924) as hereditary diseases of cystine accumulation. Following the discovery of lysosomes decades later, the molecular ba-

sis of the disease was characterized by investigating the properties of lysosomes from cystinosis patients, in which cystine was found to accumulate and form crystals (Gahl et al., 1982; Pisoni et al., 1985). Cystine accumulation in lysosomes disrupts enzymatic activity and lysosomal fusion (Cherqui and Courtoy, 2017).

Despite the identification of lysosomal cystine accumulation as a hallmark of cystinosis, it does not fully correlate with disease severity, suggesting that loss of cystinosin may cause loss of lysosomal and cellular homeostasis through additional mechanisms (Cherqui et al., 2002; Jamalpoor et al., 2021; Kalatzis et al., 2004; Nesterova and Gahl, 2008; Park et al., 2002; Racusen et al., 1995). Identified mechanisms include the dysregulation of cystinosin-mediated interactions or signaling pathways (Ragulator-Rag/mTORC1 and LAMP-2A), disruption of autophagy leading to nutrient scarcity and cell death, susceptibility to reactive oxygen species stress due to reduced GSH synthesis, and metabolic and energy (ATP) deficiencies (Figure 8) (Festa et al., 2018; Galarreta et al., 2015; Guo et al., 2022; Taub and Cutuli, 2012; Wilmer et al., 2011). In cystinosis models or patient cells, mTORC1 shows disrupted activation at the lysosomal membrane and TFEB expression is lowered, which can result in inhibition of differentiation or cell death due to dysregulation of metabolism and lysosomal activity during starvation (Andrzejewska et al., 2016; Berquezet al., 2023; Hollywood et al., 2020; Ivanova et al., 2016; Jouandin et al., 2022; Rega et al., 2016). Cystinosis has also been suggested to result from inefficient trafficking of LAMP-2A to the lysosomal membrane, disrupting chaperone-mediated autophagy (Napolitano et al., 2015; Zhang et al., 2017).

Cystinosis can manifest with different degrees of severity: infantile (severe), juvenile (milder), ocular and atypical which are milder forms of the disease. Infantile cystinosis is the most common form and is characterized by poor growth, hypothyroidism and kidney damage (renal Fanconi Syndrome) during childhood, resulting in poor nutrient absorbance (Elmonem et al., 2016; Gahl et al., 1986; Jamalpoor et al., 2021). As the disease progresses, cystine crystals form in the cornea causing blindness and end-stage renal failure occurs, making kidney transplants vital by the age of about 10 (Jamalpoor et al., 2021). Kidney transplants are typically successful with no disease recurrence in these patients (Van Stralen et al., 2011). Juvenile cystinosis patients

display similar but potentially milder phenotypes compared to infantile cystinosis patients and with a later onset (adolescence or early adulthood) (Goldman et al., 1971; Servais et al., 2008; Thoene et al., 1999). Ocular cystinosis is a rare and mild form that results from cystine accumulation in the cornea, causing photophobia (Anikster et al., 2000). These different forms of cystinosis are rare (incidence rate of 1 per 100,000 live births) and arise as a result of biallelic mutations in the CTNS gene, including over 140 different mutations (David et al., 2019; Levy and Feingold, 2000). Cystinosis mutations can disrupt transporter activity, protein interactions, localization and expression of the protein (Andrzejewska et al., 2016; Guo et al., 2022; Kalatzis et al., 2004). However, the molecular basis for cystine transport by human cystinosin remains to be determined to understand how these mutations disrupt its functions.

The most successful existing treatment for cystinosin is cysteamine (Schneider et al., 1995). Cysteamine reacts with cystine to form cysteine-cysteamine, which can be exported out of the lysosome by cationic amino acid transporter LAAT-1 (Gahl et al., 2000; Liu et al., 2012; Pisoni et al., 1985; Thoene et al., 1976; Gahl et al., 1987). If treatment is started early, it can delay kidney transplant by 6-10 years and eliminate corneal cystine crystals (Gahl et al., 2000; Kleta et al., 2004; Markello et al., 1993). However, kidney transplant is still required, the treatment causes strong body odor, gastrointestinal and bone pains, and some patients show resistance to the therapy or poor compliance due to side-effects (Cherqui, 2012; David et al., 2019). Improvements in our understanding of the mechanism of cystinosin would enable the development of improved therapies for cystinosis patients.

1.5 Nanobodies

1.5.1 Generation and Structure of Nanobodies

Antibodies are composed of two light-chains and heavy-chains that are linked by disulfide bonds. Binding to the antigen occurs through interactions formed by the variable regions of the light and heavy chains (Figure 10A). Tylopoda and sharks produce heavy-chain only antibodies, in which the variable region is present in a single domain (Flajnik et al., 2011). This region can

be isolated and expressed as a 15-kDa protein, which is referred to as a nanobody (Beghein and Gettemans, 2017; Muyldermans, 2013). Nanobodies adopt an Ig-fold with two β-sheets stabilized by a disulfide bond (Spinelli et al., 1996). They bind to their target epitope through three complementarity-determining regions (CDRs), with variations in the length of CDR3 being a determinant of their specificity and properties (Desmyter et al., 1996; Zavrtanik et al., 2018).

Heavy-chain antibodies are obtained through a series of steps, including six rounds of immunization with the protein of interest in llamas, collection of peripheral blood lymphocytes, RNA extraction, cDNA production, and finally library production by PCR (Figure 10B) (Pardon et al., 2014). High-affinity nanobodies can be identified through phage display and ELISA (Pardon et al., 2014).

The small size of nanobodies makes them easier to express (heterologously or as 'intrabodies'), increases their stability, enables them to access clefts unavailable to conventional antibodies and facilitates engineering/modification (Dong et al., 2019; Muyldermans, 2013). These advantages have been exploited in a range of applications (Muyldermans, 2021).

1.5.2 Synthetic Nanobodies (Sybodies)

Despite the numerous advantages of nanobodies over conventional antibodies, there remain a few barriers to their production. Immunization requires very large quantities of a stable purified protein (1-1.5 mg) and the process takes approximately 6 months (Pardon et al., 2014). This is not possible for numerous proteins, notably membrane proteins which tend to express poorly and may not be sufficiently stable for immunization. Most proteins display multiple conformational states. Monoclonal antibodies or nanobodies binding to a conformational epitope rather than a linear peptide will typically bind to a particular state. However, it is challenging to lock a protein in the desired state during immunization.

These limitations can be overcome by undertaking the selection *in vitro* (Liu and Yang, 2022). Numerous platforms have been developed, but most offer limited binder diversity which tends to lead to poor-quality binders (Zimmermann et al., 2020). The synthetic nanobody (sybody)

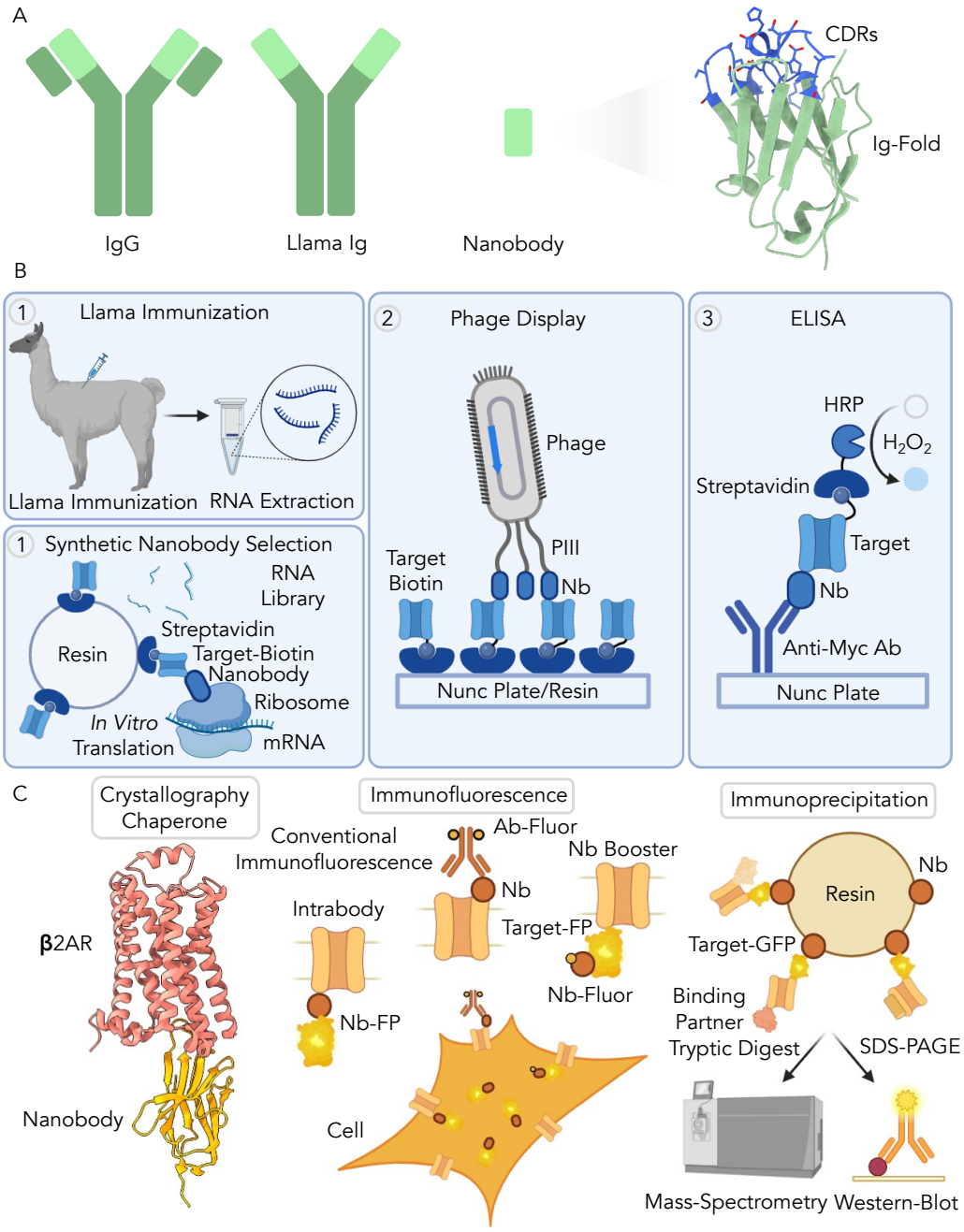

Figure 10: Nanobody (Nb) structure, selection and applications. A) Nanobodies are 15 kDa fragments (light green) derived from heavy-chain antibodies (dark green). The framework adopts an Ig-fold and it binds to its target protein through the CDRs (blue) (PDB: 5IVO). B) Nanobody selection starts with animal immunization, while sybodies are obtained through *in vitro* screening. Steps 2 and 3 are the same in both screens. C) Nanobodies have a range of applications: chaperones for structural biology applications (PDB: 3P0G), immunofluorescence and IP reagents.

selection protocol was developed with an increased library diversity of 10^{12} compared to other approaches (e.g. naïve libraries, synthetic libraries based on yeast or phage displays) with typically 10^{8}-10^{10} binders (McMahon et al., 2018; Moutel et al., 2016; Olichon and de Marco 2012; Zimmermann et al., 2020). This increased diversity is achieved by starting the selection process with ribosome display, followed by phage displays and an ELISA step (Figure 10B) (Zimmermann et al., 2020). The selection is carried out on three different libraries, with CDR regions designed based on previously characterized nanobody-protein complexes. These different designs are expected to lead to different binding modes. This protocol has been used to obtain high-affinity binders for challenging membrane proteins, such as KDELR and cystinosin (Bräuer et al., 2019; Löbel et al., 2022). The work presented here aims to apply this platform to study the structure, function and localization of lysosomal membrane proteins.

1.5.3 Application of Nanobodies to Structural Studies

Nanobodies were initially widely applied as crystallization chaperones (Figure 10C) (Koide, 2009). They served to stabilize dynamic or unstable proteins during crystallization, and facilitate structure determination through molecular replacement (Uchański et al., 2021). A notable example of this was the use of nanobodies to solve the first active β_2AR structure, which demonstrated that they can stabilize proteins in a conformation of interest (Rasmussen et al., 2011). The applications of nanobodies to structural biology has evolved since their adoption for cryo-EM structural studies. For cryo-EM, nanobodies have been used to increase the particle size, to overcome orientation bias and to lock structures in a particular state (Che et al., 2018; Parker et al., 2021; Masiulis et al., 2019). This has led to the development of larger proteins based on nanobody scaffolds, including NabFabs, megabodies and legobodies (Bloch et al., 2021; Uchański et al., 2021; Wentinck et al., 2022; Wu and Rapoport, 2021). An expected future application of nanobodies in structural biology will be their use as fiducial markers in cryo-ET.

1.5.4 Nanobodies to Investigate Protein Localization in Cells

A current barrier to characterize protein localization in the cell is the lack of specific antibodies. Nanobodies have only recently been applied to study proteins *in situ* using tags or on simple (e.g. highly-expressing and soluble proteins) targets (Dong et al., 2019; Pleiner et al., 2015; Ries et al., 2012). These applications take advantage of the small size of nanobodies. This is beneficial to express the nanobodies intracellularly in live cells ('intrabodies' or chromobodies), to easily engineer and express variants for various applications (e.g. labelled mutants or linked constructs), and minimizes linkage-error in super-resolution microscopy applications (Dong et al., 2019; Ries et al., 2012; Sograte-Idrissi et al., 2019; Virant et al., 2018).

Three main approaches have been adopted to study protein localization using nanobodies. Cells have been transfected with DNA encoding a nanobody (fused to a fluorescent or affinity tag) that binds to the target protein or to a fusion tag, which is frequently GFP (Akkermans et al., 2022; Dong et al., 2019). This approach, called intrabodies or chromobodies, is powerful to image protein localization in live cells (Mikhaylova et al., 2015; Rothbauer et al., 2006; Virant et al., 2018). This approach has been adopted to investigate the activation dynamics of β_2AR in cells using state-selective nanobodies fused with GFP (Irannejad et al., 2013). However, overexpression of the nanobody may interfere with normal protein and cellular functions. To image fixed cells, nanobody-tag fusions enable indirect labeling if stained with a fluorophore-tagged protein (e.g. antibody or streptavidin) or direct labeling if directly linked with a fluorescent protein or enzyme (e.g. sortase, horseradish peroxidase) (Ries et al., 2012; Rödström et al., 2024; Rothbauer et al., 2006; Virant et al., 2018; Yamagata et al., 2018). A third approach that has become widely used is the direct conjugation of fluorophores to nanobodies (Pleiner et al., 2015). This is typically achieved through the introduction of cysteine residues in the nanobody for maleimide labeling (Loreau et al., 2023; Pleiner et al., 2015; Pleiner et al., 2018). This approach has been used to generated GFP-boosters, in which anti-GFP nanobodies conjugated to fluorophore are used to enhance GFP signal (Cai et al., 2019; Ries et al., 2012). A lot of these approaches have been developed or applied to nanobodies that bind to protein tags, which are overexpressed and highly stable peptides or proteins (Ries et al., 2012; Rothbauer et al., 2006; Virant et al.,

2018). The current challenge is to obtain specific nanobodies against challenging proteins, including membrane proteins, modified proteins and proteins with low expression to image their endogenous localization (Viswanathan et al., 2015).

1.5.5 Nanobodies to Modulate and Investigate Protein Functions in Cells

Modulators of protein activity are essential tools to study protein function. Most available modulators for lysosomal membrane proteins are unspecific (Wang et al., 2023). This is especially the case for proteins with isoforms or other family members that show strong sequence identity, such as members of the TRPML1-3 subfamily (40% sequence identity) (Peng et al., 2024). Some of these molecules may act by interacting with regions that are important for the mechanism of the protein, which tend to be highly conserved (Schmiege et al., 2017). Antibodies tend to show higher specificity and they may target alternative regions that show lower conservation (Oo and Kalbag, 2016). Nanobodies have been adopted as an alternative to antibodies as they are potent and specific modulators of protein activity with a smaller size, enabling them to access functional clefts inaccessible to antibodies and facilitating engineering/linking with functional subunits (Caussinus et al., 2011; Zavrtanik et al., 2018).

Nanobodies with different modes of action have been identified. Some nanobodies have been found to stabilize or inhibit protein interactions with their substrate (proteins, peptides or molecules) (Akkermans et al., 2022; Bräuer et al., 2019; Bethuyne et al., 2014; Koenig et al., 2021; Kromann-Hansen et al., 2016). Nanobodies and sybodies may also act by modulating the conformation of their target protein (Deneka et al., 2021).

Nanobodies have been functionalized to investigate protein function by linking them to additional subunits. Modules have been added that can stimulate protein degradation (ligases), regulate gene expression (transcriptional repressor or regulatory domains) and (Caussinus et al., 2011; Morgenstern et al., 2019; Morgenstern et al., 2022; Tang et al., 2013). These fusions have also been used to generate a range of nanobody-based sensors to investigate protein activity

and function. This includes ion, pH and optogenetic sensors (Prole and Taylor, 2019; Queiroz Zetune Villa Real et al., 2023; Yu et al., 2019).

Nanobodies have also been used to identify functional effectors in co-IP experiments (Beghein and Gettemans, 2017). For these experiments, nanobodies have the advantage of being more stable, less disruptive and prone to epitope masking due to their small size, potentially higher affinity and more specific than antibodies, cheaper and easier to produce, and show reduced contamination of the sample upon elution (no heavy and light chain) (Smits and Vermeulen, 2016). They have been used to isolate native protein complexes (Pleiner et al., 2015; Rutz et al., 2023; Shi et al., 2015). Anti-tag (e.g. GFP or ALFA) resin has been widely adopted to characterize protein interactions (Götzke et al., 2019; Katoh et al., 2015). Resin has also been generated with nanobodies selected for specific protein of interest to identify protein-protein or protein-DNA interactions (Akkermans et al., 2022; Nguyen-Duc et al., 2013; Nishiyama et al., 2020). In these examples, the nanobody is either directly conjugated to resin with a reactive group (e.g. NHS-ester or maleimide) or through tags (e.g. streptavidin-biotin) (Platonova et al., 2015; Pleiner et al., 2015). Identification of a suitable conjugation method is critical as it may affect nanobody affinity, expression and stability (Massa et al., 2014; Pleiner et al., 2015).

1.6 Aims

This thesis aims to understand the role of transporters and ion channels in maintaining lysosomal homeostasis, focusing on the lysosomal cystine transporter cystinosin and the lysosomal ion channel TRPML1.

Aim 1: Characterize the mechanism of the human lysosomal cystine transporter cystinosin, and how it is disrupted in the lysosomal storage disorder cystinosis. *See Chapter 3*

Aim 2: Generate and characterize a synthetic nanobody toolkit to investigate the role of TRPML1 in lysosomal homeostasis, including its mechanism, functions, and localization. *See Chapter 4 and 5*

Aim 3: Engineer TRPML1 synthetic nanobodies to investigate the localization of TRPML1 in cells. *See Chapter 6*

2 | Materials and Methods

2.1 Characterization of the Human Cystine Transporter Cystinosin Using Two-Electrode Voltage Clamp.

2.1.1 Two-Electrode Voltage Clamp

Human cystinosin without its C-terminal lysosomal targeting motif (hCTNSΔGYDQLN, referred to as hCTNS) was subcloned with and without a C-terminal GFP into the pFAW vector for *in vitro* transcription. The mutants were generated by site-directed mutagenesis and were sequenced. *Xenopus laevis* oocytes were defolliculated by collagenase treatment. They were then injected with 50 nl of nuclease-free water or 75 ng (50 nl of 1500 ng/μL RNA) of hCTNS wild-type or mutant mRNA, and were incubated for 2 days at 19^{o}C in Barth's solution (54 mM NaCl, 30 mM KCl, 2.4 mM $NaHCO_3$, 0.8 mM $MgSO_4(H_2O)_7$, 0.4 mM $CaCl_2$, 0.3 mM $Ca(NO_3)_2(H_2O)_4$, 7.5 mM Tris, adjusted to pH 7.4) with gentamicin (50 μg/ml) (Ruivo et al., 2012). Two-electrode voltage clamp measurements were carried out at Room Temperature (RT) on a Roboocyte system (Multi Channel Systems) using 3 M KCl back-filled borosilicate glass pipettes with a resistance of 200-1000 kΩ (Schnizler et al., 2003). Oocytes were voltage-clamped to -40 mV for the measurements for 200 ms. For each oocyte, an initial recording was made with ND-96 solution (96 mM NaCl, 2 mM KCl, 2 mM $MgCl_2$, 1.8 mM $CaCl_2$, 5 mM MES, adjusted to pH 5 with NaOH) without cystine, followed by a second recording in ND-96 with 1 mM cystine (pH 5). For the dose-response curves, these measurement pairs were repeated on a single oocyte at the following cystine concentrations: 5 μM, 10 μM, 25 μM, 50 μM, 100 μM, 150 μM, 400 μM and 1 mM. Traces were analysed using the Roboocyte software (Multi Channel Systems). Cystine-evoked current values were obtained by subtracting the mean current after the addition of cystine from the mean current before the addition of cystine. Currents were

normalized based on the cystine-evoked currents for the wild-type hCTNS injected oocytes of the corresponding oocyte batch. All experiments were repeated on at least three different oocyte batches.

2.1.2 Oocyte Confocal Microscopy

Living oocytes that had been injected with water, wild-type or mutant hCTNS-GFP mRNA were washed in 1X PBS, stained with 0.05 mg/ml of CF-633 wheat germ agglutinin (Biotium) in 1X PBS for 5 min at RT, and washed with 1X PBS (Reed et al., 2016). Surface expression was imaged using an LSM-780 confocal microscope with a 10x 0.5 NA Dry Plan Apochromat lens, and an Argon (488 nm) and He-Ne laser (633 nm).

2.2 Generation of a Synthetic Nanobody Toolkit to Investigate TRPML1 Localization, Function and Structure

2.2.1 TRPML1 Expression and Purification

2.2.1.1 Full-Length TRPML1

The human FLAG-AVI-TRPML1 gene was synthesized and subcloned into pLEXM for transient expression in mammalian cells. HEK293F cells grown to a density of 1.3-1.4x10^6 in FreeStyle 293 Media (Thermo Fisher Scientific) were transiently transfected with TRPML1 in pLexM (1 μg of DNA per ml of culture) using PEI MAX in a 1:2 (DNA:PEI) ratio and 10 mM sodium butyrate as previously described (Parker et al., 2021). Cells were harvested 40 h post-transfection, washed with 1X PBS and snap frozen in liquid nitrogen.

For small-scale expression trials (20 ml), pellets of cells transfected with TRPML1-GFP were thawed and resuspended in 1X PBS (pH 7.4). Membrane proteins were solubilized with 1%

detergent (LMNG, LMNG:CHS, DDM, DDM:CHS; detergents from Anatrace) in 1X PBS for 1 h at 4°C. The samples were centrifuged at 200,000 g. Fluorescence size exclusion chromatography was used to analyze the solubilized fraction (supernatant). Samples were loaded onto a Superose 6 Increase 10/300 GL column (Cytiva) and GFP emission at 512 nm (excitation: 488 nm) was measured.

For large-scale expression (2-8 L), the frozen cells were thawed, resuspended in PBS with DNAse and lysed using a sonicator (Q Sonica) (4 cycles of 30s, each followed by 60s off). Debris were removed by low-speed centrifugation. Membranes were harvested by two ultracentrifugation steps at 45,000 rpm and were resuspended in 1X PBS for snap freezing (Parker et al., 2021).

Harvested membranes were solubilized with 1% LMNG or DDM dissolved in 150 mM NaCl, 1X PBS and 10% glycerol at 4°C for 60-90 min. Solubilized protein was separated from the membrane through an ultracentrifugation step at 50,000 rpm. The protein was loaded onto an anti-Flag M2 affinity column (Sigma) and eluted with 0.05 mg/ml of FLAG peptide in 0.01% LMNG, 1X PBS and 150 mM NaCl. The protein was concentrated and purified using a Superdex-200 (GE Healthcare) column equilibrated with 0.003% LMNG, 150 mM NaCl and 20 mM Tris (pH 7.5). Fractions of interest were pooled and concentrated with a Vivaspin 2 (50,000 MWCO) (Sartorius).

Purification of the TRPML1-mNeonGreen-1D4 construct was carried out from cell pellet of stable HEK293 cell line overexpressing this construct. Cells were lysed by a freeze-thaw cycle and dounce homogenization. The pellet was solubilized using 1% Digitonin (Anatrace) for 1 hour at 4°C. Debris were pelleted by ultracentrifugation at 16,000 rpm for 30 min at 4°C. The supernatant was collected and incubated with anti-1D4 antibody resin (in-house) for 2 hours at 4°C. The resin was washed with 20 CV of purification buffer (20 mM HEPES pH 8.0, 150 mM NaCl and 0.05% Digitonin), 5 CV of high salt buffer (purification buffer with 300 mM NaCl), and the protein was eluted overnight at 4°C in 5 CV of wash buffer with 20 mg/ml of 1D4 peptide (Cube Biotech).

2.2.1.2 TRPML1 Luminal-Domain

The luminal domain (residues 84-296) was amplified from the FLAG-AVI-TRPML1 gene and was subcloned in pHLSEC (Addgene #99845) for secretion in mammalian cells. 500 ml of HEK293F cells were grown to a density of 1.3-1.4x10^6 in FreeStyle 293 Media (Thermo Fisher Scientific) and were transiently transfected with luminal domain DNA (500 ug) using PEI MAX in a 1:2 (DNA:PEI) ratio as previously described (Parker et al., 2021). Media was harvested 60 hours post-transfection by centrifugation at 5000 rpm for 5 min. pH of the harvested media was adjusted to 8 using NaOH before incubation with HisPur Ni-NTA resin (Thermo Fisher Scientific) for 3 hours. Resin was washed with 25 mM Imidazole in TBS and protein was eluted with 300 mM Imidazole in TBS. The elution was concentrated using 3 kDa MWCO Amicon centrifugal filters (Millipore) and loaded on a Superdex 200 Increase column (Cytiva).

2.2.1.3 Protein Biotinylation

Concentrated protein was biotinylated using the BirA biotin ligase (Avidity) as per manufacturer protocol. Biotinylated protein was purified using a Superdex-200 Increase (Cytiva), Sepax SEC-100 or 300 column (Sepax Technologies) equilibrated in size-exclusion buffer. Biotinylation was assessed using the streptavidin shift assay in which biotinylated protein is incubated with a 3-fold molar excess of streptavidin (Sigma-Aldrich) for 10 min on ice. The sample is then loaded on a polyacrylamide gel to determine if a protein of interest-streptavidin complex has been formed.

2.2.2 Western Blot

Protein mixed with LDS Sample Buffer (Invitrogen) was loaded on a polyacrylamide gel. The protein was transferred to a Polyvinylidene Difluoride (PVDF) membrane that had been activated with 100% methanol. The membrane was incubated in PBST (0.1% Tween-20) with 5% milk powder for blocking and in PBST for the primary antibody incubation (dilution of antibody specified in Results section). Primary antibody incubation was carried out overnight at 4°C. The membrane was washed with PBST. Then, it was incubated with anti-mouse or rabbit horseradish

peroxidase-conjugated secondary antibody (Dako) (1:10000) for 1 hour at room temperature. It was washed again using PBST. The membrane was developed with Amersham ECL Prime Western Blotting Detection Reagent kit (GE Healthcare) and imaged using high-performance chemiluminescence film (GE Healthcare).

2.2.3 Differential Scanning Fluorimetry

Nanoscale Differential Scanning Fluorimetry (NanoDSF) was carried out using a Prometheus (NanoTemper Technologies) to assess protein thermal stability. Thawed purified protein (0.1-0.5 mg/ml) was centrifuged at 20,000 g for 5 min. Approximately 10 μL of protein was loaded into Prometheus Capillaries (NanoTemper Technologies). Measurements were made at a temperature range of 20-90°C with a ramp rate of 1°C/min. Emission at 330 nm and 350 nm (280 nm excitation) was measured to assess protein unfolding during the ramp protocol. Data was analysed using the Prometheus NT Software (NanoTemper Technologies).

2.2.4 Circular Dichroism

Thawed protein was diluted to a concentration of 0.1 mg/ml in Circular Dichroism (CD) buffer (10 mM potassium phosphate, 50 mM Sodium Sulfate and 0.003% LMNG, pH 7) and placed in 1 mm pathlength quartz cuvettes (Hellma analytics). Measurements were made using a JASCO 815 CD spectrometer at 240-200 nm. Unfolding of the protein was evaluated between 20-88°C with 2°C steps.

2.2.5 Sybody Selection

The sybody selection was carried out as previously described by Zimmermann et al (2020) using biotinylaled FLAG-AVI-TRPML1 in TBS with 0.003% LMNG. The sybody selection protocol is carried out by immobilizing biotinylated TRPML1 on streptavidin-coated resin or plates. The protocol comprises three selection methods: ribosome display, phage display (at least 2 rounds), and enzyme-linked immunosorbent assay (ELISA) (Figure 11A). Individual clones that can be

expressed and purified are obtained in the ELISA step of the protocol. Throughout these selection steps, poor binders are washed off during washing steps and strong binders remain bound and are eluted in the final step. The membrane protein pepTSo was used as a negative control throughout the protocol. The negative control enables to determine if the pool of obtained sybodies bind more strongly to the target protein relative to a non-target protein (enrichment), indicating that specific high-affinity binders are being obtained throughout the selection process. Selection is carried out on three different starting mRNA libraries that have been randomized with different design principles to achieve different binding modes to the target protein. The three libraries are loop (blue), convex (red) and concave (green). Each library has a starting diversity of 10^{12} binders, which throughout the process is typically reduced to approximately 10-100 binders (Zimmermann et al., 2020).

See Figure 11 for summary of pipeline results and protocol overview

2.2.5.1 Ribosome Display

Ribosome display was carried out as described by Zimmermann et al (2020). Throughout the protocol, the concentration of TRPML1 used was twice the recommended one to account for the tetrameric structure of TRPML1 while minimising the amount of protein required. At the end of the ribosome display, an agarose gel is run to purify the cDNA by gel extraction. A sufficient amount of cDNA was obtained from the gel extraction for all libraries to proceed to phage display (Figure 11B).

2.2.5.2 Phage Display

Phage display was carried out as described by Zimmermann et al (2020), except with the addition of a third phage display step to increase enrichment (typically includes two). The first phage display step led to enrichments of: 0.7 (concave), 1.0 (loop) and 11.8 (convex). The second phage display, which includes a competition step with unbiotinylated binder (carried out using two-fold recommended concentration), resulted in significant enrichment 348 (concave), 28 (loop) and 12 (convex). An additional phage display (3 steps) was carried out to increase

A

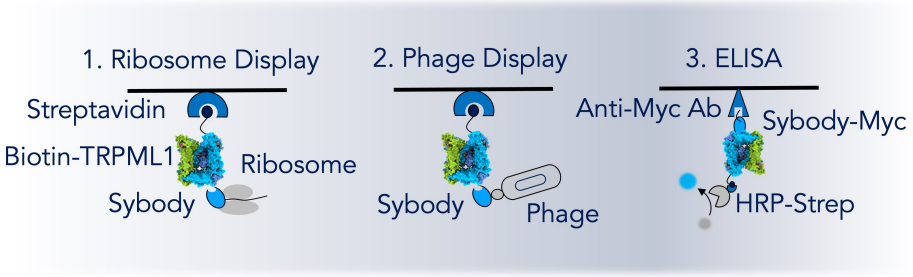

B

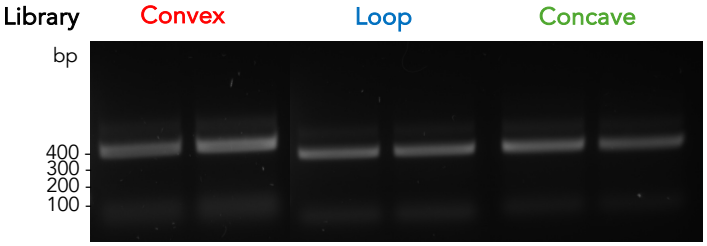

C

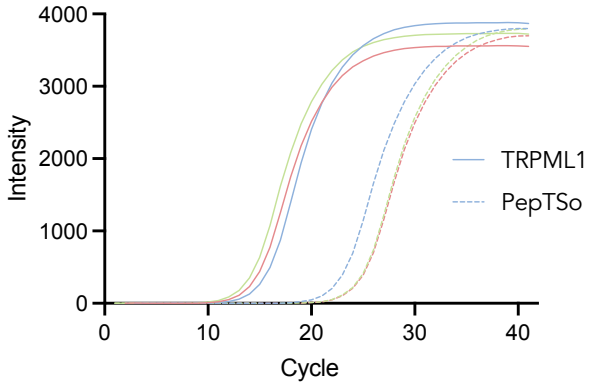

	Enrichment		
	PD1	PD2	PD3
Concave	0.7	348.2	1680.8
Loop	1.0	28.2	148.8
Convex	11.8	12.9	1095.7

Figure 11: Sybody selection protocol and results of selection steps. A) The sybody selection is carried out by immobilizing the target protein (TRPML1) on streptavidin coated resin or surface. The pipeline includes three key selection steps: ribosome display, phage display and ELISA. Throughout the protocol, strong binders remain bound during washing steps, while poor binders dissociate. At the end of each selection steps, the strong binders are eluted. At the end of the protocol, the ELISA enables the isolation of individual clones that can be expressed and purified. B) 1.5% (w/v) agarose gel with loaded cDNA from ribosome display. DNA bands were gel extracted and used to clone the obtained sybodies into a phagemid. C) qPCR data obtained following the three rounds of phage display (PD) (data from 3rd round of phage display displayed) along with the enrichment scores obtained. The enrichment scores are calculated by dividing the C_t values of the TRPML1 samples by the C_t values of the negative control (pepTSo).

binder enrichment further to maximize chances of obtaining high-affinity binders. This step was carried out using the same protocol as the second phage display, excluding the competition step. Final enrichment values were in the upper range: 1680 (concave), 148 (loop) and 1095 (convex).

2.2.6 Sybody Expression, Purification and Labelling

2.2.6.1 Sybody Expression and Purification

Sybodies were purified as previously described (Zimmermann et al., 2020). Briefly, sybodies cloned in pSBInit (Addgene #110100) were transformed in the MC1061 *E. coli* strain for expression. Cells were grown to target OD (specified in results section) and were induced with 0.02% arabinose. Expression was carried out overnight at 22°C. Sybodies were isolated by periplasmic extraction and purified using HisPur Ni-NTA resin (Thermo Fisher Scientific). Sybodies causing cell lysis upon expression were isolated by cell lysis before purification, including the poorly purifying cysteine mutants. This was carried out by resuspending the pellet in 1X PBS with bovine pancreatic deoxyribonuclease I (Thermo Fisher Scientific), freeze-thawing the resuspended cells, and separating debris through a low-speed centrifugation step (8,000 g for 30 min). Following Ni-NTA purification, the properties of the sybodies were assessed by SEC using a Sepax SRT-10C SEC100 (Sepax Technologies) equilibrated in TBS (20 mM Tris at pH 7.4, 150 mM NaCl) or PBS (pH 7.5) for sybodies purified for conjugation. Only sybodies showing monodisperse peaks within 1 column volume were selected.

2.2.6.2 Sybody Labelling

Fluorophore labeling was carried out using Alexa Fluor 647 C_2 Maleimide (Invitrogen). The fluorophore was diluted in DMSO to make a 10 mM stock, and was added in a 1:2 or 1:4 molar-excess to mutant sybody purified in 1X PBS. The reaction was incubated for 1 hour at 4°C and was quenched using 2 mM cysteine. Excess fluorophore was removed from the solution using a HiTrap Desalting column (Cytiva) equilibrated in PBS. Labeling efficiency was assessed by measuring absorbance at 280 nm and 651 nm using a BioSpectrometer (Eppendorf). Labeling efficiency was calculated using the following formulas from the manufacturer protocol:

$$[Protein](M) = \frac{(A_{280} - (A_{max} * CorrectionFactor))}{\varepsilon} \quad (1)$$

$$\frac{Mole\ of\ Dye}{Mole\ of\ Protein} = \frac{(A_{max}\ of the\ labeled\ protein)}{(\varepsilon' * [Protein](M))} \quad (2)$$

A_{280}: Absorbance at 280 nm

A_{max}: Peak absorbance of fluorophore (651 nm for Alexa-647)

$Correction\ Factor$: Absorbance correction factor (0.03 for Alexa-647)

ε: Protein extinction coefficient

ε': Fluorophore extinction coefficient (265,000 $cm^{-1}M^{-1}$)

2.2.7 Sybody Pull-Down

5 μg of full-length TRPML1 was incubated with 2.5 μg of His-tagged sybody for 1 hour on ice in TBS (pH 7.4) with 0.003% LMNG and 15 mM Imidazole. The complex was then incubated with 20 μL of HisPur Ni-NTA resin (Thermo Fisher Scientific) for 30 min at 4°C on a rotating wheel. The resin was washed three times without an incubation step and one time with a 60 min incubation in TBS (pH 7.4) containing 0.003% LMNG and 15 mM Imidazole. The protein was eluted by incubating the resin in NuPAGE LDS Sample Buffer (4X) (Invitrogen) and was loaded on a 15% polyacrylamide gel.

2.2.8 Bio-layer Interferometry

Bio-layer Interferometry (BLI) was carried out using an Octet Red385 (Sartorius) with Octet Streptavidin (SA) Biosensors (Sartorius) as previously described (Parker et al., 2021). Briefly, tips were equilibrated in 200 μL of 20 mM Tris (pH 7.4), 150 mM NaCl and 0.003% LMNG 10 min prior to the experiment, and wells were loaded with 50 μL of 20 mM Tris (pH 7.4), 150 mM NaCl and 0.003% LMNG that contained biotinylated TRPML1 (50-200 nM) for the loading step and sybody for the association step (concentration specified in Results section). All experiments included the following steps: equilibration, loading, equilibration, association and dissociation. K_Ds were determined by fitting the following model to the data:

$$Response = \frac{R_{max} * [Protein]\,(M)}{(K_D + [Protein]\,(M))} \quad (1)$$

R_{max}: Response at saturation

2.3 Structural and Functional Characterization of TRPML1-Sybody Complexes

2.3.1 Cryo-EM Sample Preparation and Data Collection

2.3.1.1 Complex Preparation

For the TRPML1-Syb94 structure in LMNG, 200 μg of purified TRPML1 in LMNG was incubated with a 1:3 molar excess of sybody for 1 hour on ice. The complex was injected on a Superose 6 Increase 10/300 GL (Cytiva) equilibrated in 20 mM HEPES (pH 8.0), 150 mM NaCl and 0.002% LMNG. Fractions were concentrated to 2.1 mg/ml using an Amicon Ultra-2 Centrifugal Filter 100 kDa MWCO (Millipore).

For the TRPML1-Syb57 structure in Digitonin, a 1:4 excess of Syb57 was added to 200 μg of purified and concentrated TRPML1 in 0.05% Digitonin. The complex was loaded on a Superose 6 Increase 10/300 GL column (Cytiva) equilibrated in the purification buffer (20 mM HEPES (pH 8.0), 150 mM NaCl and 0.05% Digitonin). The elution was concentrated to 3.3 mg/ml using an Amicon Ultra-2 Centrifugal Filter 100 kDa MWCO (Millipore). 400 μM PI(3,5)P_2 di8 lipid (Echelon Biosciences) was added and incubated with the complex for 30 min before grid preparation.

2.3.1.2 Grid Preparation

Grids were prepared by applying 3 μL of sample to freshly glow-discharged R 1.2/1.3 300 Mesh Cu grids (Quantifoil). They were then blotted for 7 s with 0 blot force at 4°C and 100% humidity before vitrification in liquid ethane with a Vitrobot Mark IV (Thermo Fisher Scientific).

2.3.1.3 Data Collection

Datasets were collected on a 300 kV Titan Krios G3i (Thermo Fisher Scientific) equipped with a K3 Summit camera (Gatan). Data collection was carried out with a 20 eV energy filter at a magnification of 81,000x with a pixel size of 0.535 Å/pixel. Datasets were acquired with a nominal dose of 49 $e^{-}/Å^2$ and -0.8 and -2.5 μm for the defocus range.

2.3.2 Cryo-EM Data Processing: TRPML1-Syb57

The dataset was processed using cryoSPARC v4.0-4.5 and RELION 4.0 (Figure 12A) (Kimanius et al., 2021; Punjani et al., 2017). The Relion implementation of MotionCorr2 and CTFFIND4 were used to process 2,496 movies (Rohou and Grigorieff, 2015; Zheng et al., 2017). The motion-corrected micrographs were imported into cryoSPARC, processed with Patch CTF Estimation and curated, resulting in a working set of 2,315 micrographs. Template and topaz picking were used to pick particles (Bepler et al., 2019). Templates for template picking were generated from a subset of micrographs, and then used for template picking for the whole dataset. 888,890 particles were picked. Two rounds of 2D classification were carried out (2.14 Å/pixel size), resulting in 160,768 particles. A topaz model was trained and 328,483 particles were picked. These particles were classified in two rounds of 2D classification (2.14 Å/pixel size), resulting in 147,744 particles. The particles were combined, while excluding duplicates, resulting in 226,846 particles. This final set was subjected to another two rounds of 2D classification, resulting in 184,003 particles. The 184,003 particles were reconstructed into Ab Initio reconstruction (four) and a single class with clear sybody and transmembrane domain (TMD) regions was selected (87,027 particles). These 87,027 particles were further classified (2D), resulting in 76,892 particles. Hetero refinement was carried out using two copies of the ab initio volume with TMD and sybody density and two copies of the ab initio volume with unclear density, from which 68,022 particles were obtained total. Particles were refined using non-uniform (NU) refinement. cryoSPARC's 3D classification was used to sort particles and two populations were obtained, with (48,890 particles) or without sybody. Particles were re-extracted at a pixel size of 1.07 Å/pixel and NU refinement with C4 symmetry enabled to obtain a structure at 3.3 Å

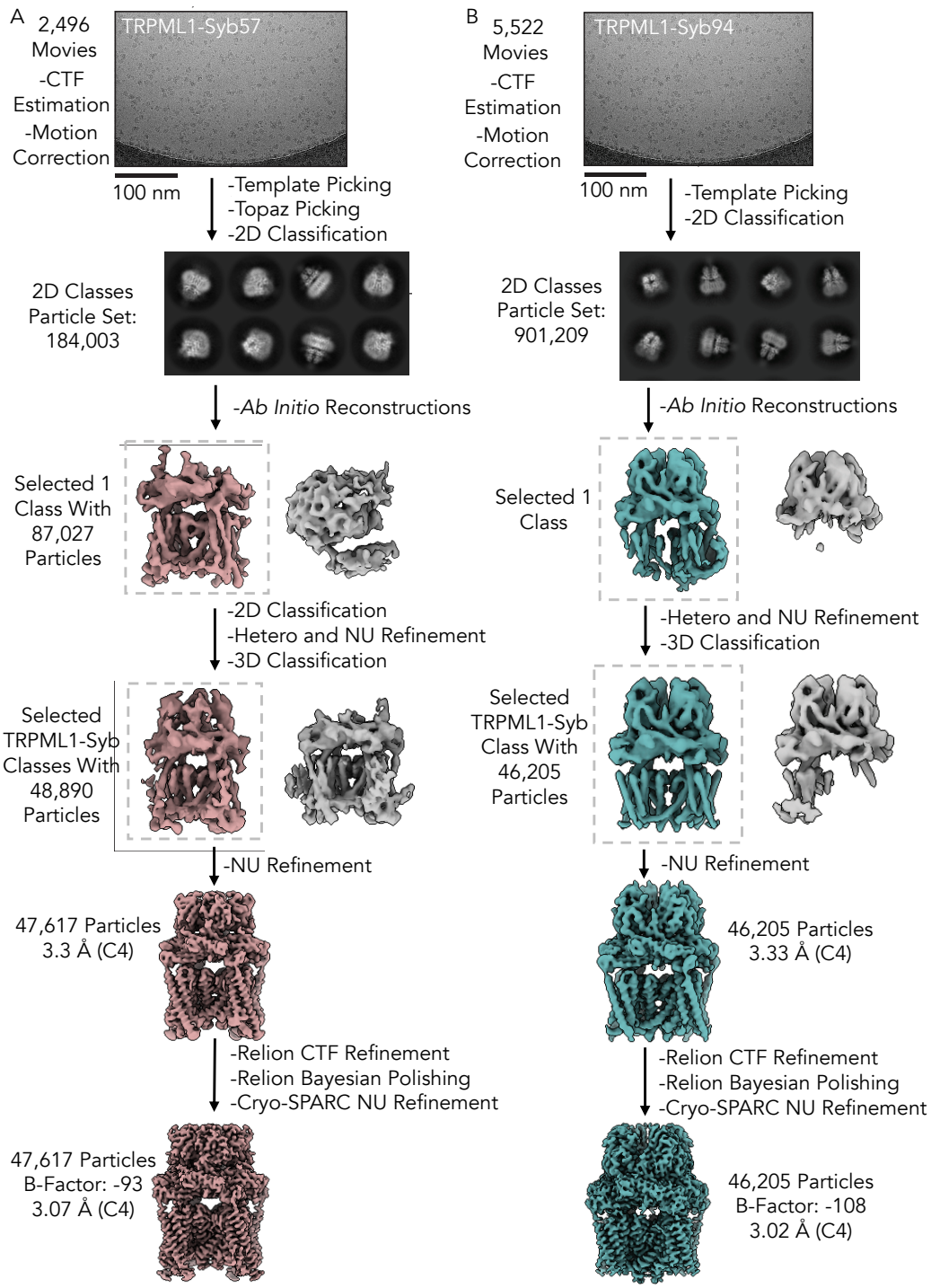

Figure 12: Cryo-EM processing pipeline. A) TRPML1-Syb57 and B) Syb94. Particles in colored maps were selected, while particles in grey maps were excluded. Images Provided by Ruth Pumroy.

(47,617 particles). The particles were used for two rounds of CTF refinements and Bayesian polishing in RELION. Finally, they were again transferred to cryoSPARC for NU refinement (C4). A structure at 3.07 Å sharpened with a B-factor of -93 was obtained.

2.3.3 Cryo-EM Data Processing: TRPML1-Syb94

The dataset was processed using cryoSPARC v4.0-4.5 and RELION 4.0 (Figure 12B) (Kimanius et al., 2021; Punjani et al., 2017). MotionCorr2 and CTFFIND4 were used to process the 5,522 movies (Rohou and Grigorieff, 2015; Zheng et al., 2017). 5,307 micrographs were obtained in cryoSPARC following Patch CTF Estimation and curation. 2,784,982 particles were picked using template picking. The particles were extracted and classified in two rounds of 2D classification, resulting in 901,209 particles (2.14 Å/pixel size). Classification was carried out to separate particles with good and poor TMD density. This was carried out by generating two Ab initio reconstructions using 901,209 particles, which produced a class with TMD + sybody and a class with sybody only. The TMD + sybody classes were used for four rounds of hetero refinement. At the end of the hetero refinement rounds, 202,717 particles were obtained. NU refinement (C4) was carried out with these particles, which produced a volume with good density for the sybody but poor density for the transmembrane region. Therefore, additional sorting was carried out following symmetry expansion using 3D classification in cryoSPARC. From this classification step, a map (46,205 particles) was obtained with high-quality density for the TRPML1 transmembrane helices after reducing symmetry. NU refinement (C4 symmetry) of the particles (1.07 Å/pixel size) resulted in a structure at 3.33 Å. CTF refinements and Bayesian polishing were carried out in RELION, and they were then transferred to cryoSPARC for NU refinement (C4) to obtain a final structure at 3.02 Å sharpened with a B-factor of -108.

2.3.4 Model Building

Human TRPML1 with PI(3,5)P_2 (PDB: 6E7P) and the AlphaFold prediction of Syb57 and Syb94 were used as starting models and in coot they were docked into the cryo-EM maps (Emsley and Cowtan, 2004; Jumper et al., 2021). These models were iteratively refined with Coot and

the PHENIX phenix.real_space_refine software package (Afonine et al., 2018). cryoSPARC's implementation of BlocRes (FSC=0.5) was used to generate local resolution maps. ChimeraX was used to generate images (Pettersen et al., 2021).

2.3.5 TRPML1 Activity Assays

2.3.5.1 FURA-2 Assay

FURA-2 Assay was carried out as described by Kilfeather et al (2024). Briefly, SH-SY5Y cells were trypsinised and seeded at a density of 1 million cells/ml in a 96 well plate (24,000 cells per well). Directly after seeding, each well was transfected with 200 ng of DNA mixed with lipofectamine-2000 (Invitrogen) in a 1:2.5 ratio (DNA:Lipofectamine) in Opti-MEM (Gibco). Media was changed 4 hours post-transfection and cells were left to express the construct at 37°C for 48 hours. Prior to measurements, cells were incubated in 2.5 mM FURA-2 AM in HBSS with calcium and magnesium (Gibco) for 1 hour at 37°C. Samples were then imaged on a FlexStation 3 Multi-Mode Microplate Reader (Molecular Devices) at 37°C with excitations at 340 and 380 nm and detection at 510 nm. Following a baseline measurement, ML-SA5 or sybodies were injected in the wells (See Results section for concentration). Data analysis was carried out using R.

2.3.5.2 Whole-Cell Patch Clamp

HEK293T cells were maintained in Dulbecco's Modified Eagle's Medium (DMEM) (Thermo Fisher) which was enriched with 10% fetal bovine serum, 50 U/ml penicillin, and 0.05 mg/ml streptomycin. The cells were incubated at 37°C with 5% CO_2. Cells were seeded at 60% confluence in a 6-well plate and transfected with Fugene-HD transfection reagent (Promega). Each well received 2.5 μg of TRPML1 plasmid (vector and mutation details unspecified) and 0.5 μg of CD8 to mark successful transfection. 24 hours post-transfection, the cells were transferred onto 6 mm borosilicate glass cover slips in a 48-well plate and used for electrophysiological studies 24-48 hours later.

Micropipettes were pulled from thin-walled borosilicate glass (Harvard Apparatus), polished, and had resistances ranging from 1.5 to 2.5 MΩ in the solutions used. The extracellular bath solution was composed of 140 mM NaCl, 6 mM KCl, 2 mM $CaCl_2$, 1 mM $MgCl_2$, 10 mM glucose, and 10 mM HEPES, adjusted to pH 7.4 with NaOH. The intracellular pipette solution contained 135 mM CsCl, 5 mM EGTA, 1 mM $MgCl_2$, 1 mM $CaCl_2$, 5 mM Na_2ATP, 0.1 mM Na_2GTP, and 10 mM HEPES, with a pH of 7.2 adjusted using CsOH. The Na_2ATP and Na_2GTP were added fresh on the day of the experiment. Final concentrations of agonists or sybodies were prepared by diluting stock solutions in the bath solution on the day of testing.

Currents were recorded from CD8-positive cells, identified using anti-CD8 coated Dynabeads (Thermo Fisher), at room temperature (20°C-22°C) under the whole-cell patch-clamp configuration using an Axopatch 200B amplifier (Molecular Devices). The setup featured 2 kHz low-pass filtering, 10 kHz digitization, and over 70% series resistance compensation when necessary. A KCl-agar bridge connected to an Ag-AgCl reference electrode was used to link the bath solution. After establishing the whole-cell configuration, cells were held at 0 mV, and 1-second voltage ramps from -100 to 50 mV were repeatedly applied.

Sybodies were administered at a concentration of 2 μM via gravity perfusion for 2 minutes, followed by a minimum 2-minute wash with control solution. The mean peak inward and outward current amplitudes were measured at -100 mV and +100 mV, respectively. Data analysis was conducted using Clampfit (Molecular Devices) and OriginPro 7.5 (OriginLab Corporation).

2.4 Engineering Synthetic Nanobodies to Investigate TRPML1 Localization

2.4.1 Sybody Fluorescence Microscopy

HeLa cells were grown in T75 flasks with DMEM supplemented with GlutaMAX (Gibco). They were seeded at a density of 100,000 cells in 6 well plates (Corning) containing 3 coverslips (#1.5) in each well. 24-hours after seeding, cells were transfected with a mixture of 1.5 μg of DNA and

3 μg of Polyethylenimine Hydrochloride MW 40,000 (PEI MAX) (Polysciences) incubated in 100 μL of OptiMEM (Gibco) for 12 min at RT. Media was changed after 4 hours to reduce cell death due to PEI toxicity. The protein was left to express for 24 hours at 37°C. Coverslips were washed with 1X PBS (137 mM NaCl, 2.7 mM KCl, 10 mM Na_2HPO_4 and 1.8 mM KH_2PO_4) and fixed with 4% paraformaldehyde (PFA) at pH 7.4 for 20 min at 4°C. Once fixed, the cells were washed with 50 mM ammonium chloride and 1X PBS. Cells were permeabilized with 0.1% Triton X-100 for 10 min at room temperature. Cells were then washed with 1X PBS and incubated with 1 sybody in a solution of 1X PBS with 1% BSA and a 1:500 dilution of primary (Anti-c-Myc antibody, Mouse monoclonal, clone 9E10, Sigma-Aldrich) and secondary (Donkey anti-Mouse IgG Highly Cross-Adsorbed Secondary Antibody, Alexa Fluor 647; Thermo Fisher Scientific) antibodies for 2 hours. Cells were washed with 1X PBS, stained with DAPI at a concentration of 1 μg/ml for 5 min at RT and washed again with 1X PBS. Coverslips were mounted using Epredia Immu-Mount mounting media (Thermo Fisher Scientific) on glass slides, and stored at 4°C before imaging. Samples were imaged on a ScanR widefield fluorescent microscope (Olympus) using a 40x lens. Confocal microscopy was carried out on an LSM-780 (Zeiss) using a 63x 1.2 NA Water C-Apochromat lens or 100x 1.4 NA Oil Plan-Apochromat lens, or an LSM-980 with AiryScan2 (Zeiss) using a 63x 1.43 NA Oil lens.

2.4.2 Sybody Fusions Expression and Purification

Purification of fusions was trialed in bacteria and in HEK293F cells. It was found that higher yields were obtained in HEK293F cells. Fusion expressions and purifications were undertaken using a similar protocol to the one used for the luminal domain purification. The modifications include expression at smaller scales (50-100 ml) and SEC purifications of the fusions were carried out using Sepax SRT-SEC100 column or SRT SEC-300 columns (Sepax Technologies) columns equilibrated in 1X PBS (pH 7.5).

2.4.3 Sybody Dimer Expression and Purification

HEK293 cells were seeded in 15 cm petri dishes 2 days prior to transfection. Cells were transfected using PEI-MAX in a 1:2 ratio with dimer DNA (1 μg per ml of media, 20 ml of media used per plate) diluted in Opti-MEM (Gibco) (1 ml per 20 μg of DNA). Dimers were expressed for 72 hours. Media was then harvested by centrifugation (3,100 g for 6 min), filtered and dialysed in 1X PBS (pH 7.5-8) using Spectra/Por 3 3.5 kD dialysis membrane (Repligen) overnight at 4°C. The pH of the media was adjusted 7.75-8 before a 2-hour incubation with Ni-NTA resin at 4°C. The resin was washed with 20 mM HEPES (pH 8), 150 mN NaCl (HBS) and 25 mM imidazole, and HBS with 150 mM NaCl and 40 mM Imidazole. Proteins were eluted with HBS (pH 8.0) with 250 mM Imidazole. The sample was injected on a Superose 6 Increase 10/300 GL (Cytiva) equilibrated in HBS (pH 8.0) and concentrated with 10 kDa MWCO Amicon Ultra Centrifugal Filter (Millipore).

2.4.4 Cryo-Electron Microscopy with Gold-Labelled Sybodies

Gold-labeling of sybodies was performed per manufacturer instructions using the 10 nm Gold Conjugation Kit (Abcam) for lysine conjugation and 5 nm gold maleimide kit (Sigma-Aldrich) for cysteine conjugation with cysteine mutants.

Negative staining was performed using 2% uranyl acetate. A 3 μL aliquot of the sample was applied to an electron microscopy grid, followed by the addition of 3 μL of 2% uranyl acetate. The sample was incubated with the stain for 2-3 minutes, after which the excess stain was gently blotted off with filter paper. A second 3 μL aliquot of uranyl acetate was then applied, incubated for another 2-3 minutes, and subsequently blotted. The grid was allowed to air dry for 15 minutes and screened on a JEOL electron microscope.

For lysosome isolation, HEK293 cells expressing TRPML1-mNeonGreen-1D4 were placed on ice, media was removed, and they were rinsed with ice-cold KPBS containing 1x HALT^{TM} protease and phosphatase inhibitors (PPI) (Thermo Fisher Scientific). Cells were then scraped into a conical tube and centrifuged at 1000 g for 2 minutes at 4°C. The pellet was resuspended

in 950 μL KPBS with 3.6% OptiPrep. The cell suspension was homogenized, passed through a 25G syringe, and centrifuged at 1000 x g for 10 minutes at 4°C. The top layer of the supernatant was transferred. The supernatant was incubated with KPBS + 3.6% OptiPrep pre-washed beads at 4°C for 2 hours, then centrifuged briefly. 100 μL of 10 mg/mL 1D4 peptide was added to the beads and incubated for 2.5 hours at 4°C for lysosome elution.

Grids were prepared as described in the cryo-EM section. The entire process was carried out in an environment maintained at 4°C with 95% humidity. Quantifoil R3.5 x 1 mm gold grids (Au H2) were used for sample preparation. TetraSpeck^{TM} microspheres (Thermo Fisher Scientific) were added to these samples for channel alignment. Confocal imaging was carried out on a Zeiss LSM 900 with Linkam cryo-stage at the Electron Microscopy Resource Lab at the University of Pennsylvania.

2.4.5 STORM

Lysosome staining for super-resolution microscopy was carried out using a protocol adapted from Bond et al (2024). Briefly, HeLa cells were seeded in LabTek-II imaging chambers (Nalge Nunc, Thermo Fisher) and transfected 24 hours after seeding using lipofectamine-3000 in a 1 μg DNA (GFP-TRPML1 WT in pcDNA5-FRT-TO) : 1.5 μL lipofectamine ratio in Opti-MEM (Gibco). 24 hours post-transfection, cells were washed with 1X PBS and fixed in 4% PFA at room temperature for 20 min. Cells were permeabilized and blocked with blocking buffer (PBS with 10% donkey serum and 0.1% saponin) for 1 hour at room temperature. Sybodies and primary antibodies were diluted (see Results section for concentration) in blocking buffer and cells were stained with the sybodies, primary and secondary antibodies sequentially at room temperature for 1 hour each. Between the sybody and primary antibody steps, cells were washed with 1X PBS (1 wash) and 0.01% saponin in PBS (2 washes) for 2 min, and between the primary and secondary staining and at the end of the staining steps, samples were washed with 1X PBS (1 wash) and 0.1% saponin in PBS (3 washes) for 2 min. Samples were imaged at 30°C in PBS for conventional imaging and overview scans or BME (143 mM β-Mercaptoethanol and 1% GLOX buffer in 10% glucose, 50 mM Tris (pH 8.0) and 10 mM NaCl as described by Xu et al., 2017)

for STORM imaging. Imaging was carried out using a Nanoimager (ONI) equipped with 405 nm, 488 nm, 561 nm and 640 nm lasers, 498-551 and 576-620 nm band-pass filters in channel 1, 666-705 nm band-pass filters in channel 2, a 100X 1.45 NA oil immersion objective (Olympus), and a Hamamatsu Flash 4 V3 sCMOS camera. For overview scans, 10x10 frames were collected of each sample. For conventional images, 10 images were collected with an exposure time of 100 ms. For STORM imaging, an exposure time of 15 ms was used and 30,000 images were collected. Images were analyzed on FIJI and NimOS (ONI) for image presentation (Schindelin et al., 2012).

2.4.6 Immunoprecipitation with Sybodies

2.4.6.1 Immunoprecipitation with Directly Conjugated Sybodies

2 mg of sybody was incubated and successfully conjugated to 40 mg of resin (1:20 w/w) overnight hr at 4°C as verified by SDS-PAGE.

Pellets of FLAG-AVI-TRPML1 HEK293F transfected cells (48 hours of expression) were thawed and resuspended in 1X PBS (1.2 ml of PBS per 5 ml of culture pellet) with the addition of 0.5 μL benzonase. The resuspended pellet was incubated on ice briefly before adding n-dodecyl-β-D-maltoside (DDM) to a final concentration of 1%. Solubilization was performed for 1 hour and 30 minutes on a rotating wheel at 4°C. Following solubilization, the unsolubilized material was pelleted through ultracentrifugation at 200,000 g for 20 minutes. The solubilized fraction was then incubated with sybody resin for 3 hours at 4°C. The resin was washed five times with TBS to remove excess detergent and contaminants. Two samples were prepared from each sybody resin, one for western blot, and another for mass spectrometry. For the western blot, the samples were eluted by incubation with SDS loading dye, loaded onto a polyacrylamide gel and analyzed using mouse anti-FLAG antibody (Thermo Fisher Scientific; 1:10,000). The experiment was repeated with untransfected HEK-293F cells (6 ml of culture per tested condition). The samples were analysed by western blot using anti-TRPML1 antibody (Santa Cruz; mouse monoclonal F10 at 1:100 dilution).

Mass spectrometry was carried out as previously described (White et al., 2017). Purified protein was run on a 10% polyacrylamide gel. The gel was coomassie stained to localize the bands of interest, which were then excised, destained with 50 mM ammonium bicarbonate and 50% acetonitrile (30 min at RT) and dehydrated with acetonitrile. Then, thiols were reduced with 10 mM TCEP in 0.1 M ammonium bicarbonate for 30 min at RT, and alkylated with 50 mM chloroacetamide in 0.1 M ammonium bicarbonate for 30 min at RT. Proteins were digested using 10 ng/μL trypsin in 10 mM ammonium bicarbonate for 16-20 h at 37°C with shaking at 650 rpm. Peptides were extracted by incubating the gel piece twice for 15 min at 37°C (650 rpm shaking) in 1.7% formic acid and 66.7% acetonitrile, collecting the supernatant each time. Peptides were dried and analysed using liquid chromatography-tandem mass spectrometry (LC-MS/MS). Data analysis was carried out by the mass spectrometry facility at the Oxford University Biochemistry Department.

2.4.6.2 Immunoprecipitation with Avi-Tagged Sybodies

Resin was prepared by incubating 12.5 μL of Pierce^{TM} High Capacity Streptavidin Agarose (Thermo Fisher Scientific) with 3 μg of biotinylated sybody for each sample. To determine the efficiency of sybody biotinylation, the binding of the sybody to the resin was assessed by SDS-PAGE.

12.5 ml of PBS-washed FLAG-AVI-TRPML1 transfected HEK-293F culture (48 hours of expression) and 10 million SH-SY5Y cells were solubilized in PBS supplemented with 1% LMNG and benzonase for a total of 2 hours at 4°C. Following solubilization, the lysate was centrifuged at 30,130 g for 5 minutes at 4°C to remove cellular debris. The resin was incubated with 100 μL of the lysate for 1 hour at 4°C, and was washed using PBS supplemented with 0.01% LMNG. For elution, 10 μL of 4X SDS loading dye with beta-mercaptoethanol and 10 μL of PBS were added to the resin, and the samples were loaded on polyacrylamide gels without boiling. Anti-FLAG antibody (Thermo Fisher Scientific; 1:10,000) was used to probe the transfected HEK-293F cells, while anti-TRPML1 antibody (Santa Cruz; mouse monoclonal F10 at 1:100 dilution) was used for the SH-SY5Y cells.

2.4.6.3 Immunoprecipitation with 1D4-Tagged Sybodies

Untransfected HeLa cells were harvested, washed twice with PBS, and pelleted by centrifugation at 1300 g for 2 minutes, yielding 50 mg of pellet per 15 cm plate. The pellets were frozen at -80°C and later lysed by thawing. Sybody-bound resin was prepared by loading 20 μg of sybody onto 40 μL of Rho1D4 antibody resin (in-house) for 1 hour at 4°C. The resin was then incubated for 1 hour with LMNG-solubilized HeLa cell lysate (equivalent to 25 mg of pellet in 500 μL PBS with 1X Halt^{TM} Protease and Phosphatase Inhibitor Cocktail) generated by a freeze-thaw cycle and clarified by centrifugation at 21,000 g. The total protein loaded on the resin (130 μg) was quantified using the Pierce^{TM} 660 nm Protein Assay Kit. The resin was washed three times with TBS (pH 7.5, 300 mM NaCl) containing 0.1% LMNG, and the bound proteins were eluted with SDS with β-mercaptoethanol. Samples were run on Novex^{TM} WedgeWell^{TM} 4-20% Tris-Glycine gels, loading approximately 20 μg of protein per well for samples with known protein concentrations.

For western blotting, the transfer was carried out using nitrocellulose membrane with the XCell II Blot Module (Thermo Fisher Scientific), which was run at 60 V at 4°C for 60 min. After transfer, the membrane was washed three times in 1X TBST, followed by incubation with rabbit polyclonal TRPML1 primary antibody (Proteintech, 5291-1-AP; 1:500) and mouse anti-beta actin conjugated to biotin (Invitrogen, MA5-15739-BTIN; 1:1000) in 1X TBST + 5% nonfat dry milk overnight at 4°C. The membrane was washed again and incubated with secondary anti-rabbit HRP conjugate antibody (1:2,500; Promega, W4011) and goat-anti-mouse IR dye (1:10,000; LI-COR, 926-68020) for 1 hour at room temperature. Following three TBST washes, the blot was developed with the ECL Prime Western Blotting reagents and imaged using the ImageQuant LAS 4000 system (GE Healthcare).

2.5 Data Presentation and Visualization

Figures in this thesis were generated with: BioRender, Microsoft Excel (Microsoft), OriginPro (OriginLab), Microsoft PowerPoint (Microsoft), Prism 10 (GraphPad), Octet Data Analysis HT

Software (Sartorius), FIJI, NimOS (ONI), JalView, ChimeraX and Python packages (Pettersen et al., 2021; Schindelin et al., 2012; Waterhouse et al., 2009). This document was compiled on Overleaf using the template: Thesis Template OxfordPav.

3 | The Molecular Basis of Proton-Coupled Cystine Transport by Human Cystinosin

3.1 Investigating Cystinosin Proton-Coupled Transport Using Two-Electrode Voltage Clamp

The results presented in this chapter have been included in the following publication: Löbel, M., Salphati, S.P., El Omari, K., Wagner, A., Tucker, S.J., Parker, J.L. and Newstead, S., (2022) Structural basis for proton coupled cystine transport by cystinosin. *Nature Communications*, 13, Article 4845.

Despite the extensive work that has been carried out to understand how cystinosis is caused by the lysosomal proton-coupled cystine transporter cystinosin, little remains known about its transport mechanism (Cherqui and Courtoy, 2017; Ruivo et al., 2012). This has limited our understanding of the effects of cystinosis mutations on cystinosin activity, which may enable to correlate clinical phenotypes with the effects of mutations. Crystal structures of plant cystinosin (apo, sybody/nanobody and cystine-bound) were obtained by Mark Löbel in the Newstead lab. Based on the mechanism suggested for the plant structure along with the AlphaFold model of the human protein, mutants were generated to investigate the mechanism of the human protein using Two-Electrode Voltage Clamp (TEVC) (Aim 1) (Jumper et al., 2021).

Cystinosin transport has previously been characterized using TEVC (Ruivo et al., 2012). In the TEVC experiments, the measured currents are generated by the movement of a proton movement across the plasma membrane and are used to assess transporter activity, assuming strict coupling between cystine and proton transport. These assumptions have been validated by Ruivo et al (2012) who demonstrated using TEVC in *Xenopus laevis* oocytes that cystinosin is a cystine:proton symporter and that the transport occurs in a 1:1 ratio using proton-selective microelectrodes, radio-ligand uptake assays and ion substitution experiments.

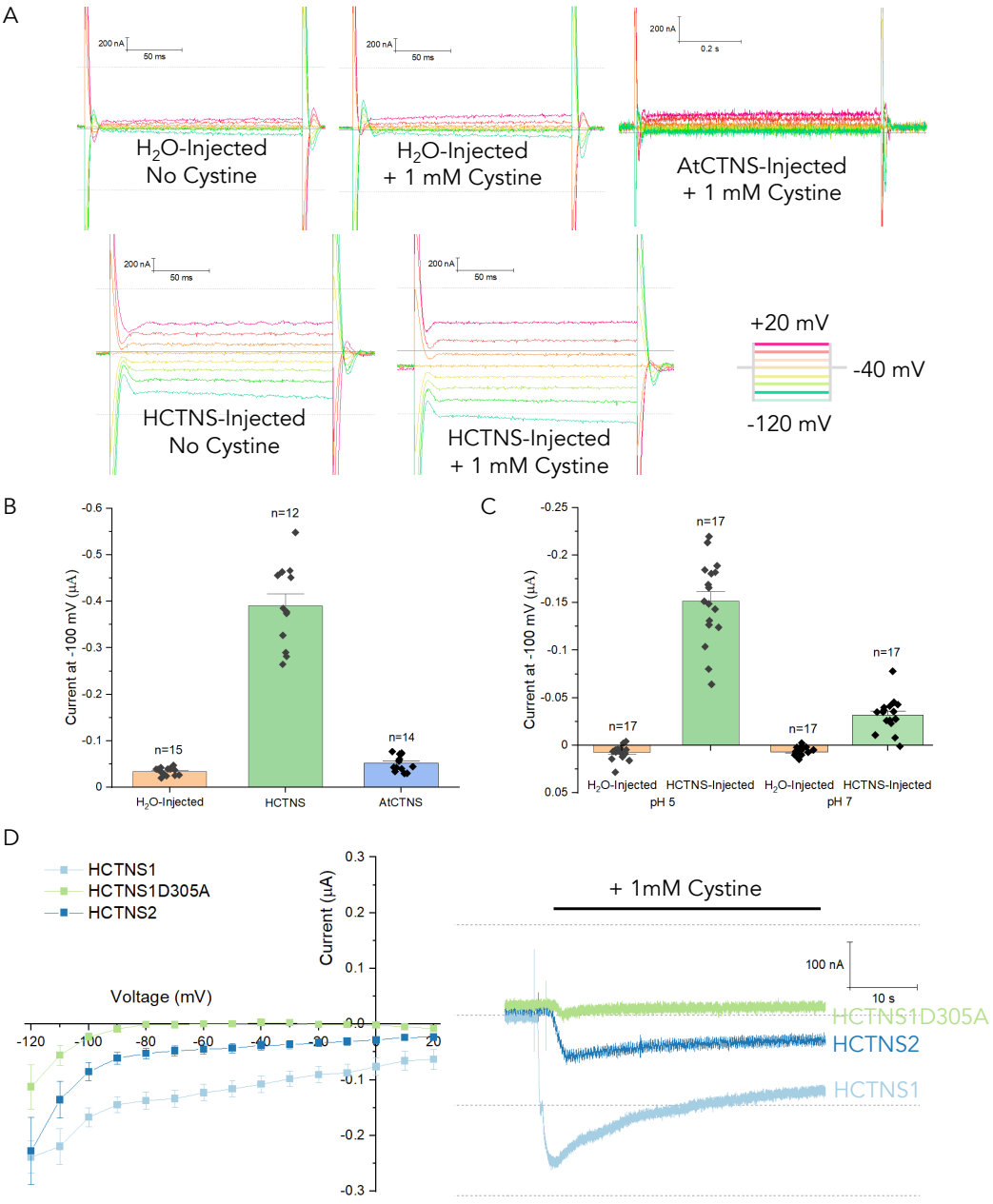

Figure 13: Initial TEVC characterization of CTNS proton currents. A) Raw currents before and following 1 mM cystine addition measured in water-injected, human CTNS-injected and plant CTNS-injected oocytes. B) Cystine-induced currents at -100 mV measured in water-injected, human CTNS-injected and plant CTNS-injected oocytes. C) Cystine-induced currents at -100 mV measured in water-injected and human CTNS-injected oocytes at pH 5 and 7. D) IV-curve (cystine-induced current) and raw currents at -40 mV for the two different isoforms of cystinosin (HCTNS1: HCTNS ΔGYDQLN ; HCTNS2: HCTNS-LKG) and a previously characterized mutant with no transporter activity due to a mutation in a proton-coupling residue (HCTNS1D305A).

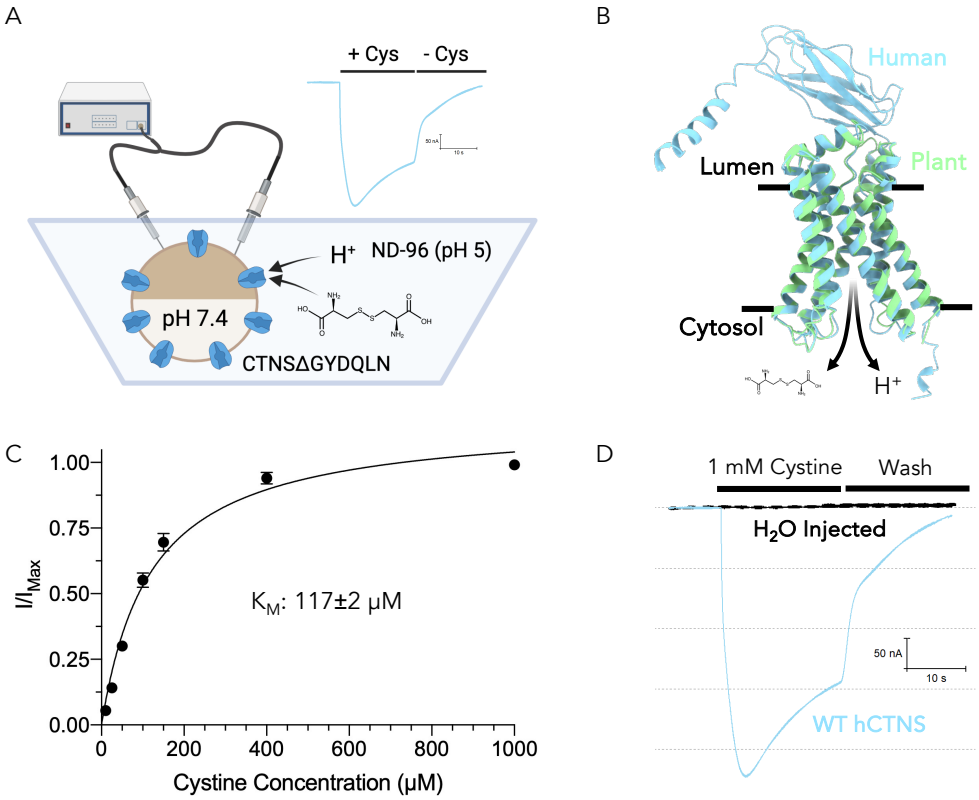

Figure 14: TEVC setup and cystine-evoked proton currents generated by wild-type human cystinosin. A) TEVC was carried out using *Xenopus Laevis* oocytes expressing wild-type human cystinosin without its lysosomal targeting motif (ΔGYDQLN). Currents were measured in a pH 5 solution with and without cystine, which was used to calculate cystine-evoked currents. B) The plant structure (obtained by Mark Löbel) and human alpha-fold model of cystinosin suggest that the two proteins are very similar. Cystinosin has 7 transmembrane helices and transporters a proton and cystine (1:1) from the lysosomal lumen to the cytosol. The main difference between the two proteins is the presence of a luminal domain in the human protein that is absent in the plant protein. C) Kinetics of proton-coupled transport by cystinosin was characterized by measuring cystine-evoked currents at different cystine concentrations (5-1000 μM). A representative dose-response curve is shown with I/I_{max} being the current measured at a concentration divided by the maximum response for that each oocyte. The data was fitted using the Michaelis-Menten equation and an apparent K_M of 117 μM was obtained (n=16). D) Cystine addition results in a ~300 nA inward proton current (negative current) in wild-type cystinosin injected oocytes (blue) clamped at -40 mV that is not observed in water-injected oocytes (black).

A series of experiments were carried out to validate the system used for the experiments presented below (Figure 14A and B). Firstly, cystine-induced currents were measured in oocytes injected with water, plasma-membrane localized human cystinosin (HCTNSΔGYDQLN; later referred to as HCTNS or CTNS) and *Arabidopsis thaliana* CTNS-injected (AtCTNS). Measurable cystine-induced currents were observed in HCTNS-injected oocytes, but not in water or plant-injected cystinosin oocytes (Figure 13A and B). It is common for plant proteins to weakly express in oocytes as they may require codon-optimization or additional post-translational modifications (Feng et al., 2013). It was also found that prior to the addition of cystine, currents were measured across the tested voltage protocol (-120 mV to +20 mV with 20 mV steps for 200 ms). These could be proton leak currents, which were also observed in experiments with AtCTNS reconstituted in liposomes (Löbel et al., 2022). Through proton leaks, cystinosin could play a role in maintaining pH homeostasis in lysosomes. These currents were later observed to be mutant-dependent, but strong variability between batches meant that quantification did not yield robust results. Further experiments would be required to characterize their properties. These leak currents have previously been observed in proton-coupled transporters (Beale et al., 2015; Mackenzie et al., 2006; Ruivo et al., 2012). The system was also validated by comparing the cystine-induced currents in CTNS-injected oocytes at pH 5 and 7 (Figure 13C). Current amplitude was significantly greater at pH 5 than pH 7, which results from the weaker proton gradient across the membrane and the deprotonation of cystine at pH 7 (net -1 charge) (Banai, 1984). When mutating the previously identified proton-coupling residue (D305A), cystine currents were fully ablated (Figure 13D) (Ruivo et al., 2012). Lastly, the cystine-induced currents from both plasma-membrane localizing constructs (construct 1: HCTNSΔGYDQLN and construct 2: HCTNS-LKG) were compared to identify the isoform that generates the strongest cystine-induced currents (Figure 13D) (Taranta et al., 2008). HCTNSΔGYDQLN produced the strongest cystine-induced currents and was therefore used for the experiments below. All analysis below was done by quantifying cystine-induced currents at -40 mV as this is the oocyte resting membrane potential and lysosome membrane potential (Xu and Ren, 2015). These measurements were all made by clamping the oocyte membrane potential to -40 mV for 200 ms.

Following initial validation of the system, the kinetics of proton-coupled transport by cystinosin

were investigated. the oocytes were perfused in solutions with different cystine concentrations ranging from 5 μM to 1 mM, and the resulting currents were measured to generate a dose-response curve. An apparent Michaelis-Menten constant (K_M) of 117 $\pm$ 2 μM was obtained based on 3 biological replicates (one replicate displayed in Figure 14C), which is significantly lower than other amino acid transporters and the concentration at which cystine will typically crystallize in lysosomes (Jézégou et al., 2012; Oude Elferink, 1983). This is higher than the 10 μM K_M of *A. thaliana* CTNS (Löbel et al., 2022). It was hypothesized that one of the key differences between the plant and human cystinosin that may explain this discrepancy is the absence of the luminal domain in the plant protein.

3.2 The Luminal Domain of Human Cystinosin is Not Required for Proton-Coupled Transport

Cystinosin was predicted to have a luminal domain with an Ig-like fold and 7 glycosylation sites. Glycosylated luminal domains or accessory subunits are found in other lysosomal membrane proteins to play a functional role or protect the protein from degradation (Li et al., 2016; López et al., 2020; Schmiege et al., 2017). The extracellular domain of CTNS shows poor conservation across eukaryotes (Figure 15B), it is not present in the plant protein and only a few mutations in this domain have been found to cause cystinosis (David et al., 2019). Therefore, the role of this domain in the transporter cycle was investigated.

Despite the significant decrease in activity resulting from the deletion of the domain (HCTNSΔ2-115), the K_M was found not to be affected (117 μM $\pm$ 2 μM compared to 117 μM $\pm$ 29 μM) (Figure 15A and C). An additional construct that includes the signaling peptide sequence of cystinosin was generated (HCTNSΔ25-115) to test if the reduced currents resulted from inefficient translation (Nevo et al., 2017). However, the currents were observed to be weaker in this construct than HCTNSΔ2-115 so this was not investigated further (Figure 15C). This suggests that the luminal domain is not essential for substrate binding and transport. The measured currents may be smaller due to reduced translation efficiency, trafficking to the plasma

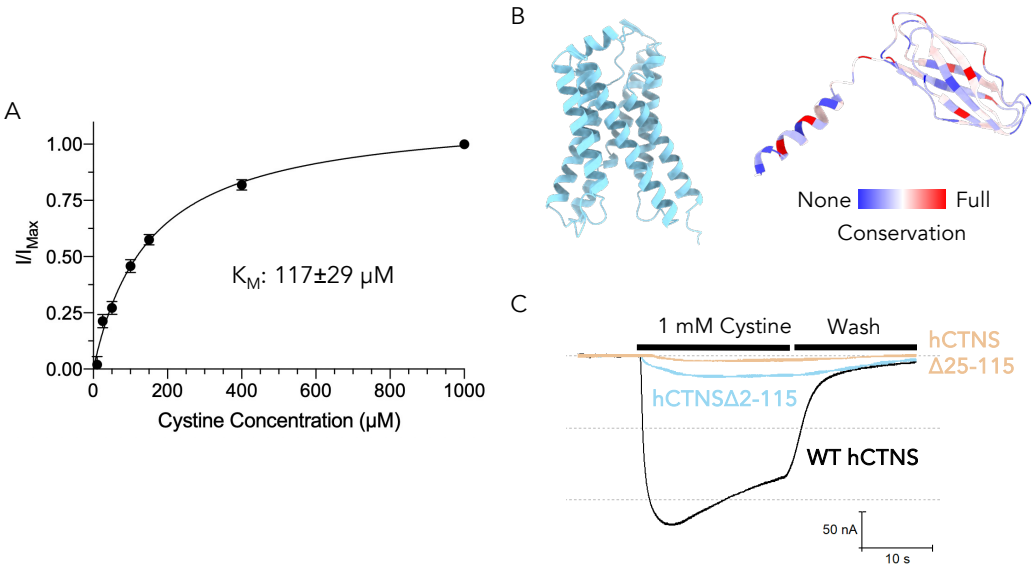

Figure 15: Effect of luminal domain deletion on proton-coupled cystine transport. A) Representative dose-response curve for cystinosinΔ2 – 115 which was fitted using the Michaelis-Menten equation. A K_M of 117 μM (n=16) was obtained, like for the construct with the luminal domain. B) On the left is displayed the model of the investigated construct without the luminal domain. On the right is displayed the model of the luminal domain with sequence conservation across eukaryotes (excluding species without the domain) mapped onto it. Sequence conservation is low relative to the transmembrane regions. C) Representative TEVC traces at -40 mV of cystine-evoked currents by cystinosinΔ2 – 115 and cystinosinΔ25 – 115. CystinosinΔ2 – 115 still generates cystine-evoked currents, while the addition of the signaling peptide results in reduced transport (cystinosinΔ25 – 115).

membrane and protein stability. Therefore, the difference in K_M between the plant and human protein may result from other minor differences between the two proteins or due to the different assays being used. Other transporters have been determined to have luminal domains or extracellular domains that are not involved in transporter activity or substrate binding (Beale et al., 2015; Zhang et al., 2016). All residues investigated from hereafter are conserved between the human and plant protein.

3.3 Identification of a Cystine Binding Site

Amino acid and peptide transporters typically transport multiple substrates (Kandasamy et al., 2018). Amino acid transporters typically transport groups of amino acids (cationic, anionic, small neutral or large neutral) and were historically classified as systems based on their amino acid specificity and ion dependence, but are now classified based on sequence homology (SLCs) (Kandasamy et al., 2018). Amino acid recognition in transporters involves hydrogen bonding with the backbone carboxyl and amino group of the amino acid, orientating it in a binding cleft that can accommodate its side chain (steric constraint) and will form amino acid-specific interactions (salt bridges and hydrogen bonds) (Jungnickel et al., 2018; Rodriguez et al., 2021). Cystinosin is highly specific for L-cystine and we thought to define the molecular basis for this specificity (Kalatzis et al., 2001). A 3.37 Å structure of cystine-bound AtCTNS in an outward-open state (open on luminal side) was obtained by Mark Löbel (Newstead Lab) (Löbel et al., 2022). Based on this structure, some residues were suggested to be essential for cystine binding. The corresponding residues in the human protein were identified to be K273 (TM5) and K280 (TM5) by aligning the human AlphaFold model and the plant structure (Figure 16A). In the structure, K273 and K280 bind to the two carboxyl groups, clamping cystine in place. These interactions were expected to be responsible for substrate specificity as they are only formed if the dipeptide is of the correct length (7 Å).

K273 was mutated to an alanine, and K280 was mutated to both alanine and asparagine. K280 and K273 mutations caused a complete loss of activity (Figure 16A) without disrupting trafficking of the protein (Figure 16C). This supports the essential of these residues in the transport

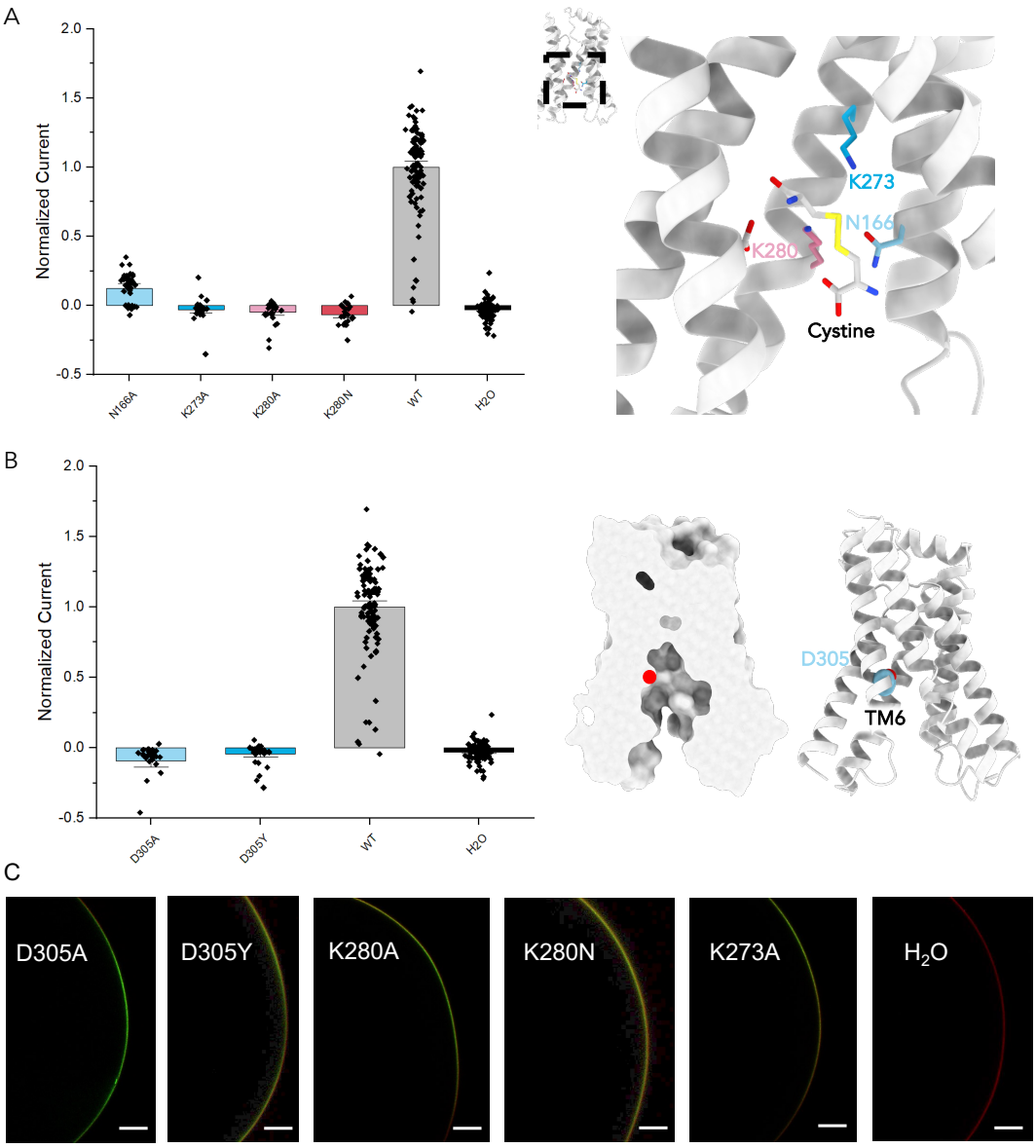

Figure 16: Identification of a cystine and proton binding site. A) Mutations in residues suggested to be involved in cystine binding eliminates cystine transport. Normalized currents are obtained by subtracting current before the addition of cystine from currents after the addition of cystine. These currents are normalized by dividing them by the mean current of wild-type cystinosin-injected oocytes from the same batch. B) Mutating the previously identified proton coupling residue eliminates proton coupled transport by cystinosin. In the obtained structure and the alpha-fold model, the transporter does not form a full channel and the proton coupling residue is exposed to the cytosolic side. This enables regulation of proton association/dissociation in the different states and prevents proton leakage. C) *X. laevis* oocytes injected with H_2O, mutant or WT CTNS-GFP (green) and stained with agglutinin (membrane; red) to assess mutant surface expression. All the mutants that no longer display activity localize to the plasma membrane. If cystinosin-GFP is not injected (i.e. H_2O), no emission is observed at 510 nm. Scale bar: 100 µm

cycle and substrate binding. N166 was suggested to be involved indirectly in cystine binding or potentially interacted with a less well-defined region of the cystine. Mutation of this residue reduced transport but did not completely abolish it (Figure 16A).

D305 was previously identified by Ruivo et al (2012) to be a proton binding site in CTNS. In the structure, D305 (TM6) is found to form a hydrogen bond with a cystine amino group, which bears a proton. To confirm the role of this residue in the transport cycle, the D305A and D305Y mutants were generated. Both mutants localized to the plasma membrane, but lost all of their activity (Figure 16B and C). This result confirms the role of D305 as a proton-binding site in CTNS.

Once the two substrates from the lysosomal lumen are bound, CTNS is expected to undergo conformational changes to transition from an outward open state to an inward open state (state of the plant structure and alphafold model) as described by the alternating access mechanism for secondary active transporters (Jardetzky, 1966).

3.4 A Salt Bridge Stabilising the Inward-Open State Acts as a Luminal Gate

Two sets of residues were suggested to be involved in inducing these conformational changes: the prolines of the PQ-loops motifs and the salt bridge that is observed on the luminal side of the protein at the site of substrate entry (Figure 17A and B). Salt bridges commonly act as gates and regulators of conformational state in SLCs (Krishnamurthy and Gouaux, 2012; Law et al., 2008; Parker et al., 2021a; Pedersen et al., 2014; Solcan et al., 2012). Therefore, the role of the luminal D205 (TM3) and K335 (TM7) salt bridge in transport was investigated.

Alanine mutations in either residues eliminated proton currents, confirming their essential role in transport (Figure 17A and C). It was observed that these mutations resulted in a weak positive current, suggesting an outward proton current. Cystine binding in this mutant may stabilize an outward open conformational state that favors outward proton leaks. Q315 is expected to interact

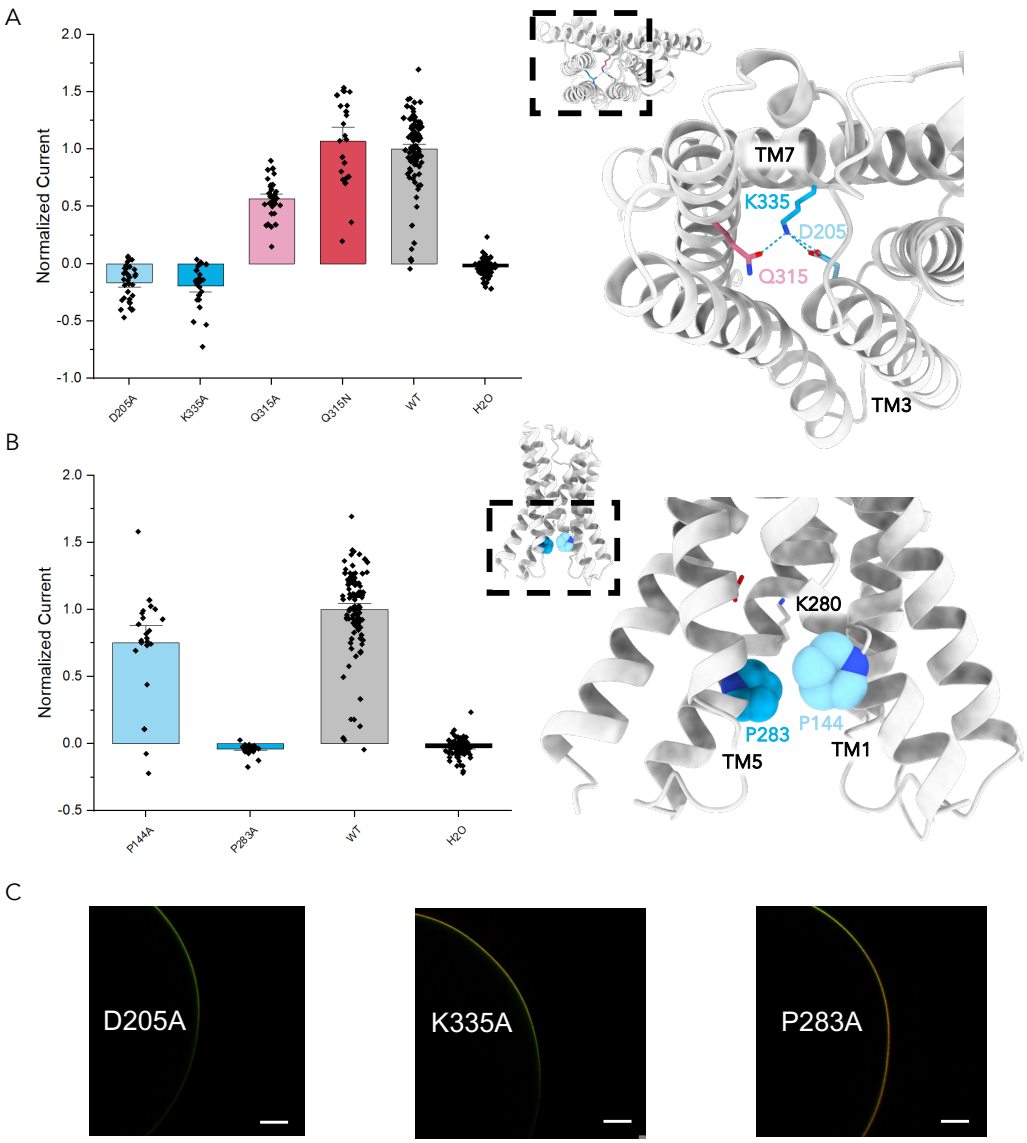

Figure 17: A salt bridge and PQ-loop motif are essential for cystine transport likely due to their role in the outward open to inward open transition. A) Mutations in the two residues forming a salt bridge on the luminal side of the protein, D205 and K335A, eliminates cystinosin transport activity. This salt bridge stabilizes the inward-open state and its formation would favor the transition to this state. Mutating Q315 only has a small effect on cystinosin activity, suggesting that the interactions that this residue forms with the salt bridge residues are not essential. B) The proline of the second PQ-loop motif is essential for transport. Mutations in the proline of the first PQ-loop motif does not strongly affect transport activity. The second PQ-loop motif is likely to be important because of its proximity to the ligand binding residue, K280. The helix break generated by P283 may be involved in coordinating ligand association/dissocation to the transition from the inward to outward open. C) The cystinosin mutants without activity localize to the plasma membrane. Scale bar: 100 µm.

with K335 and forms numerous interactions with residues on neighbouring helices. Therefore, it was mutated to an alanine or asparagine. The alanine mutation decreases transporter activity by approximately 50%, while the asparagine mutation has no effect on transporter activity. This suggests that the interactions formed by Q315 are not essential, while the D205-K335 (TM3-TM7) is a critical inter-helical salt bridge that forms the luminal gate regulating transport by cystinosin.

3.5 The Second PQ-Loop Motif of Cystinosin is Essential for Proton-Coupled Transport

Cystinosin is part of the PQ-loop family of transmembrane proteins. The PQ-loop motifs are regions of transmembrane helices 1 and 5 with a conserved proline-glutamate dipeptide (Ruivo et al., 2012). PQ-loop motifs are found in other transporters and trafficking receptors, but its function in ion-coupled transport is not well understood (Bräuer et al., 2019; Jézégou et al., 2012; Lee et al., 2015; Ruivo et al., 2012). The motifs were suggested to act as hinge points as observed in semi-SWEET transporters (Lee et al., 2015). Due to the proximity of the second PQ-loop motif (P283) with the ligand binding site, it was suggested to couple conformational changes with substrate association/dissociation.

The proline of each of the two PQ-loop motifs was mutated to an alanine. The mutation of P144 (TM1) to an alanine only had a small effect on transport activity (75% of activity retained), suggesting that this PQ motif does not play an essential role in cystine transport (Figure 17B). However, the mutation of P283 (TM5) to an alanine completely eliminated transporter activity without affecting trafficking (Figure 17B and C). Similar results were obtained for AtCTNS. P283 is located on TM5 with K280, which is an essential residue for cystine binding, and is in the vicinity of other residues involved in substrate binding (D305 and Y167). Therefore, P283 may be involved in regulating substrate binding and release by modulating the conformation of K280. Overall, D205-K335 forms the luminal gate, while P144 appears to regulate the opening of the intracellular gate formed by polar and hydrophobic residues found within loops connecting TM

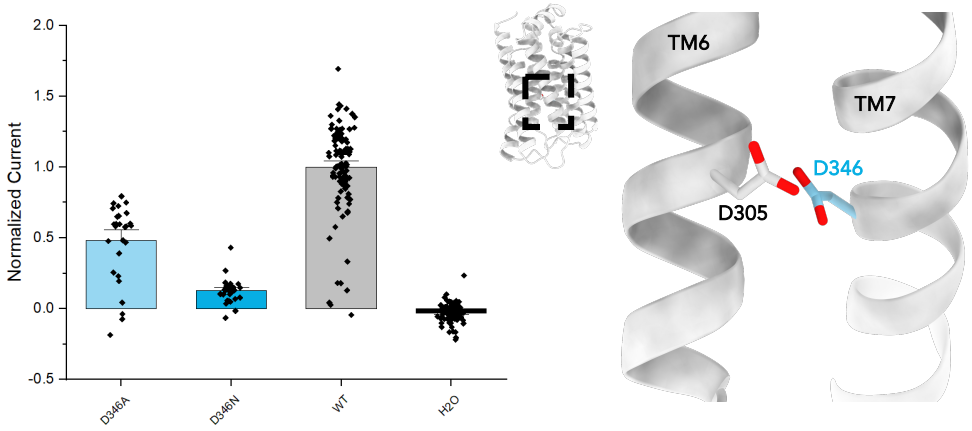

Figure 18: D346 may couple cystinosin conformational changes to substrate binding and release. Mutating D346 to an alanine halves the activity of cystinosin, while mutating it to an asparagine nearly eliminates cystinosin activity. It is suggested that D346 interacts with D305 when it is protonated. However, upon proton and cystine release, the two carboxyl groups bear a negative charge, causing the movement of TM7 away from TM3. This would favor the disruption of the D205-K335 salt bridge and facilitate the transition back to the outward open state. Additionally, D346 may modulate the pK_a of D305 based on the state of the transporter to facilitate protonation/deprotonation.

helices. Once the transporter has transitioned to the inward open state, the substrates are released on the cytosolic side due to the strong pH and cystine concentration gradients (Abu-Remaileh et al., 2017). Following substrate release, the transporter transitions back to the outward open state. The inward open state appears to be a stable state of the transporter under the tested conditions based on the obtained crystal structures (all in inward open state) and the state stabilized by the obtained sybodies/nanobodies. We aimed to investigate the mechanism that favors the transition and stabilizes the transporter in the outward open state.

3.6 Interactions Formed by the Proton-Coupling Residue May Couple Substrate Release with Conformational Changes

In a complete cycle, the transporter returns to its initial state to transport additional substrates. Along with the D305-K335 salt bridge suggested to instigate this transition, other residues may

favor the conformational change. The plant structure of cystinosin suggests that D305 interacts with D346 (TM7), which would bear a negative charge at cytosolic pH. This residue may induce conformational changes in TM7 (helix with K335 luminal gate) following the protonation/deprotonation of D305.

D346 was mutated to an alanine and asparagine residue. The D346A mutation approximately halved the transporter activity of the protein (Figure 18). Mutation of D346 to an asparagine residue reduced transporter activity down to 10% of WT activity. This mutation may favor hydrogen bonding between D346 and D305, stabilizing its deprotonated state and disrupting the normal transport cycle. This provides some evidence to support the suggested role of this residue in favoring the conformational transition from the inward open to the outward open state. Results obtained by Guo et al (2022) using double electron-electron resonance spectroscopy further support this hypothesis.

3.7 Mechanism of Proton-Coupled Transport

Based on the structures and functional data for AtCTNS, and the HCTNS electrophysiology data presented here, a mechanism of transport is suggested (Figure 19A). At lysosomal pH (≈4.5), D205 (TM3) may be partially protonated, weakening its interaction with K335 and opening the luminal gate of the transporter (outward open state) (Guo et al., 2022). In the outward open state, cystine from the luminal side can access the binding site of the transporter, where it forms key interactions with K273, K280, D305 and W138. The interactions between cystine and CTNS lead to the opening of the cytosolic gate, which is made up of polar and hydrophobic residues in the cytosolic loops of the TM helices. Full transition to the inward open state is facilitated by the second PQ-loop motif (P283 on TM5) and driven by the deprotonation of D205, favouring the formation of the D205-K335 (TM3-TM7) salt bridge. D205 deprotonation and D305 protonation may be favoured by cystine-induced conformational changes as it was previously suggested that cystine binding would favour D305 protonation by increasing its pK_a (Ruivo et al., 2012). Following the opening of the cytosolic gate and the protonation of D305, the interaction that cystinosin forms with cystine is weakened. Therefore, cystine would diffuse

out along the concentration gradient. In the inward open state, D305 becomes exposed to the cytosolic pH ($\approx$ 7.4), causing its deprotonation. As a result, D305 and D346 (TM7) would repel one another, favouring the movement of TM7 and disrupting the D205-K335 (TM3-TM7) salt bridge. Together with additional conformational changes resulting from substrate dissociation, this would drive transition back to the outward open state for another transport cycle.

Following the publication of our results, multiple HCTNS structures have been published along with functional data by Guo et al (2022) (Figure 20A). Many of the findings and the mechanism presented here are validated or further investigated using alternative methods in their work. The human inward open structure was nearly identical (RMSD: 1.397 Å) to the AlphaFold model used for this work (Figure 20A). Their structures also confirmed the suggested cystine binding site, and the roles of the luminal gate and PQ-loop motifs in the outward to inward open transition (Figure 20B-D). The authors also used ^{14}C-Cystine cellular uptake assay and double electron-electron resonance to investigate the effect of: the luminal domain truncation, cystine (W138F, N166A, K273Q and K280R) and proton binding sites (D305N), luminal salt bridge residues (D205A and N, and K335A) and residues suggested to facilitate conformational changes (D346N, and Q145A and Q284A of PQ-loop motifs). The authors showed that HCTNS with a fully truncated N-terminal domain still retains $\approx$30% of its activity as observed here. Mutations in any of the suggested binding sites or D205-K335 salt bridge residues fully abolished transporter activity by locking the transporter in the outward open conformation. Mutating the PQ-loop motif glutamines (luminal gate) and D346 residue generates gain-of-function mutants, stabilizing the transporter in the inward open state. These mutations may increase transporter activity by favouring the transition from the outward open to the inward open state, decoupling this transition from proton binding (reduced proton currents) and increasing the rate of transport (increased uptake). Any differences could also arise due to a myriad of factors (expression levels, protein stability, differing mutations etc). A key finding from the paper is that protons alone, but not cystine, can induce the conformational transitions. This result is expected as pH is a strong modulator of interactions within proteins and therefore of protein state. It suggests that the lysosomal pH gradient/protons in cystinosin act to drive and coordinate conformational changes, rather than facilitate cystine-induced changes. Albeit, cystine likely plays a strong role

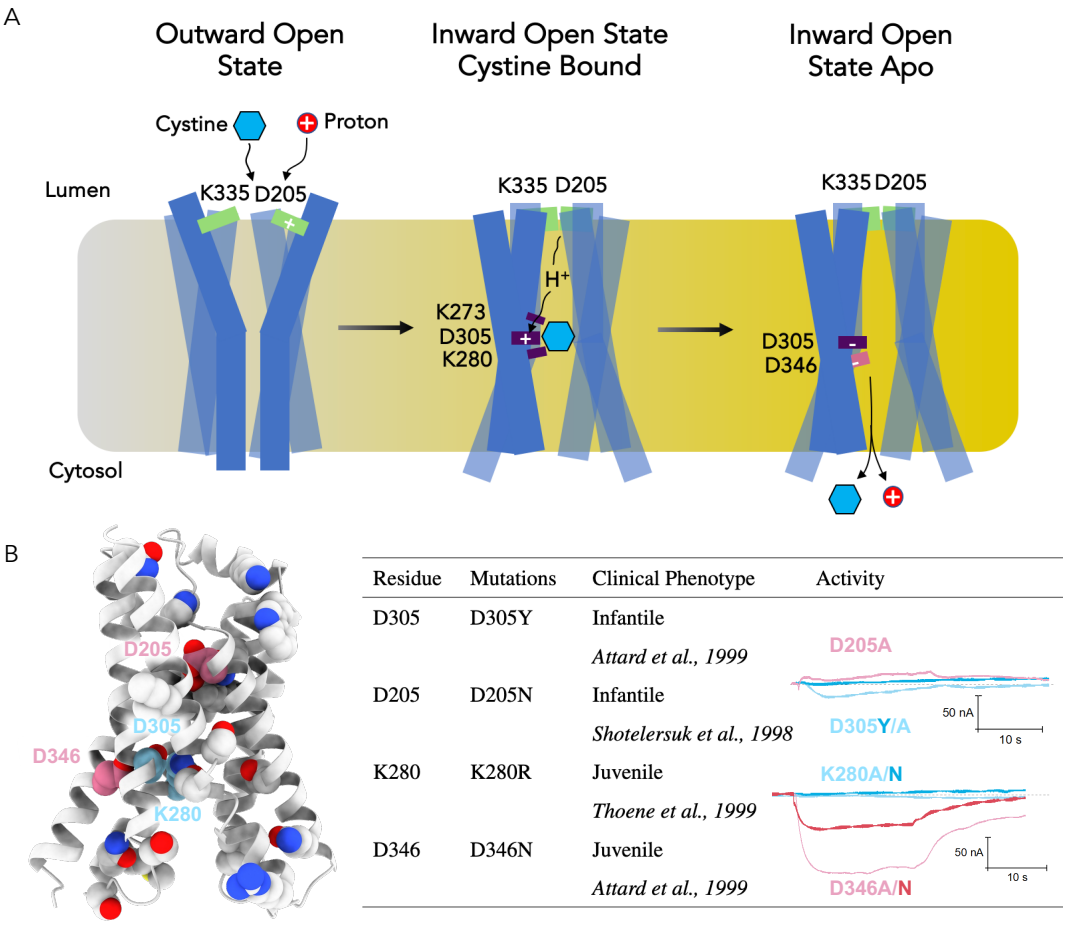

Figure 19: Mechanism of cystinosin and mutations observed in cystinosis patients that disrupt this transport cycle. A) The transport cycle of cystinosin begins with proton binding to D205, which favours the outward open state as it weakens the interaction between D205 and K335A. In the outward open state, cystine will bind to the binding pocket which includes K273, K280 and D305. This is expected to favor the transition to the inward open state. Proton shuttling may occur between D205 and D305, which would favor cystine dissociation and release in the cytosol. Then, the proton would be released as a result of the near neutral pH of the cytosol. The negative charge on the carboxyl group of D305 will be repelled by the negative charge of D346, favoring the movement of K335 away from D205 and the protonation of D205. B) Mutations observed in cystinosis patients disrupt the steps of the transport cycle described. The activity of the mutants is illustrated with representative traces from TEVC measurements. D305 mutations that cause infantile cystinosis result in a transporter without activity since this is the site for proton binding. D205 mutations cause cystinosis by disrupting the formation of the salt bridge that appears to be critical for the regulation of the conformational transitions. K280 mutations disrupt cystine binding. D346 mutations disrupt transporter activity by interfering with the potential role of D346 in favoring the inward open to outward open state transition.

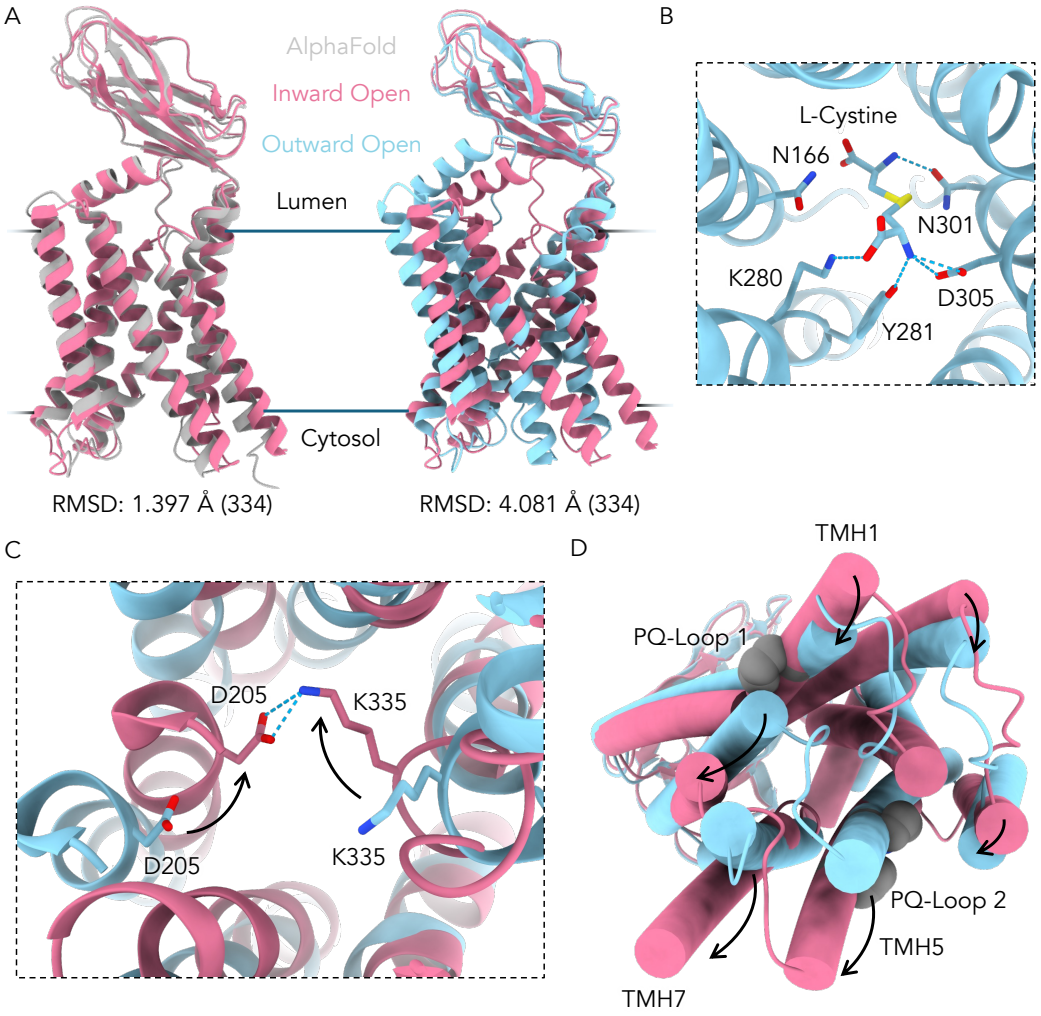

Figure 20: Comparison of HsCTNS cryo-EM structures with AlphaFold model. A) Comparison of the AlphaFold model and cryo-EM structure, which are found to be very similar. The cryo–EM inward (PDB: 8DKE) and outward open (8DKM) structures show a clear transition, and these structures can help to determine if the mechanism hypothesized here is accurate. B) In the cystine-bound structure (PDB: 8DKM), the binding site is similar to the one predicted based on the plant structure and AlphaFold models. C) Changes in the comformation of the luminal gate salt bridge in the inward and outward open structures. As predicted, the salt bridge is only formed and stabilizes cystinosin in the inward open conformation. D) The PQ-loop motifs are observed to induce the breaking of the transmembrane helices, which facilitates large conformational changes in these helices between the outward and inward open states, with the largest changes observed in TMH5.

in facilitating these conformational changes, especially in the presence of a proton gradient.

3.8 Interpretation of Cystinosis-Causing Mutations

Over 140 mutations of CTNS have been identified in cystinosis patients (David et al., 2019). Previous studies have attempted to correlate mutant activity and clinical phenotypes (Kalatzis et al., 2004; Ruivo et al., 2012). D205, K280, D305 and D346 are all mutated residues in cystinosis (Figure 20B). The D205N mutation causes infantile cystinosis, which correlates with the loss of activity of this mutant as a result of the disruption of the D205-K335 salt bridge (Shotelersuk et al., 1998). The proton-coupling residue, D305, is mutated to glycine or tyrosine in infantile cystinosis. D346N causes juvenile cystinosis as would be expected from the residual activity of D346 mutants. K280R causes juvenile cystinosis (Thoene et al., 1999). This mutation has previously been shown to abolish transporter activity (Kalatzis et al., 2004). The observation that abolishing cystinosin transporter activity is insufficient to cause infantile cystinosis suggests that cystine accumulation is not the only cause of the disease, but the patient affected by this mutation required kidney transplant (Kalatzis et al., 2004; Thoene et al., 1999). Loss of cystine transport may be sufficient to cause severe forms of cystinosis, and disruption of other cystinosin functions may accelerate the onset causing infantile cystinosis as cystine buildup and cystine crystal formation occur slowly. Some of these mutations may alter the conformational state of the protein disrupting protein interactions (e.g. Rag-Ragulator complex or lamp-2A) and signaling (Andrzejewska et al., 2016; Guo et al., 2022; Zhang et al., 2017). Some mutations may also affect cystinosin localization. This has not been investigated in patient cells (endogenous protein) due to the lack of good cystinosin antibodies. Therefore, we set out to generate reagents to investigate the effect of cystinosis mutations on cystinosin localization and protein interactions.

3.9 Sybodies to Investigate Cystinosin Functions and Localization

Genetic diseases frequently arise from mislocalization or disruption of protein interactions of mutated proteins (Hung and Link, 2011). The protein interactions and localization of endogenous cystinosin is poorly characterized. A few cystinosin antibodies are reported in the literature, but these antibodies show non-specific binding, are poorly validated, or have not been tested for immunofluorescence or co-immunoprecipitation experiments (Guo et al., 2022; Haq et al., 2002; Taranta et al., 2012; Venkatarangan et al., 2023). Obtaining specific cystinosin antibodies may be challenging for a few reasons: the low number of epitopes, the strong glycosylation pattern of the N-terminal domain and the low copy number per lysosome ($\approx$ 10 molecules per lysosome) (Thoene et al., 2013). Therefore, Mark Löbel (Newstead Lab) selected synthetic nanobodies against human cystinosin with the N-terminal truncated due to the stronger expression of this construct.

High-affinity sybodies were obtained from the selection. Then, I tested the binders for co-localization with cystinosin-GFP using immunofluorescence. It was observed that the sybodies did not colocalize with the full-length protein, but colocalized with the truncated construct (Syb30 shown in Figure 21B and C). This result was also observed in pull-down experiments and was confirmed by cryo-EM structures, which showed that the sybody binds at the position of the luminal domain (Figure 21A) (performed by Mark Löbel). This result provided evidence that the immunofluorescence assay could rapidly provide valuable information about the epitope and state of the protein being imaged. To obtain reagents to investigate cystinosin localization, the selection will need to be repeated with the full-length glycosylated protein.

3.10 Conclusions and Future Perspectives

The work presented in this chapter aimed to understand the mechanism of transport of cystinosin, the coupling between proton and nutrient transport, how patient mutations affect transport and

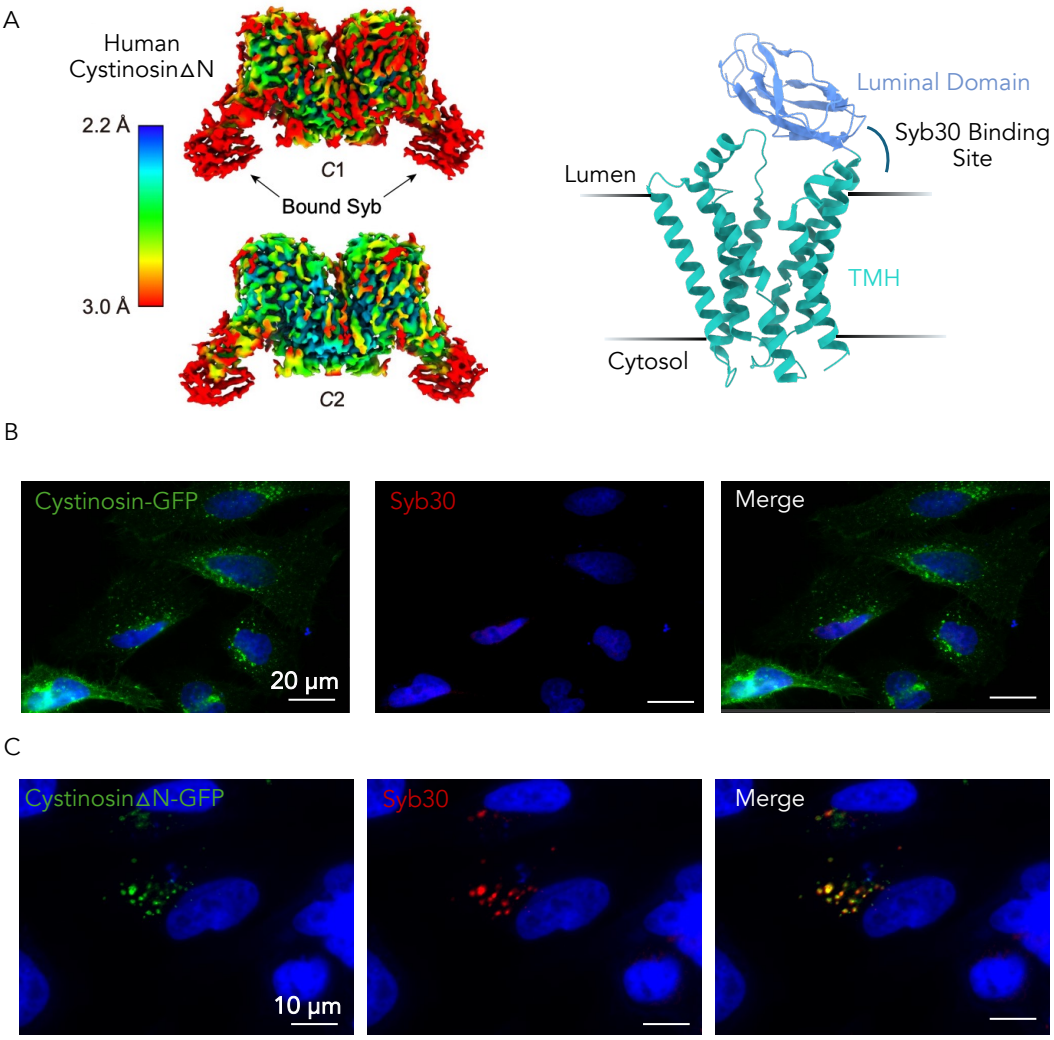

Figure 21: Human cystinosin sybodies epitope and immunofluorescence. A) cryo-EM map of human cystinosin bound to Syb30 and its binding site labelled on the AlphaFold model. B) Immunofluorescence experiment with Syb30-Myc and anti-Myc antibody in full-length human cystinosin-GFP transfected HeLa cells. Syb30 does not co-localize with the sybody signal. C) Immunofluorescence experiment in HeLa cells transfected with human cystinosinΔN-GFP stained with Syb30-Myc and Anti-Myc antibody. The signals co-localize with the truncated construct as the luminal domain does not clash with sybody binding. Map of HCTNSΔN bound to Syb30 and Syb30 samples were kindly provided by Mark Löbel.

how the PQ-loop motif is involved transport. A mechanism of transport and cystine binding site have been suggested. It was concluded based on our results and novel evidence that the proton acts to drive the conformational changes of the transporter. In our mechanism, it was suggested to regulate the opening of the luminal gate and the transition back to the outward-open state. The exact mechanism of proton transport across the protein will need to be investigated further, which may be better understood by investigating the observed proton leaks. Cystinosis mutations were tested and were consistent with the clinical phenotype. However, it was noted, as it has been observed in the past, that loss of transporter activity does not necessarily cause severe forms of cystinosis. Therefore, sybodies were selected against human cystinosin by Mark Löbel to investigate other processes that may be affected (e.g. folding, localization, interactions etc.). However, these sybodies only bound to the truncated form of cystinosin, and a selection on the full-length protein will need to be carried out to investigate this further. Lastly, we identified that the second PQ-loop motif of cystinosin plays a critical role in the transport cycle. While both glutamines appear to play an important role in transport as suggested by Guo et al (2022), only the second proline was found to be a strong regulator of activity.

4 | Generation of a Synthetic Nanobody Toolkit to Investigate TRPML1 Localization, Function and Structure

4.1 Tools to Investigate TRPML1 Functions

TRPML1 was discovered more than two decades ago when it was mapped to be the mucolipidosis type IV gene (Slaugenhaupt et al., 1999; Sun et al., 2000). A range of small molecule modulators and antibodies have been generated to investigate its functions, and the role of lysosomal calcium in lysosomal biology and cellular homeostasis (Griffin et al., 2020; Leser et al., 2021; Shen et al., 2012; Thakore et al., 2020; Yu et al., 2020). However, these agonists have been found to show poor specificity for TRPML1 as they bind to conserved transmembrane regions of TRPMLs (Spix et al., 2022). The TRPML1 antibody that has been validated by Thakore et al (2020) on smooth muscle tissue produced numerous unspecific bands in western blotting of untransfected HeLa and SH-SY5Y cells (Figure 22A). SH-SY5Y cells were used because TRPML1 expression was validated by qPCR, TRPML1 SH-SY5Y knock-down cells were generated and this cell line is used as a Parkinson's model cell line (see chapter 6) (Ioghen et al., 2023). In immunostaining experiments, this TRPML1 antibody showed partial colocalization with overexpressed GFP-TRPML1 in HeLa cells (Figure 22B). In untransfected HeLa cells, the TRPML1 antibody showed very sparse staining at the nucleus/perinuclear regions (Figure 22C) (TRPML1 is expressed in HeLa cells: Akter et al., 2023). Additional antibodies were also tested by numerous collaborators and a good antibody had not been identified. This highlights a need for new specific reagents to investigate the functions of TRPML1.

Good antibodies are difficult to generate as TRPML1 is a lowly-expressed highly modified (glycosylated, cleaved, lipidated) membrane protein, meaning that very high-affinity binders that can bind to its different proteoforms need to be obtained (Kiselyov et al., 2005). Since the start

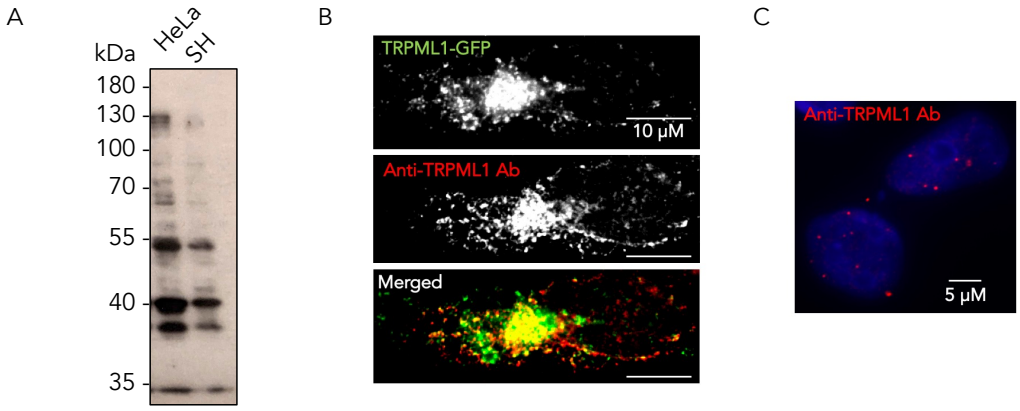

Figure 22: Test of commercial TRPML1 antibodies. A) Western blot using anti-TRPML1 mouse antibody (F-10; Santa Cruz Biotech) to detect TRPML1 in untransfected HeLa and SH-SY5Y cells. B) Anti-TRPML1 mouse antibody (red) was used in immunostaining experiments in TRPML1-GFP transfected HeLa cells (green) and samples were imaged using a widefield fluorescent microscope. C) Imaging of untransfected HeLa cells stained with anti-TRPML1 antibody (red) and DAPI (blue).

of this DPhil work, more specific modulators have been identified (e.g. ML1-SA1) (Peng et al., 2024; Rühl et al., 2021; Spix et al., 2022). Nanobody modulators that bind to novel sites are expected to have higher specificity and potency, and would provide novel information about the regulation of the channel.

In this chapter, I set out to generate a synthetic nanobody toolkit to investigate TRPML1 localization, interactions, and functions in cells (Aim 2).

4.2 TRPML1 Sybody Pipeline

Synthetic nanobody selection requires large-scale purification and biotinylation of TRPML1. To identify the detergent that would lead to the highest protein yields for sybody selection, a small-scale detergent screen to test solubilization efficiency was carried out. It was found that DDM and DDM:CHS (Cholesteryl hemisuccinate) solubilized TRPML1-GFP with a higher efficiency than Lauryl Maltose Neopentyl Glycol (LMNG) (supplementary Figure 1A and B). Following this initial screen, expression of the final construct, FLAG-AVI-TRPML1 (*Homo sapiens*) in the pLEXM vector, was trialed (20 ml HEK-293F culture). Purification with Anti-FLAG resin

was selected based on previous TRPML1 purification protocols (Schmiege et al., 2017). This construct was expressed strongly based on relative expression to a highly-expressing membrane protein (LAAT2/SLC66A2) (supplementary Figure 1C).

FLAG and Size-Exclusion Chromatography (SEC) purifications were trialed from 1 L of HEK-293F cultures with LMNG and DDM:CHS (5:1). Only LMNG resulted in yields sufficient for sybody selection (Figure 23A-F). The elution volume of 9.3 ml, corresponding to ≈500 kDa, suggested that TRPML1 was purified in its oligomeric state (275 kDa + LMNG micelle). A shoulder was observed in the TRPML1 LMNG purification. This may result from the association of TRPML1 with another protein to form larger complexes. A 100-kDa band was observed as a contaminant in the LMNG purification that was identified by western blotting and mass spectrometry to be extended-synaptotagmin 2, a calcium-binding protein (supplementary Figure 2A and B) (Woo et al., 2020).

The LMNG sample showed a transition (T_m = 68.2°C) in nano-Differential Scanning Fluorimetry (nano-DSF), while the DDM:CHS sample did not (supplementary Figure 3A). Folded proteins display a transition in fluorescence ratio (Fluorescence at 350 nm/Fluorescence at 330 nm) in nano-DSF as buried tryptophans become exposed to the solution, and their fluorescence is red-shifted (Chattopadhyay and Varadarajan, 2019). However, in unfolded proteins, this change does not occur as the protein does not denature. DDM and DDM:CHS may solubilize TRPML1 efficiently, but the protein (transmembrane regions) is likely partially unfolded in these detergents, which would explain the low purification yield (see Chapter 5 TRPML1-Syb94 LMNG structure). Circular dichroism for the LMNG-purified protein is typical of an α-helical protein with negative bands at 208 nm and 222 nm (supplementary Figure 3B) (Greenfield, 2006). This is the expected spectrum for a folded membrane protein as the transmembrane regions are α-helical.

Following purification, TRPML1 was successfully biotinylated for sybody selection (Figure 24A and B). Therefore, sybody selection was carried out (See Methods: Sybody Selection).

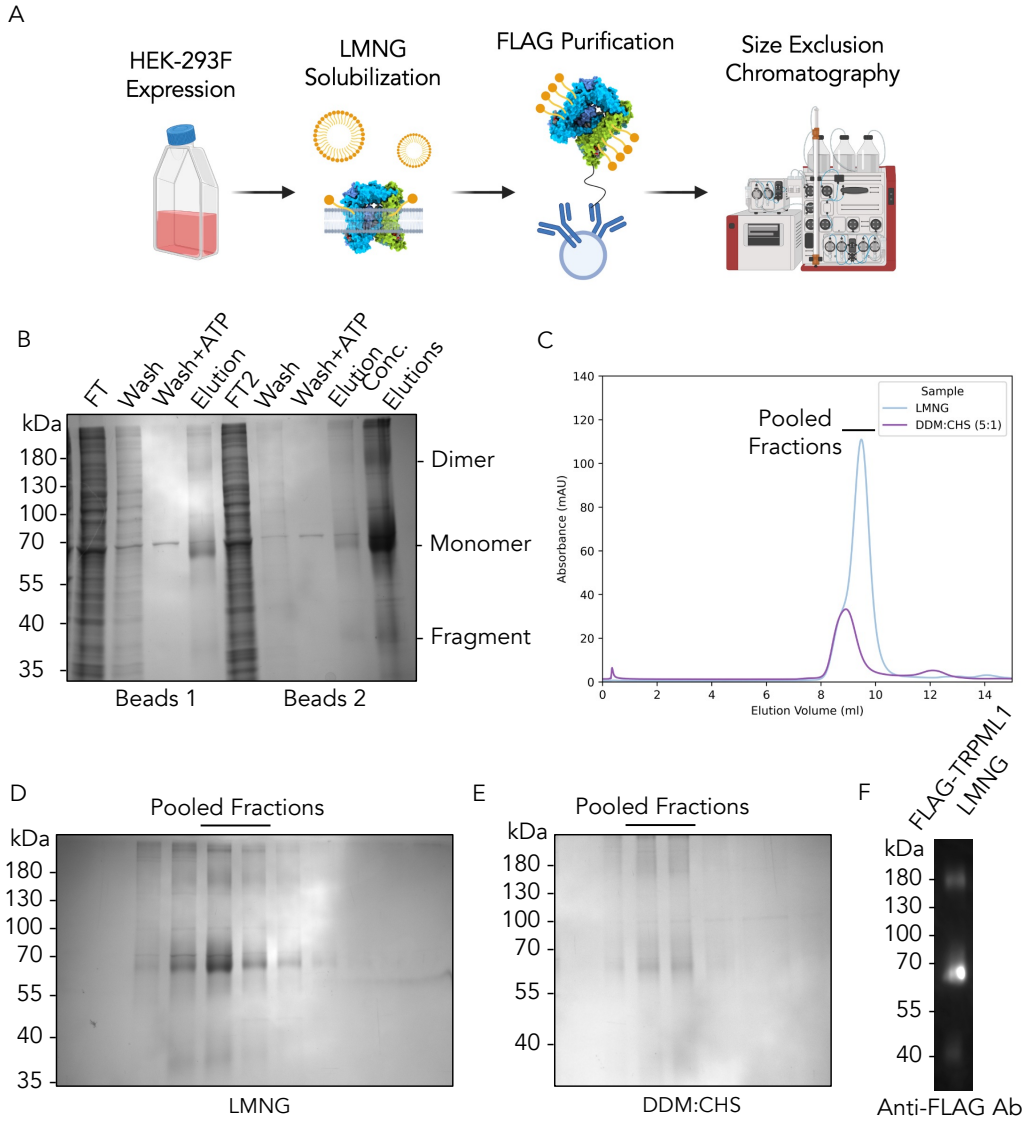

Figure 23: TRPML1 expression and purification. A) FLAG-AVI-TRPML1 was expressed in HEK-293F cells, the membrane of these cells was solubilized with LMNG, and the protein was purified using FLAG resin and Size-Exclusion Chromatography (SEC) with an S200 column. B) Large-scale (1L) FLAG purification of TRPML1. The first elution was incubated with a second set of beads to ensure that a maximum amount of TRPML1 had bound to the beads. An ATP wash was carried out to reduce Hsp70 binding to TRPML1. C) SEC (S200) profile of TRPML1 purified in LMNG or DDM:CHS (5:1). TRPML1 in LMNG displays as a monodisperse peak with a small shoulder and DDM:CHS generates a significantly smaller peak. D) Fractions from SEC for LMNG and E) DDM:CHS purification. Fractions were pooled for biophysical characterization and biotinylation. F) Western blot with anti-FLAG M2 antibody (Sigma) validates identify of band in LMNG purified sample.

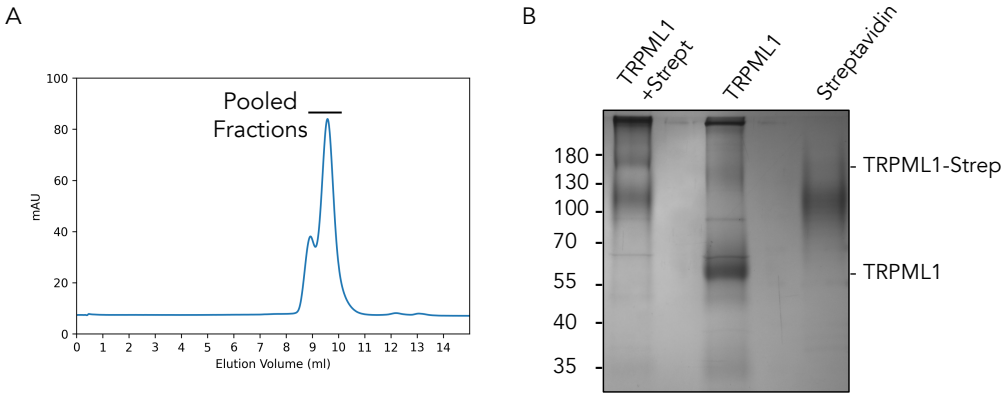

Figure 24: TRPML1 biotinylation. A) SEC (S200) profile of biotinylated TRPML1. Fractions A5-6 were concentrated and ran on a gel in Panel B. B) Biotinylation was confirmed by incubating biotinylated TRPML1 with streptavidin, which shifts the TRPML1 band to about 150 kDa as it binds biotin.

4.3 Sybody Selection Outcome

The steps of sybody selection and their respective results are presented in Methods section - Sybody Selection. Following the ribosome display and three rounds of phage display, an Enzyme-Linked Immunosorbent Assay (ELISA) was carried out as described by Zimmermann et al (2020).

212 hits (78 convex, 61 loop and 73 concave) were found to have absorbance values above the threshold value (1.5), and 137 clones (35 convex, 32 loop and 70 concave) were successfully mini-prepped and sequenced (Figure 25A; supplementary Figure 4-6). There is no clear relationship between phage display enrichment values, hit number and clone diversity. Following sequence analysis, 65 unique binders were obtained: 5 from the convex library, 9 from the loop library, and 51 from the concave library (Figure 25B and C; Figure 26).

77% of hits from the convex library were from a single sequence (Syb175), but all sequences showed few similarities in their CDRs (Figure 25B).

The loop library shows greater conservation of CDR sequences across clones, which may indicate that these residues are important for sybody binding (Figure 25C). Syb43 and 17 are related

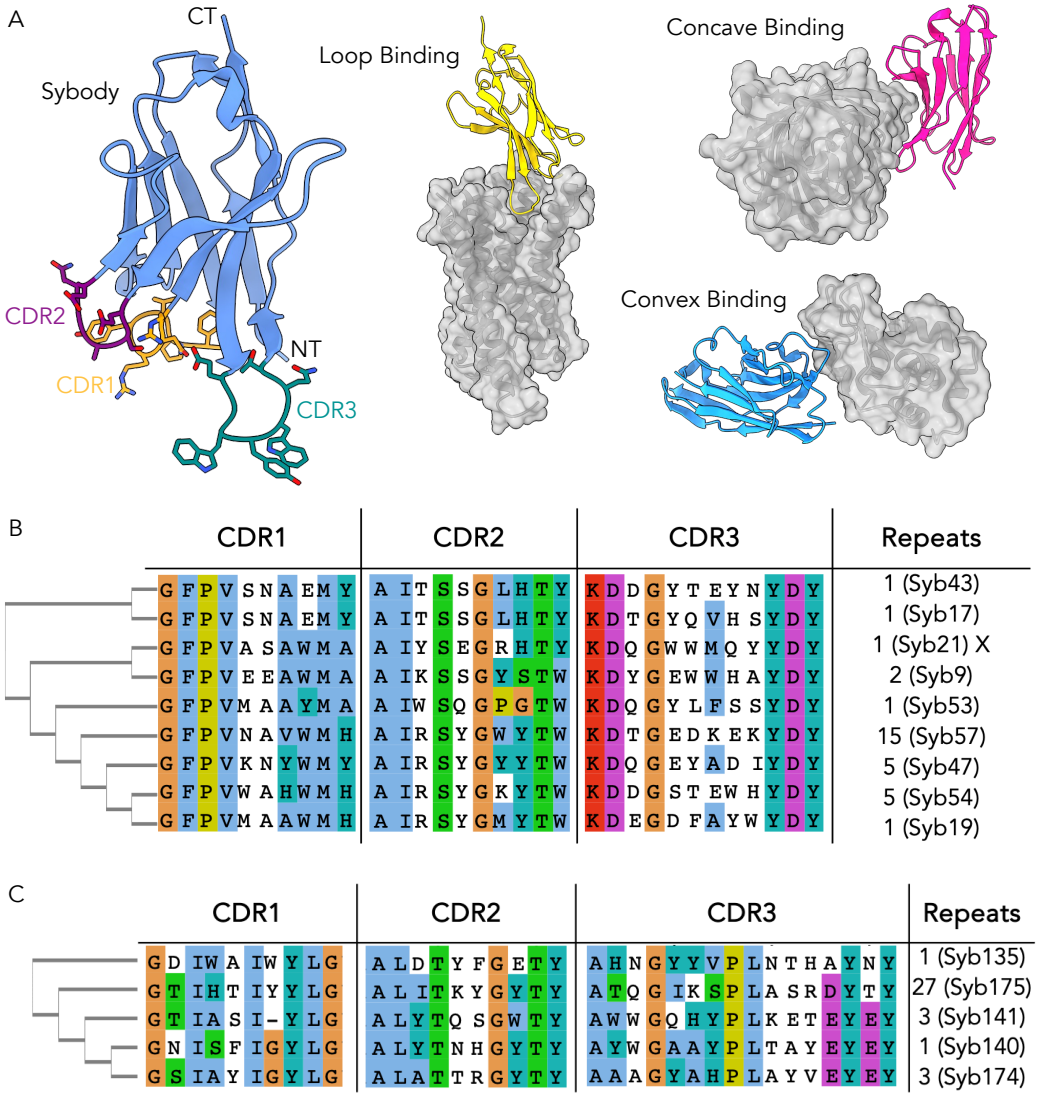

Figure 25: Unique sybody sequences from loop and convex libraries. A) Structure of Syb with annotated location of CDR1-3, and binding mode of different sybody libraries (Sybody Example PDB: 7ZKW; Loop PDB: 3P0G; Convex PDB: 1ZVH; Concave PDB: 3K1K). B) Loop library phylogenetic tree with unique sequences and number of times the sybody was sequenced. X indicates that the sybody could not successfully be purified. C) Convex library unique sequences phylogenetic tree. Color scheme of residues: Clustal X. Alignment presented using Jalview.

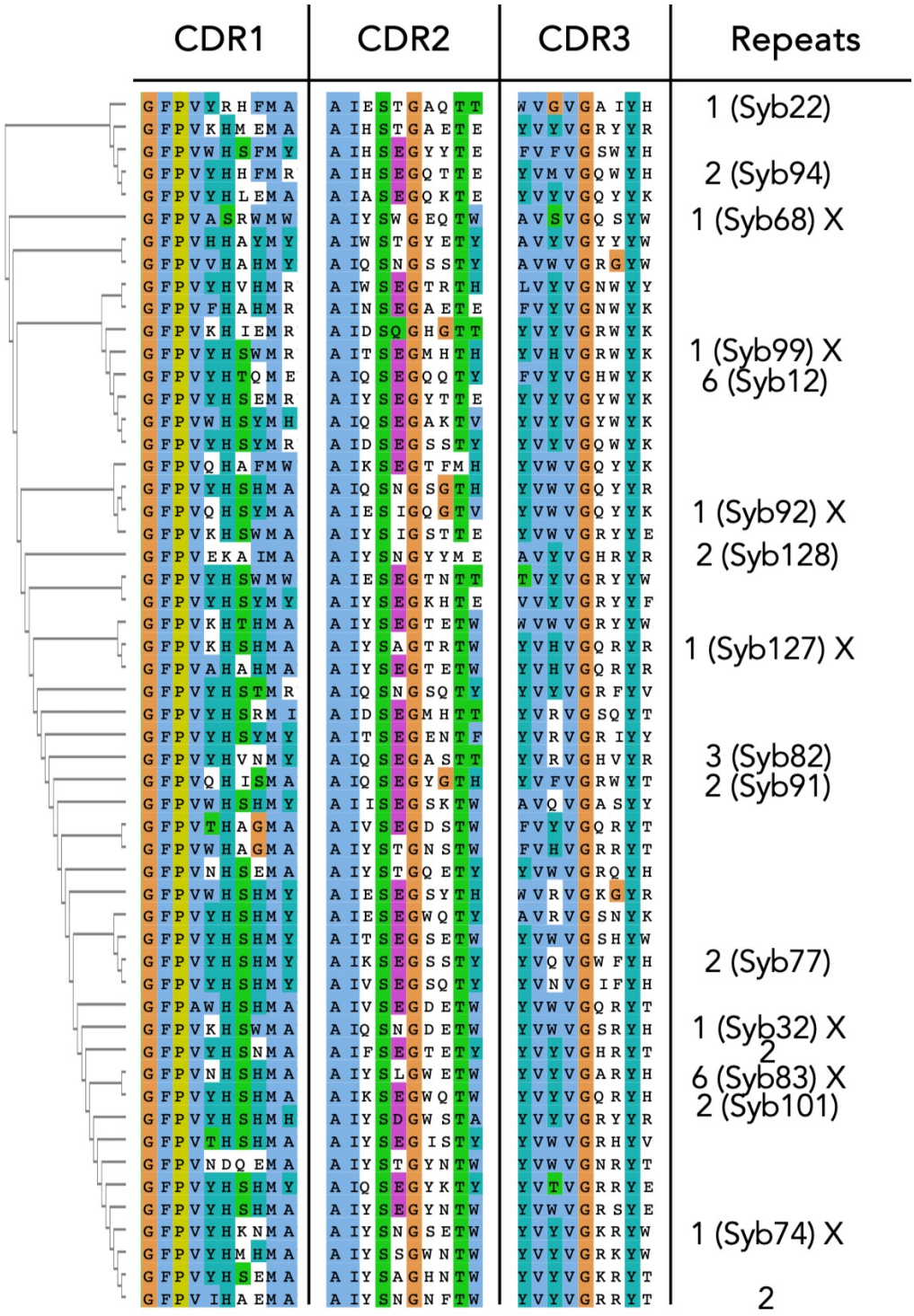

Figure 26: Unique sybody sequences from concave library. Concave library unique sequences phylogenetic tree with number of times the sybody was sequenced. X indicates that the sybody could not be purified. Color scheme of residues: Clustal X. Alignment presented using Jalview.

by their CDR1 and CDR2 sequences, Syb21 and 9 show some conservation in their CDR1, Syb57, 47, 54 and 19 show conservation in their CDR2 and some conservation in the CDR3, while Syb53 is unique suggesting it may bind to an alternative epitope.

The concave library shows strong diversity (Figure 26). The library generating the greatest diversity of binders is target-dependent based on selections in the Newstead lab. This library likely generated a large number of hits for TRPML1 due to the compatibility of this binding mode with the flat surface of the luminal domain (Figure 25A). For this library, a first family of binders, including syb94, show some conservation in their CDR1 and CDR2, notably conserved histidines (see section Binding of TRPML1 Sybodies at lysosomal pH). A second family with conservation in the CDR1 and 3 is found to be comprised of Syb12. Other families with strong conservation in the CDR3 were identified (Syb92 and Syb127). The family composed of Syb77 shows perfect conservation in its CDR1, including two histidines in the center of the CDR. A set of sequences at the bottom of the phylogenetic tree have conserved charged residues within their CDR3 (e.g. Syb74). More generally, these different families show conservation in specific CDRs, which is an indicator of the CDR(s) involved in target binding. Due to the large numbers of binders for this library, a single member of one of the described families that was sequenced more than once was expressed, purified and characterized as other members are expected to bind to a similar epitope.

4.4 Characterization of Sybody Hits

4.4.1 Sybody Purifications

Sybodies were expressed and purified as described by Zimmermann et al (2020) in 50 ml *E. coli* MC1061 cultures, extracted by periplasmic extraction, and purified using Ni-NTA resin and SEC (Sepax-100 column) (Figure 27A-C). All loop and convex binders were expressed and purified. A subset of the concave binders were expressed and purified.

Binder physicochemical properties can be inferred based on the elution volume on a Sepax

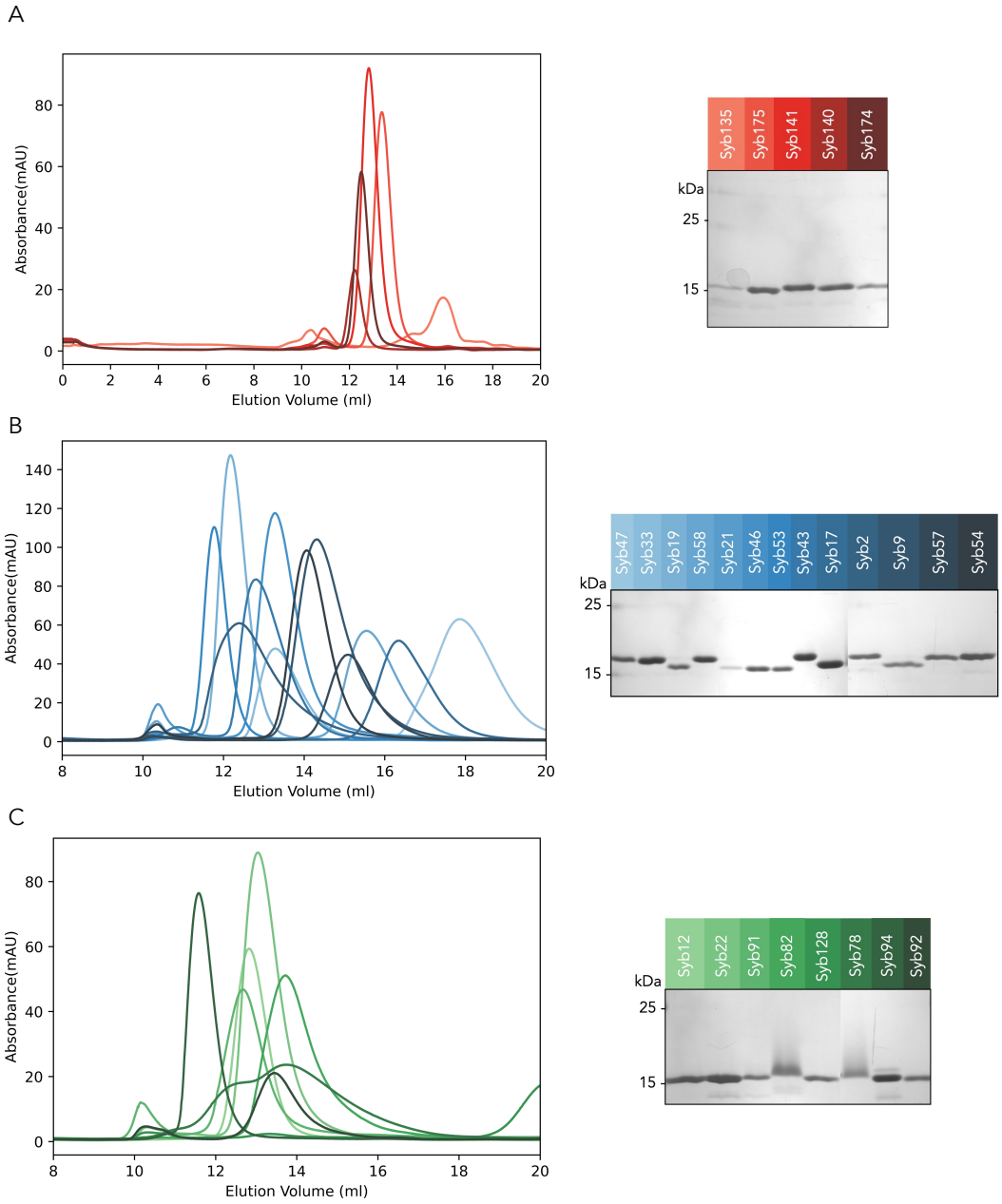

Figure 27: Sybody purifications using a sepax SRT-C SEC-100 column. SEC profile and SDS-PAGE (15%) of concentrated fractions for A) convex, B) loop, and C) concave libraries.

SEC100 column. Binders with early (≈10 ml) elution are found to form oligomers, binders eluting at 12-15 ml (≈10 ml) typically have favorable physicochemical properties, and binders eluting at >15 ml interact with the column suggesting that the binder is unstable. All loop binders, except Syb21, expressed and purified (Figure 27B). Syb21 CDR3 is rich in aromatic residues including a ditryptophan sequence, which has previously been observed to lead to unfavourable physicochemical properties.

Binders in the convex library were all found to express well and eluted at a favourable volume, except Syb135 with CDRs rich in aromatic residues (Figure 27A). Convex library binders consistently caused cell lysis upon expression, suggesting they are toxic or prone to aggregation. This could be a result of their long disordered CDR3s. However, staining with Syb175 (see Microscopy chapter) is highly specific, suggesting that they are nevertheless specific for the applications of interest.

A subset of concave library binders were expressed and purified (Figure Figure 27C). 47% of binders were found not to elute on the sepax-100. Despite the large number of binders obtained for this library, fewer were successfully expressed relative to the other libraries. Based on their sequences, it is unclear why these sybodies do not purify.

The binding of the sybodies that were successfully purified was characterized.

4.4.2 Characterization of Sybody Binding

Sybody binding to TRPML1 was characterized by pull-down and Bio-layer Interferometry (BLI) experiments. Additional characterization of the binders was carried out by co-elution and immunofluorescence as described in later chapters.

Pull-down experiments were carried out to determine if the sybodies are able to bind to the target protein. This experiment is carried out by incubating TRPML1 with individual His-tagged sybodies, the complex is incubated with Ni-NTA resin, which is washed and finally, the complex is eluted using imidazole. Most sybodies were found to pull-down TRPML1 (Figure 28). Pull-downs suggested weak binding of Syb174, 135, 140, 175, 12 and 22.

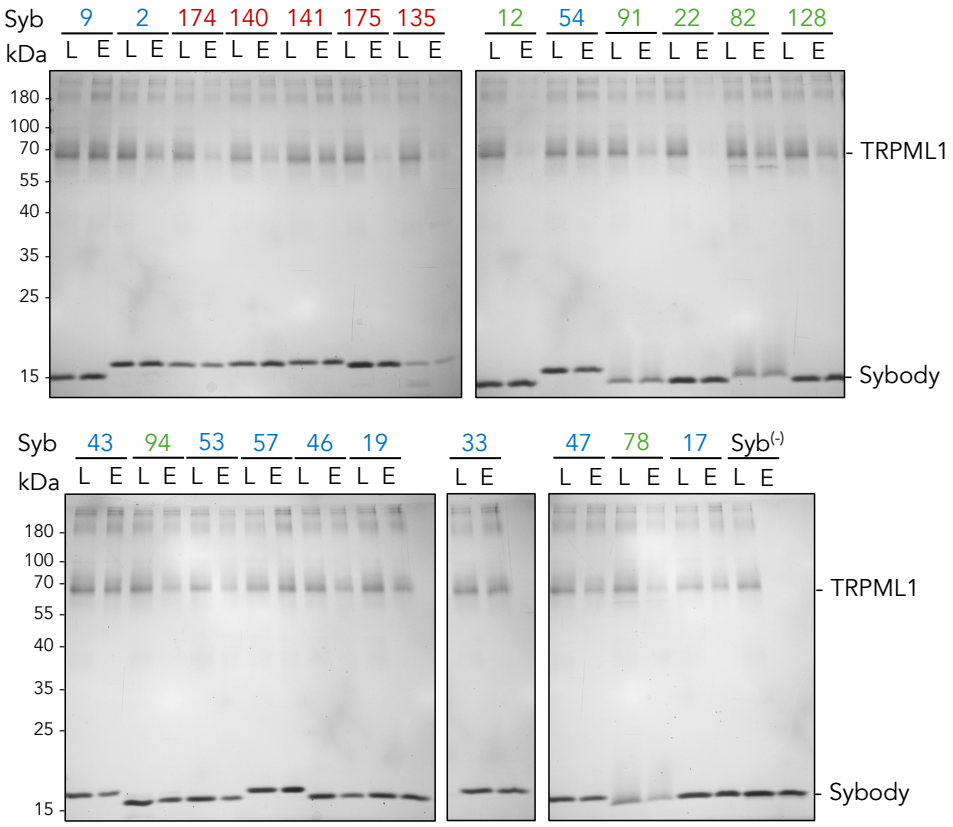

Figure 28: Sybody pull-down with full-length TRPML1. L: Load (complex loaded on Ni-NTA resin) and E: Elution (sample eluted with SDS from Ni-NTA resin following washes). Syb$^{(-)}$ is a sybody that does not bind to TRPML1 (sybody kindly provided by Dr. Oliver Adams selected against LAAT2, which was used as a negative control for all experiments). Samples ran on a 15% SDS-PAGE gel. Color coding: loop (blue), concave (green) and convex (red).

To further characterize the binding, a series of Bio-Layer Interferometry (BLI) experiments were carried out. BLI is carried out by immobilizing the target protein (biotinylated TRPML1) on a tip (streptavidin-coated). If the tip is moved to a sybody-containing solution and the sybody binds to TRPML1, a change in the interference pattern of the reflected light is measured, which is used to assess target binding (Jug et al., 2024). Initial screening was carried out at 500 nM on the binders tested by pull-down (supplementary Figure 7A-C). For the loop library, all binders, except syb9 and 53, generated a strong response (<0.1 nm). The amplitude of the response is a factor of the following variables: the size of the analyte and ligand, the affinity, the stochiometry, and the binding site. Syb54 displays the maximal observed response ($\approx$ 0.35). Syb9 and 53 show weak responses, but both sybodies pull down TRPML1 very well. This suggests that they may bind TRPML1 with a different stochiometry or to an alternative epitope that is less accessible when immobilizing TRPML1 (i.e. the cytosolic side) relative to the pull-down, in which the sybody is immobilized. k_{on} and k_{off} are parameters of binder affinity. Numerous binders from the loop library have low k_{off} (e.g. Syb57: 5.41E^{-04} s^{-1}), which is due to specific interactions as these binders were not found to interact with an empty tip. Screening of concave binders confirmed the pull-down results- all binders bind to TRPML1, except Syb12 and 22, which bind more poorly. Most binders showed a similar response of about 0.2-0.25 nm. Syb94 showed the lowest k_{off} (4.69E^{-04} s^{-1}) amongst convex binders. Most convex binders pull down TRPML1 partially. Their weak binding was confirmed by the small response obtained for all TRPML1 binders. Only Syb175 and 141 displayed a response <0.06 nm, with Syb175 having a lower dissociation rate. It was hypothesized that Syb175, and convex binders in general, may also display a weaker response due to a different interaction stochiometry (e.g. 2:4 or 1:4) by binding to alternative epitopes. Therefore, Syb175 was carried forward for further analysis.

Based on these results, 11 binders were carried forward for preliminary kinetic analysis in which the response was tested at 4 concentrations to identify binders with a K_D lower than 100 nM (10 nM, 100 nM, 250 nM, and 500 nM) (supplementary Figure 8). These binders were Syb9, 43, 19, 47, 53, 54, 57, 82, 94, 128 and 175. Based on this screen, along with binding analysis on the luminal domain of TRPML1 (see section Epitope Mapping of TRPML1 Sybodies), Syb43, 54, 57, 94 and 175 were carried forward for complete kinetic analysis. These binders were selected

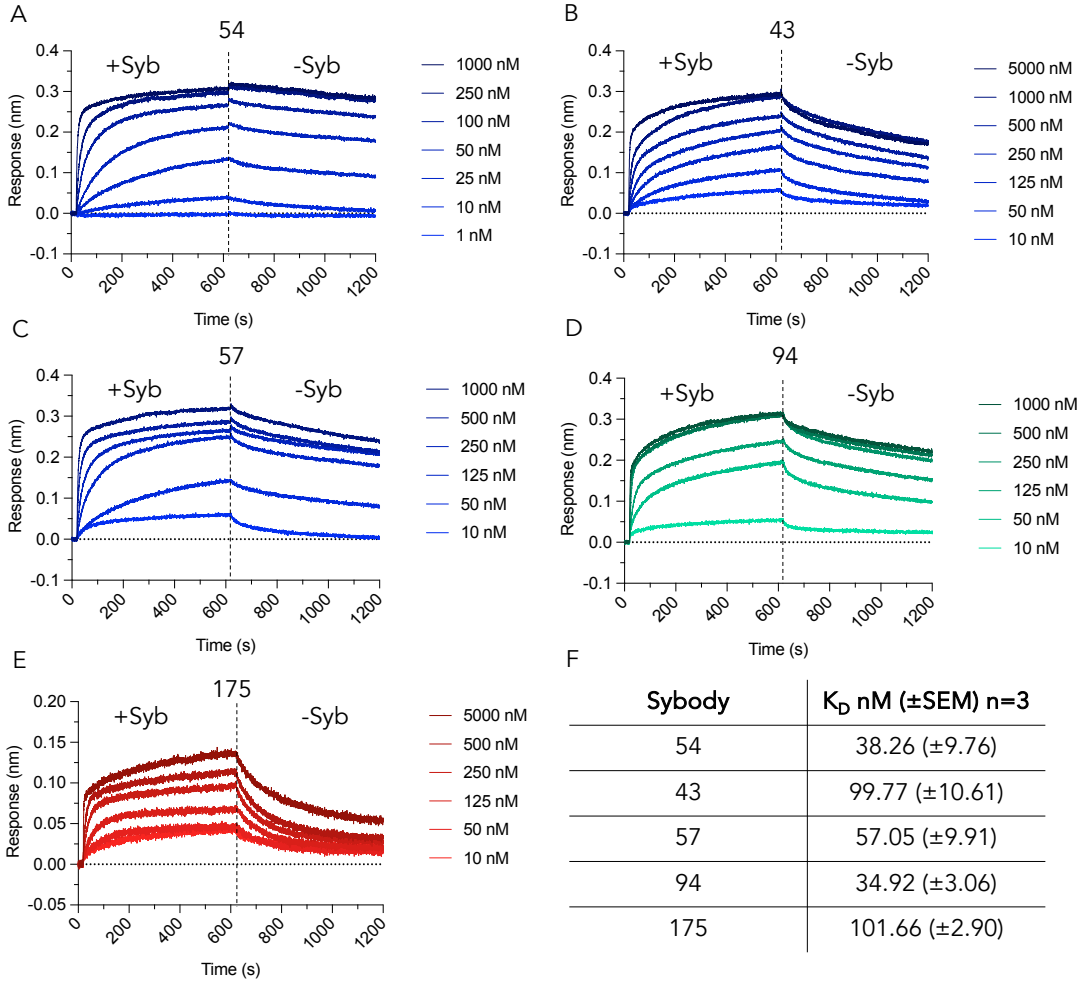

Sybody	K_D nM (±SEM) n=3
54	38.26 (±9.76)
43	99.77 (±10.61)
57	57.05 (±9.91)
94	34.92 (±3.06)
175	101.66 (±2.90)

Figure 29: Kinetics for high-affinity TRPML1 sybody binders using bio-layer interferometry. Baseline subtracted measurements made by submerging tip in sybody containing buffer (+Syb; association) for 600 s and buffer without sybody (-Syb; dissociation) (TBS pH 7.4 with 0.003% LMNG) for 600 s. Measurements made with A) Syb54, B) Syb43, C) Syb57, D) Syb94 and E) Syb175. F) Summary of K_Ds for binders with (±SEM) values based on three technical replicates. K_D calculated by fitting $\text{Response} = \frac{R_{max} \times [Syb]}{K_D + [Syb]}$ to the data (response is mean response at 590-595 s).

as they were found to approach R_{max} at 500 nM based on the 250 nM and 500 nM measurements (i.e. doubling concentration did not double the response) and their low k_{off}.

Kinetic analysis was carried out on the 5 binders with concentration ranges between 5000-10 nM or 1000-1 nM based on the initial kinetics analysis (Figure 29A-F). This analysis confirmed the initial observation that Syb94 (34.92 ±3.06 (SEM) nM) and Syb54 (38.26 ±9.76 nM) showed the highest affinity for TRPML1, followed by Syb57 (57.05 ±9.91 nM), Syb43 (99.77 ±10.61 nM) and Syb175 (101.66 ±2.90 nM). These sybodies were observed to have very low k_{off}s and lower k_{on}s relative to other sybodies with similar affinities (in similar conditions) (Bräuer et al., 2019; Deneka et al., 2021; Yao et al., 2021). It is plausible that this results from some form of cooperativity in TRPML1 binding.

4.5 Epitope Mapping of TRPML1 Sybodies

4.5.1 Purification of TRPML1 Luminal Domain

Sybodies can bind to the luminal or cytosolic side of TRPML1. To identify their binding epitopes, the luminal domain (residues 83-295) was expressed and secreted from HEK293F cells using the pHLSEC vector, purified with Ni-NTA resin and by SEC (S200), and biotinylated (Figure 30A, B and D) (Aricescu et al., 2006). Two constructs were tested, an N-terminal and C-terminal Avi-tagged construct. Both eluted at the expected retention volume for a tetrameric construct (106 kDa). The C-terminal construct was found to show a distinct transition when analysed by nano-DSF (melting temperature: 64.9°C), suggesting that it is folded (Figure 30C). Moreover, higher yields of the C-terminal-tagged construct were obtained and the N-terminal-tagged construct was not successfully biotinylated. The luminal domain is highly glycosylated based on band smearing in the polyacrylamide gel. The biotinylated C-terminal construct was used for BLI and pull-down experiments with streptavidin agarose resin.

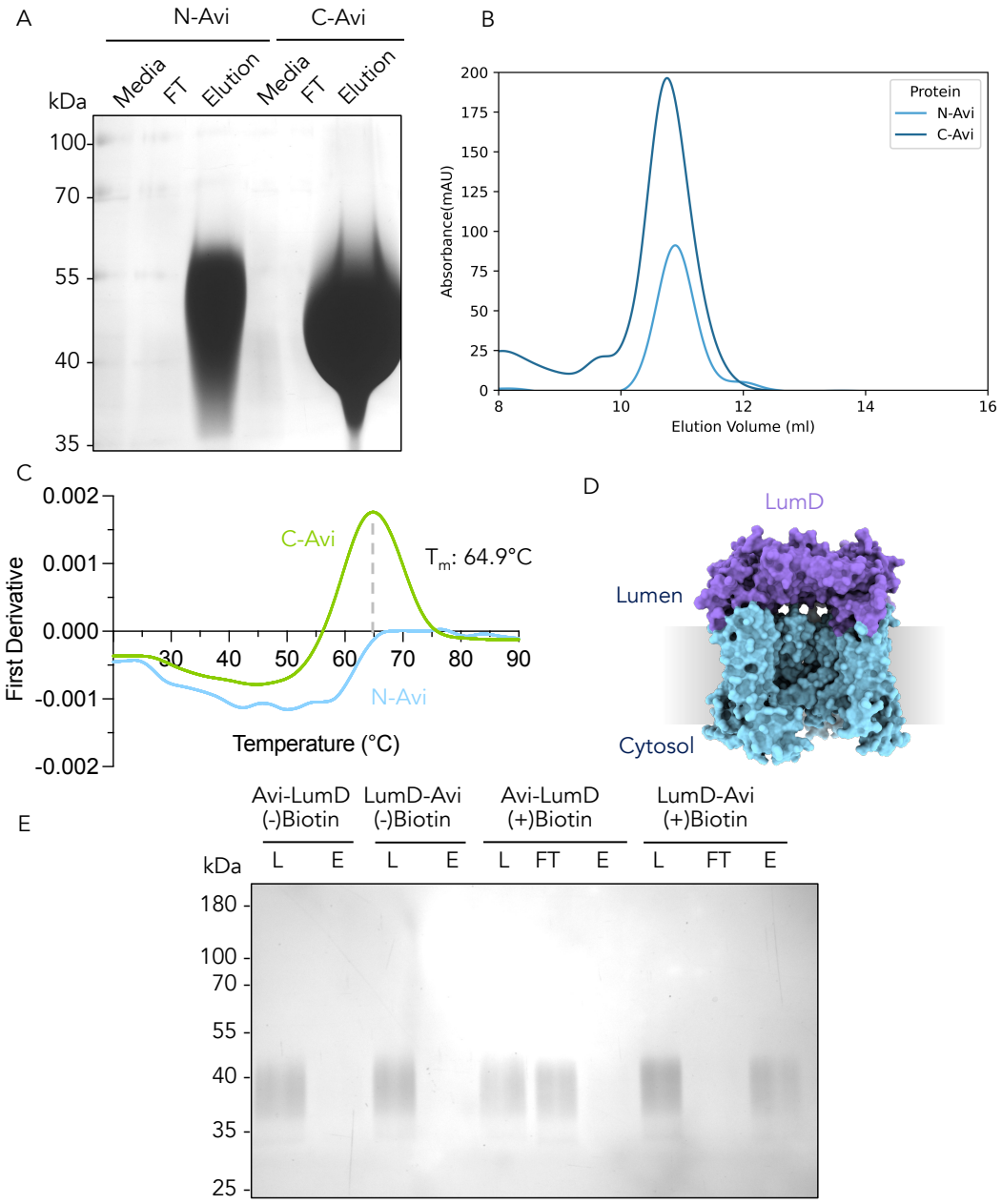

Figure 30: TRPML1 luminal domain (LumD) purification, characterization and biotinylation. A) TRPML1 luminal domain (83-295) with N or C-terminal avi-tag was secreted from HEK-293F cells (500 ml) (Media sample) and purified using Ni-NTA resin. Gel shows media, flow-through (FT) and 250 mM Imidazole elution. B) SEC purification profile (S200) following biotinylation. C) Melting curve of N and C-terminal avi-tagged constructs obtained using nano-DSF. First derivative of F_{350}/F_{330} (F: Fluorescence) values is displayed to calculate the melting temperature (inflection point). D) TRPML1 structure with LumD displayed in purple (PDB: 6E7Y). E) SDS-PAGE gel for biotinylation test with streptavidin resin for biotinylated (+) or non-biotinylated (-) N or C-terminal avi LumD. L: Load, FT: Flow-Through and E: Elution.

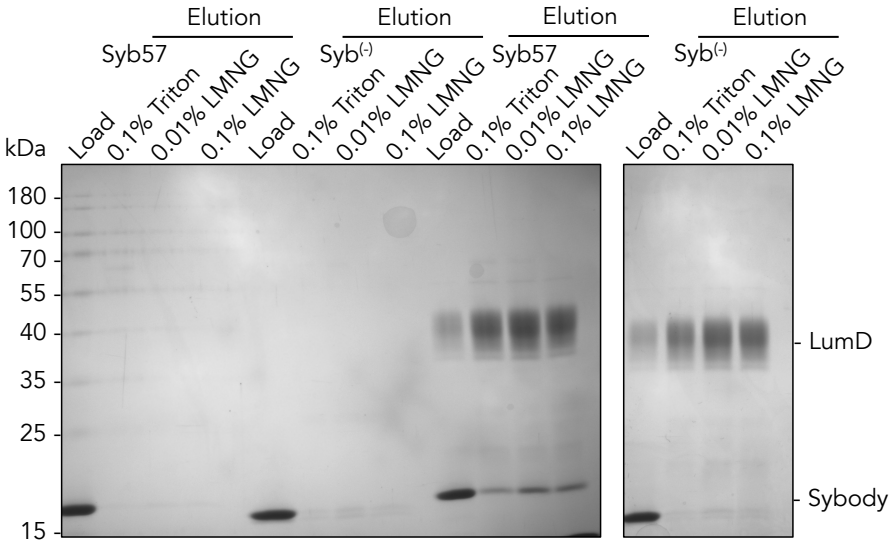

Figure 31: Optimization of luminal domain pull-down conditions with streptavidin resin. Syb57 and non-binding TRPML1 sybody (Syb$^{(-)}$) were used for the optimization in which TBS with different detergents and different detergent concentrations were tested for the wash and binding steps. Samples were run on a 15% SDS-PAGE gel. The aim was to eliminate sybody binding on resin with no LumD (first two sets of elutions). For resin with LumD, the aim was to eliminate Syb$^{(-)}$ binding without impairing Syb57 binding. The optimal condition was TBS with 0.1% LMNG.

4.5.2 Luminal Domain Sybody Binding Characterization

Using the purified luminal construct, the epitope (luminal or cytosolic) of the sybodies could be characterized.

Both in BLI and pull-down experiments, non-specific binding of the luminal domain and sybody to the resin or tip were observed. This resulted from the exclusion of the detergent (0.003% LMNG) for binding experiments, which eliminates non-specific binding (Shah and Duncan, 2014). Different conditions (salt concentration and detergent) were tested to identify conditions that would eliminate most non-specific binding (Figure 31; supplementary Figure 9). It was found that TBS with 0.01% LMNG (and 0.5 mg/ml BSA for BLI) eliminated most non-specific binding to the resin (non-specific sybody and luminal domain binding to the resin, and negative control sybody binding to the luminal domain) or tip without disrupting specific sybody binding.

Using these conditions, sybody binding to the luminal domain was tested by pull-down with

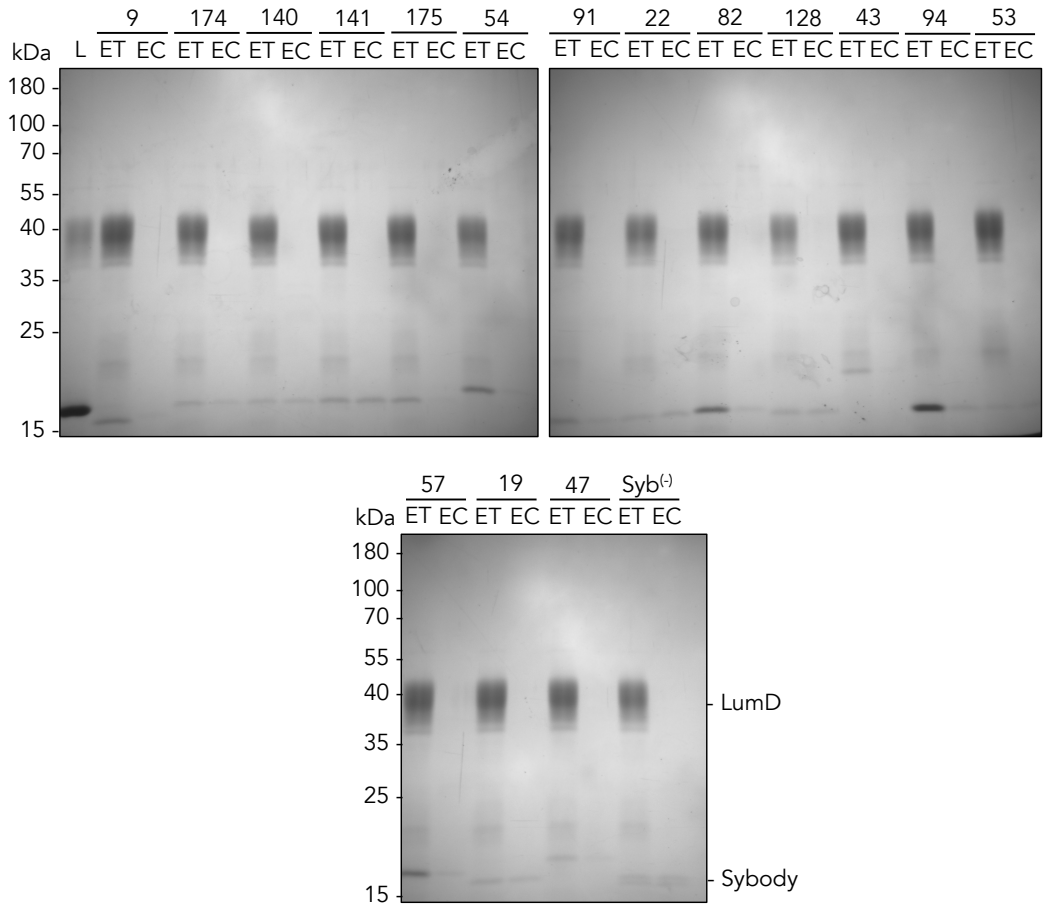

Figure 32: Luminal domain streptavidin resin pull-down with sybody. Sybodies and LumD were mixed and loaded on streptavidin resin, washed and eluted with SDS (ET). Sybodies were also loaded on empty resin, washed and eluted (EC). Samples were run on a 15% SDS-PAGE

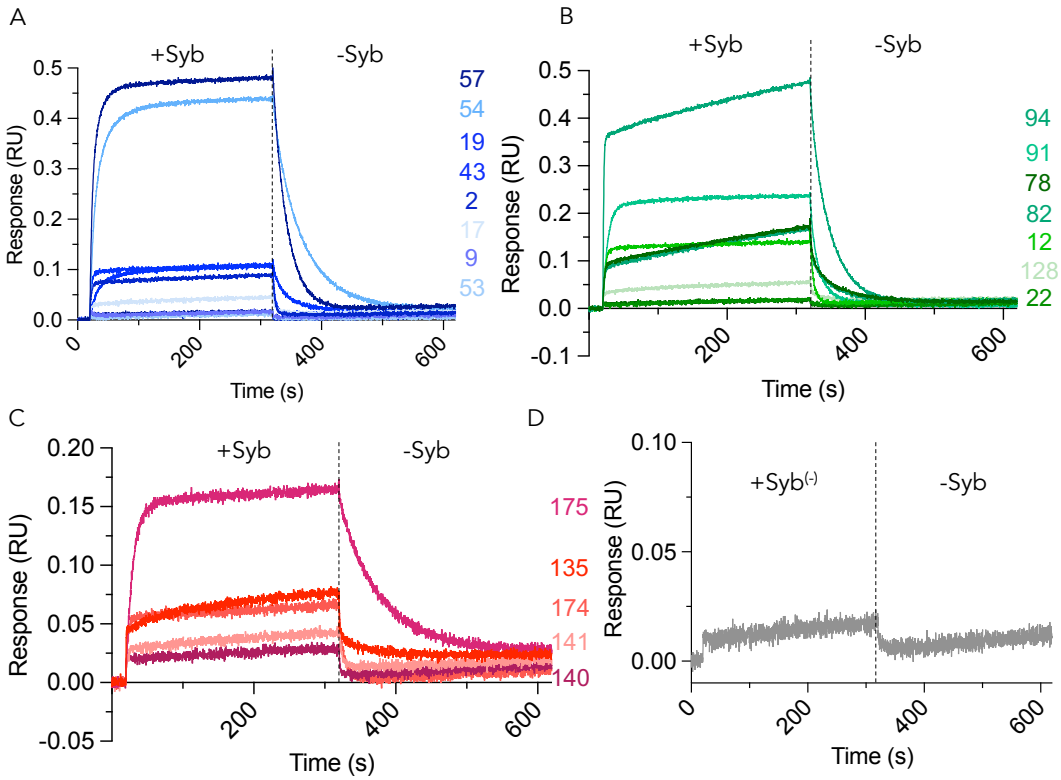

Figure 33: BLI traces for sybody binding to the luminal domain. BLI streptavidin tip with luminal domain was submerged in solution with A) loop, B) concave, C) convex library binders to identify luminal binders. (D) Negative control binder ($Syb^{(-)}$) shows little binding. The experiment was undertaken with TBS containing 0.5 mg/ml BSA and 0.01% LMNG.

streptavidin agarose. Sybody was loaded on streptavidin resin with or without luminal domain to identify luminal domain-specific binding. Comparison of the intensity of the sybody band between the two samples enables the identification of genuine binders. The following binders were clearly identified to bind to the luminal domain: Syb9, 175, 54, 91, 82, 43, 94, 57, 47 and potentially Syb174 (Figure 32). It is not clear that Syb140, 141, 22, 128, 53 and 19 bind to the luminal domain based on this assay.

To test these results further and resolve ambiguity, the binders were tested by BLI using stringent conditions (TBS with 0.01% LMNG and 0.5 mg/ml BSA) (Figure 33). The sybody negative control showed observable non-specific binding in the pull-down experiments, while this was not the case in this assay. BLI results suggest that all binders bind to the luminal domain, except Syb9, 53, 22 and 140. Strong variations are observed across binders in the response. Maximal responses (e.g. Syb57, 54 and 94) are larger than for the full-length TRPML1 since the sybody is larger relative to the luminal domain than the full-length TRPML1. Faster associations and dissociations are also observed with the luminal domain construct, potentially due to differences in the experimental conditions (Luminal domain buffer: TBS + 0.5 mg/ml BSA + 0.01% LMNG; Full-length buffer: TBS + 0.003% LMNG). Moreover, the epitopes in the full-length protein may not all be present in the truncated luminal domain construct (conformational epitopes or residues in the TM regions) and/or the luminal domain may be processed differently than the full-length protein since it does not reach the lysosomal membrane (cathepsin cleavage and glycosylation). Overall, this data suggests that all the tested binders, except Syb9 (binds in pull-down but not BLI), 53, 22 and 140 are luminal binders. To identify true cytosolic binders, epitope binning experiments were carried out using BLI.

4.5.3 Epitope Binning

In epitope binning experiment, multiple sybodies are added simultaneously to the target protein to determine if an additive effect is observed. If the response from multiple binders is additive, it suggests that they can bind to the target simultaneously and that they are binding to different epitopes.

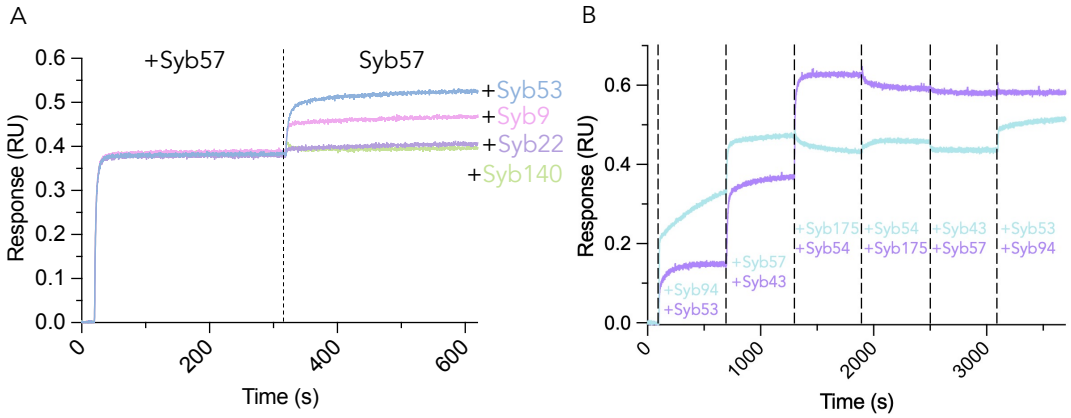

Figure 34: Epitope binning BLI experiments with full-length TRPML1. A) Streptavidin tips with TRPML1 full-length were submerged in a well with Syb57 (luminal binder) followed by a well with Syb57 along with a potential cytosolic binder. B) The experiment displayed in A was repeated but combining all the high-affinity binders with the cytosolic binder (6 binders total in final well). All experiments were carried out with sybody at 1 µM.

The first set of BLI experiments were carried out by testing if an additive effect is measured upon the addition of the potential non-luminal binders to Syb57-containing buffer, which was suggested to be a strong luminal binder based on both assays. Full-length TRPML1 was immobilized on a streptavidin BLI tip, which was submerged in Syb57-containing solution (1 μM) and then moved to a solution containing Syb57 along with one of the potential non-luminal binders (Syb9, 22, 53 or 140) (1 μM) (Figure 34). An additive signal was observed for Syb9 and 53, which generated the strongest response. Most data suggests that syb22 and 140 are poor binders and they were not considered further. To further test this result, all of the sybodies of interest (Syb43, 54, 57, 94, 175) were tested incrementally, with Syb53 being added in the first or final step. Syb53 has a clear additive effect following the addition of all the high-affinity luminal binders, which likely cover all the available epitopes on the luminal domain. This provides further evidence that syb53 is a cytosolic binder of TRPML1. If added in the first step, Syb53 generated a response of 0.14, while in the final step it generated a response of 0.07. This difference in response likely arises from the smaller relative change in molecular weight of the protein upon the addition of Syb53 to TRPML1-Syb complexes. It is also clear that there are at least two epitopes within the luminal domain as two main binding events are observed upon the addition of luminal binders.

A cytosolic binder would have a range of applications if it could be expressed intracellularly as an 'intrabody' to bind TRPML1 *in situ* (Dong et al., 2019). Therefore, the suggested cytosolic binding of syb53 was tested further by expressing them in HeLa cells.

4.5.4 Validation of Cytosolic Sybody - Intrabody Application

Syb9 and 53 were cloned into pcDNA to express them intracellularly in mammalian cells and to introduce a C-terminal mCherry tag.

Sybodies were co-transfected in HeLa cells with GFP-TRPML1 using PEI (DNA : PEI 1:2) and were expressed for 48 hours. Cells were then fixed and imaged by confocal microscopy. Syb53-mCherry was found to strongly co-localize with GFP-TRPML1 while Syb9 did not, despite its strong expression in cells (Figure 35A and B). The lack of co-localization of syb9 is a good control for the assay as it demonstrates that only true cytosolic binders will successfully colocalize with TRPML1. This resolved the ambiguity with this binder as it was found to bind the luminal domain in the pull-down assay but not in BLI (both for luminal domain and full-length). It was observed that in most cells co-transfected with Syb53-mCherry, GFP-TRPML1 localized near the nucleus. This may result from disruption of trafficking of GFP-TRPML1 due to sybody binding. In future experiments, GFP-TRPML1 was transfected and expressed for 24 hours. Cells were then transfected with Syb53-mCherry, which was also expressed for 24 hours. The cells were then fixed and imaged. Using this protocol, GFP-TRPML1 was found to localize to vesicles across the cytoplasm, and syb53-mCherry co-localization was still observed (Figure 35C). To ensure that TRPML1 colocalization was specific, the sybody was expressed with GFP-TRPML2 and a non-lysosomal membrane protein (LAAT2) (Figure 35D and E). Co-localization was not observed when co-expressing Syb53-mCherry with these membrane proteins, suggesting the effect is a result of specific binding to TRPML1.

Once epitope mapping had been completed for TRPML1 sybodies, stability and binding of luminal binders at acidic pH had to be determined.

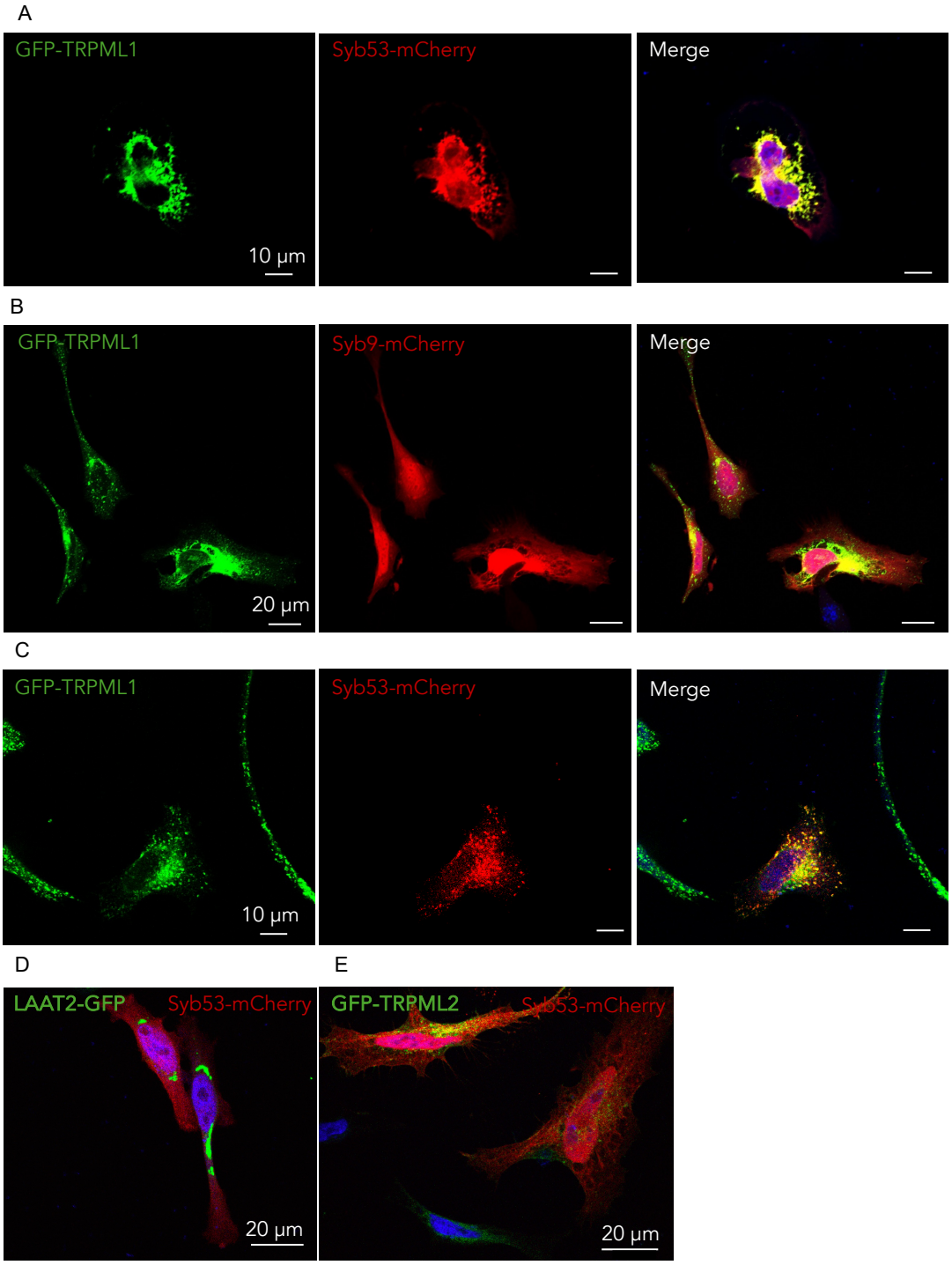

Figure 35: Intrabody application of Syb53-mCherry in HeLa cells. A) Co-transfection of Syb53-mCherry (red) or B) Syb9-mCherry and GFP-TRPML1 (green). C) Sequential transfection of Syb53-mCherry and GFP-TRPML1, D) LAAT2-GFP or E) GFP-TRPML2 (green). DAPI (blue)

4.6 Binding of TRPML1 Sybodies at Lysosomal pH

4.6.1 Stability at Lysosomal pH

Before testing sybody binding at acidic pH, sybody stability was tested.

This was carried out by measuring thermostability at pH 4.5-7.4 (lysosomal pH) using nano Differential Scanning Fluorimetry (nanoDSF). Most of the sybodies were found to show a clear transition (Figure 36A-F). A shift to lower melting temperatures was observed for all binders as lower pH is expected to destabilize protein structure. However, the sybodies remained stable to high temperatures, with melting temperatures ranging from 60.3°C (Syb57) to 80.5°C (Syb175) at pH 4.5. These melting temperatures far exceed experimental conditions and physiological temperatures. Based on these results, the sybodies would remain folded for binding analysis at acidic pH.

4.6.2 Binding at Lysosomal pH

To determine if the sybodies could be used in lysosomes, binding was tested at lysosomal pH (4.5) using BLI (Figure 37A-E).

Syb54 and 57 were observed to bind at lysosomal pH, while the other sybodies did not. For syb54 and 57, the observed response was smaller and the dissociation was significantly faster than at pH 7.4, suggesting that the binding is partially impaired at acidic pH. This was also the case for Syb57. Strong baseline drifting was observed for the pH 4.5 measurements for the sybodies that did not bind to TRPML1. This may be due to the reduced stability of the tip (streptavidin) or TRPML1 at this pH, which may in part be responsible for the weaker association of Syb54 and 57. TRPML1 also localizes to late endosomes, where disruption of TRPML1 activity may be involved in certain pathologies (Lie et al., 2022). Late endosomal pH is approximately 5.5 (Wallabregue et al., 2016). Therefore, the binding of Syb94, which does not bind at pH 4.5, was tested to identify whether it could bind to TRPML1 in less acidic environments. Syb94 is observed to bind TRPML1 up to pH 5.5 and could thus have activity in late endosomes (Fig-

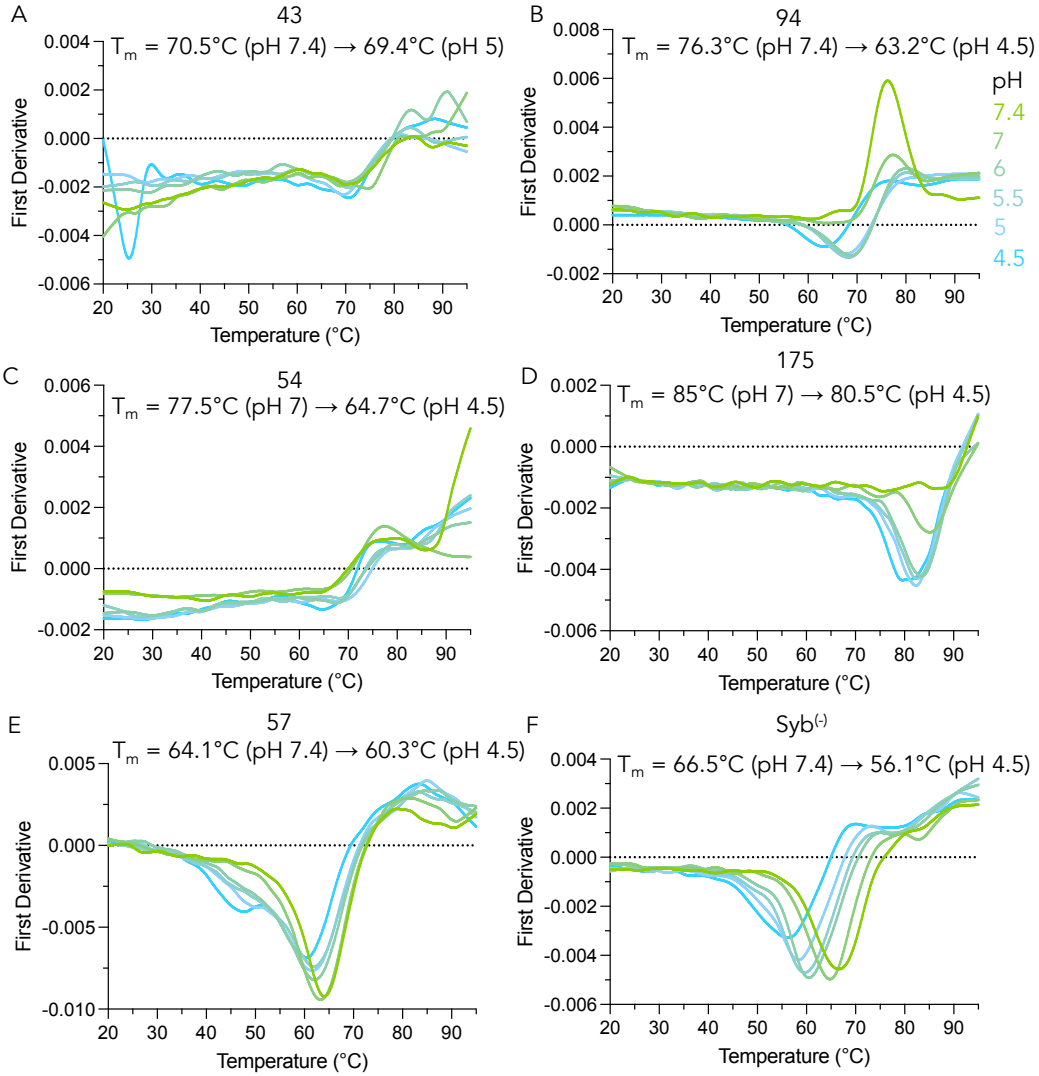

Figure 36: Thermostability (nano-DSF) of luminal binders at lysosomal pH. (A-F) Stability of high-affinity binders across pH range (pH: 7.4, 7, 6, 5.5, 5 and 4.5) between 20 and 95°C. First derivative of F_{350}/F_{330} is shown on the y-axis, from which the melting temperature (T_m) is derived.

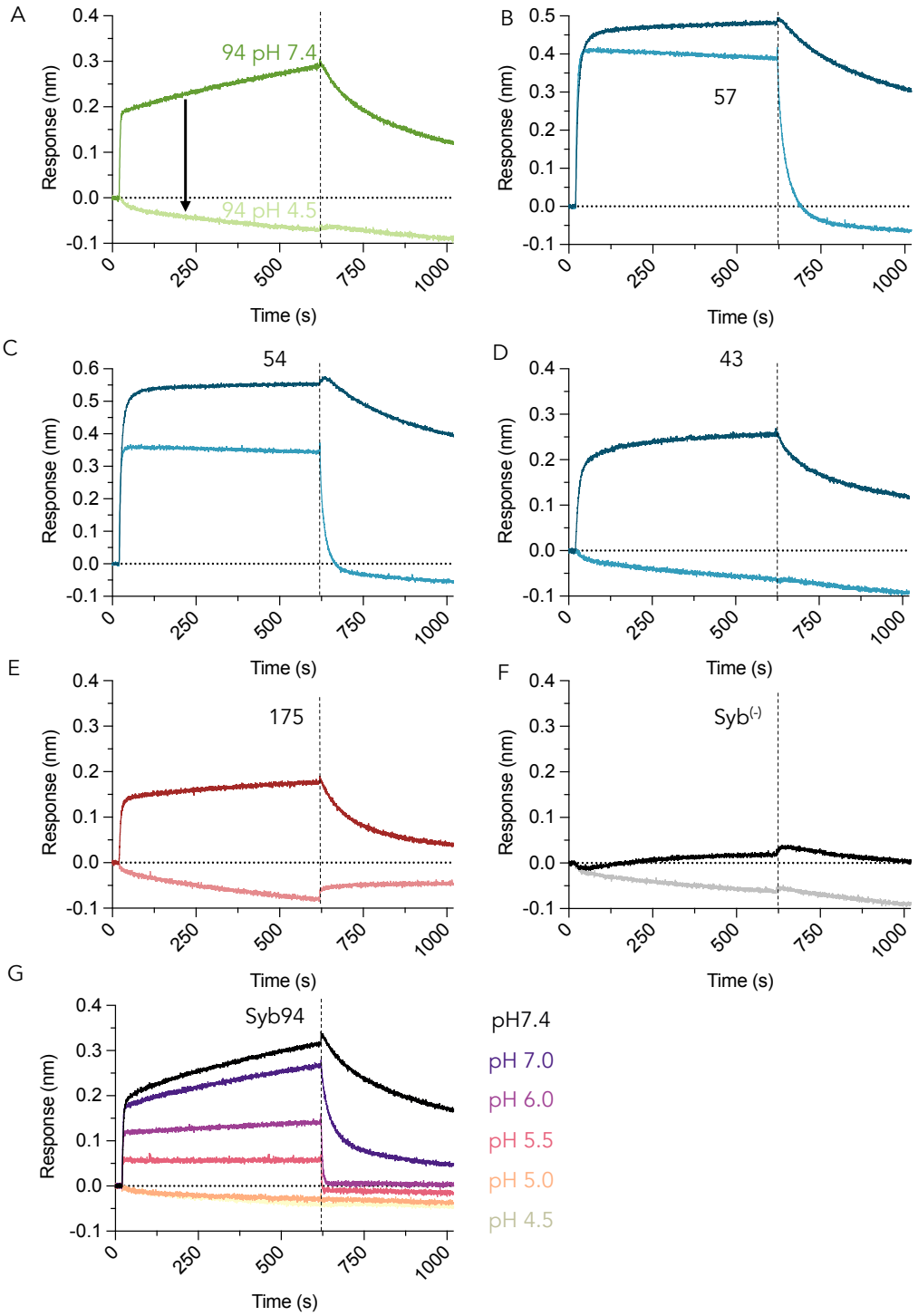

Figure 37: BLI experiments testing sybody binding to full-length TRPML1 at lysosomal pH. (A-F) Sybody (1 μM) binding at pH 7.4 (dark shade) and 4.5 (light shade). G) Syb94 binding across a pH range (4.5-7.4).

ure 37G). The binding is likely disrupted due to the deprotonation of sybody or TRPML1 side chains and pH-associated conformational changes. If pH-dependent changes in TRPML1 disrupt the binding, the sybodies could enable the identification of luminal domain hotspots that are involved in pH regulation of the channel, which is poorly understood (Li et al., 2017). Sybodies binding at specific pH ranges could also be used to target TRPML1 activity in certain organelles or could act as pH sensors as acidification of TRPML1-containing vesicles would disrupt the interaction.

As previously highlighted, there is a need for tools that would enable to investigate functions and localizations of lysosomal membrane proteins. Members of the Newstead lab have generated nanobodies and synthetic nanobodies against these lysosomal membrane proteins. Many of these binders may target luminal regions of lysosomal membrane proteins. For future selections, it would be beneficial to identify if there is a relationship between sequence features and binding at acidic pH. The imidazole ring of histidine side chains acts as a pH sensor for interactions in numerous lysosomal proteins due to its pKa of approximately 6 (Zachos et al., 2012). Histidine protonation has previously been exploited in antibodies to confer acidic environment-specific binding in tumors (Johnston et al., 2019). Syb43, 94 and 175 all have histidine residues within their side chain. The histidine in Syb43 is located in CRD2 and is conserved in Syb21 and 17, which show perfect conservation in CDR1 and 2. This suggests that CDR2 is involved in the binding of this sybody and that deprotonation of this residue would disrupt an important interaction, weakening sybody binding. Syb94 has two histidines in CDR1, one histidine in CDR2, and one histidine in CDR3. The first histidine is conserved in nearly all concave library binders for TPRML1, but not against other targets. However, sybody selections against other lysosomal targets, such as TMEM-175 (selection by Sigurbjorn Markusson), generated concave binders with strong conservation of histidines within the CDR1. These binders will likely not bind or bind weakly at lysosomal pH as this conservation suggests that the residue is important for sybody binding. Strong conservation of histidine was not observed in the other libraries, suggesting that other libraries may be more suitable for lysosomal proteins. Syb175 has one histidine in CDR1 that is not conserved, but contains a highly conserved anionic residue (aspartate) in CDR3. Binding may be disrupted by protonation of anionic side chain at acidic pHs (approxi-

mate pKa of 4 for aspartate and glutamate), but histidine residues may act as a stronger predictor (Forsyth et al., 2002). Protonation of anionic side chains may act to weaken Syb57 binding as its CRD3 contains 5 anionic residues. Both Syb54 and 57 have histidine residues in their CDRs. However, these residues are not conserved or are found in positions that are unlikely to disrupt binding (e.g. C-terminal end of CDR1). Therefore, key predictors based on the available data are strongly conserved histidine residues in the center of CDRs. In the future, mutagenesis of histidine residues to cationic amino acids could serve to stabilize binding at different pHs. Alternatively, sybody selection can be carried out at acidic pH, but this reduces the stability of the target protein significantly, impairs immobilization of the target protein and sybodies, and may eliminate important cytosolic binders.

pH-dependence of binding has previously been observed and engineered. Antibody binding at acidic pH has previously been engineered to favor binding in acidic tumors, resulting from histidine protonation (Johnston et al., 2019). Computational histidine-scanning mutagenesis testing binding free energy has been used successfully (Sulea et al., 2020). Similar approaches could be used to engineer binders that bind specifically at acidic pH, along with affinity maturation at acidic pH.

4.7 TRPML1 Sybody Selection Summary

In this chapter, the results of a sybody selection against TRPML1 purified in LMNG were described (summarized in Table 2). Five high-affinity binders, Syb43, 54, 57, 94 and 175, were identified that bind to the luminal domain, notably, with low off rates. This was critical for application of these binders to cell-based assays. Two of these sybodies, Syb54 and 57, were identified to be stable and bind at acidic pH, which will be essential information when testing the activity of these binders under lysosomal conditions. By combining a range of techniques, it was shown that one of the sybodies, syb53 and potentially Syb9, binds to the cytosolic domain of TRPML1. This sybody can be used as an 'intrabody' as it binds to TRPML1 when expressed in the cytosol of HeLa cells.

Syb	Source	Yield (µg)	Pull-Down FL	Pull-Down LD	Octet Binding Full-Length	Octet Binding Luminal Domain	K_D (±SEM) nM
9	Loop	64	✓	✓	Response of 0.06, fast on, full off after 6 min	X	
19	Loop	45	✓	X	Response of 0.22, fast on, slow off (1/4 after 6 min)	Response of .1, fast on, fast off	
43	Loop	155	✓	✓	Response of 0.2, slow on, 1/3 off in 6 min	Response of .12, slow on, slow off	99.77 (±10.61)
47	Loop	86	✓	✓	Response of 0.15, fast on, full off after 6 min	Response of .08, fast on, fast off	
53	Loop	84	✓	X	Response of 0.03, fast on, fast off	X	
54	Loop	139	✓	✓	Response of 0.26, fast on, slow off (1/3 off after 6 min); binds at acidic pH	Response of .44, fast on, slow off	38.26 (±9.76)
57	Loop	39	✓	✓	Response of 0.26, fast on, 2/3 off after 6 min; binds at acidic pH	Response of .48, fast on, fast off	57.05 (±9.91)
82	Concave	80	✓	✓	Response 0.25, fast on, 1/2 off in 6 min	Response of .2, fast on, fast off	
91	Concave	33	✓	✓	Response 0.22, fast on, nearly 1/2 off in 6 min	Response of .25, fast on, fast off	
94	Concave	128	✓	✓	Response of 0.2, slow on, slow off, remains bound; does not bind at acidic pH	Response of .5, fast on, fast off	34.92 (±3.06)
128	Concave	60	✓	X	Response of 0.2, fast on, more than 1/2 dissociates in 6 min	Response of .05, slow on, fast off	
140	Convex	160	Partial	X	Response of 0.01, signal too small to assess on and off	X	
141	Convex	138	✓	X	Response of 0.07, fast on, fast off (nearly fully dissociated within 100 seconds)	Response of 0.05, fast on, fast off	
174	Convex	80	Partial	X	Response of 0.015, signal too small to assess on and off	Response of 0.07, fast on , fast off	
175	Convex	114	Partial	✓	Response of 0.07, fast on, slow off (not fully off after 300s); does not bind at acidic pH	Response of 0.16, fast on, slow off	101.66 (±2.90)

Table 2: Sybody binder characterization summary.

5 | Structural Characterization of TRPML1-Sybody Complexes

5.1 Structural Characterization of Nanobody Complexes

Nanobodies have been used extensively to stabilize proteins for structural characterization by crystallography and cryo-EM (Uchański et al., 2020). With the approval of nanobodies for therapeutic use, nanobodies have been generated for the specific modulation of membrane proteins (Jin et al., 2023; Manglik et al., 2017; Stortelers et al., 2018). For this application, the structural characterization of nanobody-protein complexes has aimed to understand their mechanisms of action (Manglik et al., 2017; Wu et al., 2021). In turn, this can reveal novel information about the mechanisms of action of the proteins of interest, including the function of uncharacterized regions (Deneka et al., 2021). These complexes can also enable to determine the active regions/peptides of the nanobody, facilitate nanobody engineering, and facilitate the identification of novel druggable sites (Brawley et al., 2022; Koenig et al., 2021).

The obtained TRPML1 sybodies were initially screened for activity. Whole-cell patch clamp experiments enabled to identify high-affinity and potent modulators of TRPML1. The complexes these modulators form with TRPML1 were then characterized by cryo-EM to understand their mechanisms of action (Aim 2). This is important for: (1) sybody engineering, (2) to determine sybody specificity and identify novel regions that could enable specific modulation of TRPML1, and (3) to better understand the mechanism of TRPML1, which is still poorly understood despite the wealth of structural information available.

5.2 Screening of TRPML1 Sybody Modulators

5.2.1 FURA-2 Screen

Calcium indicators can be used to detect cytosolic calcium flux. FURA-2 has previously been used to measure lysosomal calcium release using a TRPML1 mutant that is mistargeted to the plasma membrane (TRPML1-L^{15}L/AA-L^{577}L/AA) (Shen et al., 2012). The main advantages of this technique are that it can enable high-throughput sybody screening and it can be used to study both the plasma-membrane variant and WT TRPML1 with the same setup. In collaboration with the Wade-Martins lab (Johanna Hoffmann), we adapted this assay to screen TRPML1 sybodies. In the assay, the luminal domain of the plasma-membrane-localized TRPML1 faces the extracellular solution (Figure 38A). Therefore, luminal binders can be added to the extracellular solution (Hanks' Balanced Salt Solution with Calcium) and probed for their activity based on FURA-2 signal.

SH-SY5Y cells were transfected with GFP-TRPML1L$^{15L/AA}$-L^{577}L/AA, the protein was expressed for 48 hours and plasma-membrane localization was confirmed by fluorescence microscopy (supplementary Figure 10A). ML-SA5 (TRPML1 activator) was injected in the wells seeded with transfected cells, resulting in calcium flux (supplementary Figure 10B). To test sybody activity, sybodies were injected at 2 μ on transfected cells. Only one sybody (Syb128) was found to potentially activate TRPML1, but the variability between experiments was too large to obtain conclusive results (supplementary Figure 10C). In an alternative experiment, cells were pre-treated with sybody (2 μM for 10 min) before agonist injection to detect both inhibitors and potentiators (supplementary Figure 11). Strong variability was again observed in the results and no clear conclusions could be made about the activity of the binders. This variability arises from the strong differences in the transfection efficiencies between experiments and technical problems with the injection system. Previous studies used a microscope system to screen expression levels based on GFP fluorescence and imaged FURA-2 signal for individual TRPML1-expressing cells (Dong et al., 2009; Shen et al., 2012). Since we could not adapt the experiment to match this setup, I identified an alternative method to determine if the sybodies modulated

TRPML1 activity.

5.2.2 Whole-Cell Patch Clamp

TRPML1 activity has previously been investigated using electrophysiology, including whole-cell patch clamp on the plasma-membrane TRPML1 mutant and lyso-patch clamp on WT TRPML1 (Schmiege et al., 2017). Lyso-patch clamp would require delivery of the sybodies to the lysosomal lumen, which would be too challenging for an initial screening experiment. Therefore, whole-cell patch clamp experiments were carried out by Bethan Cole using the protocol described by Schmiege et al (2017) with the TRPML1L^{15}L/AA-L^{577}L/AA mutant (Figure 38). The experiments were performed at pH 7.4. The setup was validated by showing that ML-SA5 (agonist) induces strong currents specifically in TRPML1-transfected HEK-293 cells (Figure 38B). Strong inward rectifying currents are observed at negative membrane potentials as previously observed upon TRPML1 activation (Figure 38B) (Schmiege et al., 2017).

Using this experimental setup, at least two potent activators of TRPML1 were identified, Syb94 and 57 (Figure 38C and D). Syb94 was found to potently activate TRPML1, even following extended washing steps. Like ML-SA5, it induced strong inward-rectifying currents at negative membrane potential. This effect was shown to be specific as Syb94 did not induce currents in untransfected cells and cells transfected with another TRP channel (TRPC3c) (Figure 38C). Syb57, which binds at acidic pH, was also found to generate currents in TRPML1-transfected cells (Figure 38D). Syb57 was found to enhance both inward and outward currents, and altered the voltage-dependence of these currents. This suggests that it alters the properties of the channel through a novel mechanism. These results were replicated in multiple experiments.

Syb94 and 57 had been identified to be high-affinity binders for TRPML1 that showed strong colocalization in IF experiments. Therefore, I set out to determine the structures of the complexes they form with TRPML1. This would enable to understand their mechanisms of action, and to design binders with improved affinity that could be used to study endogenous TRPML1.

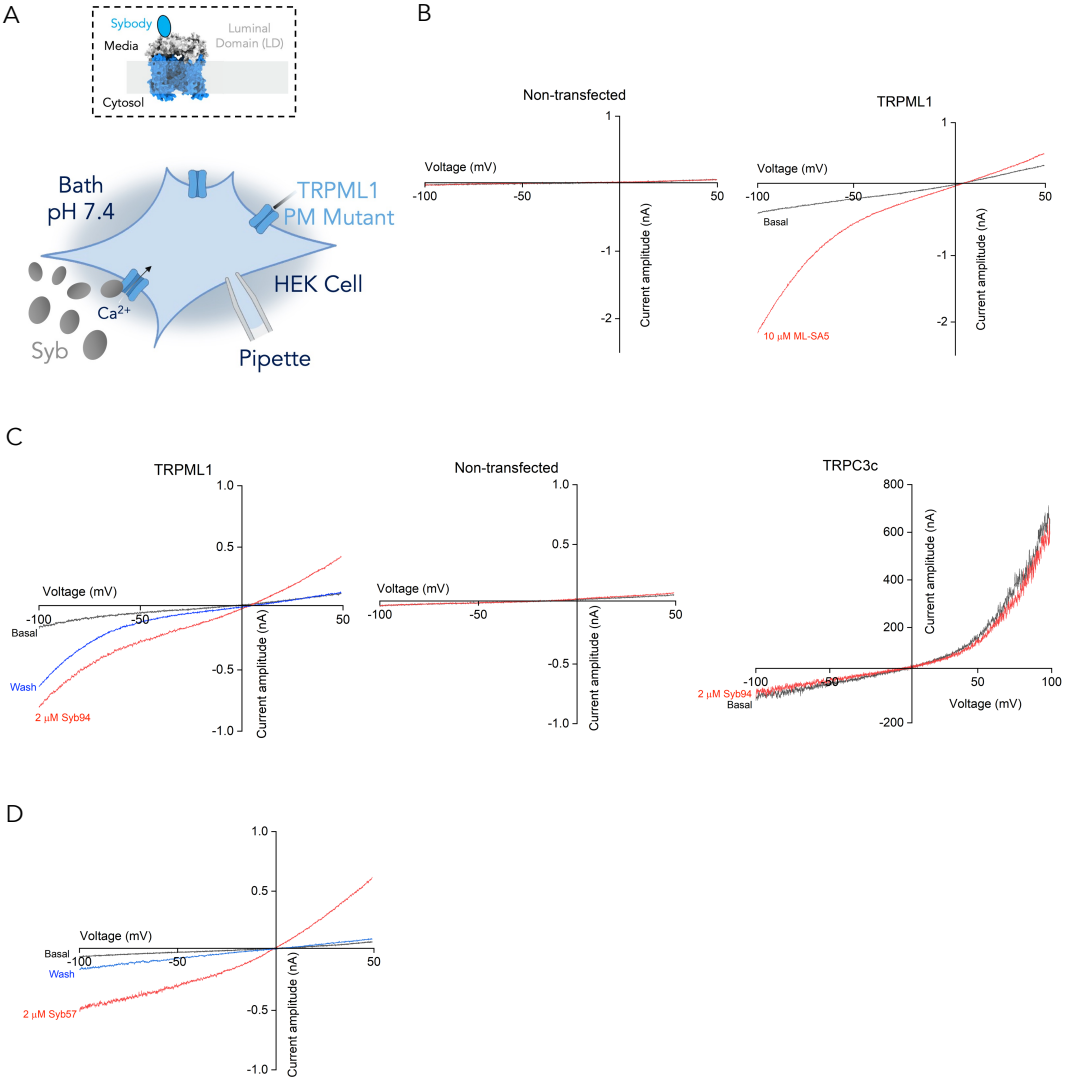

Figure 38: Whole-cell patch clamp recordings in GFP-TRPML1$^{LL/AA}$ transfected cells. A) Experimental setup for whole-cell recordings. HEK293 cells are transfected with GFP-TRPML1$^{LL/AA}$ with the luminal domain facing the bath solution. Sybodies are added to the bath solution (pH 7.4) and the resulting currents are measured. B) Whole-cell currents in non-transfected and transected cells before (basal) and after the addition of ML-SA5 (10 μM), a potent TRPML1 agonist. C) Whole-cell currents before the addition of sybody (basal), after the addition of Syb94 (2 μM) and following a wash (2 min) in bath solution without sybody in GFP-TRPML1$^{LL/AA}$-transfected cells, non-transfected cells and TRPC3c transfected cells. D) Whole-cell currents in GFP-TRPML1$^{LL/AA}$-transfected cells for Syb57 (2 μM). Data collected and plotted by Bethan Cole.

5.3 Sample Preparation and Data Processing

To structurally characterize the sybody-TRPML1 complexes using cryo-EM, the sybodies and TRPML1 were purified by Ni-NTA (Sybodies), FLAG (FLAG-AVI-TRPML1) or 1D4 (TRPML1-mNeonGreen-1D4) affinity purifications and SEC as described in the methods section. Purified Syb94 and FLAG-AVI-TRPML1 or Syb57 and TRPML1-mNeonGreen-1D4 were mixed in a 3:1 ratio and 4:1 ratio (Syb:TRPML1) respectively, incubated on ice for an hour, and the complexes were purified using a superose-6 column (Cytiva) equilibrated in HBS (pH 8) with 0.002% LMNG or 0.05% digitonin (Figure 39A and B). PI(3,5)P_2 was added at 400 μM 30 min prior to grid preparation. Copper grids (Quantifoil) were frozen with the complexes, and micrographs were collected on a Krios G3i (Thermo Scientific).

For the Syb94-TRPML1 complex, the key challenges of data processing were encountered in sorting particles with intact and damaged transmembrane regions (See Methods section for a detailed description of the processing pipeline). Using *Ab initio* reconstructions and heterogenous refinement rounds (cryo-SPARC), particles with damaged transmembrane regions were excluded. With this approach, the structure was solved to 3.02 Å (supplementary Figure 12A). Therefore, for other sybody-TRPML1 complexes samples, digitonin and PI(3,5)P_2 were used to stabilize the transmembrane regions as described in the literature (Fine et al., 2018). For the Syb57-TRPML1 complex, sorting was carried out using the same approach, but for this sample, the two main populations were sybody-bound and apo TRPML1 particles. Partial occupancy states could not be separated using 3D variability analysis (cryo-SPARC), and only two main populations (apo and sybody-bound) could be characterized. The partial occupancy may result from the change in detergent (LMNG for sybody selection and digitonin for cryo-EM), which typically impairs sybody binding. The Syb57-TRPML1 structure was solved to 3.07 Å (supplementary Figure 12B).

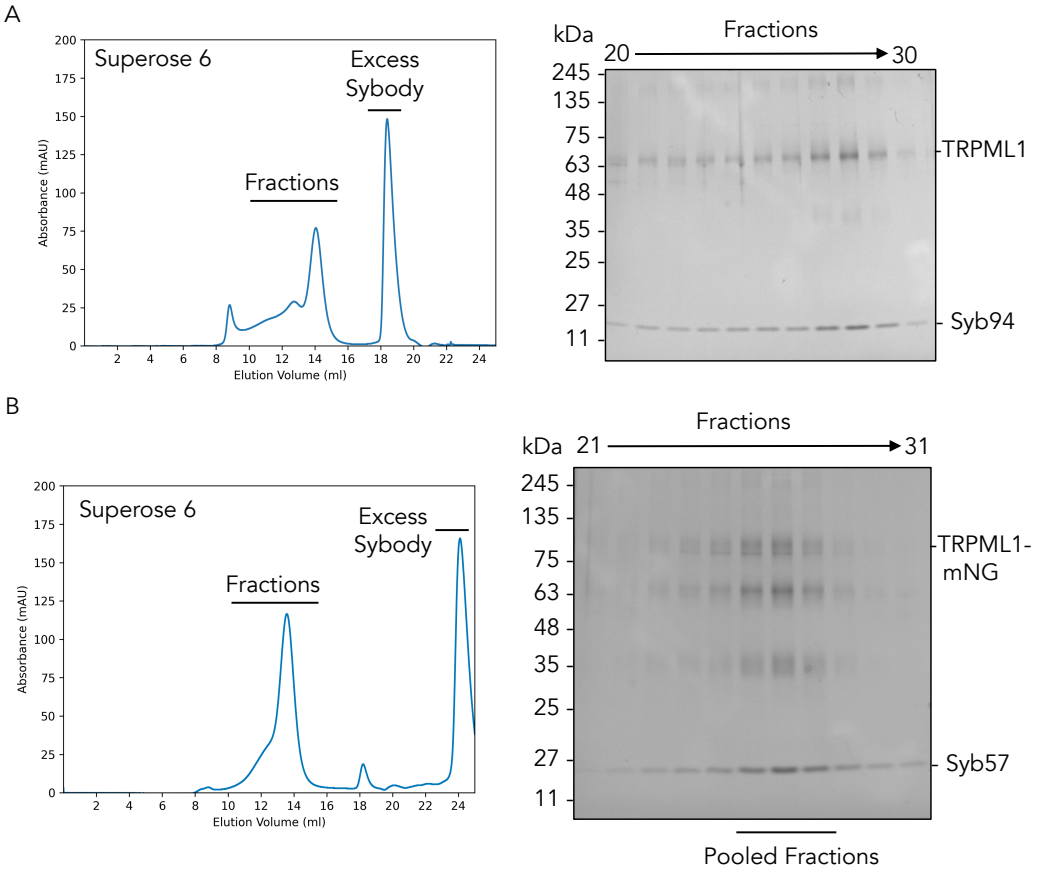

Figure 39: Sybody-TRPML1 complex co-elutions for grid preparation. A) Co-elution of FLAG-AVI-TRPML1 and Syb94 loaded on a superose 6 equilibrated in HBS with 0.002% LMNG. Fractions highlighted on the SEC profile were loaded on 4-20% Tris-Glycine gel. Syb94 co-elutes with TRPML1. B) Co-elution of TRPML1-mNeonGreen-1D4 with Syb57 loaded on a superose 6 equilibrated in HBS with 0.05% Digitonin. Fractions were loaded onto a 4-20% Tris-Glycine gel and were observed to co-elute. Fractions were pooled (pooled fractions), concentrated and QF 1.2/1.3 Cu grids were made.

5.4 Structure of TRPML1-Syb94 Complex

5.4.1 Complex Architecture

The TRPML1-Syb94 complex was solved to 3.02 Å structure in LMNG. The sybody-TRPML1 interfaces, the luminal domain and the selectivity filter are some of the best resolved regions in the map, while loop regions and the cytosolic ends of the S1-S6 helices are more poorly resolved (supplementary Figure 12A). In this structure, Syb94 binds to the luminal domain of TRPML1 in a 4:4 ratio and bridges two neighbouring monomers through an extensive set of interactions (Figure 40A-D). The sybodies do not interact with each other, but may favor binding to the neighbouring monomers through the conformational changes they induce, for example in the β4-β5 loop. The transmembrane helices (TMH) are not fully resolved on the cytosolic side, which may be due to the instability of the protein when frozen in LMNG or the sybody binding (Figure 40B).

To understand how Syb94 interacts with TRPML1, its structure was compared to those of other concave binders. In the complex, Syb94 adopts a similar fold to other concave library binders in published structures, such as a SLC22A6 sybody (PDB: 8BVR; RMSD: 0.964 Å (105)) and a LRRC8A sybody (PDB: 7P5V; RMSD: 0.631 Å (108)) displaying greater similarity with Syb94 (Figure 41A-C). The main changes are observed in the conformation of the CDR regions of the sybody, notably CDR2 and 3 which undergo the largest conformational changes as they play a critical role in target binding. Changes are also observed in the framework, which forms an extensive network of interactions in the complex structure.

In the published TRPML1 structures of different states of the protein, the observed conformational changes are typically small and complex, except at the lower gate where the changes can be correlated to function (Schmiege et al., 2017). Therefore, I aimed to do a detailed analysis of the TRPML1 structure to better understand the key regions that are altered upon sybody binding, and to determine if regions involved in channel activity are altered. Overall, TRPML1 has a similar conformation to previously solved TRPML1 structures, such as the digitonin ML-SI3-

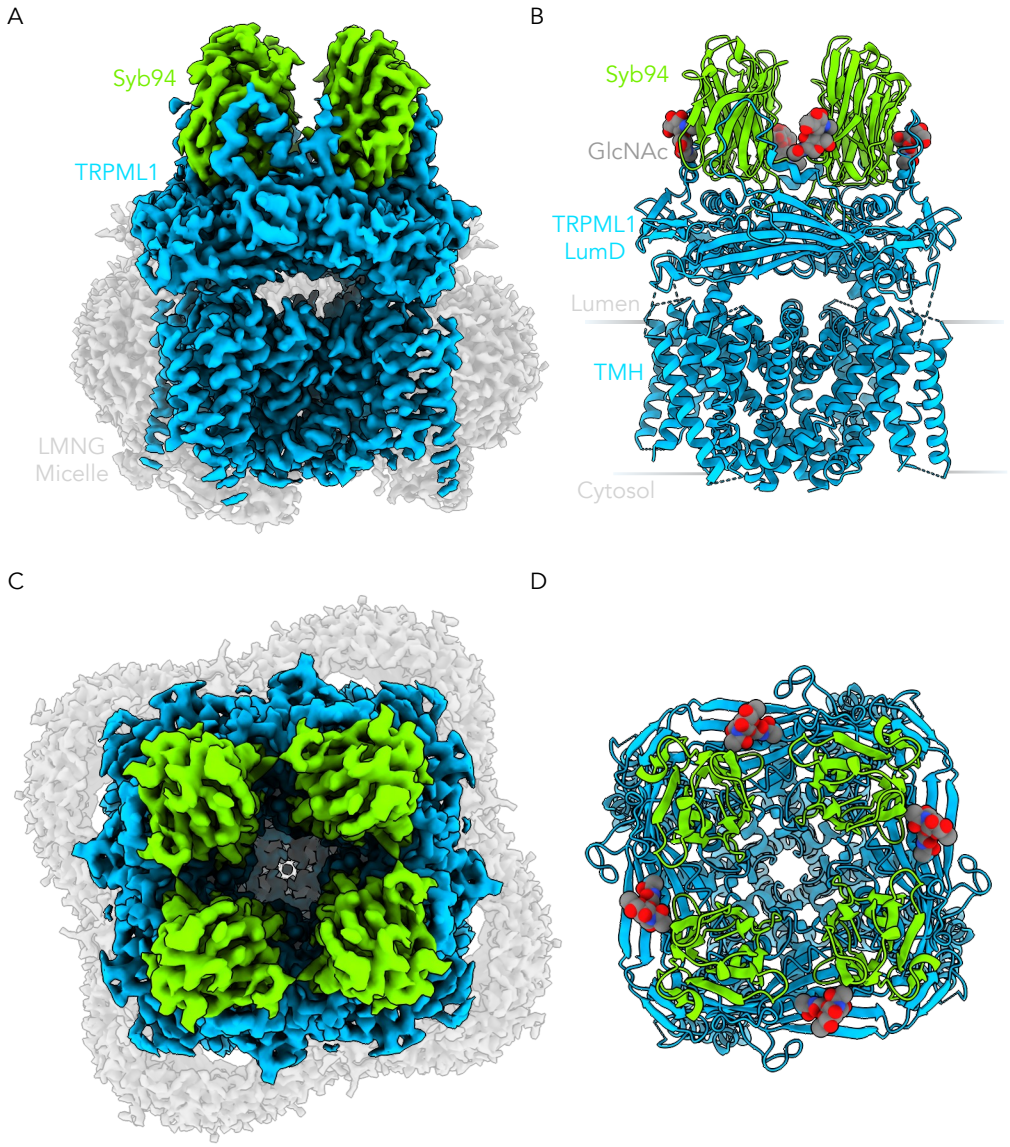

Figure 40: Cryo-EM map of Syb94-TRPML1 complex. A) Sharpened cryo-EM map of Syb94-TRPML1 complex. Syb94 (light green) binds to TRPML1 (sky blue) in a 1:1 ratio. The LMNG micelle wraps around the entire TM region up to the luminal domain-transmembrane interface. B) Cartoon representation of the Syb94-TRPML1 complex, including two GlcNAC molecules (grey). C) and D) are top views of A and B. Contour level of Syb94-TRPML1 complex: 0.36 and micelle: 0.18.

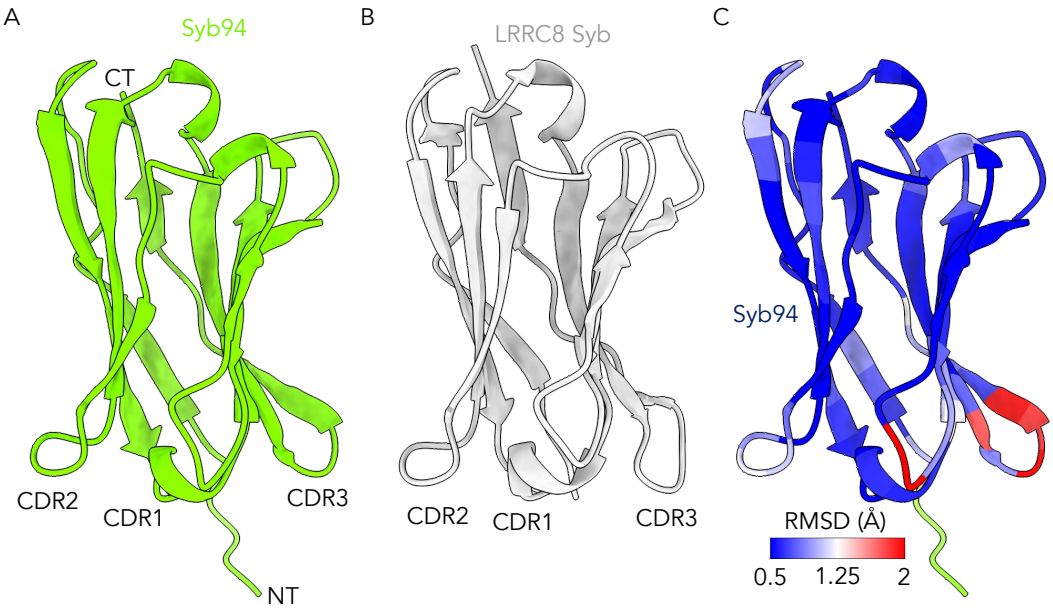

Figure 41: Structure of Syb94 and a comparison with concave LRRC8 Sybody. A) Syb94 (green) adopts the expected Ig-fold of a nanobody, including CDR1-3. B) Structure of a concave LRRC8 sybody (PDB: 7P5V) in grey. It adopts the same conformation as Syb94. C) RMSD values from the alignment between the Syb94 and LRRC8 Syb structures (RMSD: 0.631 Å (108)) mapped onto Syb94. The largest changes are observed in the CDRs, which are the main regions that interact with the target protein. The disordered N-terminal region is only observable in the Syb94 structure as it interacts with TRPML1.

bound (inhibitor) human TRPML1 structure (PDB: 7MGL; RMSD: 0.735 Å (394)). Helices S5-S6 and the pore helices show strong structural similarity between these two structures, while S1-S4 helices, which have longer cytosolic regions, display more differences in their conformation (Figure 42A and B). TRPML structures with less well-defined transmembrane helices on the cytosolic side have previously been published, including mouse TRPML2 structures in nanodiscs (PDB: 7DYS) and amphipol TRPML1 structures (PDB: 5YDZ). In the case of the TRPML1-Syb94 complex, it is plausible that this represents conformational heterogeneity in these region due to the activatory properties of the sybody, the lack of a PIP lipid to stabilize it, and the lower stability of this region in LMNG compared to the commonly used digitonin (Schmiege et al., 2017). The low stability of the TMH in LMNG (detergent for sybody selection) may in part explain the low number of cytosolic binders obtained as sybody binding is more stable in structured regions. This result also explains the challenges encountered when attempting the purification of TRPML1 in DDM, which would provide less stabilization than LMNG. Based on this observation, the TRPML1-Syb57 structure was solved in digitonin and in the presence of PI(3,5)P_2. In this structure, the lower gate constriction of TRPML1 is narrower than in the inhibitor-bound structure (0.20 Å at I514), while the selectivity filter is more dilated (0.32 Å at G470 constriction) than in the inhibitor-bound state (Figure 42E). This could potentially be one of the mechanisms through which Syb94 modulates TRPML1 activity. Overall, the conformation of the β-sheet that makes up the luminal domain is similar (Figure 42C).

The most pronounced changes are found in the loop regions of the structure, which may be involved in mediating the sybody-induced activation (Figure 42B). The map quality in some of these regions was too poor to build the loops. However, the sybody enabled to determine the structure of a previously unresolved region- the β4-β5 linker. This region (Val195-Leu228) is partially disordered and helical (α and poly-proline helix), and is rich in polar and anionic residues (Figure 42D). Its conformation is very similar to the α-fold prediction (Figure 42D). It includes a potential cathepsin cleavage site and a glycosylation site (N220) previously reported in the literature (Chandra et al., 2011; Kiselyov et al., 2005; Miedel et al., 2006). Cathepsin cleavage of this loop has been shown to regulate channel activity (Kiselyov et al., 2005; Qi et al., 2016). The cleavage is not observed in the map as Syb94-bound particles were selected for the

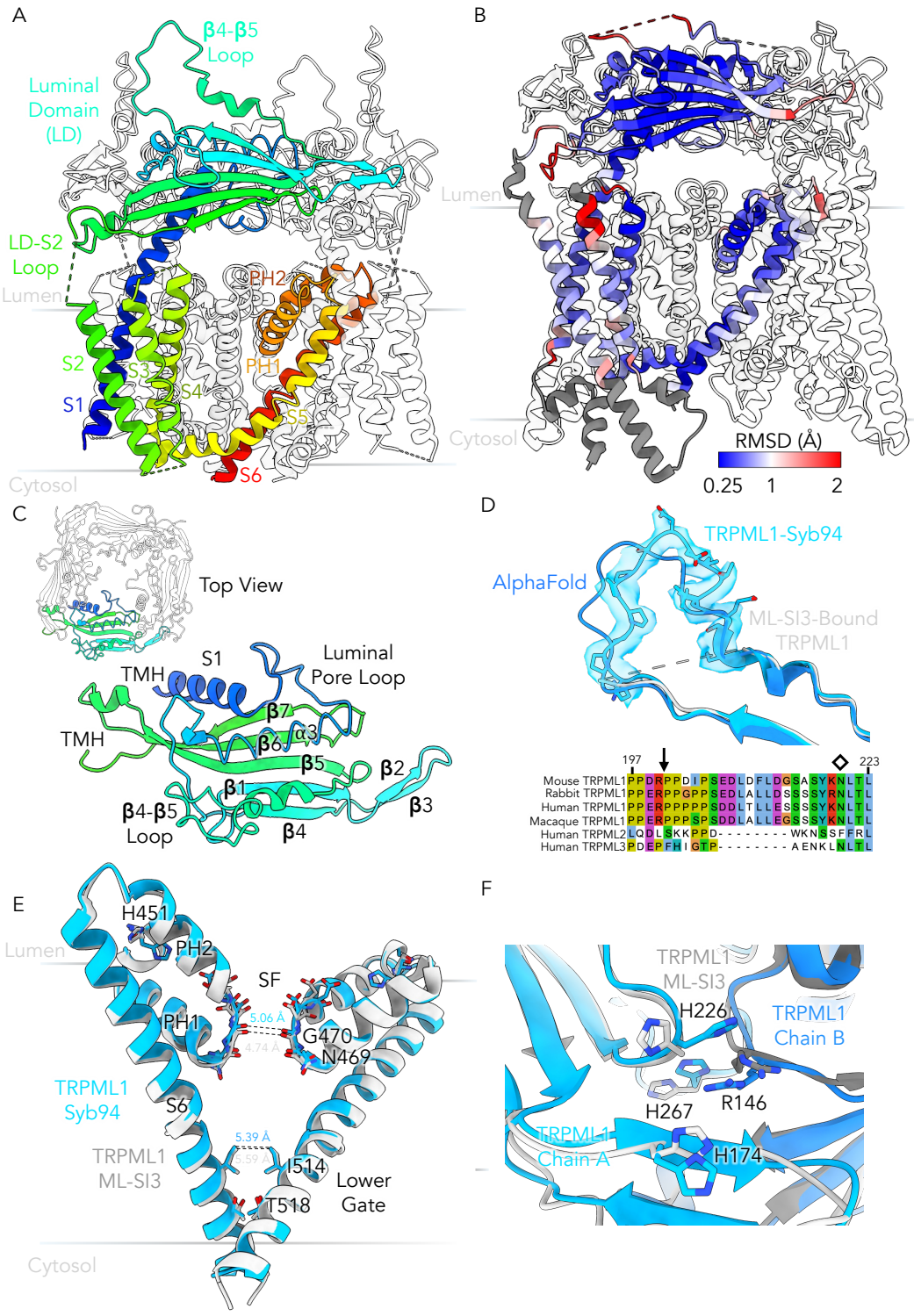
A
β4-β5 Loop
Luminal Domain (LD)
LD-S2 Loop
Lumen
PH2
S2
S3
PH1
S4
S1
S5
S6
Cytosol
B
Lumen
Cytosol
RMSD (Å)
0.25 1 2
C
Top View
S1
TMH
Luminal Pore Loop
β7
α3
TMH
β6
β5
β2
β1
β3
β4-β5 Loop
β4
D
TRPML1-Syb94
AlphaFold
ML-SI3-Bound TRPML1
197
223
Mouse TRPML1 PPDRPPDIPSEDLDFLDGSASYKNLTL
Rabbit TRPML1 PPERPPGPPSEDLALLDSSSSYRNLTL
Human TRPML1 PPERPPPPPSDDLTLLESSSSYKNLTL
Macaque TRPML1 PPERPPPSPSDDLALLEGSSSYKNLTL
Human TRPML2 LQDLSKKPPD- - - - - - - WKNSSFFRL
Human TRPML3 PDEPFHIGTP- - - - - - - AENKLNLTL
E
H451
Lumen
PH2
SF
PH1
5.06 Å
G470
N469
TRPML1 Syb94
S6
5.39 Å
TRPML1 ML-SI3
I514
Lower Gate
T518
Cytosol
F
TRPML1 ML-SI3
H226
TRPML1 Chain B
H267
R146
TRPML1 Chain-A
H174

Figure 42: Structure of TRPML1 in Syb94-TRPML1 complex. A) Cartoon representation of TRPML1 structure (rainbow color scheme). TRPML1 adopts the expected conformation, and all the key structural features are present, including S1-S6 helices, Pore Helices (PHs), the Selectivity Filter (SF) and the Luminal Domain (LD). A new structural element is observed in the structure, the **β**4-**β**5 loop in the luminal domain. B) ML-SI3-bound (inhibitor) structure (PDB: 7MGL) with RMSD mapped onto it from an alignment with the TRPML1 structure in the Syb94-TRPML1 complex (RMSD: 0.735 Å (394)). The regions with the largest conformational changes/highest RMSD values are the loop regions at the interfaces, including the LD-LD interfaces and LD-TM interfaces. Some conformational changes are also observed in the transmembrane helices (S1-S6). Regions that could not be modelled that are present in the ML-SI3-bound structure are displayed in grey. This includes the cytosolic ends of S1-S4, and loop regions across the structure. C) Top view of the luminal domain structure. The luminal domain is composed of a 7-stranded **β**-sheet, an **α**-helix (**α**3), an aspartate-rich luminal pore loop and a series of connecting loops. D) Structure of the **β**4-**β**5 loop in the Syb94-TRPML1 complex (sky blue), in the ML-SI3-bound structure (grey) and in the TRPML1 AlphaFold model (blue). The map in the Syb94-TRPML1 structure enables unambiguous modelling of side-chain densities within this region. This region is absent in most TRPML1 structures as cathepsin cleavage occurs at R200. The loop is highly conserved across species but it is not conserved in the other TRPMLs (alignment displayed with Clustal X color scheme using JalView). Contour level of loop: 0.325. E) Alignment of the S6 helix, PH1-2 and the selectivity filter between the TRPML1-Syb94 structure (sky blue) and the ML-SI3-bound TRPML1 structure (grey). The lower gate is found to be in a closed state in the two structures based on distance measurements at I514 (constriction point). The selectivity filter is more dilated in the TRPML1-Syb94 structure than in the inhibitor-bound structure. H451 is found to adopt a conformation only observed in the agonist-bound state. F) Conformational changes at the LD-LD interface, including the network of histidines at the interface. The histidines are found to adopt a novel conformation.

reconstruction, and Syb94 likely preferentially binds to TRPML1 subunits with an uncleaved loop. In published structures, the loop is typically not observable at residues beyond R200, which is the suggested cleavage site (Kiselyov et al., 2005). This region is likely to have a functional role as it is strongly conserved across TRPML1 homologs, while it is not conserved in other TRPMLs (Figure 42D). Therefore, Syb94 may act to modulate channel activity through its binding to this region.

Conformational changes are also observable at the interfaces between the luminal domains and the neighboring luminal domains and the transmembrane regions, in the vicinity of the S1 and S2 helices (Figure 42B). The changes across the luminal loops alter the contacts formed at the interfaces. Notably, the network of conserved pH-sensitive histidines adopts a novel configuration, which may contribute to the activity of Syb94 (Figure 42F; supplementary Figure 14).

5.4.2 TRPML1-Syb94 Interface

To better understand how Syb94 modulates TRPML1 activity and to identify the conformational changes induced by its binding, the full interface it forms was investigated. Syb94 interacts with the luminal domain of two neighbouring TRPML1 monomers (Figure 43A). It interacts with the β4-β5 loop and the α3 helix of both monomers, and the S1 helix of one monomer (Figure 43A). The extensive interface of 1494.6 Å^2 is formed through interactions that involve both β-sheets of the Ig domain and the CDR regions.

The first β-sheet of the sybody interacts with two N-acetylglucosamine molecules at Asn220 (Figure 42C). The first GlcNAc molecule forms contacts with R76-A79, and the second molecule forms contacts with R23, S75-D77 and Y84 with a total buried surface area of 187.3 Å^2. Nanobody-glycan interactions have previously been observed and can confer the binder with additional specificity (Gupta et al., 2023). The sybody also interacts with this TRPML1 chain through CDR1 and 2 which form hydrogen bonds and salt bridges with TRPML1, including G30-E123 and H35-R122/Y126 (CDR1), and E58-R122 (CDR2) (Figure 42C). The central role of H35 in stabilizing the interface is likely responsible for the pH sensitivity of Syb94 binding. The β5-β6 loop of the sybody also stabilizes the complex through an additional hydrogen bond (N78-N220). The N-terminal peptide of the sybody, GSSSN, is inserted inside the luminal domain at the interface of the two neighbouring subunits, near the luminal pore loop, and interacts through its N-terminal residue and Ser2 with S1, which transmits conformational changes between the luminal domains and transmembrane regions (Figure 42B). The N-terminal glycine is found in the vicinity of a mucolipidosis type IV disease mutations, L106P (Figure 42B) (Wakabayashi et al., 2011). The sybody forms extensive contacts with the neighbouring monomer by interacting with the β4-β5 loop and the α3 helix (Figure 42D). The proline-rich region is stabilized by a ladder of hydrogen bonds along the surface of the sybody, and hydrogen bonds formed by CDR3 (Figure 42D). This extensive network of interactions enables Syb94 to bind to TRPML1 with a high affinity (K_D: 34.92 $\pm$3.06 nM). The β4-β5 loop and key residues (e.g. R122) are absent from other TRPMLs, conferring Syb94 with TRPML1 specificity. This suggests that Syb94 acts as a TRPML1-specific modulator. Based on its interface, this sybody is

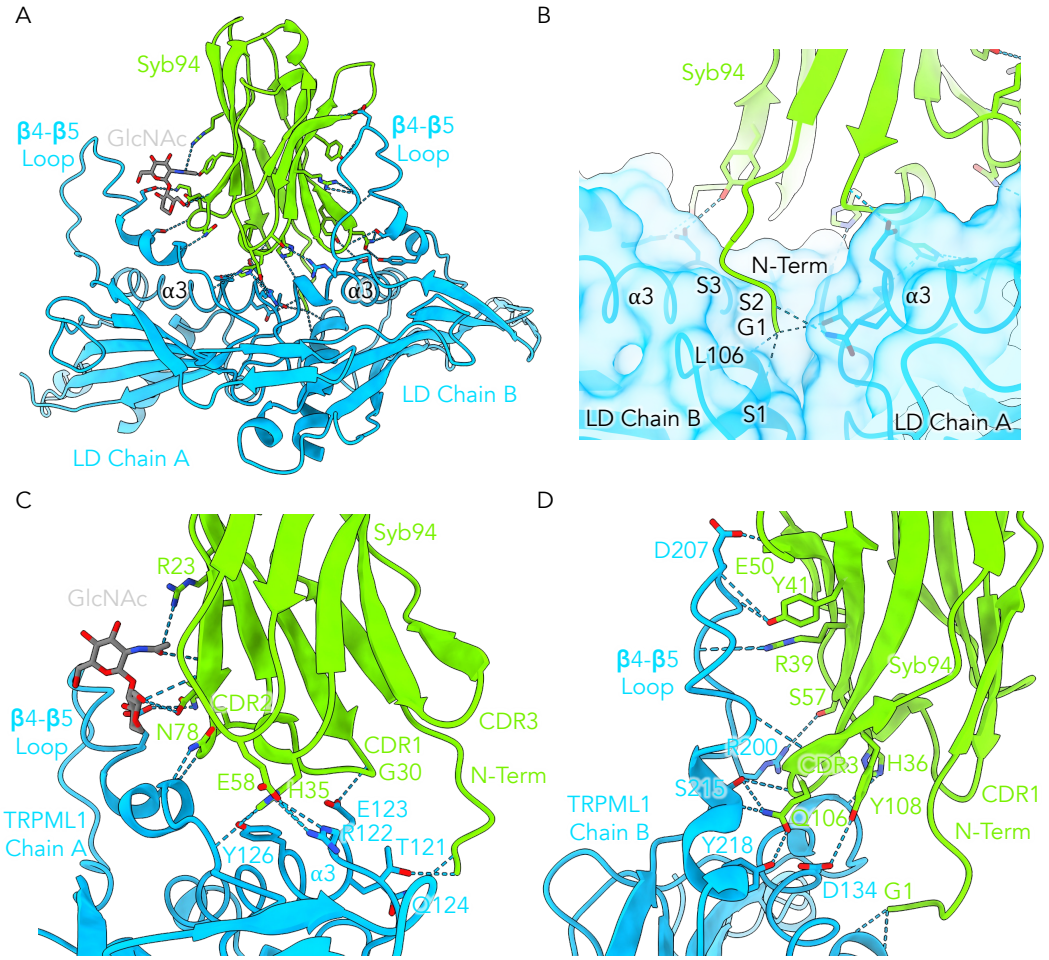

Figure 43: Syb94-TRPML1 interface. A) Syb94 interacts at the luminal domain, with two neighbouring subunits (chain A and B). This enables it to form a 1494.6 Å^2 interface with the luminal domains. Hydrogen bonds and salt bridges are marked with dotted lines (sky blue). B) The N-terminal peptide of Syb94 interacts with the LD of both subunits of TRPML1 through G1 and S2. The interactions are formed in the vicinity of the mucolipidosis type IV mutation L106. C) Syb94 interacts with two GlcNAc molecules on Chain A and forms hydrogen bonds and a salt bridge with the **β**4-**β**5 loop and **α**3 helix of TRPML1. These interactions are formed by the framework of the sybody and CDR1-2. A key residue at the interface is H35, which is likely partially responsible for the pH-dependence of Syb94 binding. D) Syb94 also binds to the neighbouring subunit and interacts extensively with the **β**4-**β**5 loop through its framework and CDR3. This large interface stabilizes the **β**4-**β**5 loop and enabled its structural characterization.

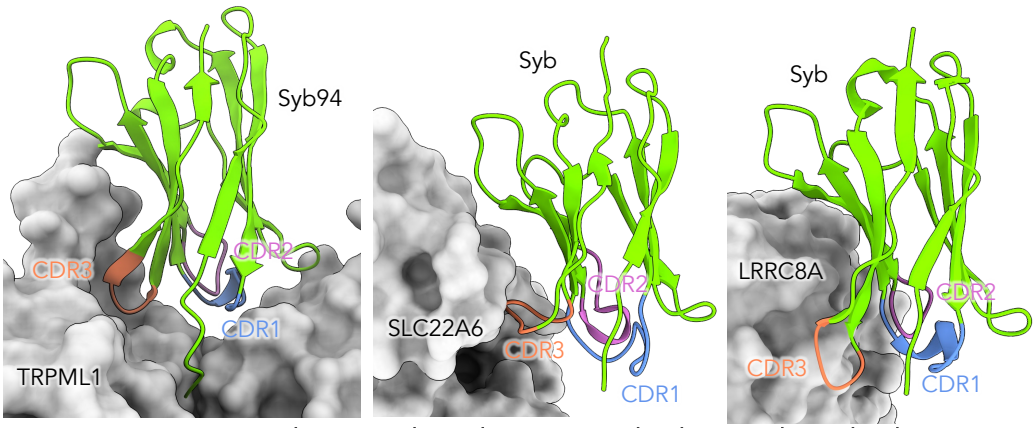

Figure 44: Comparison between the Syb94-TRPML1 binding mode and other concave sybodies. Syb94 wraps around the TRPML1 structure through its framework like the SLC22A6 (PDB: 8BVR) and LRRC8A (PDB: 7P5V) concave binders. However, Syb94 forms a larger interface with its target as TRPML1 wraps around its structure, and forms interactions through CDR1-3 and its N-terminal peptide.

expected to act by modulating the conformation of the β4-β5 and the S1 helix.

The key residues involved in forming the syb94-TRPML1 interactions have been identified, which could enable to identify other concave binders that would still bind tightly and activate TRPML1 but with a weaker pH sensitivity. H35, which plays a key role in Syb94 binding, is strongly conserved in the CDR1 of the concave library hits. However, some hits, including Syb22, 68 and 128, have a polar or cationic residue substituting H35. Syb22 was found to bind TRPML1 and could be investigated further. Syb68 was found not to express, but optimization of the expression could enable purification of the protein, and Syb128 was found to have favorable binding properties and could be investigated further as a non-pH-dependent binder modulating TRPML1 activity. The AlphaFold3 model (see AlphaFold section) predicts that it does not form key interactions with histidine, suggesting its binding should show lower pH sensitivity. In fact, Syb128 was suggested to activate TRPML1 based on the initial FURA-2 experiments and was found to be the only potential hit using this assay (supplementary Figure 10C). Further work could aim to characterize the activity of these binders.

Syb94 binds through a similar binding mode to other concave binders (Figure 44). The sybody interacts with the protein (loop and glycan) through its β-sheet framework. However, such

an extensive interaction surface has not previously been observed for a concave binder. This confers the sybody with high proteoform and conformational specificity. This binding mode is also observed in the AlphaFold predictions of the other concave TRPML1 sybodies. The structure obtained here demonstrates the applications of sybodies to resolve new protein regions and their potential for strong conformational specificity.

5.5 Structure of TRPML1-Syb57 Complex

5.5.1 Complex Architecture

To understand the mechanism of activation of Syb57, the structure of the complex it forms with TRPML1 was also characterized. The TRPML1-Syb57 complex was solved to 3.07 Å structure with PI(3,5)P_2 and in digitonin (Figure 45). As observed for the Syb94-TRPML1 complex, the sybody-TRPML1 interfaces, the luminal domain and the selectivity filter are some of the best resolved regions in the map, while loop regions, regions in the vicinity of the PIP-binding site and the top regions of Syb57, due to the partial sybody occupancy, are more poorly resolved (supplementary Figure 12B). Syb57 binds to the luminal domain of TRPML1, as predicted based on the pull-down and BLI data. The sybody forms a 4:4 complex with TRPML1 (Figure 45A-D). Each sybody forms most of its interactions with a single TRPML1 subunit through CDR1 and 2, and interacts with the neighboring sybody through a hydrogen-bond between N88 and S11 of the neighboring monomer. This interaction would stabilize complexes with full occupancy, leading to the low k_{off} observed in the BLI experiments. PI(3,5)P_2 molecules are observed on the cytosolic side in the previously described PIP-binding site (Figure 45B) (Fine et al., 2018).

In the TRPML1-Syb57 complex, Syb57 displays strong structural similarities with previously published loop library sybodies, such as UCP1 (PDB: 8HBV; RMSD: 0.752 Å (105)) and IrtAB (PDB: 6TEJ; RMSD: 0.714 Å (108)) sybodies (Figure 46A-C). The β-strands of Syb57 are found to be partially distorted, which may result in reduced structural stability as observed in nano-DSF (T_m= 64.1 for Syb57 compared to $>$70°C for the other loop binders). However, Syb57 interacts with TRPML1 through an alternative binding mode as noted from the strong

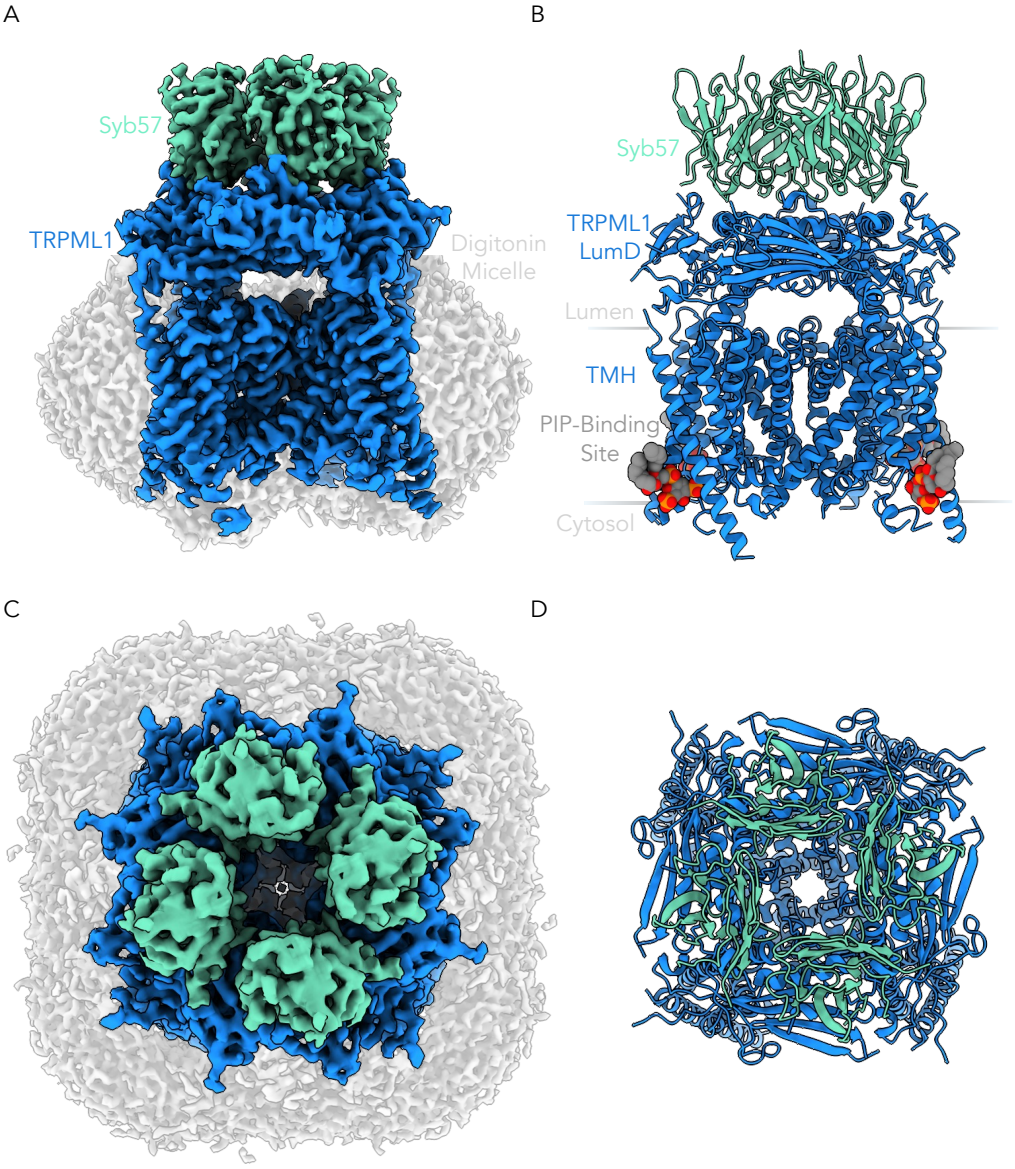

Figure 45: Cryo-EM map of TRPML1-Syb57 complex. A) Syb57 (green) interacts with TRPML1 (blue) in a 1:1 ratio. The transmembrane region of TRPML1 is surrounded by the digitonin micelle (grey). B) Cartoon representation of the TRPML1-Syb57 structure. PI(3,5)P_2 (grey) binds on the cytosolic side of TRPML1 at the previously characterized PIP binding pocket. Top views of C) cryo-EM map and D) structure. Contour level of Syb57-TRPML1 complex: 0.30 and micelle: 0.15.

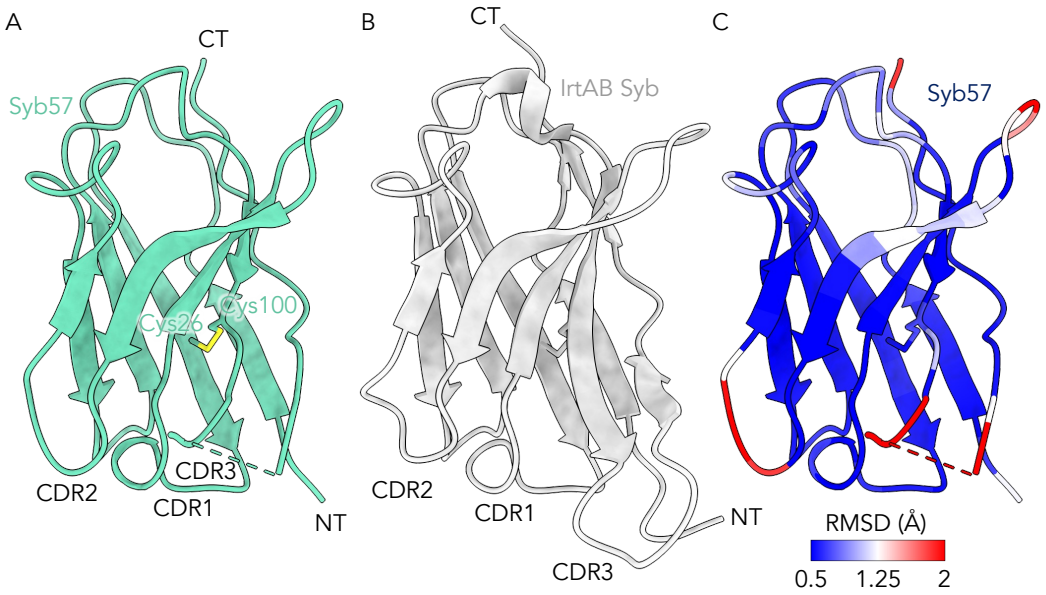

Figure 46: Syb57 structure and comparison with another loop library sybody (IrtAB). A) Syb57 adopts the expected Ig-fold, but its CDR3 is disordered as it does not interact with TRPML1 B) The IrtAB loop sybody (PDB: 6TEJ) has a long CDR3 region, which is inserted into the cavity of the transporter. C) RMSD values mapped onto the Syb57 structure from the alignment between the Syb57 and IrtAB Syb structures (RMSD: 1.221 Å (114)). The main changes are observed in the CDRs and the other loop regions of the sybodies.

conformational differences in CDR2 and 3, which is not resolved in the structure likely because it is partially disordered (Figure 46C). The CDR3 of Syb57 is found to be highly charged with alternating anionic and cationic residues, which is a sequence feature of intrinsically disordered regions (Bianchi et al., 2022). The CDR3 is typically essential for loop library sybody binding to their target protein and all published structures of loop sybodies have a resolved CDR3 based on a PDB search. In the Syb57-TRPML1 complex, the CDR3 is positioned over a positively charged patch at the luminal domain-luminal domain interface. It may interact transiently with this region as it can be observed potentially near the poorly defined β1-β4 loop at higher counter levels. An interaction in this region would be expected to affect the luminal domain-luminal domain interface, which may modulate the conformation of the transmembrane regions.

In this structure, TRPML1 is found to adopt a conformation that is nearly identical to the PI(3,5)P_2-bound human TRPML1 structure solved at pH 5.0 in digitonin (PDB: 6E7P; RMSD: 0.809 Å (403)) (Figure 47A and B) (Fine et al., 2018). The two constriction points of the lower gate, I514 and T518, have nearly identical conformations in the two structures (0.02 Å difference at I514 constriction point) (Figure 47D). Differences are observed in the selectivity filter, where D471 and 472 are found to rotate away from the center of the pore, and D472 is found to be in the same conformation as the 'open' state (PI(3,5)P_2+ML-SA1: 6E7Z) (Figure 47D). G470, a constriction point in the selectivity filter, is more dilated than in the agonist-bound structures (later discussed) (Figure 47D). Therefore, the sybodies appear to act by modulating the conformation of the selectivity filter rather than the lower gate.

The strongest differences between the structures are observed at S1 and the PIP binding site, and the loop regions across the structure, some of which are found to be less well resolved (Figure 47B). In the luminal domain, the following loops could not be modeled: β1-β4 loop, β4-β5 loop, and the loop linking the luminal domain and the S2 helix. These regions are located at the luminal domain subunit interfaces, which is in the vicinity of the sybody binding site. In the Syb94 structure and all the high-resolution TRPML1 structures, the β2-β3 strands are resolved, while they are poorly resolved in the Syb57 structure (Figure 47C). This suggests that this region is destabilized by sybody binding, which may in part be due to interactions with the CDR3.

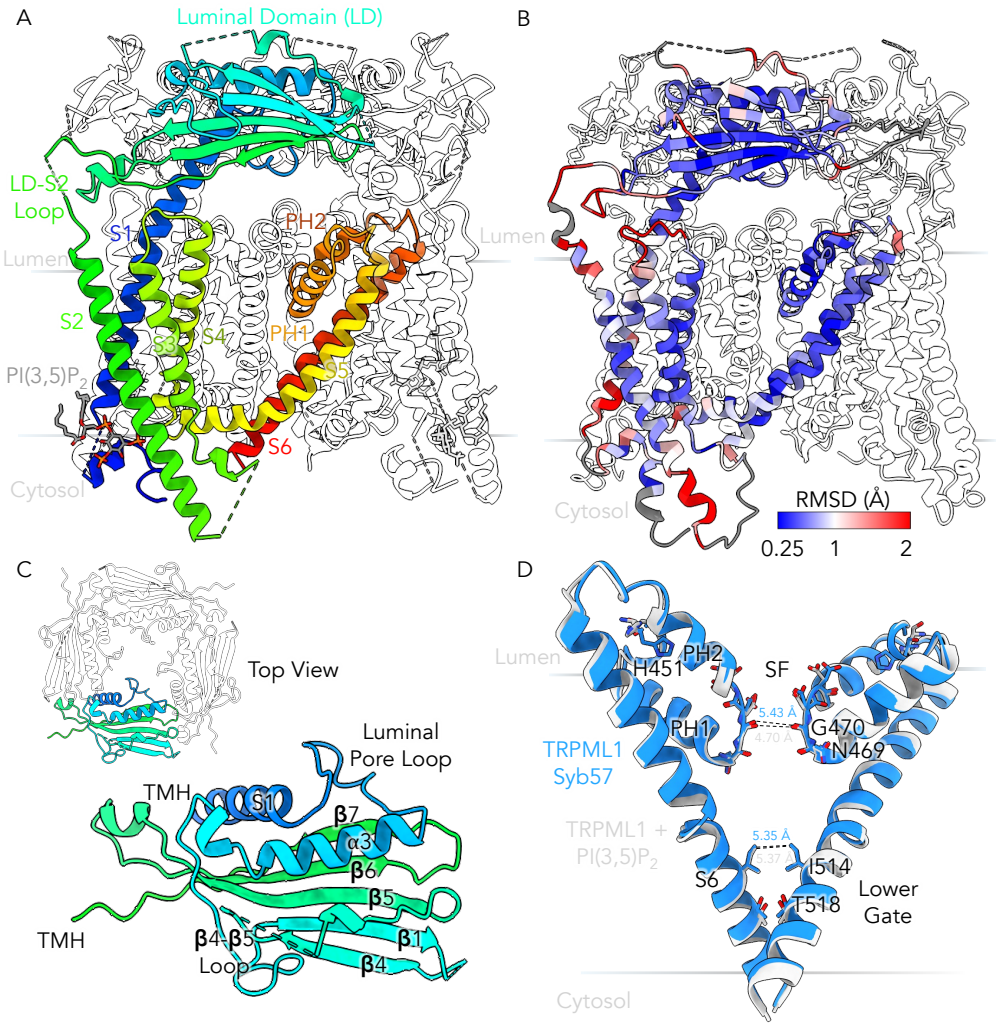

Figure 47: TRPML1 structure in the Syb57-TRPML1 + PI(3,5)P_2 complex. A) Cartoon representation of the TRPML1 structure (rainbow color scheme). B) RMSD values for the structure alignment between TRPML1 + PI(3,5)P_2 from the TRPML1-Syb57 complex and a published TRPML1 + PI(3,5)P_2 (PDB: 6E7P) structure solved at pH 5 and in digitonin (RMSD: 0.809 Å (403)) mapped on this published PIP-bound structure. The TRPML1 structure from the TRPML1-Syb57 complex is nearly complete (regions not modelled in sybody complex structure are in grey). Most of the conformational changes are in the loop regions and some changes are also observed in the S1-S4 helices, as observed in the TRPML1-Syb94 structure. Some of the conformational changes in the helices are induced by PIP binding. C) The luminal domain structure in the TRPML1-Syb57 complex. The domain adopts the expected fold, but the **β**4-**β**5 loop is disordered as observed in the other TRPML1 structure, and the **β**1-**β**4 linker which includes **β**2 and **β**3 could not be modelled. D) Alignment of the S6 helix, PHs and SF with the TRPML1-Syb57 (blue) structure and the TRPML1 + PI(3,5)P_2 (grey). The SF is observed to be dilated relative to the PIP-bound structure, while the lower gate is in the same state.

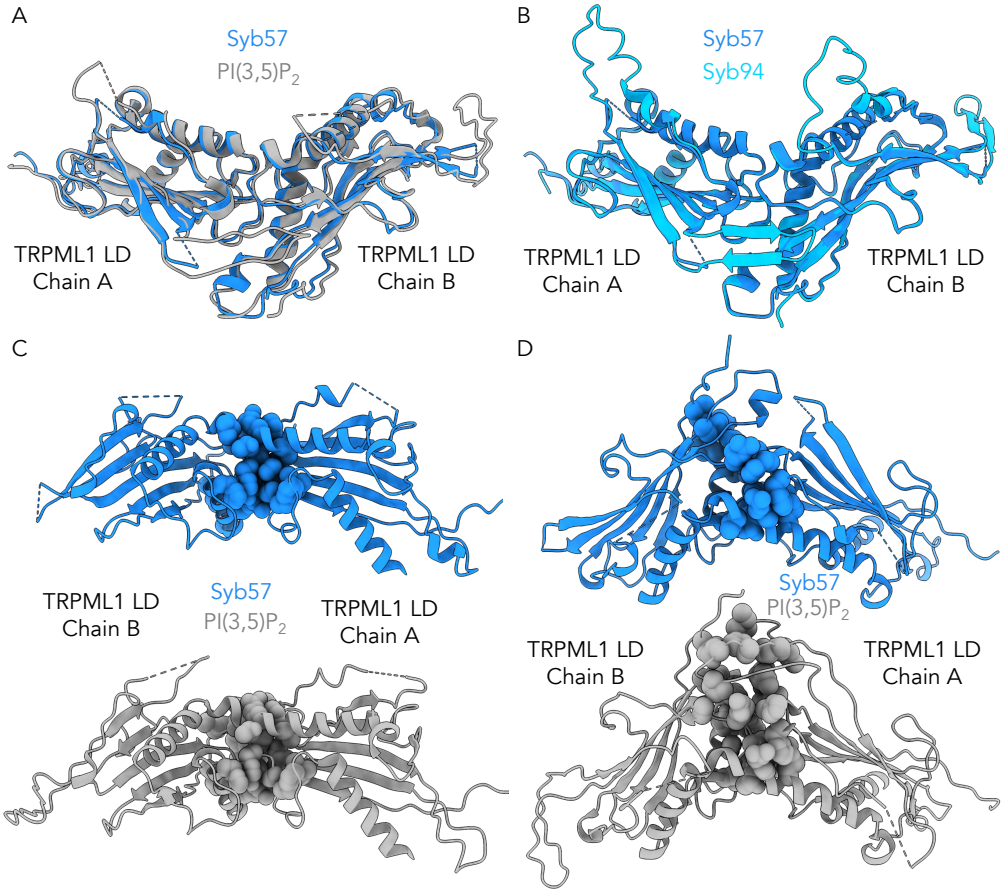

Figure 48: Conformational changes at the luminal domain-luminal domain interfaces. A) Alignment of the luminal domains of the Syb57-TRPML1 and PI(3,5)P_2-bound structures or B) Syb94-TRPML1 structure. Conformational changes are observed in the loop regions at the luminal domain-luminal domain interfaces when comparing Syb57 and PI(3,5)P_2-bound structures, but the Syb94-TRPML1 and Syb57-TRPML1 structures show similar conformational changes despite the differences in conditions. C) Side and D) top views of contacts between the luminal domains in the different structures (atoms displayed as spheres). Changes are observed in the contacts, notably due to the absence of the **β**2 and **β**3 strands.

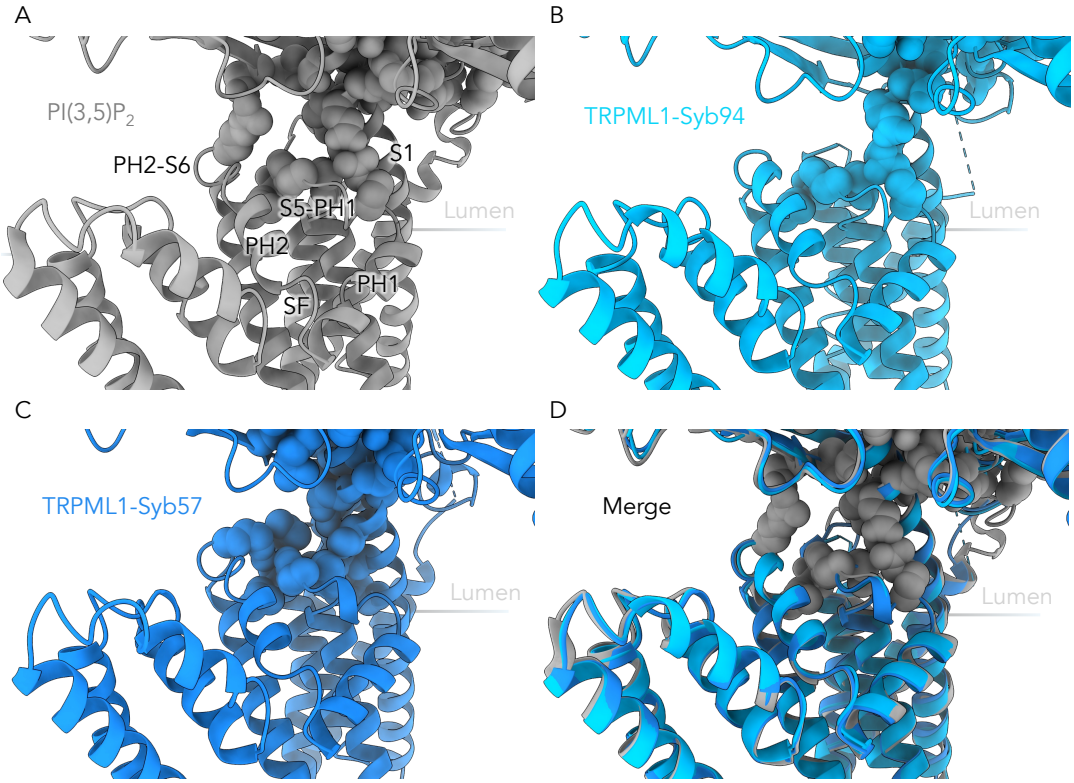

Figure 49: Contacts between the luminal domain and the transmembrane domain. Contacts between the luminal domains and transmembrane regions in the A) PI(3,5)P_2-bound structure, B) TRPML1-Syb94 structure, C) TRPML1-Syb57 structure and D) a merge between A-C. Many contacts from the PI(3,5)P_2 structure are disrupted in the sybody-bound structures, leading to conformational changes in the TMH connecting loops and the helices.

The loops at the luminal domain interface adopt the same conformation in both sybody-bound structures, which is different than existing structures, despite the differences in conditions for both complexes (Figure 48A and B). The changes in these luminal domain loops at the subunit interface propagate to other regions of the luminal domain, resulting in altered contacts between the luminal domain and the S3-S4 loop, S5-PH1 loop, PH2-S6 loop and the S1 helix (Figure 48C and D; Figure 49 A-D). In turn, these conformational changes propagate along the pore helices and alter the conformation of the selectivity filter as discussed later in this chapter. Despite the conformational changes at these domain interfaces, the luminal domain rotation observed in the active state of the channel is not observed (Gan et al., 2022). Large differences are also observed near the PIP-binding site, including at the cytosolic ends of the S1 and S2 helices. Differences in this region arise from an alternative PI(3,5)P_2 binding mode.

In the obtained structure, PI(3,5)P_2 is found to interact with the previously described cytosolic positively charged patch, comprised of two short helices H1-H2 and the S1-S3 transmembrane helices (Figure 50A). Previously, PI(3,5)P_2 has been suggested to control channel activation through conformational changes in the S4-S5 linker (Fine et al., 2018). While changes are observed relative to the structures lacking PI(3,5)P_2, they do not lead to the pronounced conformational changes observed in the S5 helix of the PI(3,5)P_2 + ML-SA1 structure that lead to channel opening. Variations in the PI(3,5)P_2 binding mode is observed across structures. The PI(3,5)P_2-bound mouse TRPML1 structure in glyco-diosgenin (GDN) solved at pH 8 shows the greatest similarity with the TRPML1-Syb57 structure in terms of the PIP pose and side chain conformations in the binding pocket (Figure 50C) (Gan et al., 2022). In the human PI(3,5)P_2-bound structure obtained at acidic pH (5.0), the fatty acid chains face downwards away from the TMH and membrane, while in the sybody complex and mouse TRPML1 structures obtained at near neutral pH (8.0) the fatty acid chains face point towards the membrane (Figure 50B). The PIP_2 binding mode presented here is likely to be more physiological as PIP molecules bind to the cytosolic side of the protein at cytosolic pH (pH = 7.4). PI(3,5)P_2 binding induces some conformational changes in S1-S3 helices that may in part be responsible for some of the differences observed between the sybody-TRPML1 complexes. However, the PI(3,5)P_2 lipids are not essential for the activation mechanism as in the electrophysiology experiments, PI(3,5)P_2 is

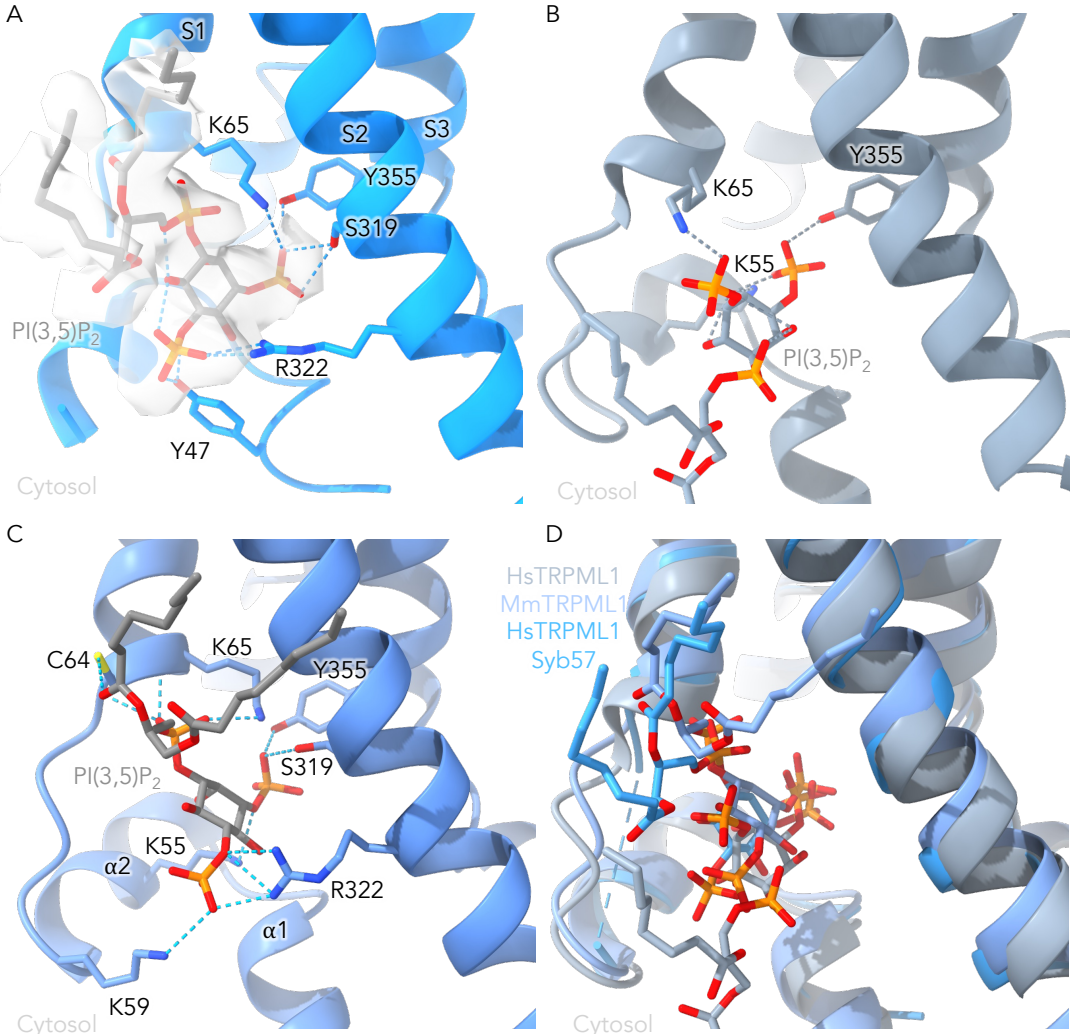

Figure 50: PIP binding site in PI(3,5)P_2-bound TRPML1 structures. PI(3,5)P_2 binding site in the A) TRPML1-Syb57 structure, B) PI(3,5)P_2-bound human TRPML1 structure at pH 5.0 in digitonin (PDB: 6E7P), C) PI(3,5)P_2-bound mouse TRPML1 structure at pH 8.0 in 0.04% Glyco-DiosgeniN (GDN) (PDB: 7SQ7) and D) an alignment of these structures. In the Syb57-TRPML1 structure, phosphates at position 3 and 5 form salt bridges and hydrogen bonds with residues in S1-S3 (PIP lipid density displayed in grey). Similar contacts are formed in the mouse structure as the acyl chain points toward the membrane, but the sugar group is buried more deeply into the binding cavity than in the Syb57-TRPML1 structure, leading to the formation of additional contacts. In the human structure, the acyl groups are lower than in the other structures, leading to a different binding pose with fewer interactions.

absent from the plasma membrane. Nevertheless, in the structure, PI(3,5)P_2 may partially stabilize the sybody-induced conformational changes as it interacts with regions that are suggested to be involved in the mechanism of the sybody, including the S1 and S3 helices. The presence of PI(3,5)P_2 may also explain why stronger conformational changes are observed at the interfaces of the domains and within the PHs and SF in the Syb57-TRPML1 structure.

5.5.2 TRPML1-Syb57 Interface

To better understand how Syb57 binding induces conformational changes at the interfaces and activates the channel, the full Syb57-TRPML1 interface was studied further. Syb57 interacts with TRPML1 through a 444.9 $Å^2$ interface. This interface mostly involves the CDR1 and 2 of Syb57. These CDRs pack tightly against the α3 helix of a single TRPML1 subunit to form hydrogen bonds that stabilize the interface, including N34-E123 (CDR1), and R56-Y126/L221, Y58-R122 and Y61-D134 (CDR2) (Figure 51A and C). Aromatic residues at the interface further stabilize the interface through cation/anion-pi stacking and van der Waals interactions, including R56-F130, Y58-E123, W60-E127 and W63-K219. Syb57 forms one hydrogen bond with the neighboring TRPML1 subunit (Y58-D141). Most of these contacts are located in α3 and at the end of the β3-β4, which is similar to the interface formed by Syb94 and they may thus activate the channel through a similar mechanism. Syb57 was found to bind to TRPML1 at acidic pH (Chapter 4), which results from the lack of histidine residues at the interface. Like Syb94 binding, Syb57 binding is expected to be TRPML1-specific based on the lack of conservation of key residues, such as R122 (mutated to Q) and D134 (mutated to N) (Figure 51D).

This sybody-protein interface differs from the expected loop library binder interface because the CDR3 is disordered and is not involved in specific interactions. The CDR3 typically forms extensive contacts by inserting itself into clefts as observed for CTNS, or by creating contacts with an exposed surface as observed for LRRC8A (Figure 52). The CDR3 may interact non-specifically with charged patches on the surface of TRPML1 (Figure 51E). In agreement with this, AlphaFold models suggest that the CRD3 may form interactions with this region, leading to a binding mode comparable to LRRC8. Further analysis was carried out with AlphaFold to

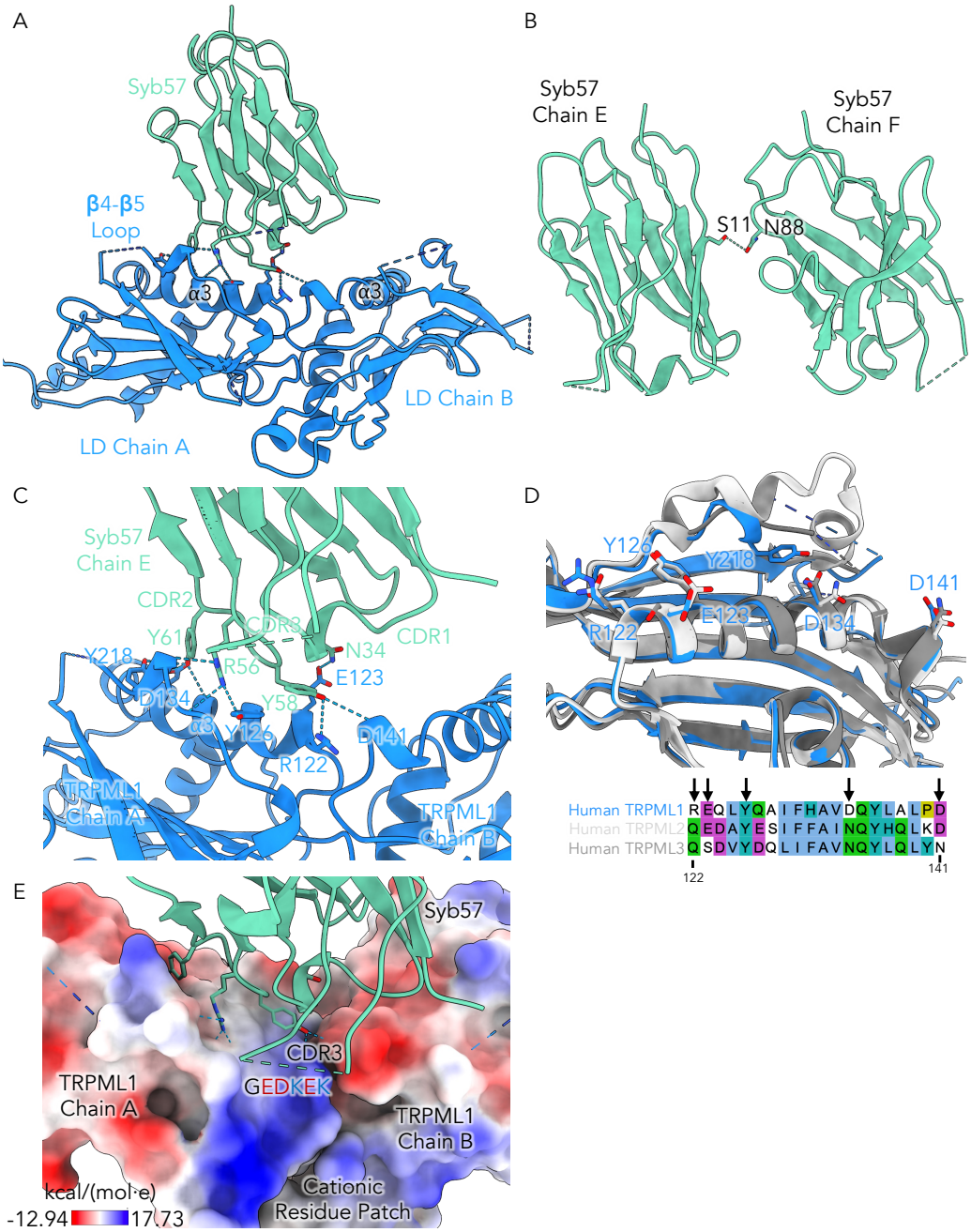

Figure 51: TRPML1-Syb57 interface. A) Syb57 forms most of its interactions with a single subunit at the luminal domain. B) Neighbouring Syb57 monomers interact through a hydrogen bond (S11-N88). C) Syb57 interacts to one monomer at α3 and the **β**4-**β**5 loop through CDR1 and 2, and to the α3 of a neighbouring monomer through its CDR2 with D141. D) Conservation of binding site in other TRPMLs (alignment for α3, arrows are interacting residues PDB: 6HRR for TRPML2 and 6AYF for TRPML3). E) Surface representation with electrostatic potential displayed on TRPML1. The CDR3 of Syb57 is rich in anionic residues that may interact with the cationic patch of TRPML1.

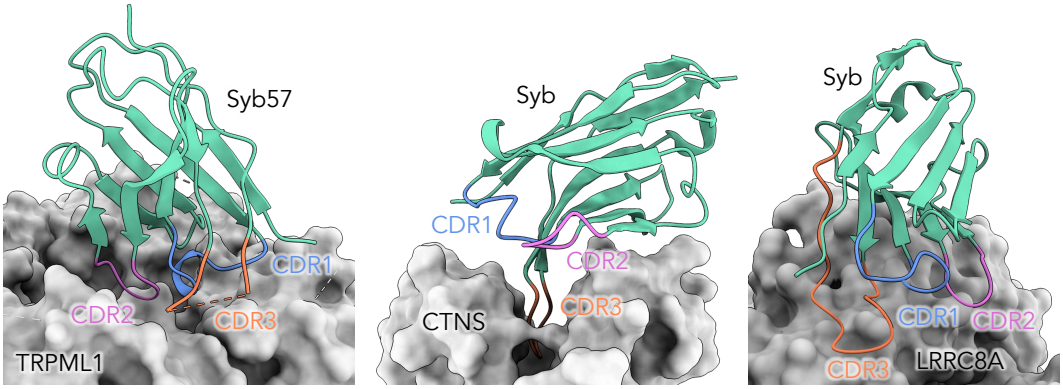

Figure 52: Comparison of the Syb57 binding mode and binding mode of other loop binders. Syb57 interacts through CDR1 and 2, which come into contact with the surface of TRPML1. In the CTNS-Syb complex (PDB: 7ZKW), the CDR3 is inserted into the substrate binding cleft. In the LRRC8A-Syb complex (7P5W), the CDRs are all involved in the interactions, and they interact with a flat surface on the soluble cytosolic domain of LRRC8A.

characterize the binding of TRPML1 sybodies and determine if their binding mode could be predicted, despite potential differences with existing sybody-protein complexes.

5.6 States of the Complexes

There are two main constriction points along the pore of TRPML1: (1) the selectivity filter (SF) and (2) the lower gate. To determine the mechanisms of action of the sybodies, the pore profile was analysed using PoreAnalyser (Seiferth and Biggin, 2024).

Existing TRPML1 agonists bind to the transmembrane region and activate the channel by opening the lower gate (Schmiege et al., 2017). The pore radius at the lower gate is regulated by two constriction points, I514 and T518. The S6 helix, which forms the lower gate in TRP channels, is the main regulator of channel conductance (Huffer et al., 2020). In the two sybody-bound structures, the lower gate is found to be in a closed state (Figure 53A and B). Lower gate opening could require an acidic environment and the structures were obtained at an alkaline pH (8.0). However, for the mouse homolog of TRPML1, structures with an open lower gate were obtained at pH 8.0 in the presence of agonists, which does not support this hypothesis (Gan et al., 2022). This suggests that the sybodies may act to activate the channel by modulating the conformation

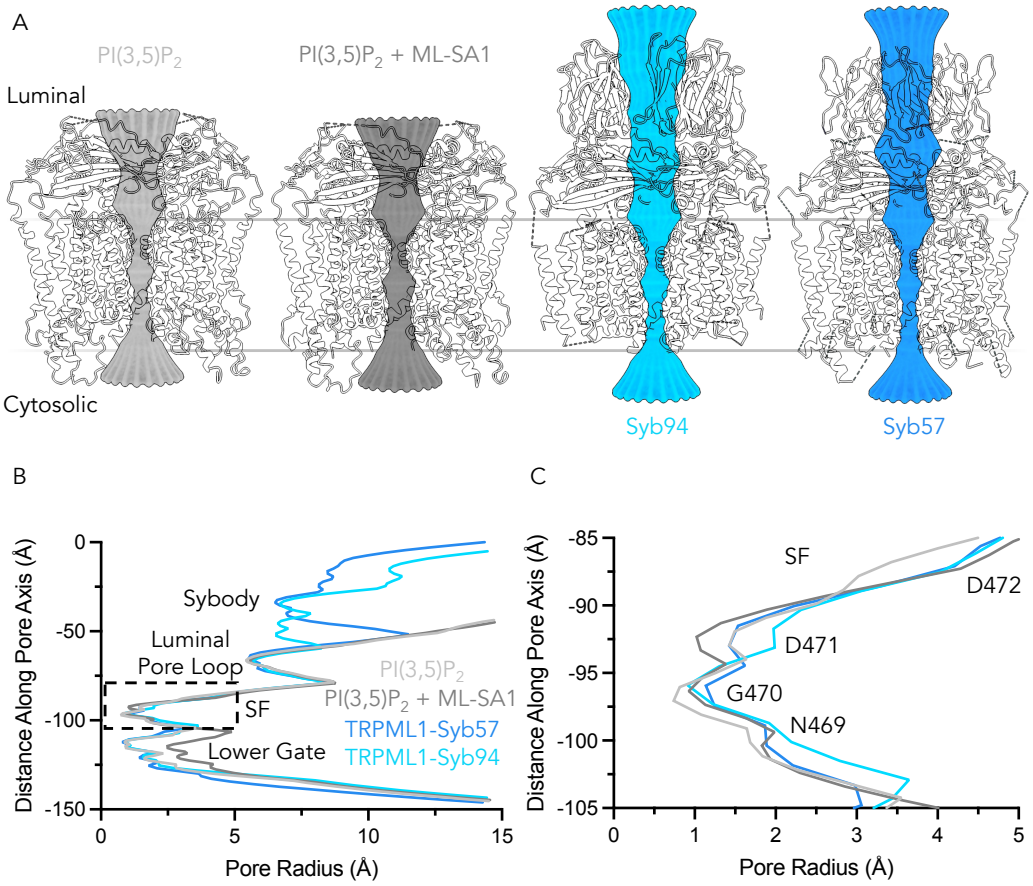

Figure 53: Pore profile of Syb-TRPML1 structures. A) Pore profile for the PI(3,5)P_2-bound (PDB: 6E7P; light grey), PI(3,5)P_2-bound + ML-SA1 (PDB: 6E7Z; grey), TRPML1 + Syb94 (sky blue) and TRPML1 + Syb57 + PI(3,5)P_2 (blue) structure. B) Pore profile plot and C) zoom-in on selectivity filter (SF) region of the pore profile (dotted region in B). At the top of the pore profile (B) a constriction is formed by the sybody and the luminal domain. The next constrictions are formed by the SF and the lower gate. The lower gate is open in the PI(3,5)P_2-bound + ML-SA1 bound structure , while it is closed in all the other structures. Differences are observed in the SF: the D471 region is more dilated than in the syb94-TRPML1 and Syb57-TRPML1 structures than in the PI(3,5)P_2 + ML-SA1-bound structure, and the N469-G470 region is more dilated in the sybody-bound structures than the PI(3,5)P_2-bound structure. Pore profiles were obtained using PoreAnalyser (Seiferth and Biggin, 2024).

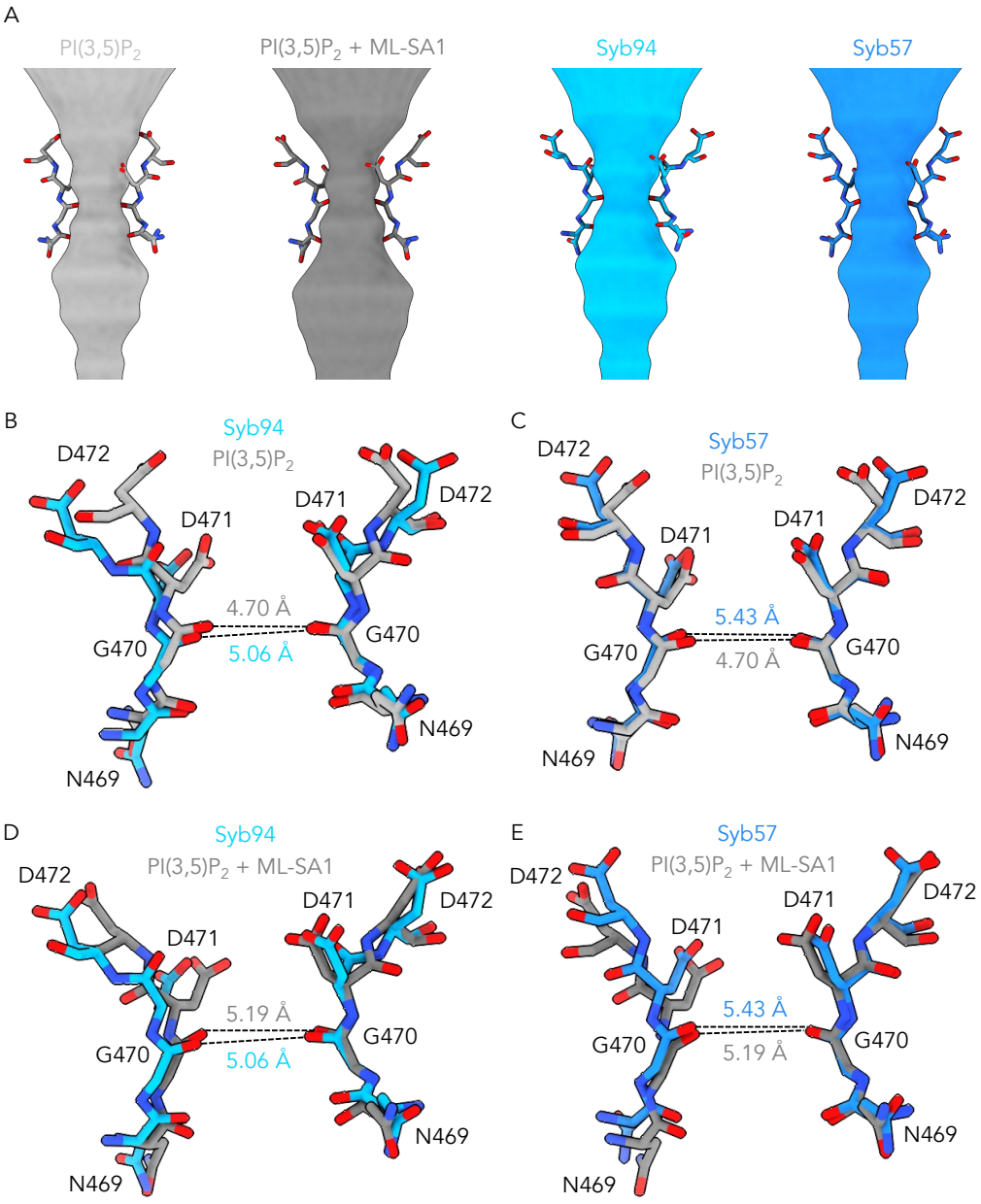

Figure 54: Pore profile and conformation of the selectivity filters. A) Pore profile for the $PI(3,5)P_2$-bound (PDB: 6E7P; light grey), $PI(3,5)P_2$-bound + ML-SA1 (PDB: 6E7Z; grey), TRPML1 + Syb94 (sky blue) and TRPML1 + Syb57 + $PI(3,5)P_2$ (blue) structure with a stick representation of residues N469-D472 of the selectivity filter. B-E) Stick representation of the selectivity filter (N469-D472) in the structures cited above annotated with the distances between the carbonyl oxygens of G470 in chain A and C.

of the SF rather than the lower gate. ML-SA1, a TRPML1 agonist, induces a slight dilation of the SF as observed when comparing the pore profile of the PI(3,5)P_2 (PDB: 6E7P) and PI(3,5)P_2 + ML-SA1 (PDB: 6E7Z) human TRPML1 structures obtained at pH 5.0 (Figure 53C) (Fine et al., 2018). The two constriction points of the SF are G470 and D471. In the PI(3,5)P_2 + ML-SA1 structure, the carbonyl group of G470 may slightly alter its conformation (0.18 Å) to lead to a more open state (Figure 53C). However, the SF remains closed as it has a radius of 0.927 Å, which is less than the radius of a calcium ion (0.99 Å) (Mann, 1968). Nevertheless, the dilation of the pore suggests that the agonist may favor ion conductance by modulating the conformation of the selectivity filter, and the interactions that stabilize it.

The pore profile of the TRPML1-sybody complexes shows that the selectivity filter is dilated in both complexes (Figure 53C; Figure 54A-E). In the Syb94-TRPML1 complex, G470 dilates and remains the constriction point at a radius of 0.913 Å (0.014 Å less open than PI(3,5)P_2 + ML-SA1), and D471 also dilates to a radius of 1.99 Å (0.92 Å more open than PI(3,5)P_2 + ML-SA1) (Figure 53C). Therefore, the SF dilates to reach a similar diameter as the PI(3,5)P_2 + ML-SA1 structure SF, despite the neutral pH and the absence of PI(3,5)P_2. The Syb57-TRPML1 structure is the human TRPML1 structure with the most dilated SF. The selectivity filter has a radius of 1.138 Å at G470 and 1.426 Å at D471 (Figure 53C). This suggests that the sybodies activate TRPML1 by altering the state of the selectivity filter. It is plausible that in the same detergent and in the presence of PI(3,5)P_2, Syb94 may cause further dilation of the selectivity filter.

A key observation from the whole-cell electrophysiology recordings is that the voltage dependence of TRPML1 currents is altered in the presence of Syb57 and 94 relative to ML-SA1. The opening of the selectivity filter has been suggested to reduce the voltage dependence of TRP channels by altering the conductance of the channel for specific ions (Chung, et al., 2008; Garcia-Avila et al., 2024). Additional electrophysiology experiments will need to be carried out to confirm the suggested role of the selectivity filter in the mechanism of Syb57 and 94.

The conformational changes observed at the constriction points are minor and the cryo-EM maps do not allow these differences to be asserted with a high degree of confidence. Nevertheless, clear conformational changes were observed in the side chains of the SF (D471 and D472),

confirming the hypothesis that changes in SF conformation and contacts may be responsible for the activity of the sybodies. To determine with greater confidence whether the sybodies act by modulating the SF conformation, I investigated whether the contacts between the PHs and SF were altered, and how such changes may be propagated from the sybody binding site.

5.7 Mechanism of Modulation

5.7.1 Sybody Modulation of Selectivity Filter State

Syb57 and 94 interact at the luminal domain-luminal domain interfaces. Two functions have been suggested for the luminal domain of TRPML1 in the regulation of channel activity: (1) the pH regulation of channel activity through protonation of an aspartate cluster at the suggested luminal pore loop, and (2) the regulation of channel conformation through the rotation of the luminal domain (Gan et al., 2022; Li et al., 2017). The luminal pore loop is expected to regulate channel activity by restricting the flow of ions when the aspartate cluster is deprotonated (neutral pH) and allowing ions to flow through when it is protonated (lysosomal acidic pH) (Li et al., 2017). Moreover, changes in its conformation may regulate S1 conformation as it forms direct interactions with it. The N-terminal peptide of Syb94 forms interactions in the vicinity of this loop with S1, but does not directly interact with it. While major structural rearrangements are observed in this loop with pH changes in TRPML3, no major conformational changes are observed in TRPML1 (Li et al., 2017; Zhou et al., 2017). Some potential minor conformational changes and new interactions (e.g.Y109-D114) are observed in this region that are consistent between the two sybody-bound structures, but they are unlikely to have a strong effect on channel conformation (Figure 55A). The rotation of the luminal domain that is observed in activated TRPML1 structures is not observed here (Gan et al., 2022; Schmiege et al., 2017). The key effects of this rotation are changes in the luminal domain-luminal domain interface as the β2 and β3 strands in the luminal domain alter the contacts formed. This region was noted earlier to have some of the most pronounced conformational changes in the Syb-TRPML1 structures. In TRPML3, the luminal domain interfaces have been suggested to regulate channel activity by

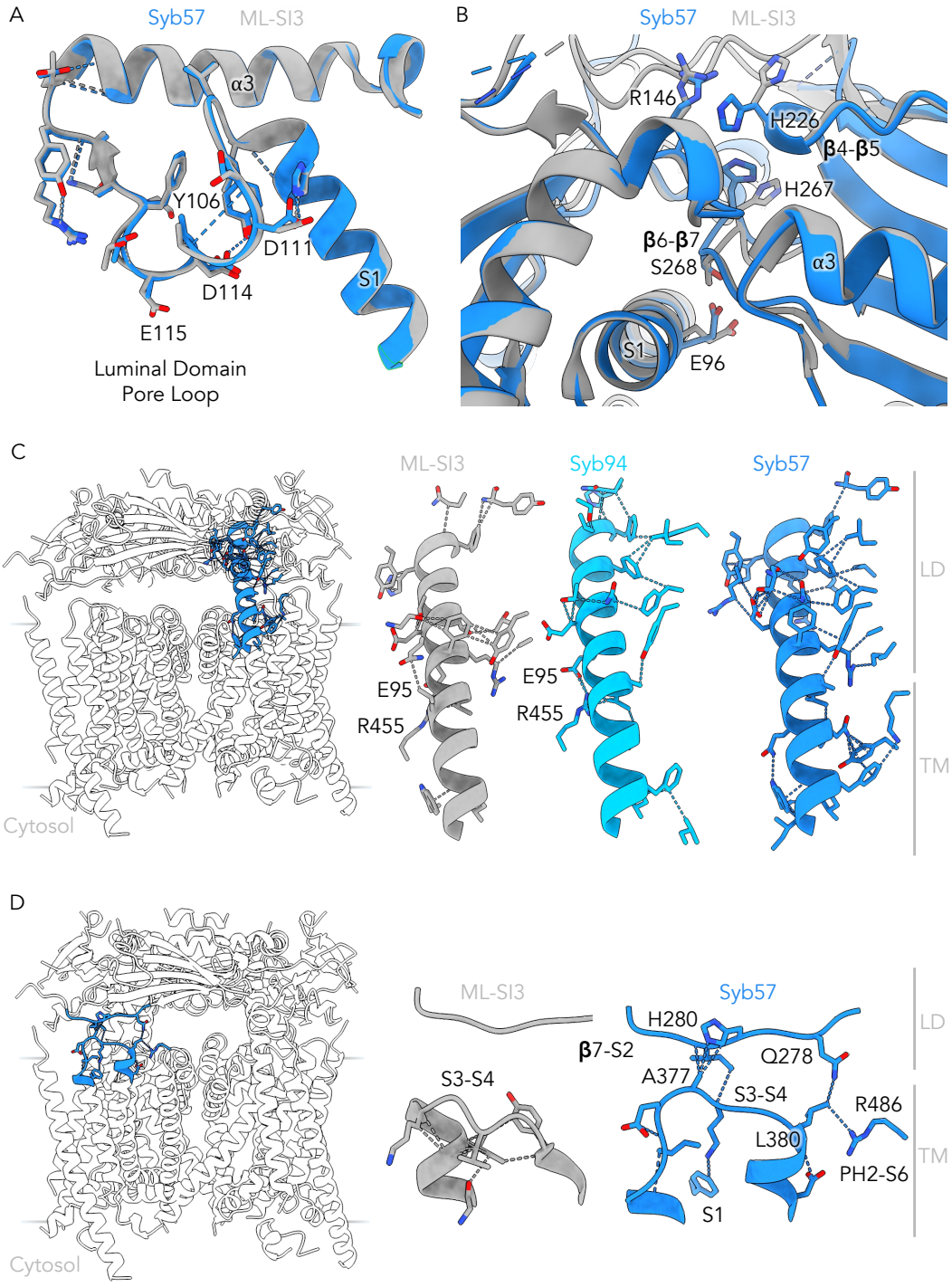
A
Syb57
ML-SI3
α3
Y106
D111
D114
S1
E115
Luminal Domain
Pore Loop
B
Syb57
ML-SI3
R146
H226
β4-β5
H267
β6-β7
S268
α3
S1
E96
C
Cytosol
ML-SI3
Syb94
Syb57
E95
R455
E95
R455
LD
TM
D
Cytosol
ML-SI3
Syb57
β7-S2
S3-S4
H280
Q278
A377
S3-S4
R486
L380
PH2-S6
S1
LD
TM

Figure 55: Conformational changes in luminal regions and at the luminal domain-transmembrane interface. A) Very few conformational changes are observed at the luminal pore loop between the ML-SI3-bound structure and the TRPML1-Syb57 structure, except the formation of an additional hydrogen bond between Y106 and D114. Contacts are depicted with dotted lines. B) Pathway through which Syb57 and 94 binding to the **β**4-**β**5 loop induce conformational changes in the transmembrane regions. C) Contacts (dotted lines) between the S1 helix, and the luminal domain and the transmembrane regions. The contacts it forms are altered between the ML-SI3 structure and the sybody-bound structures at the luminal domain, which propagates to the transmembrane region. This includes the weakening of the E95-R455 contact in the Syb57-TRPML1 structure. D) New contacts (dotted lines) are formed between the luminal domain **β**7-S2 loop and S3-S4 loop of the transmembrane region, including a contact between H280 and A377, and Q278 and L380 which results in the formation of an additional direct contact with the PH2-S6 loop. This affects the conformation of the PHs.

propagating pH-induced (histidine) conformational changes to the TMH (Hirschi et al., 2017). Therefore, the contacts formed within this region were investigated further.

The luminal domain-luminal domain interface region includes the largest cluster of histidine residues across TRPML1. Therefore, it was hypothesized that these histidine residues modulate this interface in a pH-dependent manner, and the conformational changes induced by the sybodies regulated channel activity potentially through a similar pathway. A luminal histidine cluster has also been found to be involved in TRPML3 pH regulation (Kim et al., 2008). The histidine residues were found to adopt the same conformation in both Syb-TRPML1 structures, and this conformation had not previously been observed in any other TRPML1 structure. Therefore, I aimed to further investigate how sybody binding induces conformational changes at this interface, and how these conformational changes may propagate to the selectivity filter.

Sybody binding causes structural rearrangements through the interactions it forms with α3 and the β4-β5 loop. The structural rearrangements in these regions propagate to the loops that are located in their vicinity and form the luminal domain interfaces, causing structural rearrangements in the transmembrane regions they interact with. For example, sybody binding to the β4-β5 loop drives its movement. This propagates to the luminal domain-luminal domain interface and leads to a novel conformation and cation-pi interaction between H226 and R146 (Figure 55B). Another histidine residues located below it, H267, is rearranged which causes the movement of the β6-β7 loop, altering the contacts it forms with the S1 helix (Figure 55B). The changes in the S1 helix may destabilize an interaction between E95 and R455, which is found in

the S5-PH1 loop that modulates the PH and SF conformations (Figure 55C). The S1 helix acts to relay changes in the luminal domain to the transmembrane region as it forms extensive contacts both with the luminal and transmembrane loops (Figure 55C). In addition to the changes in the S1 helix, the S3-S4 loop also undergoes large conformational changes as a result of the novel contact it forms with H280 and Q278 in the luminal domain of the syb57-TRPML1 structure (Figure 55D). These changes propagate to the PH2-S6 loop of the neighboring subunit as the S3-S4 loop/S4 helix forms direct contacts with it, affecting the conformation of the PHs (Figure 56A).

These changes at the interface drive rearrangements in the PHs and SF. The sybody-bound structures display contacts only observed in the agonist-bound structures, which likely stabilize the selectivity filter in the conductive state (Figure 56B). In the sybody-bound and agonist-bound structures, the imidazole ring of H451 is displaced closer to the SF to form new contacts, D472 stabilizes the SF through the interaction it forms with K453, and L467 stabilizes M473 (Figure 56B). While the observed changes at the constriction site (G470) are small, the new network of interactions formed as a result of sybody binding is likely to shift the conformational ensemble of the SF towards a conductive state as it mimics the agonist-bound state (for map quality in these regions see supplementary Figure 13C and D).

Overall, Syb57 binding with PI(3,5)P_2 leads to more pronounced conformational changes in TRPML1, which is consistent with the potentially more dilated SF observed in the structure and experimentally its strong effect on voltage dependence. Through contact analysis, it was observed that the sybodies cause conformational changes at the luminal domain-transmembrane domain interface, partly through a network of histidines, allosterically regulating the SF conformation. Some of the histidine side chain conformations observed here have not previously been observed in structures obtained at neutral or acidic pH in the presence of synthetic agonists. Therefore, the sybodies appear to activate the channel through an alternative mechanism.

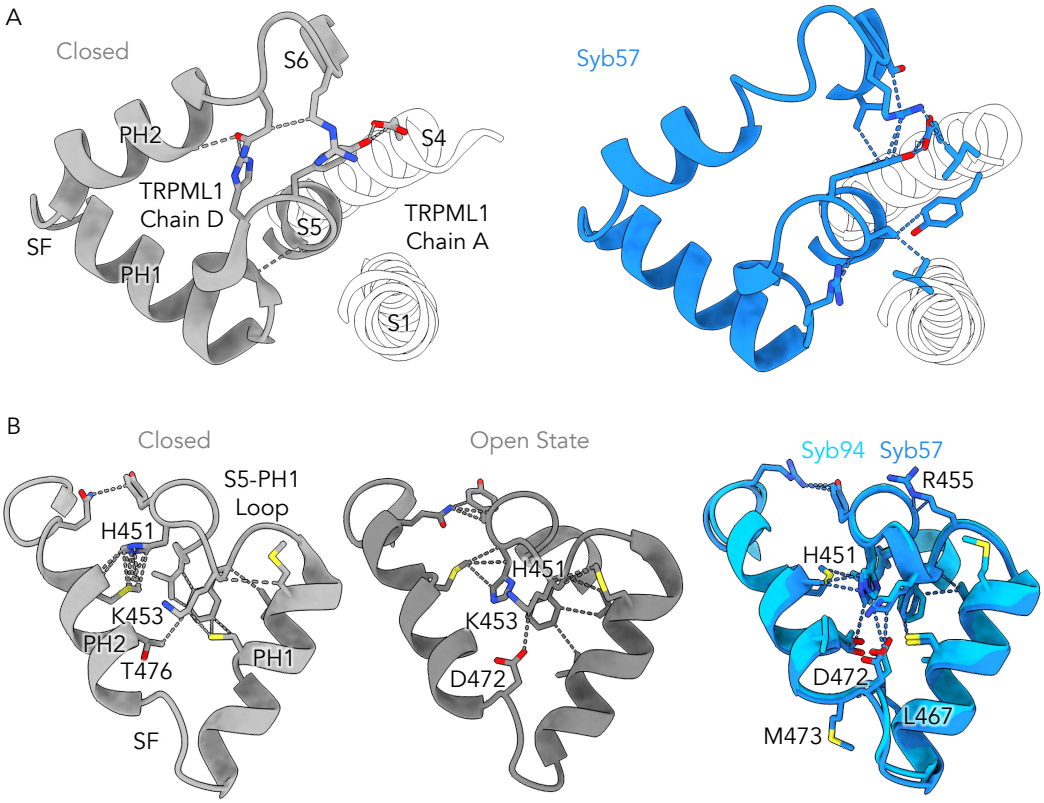

Figure 56: Changes at the subunit interfaces and the conformations of the Pore Helices (PHs) and Selectivity Filter (SF) in the sybody structures. A) Contacts between neighbouring subunits (colored: chain D; transparent: chain A) in closed structure (PDB: 7MGL) and Syb57-bound structure. Syb57 binding alters contacts formed by S1 and S4 of one subunit with the PHs and loops of the neighbouring subunit. B) Conformations of the PHs and SF in $PI(3,5)P_2$-bound (grey), $PI(3,5)P_2$ + ML-SA1-bound (dark grey), Syb57 (blue) and Syb94-bound (sky blue) structures. The main changes are observed in the conformation of H451, altering the contacts it form. A salt bridge is also formed by D472 and K453 in the agonist and sybody-bound structures, and additional contacts within the SF (by M473) or in the vicinity of the selectivity filter are formed in the sybody-bound structures.

5.7.2 Potential Functions of the Luminal Loop

Structural characterization of the Syb94-TRPML1 complex enabled to determine the structure of the β4-β5 loop, which is strongly conserved across TRPML1 homologs. This loop is the longest β4-β5 linker in the TRPML family and no homologous sequences were found through a blast search. It has been suggested that cleavage of the loop would reduce TRPML1 stability and activity (Kiselyov et al., 2005). However, the strong conservation across its 34 amino acid sequence (Val195-Leu228) across species could suggest a more complex function (supplementary Figure 14).

Like numerous lysosomal membrane proteins, it is expected that TRPML1 may have an auxiliary subunit or binding partners (Rudnik and Damme, 2021). The loop could be involved in the regulation of protein interactions and Syb94 may mimic the configuration of TRPML1 binding partners. As described in this chapter, luminal domain interactions can modulate channel activity. Therefore, a binding partner could act as an endogenous modulator of channel activity as discovered for TMEM-175 and lamp-1 (Zhang et al., 2023). In support of this hypothesis, the loop is comprised of a proline-rich region, which are typically involved in protein-protein interactions, and is rich in anionic residues that could form electrostatic interactions (Figure 57A and B) (Ball et al., 2005). In the syb94-TRPML1 structure, it forms a cup-like structure, forming a large interface for protein interactions (Figure 57A). In the vicinity of the loop, at the luminal domain-luminal domain interface, there is a positively charged patch (R122, R146, H226, and K227) that is only present in TRPML1 that could also be involved in protein interactions (Figure 57B).

Another possibility is that the loop itself may be involved in the regulation of the channel. Upon cleavage, interactions formed by the loop may be disrupted or its conformation might be altered, inactivating the channel. Alternatively, the loop may only form interactions or adopt an active conformation upon cathepsin cleavage, ensuring it is only active once it is in contact with lysosomal proteases. Proteolytic cleavage is a known mechanism for the regulation of ion channel activity (Wang and Yule, 2018). There are multiple potential binding sites for this loop (Figure

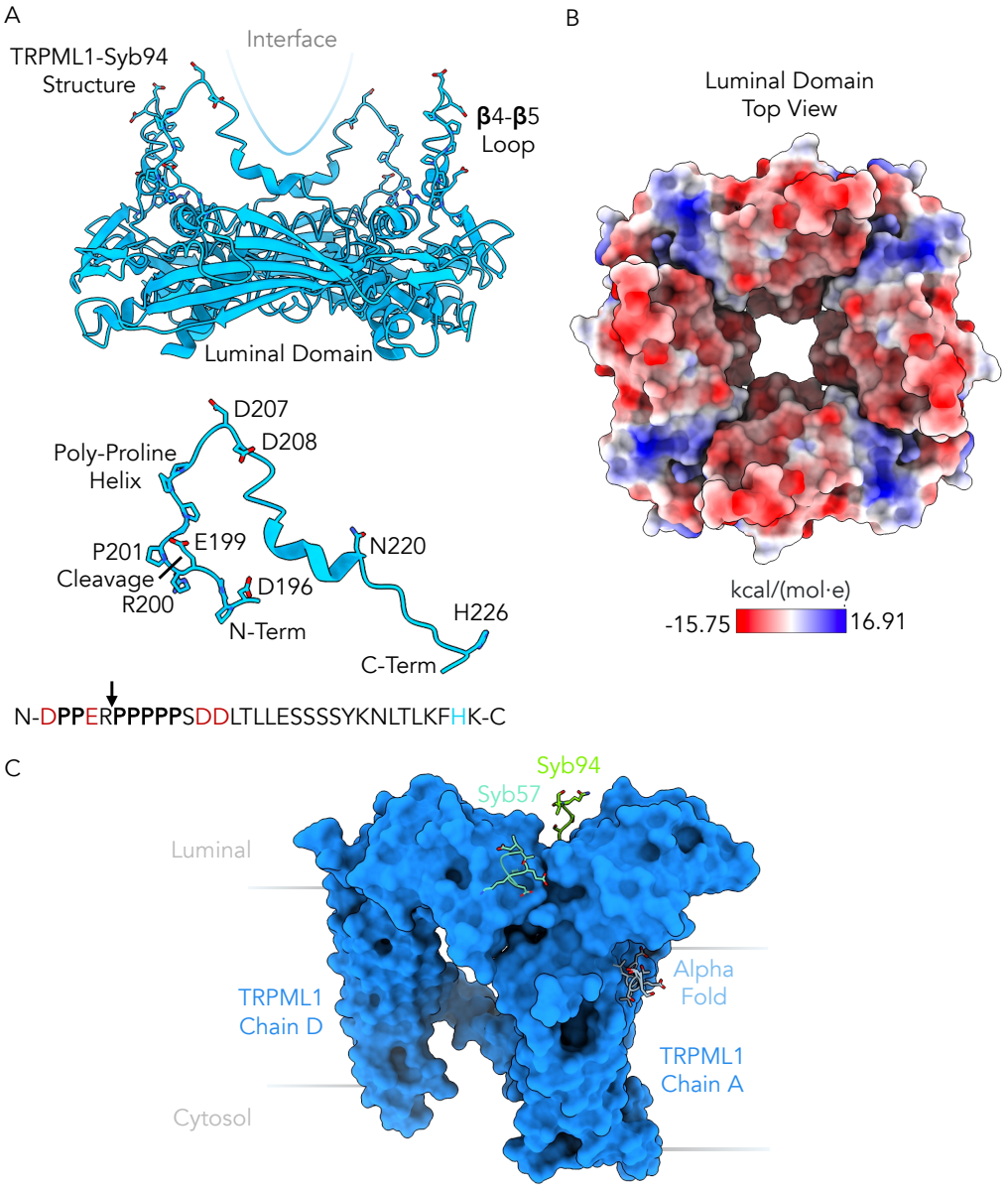

Figure 57: Potential functions of the β4-β5 loop in TRPML1. A) In the Syb94-TRPML1 structure, the **β**4-**β**5 loop forms a cup-like structure that could form a large interface for protein interactions at the luminal domain. This region also contains a poly-proline helix and anionic residues that could be involved in forming protein interactions (sequence displayed below, arrow shows cleavage site). B) The luminal domain of TRPML1 displays a unique charge distribution on its surface, with alternating cationic and anionic charges. These charges may be involved in protein interactions. Alternatively, it may suggest that the mostly negatively charged **β**4-**β**5 loop interacts with the cationic patch in its vicinity. C) Potential peptide binding poses on the Syb57-TRPML1 structure (blue), including Syb57 CDR3 AlphaFold predicted binding pose to the cationic patch, Syb94 N-terminal peptide binding pose and the AlphaFold predicted binding pose for the **β**4-**β**5 loop peptide. The **β**4-**β**5 loop could interact through a combination of these different binding poses.

57C). A first site could be the strongly cationic luminal domain interface. It is plausible that the anionic and disordered CDR3 of Syb57 mimics this binding mode (Figure 57C). The N-terminal peptide of Syb94 (GSSSQVQ) shows sequence homology with the loop and it may thus mimic its binding mode (Figure 57C). Binding of the N-terminal peptide occurs at the S1 helix and at the subunit interface, which could enable it to regulate channel activation. A third binding mode was suggested by AlphaFold 3 when adding different peptide fragments to the full-length proteins. AlphaFold predicts the peptide to bind under the luminal domain at the interface of the transmembrane region. Combinations of these sites could accommodate the loop. Alternatively, cleavage of the loop alone may be sufficient to induce conformational changes that modulate channel activation as small conformational changes in the sybody-bound structures were suggested to alter the SF state.

The function of this peptide could be determined by investigating its effect or the effect of its fragments on channel activity in whole-cell patch clamp experiments. If this peptide does not have activity against TRPML1, it is likely involved in protein interaction which could be investigated further in co-IP experiments using the sybodies.

5.7.3 Suggested Mechanism of Modulation

The structures of two activatory sybodies bound to TRPML1 were obtained. This enabled characterization of their interfaces at the luminal domain, including a previously unresolved region (β4-β5 loop). The SF and PHs are suggested to have an altered conformation compared to PI(3,5)P_2-bound or apo TRPML1 structures, while no significant changes were observed in the lower gate. Therefore, it was suggested that the sybodies modulate channel activity by altering the SF conformational dynamics (Figure 58). The sybodies induce local conformational changes at the luminal domain through the interactions they form, which are propagated by a network of contacts between the luminal domain and the transmembrane helices. These contacts are formed by the S1 helix, which connects the luminal domain with the TMH, and the loops linking the TMH, which undergo large conformational changes. The changes at the loops and helices are propagated to the PH1-SF-PH2 region, stabilizing a conformation of the selectivity filter

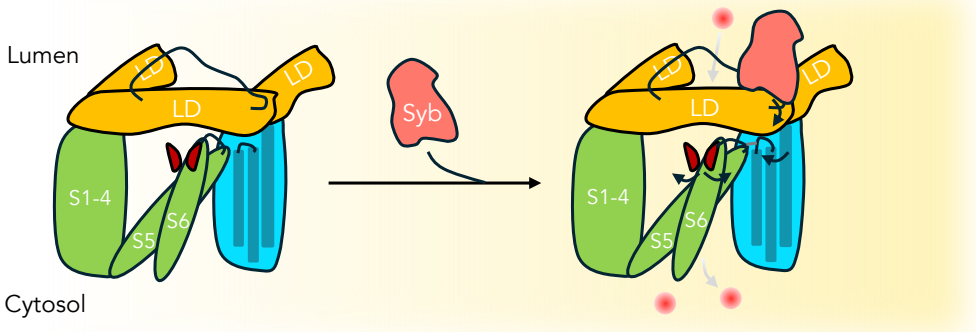

Figure 58: Mechanism of TRPML1 activation by sybodies. TRPML1 has a domain swapped architecture in which the S5-S6 and PHs of one subunit interacts with the S1-S4 helix bundle of a neighbouring subunit. The S1-4 bundle (voltage sensor–like domain) contains two key regions that interact with the luminal domain, the S3-S4 connecting loop and the S1 helix. Changes in these regions are propagated from one subunit to the S5-S6 and PHs region of the neighboring subunit, leading to changes in the selectivity filter. Sybody binding occurs at the luminal domain and through its interactions, potentially with **β**4-**β**5 (LD loop), alters the conformations of the loops at the LD-LD interfaces. This propagates to S1 (blue helix) and the S3-S4 loop (black loop) which support the luminal domain interface. The altered conformations of the residues in these regions (blue) propagate to the S5-S6 and PHs regions of the neighboring subunit (green), altering the contacts in the PHs (red). This is suggested to stabilize the selectivity filter in a more dilated conformation, favoring the conductive state of the channel. This may be partly regulated by a histidine network at the luminal domain, and the sybodies may mimic the activation mechanism of a protein binding partner as observed for other lysosomal channels.

observed in the agonist-bound structures. These changes are coordinated by a conserved network of histidines throughout the structure. A histidine network at the luminal domain-luminal and transmembrane domain interface has also been suggested to regulate channel activity in TRPML3 and other ion channels (Kim et al., 2008; Rajan et al., 2000; Sandoz et al., 2009). The sybodies are suggested to mimic the interactions and mechanisms of endogenous protein binding partners, which would bind to the β4-β5 loop. Since this mechanism is coordinated by a network of histidine residues, it would enable pH regulation of the channel and specific activation at the lysosomal membrane. Dissociation of the binding partner from TRPML1 would leave the loop exposed, potentially causing cathepsin cleavage and preventing further activation of the channel.

Many of the available nanobody-ion channel complex structures show that nanobodies act through allosteric modulation as described here (Brams et al., 2020; Deneka et al., 2021; Rödström et al., 2024). These nanobodies act by binding to highly immunogenic extra-membrane soluble regions that can allosterically modulate channel activity. Overall, this reveals that ion channel activity can be modulated by allosteric sites situated across their surfaces. This has enabled the identification of regions that are more poorly conserved for specific targeting and more controlled regulation of channel activity compared to conventional agonists. In the future, small molecules or peptides that bind to the luminal domain of TRPML1 could be used for specific modulation of TRPML1 activity.

5.8 *In Silico* Predictions of Interfaces

With the undeposited experimental structures available, I aimed to determine if AlphaFold 3 could accurately predict the Syb57 and Syb94-TRPML1 complexes (Abramson et al., 2024). I also aimed to determine whether AlphaFold 3 predictions for unsolved complexes could be correlated with biophysical experimental data. These predictions may provide insights into the mechanisms of action of the sybodies and would enable to determine if AlphaFold is an accurate method to predict sybody-protein complexes for applications presented in chapter 6. Such predictions would be powerful to rationalize why certain sybodies label TRPML1 in cells better

than others in immunofluorescence experiments.

Four TRPML1 subunits (full-length) and four sybodies were used for the predictions. The runs were repeated with a single sybody and four TRPML1 subunits, enabling to validate the prediction if the interface is predicted to be the same. For both Syb57 and Syb94, the binding poses were found to be similar for a 1:4 and 4:4 ratio. The addition of two GlcNAc molecules at Asn220 resulted in inaccurate poses for the Syb94-TRPML1 complex, in which the glycan is involved in sybody binding. Therefore, post-translational modifications were not included for the predictions. This is likely due to the lower number of deposited structures with glycan protein interactions, and the challenges associated with predicting these interactions (Carpenter et al., 2022). The Syb57-TRPML1 complex was accurately predicted with an RMSD of 2.123 Å (547), 1.797 Å (433) for TRPML1 alone and 0.738 Å (114) for the sybody (Figure 59A). Four key hydrogen-bonds are accurately predicted in the model (Figure 59B). Some interactions of interest that could not be built in the structure, potentially due to their transient nature, are observed, including the CDR3 E107-Y126 hydrogen-bond and the interactions between the N-terminal peptide of the sybody and the β4-β5 loop (Figure 59A). In contrast, the accuracy of the prediction for the Syb94-TRPML1 complex was found to be poorer with an RMSD of 3.214 Å (539) for the complex, 1.753 Å (422) for TRPML1 alone and 1.001 Å (117) for the sybody alone. Only the H35-Y126 interaction is accurately predicted (Figure 59C and D). Nevertheless, the binding region at the luminal domain is correctly predicted, the N-terminal peptide of the sybody is correctly predicted to point to the inside of the luminal domain and the β4-β5 loop is predicted to form extensive contacts with the framework of the sybody as observed (Figure 59C). In both predictions, TRPML1 adopts the expected fold. It was found that the sybody-bound AlphaFold model had a dilated selectivity filter and a closed lower gate relative to the apo model, as observed experimentally (see section State of Complexes). However, this was also observed with a sybody shown not to bind to TRPML1 experimentally, suggesting that this approach cannot be used to infer the activity of sybodies.

From these results, it can be noted that AlphaFold 3 predicts the interface accurately when the sybody binds to a simple conformational epitope. Therefore, loop library binder predictions may

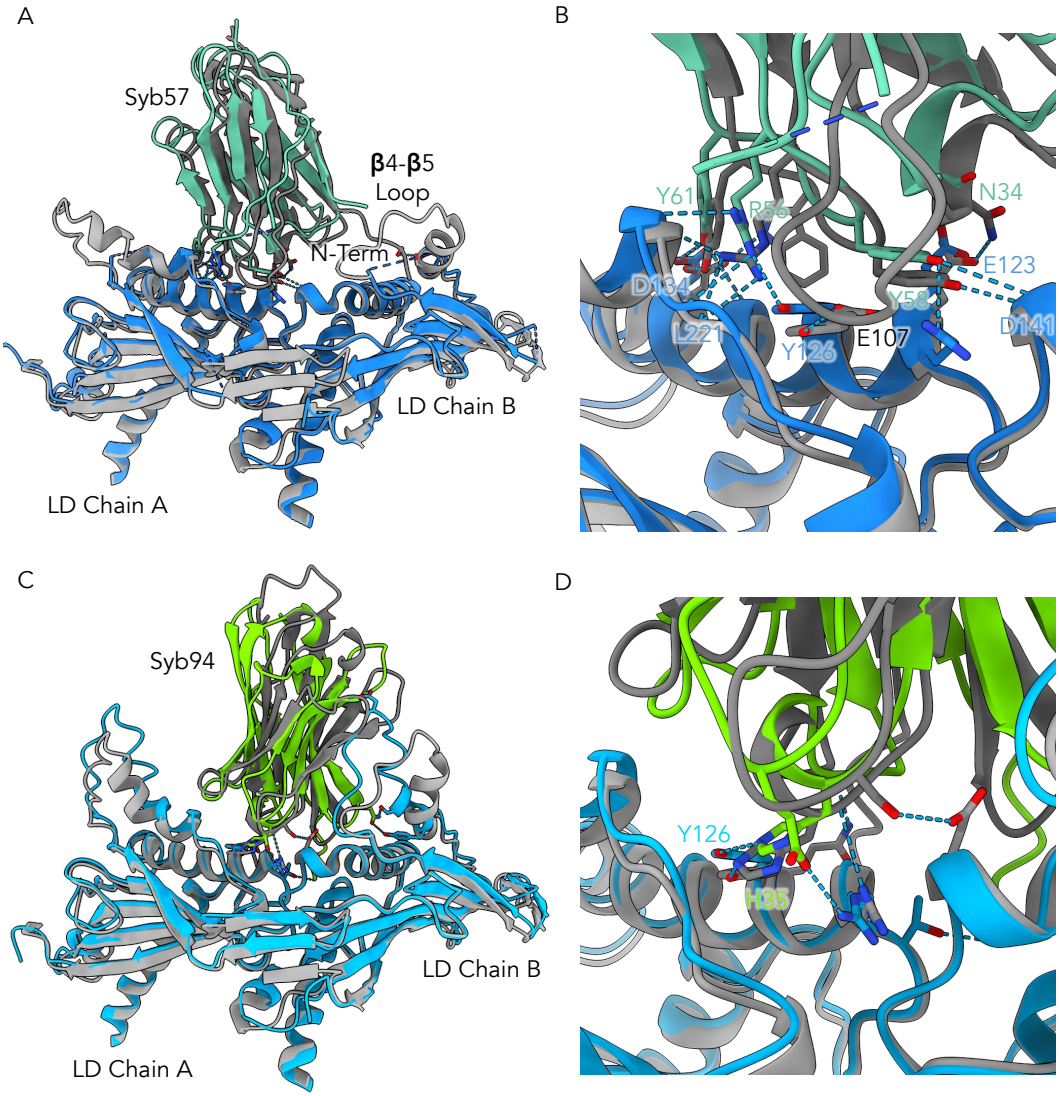

Figure 59: AlphaFold model of Syb57 and Syb94-TRPML1 complexes. A) Comparison of the Syb57-TRPML1 complex structure (TRPML1: blue and sybody: green) and AlphaFold model (TRPML1: light grey and sybody: dark grey) and B) zoom-in on the interface (RMSD: 2.123 Å (547)). Residue pairs that are labelled are present in both the model and the structure. Additional potential interactions of interest are observed in the model, including an interaction between E107(CDR3)-Y126 and between the N-terminus and the β4-β5 loop of the neighbouring monomer. C) Comparison of the Syb94-TRPML1 complex structure (TRPML1: sky blue and sybody: green) and AlphaFold model (TRPML1: light grey and sybody: dark grey) and D) zoom-in on the interface (RMSD: 3.214 Å (539)). The interface between the prediction and structure are similar, but only one specific interaction is predicted accurately (H35-Y126). The orientation of the sybody is accurately predicted as the N-terminus of the sybody points inside the luminal domain.

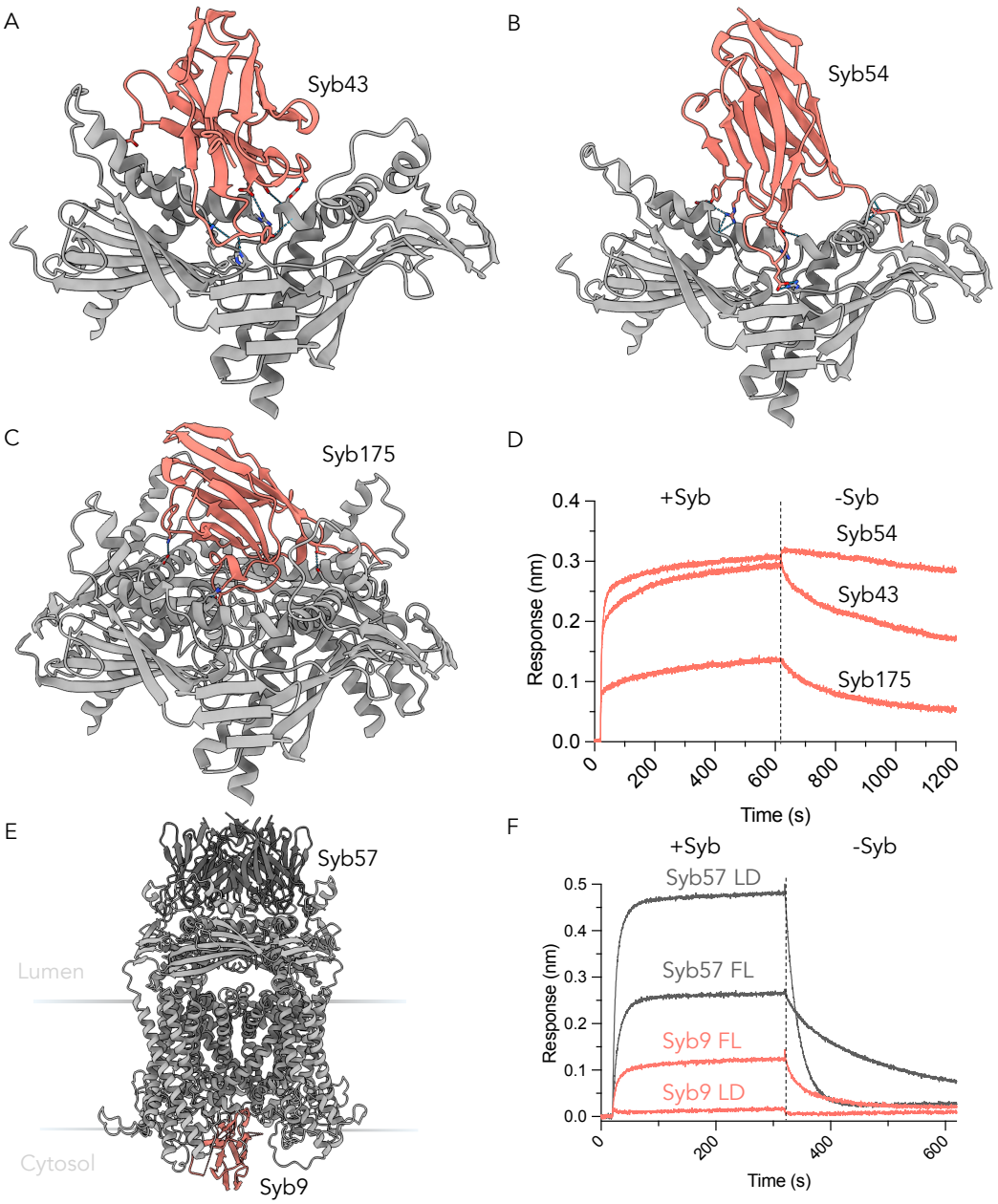

Figure 60: AlphaFold prediction of unsolved sybody-TRPML1 complexes. A) Syb43-TRPML1 AlphaFold prediction (sybody: salmon; TRPML1: grey). The sybody forms extensive contacts with the luminal domain, including the **β**4-**β**5 loop, and the binding mode is compatible with a 1:1 binding ratio. B) Syb54-TRPML1 AlphaFold prediction. Syb54 binds through a very similar interface to Syb57, compatible with 1:1 ratio. C) Syb175-TRPML1 AlphaFold prediction. Syb175 is suggested to interact in a 1:4 ratio. It is predicted to interact by binding to the residues that line the luminal domain pore. D) BLI with full-length TRPML1 for Syb43, Syb54 and Syb175. The response is found to match the binding ratio in the AlphaFold model. E) AlphaFold predictions for Syb57 (dark grey) and Syb9 (salmon) and F) corresponding BLI data for the full-length (FL) and luminal domain (LD).

be more accurate than convex binders, which can typically interact with complex conformational epitopes due to their binding mode.

Since the predictions of AlphaFold 3 were found to be accurate, it was used to predict the structure of the three complexes that had not been structurally characterized, including Syb43 (loop), 54 (loop) and 175 (convex). Different TRPML1:Sybody ratios were trialed to determine the accuracy of the predictions. Syb43 and 54 were found to bind the same epitope regardless of the ratio, while the binding pose of syb175 was altered by the ratio (Figure 60A-C). The highest scoring (1 Syb175: ipTM = 0.72 and pTM = 0.74; 4 Syb175: ipTM = 0.63 and pTM = 0.67) and most reasonable pose was obtained with the 1:4 ratio for Syb175 (Figure 60C). This correlates well with the magnitude of the responses in the BLI experiments with Syb175 showing about a 3-fold smaller response than the other binders, which was suggested to result from different binding ratios (Figure 60D). Future work should aim to test the activity of Syb175 as its predicted complex structure suggests it blocks the pore and interacts with the luminal pore loop, which is expected to inhibit the channel (Figure 60C). Syb43 was found to interact in a 4:4 ratio with the luminal domain and the β4-β5 loop (Figure 60A). For Syb54, its weaker pH dependence is consistent with the predicted structure as it does not interact with any histidine residues and binds through a very similar binding mode to Syb57, which is the only other sybody displaying a weaker pH dependence (Figure 60B). Other loop binders (Syb19 and Syb47) were found to bind to the same interface.

The predictions were expanded further to a range of sybodies that were described throughout chapter 4. These results are summarized in Table 3, including CDR sequence, experimental binding data and the predicted top model (model_0). The aim was to do further testing on the accuracy of AF3 predictions and obtain information about sybody binding epitopes based on correlations with experimental data. Overall, the experimental data is in agreement with the predicted models.

A few conclusions can be drawn from this analysis. Most binders interact with the luminal domain of TRPML1 as suggested by the experimental data. This suggests that the luminal domain is highly immunogenic. Two cytosolic binders were predicted (Syb9 and 135). Limited

Syb	CDR Sequences	Experimental Binding AF: pTM and ipTM	Epitope	Top Model
82	**CDR1:** YHVNMY **CDR2:** QSEGASTT **CDR3:** YVRVGHVYR	FL: Strong PD and Est K_D >500 nM R ≈ 0.25 nm LD: Does PD and R ≈ 0.2 nm ipTM = 0.75 and pTM = 0.76 **(1:4)** ipTM = 0.73 and pTM = 0.75 (4:4)	Syb94-like binding mode, including Syb framework interactions with **β**4-**β**5 loop	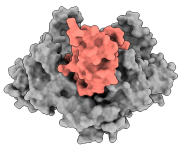
91	**CDR1:** QHISMA **CDR2:** QSEGYGTH **CDR3:** YVFVGRWYT	FL: Strong PD and BLI (strong response) R ≈ 0.22 nm LD: Does PD and R ≈ 0.25 nm ipTM = 0.76 and pTM = 0.77 **(1:4)** ipTM = 0.66 and pTM = 0.69 (4:4)	Syb94-like binding mode, including Syb framework interactions with **β**4-**β**5 loop	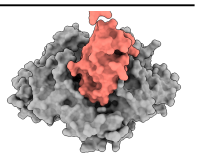
94	**CDR1:** YHHFMR **CDR2:** HSEGQTTE **CDR3:** YVMVGQWYH	FL: Strong PD and K_D = 34.92 (±3.06) nM R ≈ 0.2 nm LD: Does PD and R ≈ 0.5 nm ipTM = 0.75 and pTM = 0.76 **(1:4)** ipTM = 0.66 and pTM = 0.69 (4:4)	N-term Syb points inside, α3 and framework interactions with **β**4-**β**5 loop	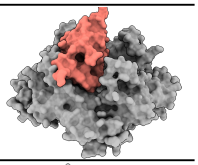
128	**CDR1:** EKAIMA **CDR2:** YSNGYYME **CDR3:** AVYVGHRYR	FL: Strong PD and Est K_D >500 nM R ≈ 0.2 nm LD: Does not PD and R ≈ 0.05 nm ipTM = 0.74 and pTM = 0.76 **(1:4)** ipTM = 0.64 and pTM = 0.68 (4:4)	LD-LD domain interface interactions and extensive **β**4-**β**5 interactions	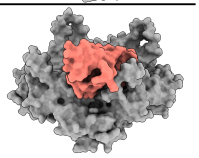
135	**CDR1:** DIWAIW **CDR2:** DTYFGE **CDR3:** HNGYYVPLNTHAYN	FL: Weak PD and BLI (small response) LD: R ≈ 0.07 nm ipTM = 0.73 and pTM = 0.74 **(1:4)** ipTM = 0.65 and pTM = 0.68 (4:4)	Interacts with cytosolic region, away from pore and bridging subunits	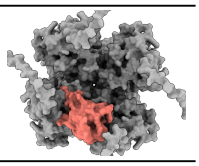
140	**CDR1:** NISFIG **CDR2:** YTNHGY **CDR3:** YWGAAYPLTAYEYE	FL: Weak PD and BLI (small response) LD: Does not PD and no response ipTM = 0.74 and pTM = 0.75 **(1:4)** ipTM = 0.63 and pTM = 0.66 (4:4)	LD-LD interface interactions facing the outside of the LD	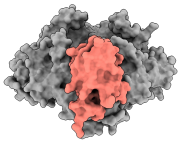
141	**CDR1:** TIASI- **CDR2:** YTQSGW **CDR3:** WWGQHYPLKETEYE	FL: Strong PD and Weak BLI R ≈ 0.07 nm LD: Does not PD and R ≈ 0.05 nm ipTM = 0.74 and pTM = 0.76 **(1:4)** ipTM = 0.72 and pTM = 0.74 (4:4)	LD-LD interface interactions facing the outside of the LD	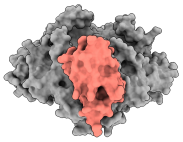
174	**CDR1:** SIAYIG **CDR2:** ATTRGY **CDR3:** AAGYAHPLAYVEYE	FL: Weak PD and BLI (small response) LD: Does not PD and R ≈ 0.075 nm ipTM = 0.73 and pTM = 0.75 **(1:4)** ipTM = 0.65 and pTM = 0.68 (4:4)	Stretches across LD pore by interacting with α3, does not occlude pore and forms few interactions	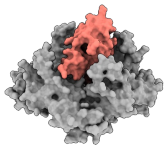
175	**CDR1:** TIHTIY **CDR2:** ITKYGY **CDR3:** TQGIKSPLASRDYT	FL: Weak PD and K_D = 101.66 (±2.90) nM R ≈ 0.16 nm LD: Does PD and R ≈ 0.15 nm ipTM = 0.72 and pTM = 0.74 **(1:4)** ipTM = 0.63 and pTM = 0.67 (4:4)	Binds to center of LD by interacting with luminal pore loop and α3	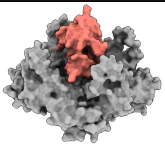

Syb	CDR Sequences	Experimental Binding AF: pTM and ipTM	Epitope	Top Model
9	**CDR1:** EEAWMA **CDR2:** KSSGYSTW **CDR3:** YGEWWHA	FL: Strong PD and Est K_D >500 nM R ≈ 0.06 nm LD: Does PD and no binding in BLI ipTM = 0.73 and pTM = 0.74 **(1:4)** ipTM = 0.63 and pTM = 0.67 (4:4)	Binds occludes the cytosolic side of the pore	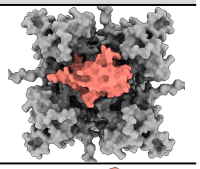
19	**CDR1:** MAAWMH **CDR2:** RSYGMYTW **CDR3:** EGDFAYW	FL: Strong PD and Est K_D >500 nM R ≈ 0.22 nm LD: Does not PD and R ≈ 0.1 nm ipTM = 0.78 and pTM = 0.79 (1:4) ipTM = 0.79 and pTM = 0.81 **(4:4)**	Syb57-like binding mode, including additional contacts with **β**4-**β**5 loop	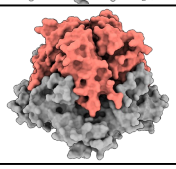
43	**CDR1:** SNAEMY **CDR2:** TSSGLHTY **CDR3:** DGYTEYN	FL: Strong PD and K_D = 99.77 (±10.61) nM R ≈ 0.2 nm LD: Does PD and R ≈ 0.12 nm ipTM = 0.74 and pTM = 0.75 **(1:4)** ipTM = 0.65 and pTM = 0.68 (4:4)	Interacts with the luminal-luminal domain interface and the **β**4-**β**5 loop	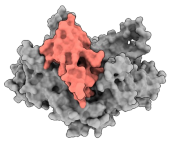
47	**CDR1:** KNYWMY **CDR2:** RSYGYYTW **CDR3:** QGEYADI	FL: Strong PD and Est K_D >500 nM R ≈ 0.15 nm LD: Does PD and R ≈ 0.08 nm ipTM = 0.78 and pTM = 0.79 (1:4) ipTM = 0.79 and pTM = 0.8 **(4:4)**	Syb57-like binding mode, including additional contacts with **β**4-**β**5 loop.	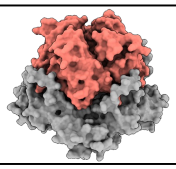
53	**CDR1:** MAAYMA **CDR2:** WSQGPGTW **CDR3:** QGYLFSS	FL: Strong PD and Est K_D >500 nM R ≈ 0.03 nm LD: Does not PD and no binding in BLI ipTM = 0.73 and pTM = 0.75 **(1:4)** ipTM = 0.65 and pTM = 0.65 (4:4)	Interacts with center of LD, mostly forming interactions with α3	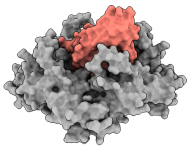
54	**CDR1:** WAHWMH **CDR2:** RSYGKYTW **CDR3:** DGSTEWH	FL: Strong PD and K_D = 38.26 (±9.76) nM R ≈ 0.26 nm LD: Does PD and R ≈ 0.44 nm ipTM = 0.79 and pTM = 0.79 (1:4) ipTM = 0.8 and pTM = 0.81 **(4:4)**	Syb57-like binding mode with few **β**4-**β**5 loop interactions and greater spacing between sybodies than Syb57	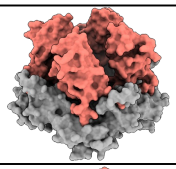
57	**CDR1:** NAVWMH **CDR2:** RSYGWYTW **CDR3:** TGEDKEK	FL: Strong PD and K_D = 57.05 (±9.91) nM R ≈ 0.26 nm LD: Does PD and R ≈ 0.48 nm ipTM = 0.8 and pTM = 0.8 (1:4) ipTM = 0.8 and pTM = 0.81 **(4:4)**	Interactions with α3 and **β**4-**β**5 loop as observed in the structure	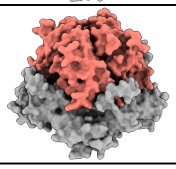

Table 3: AlphaFold 3 predictions of Sybody-TRPML1 complexes and correlation with experimental data. Table displaying the different sybodies with their CDR, experimental and AF3 confidence scores, binding epitope based on the AF model and surface representation of the top (model_0) prediction. In the experimental binding AF parameter column, PD refers to pull-down and how well this sybody pulls-down to TRPML1, K_Ds or Estimated (Est) K_D are provided and R refers to the response that the sybody generates in BLI at a concentration of 500 nM. Values were included for the FL (full-length) and LD (luminal domain). ipTM and pTM scores for the 1:4 and 4:4 predictions are provided (Syb:TRPML1), and the prediction displayed in the top model column with the highest score is shown in bold. The epitope column describes the epitope the sybody binds to. The top model column shows the surface representation of the prediction with the highest score (sybodies: salmon and TRPML1: grey). Syb libraries loop (blue), concave (green) and convex (red)

testing was carried out on Syb135 because it was found to pull down TRPML1 poorly and it was found to stain TRPML1 non-specifically (see Chapter 6). This suggests that the cytosolic domain potentially favors binding to weaker and less specific sybodies, which would explain why few cytosolic binders were obtained. Moreover, the epitope Syb135 binds to is partially shielded by the detergent micelle, which would weaken its binding. A key finding from this screen is the cytosolic binding of Syb9, which acts to block the pore of TRPML1. Syb9 was found to pull down TRPML1 well, and epitope binning along with the luminal domain BLI results suggested it was a cytosolic binder. This binder should be investigated further as it may show inhibitory activity by blocking the pore.

For the other loop library binders, 3 binders (Syb19, 47 and 54) were found to have a similar binding to Syb57 as expected based on the conservation of the CDR2, which plays an important role in Syb57 binding. The models suggest that Syb19 and 47 are weaker binders because they are tilted relative to the plane of the LD, causing changes in the interactions they form with the luminal domain and leading to the formation of contacts with the β4-β5. An attempt was made to rank these sybodies based on affinity predictions using the model but this was unsuccessful. The responses in BLI experiments were found to correlate with the models as lower responses were found for sybodies that bound to the middle of the luminal domain or cytosolic regions in a 1:4 ratio. For sybodies that may interact in a 4:4 ratio, the ipTM and pTM scores were found to be similar for the 1:4 and 4:4 predictions. In sybodies with weaker predictions, potentially due to more complex binding modes, the score degraded significantly in the 4:4 prediction as the sybody-TRPML1 interface becomes a more prominent part of the model (Syb43 1:4: ipTM = 0.74 and pTM = 0.75; 4:4: ipTM = 0.65 and pTM = 0.68). These sybodies with more complex binding modes may also clash in the tetrameric state, leading to a slightly altered and weaker model in the 4:4 prediction.

The concave binders interacted with TRPML1 through their expected binding mode, including interactions formed by the CDRs and the sybody framework. As observed in the loop library, most tested concave binders, including Syb82, 91 and 94, adopt the same binding mode.

As observed for the loop library, the convex binders showed great diversity in binding modes.

Syb135 was found to bind on the cytosolic side, Syb140 and 141 bound to the exterior of the luminal domain, and Syb174 and 175 bound to the center of the luminal domain. Syb140 and 141 show similarities in their CDRs and could be predicted to bind through a similar binding mode. Their binding may be weak due to glycosylation of their epitope at N179 and 220. The diversity in the sequences in this library are responsible for the diversity of binding modes. Poor binders in the convex library were found to form fewer interactions, which typically led to lower pTM and ipTM scores. However, the score was not found to necessarily correlate with affinity.

Overall, these predictions explain why certain high-affinity sybodies bind efficiently to their target protein in the cell, while others do not (see Chapter 6). Sybodies that form fewer interactions with the flexible and post-translationally modified β4-β5 loop show improved co-localization (Syb54, 57 and 175) compared to those that do (Syb43 and 94). Overall, the predictions were consistent with the structural data, and thus AlphaFold may act as a useful tool to predict the epitopes of the sybodies, which can be applied to the design of high-affinity sybody multivalent constructs and for sybody mutagenesis.

5.9 Outlook

The work presented here has enabled to suggest a novel mechanism for the activation of TRPML1.

Further electrophysiology experiments will be required to: (1) to test the activity of syb57 at acidic pH or in the lysosomal environment (lyso-patch), (2) test the hypothesis that the sybodies act by modulating the conformation of the selectivity filter, (3) test the role of the histidine network in channel activation, (4) test the activity and specificity of peptides extracted from the CDRs of the activatory sybodies and (5) investigate the role of the β4-β5 loop on channel activity (effect of cathepsin cleavage or loop peptide addition). Co-IP experiments could be carried out to identify an endogenous protein modulator and its activity could be tested.

Additional insights into the mechanisms of the sybodies could be obtained by: (1) obtaining a structure of Syb94-TRPML1 in the presence of PI(3,5)P_2 in digitonin for comparison to the

Syb57 structure and (2) obtaining a structure of Syb57-TRPML1 at acidic pH to determine if additional conformational changes are observed.

It was shown that AF3 makes highly accurate predictions of binding by comparing BLI data with the obtained models. Combinations of BLI experiments, such as measurements at saturating concentrations, measurements with isolated domains from the protein and epitope binning experiments, with AF3 can act as a powerful predictive tool to identify the epitope of the sybodies obtained in the screen. This can enable to rationalize functional data, predict binding of the sybodies to endogenous protein based on the complexity of the epitope and can facilitate sybody engineering.

6 | Engineering Synthetic Nanobodies to Investigate TRPML1 Localization

6.1 Lysosomal Membrane Protein Imaging

Lysosomes can be studied by microscopy in a fixed or live state. Lysotracker, a pH-sensitive dye, has been used extensively to study the trafficking of lysosomes through live imaging (Lie et al., 2022; Sun et al., 2022). However, loading of lysosomes with dyes significantly impairs their functions, lysotracker photobleaches rapidly and the dye is not lysosome-specific (Pierzyńska-Mach et al., 2014). In recent years, new antibodies have been generated against a range of lysosomal membrane proteins, but most of these antibodies show poor specificity (Nelson et al., 2017). Specific antibodies have mostly been obtained against soluble lysosomal proteins and lysosomal markers, which are highly expressed lysosomal membrane proteins (Bond et al., 2024). However, most lysosomal membrane proteins are weakly expressed (Akter et al., 2023). This challenge along with other challenges, including extensive processing of lysosomal membrane proteins (PTMs, cleavage etc.), low stability, detergent specificity and epitope shielding due to protein complex formation, make it highly challenging to generate reagents that can be used to stain lysosomal membrane proteins in cells.

We aimed to determine if the sybody platform could be used as a method to rapidly generate reagents to map the localization of endogenous lysosomal membrane proteins (Aim 3). This method would be attractive for these targets because they tend to be unstable and are often obtained in low yields, which are challenges that the sybody pipeline aims to overcome (Zimmermann et al., 2020).

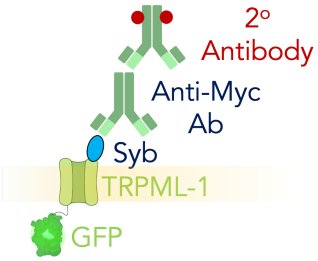

Figure 61: Staining protocol for immunofluorescence experiments with the sybody-Myc constructs. HeLa cells are transfected with GFP-TRPML1 or other targets of interests fused with a GFP tag. The cells are then fixed, permeabilized and stained simultaneously with sybody-Myc, primary anti-Myc antibody and secondary antibody conjugated to a fluorophore. This initial setup is modified when using alternative constructs in other sections of this chapter.

6.2 Determining Sybody Specificity and Binding in Cells

Before testing sybodies with endogenous lysosomal membrane protein imaging, it needed to be determined if they are specific and can bind to the target protein of interest in cells. Sybody binding to target proteins can be strongly impaired by detergent changes and has been observed to be highly conformation/environment dependent. Moreover, many obtained sybodies display unfavorable physicochemical properties, which can be synonymous with a lack of specificity. Therefore, I aimed to establish an assay that would enable to quickly identify binders that could be used for immunofluorescence experiments.

The designed assay makes use of the myc-tag that is already present on the sybody constructs from the ELISA (Figure 61). The GFP-tagged target protein is transfected in HeLa cells that have been grown for 24 hours on coverslips or imaging chambers. After 21-24 hours of expression, the cells are fixed with 4% PFA and permeabilized with 0.1% Triton X-100. Cells are simultaneously stained with 500 nM of sybody-myc, anti-myc mouse antibody (clone 9E10; Invitrogen) and donkey anti-mouse secondary antibody conjugated to alexa fluor 647 (Invitrogen). The cells are then washed, mounted, and imaged. The simplicity of this assay makes it scalable to screen large numbers of binders at once. Moreover, the use of a primary and secondary antibody leads to significant signal amplification.

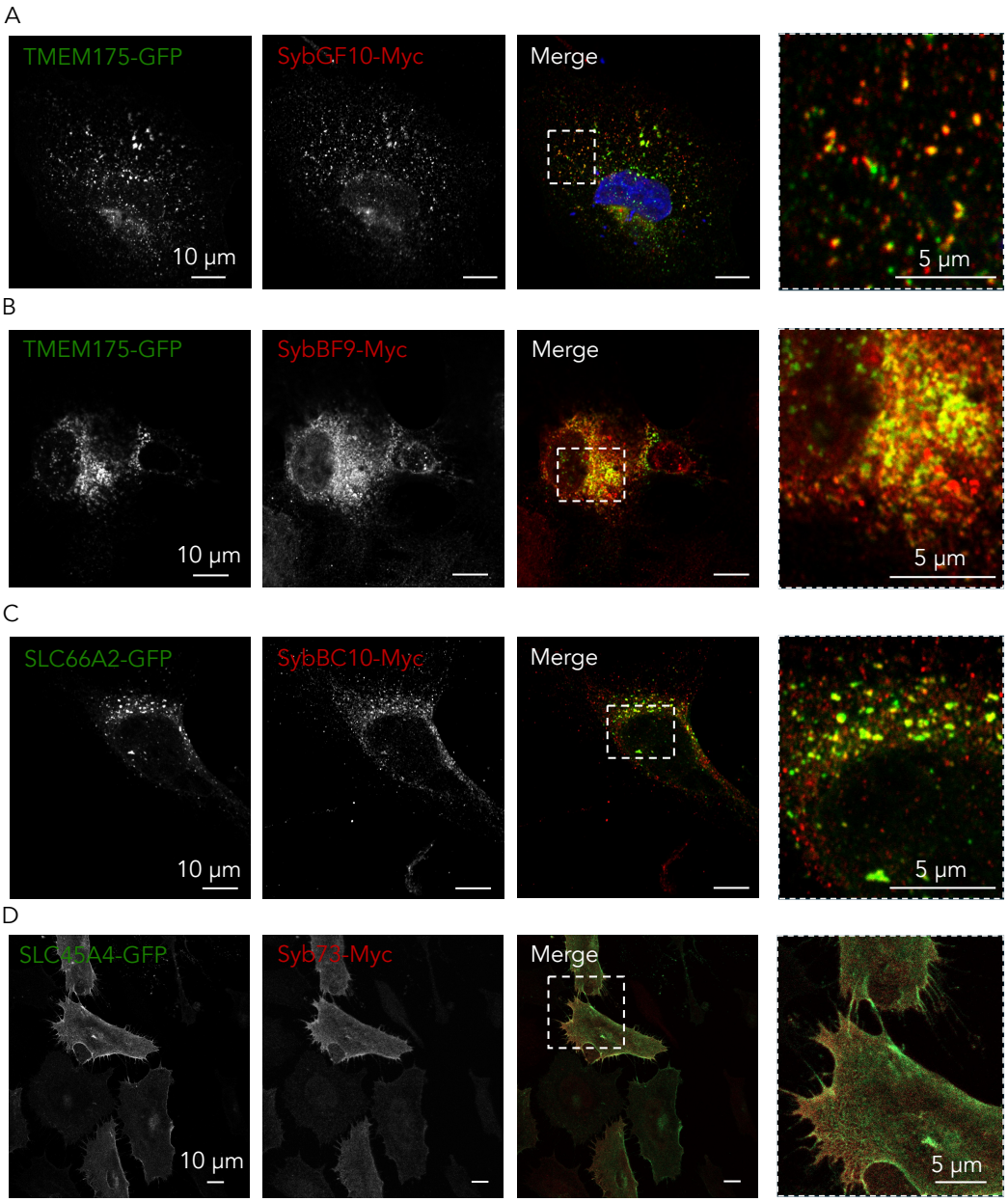

Figure 62: Confocal imaging of overexpressed human membrane protein-GFP fusions in HeLa cells using sybody-Myc constructs. A) Staining of TMEM175-GFP (green) overexpressing HeLa cells with SybGF10 (red) and B) SybBF9 (red). A specific region highlighted with white dotted lines is shown to the right of the merged image. Strong colocalization is observed between SybGF10 and TMEM-175-GFP signal, while SybBF9 shows non-specific binding that does not co-localize with TMEM175-GFP. C) Staining of SLC66A2-GFP with SybBC10-Myc (Syb$^{(-)}$). The sybody and GFP signal show strong co-localization. D) Staining of SLC45A4-GFP with Syb73-Myc. Co-localization is more challenging to visualize in low-expressing plasma-membrane proteins like SLC45A4. The signals co-localize as only transfected cells (GFP-positive) show sybody signal.

This assay was initially trialed on a range of membrane proteins, including TMEM175, SLC66A2, TRPML1 and SLC45A4 (Figure 62 A-D). By trialing this on a range of proteins, it could be determined how widely applicable these binders would be for imaging studies, and any potential limitations of the binders or assay could be identified. By observing the different samples, it was found that nearly all sybodies, including low-affinity binders (e.g. SLC45A4 sybodies), showed some colocalization with the target protein in low-stringency staining (PBS with 1% BSA) and washing (5 times with 1X PBS washes) conditions (Figure 62A-D). The notable difference between binders was the labeling efficiency and the staining of regions with no target protein. Incomplete labeling of the target protein is due to the low affinity of the sybody for the protein or a low affinity for the state present in cells (modified, protein complex, unfolded etc.). For example, SybGF10 (provided by Sigurbjörn Markusson), a high-affinity TMEM175 sybody (40.7 $\pm$5.9 nM), shows strong but partial co-localization, which may be due to steric occlusion of the binding site by one of its binding partners, such as lamp-1 (Figure 62A) (Zhang et al., 2023). SybBF9, also a high-affinity TMEM175 sybody (22.0 $\pm$2.3 nM), was observed to stain regions that showed no GFP fluorescence. This could be due to binding of endogenous protein, which may localize to non-GFP-containing compartments (Figure 62B). However, the location of the signal is not specific and is stronger than expected based on the low expression of TMEM175 in cells, suggesting this is due to non-specific binding (Akter et al., 2023). Therefore, with a simple qualitative analysis, this assay enables to identify low-specificity binders. SLC66A2 and SLC45A4 sybodies (153.0 $\pm$13.3 nM) (provided by Oliver Adams and Sigurbjörn Markusson) were found to show some but incomplete colocalization to their target protein (Figure 62C-D). Overall, this showed that the sybodies and the assay could be applied to a range of proteins. It also enabled to identify the key challenge, which is partial labeling of the target protein. Although this could demonstrate the existence of different states of the protein in the cell, near-complete labeling of the protein is desired for super-resolution microscopy and would be necessary to comprehensively map out the localization of the lysosomal proteins of interest (Hellmeier et al., 2024).

This protocol was then applied to TRPML1 sybodies. Two main experiments were carried out on TRPML1 sybodies: (1) high-throughput wide-field imaging on the convex library binders as

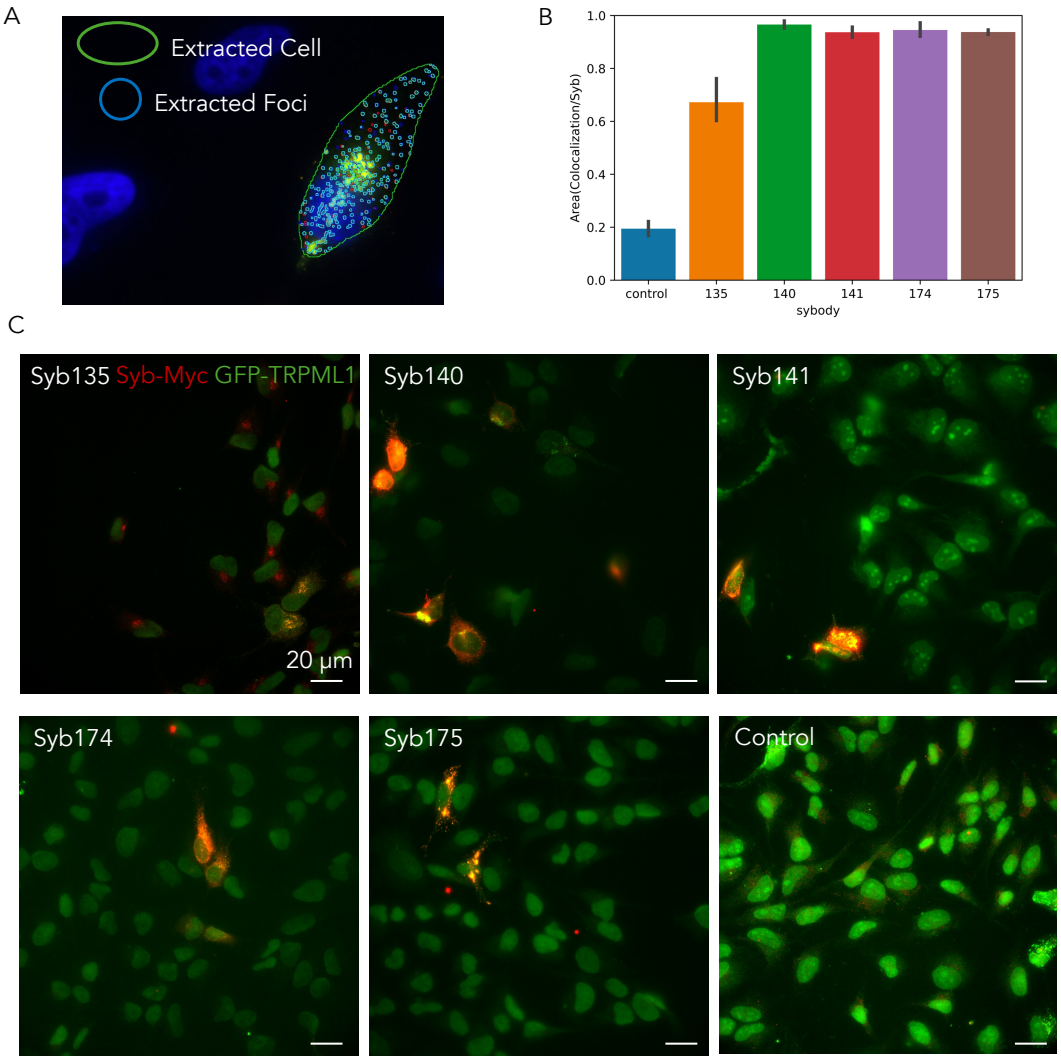

Figure 63: Screen of convex sybody co-localization with GFP-TRPML1 in HeLa cells using the widefield ScanR screening station (Olympus). A) Deep-learning model and data analysis pipeline for automated data analysis. The deep-learning model extracts the cells (green) and lysosomes (blue) based on GFP channel. B) Object-based co-localization analysis using the automated pipeline with values displayed showing the total area of co-localization in the extracted regions divided by the total area in the extracted regions. All sybodies co-localize well with GFP-TRPML1, except Syb135 which is a weak binder of TRPML1. Control sample includes anti-Myc antibody and secondary antibody without sybody. Control: n=116, Syb135: n=9; Syb140: n=142; Syb141: n=96; Syb175: n=22; Syb174: n=17. Number of cells are low for Syb135 because cells with fewer than 10 spots in the red channel were excluded to eliminate artifacts, and the staining by this sybody was weak. Error bars are standard deviation values. C) Raw merge images for the convex library binders (TRPML1-GFP and secondary antibody alexa-647 channels).

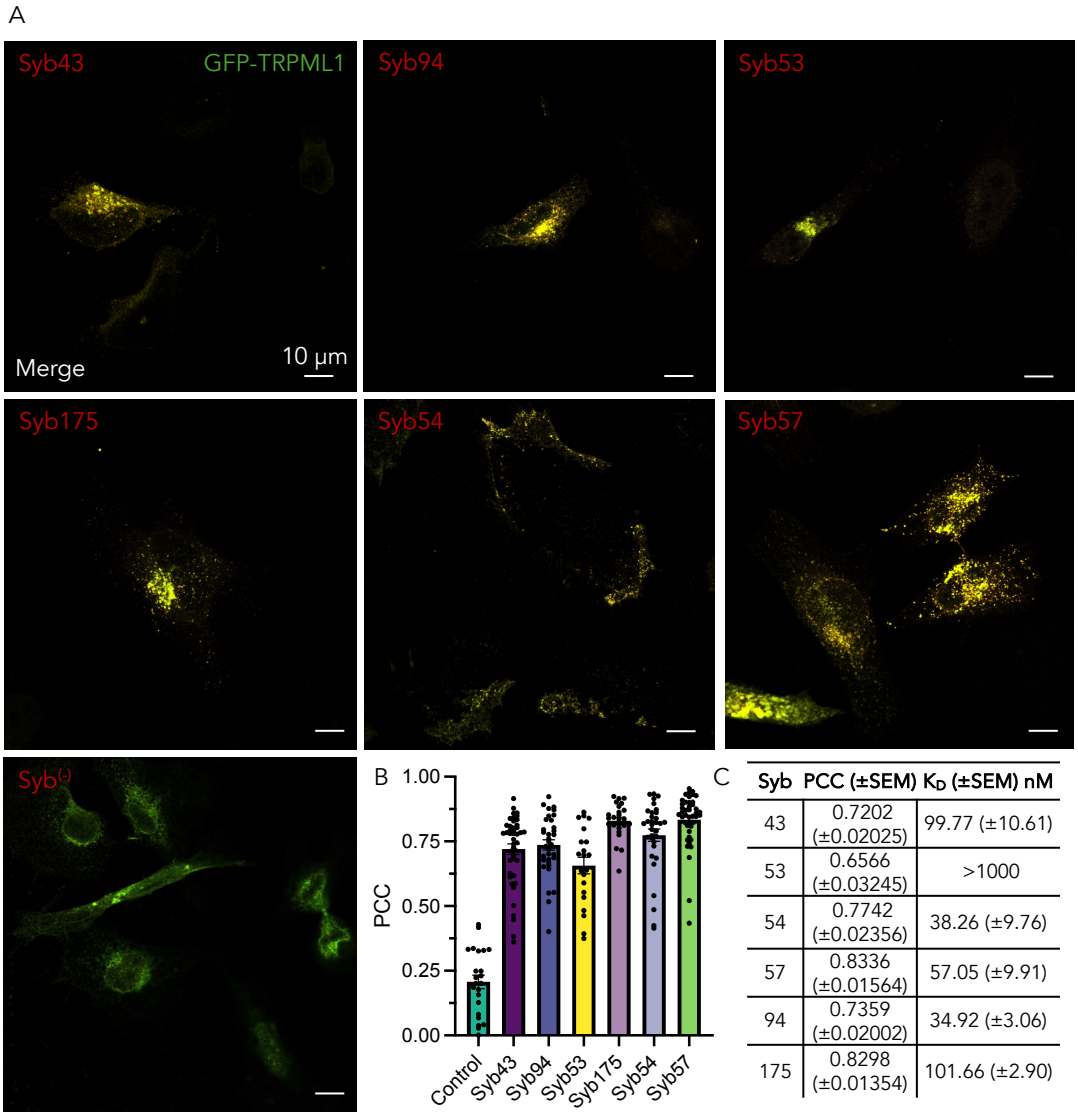

Syb	PCC (±SEM)	K_D (±SEM) nM
43	0.7202 (±0.02025)	99.77 (±10.61)
53	0.6566 (±0.03245)	>1000
54	0.7742 (±0.02356)	38.26 (±9.76)
57	0.8336 (±0.01564)	57.05 (±9.91)
94	0.7359 (±0.02002)	34.92 (±3.06)
175	0.8298 (±0.01354)	101.66 (±2.90)

Figure 64: Confocal microscopy co-localization screen of high-affinity TRPML1 sybodies. A) Raw merged images of GFP-TRPML1 (green) and sybody-Myc (red) signal. Control sample includes Syb$^{(-)}$ with primary and secondary antibodies. B) Pearson's correlation coefficient (PCC) for confocal data set of different sybodies. Correlation values were obtained by measuring co-localization of GFP-TRPML1 signal with sybody-Myc signal in extracted cells (GFP positive transfected cells were selected for the analysis). Control: n=23, Syb43: n=44, Syb53: n=21, Syb54: n=33, Syb57: n=43, Syb94: n=34, Syb175: n=25. Displayed data points represent PCC for a single extracted cell and error bars are standard error of the mean values. C) Table displaying side-by-side PCC values with K_D values for the sybodies, showing the lack of a correlation between affinity and co-localization except for low-affinity binders (e.g. Syb53).

a case study (Figure 63A-C), and (2) confocal imaging on the high-affinity TRPML1 binders to identify the best binders for super-resolution experiments (Figure 64A). The scanR microscope system (Olympus) automates data acquisition and analysis, which made it an ideal tool to screen binding specificity (co-localization) using immunofluorescence (IF). Samples were stained as described above, imaged, and the images were processed using automated object-orientated (lysosome extraction) co-localization analysis (Figure 63A). This analysis confirmed the visual observation that the assay is specific (anti-Myc antibody only control Mander's coefficient: 0.19 $\pm$0.14) and that all the convex library sybodies colocalized well with TRPML1 (Mander's co-efficient: 0.94-0.97), except the low-affinity binder Syb135 (Mander's coefficient: 0.67 $\pm$0.13) which also displayed non-specific binding. This experiment demonstrates that the assay can be used qualitatively and quantitatively to discriminate specific binders from non-specific binders.

High-affinity binders, as determined by kinetic studies, were imaged by confocal microscopy (Figure 64A). The data was analysed by segmenting the cells and measuring Pearson's Correlation Coefficient (PCC) between the GFP and Alexa-647 channels using JACOP (Bolte and Cordelières, 2006). All binders, except Syb53 (PCC: 0.6566 $\pm$0.03245), were found to colocalize well with GFP-TRPML1. In these experiments, it was observed that weakly-expressing cells enabled to differentiate the labeling efficiencies of the sybodies as strong co-localization is generally observed in highly-expressing cells/regions regardless of the quality of the binder. Syb54 (PCC: 0.7742 $\pm$0.02356), Syb57 (PCC: 0.8336 $\pm$0.01564) and Syb175 (PCC: 0.8298 $\pm$0.01354) were observed to label GFP-TRPML1 in low-expressing cells and co-localized best with TRPML1. Low-affinity binders, such as Syb53, display poorer co-localization. However, for high-affinity binders ($K_D < 100$ nM), affinity is not a good predictor of co-localization (Figure 64B and C).

As described in Chapter 5, the determining factor for the high-affinity binders appears to be the presence of their conformational epitope in cells. The best co-localizing sybodies are those that form few interactions with the modified and flexible β4-β5 loop, which sybodies are unlikely to bind to with a high affinity in the cell. Therefore, epitope binning should be carried out before IF to ensure that multiple epitopes across the protein are targeted. This data can be combined

with AlphaFold predictions in the future for panels of sybodies against other lysosomal targets to predict sybody binding sites and in turn, correlate this with co-localization. Another factor to consider from these predictions is whether the binding mode is compatible with the staining protocol, for example, does the staining protocol require acidic conditions that would disrupt interactions formed by histidine residues. An important consideration when using nanobodies/sybodies in immunostaining experiments is that they interact with a conformational epitope while many conventional antibodies interact with linear epitopes/peptides, which are more likely to be present in a fixed cell. Therefore, while affinity values may be useful for these antibodies, the epitope is significantly more important when looking to predict the usability of a nanobody for immunostaining experiments.

The main goal of this work was to image the localization of endogenous protein. Therefore, untransfected HeLa cells were fixed, permeablized and stained with Syb57 along with primary and secondary antibody as detailed above (Figure 65A-B). Syb57 was chosen for this experiment and experiments in the sections below because it co-localized best with GFP-TRPML1 (PCC: 0.8336 $\pm$0.01564). This was trialed with two anti-myc (rabbit and mouse) and anti-lamp-1 (mouse and sheep) antibody combinations, but the signals did not co-localize. Significant background was observed from the anti-myc antibody, which was also observed in the confocal sybody screen (PCC: 0.2070 $\pm$0.02634). It was hypothesized that direct conjugation of the sybody to a fluorophore may reduce the background from the staining, which would enable to differentiate the weak signal of the endogenous protein from the background. Moreover, this would reduce the linkage error for super-resolution microscopy experiments. Therefore, sybodies were engineered to directly conjugate them to fluorophores.

6.3 Sybody Engineering for Fluorescence Microscopy

6.3.1 Sybody Fusions

To image endogenous TRPML1 localization, sybodies were fused with the HaloTag. The HaloTag is derived from the enzyme haloalkane dehalogenase, which can form covalent bonds

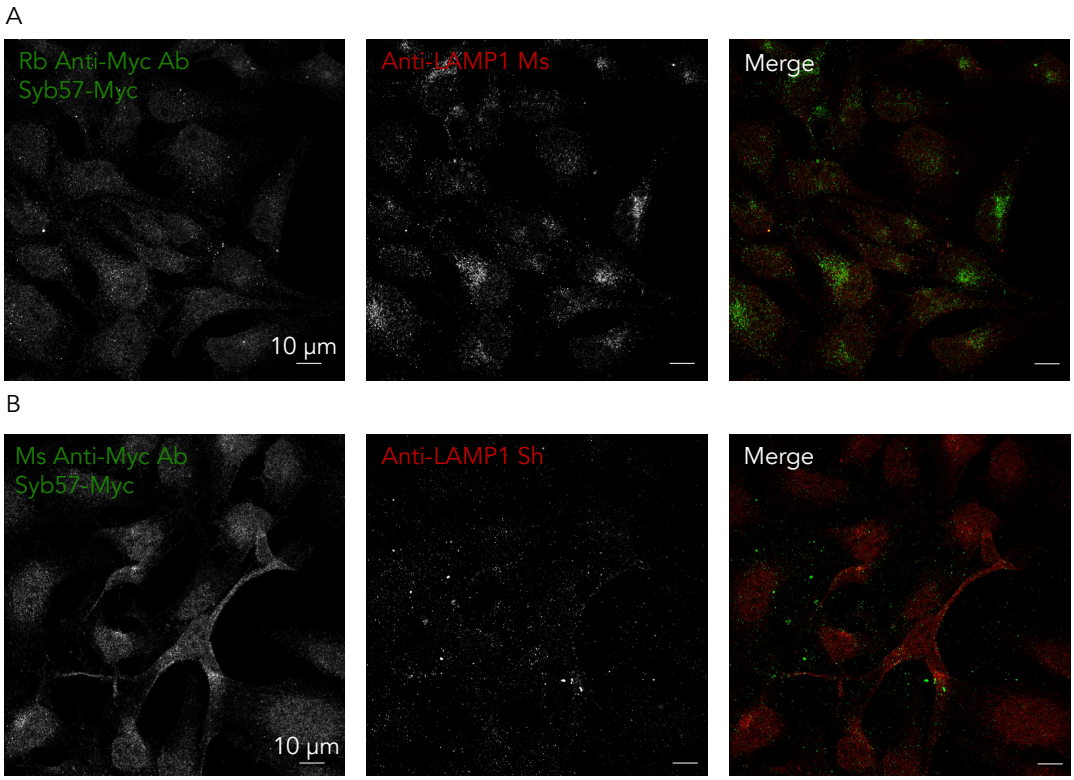

Figure 65: Confocal microscopy of untransfected HeLa cells stained with sybody and lamp-1 antibody. A) Confocal images of cells stained with Syb57-Myc and rabbit anti-Myc antibody (green) and mouse anti-LAMP1 antibody (red) or B) mouse anti-Myc antibody (green, used for previous experiments) and sheep anti-LAMP1 antibody. The LAMP1 and sybody signals do not co-localize.

with substrates that have chloroalkane linkers (Los et al., 2008). This tag was selected because it can be conjugated to a range of fluorophores that are super-resolution compatible (Kompa et al., 2023).

The HaloTag was fused to the N and C-terminal ends of Syb57 in the pSBINIT vector (vector used for WT expression) through a 5xGSSS linker. The constructs were expressed in MC1061 cells for periplasmic extraction and were purified with Ni-NTA resin, as described for WT sybodies. Syb57 was selected due to its strong expression, high affinity and colocalization with GFP-TRPML1. Both constructs were found to express weakly and generate low protein yields from 1 L of culture (Figure 66A and B). The N-terminally tagged construct was purer and higher yields were obtained (Figure 66B). To improve the yield, induction at different temperatures and ODs were tested, and lower ODs were found to lead to higher protein yields (Figure 66C and D). However, yields remained low. Nevertheless, the Halo-Syb57 fusion was successfully purified with Ni-NTA and with a sepax SEC-300 column (Figure 66E). The fusion was successfully labeled with Janelia Fluor-646 HaloTag ligand (Promega) in a 1.15:1 ratio for 1 hour at RT, and labeling was confirmed by running the labeled fusion on an SDS-PAGE (Figure 66F). Fusion concentrations were too low to assess labeling efficiency. Previously, HaloTag fusions have been successfully expressed in the periplasm of *E. coli*, but this was shown to be construct-dependent as some constructs were found to aggregate upon fusion to the HaloTag (Ke et al., 2016). Many nanobody fusions have previously been found to be challenging to express and purify due to the lack of important chaperones in *E. coli* (Su et al., 2023). To increase the yield, expression of the fusion was successfully carried out in HEK293F cells without dialysis (500 ml; 60 hours of expression following PEI transfection) (Figure 67A). Purification of the N and C-terminal tagged Syb57 and SybGF10 (TMEM175 sybody) was found to be successful and significantly higher yields were obtained in HEK cells (50 ml) with dialysis (500 ml without dialysis in Figure 67A compared to Figure 67B-C 50 ml with dialysis). TMEM175 sybody-Halo fusions were purified to test the protocols for multiple targets, but the focus of the analysis was on TRPML1 sybodies. Interestingly, C-terminally Halo-tagged fusions displayed a double band pattern (boiled and reduced with DTT) potentially due to a post-translational modification, while the N-terminal fusions did not (Figure 67B). This suggests that the two fusions are processed differently and

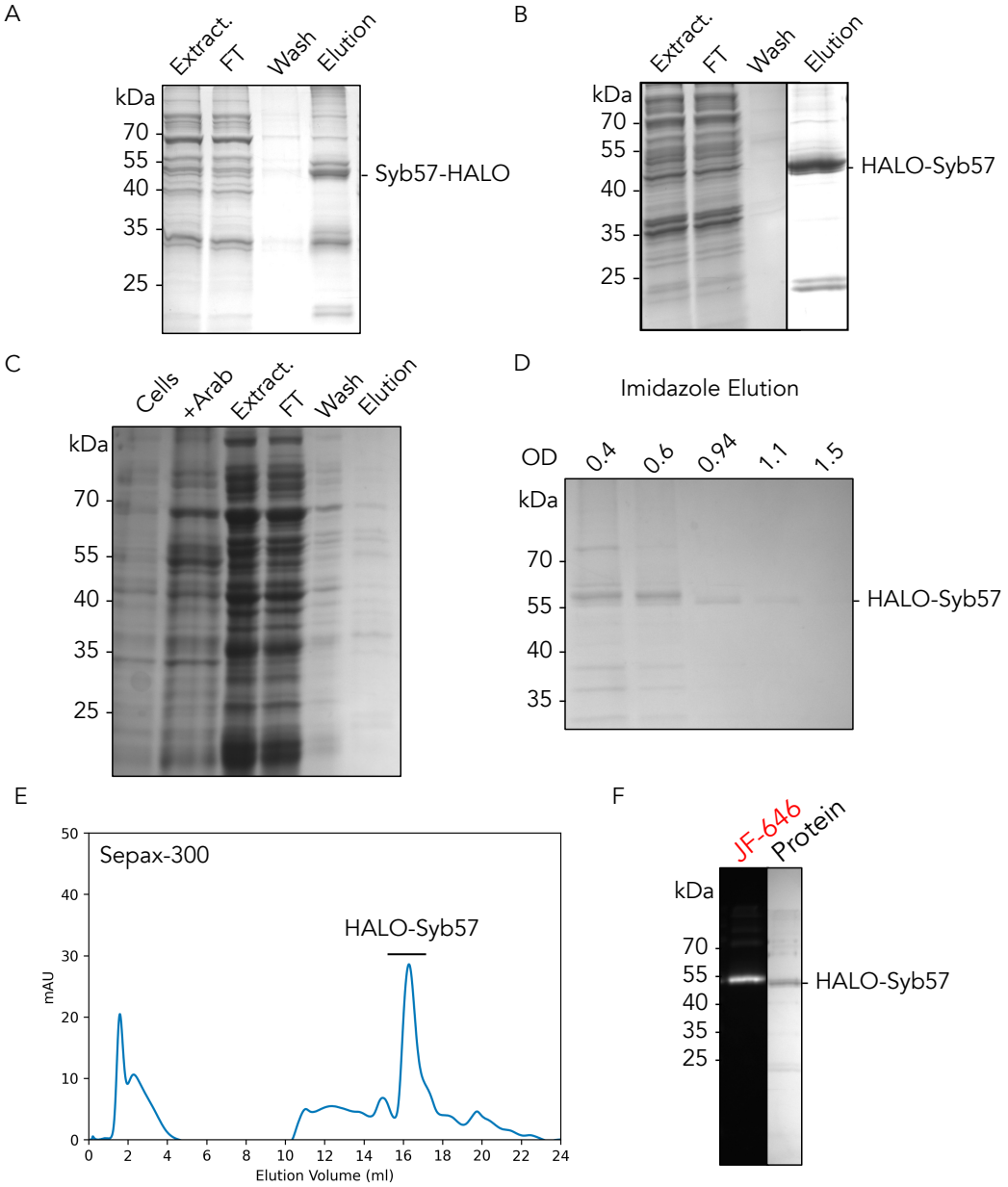

Figure 66: Syb57 HaloTag fusions expressions in bacteria, purifications, and labelling. A) SDS-PAGE of Syb57 C-terminal and B) N-terminal HaloTag fusion expression and purification samples with induction at 22°C and expression overnight or C) Induction at 37°C and expression for 4 hours (N-terminal HaloTag fusion). Extract: Periplasmic extraction, FT: Flow-through, Wash: TBS + 25 mM Imidazole wash and Elution: 250 mM imidazole + TBS elution. D) Expression trials at 22°C with induction at different ODs and small-scale purification. E) SEC (Sepax SRT-C SEC-300) profile of HALO-Syb57 fusion purification from 1 L of *E. coli* culture. F) SDS-PAGE following the labelling of the Halo-Syb57 fusion with Janelia Fluor-647 HaloTag ligand (JF-646; Promega). The left lane shows the in-gel fluorescence for the cy5 Channel (similar spectrum as JF-646) and the right lane shows the result of the Coomassie stain. The fusion was successfully labelled.

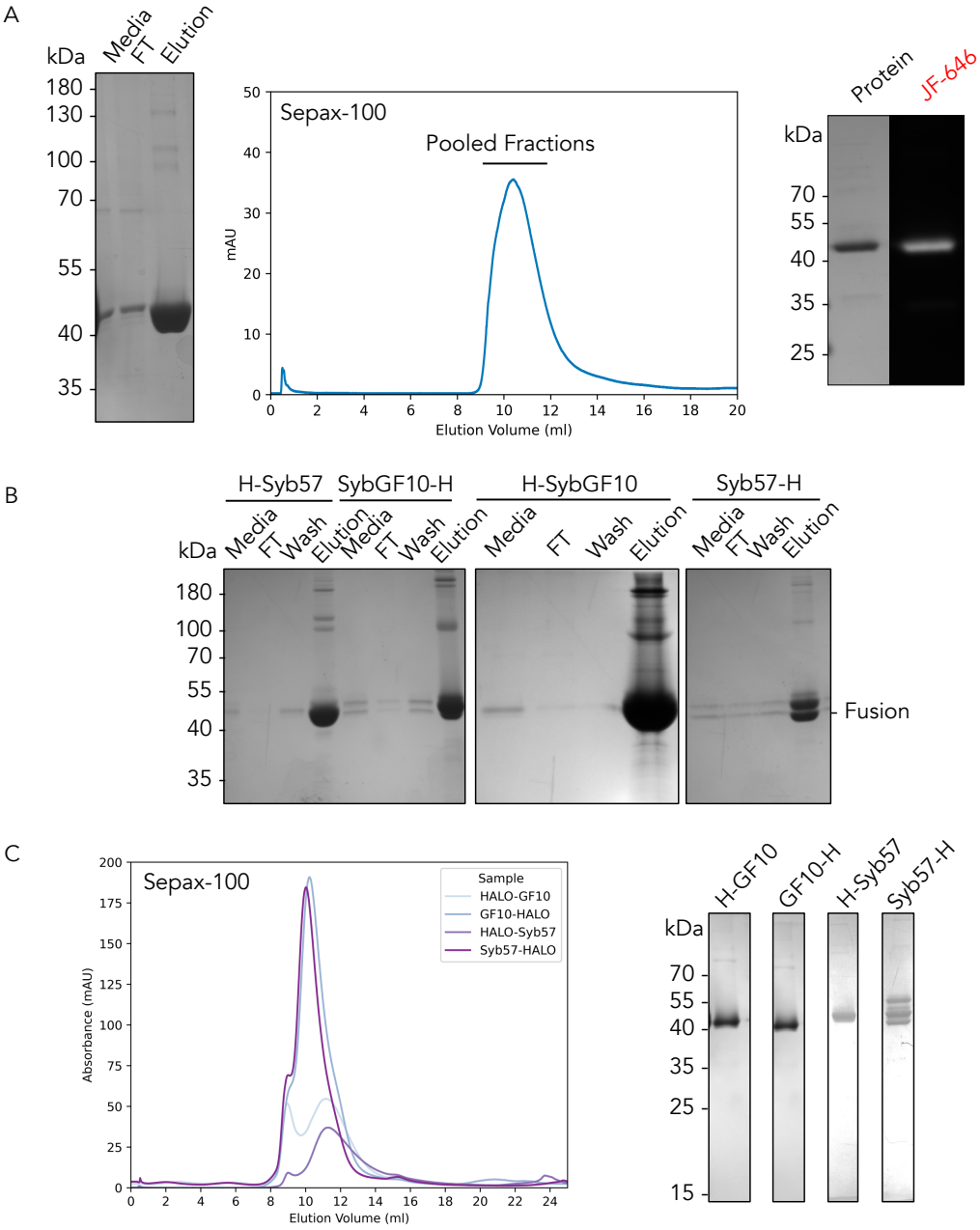

Figure 67: HEK-293 FreeStyle cell (Thermo Fisher Scientist) expression of sybody HaloTag fusions. A) Expression of the Halo-Syb57 fusion in HEK cells, and purification with Ni-NTA and SEC (Sepax SRT SEC-100). Fusions were purified by adding Ni-NTA resin to non-dialyzed media (media sample) (500 ml), the flow-through following the incubation was collected (FT), the resin was washed with TBS + 25 mM Imidazole (Wash), eluted with TBS + 250 mM Imidazole and eluted in a sepax column equilibrated in PBS (pH 7.5). The fusion was successfully labelled based on SDS-PAGE analysis. B) 50 ml expression of multiple fusion constructs (H: Halo) and purification by Ni-NTA on dialyzed media and C) SEC profile and SDS-PAGE analysis of the purified constructs.

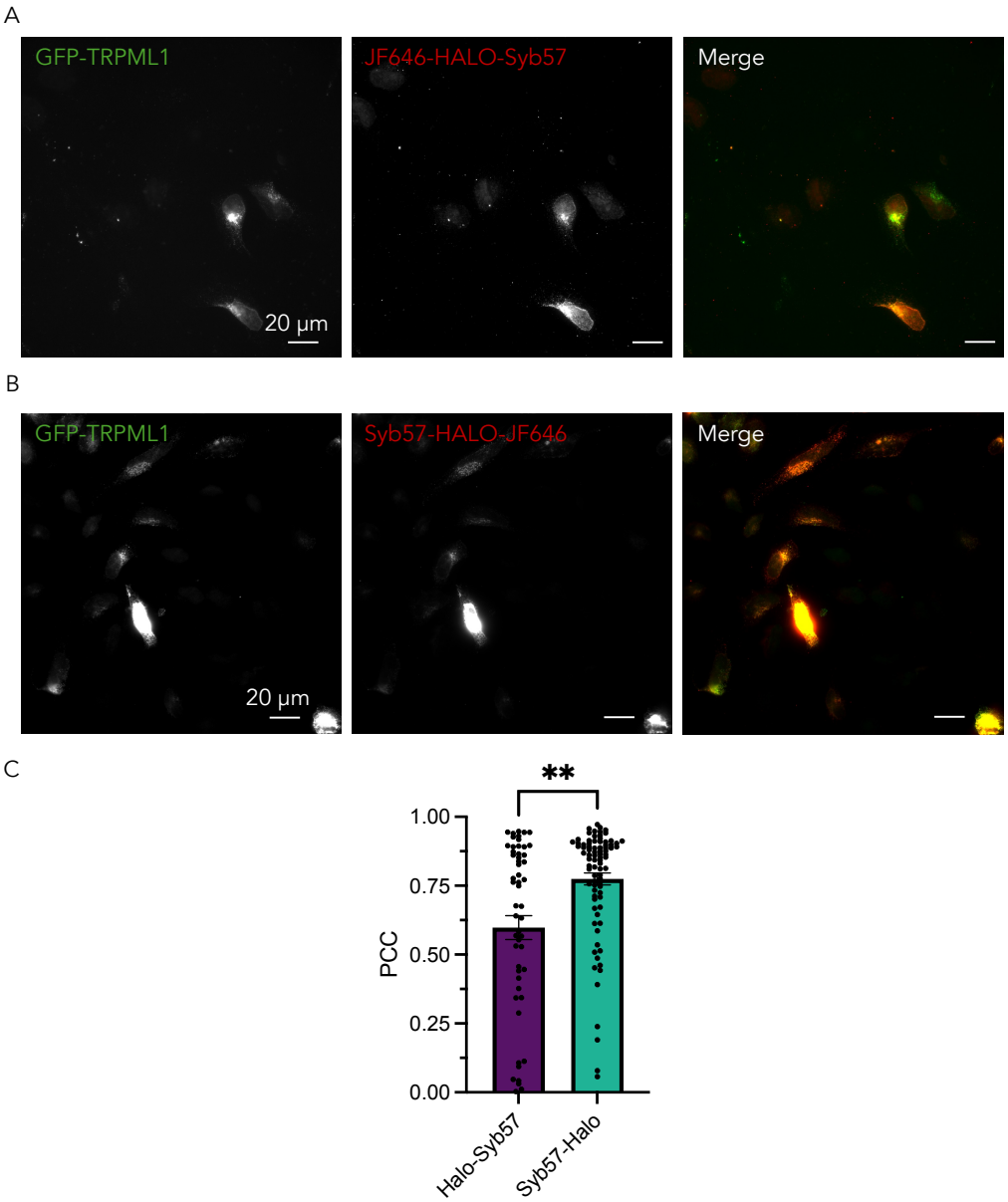

Figure 68: Staining of GFP-TRPML1 transfected fixed HeLa cells with the Syb57 HaloTag fusions. A) Widefield fluorescence microscopy on GFP-TRPML1 transfected cells (green) stained with 4 µM of Halo-Syb57 or B) Syb57-Halo fusion labelled with JF-646. C) Co-localization (Pearson's Correlation Coefficient (PCC)) quantification carried out as described for the confocal high-affinity binder screen between the GFP-TRPML1 channel and JF-646/Cy5 channels. Data points represent PCC values for individual GFP-TRPML1 expressing segmented cells, and error bars represent the standard error of the mean (SEM). Halo-Syb57: n=55, Syb57-Halo: n=84. **: p=0.0015 Mann-Whitney test.

could explain differences in their behaviors. The construct may be phosphorylated, for example in the GS linkers, which could be tested by adding phosphatases (Tyshchuk et al., 2017).

Purified and labeled syb57-Halo fusions were used for IF experiment (Figure 68A-B). GFP-TRPML1 transfected HeLa cells were fixed and permeabilized, stained with the fusions at 4 μM for 2 hours at room temperature, and imaged on a widefield fluorescent microscope. The Syb57-Halo fusion co-localized well with GFP-TRPML1 (0.7745 $\pm$0.02178), while the Halo-Syb57 fusion colocalized more poorly overall (0.5981 $\pm$0.04319) as the fusion was only found to colocalize well in some of the cells (Figure 68A-C). This is expected based on the Syb57-TRPML1 structure as the C-terminal region faces away from the luminal domain, while the N-terminal region faces toward it potentially disrupting sybody binding. These differences could also partly result from post-translational modification of the constructs.

Therefore, I aimed to determine if fusion to the HaloTag affected sybody binding to the target protein. BLI was used to test the K_D of both Syb57 and SybGF10 fusions (Figure 69A and B). Due to the larger sizes of the constructs, the maximal response amplitude was more than doubled for SybGF10 constructs, and 40% greater for Syb57 constructs. The binding of all the HaloTag constructs was significantly weaker. The K_D values of the fusions were found to increase to 860 nM (Halo-Syb57) and 500 nM (Syb57-Halo), relative to 80 nM for Syb57 (Figure 69A). The same observation was made for SybGF10 fusions (SybGF10: 33 nM; Halo-SybGF10: 140 nM; SybGF10-Halo: 110 nM) (Figure 69B). The addition of the tag on the C-terminal end was less disruptive to the binding, as observed in the IF experiments. The HaloTag was designed to be used in the reducing environment of the cytoplasm. Expression in an oxidizing environment can lead to intramolecular disulfide bond formation in the tag, potentially affecting its behavior (Deprey and Kritzer, 2021). The biphasic dissociation curves measured for the different fusions are characteristic of non-specific binding in BLI. The HaloTag may behave poorly when purified and may interact non-specifically with the sybody, disrupting its binding. The HaloTag had been selected to facilitate sybody labeling, but a range of challenges were encountered when adapting it to this application. Therefore, direct labeling was trialed instead to further minimize the linkage error. However, the insights gained from the expression and purification of fusions

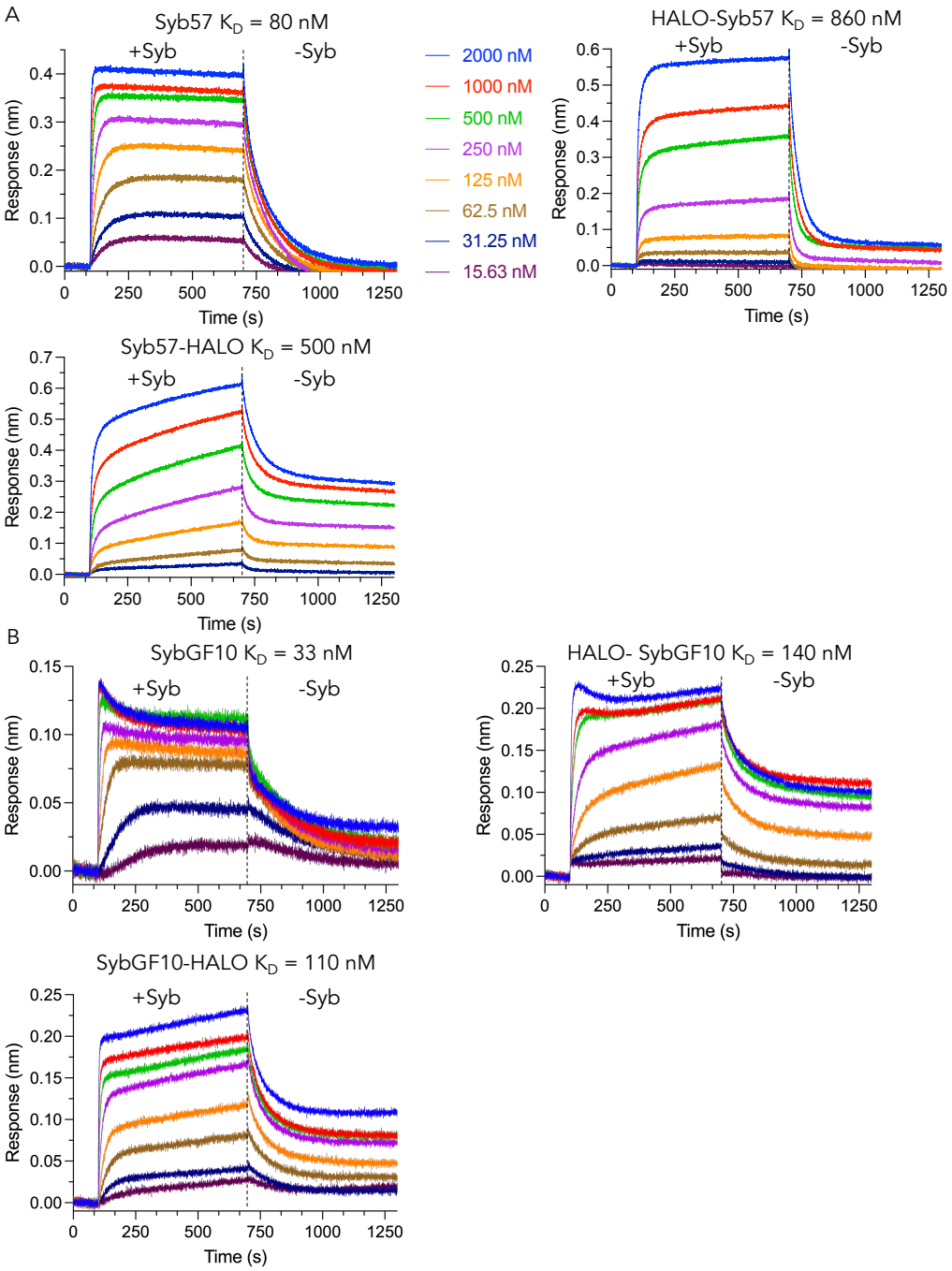

Figure 69: Binding kinetics of TRPML1 and TMEM175 sybody Halotag fusions. A) TRPML1 (Syb57) and B) TMEM175 (SybGF10) sybody HaloTag fusion kinetics. K_D values are displayed above the graphs. Tips were loaded with biotinylated TRPML1 for Syb57 fusions, and with biotinylated TMEM175 for SybGF10 fusions. Protein concentrations are displayed on the 1st graph.

were later applied to generate sybody dimers.

6.3.2 Direct Sybody Labeling

Ligands can be covalently conjugated to substrates through lysine and cysteine residues. Lysine conjugation can be undertaken with ligands containing an N-hydroxysuccinimide (NHS) ester group, while cysteines can react with maleimide-containing substrates (Ries et al., 2012; Pleiner et al., 2015). Lysine conjugation can disrupt sybody binding, especially for binders with lysines in their CDRs (e.g. Syb57) (Pleiner et al., 2015). Cysteine conjugation requires mutagenesis of the sybody to introduce free cysteines for maleimide labeling. These are introduced away from the CDR regions to avoid interference with target binding (Galazzo et al., 2020; Pleiner et al., 2015). The following mutants were trialed on the obtained sybodies: A65C, S75C, S89C, and a C-terminal cysteine insertion (Figure 70A-C) (from: Galazzo et al., 2020; Pleiner et al., 2015). These mutations are mostly located away from the binding and sybody-sybody interfaces for Syb94, except S75C which may clash with the glycan but this is not expected to strongly impair sybody binding (Figure 70B). For Syb57, A65C and the C-terminal insertion are expected to be the least disruptive for sybody binding (Figure 70C).

Syb57 and Syb94 mutants were generated, expressed and purified using the standard sybody purification protocol with periplasmic extraction. Following Ni-NTA elution with 250 mM imidazole, sybodies were incubated for an hour on ice with 0.2 mM DTT, concentrated, and injected on a sepax SEC-100 column. Using this approach, only one mutant was successfully purified, Syb94S75C which has a retention volume (11.4 ml) similar to WT Syb94 (10.8 ml) on the sepax SEC-100 (Figure 71B). Low yields of the other Syb57 and 94 mutants were obtained (1 L culture) (Figure 71A and B). It was noted from the purification of numerous mutants and fusions that the retention volume of the WT sybody is a strong predictor of binder behavior. For example, syb94 WT eluted 6.8 ml earlier than syb57 WT on a sepax SEC-100 and remained stable when mutated.

Syb94S75C was labeled with maleimide alexa-647 fluor C2 maleimide (Invitrogen), testing a range of conditions (Figure 72A-C; supplementary Figure 15A-D). It was found that increas-

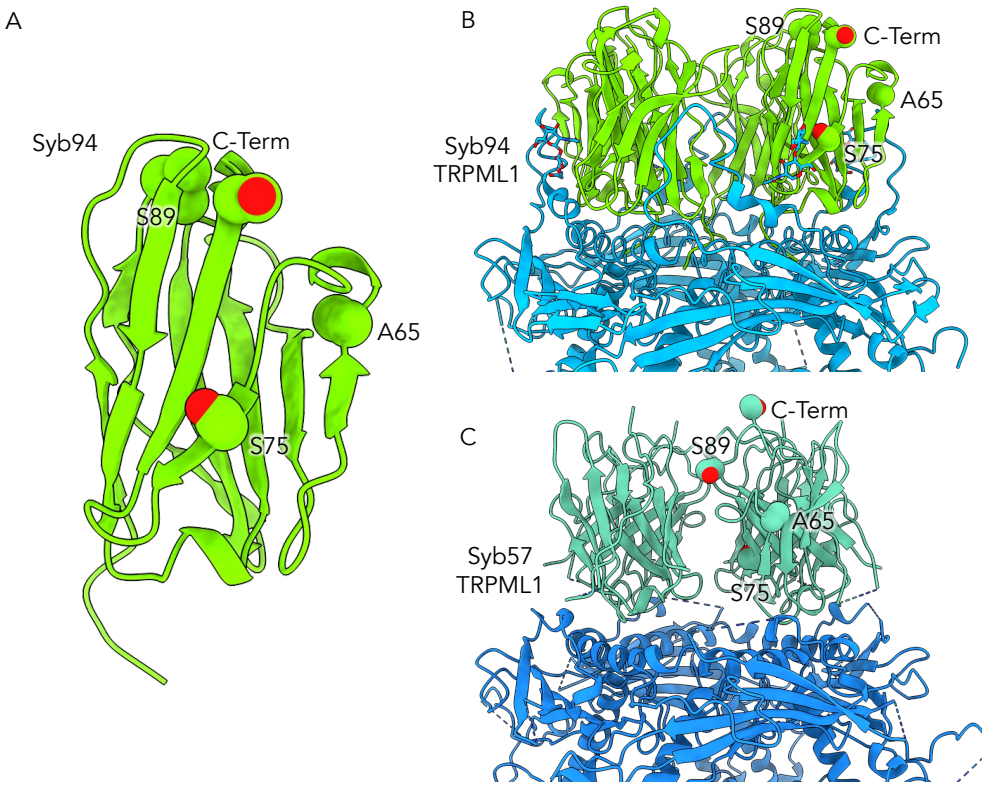

Figure 70: Site of cysteine mutations in Syb94 and Syb57. A) A65, S75, S89 and the C-terminus were mutated with a cysteine residue B) In the Syb94-TRPML1 structure, these residues are not located in the vicinity of another sybody or TRPML1, except S75 that may clash with the glycan. C) In the Syb57-TRPML1 structure, S75 and S89 are located in the vicinity of the neigbouring sybody and may thus disrupt sybody binding, while A65 and the C-terminus are isolated and should not disrupt binding.

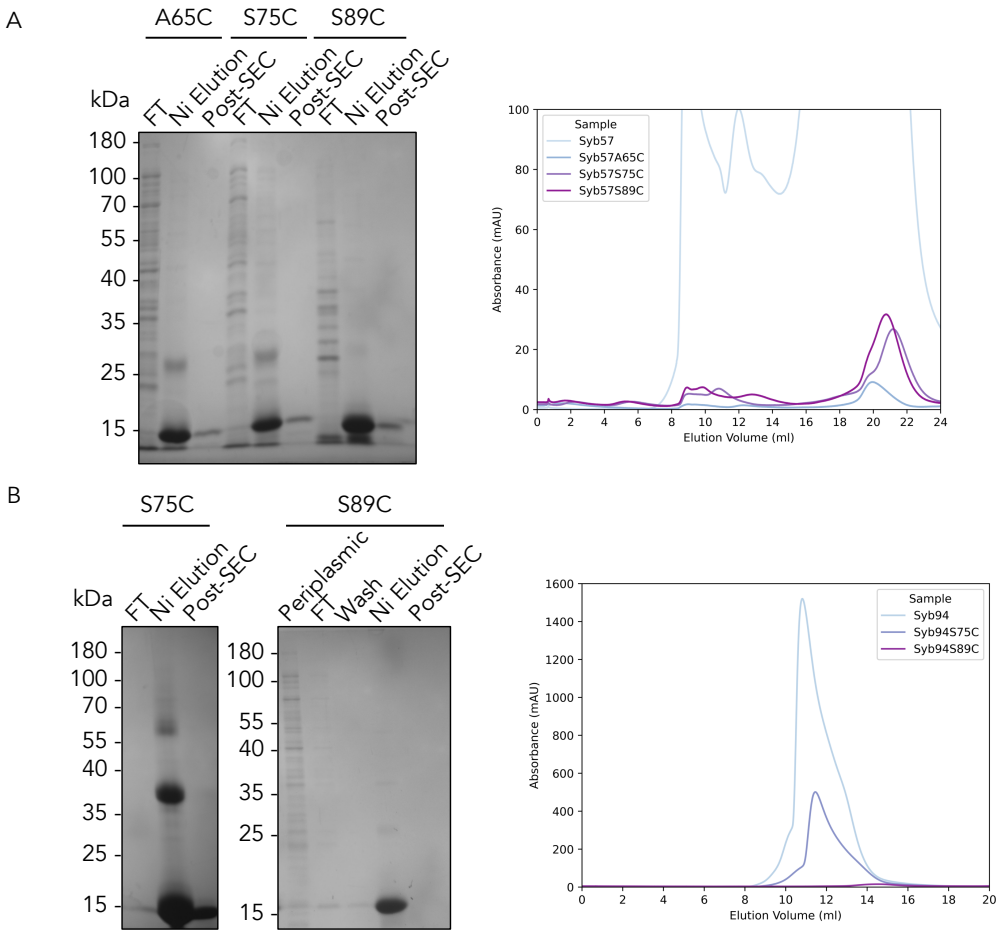

Figure 71: Purification of Syb57 and Syb94 cysteine mutations by periplasmic extraction. A) SDS-PAGE of Ni-NTA purification and SEC profile (Sepax SRT SEC-100) of Syb57 cysteine mutants and B) Syb94 cysteine mutants.

A

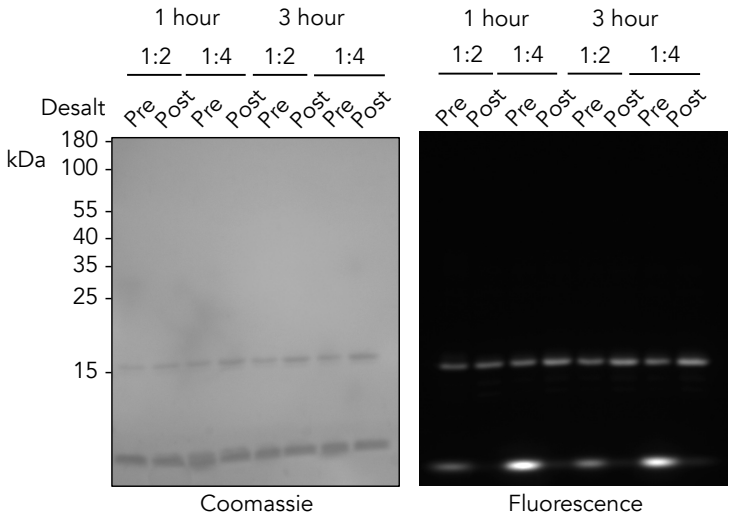

$$\text{Protein Concentration (M)} = \frac{A_{280} - (A_{max} \text{ x CF})}{\varepsilon}$$

$$\text{Moles Dye Per Mole Protein} = \frac{A_{max} \text{ of the Labeled Protein}}{\varepsilon' \text{ x Protein Concentration (M)}} \text{ x Dilution Factor}$$

B

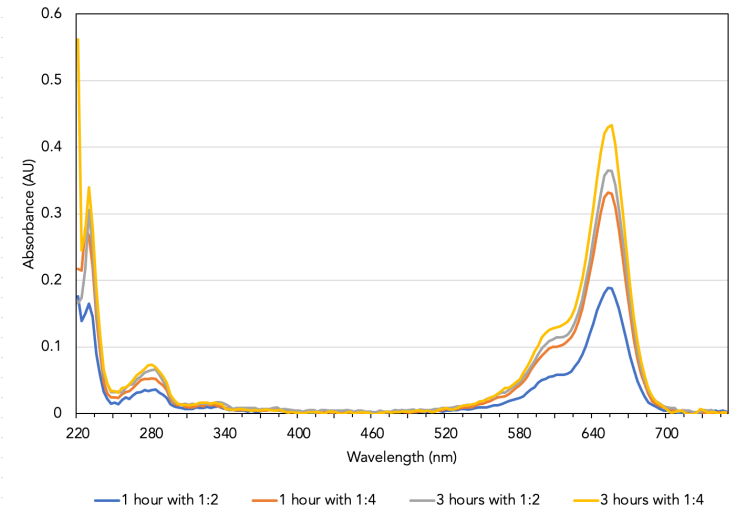

Condition	Ratio: 1:2 1 hour 4°C	Ratio: 1:4 1 hour 4°C	Ratio: 1:2 3 hours 4°C	Ratio: 1:4 3 hours 4°C
Labelling Efficiency (%)	71	84	72	77

Figure 72: Optimization of Syb94S75C labeling conditions with Alexa Fluor-647. A) SDS-PAGE or B) spectrometer analysis of labeling efficiency of Syb94S75C samples labelled with Alexa Fluor-647 under different labeling conditions: ratios (1:2 and 1:4) and incubation times (1 and 3 hours). Panel A includes samples pre and post desalting, and labeling efficiency equations.

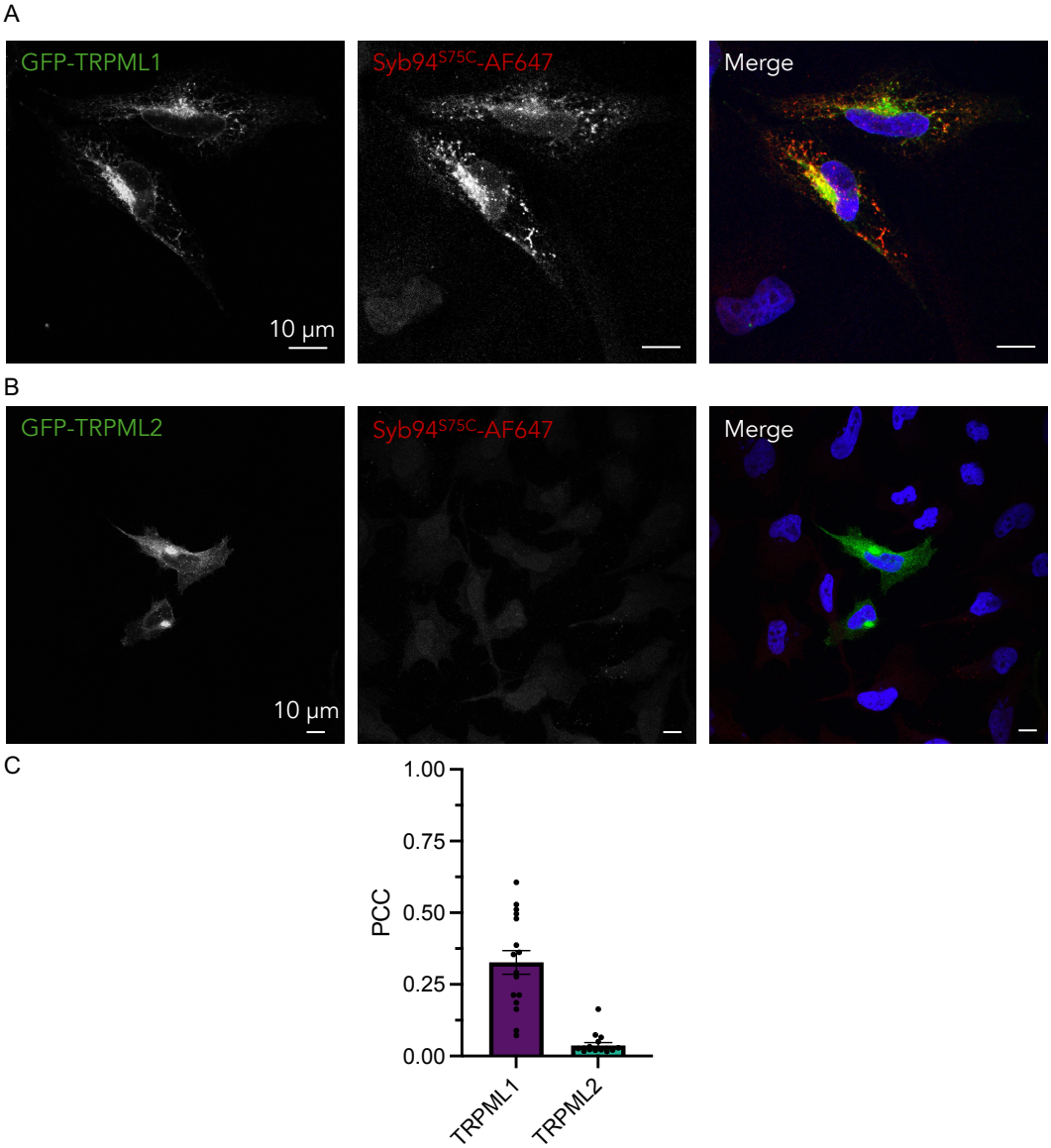

Figure 73: Immunostaining of GFP-TRPML1 and 2 transfected HeLa cells labelled with Syb94S75C-AF647 imaged using a confocal microscope. A) GFP-TRPML1 and B) GFP-TRPML2 transfected HeLa cells were fixed, permeabilized and stained with 1 µM Syb94S75C-AF647. The samples were imaged using a confocal microscope (LSM980). C) Co-localization (PCC) between Syb94S75C-AF647 and GFP-TRPML1 or GFP-TRPML2 as described for previous figures. TRPML1: n=16, TRPML2: n=16. Error bars represent SEM.

ing the ligand excess to a 1:4 molar ratio had the greatest effect on labeling efficiency (84%). Labeling in a 1:4 ratio for 1 hour at 4°C was used for the remainder of the discussed mutants.

Following labeling, Syb94S75C (1 μM) was used to stain GFP-TRPML1 and GFP-TRPML2 transfected HeLa cells for 2 hours at RT (Figure 73A and B). Partial colocalization was observed with GFP-TRPML1 (PCC: 0.3269 $\pm$0.04123) and no colocalization was observed with GFP-TRPML2 (PCC: 0.03750 $\pm$0.009827), demonstrating the TRPML1 specificity of Syb94 and the cysteine mutant (Figure 73A-C). The GFP-TRPML2 sample also shows that significantly less background is observed when using the directly labeled mutant rather than the anti-myc antibody (PCC: 0.2070 $\pm$0.02634). However, co-localization of the mutant was significantly lower than Syb94 WT with the anti-myc antibody (PCC: 0.7359 $\pm$0.02002). Weaker signal results from the lack of signal amplification which occurs when using a secondary antibody, or potentially due to disruption of binding to the target protein (later discussed). In the GFP-TRPML1 sample, strong heterogeneity in labeling efficiency was observed at the cellular level and across the sample (some cells were not labeled). The reasons for this heterogeneity may be related to cell permeabilization variations or to steric clash of the fluorophore with PTMs (variations in the glycosylation or cleavage of the overexpressed protein) or TRPML1 binding partners. Since the labeling of GFP-TRPML1 was partial and signal intensity was weak with Syb94S75C, additional mutants were trialed.

It was previously observed that periplasmic extraction is inefficient for the expression and purification of cysteine mutants as they may aggregate within the crowded environment of the periplasm (Pleiner et al., 2015). This was confirmed by the observation that cells were lysed following overnight expression of the mutants. Therefore, cysteine mutants have previously been expressed in the cytosol (Pleiner et al., 2015). Expression of Syb57A65C was optimized by trialing expression (50 ml culture) at different ODs and different temperatures (22 and 37°C) (Figure 74A). In this expression trial, cells were lysed by a freeze-thaw cycle, the supernatant was separated from cellular debris by low-speed centrifugation and incubated with Ni-NTA resin (see Methods section). The protein was eluted with imidazole, and run on a gel to compare yields. The highest yield was obtained at OD 1.19 (Figure 74A). Therefore, expression of the different

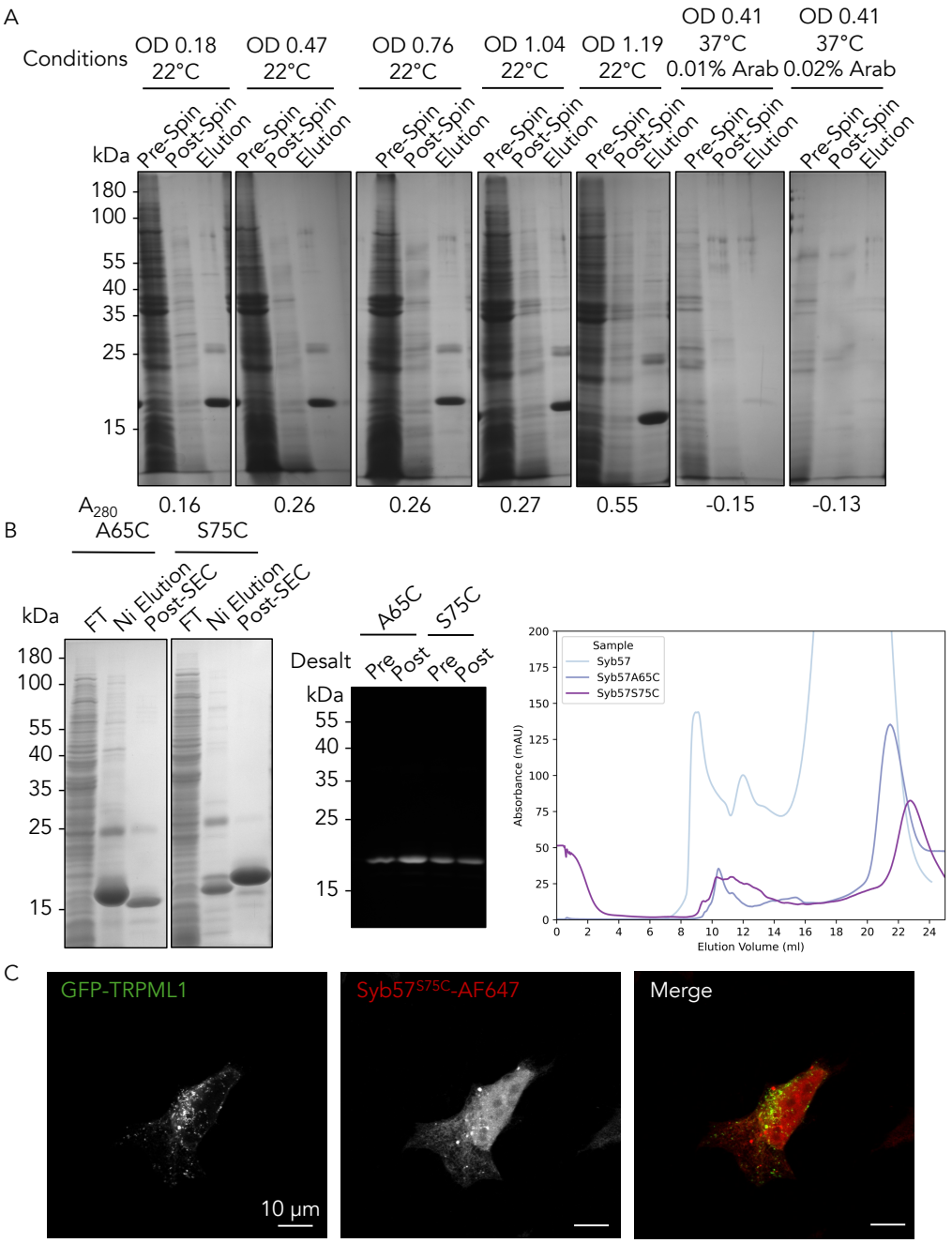

Figure 74: Optimization of Syb57 cysteine mutant expression and purification. A) Syb57A65C expression trials (50 ml culture) in bacteria with induction and expression at different ODs (22°C) and at different temperatures (37°C), and small-scale Ni-NTA purifications. B) Purification and labeling of Syb57A65C and S75C mutants as previously described (Sepax SRT SEC-100). C) Staining on GFP-TRPML1 transfected HeLa fixed cells with Syb57S75C-AF647, and imaged using a confocal microscope (LSM-980).

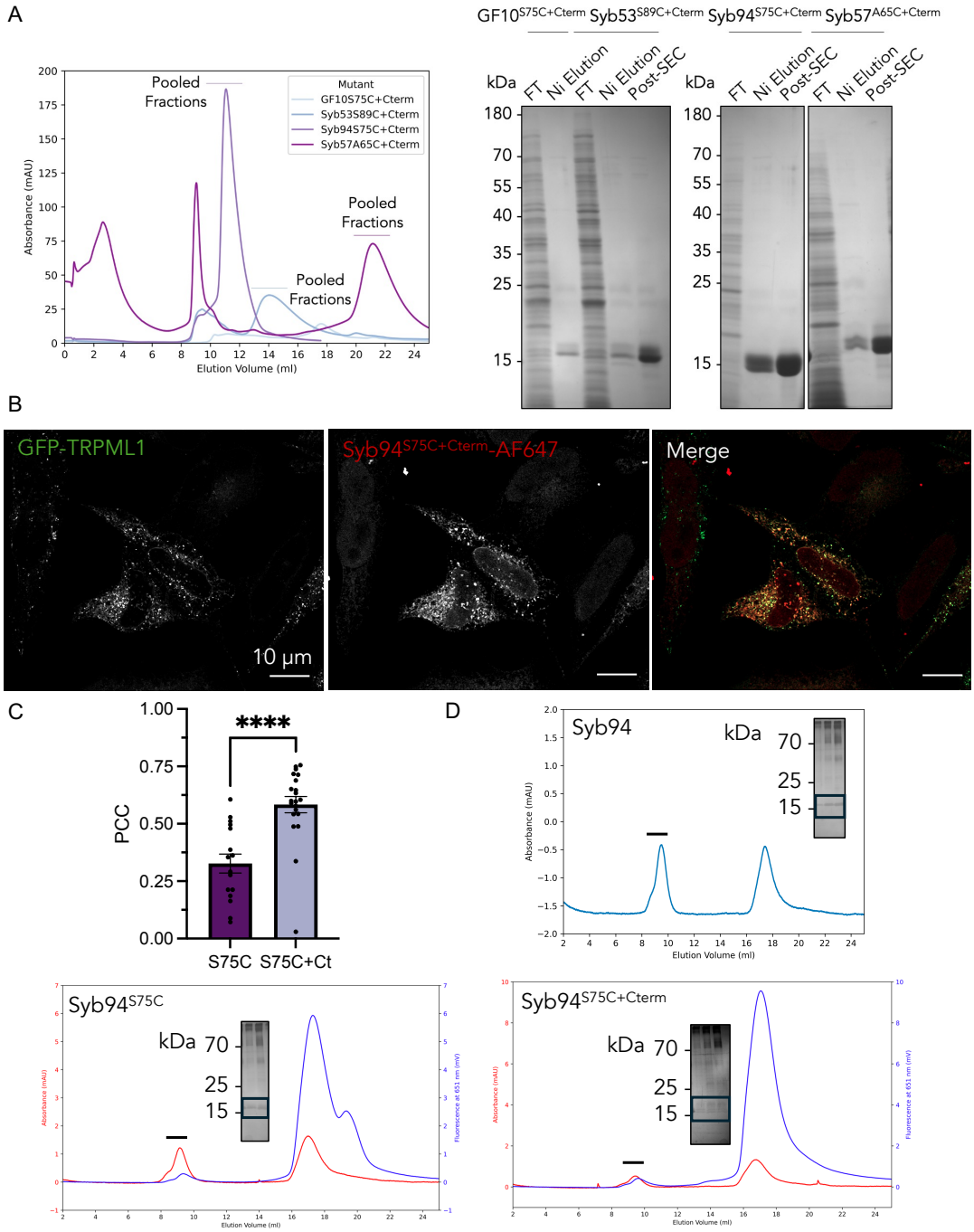

Figure 75: Purifications of sybody cysteine double mutants, staining with the Syb94 double mutant and analysis of binding by co-elutions. A) Ni-NTA and SEC (Sepax SRT SEC-100) purifications of sybody double mutants (mutation A + C-terminal insertion of cysteine). B) Imaging and C) co-localization (PCC) between Syb94 mutants and GFP-TRPML1 in transfected fixed HeLa cells. Syb94S75C: n=16, Syb94S75C+Cterm: n=21. ±SEM. ****: p<0.0001 Mann–Whitney test. D) Co-elution of TRPML1 with Syb94 and mutants loaded on a S200 Increase column connected to UV (left axis) and fluorescence detectors (right axis). Fractions (line) loaded on displayed gel.

mutants was repeated at this OD and using this protocol (freeze-thaw lysis). Yields of folded protein were significantly increased, and protein was obtained post-SEC (Figure 74B). The Syb57 mutants eluted later (Syb57: 17.6 ml; A65C: 21.4 ml and S75C: 22.7 ml) than WT Syb57, suggesting that the mutation impacts their physicochemical properties (Figure 74B). This protocol was also used to successfully purify a set of double mutants (Mutant X + C-Term cysteine insertion) of TRPML1 and TMEM175 sybodies with the aim of enhancing labeling efficiency and signal intensity in IF (Figure 75A). Labeling efficiency was doubled for the Syb94 double mutant (Table 4).

These mutants were tested on GFP-TRPML1 transfected cells to determine if they showed improved colocalization and signal. It was found that syb57 mutants did not colocalize well with GFP-TRPML1 and strong nuclear staining was observed, suggesting that it binds non-specifically (Figure 74C). The Syb94S75C+C-Term mutant was also tested to determine whether double labeling would improve colocalization in IF. The double mutant (PCC: 0.5835 $\pm$0.03545) showed significantly improved co-localization (Mann-Whitney test: $p<0.0001$) relative to the single mutant (PCC: 0.3269 $\pm$0.04123) (Figure 75B and C). As observed with the single mutant, double mutants were found to only label some of the cells and certain lysosomes within these cells. To better understand the cause of this partial labeling, the effects of the mutations on TRPML1 binding were tested by co-elution. Co-elution experiments were carried out by incubating 20 μg of syb (8-fold excess) with 10 μg of TRPML1 for 1 hour on ice, followed by injection on an S200 column connected to UV and fluorescence (651 nm) detectors. It was found that all three constructs of syb94 (WT, S75C and S75C+CTerm) co-eluted with TRPML1 based on the silver stain and the FSEC (Figure 75D). Therefore, partial co-localization may be due to steric clashing in cells upon the addition of the fluorophore, reduced sybody stability as fluorophores can display unfavourable behaviors when undergoing freeze-thaw cycles and reduced signal amplification as antibodies are not used in these experiments.

The information obtained from these studies was applied to directly conjugate the cytosolic binder to fluorophores and gold for lysosome labeling.

6.3.3 Cryo-Correlative Light-Electron Microscopy (CLEM)

A key long-term challenge for structural biology is to solve the structure of proteins in their native environment. This cannot be achieved for most proteins as their location in the crowded environment of the cell cannot be accurately determined (Rice et al., 2023). Binders can be used as fiducial markers to localize the protein of interest at the lysosomal membrane.

Syb53 mutants, syb53S75C and syb53S89C, were successfully expressed, purified (freeze-thaw, Ni-NTA and SEC), and labeled (Figure 76A). WT and mutant sybody binding was tested by co-elution and IF. WT and both mutant sybodies co-eluted with TRPML1, and syb53S75C conjugated to alexa-647 fluor was found to colocalize with TRPML1-mNeonGreen(mNG)-1D4 in overexpressing HEK-293 cells (Figure 76B and Figure 77A). Bridget McVeigh (Moiseenkova-Bell lab) used the lyso-immunoprecipitation protocol with 1D4 antibody resin to isolate lysosomes from HEK-293 cells overexpressing TRPML1-mNG-1D4 (Figure 77B) (Abu-Remaileh et al., 2017). The purified lysosomes were added to grids and plunge frozen using a vitrobot. The grids were visualized on a cryo-confocal (LSM-900) to determine if the TRPML1-mNG signal colocalized with the Syb53S75C signal (cryo-CLEM). Perfect colocalization was observed between the mNG and alexa-fluor 647 channels, suggesting that the sybody can successfully label the TRPML1 in lysosomes (Figure 77C). To use the cytosolic binder for EM, the sybody was conjugated to 10 nm gold (20 OD) (Abcam) as per manufacturer instructions. Binding of the gold-labeled sybody was tested by negative-staining (experiment carried out by Dr. Ruth Pumroy). Gold particles, each containing multiple copies of the sybody, were consistently observed to be surrounded by multiple TRPML1 molecules (Figure 77D). The gold-labelled sybody was then added to a TRPML1-1D4 lyso-IP preparation (Prerana Gogoi). In this experiment, the gold was found to be too sparse (Figure 77E). In the future, a range of dilutions will need to be tested.

See Table 4 for summary of mutant results.

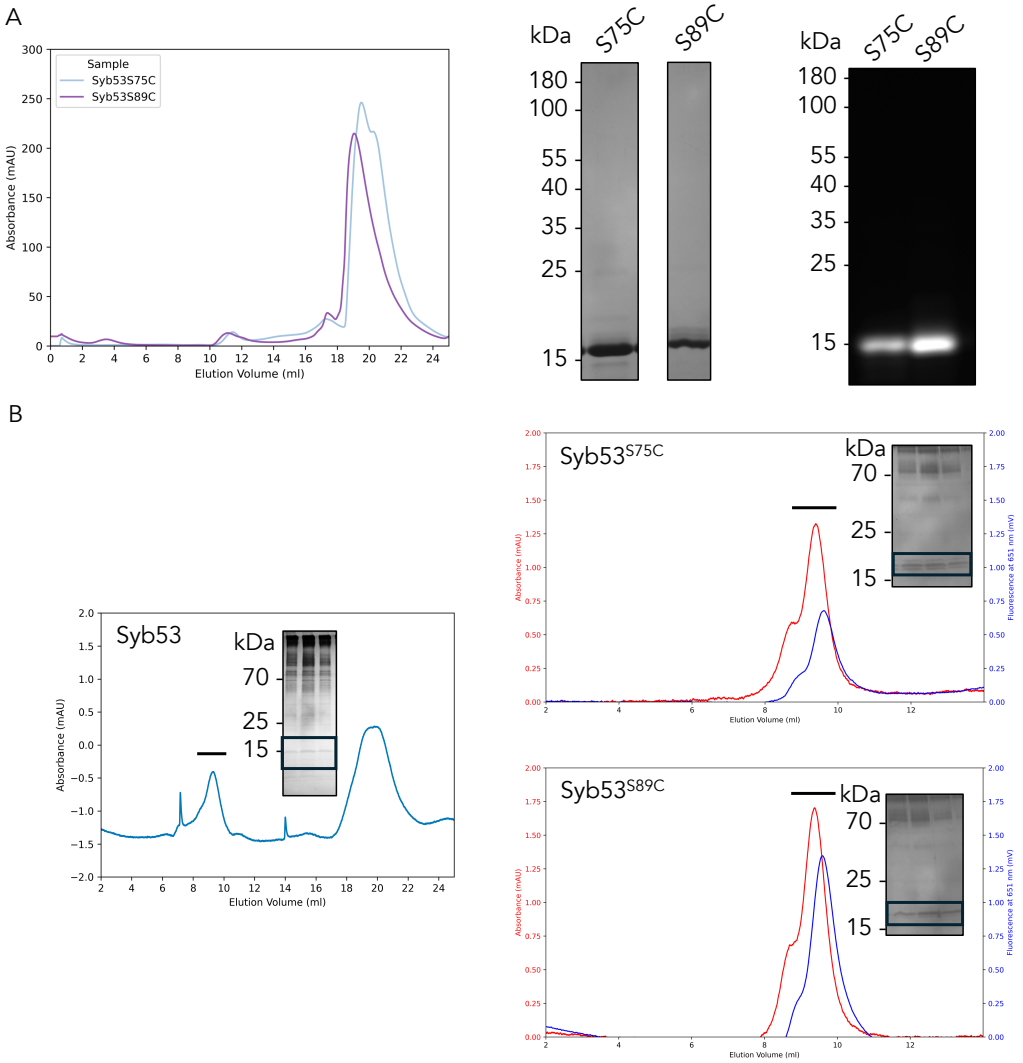

Figure 76: Purification and co-elution of Syb53 cysteine mutants. A) Purification of Syb53S75C and Syb53S89C mutants by Ni-NTA and SEC. Mutants labelled with Alexa Fluor-647 were loaded on a 15% polyacrylamide gel to determine labeling efficiency. B) Co-elution of TRPML1 with Syb53, Syb53S75C and Syb53S89C mutants loaded on a S200 Increase column connected to UV (left axis) and fluorescence detectors (right axis). Fractions (line) loaded on displayed gel. Both mutants co-elute with TRPML1.

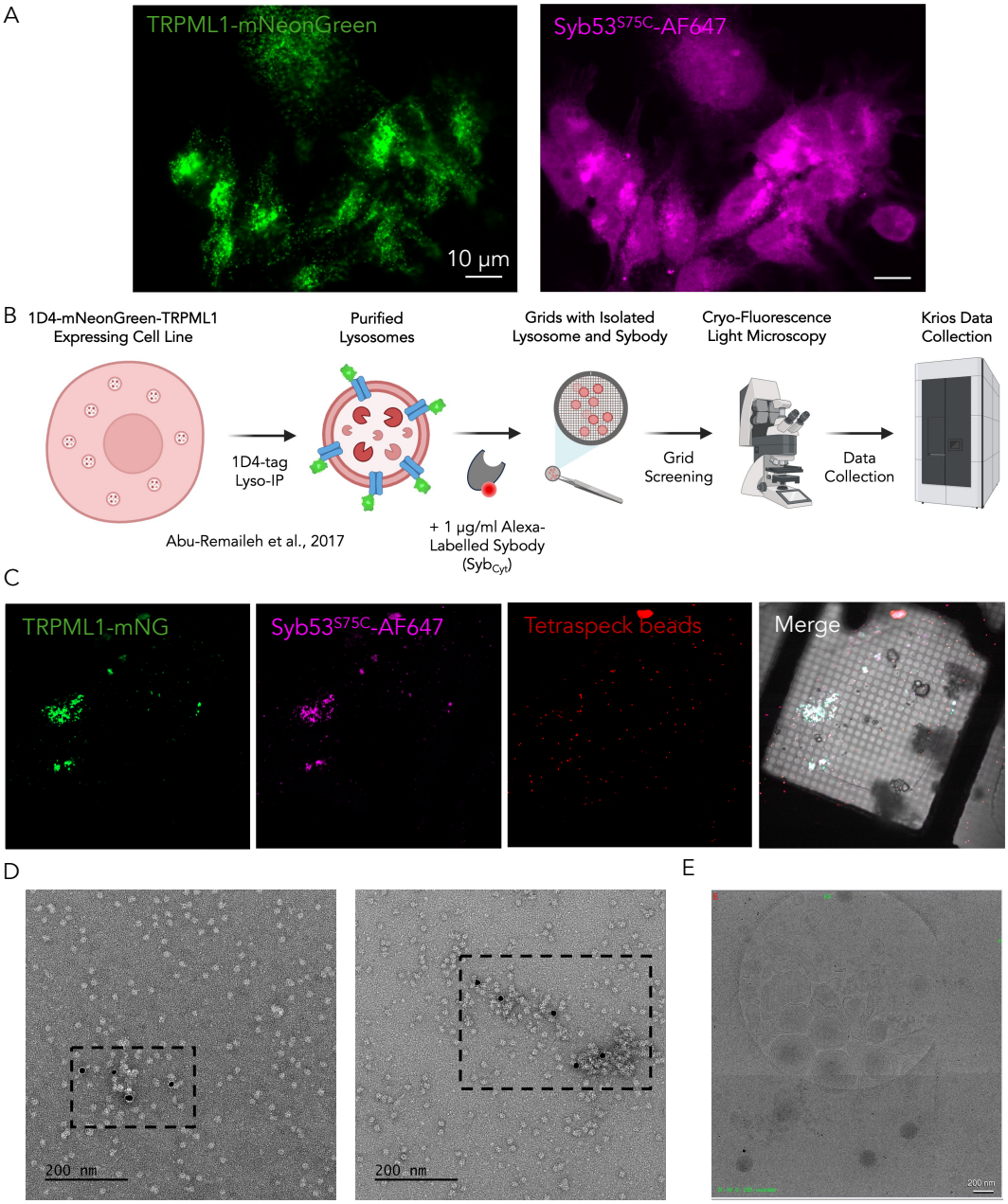

Figure 77: Immunofluorescence, cryo-confocal and negative-staining analysis of Syb53 mutants. A) Imaging of fixed and permeabilized TRPML1-mNeonGreen-1D4-expressing HEK-293 cells (green channel) stained with Syb53S75C-AF647 (magenta channel). B) Protocol for the isolation of lysosomes from HEK-293 cells expressing TRPML1-mNeonGreen-1D4 by lyso-immunoprecipitation, and cryo-confocal analysis of sample. C) Cryo-confocal imaging (LSM-900 Zeiss) of TRPML1-mNeonGreen (mNG) containing lysosomes labelled with Syb53S75C-AF647. D) Negative stain with purified TRPML1 and E) lysosomes from lyso-IP (Panel B) labelled with gold-labeled Syb53S75C. Tetraspeck beads were added for channel alignment. IF and cryo-confocal data obtained by Bridget McVeigh, negative stain data obtained by Dr. Ruth Pumroy and Lyso-IP data obtained by Dr. Prerana Gogoi.

Tube Name	Expected Binding Region	Labelling Efficiency	Validation
Syb57A65C	Luminal	88 %	Co-elutes; Poor colocalization in IF
Syb57S75C	Luminal	113 %**	Poor colocalization in IF
Syb53S75C	Cytosolic	62 %	Co-elutes; Colocalizes in IF and with isolated lysosomes
Syb53S89C	Cytosolic	98 %	Co-elutes; Colocalizes in IF and with isolated lysosomes
Syb94S75C	Luminal	79 %	Co-elutes; Colocalizes in IF
Syb94S75C + Cterm	Luminal	208 %**	Co-elutes; Colocalizes in IF

Table 4: Summary of TRPML1 Sybody mutant results. **Lower labeling efficiency accuracy due to low sample concentration.

6.4 Super-Resolution Imaging with TRPML1 Sybodies

6.4.1 Sybody Lysosomal Imaging Protocol for Super-Resolution Microscopy

As hitherto discussed, TRPML1 sybodies were shown to be able to bind to TRPML1 in cells in immunofluorescence experiments using widefield and confocal microscopy. However, these techniques have a limited resolution (diffraction-limited) and their applications to quantitative studies is limited. Using a high-resolution technique for the study of lysosomes is important because they are small organelles potentially in close spatial proximity (Bond et al., 2024). Moreover, numerous lysosomal membrane proteins, including TRPML1, are weakly expressed, and thus a sensitive technique is required to map their localization (Akter et al., 2023). Super-resolution experiments have previously been carried out on ion channels, for example, to determine their organization at synapses (Heck et al., 2019; Liu et al., 2020; Schneider et al., 2015). I set out to investigate the localization of TRPML1 localization using super-resolution methods

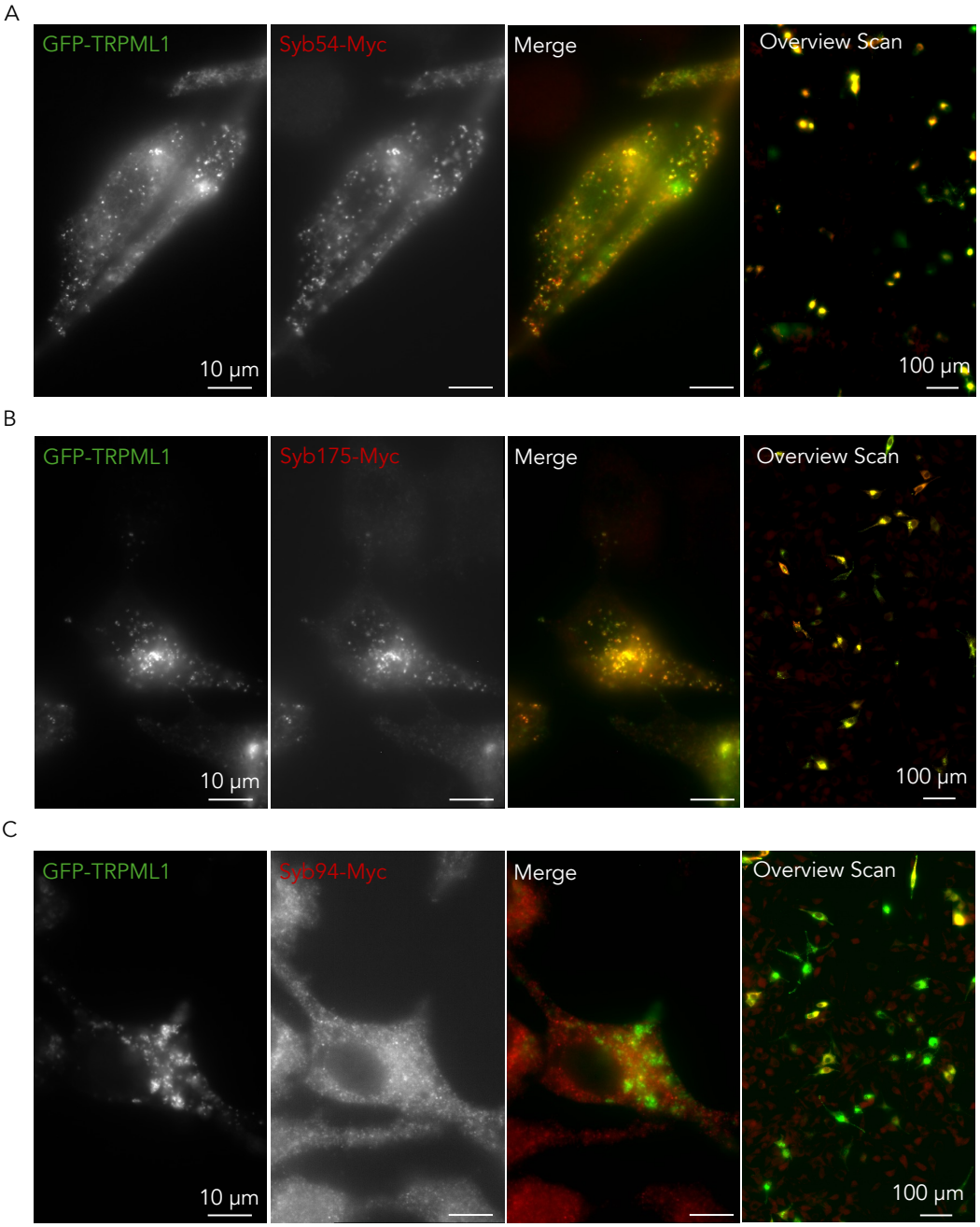

Figure 78: Immunostaining with with super-resolution protocol using sybody-Myc constructs in fixed GFP-TRPML1 transfected HeLa cells. A) Conventional image of fixed GFP-TRPML1 (green) transfected HeLa cell stained with anti-Myc primary antibody, secondary antibody conjugated to Alexa Fluor-647 and Syb54-Myc, B) Syb175-Myc or C) Syb94-Myc (red). 10x10 frames overview scans are displayed to the right of the conventional image with merged GFP and Alexa Fluor-647 channels.

and sybodies.

Super-resolution microscopy staining protocols require more stringent staining and washing conditions. Preliminary experiments were carried out with the protocol described by Bond et al (2024) to determine if sybody binding could withstand these stringent conditions. It was observed in these preliminary experiments that the sybody was potentially washed out if left in imaging buffer (Mass Photonics) for prolonged periods during imaging. To minimize sybody dissociation, an additional fixation step was added after primary antibody staining (4% PFA for 10 min at RT). To maximize labeling, sybody and antibody staining steps were carried out sequentially with three washes with 2 min incubations in between (PBS with 0.01% saponin). The sybodies were tested for colocalization with overexpressed GFP-TRPML1 in HeLa cells using the anti-myc antibody and donkey anti-mouse secondary antibody conjugated to alexa 647 (Invitrogen). Overview scans of the chambers were collected using an ONI microscope (supplementary Figure 16A-F). Syb54 and Syb175 were observed to strongly colocalize with GFP-TRPML1, while the other sybodies that colocalized in the other assays were found to colocalized poorly (note overview scan intensity values cannot be quantified) (Figure 78A-C; supplementary Figure 16A-F). This is likely due to more stringent staining (PBS with 0.1% saponin and 10% donkey serum compared to PBS with 1% BSA) and washing conditions (PBS with 0.01%-0.1% saponin compared to PBS), and changes in the detergent (Triton-X100 and saponin). In this assay, it was found that the high-affinity binder (Syb54) showed the strongest co-localization (Figure 78A). Despite the strong co-localization of GFP-TRPML1 with Syb54, labeling of GFP-TRPML1-containing lysosomes was still partial, and some cells in the overview scan (weakly expressing) were found not to be labeled (Figure 78A). It was hypothesized that nearly complete labeling could be achieved by increasing sybody affinity as dissociation was observed for all the sybodies in non-stringent conditions (TBS + 0.003% LMNG) in the BLI experiments in 10 minutes, which would reduce labeling efficiency significantly across the course of an IF experiment.

6.4.2 Generation and Characterization of TRPML1 Super-Binders

Using the epitope mapping and structural data (cryo-EM and AlphaFold), dimers of the luminal binders were generated to obtain 'super-binders' to achieve complete labeling of GFP-TRPML1 in cells with the stringent super-resolution protocol (Figure 79A). Another advantage of multivalent binders is that they can bind to a larger population of the target protein if specific epitopes are modified in subpopulations. Nanobodies have previously been linked using GS linkers to obtain multivalent high-affinity binders (Schoof et al., 2020). All dimers were linked through a (5xGGGGS linker) based on the max distance between the N and C-terminus of Syb57 and 94 (Distance: 58 Å) (Figure 79A). A 8xHis-tag was added for purification and a high-affinity 1D4 tag, which is derived from rhodopsin, was added to the C-terminal end of the construct for immunoprecipitation and immunofluorescence experiments (Molday and Molday, 2014). The 1D4-tag was used rather than the myc-tag due to the availability of the resin and antibody in the Moiseenkova-Bell lab, and the high affinity and specificity of this tag.

Previous attempts to express sybody dimers in *E. coli* were unsuccessful. This matched the observation that was made when attempting bimodal/fusion protein expression with the HaloTag. Therefore, the same approach was adopted and the dimers were cloned in pcDNA with a signal peptide, expressed and secreted from HEK-293 cells. Initial, expression trials were carried out to determine an optimal expression time, and to determine which dimer combination could successfully be expressed (Figure 79B-C). Small-scale Ni-NTA purifications (1 ml) were carried out on samples collected at 27, 48 and 74 hours post-transfection. It was found that the expression of the construct (Syb94-57) was only observed after 48 hours, and that increasing the expression time increased expression without causing cleavage of the GS linker (Figure 79B). Small-scale purifications (20 ml) were also carried out on six different dimer combinations (Figure 79C). All combinations were purified successfully using Ni-NTA and the samples were dialyzed in HBS (pH 8.0). A double band is obtained from boiled and reduced samples (β-mercaptoethanol) when purifying the dimers in HEK cells, suggesting that they are post-translationally modified like the HaloTag fusions.

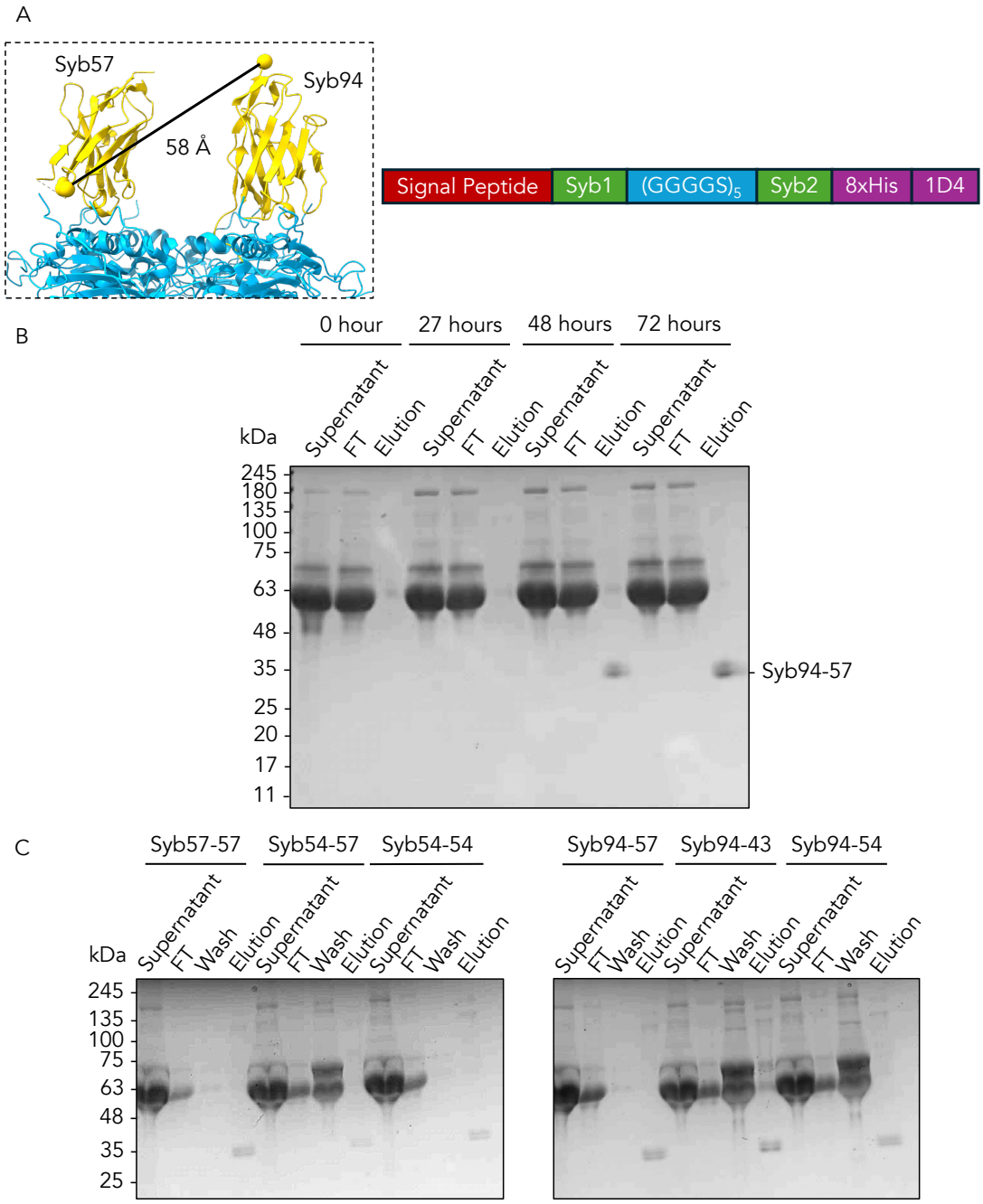

Figure 79: Design and purification of sybody dimers. A) Design of Syb94-Syb57 dimer based on Syb94-TRPML1 and Syb57-TRPML1 structure distance measurement between N and C-terminal ends. The final construct includes a signal peptide for the secretion of the dimer in mammalian culture media, the first sybody, a 5xGGGGS linker, the second sybody, a 8xHis tag for purification and a 1D4 tag for IF and IP experiments. B) Small-scale (1 ml of media) Ni-NTA purification of the Syb94-Syb57 construct at different expression time points in HEK-293 cells. C) Small-scale Ni-NTA purification (20 ml of media) of different combinations of sybody dimers. All dimers were successfully purified. Samples were dialysed in TBS following purification.

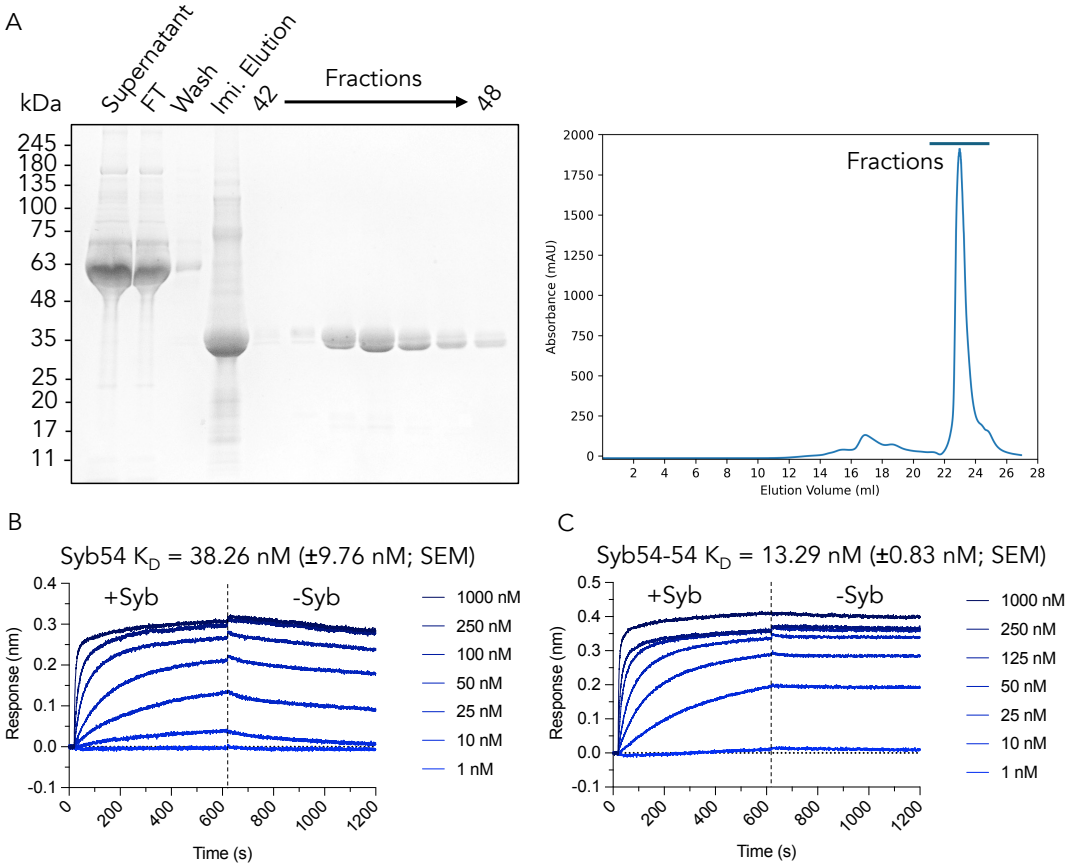

Figure 80: Purification and kinetic analysis of Syb54-54 construct using BLI. A) Large-scale purification (800 ml media) of Syb54-54 fusion by Ni-NTA and SEC (Superose 6) with the polyacrylamide gel (4-20% gradient) of the purification, including SEC fractions, displayed on the left and the SEC profile displayed on the right. B) Binding kinetics (BLI) of Syb54 and C) Syb54-54 with immobilized full-length biotinylated TRPML1 in TBS + 0.003% LMNG. K_D values obtained from response at equilibrium (590s-595s) as described in previous sections. Syb54: n=4 and Syb54-54: n=3. SEM: Standard Error of the Mean

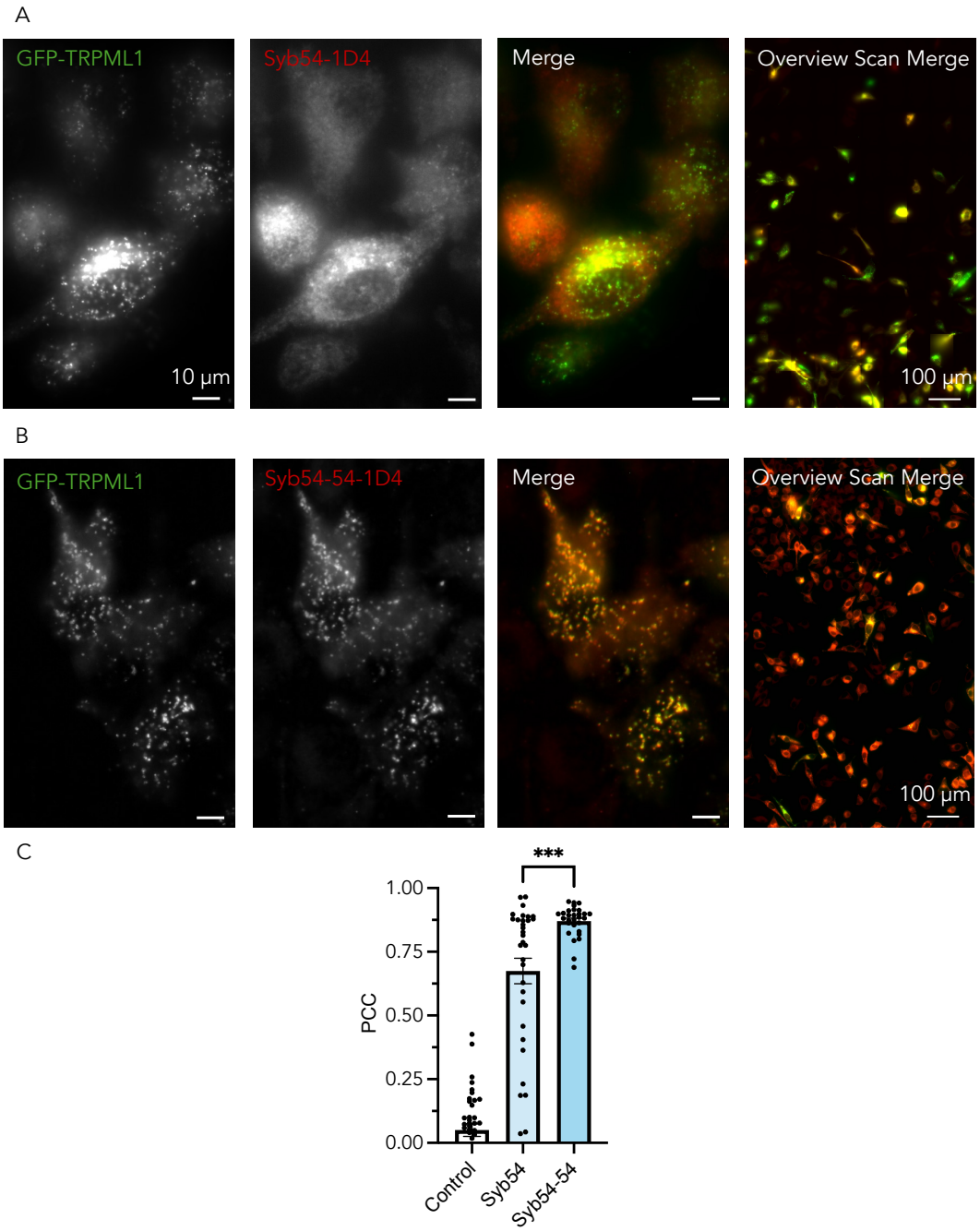

Figure 81: Comparison of labeling efficiency of Syb54-1D4 and Syb54-54-1D4 constructs in GFP-TRPML1 transfected HeLa cells. A) Conventional imaging and overview scan in GFP-TRPML1 transfected fixed and permeabilized HeLa cells stained with Alexa Fluor-647-conjugated anti-1D4 antibody and Syb54-1D4 or B) Syb54-54-1D4. C) Quantification of co-localization (PCC) between GFP-TRPML1 and sybody (anti-1D4 antibody) signal. Error bars are SEM. Control: n=41, Syb54: n=32, Syb54-54=29. ***: p=0.0007 Mann-Whitney test.

Syb94-57, 94-43 and 54-54 were used for BLI and IF experiments as sufficient concentrations were obtained for these experiments. It was found that Syb94-57 (2.1-fold increase) and Syb54-54 (2.8-fold increase) had a significantly higher affinity than the monomeric construct (Figure 80B and C; supplementary Figure 17A and C). In the future, shorter linkers may be trialed to increase the affinity further. Syb54-54 was found to display no dissociation in the BLI experiment, demonstrating its very tight binding to TRPML1. IF experiments showed that Syb54-54 colocalized nearly fully with GFP-TRPML1, while the other dimeric constructs did not (Figure 81B; supplementary Figure 17B and D). Syb54-54-1D4 (PCC: 0.8704 $\pm$0.01130) was found to have significantly (Mann-Whitney test: p=0.0007) improved co-localization relative to Syb54-1D4 (PCC: 0.6746 $\pm$0.05004) (Figure 81 C). Syb54-54-1D4 essentially labels all the cells in the overview scans (Figure 81B). As was observed in other co-localization experiments, there are two populations for Syb54 in the PCC bar chart: a highly co-localizing population and a population with poorer co-localization (Figure 81C). This likely represents cells with different GFP-TRPML1 expression levels (high co-localizing with high expression). Only a single population is observed for Syb54-54 as all cells are stained (Figure 81C). Note that these experiments were carried out with Alexa-647-conjugated 1D4 antibody, bypassing the need to use a secondary antibody and reducing the linkage error, and the samples were not primary-fixed as both binders have a high affinity for TRPML1. It was observed that Syb54-1D4 staining was poorer than Syb54-Myc staining, but the 1D4 tag system was used regardless due to the availability of the reagents and because it was successful with the dimer. These results showed that Syb54-54 was the best candidate for super-resolution imaging of TRPML1, and it was thus expressed and purified on a large scale (800 ml) for further experiments (Figure 80A).

6.4.3 STORM Imaging

A range of super-resolution methods have been developed, including Structured Illumination Microscopy (SIM), Photo-Activated Localization Microscopy (PALM), Stochastic Optical Reconstruction Microscopy (STORM) and Stimulated Emission Depletion (STED). STORM was used for this project because: (1) it provides high-resolution localization data, (2) the chosen

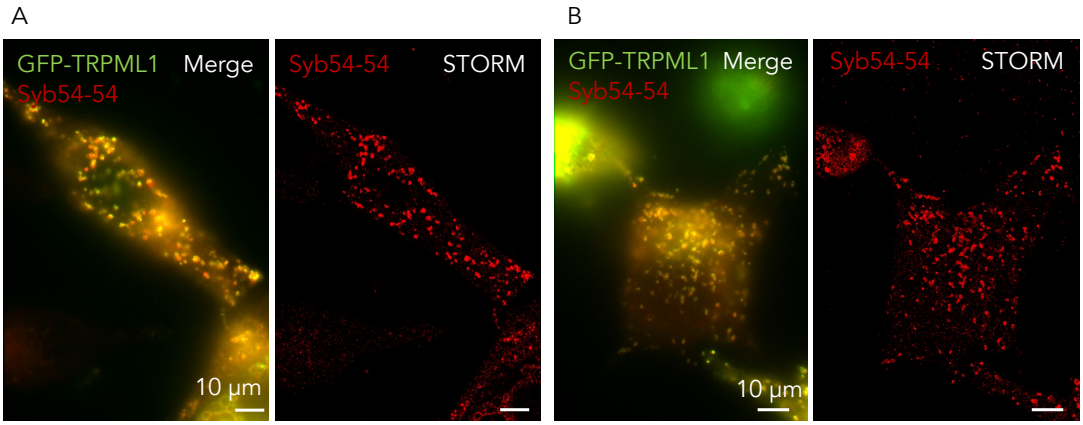

Figure 82: STORM imaging with Syb54-54-1D4 in GFP-TRPML1 transfected HeLa cells. A-B) Conventional merged images in HeLa transfected cells of GFP-TRPML1 signal (green) and Syb54-54-1D4 stained with anti-1D4 antibody conjugated to Alexa-647 (red) (left image), and STORM image of the Syb54-54 signal in the same cell (right image).

setup was compatible with this method (Alexa Fluor-647 is STORM compatible), and (3) because it is quicker than other techniques. In STORM experiments, the activated state of individual photoswitchable fluorophores emits photons. Blinking of the fluorophores, before they are bleached or transition to a dark state, enables precise determination of their location (20-30 nm resolution) past the Abbe diffraction limit (Rust et al., 2006).

Cells were prepared as described above. Cells with very low GFP-TRPML1 expression levels ($<$500 GFP photon count threshold) were selected for imaging on an ONI microscope. These cells were selected because they are expected to have less overexpression-induced artifacts and the localization of the protein is expected to be more similar to the endogenous localization (Moriya et al., 2015). STORM images were successfully obtained with Syb54-54-1D4 (100 nM) with Alexa-647-conjugated 1D4 antibody (1:500) (in-house) (Figure 82A and B). In these STORM images, the Syb54-54 signal is present in puncta with a diameter of $\approx$500 nm, the expected size of a lysosome (Mellman, 1989). For these samples, conventional microscopy images were collected for the GFP channel for the segmentation of GFP-containing organelles to evaluate co-localization of sybody puncta with GFP-TRPML1 puncta (Figure 82A and B). Overall, these STORM experiments show that the sybody dimer can be used in STORM experiments if GFP-TRPML1 is overexpressed, which would enable detailed mapping of the localization of

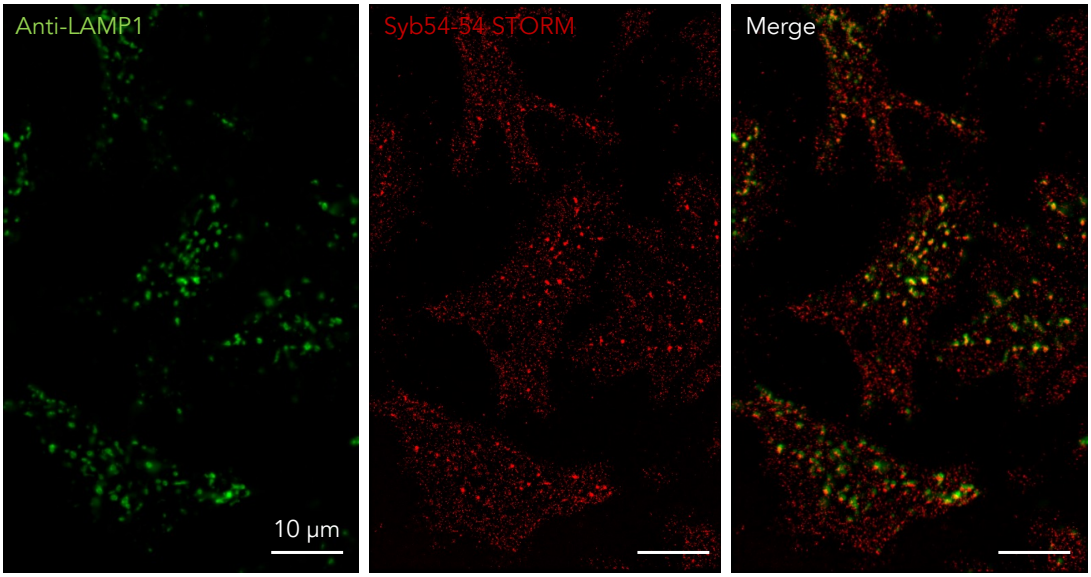

Figure 83: STORM imaging with Syb54-54-1D4 in GFP-TRPML1 untransfected HeLa cells. Conventional image of anti-LAMP1 (green, image 1) stained with Cy3 secondary antibody and Syb54-54 stained with anti-1D4 antibody conjugated to Alexa-647 (red, image 2) in untransfected HeLa cells. The image on the right is a merged image of the conventional and STORM images.

overexpressed TRPML1.

Since STORM was successfully applied to transfected cells using syb54-54, the experiment was repeated with untransfected HeLa cells. In this experiment, cells were stained with syb54-54 (100 nM) with anti-1D4 antibody conjugated to alexa-fluor 647 (in-house), and anti-LAMP-1 sheep antibody with anti-sheep secondary antibody conjugated to cy3 (Jackson ImmunoResearch). The LAMP-1 signal (Cy3) was imaged by conventional microscopy, which will be used to determine the co-localization between LAMP-1 and TRPML1 in the STORM images. Nearly all LAMP-1 lysosomes are sybody/TRPML1-positive in the STORM images, which confirms the results from tagged/overexpressed protein suggesting that TRPML1 specifically localizes to LAMP-1-positive organelles (Figure 83) (Pryor et al., 2006). However, some TRPML1 appears to localize to other vesicles and additional markers of the endo-lysosomal pathway will need to be tested to characterize these regions. The signal is significantly weaker than in the overexpressing cells as expected from the low expression levels of TRPML1 in the cell. Sybody signal is found in all cells since all cells require TRPML1 expression. These results have now been

replicated in 3 independent experiments. Overall, this demonstrates that Syb54-54 can be used to image endogenous TRPML1, which fulfills aims 3 of this thesis.

Follow-up work will focus on qualitative analysis of the STORM data to quantify the co-localization between LAMP-1 and TRPML1-positive lysosomes. Additionally, more lysosomal markers will be tested to determine which lysosomal population TRPML1 is present in using the antibody panel characterized by Bond et al (2024).

6.5 Validation of Sybody Specificity by Immunoprecipitation

6.5.1 TRPML1 Immunoprecipitation Optimizations

Nanobodies are commonly used for immunoprecipitation, and are commercially available for this application. Commercially available nanobody resin is generated by covalent conjugation of nanobodies to resin (e.g. ChromoTek GFP-Trap®). Different binding/conjugation methods were trialed to identify a method that would be compatible with sybodies.

In the first method, sybodies were purified and conjugated to NHS-activated agarose (supplementary Figure 18A-F). This method was trialed because this resin can be generated from WT sybody, which can easily be purified. Sybody was successfully conjugated to the resin, as validated by SDS-PAGE (supplementary Figure 18A). The resin was incubated with DDM-solubilized membrane protein from HEK293F cells transfected with FLAG-AVI-TRPML1. Following the washes, the protein was eluted using SDS for SDS-PAGE analysis or through on-bead tryptic digest for mass spectrometry analysis. TRPML1 was successfully pulled-down using this method, but when repeating this experiment on untransfected cells, the enrichment of TRPML1 was weak in the western blot and the protein was not detected in mass spectrometry samples (supplementary Figure 18B-F). Lysine conjugation has previously been found to disrupt nanobody binding, especially in nanobodies containing lysine residues within their CDRs (Pleiner et al., 2015). Nanobody biotinylation and binding to streptavidin resin has been used

as an alternative IP strategy for lower affinity in-house generated binders (Akkermans et al., 2022). The avi-tagged constructs of the sybodies were: (1) strongly degraded in the presence of cOmplete Protease Inhibitor Cocktail (Roche), (2) precipitating when they were concentrated, (3) eluting later than the WT constructs in SEC, and (4) weakly enriching TRPML1 in untransfected cells (supplementary Figure 19A-D).

Then, the 1D4 tag was trialed because it enables specific and stable immobilization of proteins without chemical modification due to the very high affinity of the Rho1D4 antibody for the 1D4 tag (K_D: 20 nM). Moreover, with this system, the sybody-TRPML1 complexes could be eluted from the resin with peptide, which enables gentle elution of pure protein complexes. Sybody-1D4 constructs were successfully expressed, purified and bound to 1D4 resin (Figure 84A and B). It was observed that myc-tagged sybodies precipitated upon freeze-thawing but this was not observed with 1D4-tagged constructs, suggesting that this tag stabilizes the sybodies. Since syb54 was used for STORM experiments, I aimed to test its ability to IP endogenous TRPML1. By using the 1D4-tagged sybodies, clear enrichment of endogenous TRPML1 (LMNG-solubilized) was observed in the syb54 sample relative to the negative control ($Syb^{(-)}$) by western blotting with a polyclonal anti-TRPML1 antibody (Proteintech Rabbit Polyclonal; 1:500) (see Methods section for IP protocol) (Figure 84C). The antibody shows strong unspecific bands in the lysate samples, but the TRPML1 bands (five bands: degradation product ($\approx$36 kDa), monomer ($\approx$65 kDa), dimer ($\approx$130 kDa), trimer ($\approx$195 kDa) and tetramer ($\approx$260 kDa)) become apparent in the enriched fraction (Figure 84C). Nearly complete depletion of TRPML1 in the load can be observed by comparing the load and flow-through fractions in the regions where the TRPML1 bands are found. Since this protocol was found to be successful, it was optimized by: (1) trialing solubilization with a more gentle and mass-spectrometry compatible detergent (DDM), (2) loading different sybody amounts on the resin, (3) increasing washing steps, (4) trialing elution with 1D4 peptide and (5) pulling-down the protein with Syb54-54. It was found that: (1) 1% DDM (in TBS) could be used for TRPML1 IP, (2) $\approx$2 μg of sybody can be loaded per μL of resin to saturate the resin (theoretical capacity: $\approx$3 μg/μL), (3) TRPML1 does not dissociate during washes with incubations (2 x 30 min), (4) multiple 1D4 peptide elutions (30 mg/ml peptide for 30 min x 3) are required to elute TRPML1 but the affinity of the

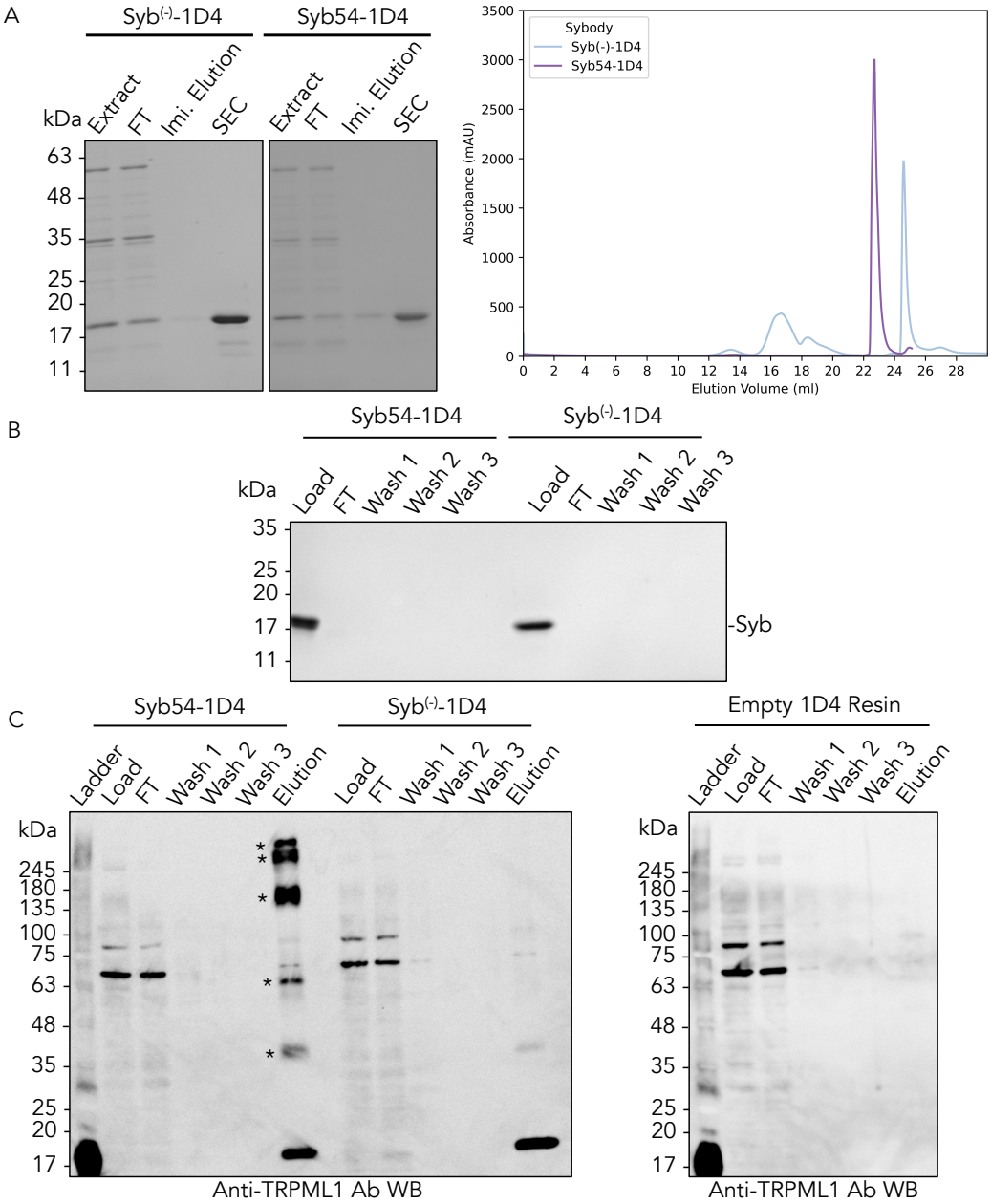

Figure 84: Purification, resin binding and immunoprecipitation (IP) with 1D4-tagged sybodies. A) Purification of 1D4-tagged Syb(-) and Syb54 by periplasmic extraction (extract), Ni-NTA (FT and Imi. Elution) and SEC (superose 6) (Polyacrylamide gel (4-20%) left and SEC profile right). B) Binding efficiency test of 20 µg of Syb-1D4 to 40 µL of anti-1D4 resin. Polyacrylamide gel displays complete binding as the protein in the load is no longer present in the FT following resin binding (Washes: TBS with 300 mM NaCl + 0.1% LMNG). C) Western blot of IP with Syb-1D4 or empty 1D4 resin on LMNG-solubilized protein from untransfected HeLa cells. Samples were run on a 4-20% gel and the membrane was bound to Rb anti-TRPML1 Ab and HRP secondary. Load is the soluble fraction, FT is load after resin incubation, washes of resin, and loading buffer elution of IP. Stars (*) are TRPML1 bands (from low to high MW): degraded fragment, mono, di, tri and tetramer.

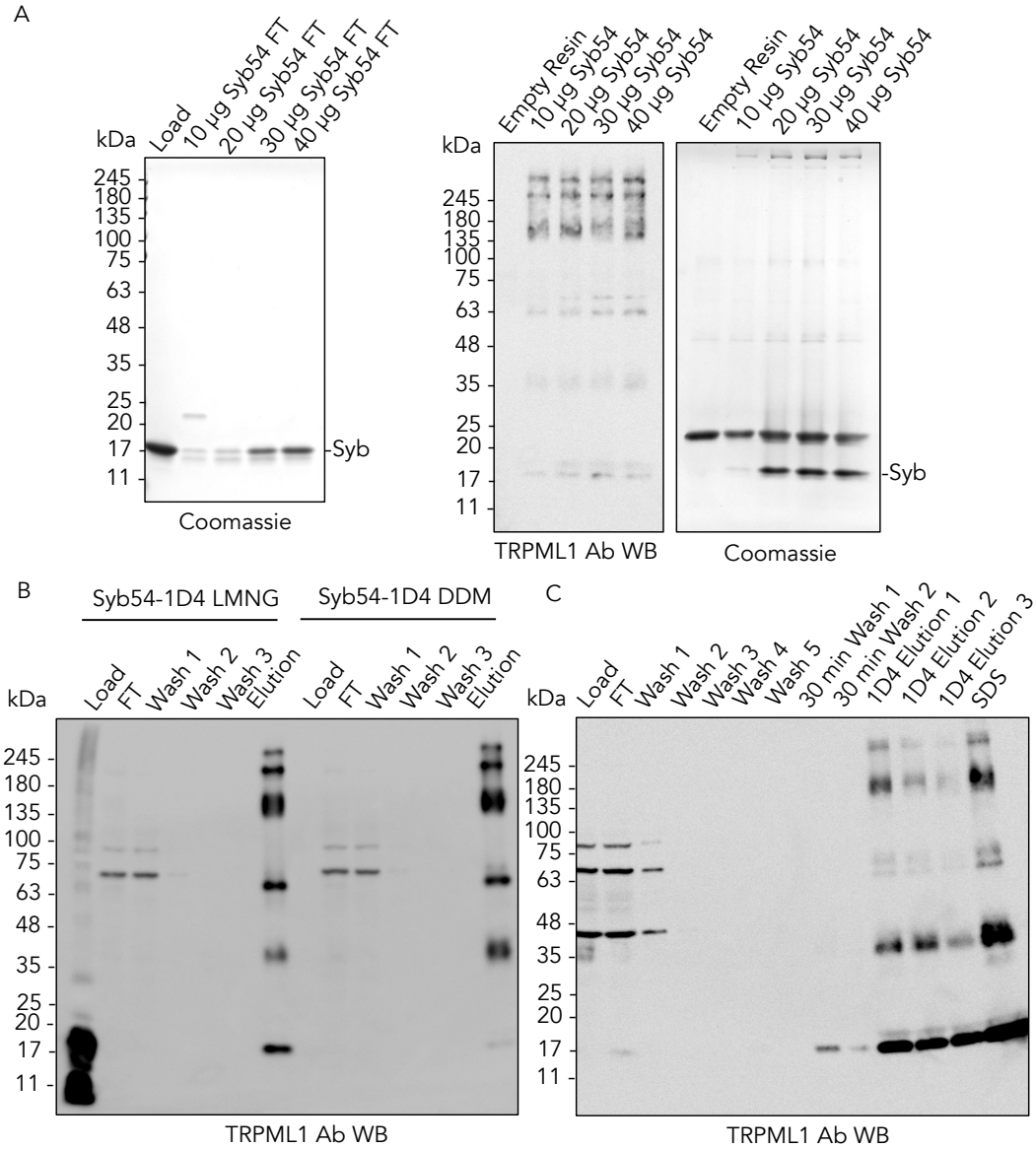

Figure 85: Optimization of Syb54-1D4 resin IP, including sybody loading amount, detergent, washes and elution. A) Binding efficiency of different amounts (10-40 µg) of Syb54-1D4 loaded on 10 µL of anti-1D4 antibody resin assessed by SDS-PAGE (left) and a western blot of the IP, as described for the initial experiment, carried out with the resins with different amounts of Syb54-1D4 loaded (right). Approximately 20 µg of sybody fully saturates resin. B) Western blot of an IP experiment with Syb54-1D4 resin incubated with LMNG-solubilized or DDM-solubilized proteins from untransfected HeLa cells. Syb54 can pull-down TRPML1 in either detergents. C) Western blot of an IP experiment with Syb54-1D4 on DDM-solubilized untransfected HeLa cells with added washes, including 5 washes and 2 x 30 min washes in TBS (pH 8.0, 300 mM NaCl) + 0.1% DDM, 3 elutions with 30 mg/ml 1D4 peptide in TBS (pH 8.0), and a final elution on the same resin with SDS-loading buffer to determine if any protein was left on the resin. The added washes do not cause the loss of TRPML1 and the 1D4 elutions do not enable complete elution of TRPML1-Syb54.

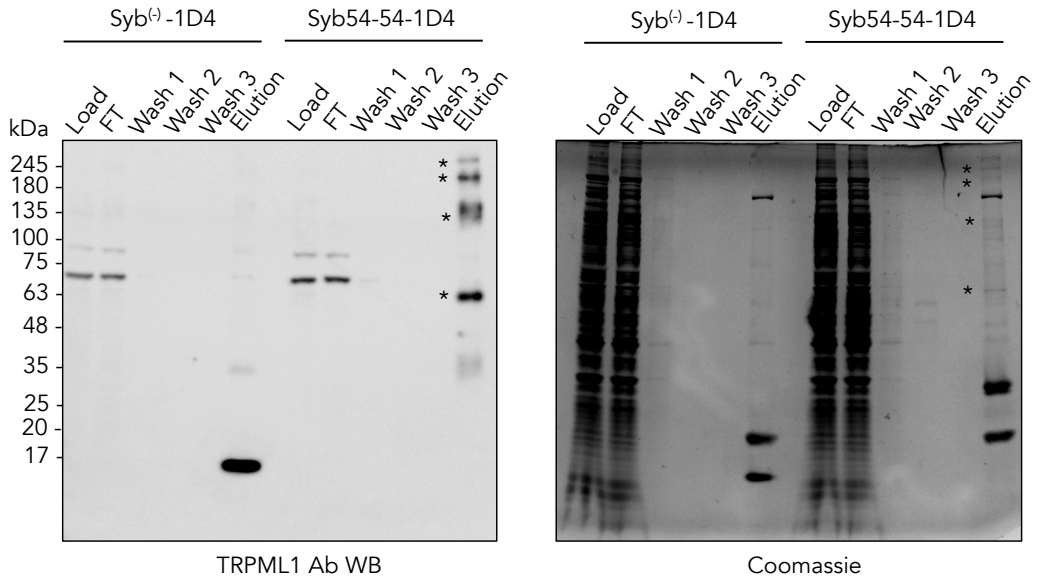

Figure 86: IP in HeLa untransfected cells with Syb54-54-1D4 construct. IP was carried out on DDM-solubilized fraction from untransfected HeLa cells, which was incubated with Syb54-54-1D4 resin or negative control resin. Samples were eluted with gel loading buffer, and were loaded on a gel for Coomassie staining or western blot analysis as described earlier. The dimer successfully pull-downs TRPML1, and bands in the Coomassie that may correspond to TRPML1 are marked with *.

tag is too strong to have complete elution, and (5) the dimer can IP TRPML1 efficiently (Figure 85A and B; Figure 86). Once this protocol had been successfully optimized to IP endogenous TRPML1, it was used to validate the specificity of the sybody.

6.5.2 Validation of Sybody specificity

Reagent specificity is validated using knock-down or knock-out cell lines or tissues. A TRPML1 knockdown SH-SY5Y cell line was generated by Johanna Hoffmann (Wade-Martins lab) and validated by qPCR (Figure 87C). TRPML1 knock-down cells and cells with control non-targeting sgRNA were provided. Aliquots of 2 million cells were frozen and thawed for lysis, were resuspended in 300 μL of TBS with 1% DDM and 1X PPI, solubilized, and the lysate was clarified with a low-speed spin (21,000 g). Protein was quantified and equivalent amounts (300 μg) of knockdown and control cells were incubated with syb54 or syb$^{(-)}$ 1D4 resin. Following

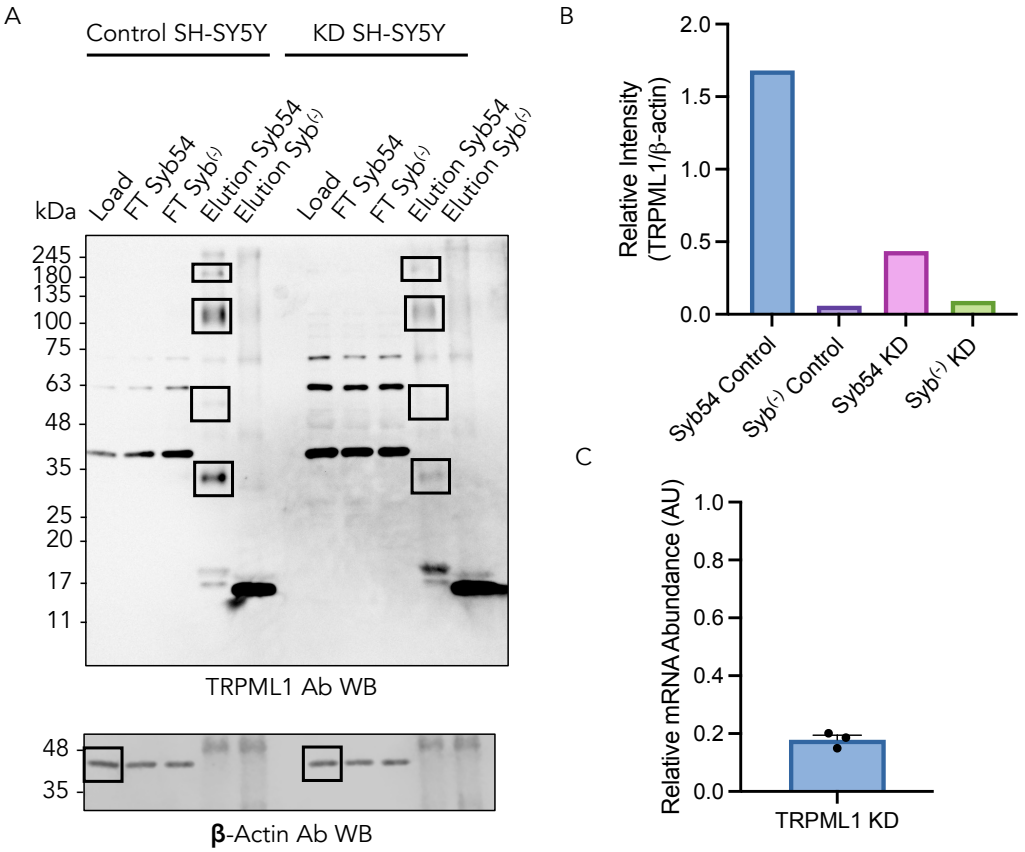

Figure 87: Validation of Syb54-1D4 specificity by IP using a TRPML1 Knock-Down (KD) SH-SY5Y cell line. A) Western blot from IP with Syb54-1D4 or Syb$^{(-)}$-1D4 on DDM-solubilized protein from TRPML1 knock-down and control (non-targeting sgRNA) SH-SY5Y cells. B) Quantification of band intensity (band used marked with black box) in western blot. Values were normalized based on the beta-actin levels in the load for the respective samples. C) TRPML1 mRNA expression in knock-down cell line normalized by GAPDH expression and the control cell line TRPML1 expression levels. The knock-down generation and qPCR were performed by Johanna Hoffmann.

the washes, bound protein was eluted from the resin with SDS. The presence of TRPML1 in the elution was determined by western blotting (Beta-actin antibody conjugated to biotin from Invitrogen at 1:1000 and goat anti-mouse IR dye 1:10000; Proteintech anti-TRPML1 Ab 1:500 and anti-rabbit HRP promega 1:2500). Knock-down cell TRPML1 expression was found to be 74% lower than the control cells (Figure 87A and B). This decrease in expression is consistent with the decrease measured by qPCR (82% $\pm$0.01539). The specificity of the enrichment is also shown by the loss of beta-actin in the elutions. It was found that the degraded fragment makes up a large proportion of the total TRPML1, suggesting that TRPML1 is mostly in its cleaved state in the cell. Moreover, this shows that Syb54 can bind both the full-length and truncated version of TRPML1. In the future, it would be interesting to repeat this experiment with a binder that interacts with the β4-β5 loop, such as Syb94, to compare the amount of cleaved TRPML1 that is pulled down. If it does not pull down the cleaved fragment, these different reagents could be used to image different states of the protein in the cell (cleaved and uncleaved). Overall, this result shows that syb54 and the anti-TRPML1 Ab are TRPML1-specific binders, and this is the first time endogenous TRPML1 has been successfully pulled down.

6.6 Outlook

In this thesis, methods have successfully been established to study endogenous TRPML1. The super-resolution data and the protocol that has been established will enable to precisely map out the localization of endogenous TRPML1 in cells for the first time and study its protein interactions. Syb54 and its bivalent construct (Syb54-54) were shown to successfully IP and stain endogenous TRPML1 in untransfected HeLa cells. The specificity of these constructs were also validated using knockdown cell lines, which demonstrated that Syb54 specifically pull-downs TRPML1. Syb175 was also found to be an excellent candidate for immunostaining experiments, but due to its predicted 1:4 binding mode, bivalent constructs are unlikely to bind with a higher affinity.

In the future, the protocols described here can be applied to stressed or diseased cells to investigate how TRPML1 localization is affected in these states in which lysosomal homeostasis is

disrupted. For example, the localization of TRPML1-positive lysosomes has been suggested to be disrupted in Alzheimer's model neurons and TRPML1 has been suggested to play a key role in preserving lysosomal homeostasis under nutrient starvation (Lie et al., 2022; Wang et al., 2015). Some of the protocols described here could be combined effectively for super-resolution microscopy, such as the generation of dimeric constructs with cysteine mutations which would decrease the linkage error for super-resolution experiments.

The IP protocol has been optimized for co-IP experiments with mass spectrometry for Syb54. This protocol will form the basis for important work as there is currently no co-IP data for endogenous TRPML1 due to the lack of specific antibodies. This data would enable to identify TRPML1 effectors for its functions as the mechanisms of action of TRPML1 remain poorly characterized. The IP protocol could also be applied to the structural characterization of endogenous protein (Sun et al., 2023). TRPML1 is known to form heteromers (Zeevi et al., 2010). Syb54 could be used to isolate endogenous heteromeric TRPMLs and their protein complexes for structural characterization.

When setting up the protocols described here, multiple sybodies, including some with unfavourable physicochemical properties were tested. This makes these protocols broadly applicable to other sybodies for a range of lysosomal targets in the future to understand their role in lysosomal homeostasis. Future work on novel targets should leverage the power of combining biophysical techniques like BLI with AlphaFold to engineer high-affinity sybodies and identify binders that interact with epitopes that are likely to be present in the cellular context.

7 | Conclusions

This thesis aimed to develop our understanding of the role of transporters and ion channels in lysosomal homeostasis.

This was achieved by investigating the transport mechanism of cystinosin, which maintains cystine homeostasis in lysosomes. Using two-electrode voltage clamp experiments, key residues in gating, and cystine and proton binding were identified (Chapter 3). These results constitute an important step in understanding the roles and mechanisms of transporters in preserving lysosomal and cellular homeostasis. Secondary transporters couple the transport of their substrate to an electrochemical gradient (Drew and Boudker, 2024). Some lysosomal transporters couple the transport of substrates enriched in the lysosomal lumen to proton movement (Ruivo et al., 2012; Schmiege et al., 2024). The results presented here along with results published by Guo et al (2022) demonstrate that the proton gradient and its coupling to the transport cycle play a critical role in facilitating the conformational changes of cystinosin, conferring the transporter with directionality and organelle specificity. The proton leaks observed here may occur in a physiological context as a release valve upon the loss of proton homeostasis in lysosomes. Novel insights were also revealed from the results presented here regarding the mechanisms that confer amino acid/peptide transporters with their specificity. Based on the identified binding site, the specificity is conferred through a molecular clamp where the extremities of the dipeptide form extensive interactions with the transporter, ensuring that only substrates of the correct length interact with cystinosin. Lysosomal membrane proteins commonly associate with an accessory subunit or contain a soluble luminal domain region (Rudnik and Damme, 2020). The results presented here suggest that in some transporters the luminal domain does not play an important role in the transporter's activity, and they are perhaps instead involved in maintaining transporter stability at the lysosomal membrane.

Lysosomal homeostasis is disrupted in lysosomal storage disorders like cystinosis, and I aimed to determine whether proton transport activity of mutants could be linked with disease severity. Binding site mutations (e.g. D305) and key regions for conformational transitions (e.g. D205)

eliminate transporters activity and cause the most severe form of cystinosis (David et al., 2019). This establishes a link between the loss of transporter activity and the phenotypes in these patients, suggesting potential mechanisms of intervention (transporter modulators or activation of alternative pathways for the restoration of cystine homeostasis). It also provides further evidence that lysosomal homeostasis is a fragile equilibrium and can be disrupted by the loss of activity of a single transporter, suggesting a lack of redundancy for some lysosomal transporters (Huizing and Gahl, 2020). Cystinosin is known to have other functions in addition to cystine transport and the severity of cystinosis does not always correlate with transporter activity (David et al., 2019; Zhang et al., 2017). To investigate this, synthetic nanobodies were generated by Mark Löbel, but unfortunately, they did not bind to the full-length target protein. In the future, the selection should be carried out on the full-length protein to obtain binders that interact with TRPML1 in cells.

Our understanding of the role of lysosomal membrane proteins in maintaining lysosomal homeostasis has been limited by our lack of tools to study them. Therefore, I set out to generate sybody tools to investigate TRPML1, a lysosomal ion channel with a wide range of functions involved in preserving lysosomal homeostasis. High-affinity synthetic nanobodies were obtained for TRPML1, including Syb43, 54, 57, 94 and 175, which were all found to have a K_D of approximately 100 nM or lower (Chapter 4). BLI was applied to identify the sybody epitopes, and remarkable consistency was found between these measurements and AlphaFold3 models. It was noted that a range of sybodies that have been selected for TRPML1 and other lysosomal targets are histidine rich, especially amongst concave binders. When choosing sybodies to develop further for cellular assays, the presence of histidines within the CDRs should be verified or the histidines may have to be substituted by site-directed mutagenesis. Alternatively, a strategy should be selected to favor cytoplasmic binding by isolating a cytosolic region of the protein or shielding the luminal regions. All high-affinity binders were found to be luminal, which was expected as it displays the most epitopes. When selecting future lysosomal targets to investigate with sybodies in cellular assays, it will be best to choose those containing highly-immunogenic rigid soluble regions with fewer post-translational modifications or by selecting the binders that do not interact with challenging regions, which could be identified by combining

enzymatic digestion, AlphaFold3 and binding analysis. It was found that AlphaFold3 shows the greatest accuracy for interactions with these soluble rigid regions. Following these observations would enable the selection of high-affinity binders to investigate the role of lysosomal membrane proteins in preserving homeostasis. The great conformational and isoform specificity of sybody binding to flexible/modified regions presents an opportunity to study proteins in greater detail. The main barrier to achieving this remains that the post-translational modification of overexpressed proteins is different to endogenous proteins as observed for TRPML1.

Two of the obtained sybodies, Syb57 and Syb94, were identified to be specific activators of TRPML1 using whole-cell patch-clamp (Chapter 5). The complexes these binders form with TRPML1 were structurally characterized using cryo-EM to a resolution of 3 Å. Based on these structures, a mechanism of channel modulation was suggested. The sybodies were suggested to alter the contacts formed between the luminal domain and transmembrane regions through the interactions they form with the luminal domain. This was in turn suggested to alter the conformation and dynamics of the PHs and SF. This represents a novel mechanism for the activation of TRPML1 as all characterized agonists activate the channel by opening its lower gate by interacting with the transmembrane region or the PIP binding site (Gan et al., 2022; Schmiege et al., 2017). It was suggested that the sybodies may mimick the modulation by an endogenous TRPML1 binding partner that may regulate channel activity by modulating the conformation of the SF. The luminal domain may regulate the channel conformation through a conserved set of histidine residues, which potentially enables coupling of luminal pH changes to channel activity. This would be critical to ensure that TRPML1 is only activated once it reaches the lysosomal membrane. Overall, the conformational changes observed in the structures are minor, which may not be a true reflection of the effects of the sybodies. It has proven challenging for other channels to decipher a mechanism of activation for nanobodies as they frequently target allosteric sites that may have more subtle effects on channel conformation. In the case of the Syb94-TRPML1 complex, activation of the channel by the sybody may lead to pronounced conformational changes that affect its stability and would result in the exclusion of the activated channels in the analysis. Although nanobodies may prove useful to reveal details about the mechanisms of channels, many of the published complexes modulate the channels through known pathways

because these stabilize stable active states of the channel or target regions known to be involved in channel function, but few reveal novel and potentially more physiological mechanisms of modulation (Wu et al., 2021). These mechanisms may be revealed through novel techniques such as time-resolved cryo-EM or more detailed analysis of the datasets (Dandey et al., 2020). In the TRPML1-Syb94 structure, a cathepsin cleaved and glycosylated region was resolved (β4-β5 loop) as it interacts extensively with Syb94. Cathepsin cleavage is observed in a range of lysosomal proteins (Rudnik and Damme, 2020). This structure and the potential involvement of this region in the activation mechanism of the sybodies may indicate more complex mechanisms through which cathepsins modulate lysosomal protein activity than previously suggested (Kiselyov et al., 2005; Rudnik and Damme, 2020). These undeposited structures also enabled to evaluate the accuracy of AlphaFold3 to predict TRPML1-sybody complexes. AlphaFold3 was found to predict the complexes with very high accuracy. AlphaFold3 was used to predict unsolved complexes formed by the high-affinity binders (Syb43, 54 and 175) and the predictions were found to be consistent with BLI data.

Following characterization of the sybody properties and epitopes, their ability to bind to TRPML1 in cells was tested (Chapter 6). No clear correlation was present between K_D and co-localization. However, it was found based on the structures and models that all highly co-localizing sybodies formed fewer interactions with the highly flexible and modified β4-β5 loop. Syb54 and Syb175 were identified to be the best co-localizing sybodies, and Syb54 was carried forward as it interacts with TRPML1 in a 4:4 ratio enabling the generation of a high-affinity multivalent construct. Using STORM imaging, the localization of endogenous TRPML1 was mapped in the cell with Syb54-54, confirming the lysosomal localization of the endogenous protein. Moreover, the obtained reagents (Syb54 and Syb54-54) were shown to be highly specific in immunoprecipitation experiments of endogenous TRPML1. Additional studies will need to be carried out to determine whether it co-localizes with other lysosomal markers and whether its localization and expression is affected under stress conditions. Moreover, it will need to be tested whether the staining pattern is lost in the knock-down cell line. The use of nanobodies and sybodies in cell biology has so far mostly been limited to well characterized proteins or protein tags (Götzke et al., 2019; Pleiner et al., 2015; Ries et al., 2012). Therefore, these

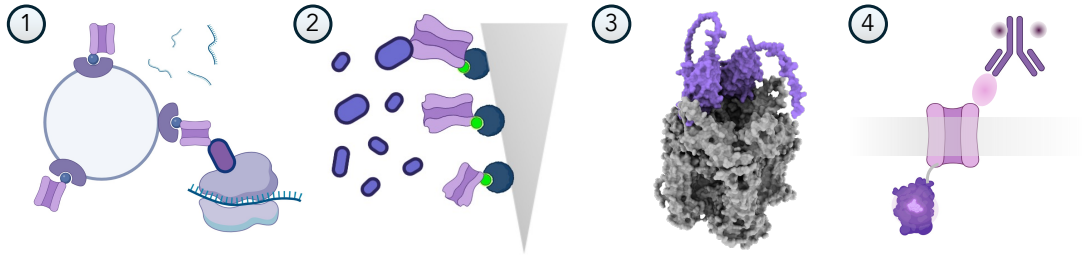

Figure 88: Pipeline for the structure-guided design of synthetic binders against lysosomal membrane proteins. High-affinity conformationally-specific multivalent nanobodies can be obtained by combining the sybody pipeline which enables to obtain high-affinity binders against labile proteins (1), biophysical assays which enable to measure sybody affinities (2) and *in silico* predictions with AF3 that enable to determine the conformational epitopes (3). The affinity of the construct for the target protein in the cell can then be determined using the simple immunofluorescence screening method developed here (4). The most successful binders can then be tested for their ability to bind endogenous protein with IP and IF experiments.

results represent a significant advancement for reagent design for the study of lysosomal membrane proteins. A similar study has recently been carried out on the SLC class of proteins with nanobodies and sybodies, which showed the great challenges and attrition rates observed when generating reagents for challenging membrane proteins (Gelová et al., 2024). Sybody design using this approach is expected to significantly improve our understanding of lysosomal biology by enabling studies on the protein interactions/effectors of lysosomal membrane proteins, the isolation of the intact complexes they form for structural studies, and the characterization of localization changes in stress conditions or disease states.

Overall, the TRPML1 sybody work presented here provides a rapid strategy for generating reagents against lysosomal membrane proteins to investigate their role in lysosomal homeostasis. This strategy combines the sybody selection pipeline, biophysical assays (BLI) and *in silico* predictions of sybody-protein complex structures to engineer multivalent high-affinity binders. This strategy is broadly applicable but would be most effective on multimeric proteins or proteins with a large immunogenic region. However, a key advantage of nanobodies is that they are small, enabling multiple nanobodies to potentially interact to small exposed regions. This strategy can be applied to any protein in the cell but it overcomes specific challenges associated with generating reagents for lysosomal membrane proteins.

8 | Appendix

8.1 Supplementary Figures and Data

A

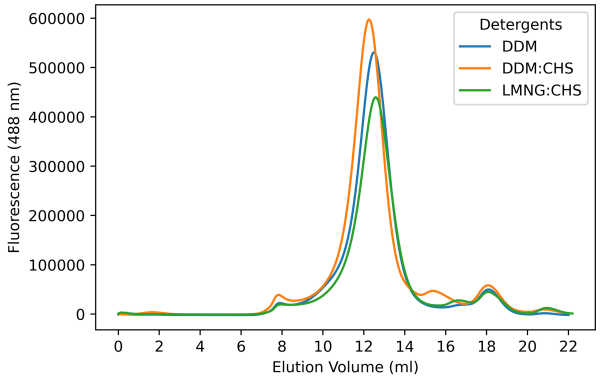

C

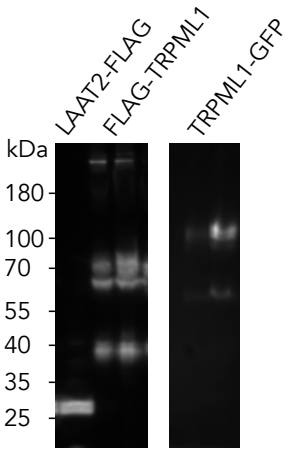

B

	DDM	DDM+CHS	LMNG	LMNG+CHS
Pre-Spin	2407	3334	2803	3575
Post-Spin	1617	2117	1529	2148
Solubilization Efficiency (%)	67%	63%	54%	60%

Supplementary Figure 1: TRPML1 expression trials and detergent screen. A) Fluorescence SEC profile with superose 6 column for FLAG-AVI-TRPML1-GFP-6xHIS (small-scale expression) solubilized in different detergents. B) Solubilization efficiency of different detergents based on GFP counts after detergent solubilization (1% for all detergents), and before or after an ultracentrifuge spin (200,000g for 20 min at 4°C) (Post-Spin Counts / Pre-Spin Counts). C) Western blot of FLAG-tagged TRPML1 (FLAG-AVI-TRPML1) and LAAT-2-FLAG (positive control) using anti-FLAG antibody, and in-gel fluorescence of FLAG-AVI-TRPML1-GFP-6xHIS. Each lane was loaded twice with 2 or 10 µL.

A

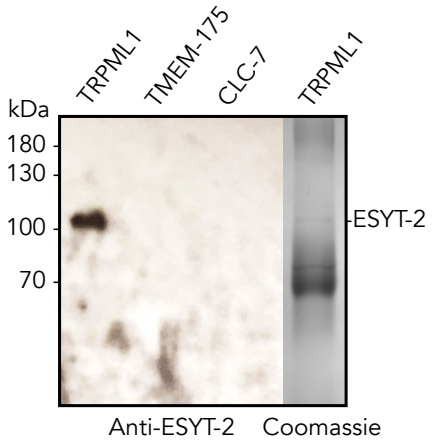

B

MW [kDa]	Description	Score	Coverage
68.7	TRPML1	99.51	18.33
70.0	Hsp-70	49.24	19.03
67.5	Calnexin	43.28	16.22
102.3	**ESYT-2**	**40.80**	**12.38**

Supplementary Figure 2: Identification of a potential TRPML1 protein interactor. A) An unknown band was observed in the TRPML1 purified sample. This band was identified to be extended synaptotagmin-2 (ESYT-2) by mass spectrometry, which was confirmed by doing a western blot using anti-ESYT-2 antibody (Sigma-Aldrich; HPA002132). The band is not present in samples of other purified lysosomal membrane proteins. B) Mass spectrometry results for the excised 100 kDa band. Extended Synaptotagmin-2 was one of the top hits.

A

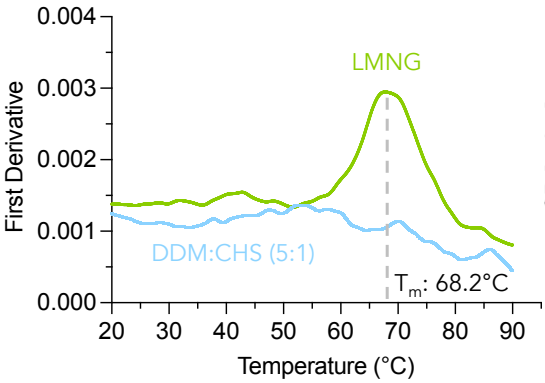

B

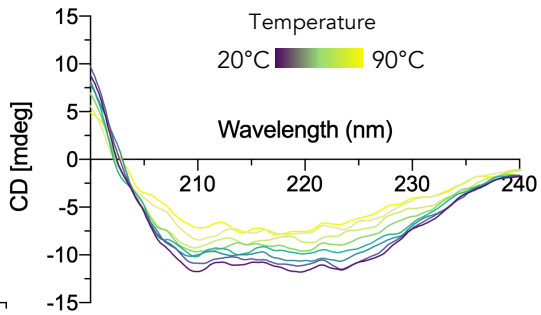

Supplementary Figure 3: Biophysical characterization of purified full-length TRPML1. A) Nano-differential scanning fluorimetry (nano-DSF) of TRPML1 with a temperature gradient. TRPML1 in LMNG shows a weak transition at approximately 68.2°C, but the DDM:CHS (5:1) sample does not show a clear transition. B) TRPML1 shows elements of secondary structure in circular dichroism, suggesting it is folded. However, it does not show a clear transition between 20°C to 90°C.

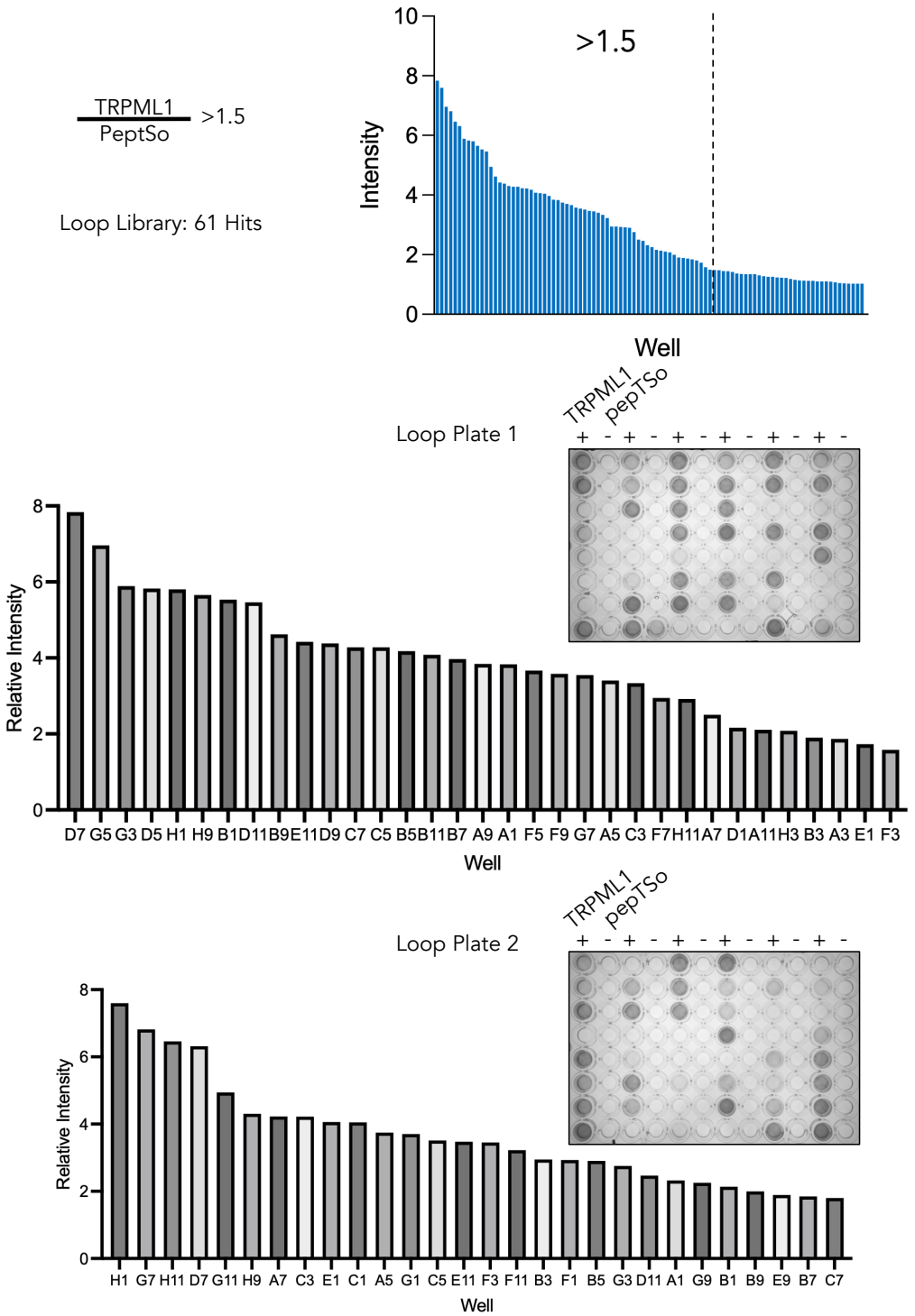

Supplementary Figure 4: ELISA significant hits for loop library. 61 hits were found to be above the threshold (1.5). Graphs below show significant hits ranked in terms of relative intensity (intensity TRPML1/intensity pepTSo negative control well) with the well number in the ELISA plate.

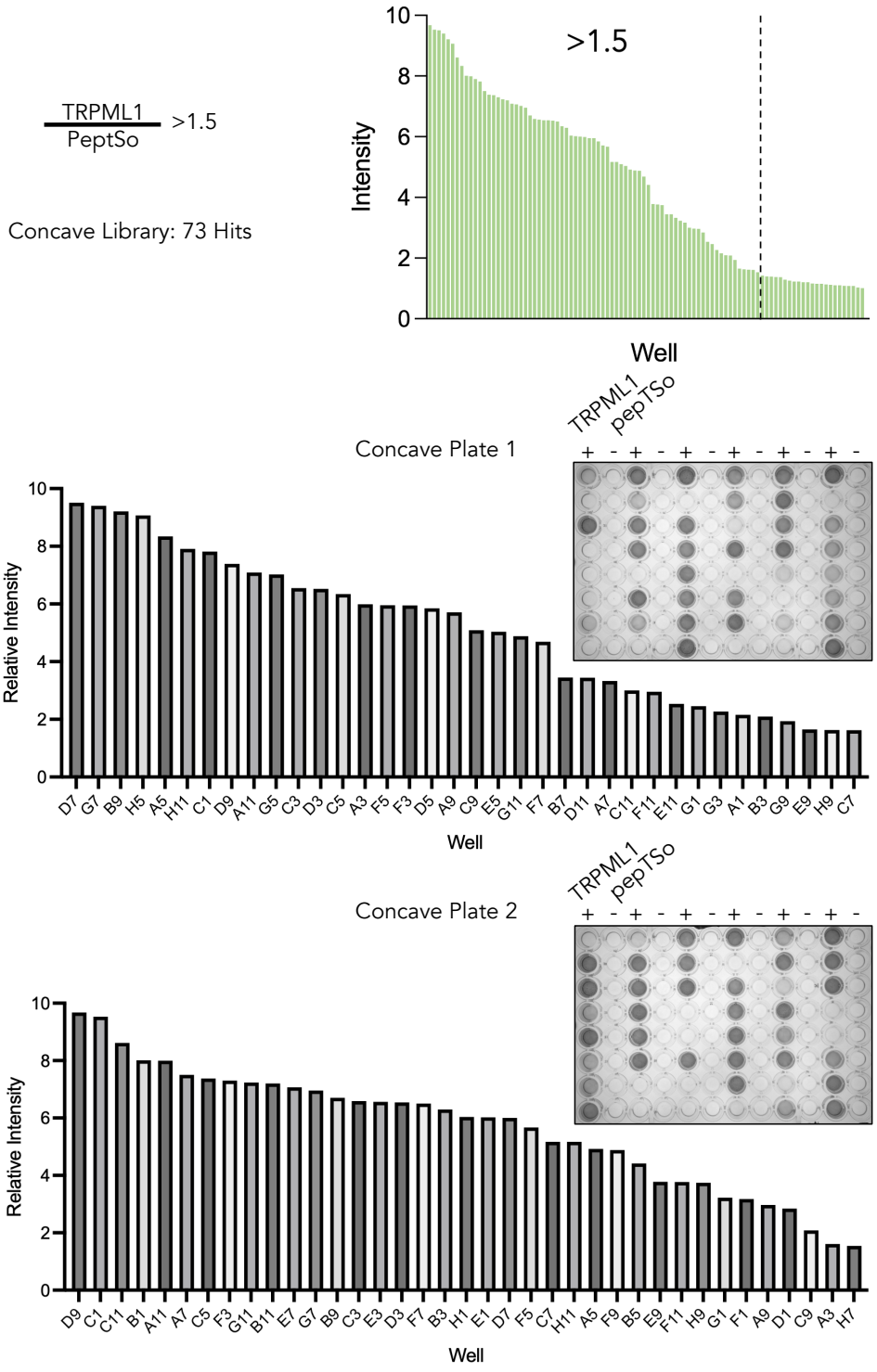

Supplementary Figure 5: ELISA significant hits for concave library. 73 hits were found to be above the threshold (1.5). Graphs below show significant hits ranked in terms of relative intensity (intensity TRPML1/intensity pepTSo negative control well) with the well number in the ELISA plate.

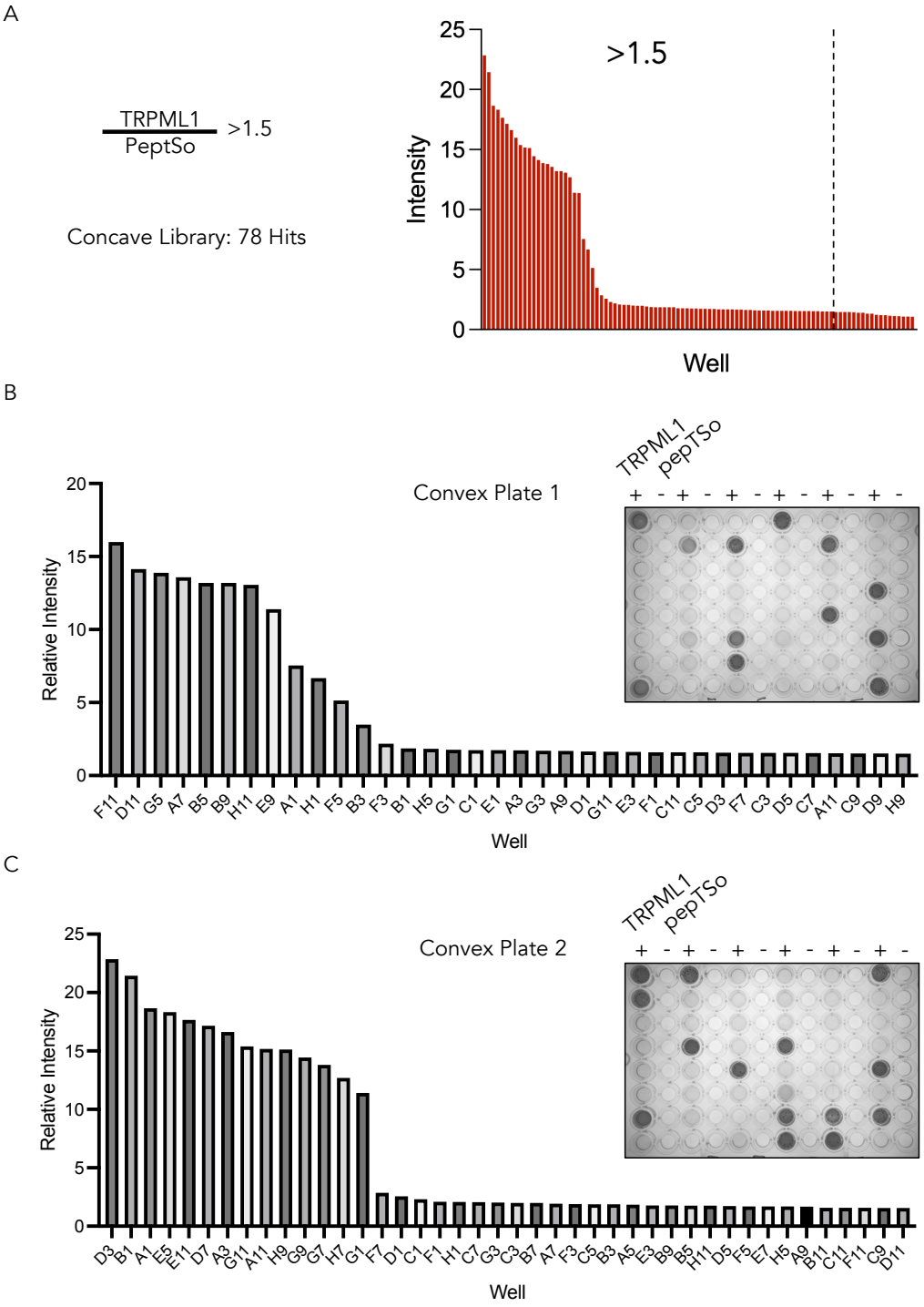

Supplementary Figure 6: ELISA significant hits for convex library. 78 hits were found to be above the threshold (1.5). Graphs below show significant hits ranked in terms of relative intensity (intensity TRPML1/intensity pepTSo negative control well) with the well number in the ELISA plate.

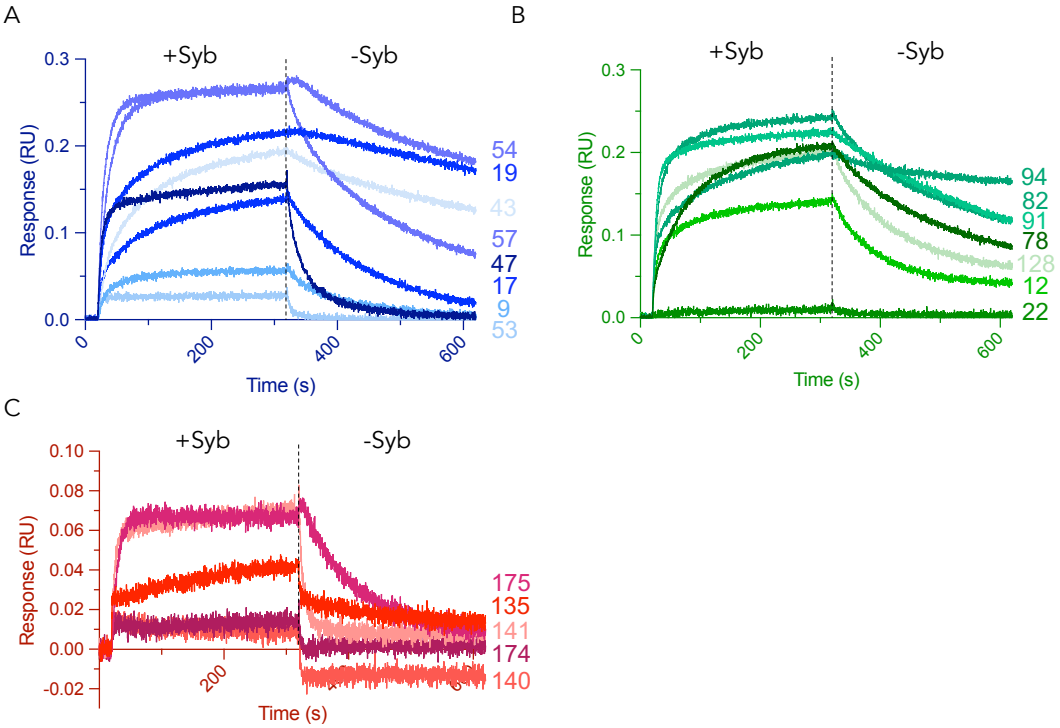

Supplementary Figure 7: Initial Bio-layer Interferometry (BLI) traces for full-length TRPML1. (A-C) Traces for loop, concave and convex libraries, respectively with sybody concentration of 500 nM in TBS with 0.003% LMNG.

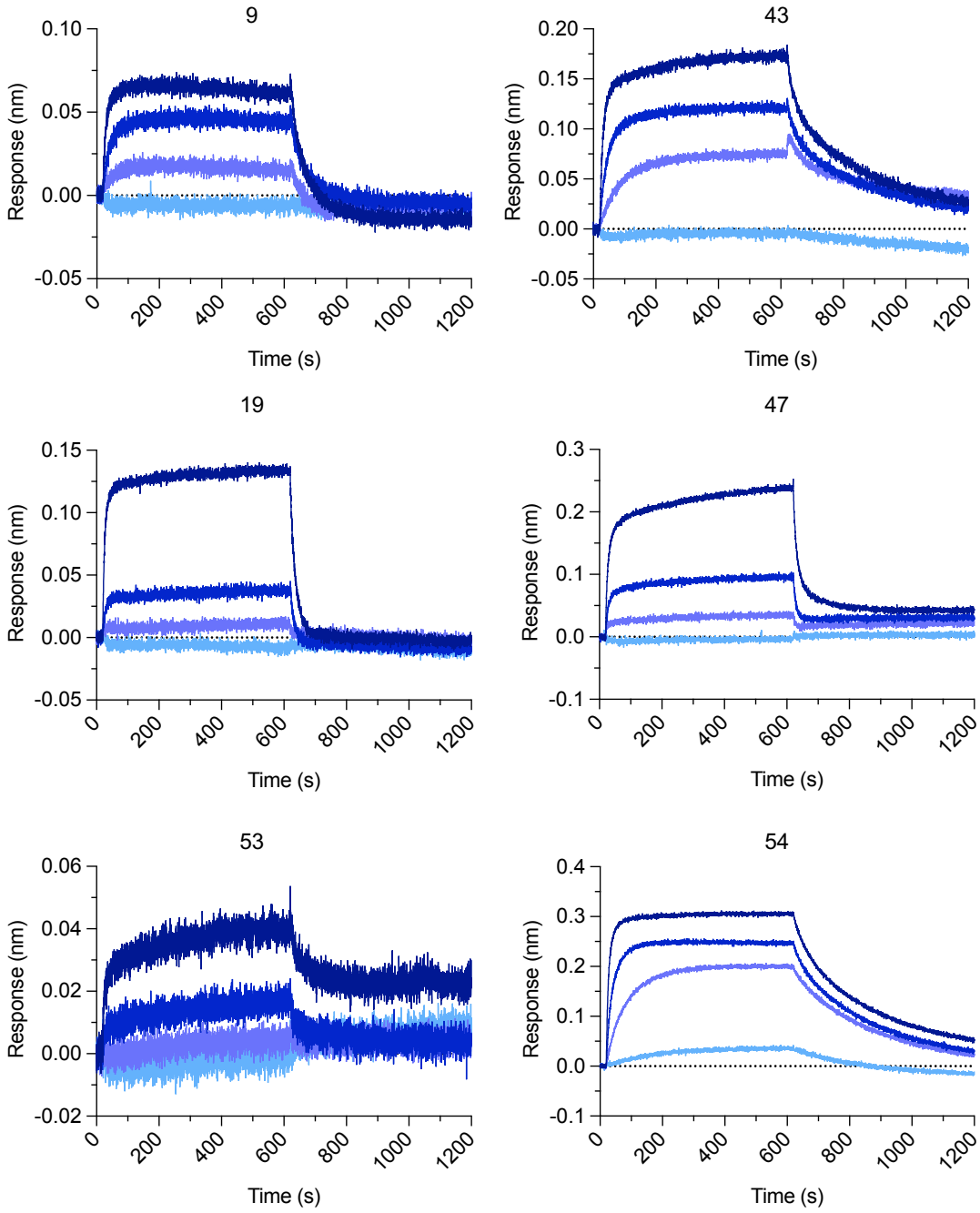
9
Response (nm)
0.10
0.05
0.00
-0.05
0
200
400
600
800
1000
1200
Time (s)
43
Response (nm)
0.20
0.15
0.10
0.05
0.00
-0.05
Time (s)
19
Response (nm)
0.15
0.10
0.05
0.00
-0.05
Time (s)
47
Response (nm)
0.3
0.2
0.1
0.0
-0.1
Time (s)
53
Response (nm)
0.06
0.04
0.02
0.00
-0.02
Time (s)
54
Response (nm)
0.4
0.3
0.2
0.1
0.0
-0.1
Time (s)

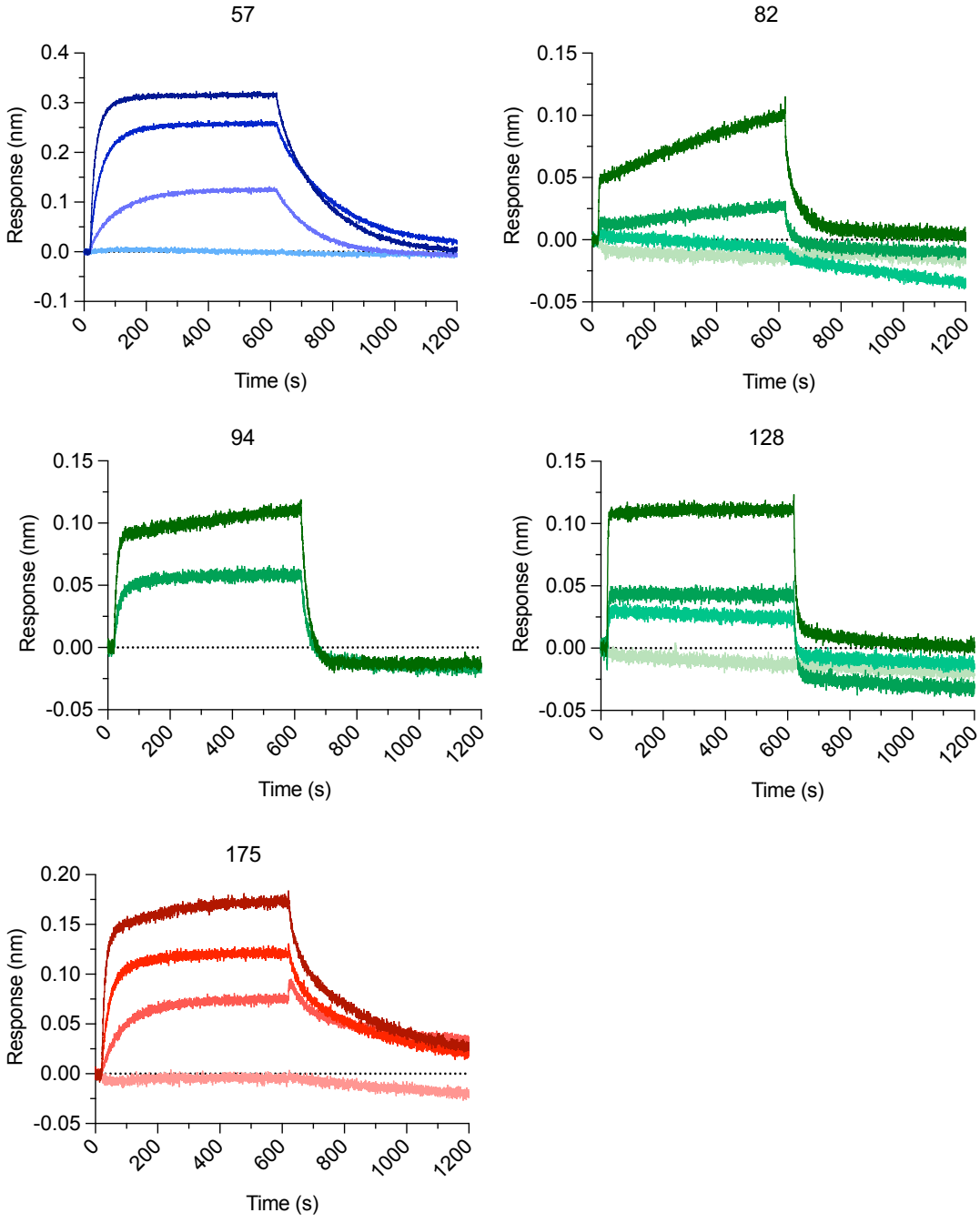

Supplementary Figure 8: Initlal kinetics measurements for sybodies of interest on full-length TRPML1 using BLI. Sybodies were tested at 10, 100, 250 and 500 nM (measurement at 10 and 100 nM not included for Syb94) in TBS with 0.5 mg/ml BSA and 0.01% LMNG.

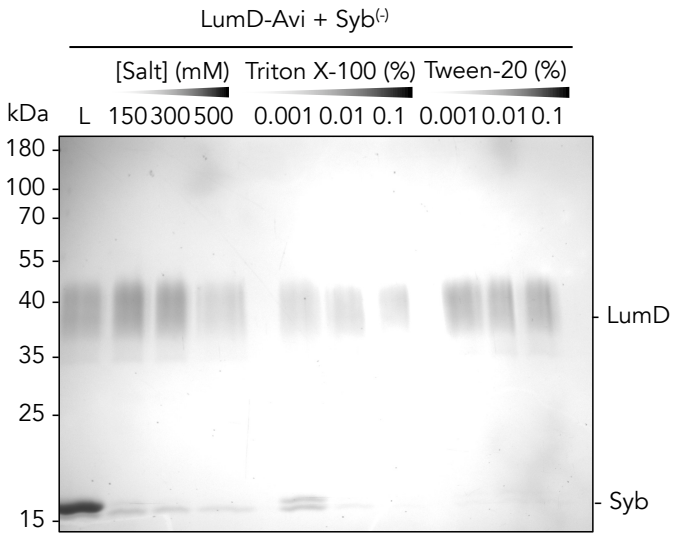

Supplementary Figure 9: Optimization of luminal domain pull-down with streptavidin resin. Different NaCl (salt), and detergent types and concentrations were tested to eliminate non-specific binding. Detergent changes were found to eliminate most non-specific binding, but not salt. L: Load; remainder of samples are elutions following washes with TBS + X (reagent indicated above lane).

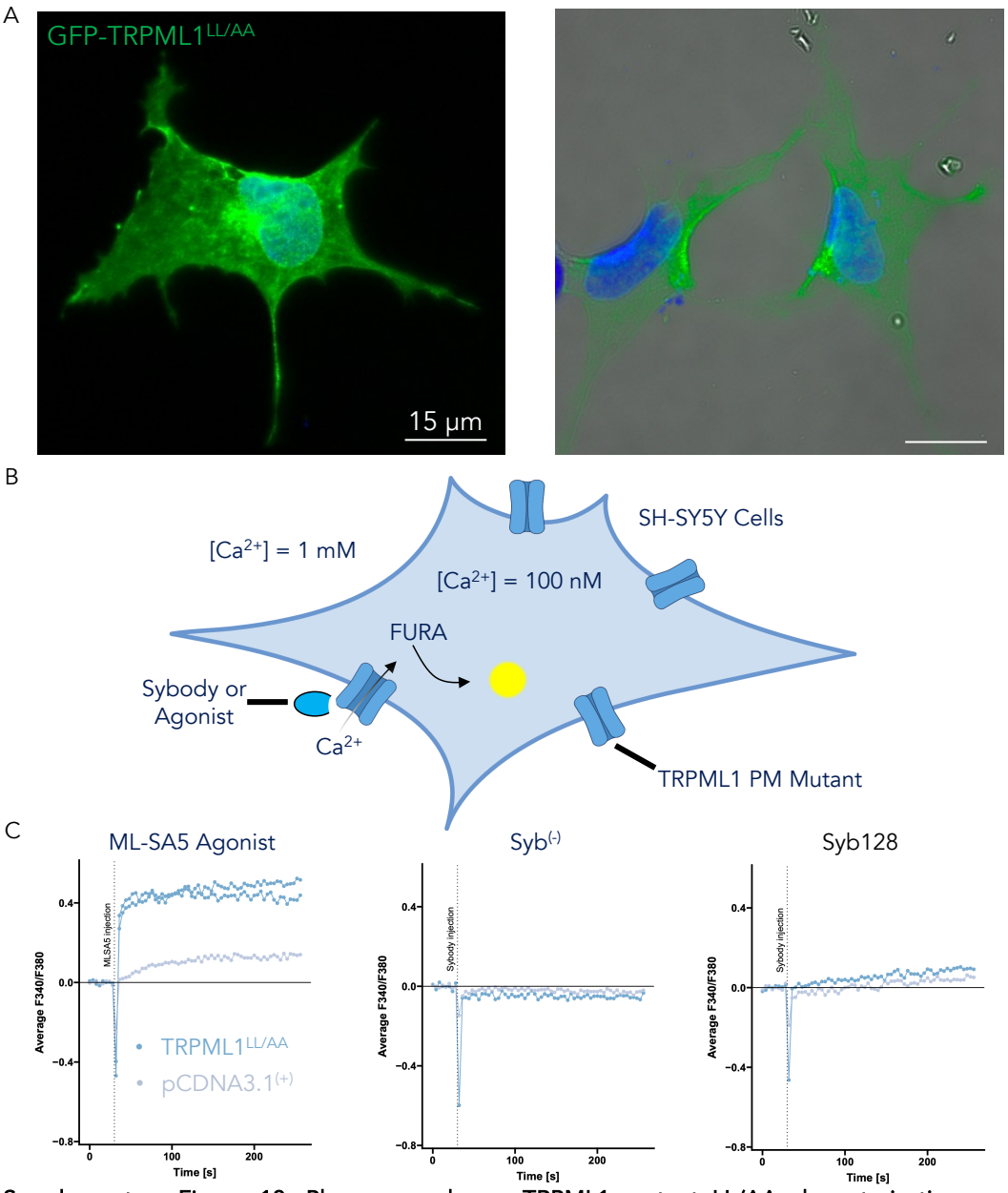

Supplementary Figure 10: Plasma membrane TRPML1 mutant LL/AA characterization and FURA-2 assay. A) HeLa cells were transfected with GFP-TRPML1$^{LL/AA}$ (green) to determine if it localizes to the plasma membrane as previously described. The GFP signal (green) was observed to localize along the contour of the cell using a widefield fluorescent microscope (blue: DAPI). B) Setup for FURA-2 experiments. Cells are transfected with the TRPML1 mutant and loaded with FURA-2. The luminal domain is expected to face the extracellular solution. Upon sybody/agonist-injection, FURA-2 fluorescence is measured. C) FURA-2 assay results with technical replicates (n=4) in TRPML1 and empty vector transfected cells. ML-SA5 agonist generates strong FURA-2 fluorescence specifically in TRPML1 transfected cells. Syb$^{(-)}$ was found not to increase FURA-2 signal, while Syb128 potentially slightly increases FURA-2 signal and activates the channel. Panel C was made by Johanna Hoffmann.

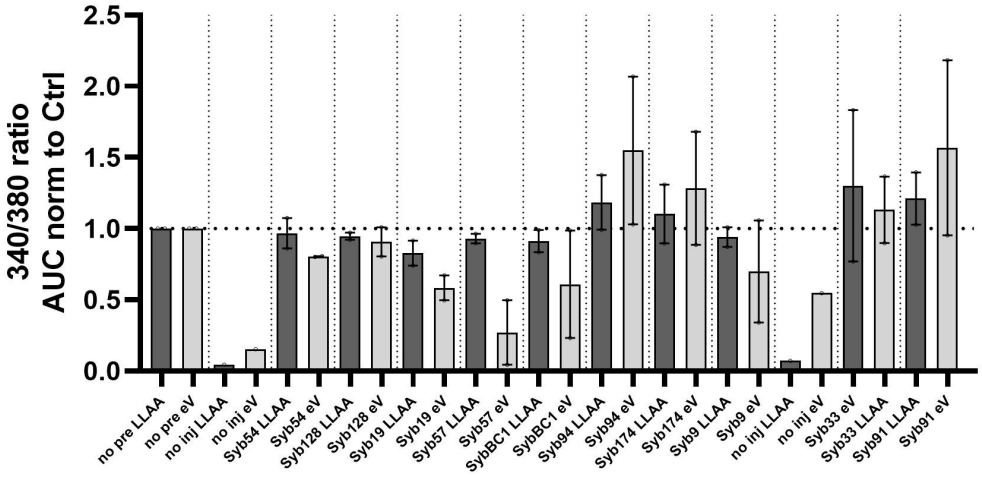

Supplementary Figure 11: FURA-2 assay with sybody pretreatment. Cells transfected with mutant TRPML1 (dark grey) or empty vector (light grey) were pretreated with sybody before the addition of TRPML1 agonist and FURA-2 fluorescence measurements. Results were normalized to the fluorescence of the control experiment (agonist without pretreatment in the matching cell line). Figure made by Johanna Hoffmann. Two biological replicates.

	TRPML1+Syb57	TRPML1+Syb94
cryoEM data collection and processing		
Magnification	81,000x	81,000x
Voltage (kV)	300	300
Camera	K3	K3
Dose (e-/Å^2)	49	49
Defocus range (μm)	-0.5 to -2.5	-0.5 to -2.5
Pixel size (Å/pixel)	1.07	1.07
Micrographs	2,496	5,522
Particles going into initial 3D reconstruction	184,003	901,209
Final particles	47,617	46,205
Symmetry	C4	C4
Map resolution, FSC=0.143, Masked/Unmasked (Å)	3.1/3.5	3.0/3.4
Map Sharpening B-factor (Å^2)	-93	-108
Model Refinement		
Model Composition		
Non-hydrogen atoms	17,500	17,084
Protein residues	2,188	2,156
Ligands	EUJ: 4	NAG: 8
B-factors (mean, Å^2)		
Protein	58.03	68.1
Ligand	125.2	69.82
R.M.S. deviations		
Bond lengths (Å)	0.003	0.002
Bond angles (°)	0.609	0.465
Validation		
MolProbity score	1.22	1.35
Clashscore	4.48	5.97
Rotamer outliers (%)	0.05	1.07
Cαβ BLAM (%)	0.58	1.16
Ramachandran plot		
Favored (%)	98.87	98.63
Allowed (%)	1.13	1.37
Disallowed (%)	0.00	0.00

Supplementary Table 1: Data collection and refinement statistics for TRPML1-Syb57 and TRPML1-Syb94 structures.

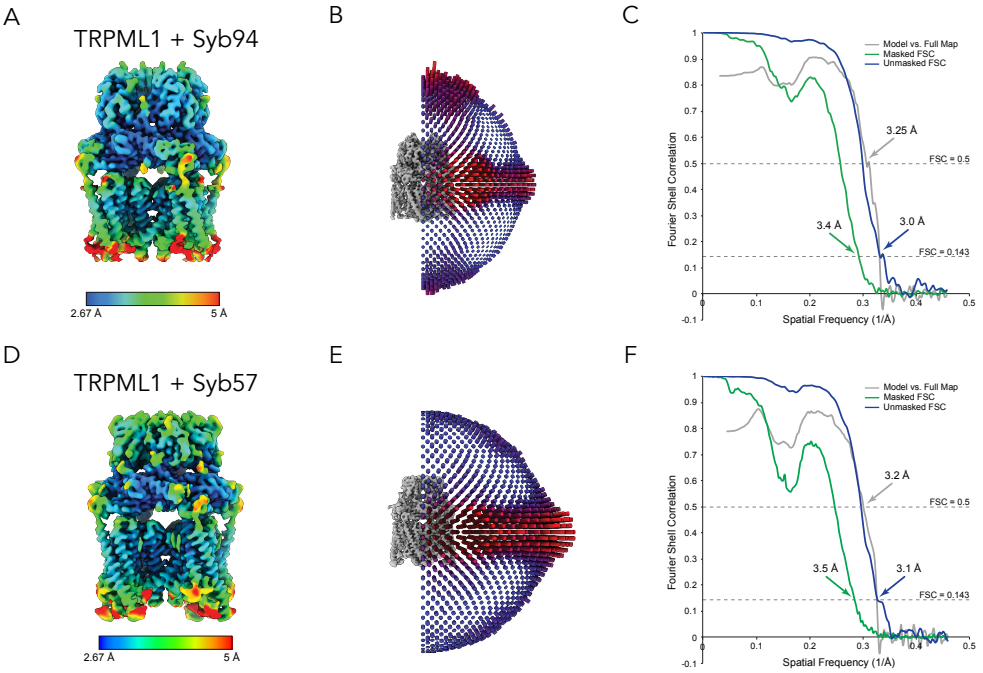

Supplementary Figure 12: Local resolution, angular distribution and FSC curves. A) Local resolution estimates for TRPML1-Syb94 complex. B) Angular distribution of TRPML1-Syb94 particles. C) Masked (green), unmasked (blue) and model to map (grey) FSCs. D) Local resolution estimates for TRPML1-Syb57 complex. E) Angular distribution of TRPML1-Syb57 particles. F) Masked (green), unmasked (blue) and model to map (grey) FSCs. Figure made by Dr. Ruth Pumroy.

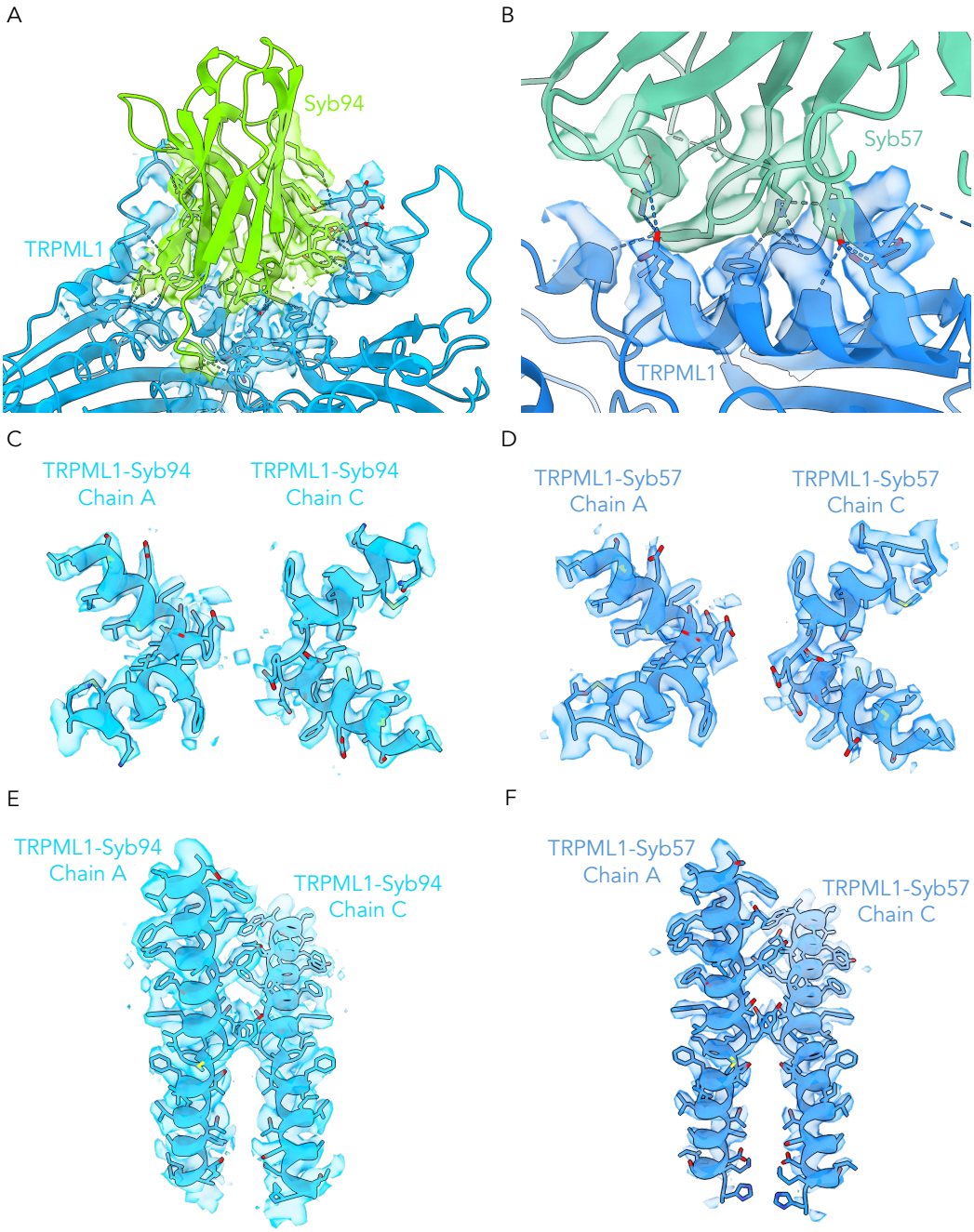

Supplementary Figure 13: EM density quality in key regions of the structures. A) EM density with cartoon and stick representation of the Syb94-TRPML1 interface (sybody contour: 0.237 and TRPML1 contour: 0.237) and B) Syb57-TRPML1 interface (sybody contour: 0.374 and TRPML1 contour: 0.22). C) EM density for the PHs and SF for the Syb94-TRPML1 structure (contour: 0.237) and D) Syb57-TRPML1 structure (contour: 0.297). Ion density is observed in the TRPML1-Syb94 selectivity filter map. E) EM density for the S6 helix in the Syb94-TRPML1 structure (contour: 0.237) and F) TRPML1-Syb57 structure (contour: 0.475).

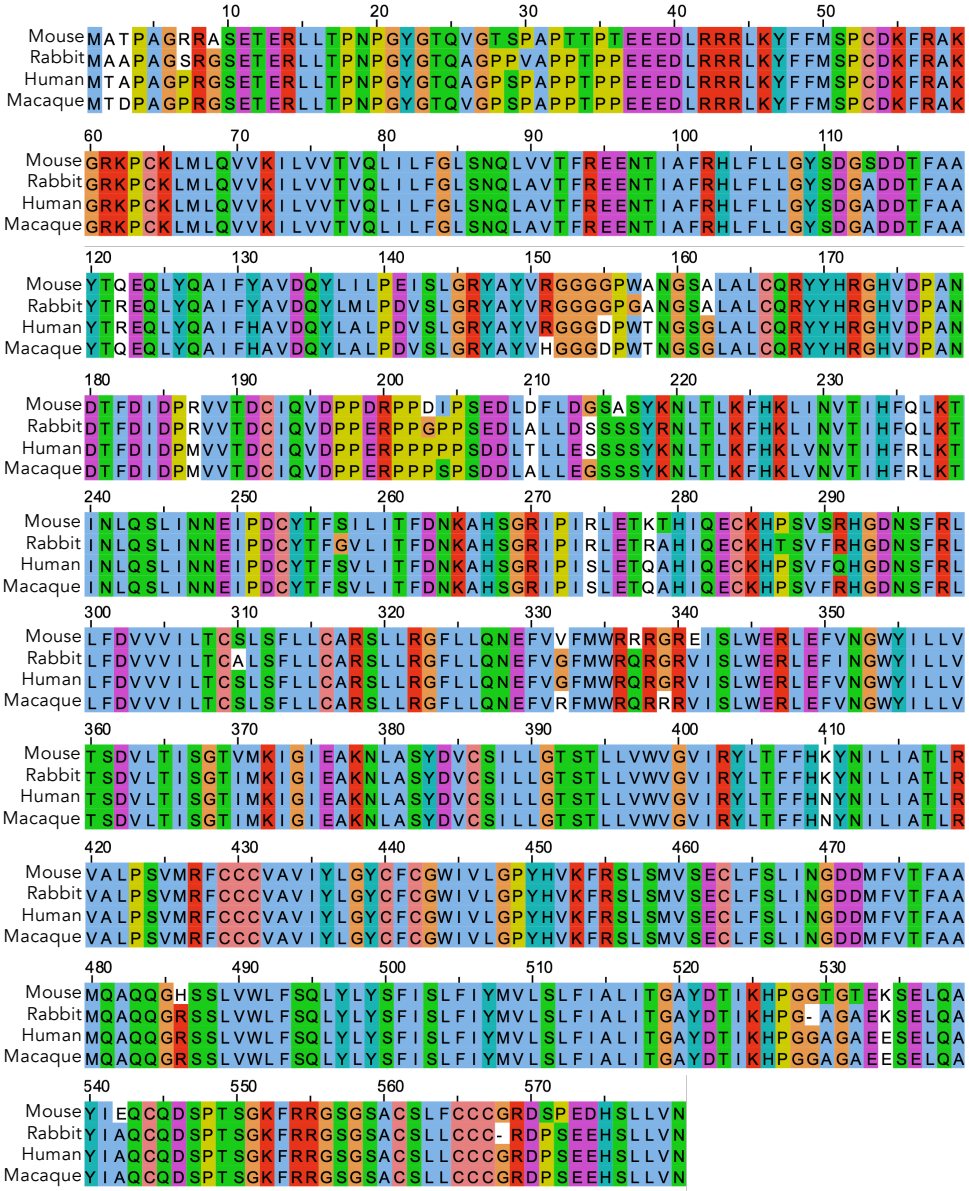

Supplementary Figure 14: Full-length TRPML1 homologs global sequence alignment. Sequences were obtained from uniprot (mouse: Q99J21; rabbit: G1T1X3; human: Q9GZU1; macaque: Q60HE8), the alignment was made using the uniprot alignment tool and displayed using JalView.

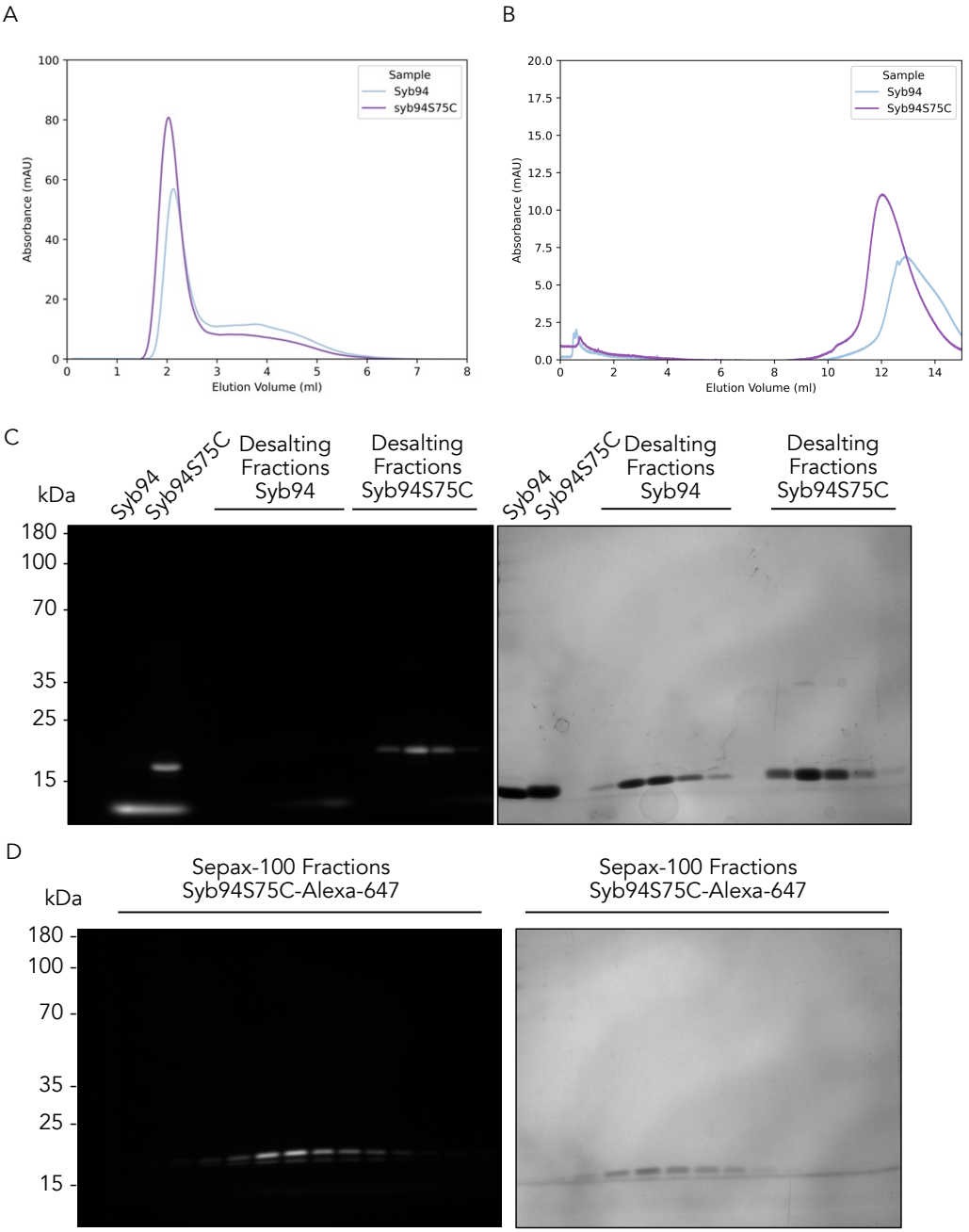

Supplementary Figure 15: Desalting and SEC of Syb94 WT (control) and Syb94S75C following labeling with Alexa Fluore-647. A) Desalting of Syb94 and Syb94S75C using a HiTrap Desalting column (Cytiva) connected to an Akta Go and equilibrated in PBS. B) SEC profile of Syb94 and Syb94S75C following desalting. Labeling has little effect on retention volume as the WT sybody, which was incubated with fluorophore but was not labelled successfully, has a similar retention volume to the labelled mutant. C) In-gel fluorescence (left) and Coomassie (right) for desalting (A) fractions or SEC fractions (B) ran on a 15% polyacrylamide gel.

A

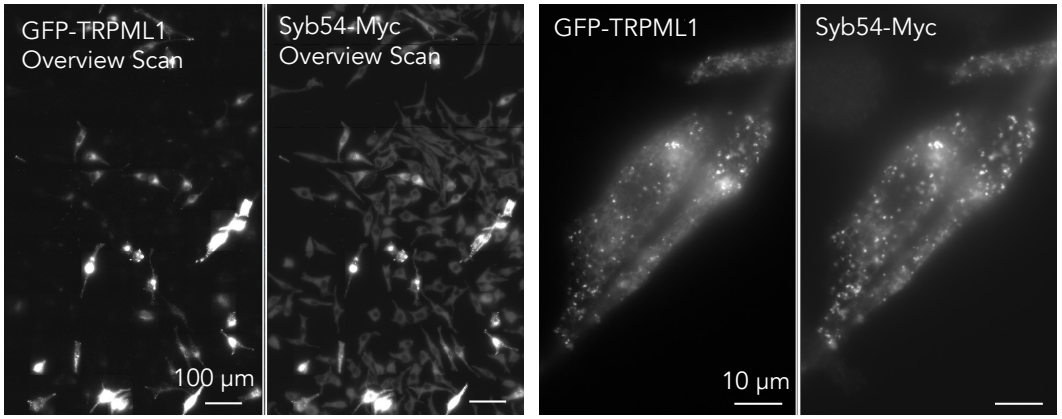
GFP-TRPML1
Overview Scan
Syb54-Myc
Overview Scan
GFP-TRPML1
Syb54-Myc
100 µm
10 µm

B

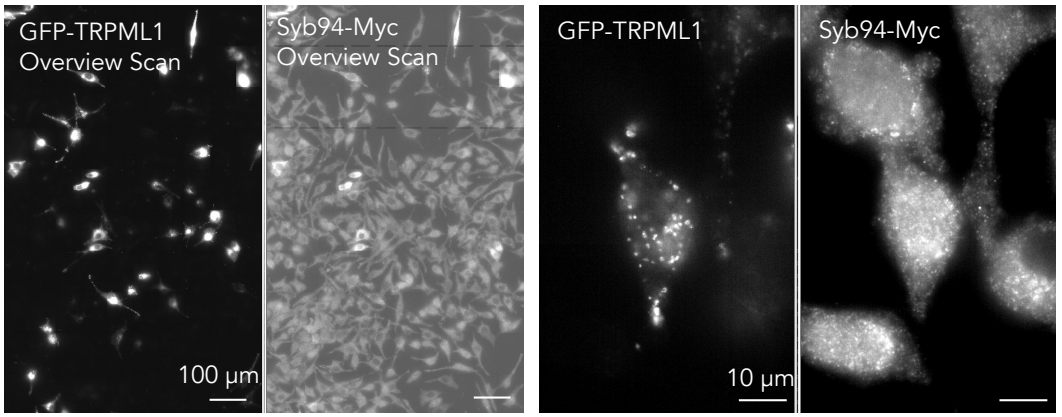
GFP-TRPML1
Overview Scan
Syb94-Myc
Overview Scan
GFP-TRPML1
Syb94-Myc
100 µm
10 µm

C

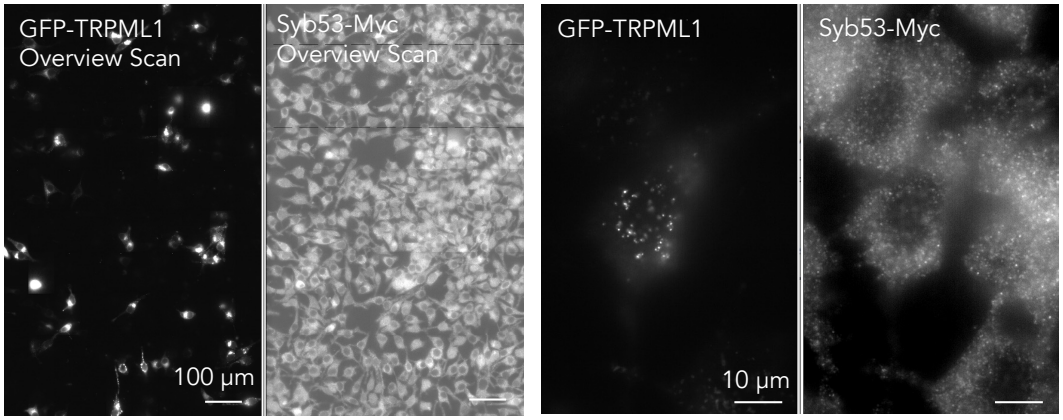
GFP-TRPML1
Overview Scan
Syb53-Myc
Overview Scan
GFP-TRPML1
Syb53-Myc
100 µm
10 µm

D

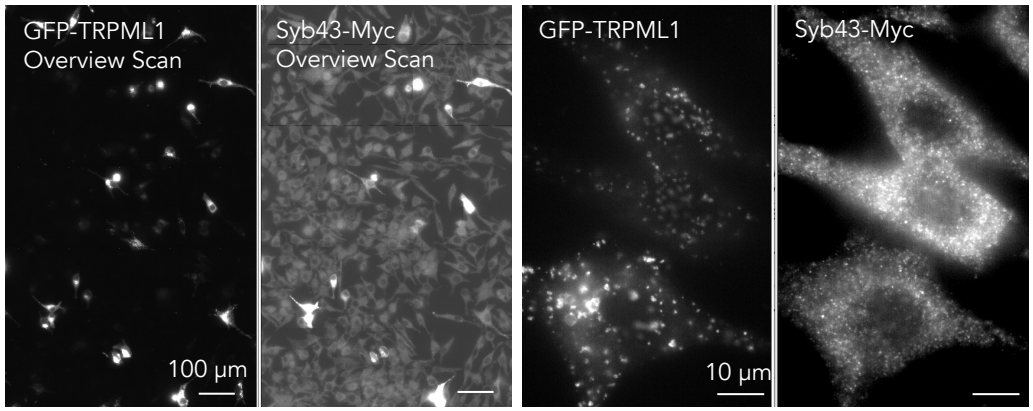

E

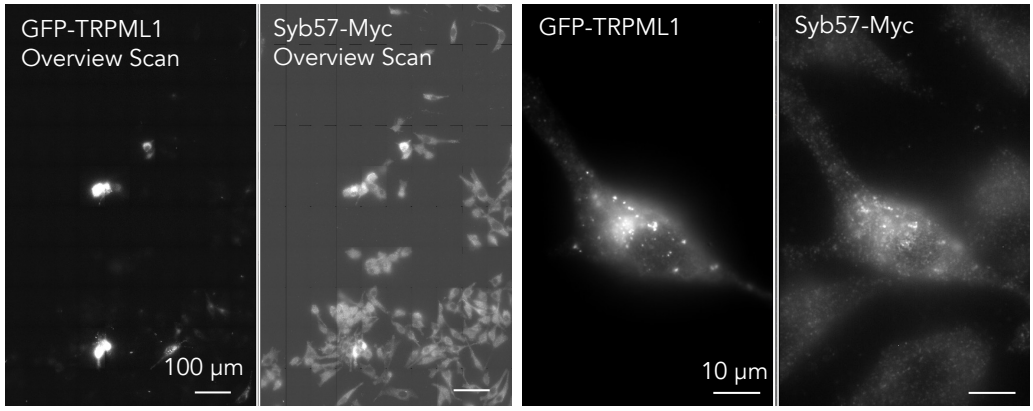

F

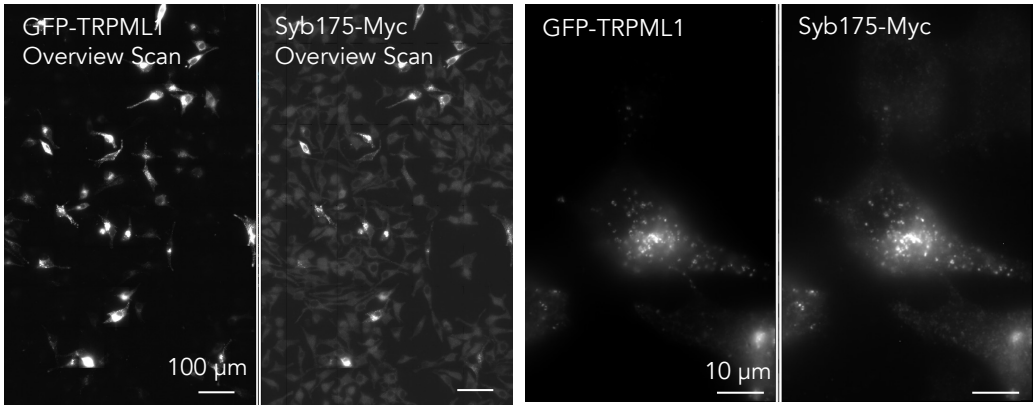

Supplementary figure 16: Overview scans (left) and conventional images of samples stained using the super-resolution protocol with sybody-Myc constructs (right). A-F) Images of immunostaining with super-resolution protocol on fixed and permeabilized GFP-TRPML1-transfected cells stained with sybody-Myc constructs, primary anti-Myc antibody and secondary antibody conjugated to Alexa Fluor-647. Overview scans are shown on the left and conventional images are shown on the right. Ranking of co-localization: Syb54, 175, 57, 43, 94 and 53.

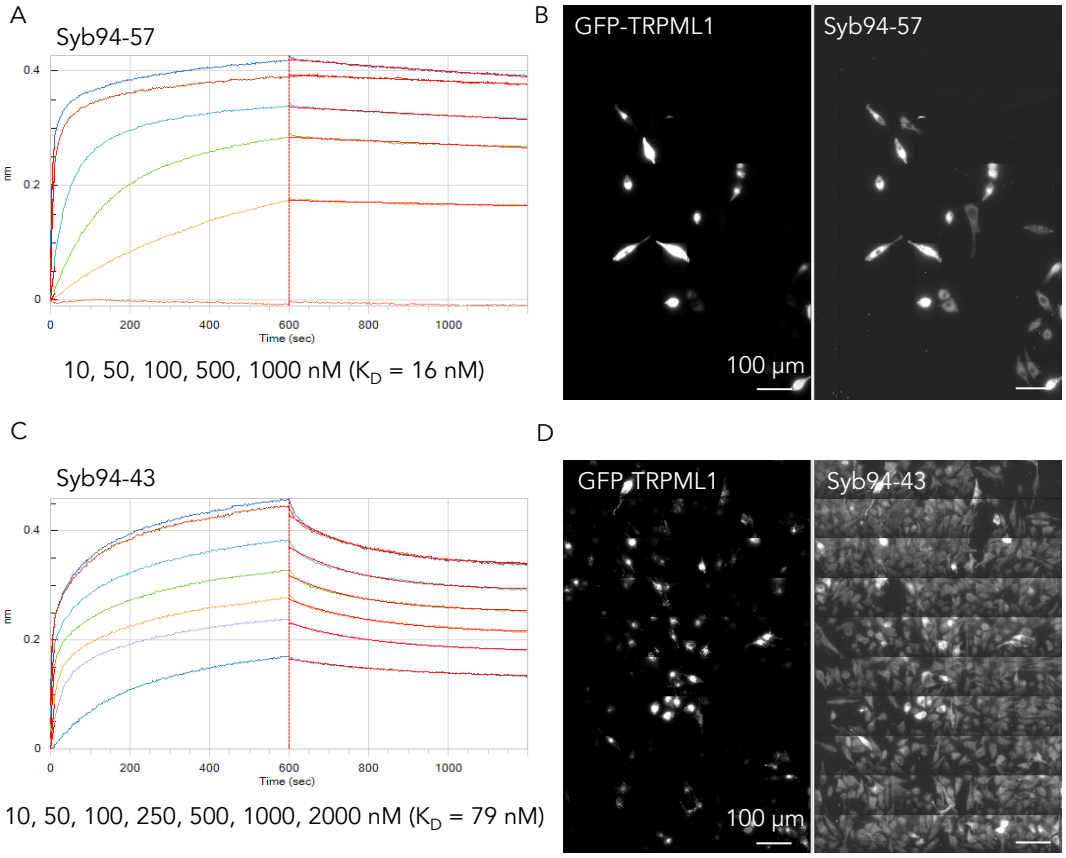

Supplementary figure 17: Kinetics and overview scans of immunostaining with 1D4-tagged sybody dimer constructs. A) BLI kinetics on full-length TRPML1 in LMNG with Syb94-57 at the displayed concentrations (below graph). Calculated K_D = 16 nM. B) Overview scan of immunostaining with Syb94-57-1D4 stained with anti-1D4 antibody and secondary antibody conjugated to Alexa Fluor-647 in GFP-TRPML1 transfected HeLa cells. C-D) Same experiments as A-B for Syb94-43 dimer. Calculated K_D = 79 nM.

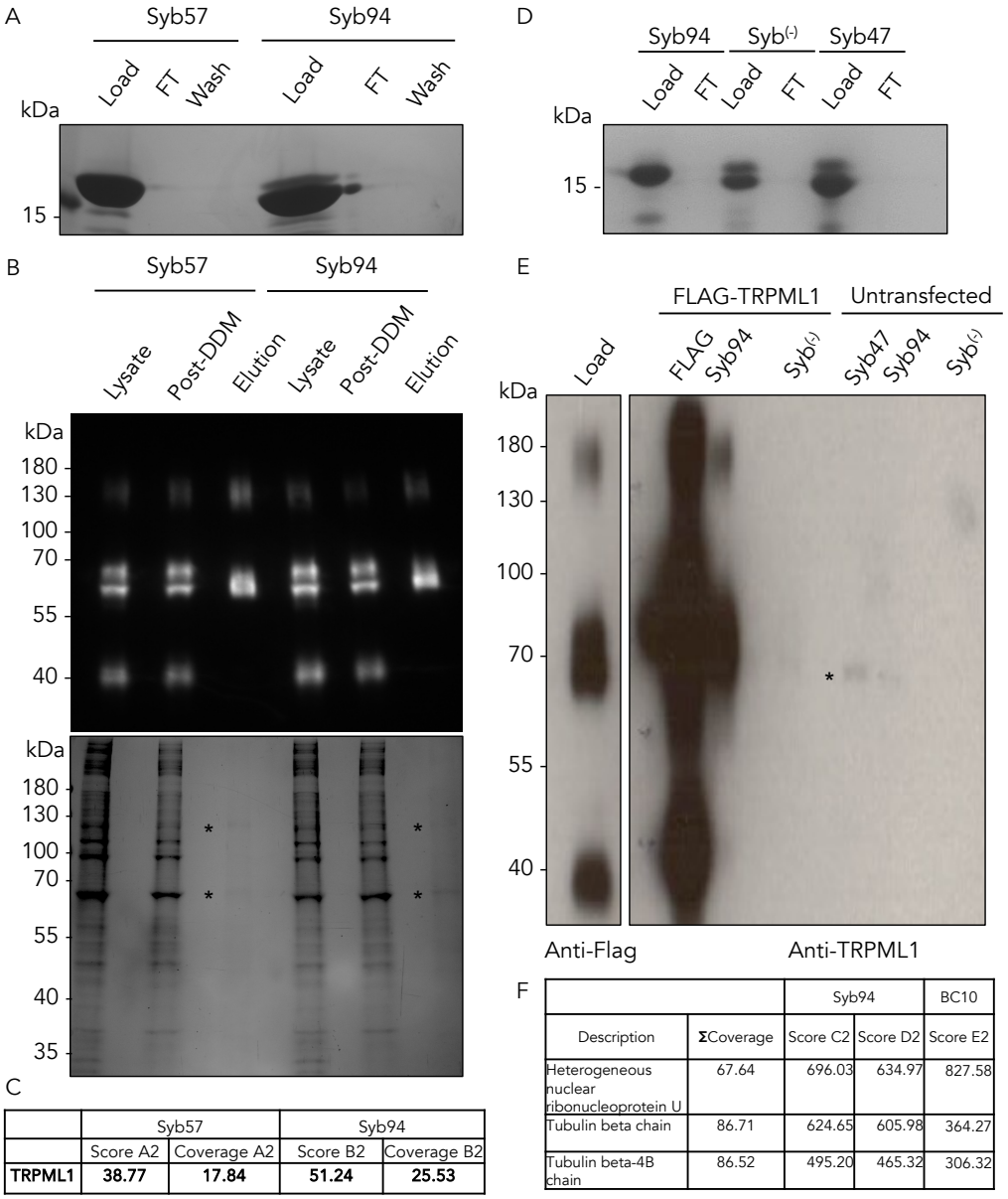

C

	Syb57		Syb94	
	Score A2	Coverage A2	Score B2	Coverage B2
TRPML1	**38.77**	**17.84**	**51.24**	**25.53**

F

		Syb94		BC10
Description	ΣCoverage	Score C2	Score D2	Score E2
Heterogeneous nuclear ribonucleoprotein U	67.64	696.03	634.97	827.58
Tubulin beta chain	86.71	624.65	605.98	364.27
Tubulin beta-4B chain	86.52	495.20	465.32	306.32

Supplementary figure 18: IP experiments with sybodies conjugated to NHS-activated resin. A,D) Syb47, Syb57, Syb94 and Syb$^{(-)}$ were successfully conjugated to the resin as the protein in the load is absent from the FT following the conjugation. B) Anti-FLAG western blot on IP samples obtained by solubilizing FLAG-AVI-TRPML1 overexpressing HEK-293F cells with DDM (Lysate and Post-DDM), incubating the resin with the post-DDM sample, washing it and eluted the sample with SDS loading buffer (anti-FLAG WB on top and Coomassie of the same gel at the bottom). C) TRPML1 was obtained as one of the top hits for a sample prepared with the same method for mass spectrometry D-E) The experiment was repeated with overexpressed (HEK-293F) and untransfected cells, but the enrichment was low in the TRPML1 WB (* is a potential TRPML1 band) and it was not detected in the mass spectrometry experiment.

Publication

nature communications

Article

https://doi.org/10.1038/s41467-022-32589-2

Structural basis for proton coupled cystine transport by cystinosin

Received: 20 April 2022

Accepted: 8 August 2022

Published online: 17 August 2022

Check for updates

Mark Löbel[1], Sacha P. Salphati[1,2], Kamel El Omari[3], Armin Wagner[3], Stephen J. Tucker[2,4], Joanne L. Parker[1] ✉ & Simon Newstead[1,4] ✉

Amino acid transporters play a key role controlling the flow of nutrients across the lysosomal membrane and regulating metabolism in the cell. Mutations in the gene encoding the transporter cystinosin result in cystinosis, an autosomal recessive metabolic disorder characterised by the accumulation of cystine crystals in the lysosome. Cystinosin is a member of the PQ-loop family of solute carrier (SLC) transporters and uses the proton gradient to drive cystine export into the cytoplasm. However, the molecular basis for cystinosin function remains elusive, hampering efforts to develop novel treatments for cystinosis and understand the mechanisms of ion driven transport in the PQ-loop family. To address these questions, we present the crystal structures of cystinosin from *Arabidopsis thaliana* in both apo and cystine bound states. Using a combination of in vitro and in vivo based assays, we establish a mechanism for cystine recognition and proton coupled transport. Mutational mapping and functional characterisation of human cystinosin further provide a framework for understanding the molecular impact of disease-causing mutations.

The lysosome is the main site of macromolecule degradation in mammalian cells and functions as a major signalling centre, integrating multiple inputs to regulate cellular metabolism via mTOR[1–3]. Central to lysosomal function and cell homoeostasis is the transport of amino acids across the lysosomal membrane via solute carrier (SLC) systems[4–6]. Solute carrier proteins are secondary active transporters that control the flow of nutrients between and within cells, often linked to ion gradients that function to concentrate nutrients and regulate levels in response to cellular energy demands[7–9]. Dysregulation of SLC function in the lysosome is linked to several lysosomal storage disorders, which are inherited metabolic diseases resulting from defective lysosomal function[10]. Mutations in the gene encoding cystinosin, *CTNS*, result in cystinosis, an autosomal recessive metabolic disease characterised by abnormal accumulation of cystine, the oxidised form of cysteine, inside lysosomes[11,12]. The *CTNS* gene was identified in 1998 and to date more than 140 mutations have been linked to nephropathic cystinosis in patients around the world[11,13]. Cystinosis often leads to renal Fanconi syndrome in paediatric patients, characterised by reduced kidney function and impaired growth and bone development due to mineral depletion[14]. Less severe forms of the disease result in blindness due to cystine crystallisation in the cornea, referred to as ocular cystinosis[15]. Defective lysosomal cystine transport also contributes to acute cellular oxidative stress, mitochondrial dysfunction, trafficking defects, and proteolysis defects in the cell[13,16,17]. However, a mechanistic link between cystinosis symptoms in patients and mutations in the *CTNS* gene is not fully established at the molecular level, hampering efforts to develop new treatments[18].

Cystinosin is a proton coupled lysosomal cystine transporter[19], which functions as the primary route for the export of cystine out of the lysosome (Fig. 1a). The transporter comprises seven transmembrane helices (TMs) and uses the outwardly directed proton electrochemical gradient, generated by the V-ATPase, to drive cystine export from the lysosome in a 1:1 stoichiometry[20]. Cystinosin is also a member of the so-called PQ-loop family[21,22], members of which function as trafficking receptors[23], lipid flippases[24], amino acid transporters[25] and sugar transporters in plants and mammals[26]. Eukaryotic PQ-loop

[1]Department of Biochemistry, University of Oxford, Oxford, UK. [2]Clarendon Laboratory, Department of Physics, University of Oxford, Parks Road, Oxford, UK. [3]Diamond Light Source, Harwell Science and Innovation Campus, Didcot, UK. [4]Kavli Institute for Nanoscience Discovery, University of Oxford, Oxford, UK. ✉e-mail: Joanne.parker@bioch.ox.ac.uk; Simon.newstead@bioch.ox.ac.uk

https://doi.org/10.1038/s41467-022-32589-2

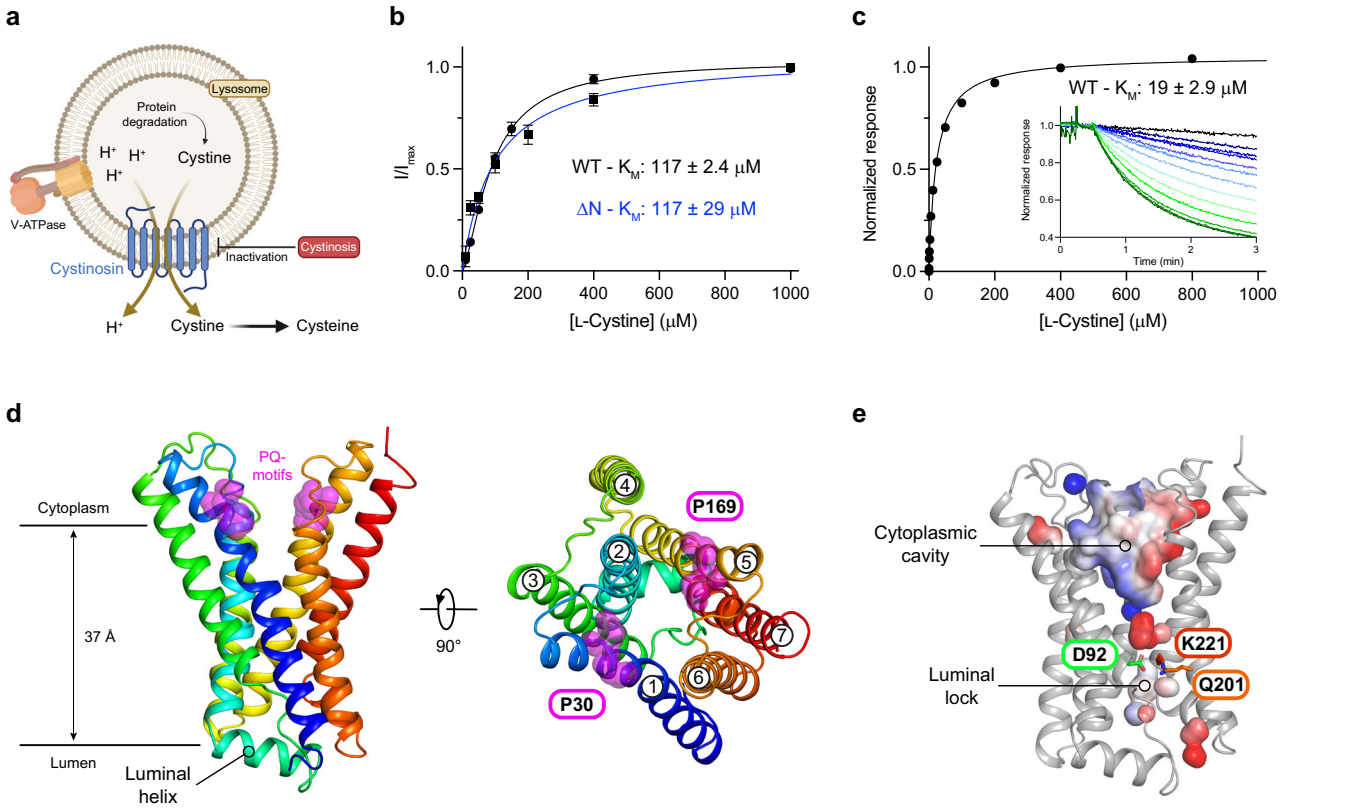

Fig. 1 | Functional characterisation and structure determination of cystinosin. **a** Cystinosin resides within the lysosomal membrane where it is responsible for the export of cystine from the lysosomal lumen. Transport is proton coupled, utilising the proton gradient across the membrane generated through the action of V-ATPase. Mutation of the CTNS gene, which encodes cystinosin, lead to cystinosis. **b** Representative K_M curve derived from TEVC for full length human cystinosin (WT – black) and a construct lacking N-terminal amino acids 2-115 (ΔN – blue). $n = 16$ independent experiments for every WT data point, $n = 10$ for ΔN, error bars SEM. K_M values were calculated from three biologically independent experiments, error SD. **c** Representative K_M analysis of plant cystinosin derived using a pyranine based in vitro assay. K_M was calculated from three independent experiments, error SD. Inset shows a typical set of raw data generated from the assay (lines are coloured according to cystine concentration dark green 800 via lighter colours to dark blue 0 µM). **d** Crystal structure of plant cystinosin with helices coloured blue to red from the N-terminus. Highlighted (magenta spheres) are the two PQ loop motifs which sit in the open cavity facing the cytoplasm in the conformation captured in the structure. **e** View of cystinosin highlighting the salt bridge network which forms the luminal lock and seals the binding site on the luminal side. Source data are provided as a Source Data file.

proteins contain two PQ-motifs, located on TM1 and TM5, which play important roles in facilitating the structural changes required for alternating access transport within these proteins[22,27].

Insights into the structural changes that occur in transporters belonging to the PQ-loop family were revealed through crystal structures of the bacterial PQ-loop transporters, which were captured in both the inward (cytoplasmic) and outward (extracellular) states of their transport cycles[27–29]. However, unlike eukaryotic PQ-loop family transporters, the bacterial homologues are obligate dimers, consisting of two 3-TM domains and function as facilitators, allowing sugar molecules to equilibrate across the membrane[30]. Although a plant homologue of the bacterial semi-SWEET transporters was also crystallised[31], revealing the architecture of the eukaryotic hepta-helical PQ-fold, we still have little insight into how PQ-loop transporters couple ligand binding and transport to secondary ion gradients. Previous work on human cystinosin, using two electrode voltage clamp (TEVC) assays, revealed the presence of several conserved aspartate residues, one of which undergoes reversible protonation during transport[20]. Cystine binding was proposed to alter the pK_a of this side chain, providing a mechanistic link for coupled transport. However, several key questions concerning the mechanism of cystinosin remain, including how cystine is recognised, how proton binding and release drive the full transport cycle and the rationalisation of patient mutations within the mechanism of transport.

To address these questions and understand the molecular basis for proton coupled cystine transport, we determined the structure of the plant cystinosin transporter from *Arabidopsis thaliana*. Using both Llama derived[32] and synthetic nanobodies[33], cystinosin was captured in both apo and ligand bound states, revealing a key role for conserved lysine side chains in cystine recognition. Combined with in vitro transport assays and TEVC comparisons on the human transporter we propose a mechanism for proton coupled cystine transport across the vacuolar and lysosomal membranes.

Results

Characterisation of *Arabidopsis thaliana* cystinosin

To identify homologues of cystinosin suitable for structural and biochemical analysis we screened several homologues from different organisms (Supplementary Fig. 1a). The homologue from *Arabidopsis thaliana* showed high expression levels in our yeast-based system[34] relative to other homologues and was therefore chosen for further analysis. Cystinosin from *A. thaliana*, however, does not contain the N-terminal lysosomal luminal domain found in human and other eukaryotic cystinosin proteins (Supplementary Fig. 1b), prompting us to determine the importance of this domain for transport function. Analysing the human transporter expressed in *Xenopus laevis* oocytes and measuring currents elicited by L-cystine under two electrode voltage clamp (TEVC), we found that the N-terminal domain of the human transporter does not impact the transport kinetics, with both having

Table 1 | X-ray data collection and refinement statistics

		S-SAD data	Cystinosin apo (Syb39 & Nb4)	Cystinosin apo (Nb1 & Nb4)	Cystinosin cystine complex (Syb39)
Data collection	PDB	–	7ZK1	7ZKZ	7ZKW
	Space group	$P\,2_1\,2_1\,2$	$P\,2_1\,2_1\,2$	$C\,2$	$C\,2$
	Cell dimensions a, b, c (Å)	62.60, 319.49, 45.48	62.79, 319.96, 45.65	210.28, 77.46, 46.30	283.37, 64.07, 55.44
	Cell angles α, β, γ (°)	90, 90, 90	90, 90, 90	90, 93.25, 90	90, 99.95, 90
	Wavelength (Å)	2.7552	0.9999	0.9795	0.9762
	Resolution (Å) [a]	29.24–3.20 (3.28–3.20)	79.99–2.65 (2.69–2.65)	104.76–2.33 (2.37–2.33)	70.10–3.37 (3.52–3.37)
	CC1/2 (%) [a]	99.9 (67.1)	99.8 (35.7)	99.5 (42.7)	79.7 (10.0)
	R_{pim} (%) [a]	5 (99.2)	11.4 (227.6)	7.2 (91.7)	49.7 (120.5)
	I/σI [a]	13.7 (1.1)	5.9 (0.4)	7.9 (0.6)	2.0 (0.6)
	Completeness (%) [a]	99.7 (99.5)	100 (99.9)	100 (100)	99.7 (95.3)
	Multiplicity [a]	44.6 (38.6)	23.9 (13.3)	6.4 (6.7)	6.1 (5.9)
Refinement	Resolution (Å)		79.99–2.65	20.79–2.33	69.78–3.37
	Number of reflections		26170	31641	12426
	R_{work}/R_{free}		23.4/27.49	23.5/26.5	23.5/27.7
	F_o,F_c correlation		0.83	0.94	0.83
	Average B, all atoms (Å^2)		84.8	66.9	67.5
R.m.s deviations	Bond lengths (Å)		0.009	0.008	0.014
	Bong angles (°)		1.05	0.97	1.55
	Ramachandran statistics Favoured/outliers (%)		91.55/2.47	97.88/0.64	89.72/2.50
	Molprobity score		2.97	1.77	2.94

[a]Highest resolution shell shown in parentheses.

similar K_M values for cystine (117 ± 2.4 µM for WT compared to 117 ± 28.9 µM for the Δ2-115 variant) (Fig. 1b & Supplementary Fig. 2a). We then determined the K_M for cystine transport using a reconstituted system and employed pyranine to monitor proton movement[35]. These results establish *A. thaliana* cystinosin as a proton coupled cystine symporter with a K_M for cystine of 19 ± 2.9 µM, (Fig. 1c & Supplementary Fig. 2b) suggesting a slightly higher affinity for L-cystine than the human protein. Having established the plant transporter as a suitable functional homologue of human cystinosin, we sought to determine the structure using crystallisation in the lipidic cubic phase.

Structure of cystinosin

Single chain binders have been successfully used to obtain the structures of small, dynamic membrane proteins[36]. Using a similar strategy to our recent work on the KDEL receptor[23], we screened both a synthetic nanobody (sybody) library and a library generated via llama immunisation to identify specific binders to cystinosin (Supplementary Fig. 3). The structure was initially determined in complex with both a cytoplasmic binding sybody and luminal binding nanobody to 2.65 Å and phases calculated using long wavelength sulfur single wavelength anomalous dispersion (S-SAD) (Table 1 & Supplementary Fig. 4a). The transporter adopts a compact V-shaped structure, consisting of seven transmembrane (TM) alpha helices and adopts an inward (cytoplasmic) open state, with the CDR3 loop of the sybody (Syb39) extending into the cytoplasmic entrance of the binding site (Fig. 1d & Supplementary Fig. 4b). On the luminal side of the transporter the llama derived nanobody (Nb4) interacts with the N-terminus of TM1 and the luminal end of TM7 (Supplementary Fig. 4a, b). Within the crystal the binders act to bridge two of the transporters together, aiding crystal packing within the lipidic cubic phase. We also identified a second binder combination, consisting of two llama nanobodies, which diffracted to a slightly higher resolution of 2.33 Å (Table 1). The structures of the transporter in both crystal forms are very similar (root mean square deviation (RMSD) of 0.776 Å over 224 C_α atoms), with the only difference being loss of density for the cytoplasmic end of TM4 and the connecting loop to TM5 in the 2.33 Å structure (Supplementary Fig. 4c, d).

The structure has similarities to both the eukaryotic SWEET transporter, the bacterial semi-SWEET transporters and KDEL receptor[23,28,29,31], although with some notable differences. Cystinosin aligns with the previously determined SWEET transporter from *Oryza sativa* (rice) with an RMSD of 4.9 Å over 208 C_α atoms, which also adopts an inward open conformation[31]. However, the inversion helix (TM4) is positioned closer to TM5 forming a more spherical molecule. Another notable difference observed in cystinosin is the presence of a luminal helix connecting TM2 and TM3. This feature is likely to be present in all cystinosin homologues given the sequence conservation in this region (Supplementary Fig. 1b) and as discussed below, may play an important role in the transport mechanism by stabilising a shortunwound region of TM3. PQ-loop transporters contain a pair of three TM bundles, TMs 1-3 and TMs 5-7, which frame a central binding site[27]. In the structure of cystinosin, a polar cavity extends 23 Å into the centre of the transporter from the cytoplasmic side of the molecule, which contains a high density of positively charged side chains (Fig. 1e). The positive charges continue down into the binding site, which is dominated by the presence of two lysine side chains Lys55 (TM2) and Lys166 (TM5) and His56 (TM2), which as discussed below play an important role in cystine recognition. The luminal side of the transporter is sealed through the packing of TMs 3, 6 and 7, which are stabilised through interactions between Asp92 (TM3), Gln201 (TM6) and Lys221 (TM7) (Fig. 1e). This interaction network is strictly conserved within cystinosin homologues and as discussed below plays an important role in the transport mechanism.

Molecular basis for cystine recognition

To understand the structural basis of the recognition and transport of cystine we employed our previous binder trap methodology to stabilise the ligand bound state for structure determination[37]. Following

https://doi.org/10.1038/s41467-022-32589-2

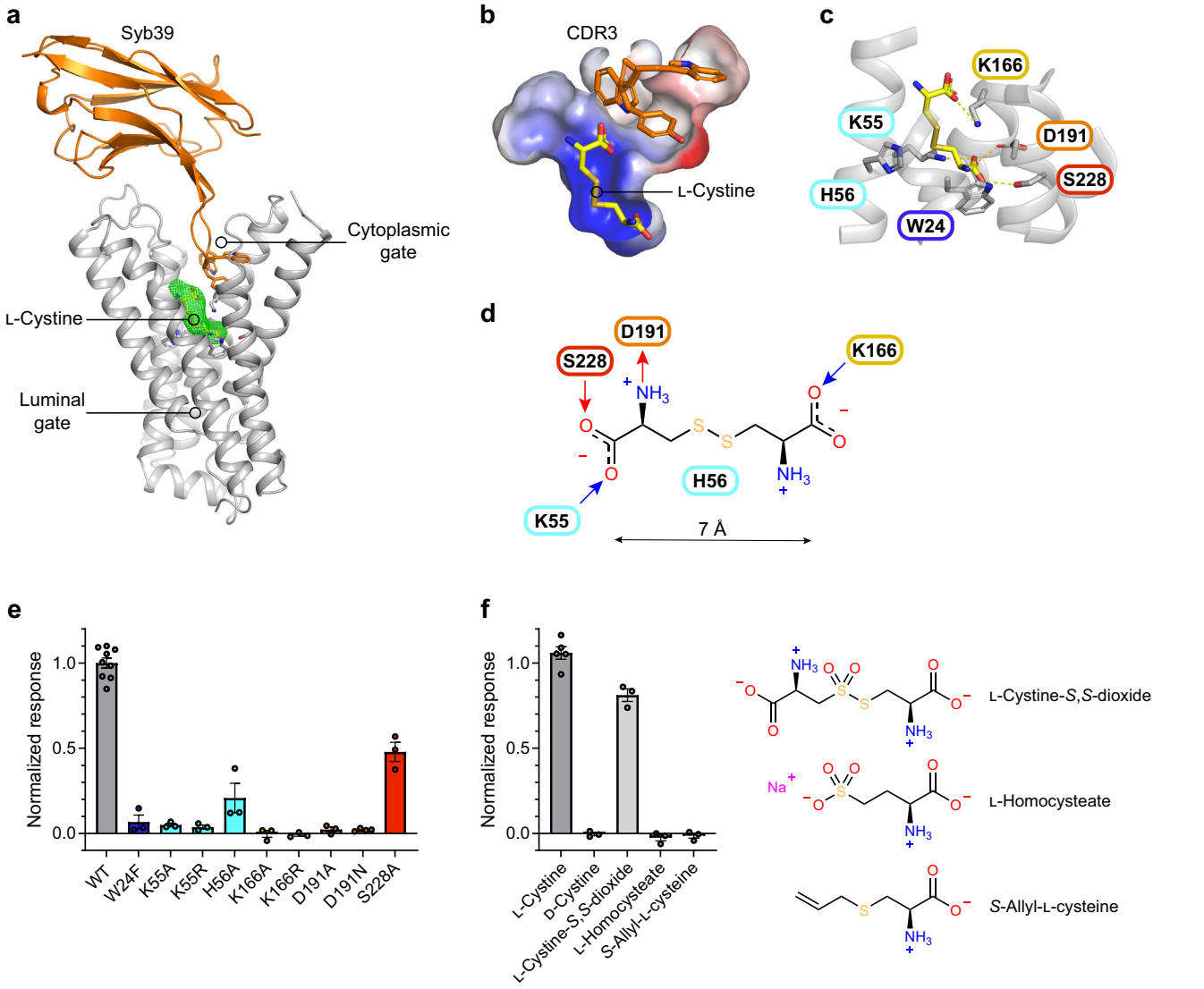

Fig. 2 | Structural basis for L-cystine recognition. a Crystal structure of cystinosin showing sybody 39, which aided in trapping the cystine ligand within the binding site. Cystine mFo-DFc difference electron density map (green mesh) contoured at 3σ. **b** The central binding site is positively charged complementing the negative charge on cystine. **c** Zoomed in view of the binding site showing the interaction network between cystinosin and cystine. **d** Schematic of cystine highlighting key interactions in the binding site. **e** Impact of binding site variants on cystine transport using a pyranine based in vitro assay. All variants were tested using 200 µM L-cystine. $n = 3$ independent experiments for variants ($n = 4$ for D191N) and $n = 9$ for WT, error bars SEM. **f** Substrate specificity of cystinosin analysed using a pyranine based in vitro assay system. All substrates were tested at 500 µM. $n = 5$ for L-cystine and $n = 3$ for all other substrates, error bars SEM. Source data are provided as a Source Data file.

several rounds of screening with different binder combinations we determined the structure of the ligand bound state in complex with Syb39 to 3.37 Å (Table 1). The ligand bound conformation of cystinosin is very similar to the apo state, with an RMSD of 0.48 Å over 240 C_α atoms. The cystine ligand was clearly resolved in the electron density map and sits at the base of the polar pocket observed in the apo state (Fig. 2a, b). Cystine adopts an extended conformation within the binding site and makes several notable interactions to conserved side chains (Fig. 2c, d). Cystine can exist in three different ionic forms depending on the pH of the environment[38]. Within physiological pH the carboxyl groups will be fully dissociated, however, the two amino groups have different pKa values of 7.48 and 9.02. Our crystallisation trials were conducted at pH 6.5, favouring the zwitterionic form of cystine, which we modelled into the structure. Indeed, we observe a salt bridge interaction between one of the amino groups of cystine and Asp191 (TM6). In addition, we observe two further salt bridge interactions between the two carboxylate groups and Lys55 (TM2) and Lys166 (TM5). A further hydrogen bond interaction is made to a conserved serine, Ser228 (TM7). The disulfide bond is sandwiched between Lys166 (TM5) and His56 (TM2), which would help to stabilise the delocalised negative charge, whereas the second amino group makes no specific interactions and points towards a hydrophobic cavity between TM2 and TM3.

To assess whether these observed interactions are important for L-cystine transport, we generated a series of variants in the plant transporter and tested their function using both a pyranine-based transport assay and a differential scanning fluorimetry (nanoDSF) binding assay. We found that alanine variants of the main interaction sites Lys55, Lys166 and Asp191, resulted in inactive protein in both assays (Fig. 2e and Supplementary Fig. 5). Furthermore, even conservative mutations of these side chains to arginine and asparagine respectively, could not recover transport activity, highlighting their importance to the mechanism. Interestingly the tryptophan, Trp24, which sits at the base of the binding site, is also important for L-cystine uptake, with even a

https://doi.org/10.1038/s41467-022-32589-2

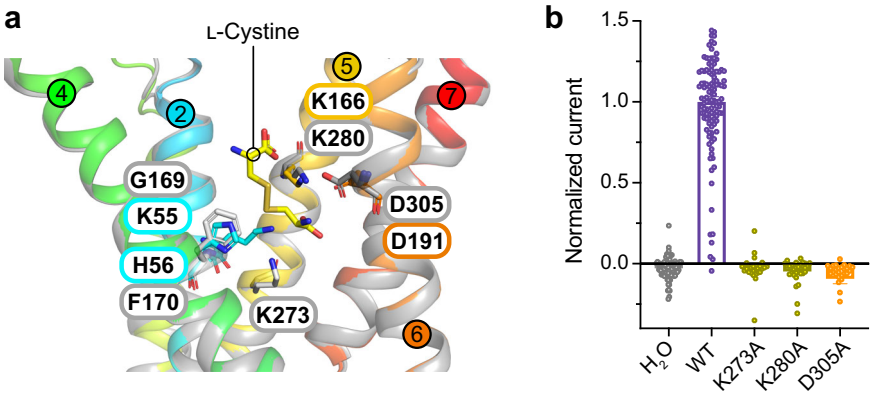

Fig. 3 | Differences in the binding site between plant and human cystinosin. **a** Structural superimposition of the plant crystal structure (coloured helices and numbers) and human AlphaFold2 model (grey) revealing the movement of key residues within the binding site. **b** TEVC data showing the effect of mutations within the binding site of human cystinosin. $n = 109$ independent experiments for H_2O, $n = 113$ for WT, $n = 28$ for K273A and D305A, $n = 30$ for K280A, error bars SEM. Source data are provided as a Source Data file.

conservative mutation to phenylalanine only exhibiting ~10% WT transport levels. In the binding assay this variant loses ~50% binding. Together these results suggest a possible cation-π interaction with the amino group that sits ~3.4 Å away in the binding site and demonstrates an essential role for Trp24 in the conformational changes required for transport. The His56Ala variant retained ~20% transport activity, indicating that this side chain is not essential for L-cystine recognition. L-Cystine also contacts Ser228 in the base of the binding site. An alanine variant of this side chain reduces both binding and transport by ~50%, indicating this side chain plays only a supporting role in transport (Fig. 2e and Supplementary Fig. 5).

A noticeable feature of the L-cystine binding pose are the interactions observed between the two carboxylate groups of the ligand and the Lys55 and Lys166 side chains. To assess the importance of these interactions we screened a library of structural analogues of L-cystine (Fig. 2f). We observed that only L-cystine-*S*,*S*-dioxide, which contains two carboxylates could be transported, at ~80% WT levels and consistent with previous assays conducted using the human transporter[20]. The uptake of L-cystine-*S*,*S*-dioxide also suggests that the position of the disulfide group is likely to be flexible to accommodate the additional two carbonyl groups which bind to one sulfur atom of the disulfide, consistent with our crystal structure. Interestingly, neither *S*-allyl-L-cysteine, which has an amino acid group replaced with an allyl group, nor L-homocysteate, which contains a sulfonate group in place of the second L-cysteine moiety, could be transported. These results show that the length of the ligand, in addition to the presence of the two carboxylate groups is important. Finally, D-cystine was also not transported, demonstrating that cystinosin is stereospecific. These results thus establish a preliminary binding model for plant cystinosin (Fig. 2d) emphasising the importance of the two salt bridges and an ideal distance of ~7 Å between the two carboxylate groups.

We next compared our structure to that predicted by AlphaFold2 for the human protein[39]. Many of the side chains identified in the binding site of plant cystinosin are strictly conserved within the human transporter, nevertheless, notable differences exist. In human cystinosin the equivalent side chain to His56 is phenylalanine (Phe170) and Lys55 is a glycine (Gly169) (Supplementary Fig. 1b). However, the AlphaFold2 model shows that in the human transporter a lysine, Lys273, extends from TM5 to sit in a similar position in the binding site (Fig. 3a). Using our oocyte transport assay, we tested the Lys273Ala variant and found this lysine is essential for function (Fig. 3b & Supplementary Fig. 6), similar to the structurally equivalent lysine in plant cystinosin. We then analysed the alanine variants of Lys280 and Asp305, which are the equivalent side chains to Lys166 and Asp191 in the plant transporter. These side chains are also essential for L-cystine transport, highlighting an evolutionary conserved mechanism of L-cystine recognition.

Mechanism of cystine transport

Secondary active transporters operate via an alternating access mechanism, whereby the transporter switches between outward and inward facing states to move ligands and ions across the membrane[40]. Within the PQ-loop family, alternating access transport is understood to occur following the symmetrical movement of helices within the two 3TM bundles[22]. Specifically, the PQ-motifs on TM1 and TM5 are required to enable the bending of these helices to open and close the intracellular gate in response to ligand and/or ion binding. In the plant SWEET transporter, the glutamine residues are absent from both PQ-motifs, with the transporter still functional in cells, however, the prolines were essential for function[31]. Therefore, to understand the role of the prolines within the transport mechanism of cystinosin, we assayed the proline to alanine variants in the human and plant transporters (Fig. 4a). In human cystinosin the proline of the first PQ-motif is dispensable, with transport levels of an alanine variant exhibiting ~75% WT levels. The equivalent alanine variant in plant cystinosin proved too unstable to purify and assay, however, a glycine variant was stable and surprisingly exhibited almost WT transport levels (~90%) (Fig. 4a & Supplementary Fig. 5c). We next analysed the Pro169Gly variant using our binding assay, and discovered that although this variant and the Pro169Ala variant are transport defective, it still retains WT levels of L-cystine binding (Supplementary Fig. 5a). Together, these results indicate the second PQ-motif proline facilitates the conformational changes during transport. The importance of the second PQ-motif proline is perhaps explained through its proximity to Lys166, which sits adjacent to Tyr167 and Asp191 (Supplementary Fig. 7a). Scanning mutagenesis previously identified the equivalent aspartate in the human transporter, Asp305, as being a potential site of proton binding[20].

To further explore the role of these side chains in cystinosin, we mutated Asp191 to asparagine and Tyr167 to phenylalanine. Interestingly, we observed increased proton flux through the Tyr167Phe variant, as measured using our pyranine-based assay (Supplementary Fig. 7b), indicating that either more protons are moving during the transport cycle or that the kinetics of transport have been altered. However, when we analysed the uptake of radioactive cystine we also observed an increase in the amount of substrate moved (Supplementary Fig. 7c). Further kinetic analysis of the Tyr167Phe variant demonstrated that Vmax increased ~30% relative to WT and the K_M increased from 19 µM to 73.3 ± 12.8 µM (Fig. 4b), confirming the role of this side chain in

https://doi.org/10.1038/s41467-022-32589-2

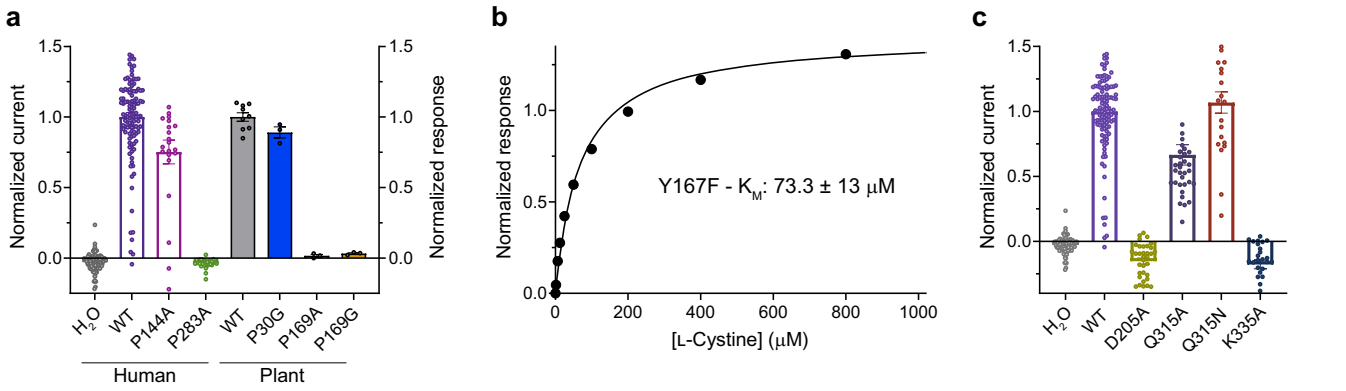

Fig. 4 | Role of PQ motifs in cystinosin. a Effect of mutating the PQ motifs in both human and plant (*A. thaliana*) cystinosin. The human protein was assayed using TEVC ($n = 109$ independent experiments for H_2O, $n = 113$ for WT, $n = 22$ for P144A and $n = 31$ for P283A) whereas the plant transporter was analysed in reconstituted liposomes ($n = 9$ independent experiments for WT and $n = 3$ for variants). Error bars SEM. **b** Representative K_M of plant cystinosin variant Tyr167Phe. K_M was calculated from three independent experiments, error SD. **c** Summary data showing the effect of mutations on the proposed luminal lock of human cystinosin expressed in Xenopus oocytes. $n = 109$ independent experiments for H_2O, $n = 113$ for WT, $n = 35$ for D205A, $n = 34$ for Q315A, $n = 22$ for Q315N, $n = 27$ for K335A, error bars SEM. Source data are provided as a Source Data file.

regulating transport kinetics. These results are consistent with the previous analysis of the human transporter and demonstrate that Tyr167 is important for modulating L-cystine recognition[20]. In contrast, the asparagine 191 variant displayed a marked, but slow proton leak and was unable to transport L-cystine, suggesting this variant is uncoupled (Supplementary Fig. 7d). The presence of a slow proton leak indicates a second site of proton binding is involved to gate the transporter, consistent with suggestions from the previous functional analysis using TEVC[20]. Our structure highlighted an interaction between Asp92 on TM3 with Lys221 on TM7 and Gln201 on TM6, which forms the only inter bundle salt bridge between the two 3TM repeats (Fig. 1e). Alanine variants of these side chains proved too unstable to purify (Supplementary Fig. 5c), highlighting their importance for structural stability. To address the role of these side chains in the transport mechanism of cystinosin, we made the equivalent mutations in the human transporter and assayed their function using our TEVC assay (Fig. 4c). Unlike the plant variants, the human proteins all expressed in the oocytes (Supplementary Fig. 6). Our results indicate that whilst the glutamine in the human transporter (Gln315) is not required for function, both the aspartate (Asp205) and lysine (Lys335) are essential and as discussed below, mutation of Asp205 to asparagine in the human transporter leads to infantile cystinosis[41].

As noted above, a major difference between human and plant cystinosin is the presence of His56 on TM2, which is located close to the disulfide bond of the ligand (Fig. 2b). In the human protein, His56 is a phenylalanine; however, a His56Phe plant cystinosin variant was still functional, displaying ~50% WT activity (Supplementary Fig. 7e). Although this side chain is not essential for transport, the proximity to Lys55 suggested a functional role, which combined with the slightly different pH environments found between the plant vacuole and mammalian lysosome[42,43], prompted us to study the effects of different pH conditions on the His56Phe variant in the plant transporter. The WT transporter shows transport activity across a wide pH range (6.5–8.2), whereas the His56Phe variant is unable to transport at pH 6.5 but remains functional at pH 7.2 and 8.2 (Supplementary Fig. 7e). As the pH gradient across the plant tonoplast membrane is less steep than observed in mammalian lysosomes, this adaption may have evolved to facilitate more efficient transport under the conditions found within plant cells.

Discussion

The crystal structure of the plant homologue provides a framework for understanding how disease-causing mutations in human cystinosin lead to different severities of cystinosis. Currently, 42 missense mutations have been identified (Supplementary Table 1), which are categorised into four broad groups and relating to age of onset: infantile, juvenile, atypical and ocular[13,15,18]. Omitting those mutations that occur in the N-terminal domain, we can map on the remaining mutations using the model of the human transporter (Fig. 5a and Supplementary Table 1). Many of these mutations map to the functionally important regions, and in particular cluster around the cytoplasmic gate, ligand binding region and luminal gate (Fig. 5b, c).

Previous structures of the bacterial PQ-motif transporters revealed that alternating access transport within this family is likely to occur following the movement of the two 3TM helical bundles around the central ligand, aided by the location of the two PQ-motifs in TM1 and 5[27,28]. However, unlike the bacterial transporters, cystinosin is proton coupled, which introduces the need to couple ligand binding to proton translocation. Our results suggest this occurred in cystinosin through the introduction of two conserved salt bridge interactions that exist on either side of the cystine binding site, which function to couple the open/closed state of the cytoplasmic and luminal gates to proton and cystine binding.

Taken together, our data enables us to propose a working model for proton coupled L-cystine transport (Fig. 6). The transporter adopts an outward open state in the lysosome (state i), with the cytoplasmic gate closed and TMs 1-2 and TMs 5-6 packed together. In this conformation, the luminal gate is open, with TMs 3 and 7 separated. In this state, Asp92 (Asp205; human numbering in parentheses) would be protonated, given the acidic luminal pH. The protonation of Asp92 would function to keep the luminal gate open, as it would weaken the interaction with Lys221 (Lys335). Following L-cystine binding, Asp92 (Asp205) likely deprotonates to engage Lys221 (Lys335), closing the luminal gate (state ii). L-Cystine engages both Lys166 (Lys280) and Asp191 (Asp305), which reside on TM5 and 6 respectively, triggering opening of the cytoplasmic gate, aided through interactions to Trp24 (Trp138) and Lys55 (Lys273). The transporter will transition to the inward (cytoplasmic) open state following the movement of the cytoplasmic ends of TMs 1 and 2 and TMs 5 and 6 away from one another (state iii). There are no salt bridge interactions coordinating the closure of the cytoplasmic gate (i.e., connecting helices of the first and second 3TM bundle), instead the loops connecting these helices contain polar and bulky hydrophobic side chains that pack together to seal the binding site from the cytoplasm. A similar feature is observed in the bacterial PQ-loop homologues[27]. Following opening of the cytoplasmic gate, L-cystine release could be triggered by protonation of Asp191

https://doi.org/10.1038/s41467-022-32589-2

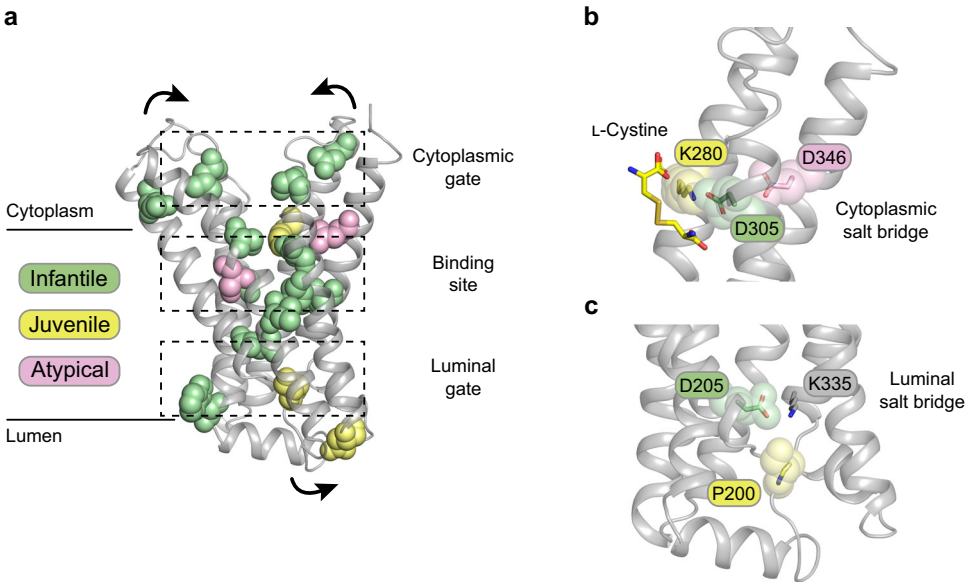

Fig. 5 | Structural context of cystinosis-causing mutations. a A subset of the missense mutations that localise to the cytoplasmic and luminal gates or binding site mapped onto the AlphaFold2 model of human cystinosin. Mutations are coloured according to the severity and onset of disease. Arrows indicate structural movements that occur during transport. **b** Zoomed in view of the cytoplasmic gate with the position of L-cystine superimposed. **c** Zoomed in view of the luminal gate with the inter bundle salt bridge residues highlighted.

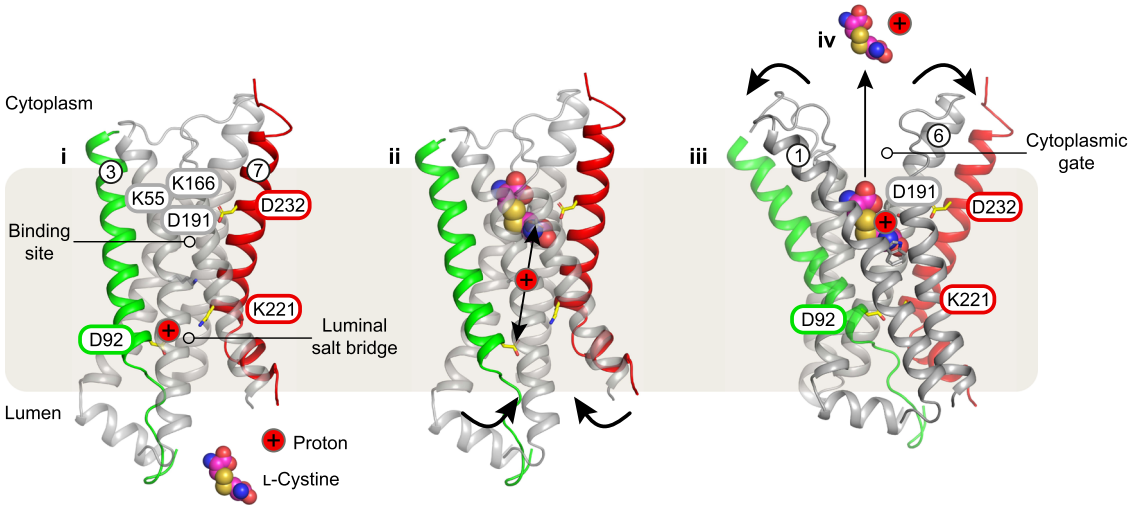

Fig. 6 | Conserved salt bridge interactions mediate L-cystine transport. Proposed mechanism for proton coupled cystine transport via cystinosin. **i** in the apo state the transporter adopts an outward open state due to protonation of Asp92 on TM3. **ii** cystine binding results in deprotonation of Asp92 and promotes opening of the cytoplasmic gate through interactions within the binding site, with Asp191, Lys55 and Lys166 playing important roles in ligand recognition. Closure of the luminal gate is facilitated through a salt-bridge interaction between Asp92 and Lys221. Movement of Lys221 towards Asp92 would reinforce the movements required to open the cytoplasmic gate as the helices pivot around the bound cystine ligand. **iii** transition to the inward open state occurs and Asp191 become protonated, weakening the interaction with cystine, and promoting release of the ligand and proton into the cytoplasm (**iv**). Deprotonation of Asp191 would create the conditions necessary for the return of the transporter to restart the cycle, facilitated by the proximity of Asp232.

(Asp305), as this would weaken the salt bridge interaction we observe with the amino terminus of the ligand (Fig. 2c, d). The movement of protons between Asp92 (Asp205) and Asp191 (Asp305) could occur through ordered water molecules, as shown for POT family peptide transporters[44] or may be facilitated directly by L-cystine. Following L-cystine release, Asp191 (Asp305) would be expected to deprotonate on exposure to the cytoplasm and further protonation of Asp92 (Asp205) would result in the transporter resetting for another cycle. The absence of a pH sensitive element within the cytoplasmic side of the helices suggests this gate is structurally coupled to the luminal gate, which contains the pH responsive element, Asp191. Mechanical coupling between the two gates is achieved by having Lys221 (Lys335) and Asp232 (Asp346) on TM7. Aspartate 232 (Asp346) interacts with Asp191 (Asp305) in the cystinosin structure (Fig. 6), providing a link between movement in the luminal gate to structural changes in the cytoplasmic region of the transporter and L-cystine binding.

Finally, our observation that the first PQ-motif is not required for cystinosin function suggests a division of labour within the transporter, with the second 3TM bundle coordinating a more sensitive interaction network. Certainly, more mutations map to the second 3TM

bundle in cystinosis patients, supporting a more prominent role in the transport mechanism (Fig. 5a & Supplementary Table 1). Fusing the two 3TM bundles together clearly represented an important step in the evolution of function within the PQ-loop family and provided an ideal framework to evolve more complicated coupling mechanisms. It would also provide opportunities for oligomerisation and asymmetric assemblies in the membrane, for which we currently have little insight. It will be important to pursue this aspect of PQ-protein biology to fully understand their role in the cell. Nevertheless, the structures and functional data presented, combined with the functional annotation of key disease-causing mutations now provides a firm foundation for developing a molecular blueprint for proton coupled lysosomal cystine transport and cystinosis.

Methods

Cloning, expression, and purification of *Arabidopsis thaliana* cystinosin

The gene encoding *Arabidopsis thaliana* cystinosin (Uniprot code P57758) was codon optimised, synthesised (Geneart, ThermoFisher) and cloned into pDDGFP-Leu2d[34] for expression as a cleavable GFP^{His} fusion in *Saccharomyces cerevisiae* strain BJ5460[45]. Variant forms of plant cystinosin were created by site-directed mutagenesis using overlap PCR. Yeast cells transformed with their respective plasmids were cultivated in synthetic complete medium minus leucine (-leu) with 2% (w/v) D-glucose for 32 h before diluting ninefold into -leu containing 2% (v/v) DL-lactate; wild type protein was expressed using a 15 l fermentation vessel (Eppendorf BioFlo 415) whilst variants were grown in baffled flasks, using 6 l volumes. Following overnight culture, expression was induced at an optical density (OD_{600}) of 2.5 by addition of 1.5% (w/v) D-galactose, dissolved in -leu media. After 20–23 h the yeast cells were harvested by centrifugation and lysed using a high pressure (38 kpsi). Following a low-speed centrifuge spin to remove cell debris and unlysed cells (30,000 x *g*) membranes were isolated through two spins at 200,000 x *g* with a resuspension in between using 20 mM HEPES-NaOH, pH 7.5, 1 M K-acetate, and finally resuspended in phosphate-buffered saline (PBS). Wild type cystinosin and variants were solubilized in *n*-dodecyl-β-D-maltoside (DDM, Anatrace) and purified to homogeneity using standard immobilised metal affinity chromatography (IMAC) steps. Solubilisation was carried out for 1 h in 1% (w/v) DDM, 1 × PBS, 150 mM NaCl and 10% (v/v) glycerol. Following ultra-centrifugation at 200,000 x *g* for 1 h at 4 °C, the soluble fraction was supplemented with 25 mM imidazole and bound to Ni-NTA resin (Thermo) in batch for 2.5–3 h at 4 °C. The resin was transferred into a gravity flow column, washed with 25–30 CV of solubilisation buffer supplemented with 0.1% (w/v) DDM and 35 mM imidazole and subsequently eluted with 250 mM imidazole. After overnight dialysis (20 mM Tris-HCl, pH 7.5, 150 mM NaCl, 0.02% (w/v) DDM) at 4 °C in the presence of Tobacco Etch Virus (TEV) protease, a reverse IMAC step was performed using the same resin (1.5 h binding at a final concentration of 10 mM imidazole). The flow-through, containing the purified cystinosin protein, was concentrated using a 50 kDa MWCO centricon (Amicon, Sigma Aldrich) and applied to a Superdex 200 Increase 10/300 GL column (Cytiva) equilibrated in size exclusion buffer (20 mM MES-NaOH pH 6, 150 mM NaCl and 0.03 (w/v) DDM). For crystallisation the detergent concentration was reduced to 0.013% (w/v) DDM. C-terminally Avi-tagged protein was purified as above, and subsequent biotin modification was carried out using the BirA ligase according to the manufacturer's instructions (Avidity).

Nanobody selection and purification

To identify cystinosin-specific nanobodies a library was raised through immunisation of a llama using reconstituted protein and screened using C-terminally Avi-tagged and biotinylated protein (method modified from[32]). Specifically, nanobodies were raised in a llama following intramuscular immunisation with purified protein reconstituted into liposomes and using Gerbu LQ#3000 as the adjuvant. Immunisations and handling of the llama were performed under the authority of the project license PPL 70/8108. Blood (150 ml) was collected, and peripheral blood mononuclear cells were prepared using Ficoll-Paque PLUS according to the manufacturers protocol. Total RNA was extracted using TRIzol™ and VHH cDNAs were generated by reverse transcription-PCR using primer as detailed previously[46]. The pool of VHH encoding sequences were amplified by two rounds of nested PCR: firstly with 'CALL_001' and 'CALL_002', followed by 'VHH_For' and 'VHH_Rev_IgG2' and 'VHH_Rev_IgG3', and cloned into the SfiI sites of the phagemid vector pADL-23c. In this vector, the VHH encoding sequence is preceded by a pelB leader sequence followed by a linker, His_6- and cMyc-tag (GPGGQHHHHHHGAEQKLISEEDLS). Electro-competent *E. coli* TG1 cells were transformed with the recombinant pADL-23c vector resulting in a VHH library of about 2×10^8 independent transformants. The resulting TG1 library stock was then infected with M13K07 helper phage to obtain a library of VHH-presenting phages. Phages displaying VHHs specific for cystinosin were enriched after two rounds of bio-panning on 50 nM of biotinylated cystinosin, through capturing with Dynabeads™ MyOne™ Streptavidin T1 (Thermo Fisher). Enrichment after each round of panning was determined by plating the cell culture with 10-fold serial dilutions. After the second round of panning, 192 individual phagemid clones were picked, VHH displaying phages were recovered by infection with M13K07 helper phage and tested for binding to cystinosin by ELISA. ELISA positive clones were sequenced and unique nanobodies identified and grouped according to sequence identity. These were analysed by small scale pull-down using the His_6-tagged constructs as well as co-elution using a Sepax SRT-C SEC-300 size exclusion column (Chromex). The better binders were further characterised using biolayer interferometry using an Octet Red384 (Sartorius) and streptavidin biosensors loaded with biotinylated cystinosin at 20 nM in 20 mM MES-NaOH pH 6, 150 mM NaCl, 0.03% (w/v) DDM to compare k_{on} and k_{off}. To calculate the K_D a serial dilution of the nanobody was made and following a short baseline step the nanobody was allowed to associate for 10 min followed by a dissociation step of 10 min. Data were analysed in the Octet v9.0 software package and fit to a single binding site model in Prism (GraphPad). All raw data was baseline and reference subtracted, in-step corrected, *y*-axis aligned and filtered with a Savitzky–Golay filter.

Synthetic nanobody (Sybody) selection

Sybody selection was performed against C-terminally Avi-tagged and biotinylated cystinosin, prepared using the same procedure as above for the llama based nanobody screen. The protocols for sybody selection have been described elsewhere[33,47]. A high affinity sybody, Syb39, was identified from the loop library[47], which formed a stable complex with the transporter and co-eluted down a Sepax SRT-C SEC-300 column (Chromex). High affinity binders were identified using small scale pull-down assays using the His_6-tagged binders. Biolayer interferometry was performed on an Octet Red 384 (Sartorius) as described above to compare k_{on} and k_{off} and calculate K_D. The identified sybodies were cloned and expressed as tag-free binders using the protocols previously described[33].

Crystallisation

Crystallisation was performed using protein at 30–37.5 mg ml^{-1} final concentration, as determined using absorbance at 280 nm. L-Cystine was added to a final concentration of 0.5 mM and the protein was left on ice for at least 2 h prior to crystallisation using the lipidic cubic phase method[48]. Protein-laden mesophase was obtained by monoolein with protein in a 60:40 (w:w) ratio using a coupled syringe device (Art Robbins, USA). Initial crystals appeared at 20 °C after 1–3 days in

27–28% PEG 500DME, 100 mM MES-NaOH, pH 5.50–5.75, 100–150 mM K-formate and matured after 5–7 days. Wells were opened using a tungsten carbide glasscutter and the crystals were harvested using 50 or 100 µm micromounts (MiTeGen). Crystals were cryo-cooled directly in liquid nitrogen and stored in unipucks.

Structure determination

X-ray diffraction data were collected at beamlines I24 and I04, Diamond Light Source, UK (Table 1). Indexing and integration were performed with XIA2 using either the DIALS[49–51] or autoPROC[52] pipeline, followed by scaling and merging with AIMLESS[53]. Initial phases were obtained by sulfur SAD phasing. Model building into the electron density map was performed in COOT[54], with structure refinement carried out using BUSTER[55]. The cystine bound crystal structure (PDB: 7ZKW) contained two molecules in the asymmetric unit and exhibited pseudo merohedral twinning in space group C2 with twin law -h-4/2 l,-k,l applied during refinement using Refmac[56]. The twin fraction was 0.204. The figures and interactions detailed in the study are based on chain B, which gave the strongest density in the refined maps. Geometry restraints for L-cystine were calculated using the grade server supplied by Global Phasing Ltd. Model validation was carried out using the Molprobity server[57]. Images were prepared using PyMol[58].

Sulfur-SAD phasing

X-ray diffraction images were collected at the Diamond Light Source I23 beamline[59] on a PILATUS 12 M detector (Dectris). A single dataset of 360° (rotation increment 0.1°, exposure 0.1 s) was collected at a temperature close to 60 K and a wavelength of 2.7552 Å. The dataset was automatically processed with DIALS[60] in the $P2_12_12$ space group to a resolution of 3.2 Å. The structure was solved by sulfur-SAD using the increased sulfur anomalous signal at longer wavelengths, Fast_EP[61], Anode[62] and Phenix.autobuild[63] as implemented in the Diamond automatic downstream processing pipelines.

Proteoliposome reconstitution

Purified wild type and mutated cystinosin were reconstituted into lipid vesicles consisting of a 3:1 (w:w) ratio of POPE:POPG by rapid dilution. To do so, the proteins were first exchanged into *n*-decyl-β-D-maltoside (DM, Glycon) by gel filtration using the same buffer as before but supplemented with 0.3% (w/v) DM, and subsequently mixed with the extruded vesicles at a 40:1 (w:w) lipid:protein ratio. The lipid protein mix was incubated at room temperature for 20 min before diluting it 27-fold into cold reconstitution buffer (50 mM K-phosphate, pH 7.0). Proteoliposomes were harvested by ultracentrifugation at 200,000 × g for >2 h and dialysed extensively overnight against two batches of reconstitution buffer. Proteoliposomes were recovered and resuspended to a final concentration of 0.5 µg µl^{-1} as analyzed by SDS-PAGE using ImageJ, comparing all bands of reconstituted protein to a known concentration of detergent-solubilized protein. Proteoliposomes were subjected to two rounds of freeze-thaw using liquid nitrogen and stored at −80 °C. For llama immunisation to raise nanobodies, a total of 600 µg of cystinosin was reconstituted at a lipid to protein ratio of 30:1 and proteoliposomes were resuspended to a final concentration of 1 mg ml^{-1}.

Transport assay using pyranine

Proteoliposomes were pelleted by ultra-centrifugation at 108,000 × g and 4 °C for 25 min and subsequently resuspended in INSIDE buffer consisting of 5 mM HEPES-NaOH, 120 mM KCl, 2 mM $MgSO_4$ and 2 mM pyranine (trisodium 8-hydroxypyrene-1,3,6-trisulfonate) at pH 7.2. Proteoliposomes were subjected to eight rounds of freeze-thaw before being extruded through a 0.4 µm polycarbonate membrane. The uniquely formed vesicles were then harvested through ultracentrifugation as before but at 18 °C and external pyranine was removed by applying the sample to a G-25 column (Cytiva) equilibrated in INSIDE buffer without pyranine. Vesicles were collected again and finally resuspended in INSIDE buffer without pyranine. Transport assays were performed at 25 °C in a cuvette equipped with a small magnetic flea using a Cary Eclipse Fluorescence Spectrophotometer (Agilent) set at dual excitation at 460 and 415 nm and emission at 510 nm. At the start of each assay, vesicles containing 5 µg of cystinosin were diluted into 545 µl of OUTSIDE buffer (5 mM HEPES-NaOH, 120 mM NaCl, 2 mM $MgSO_4$ at pH 7.2). After 15 seconds substrates were added per 100 µl from a freshly prepared stock in OUTSIDE buffer (200 µM final if not stated otherwise) and transport was initiated with a final concentration of 1 µM valinomycin (v) in OUTSIDE buffer after 30 seconds. The ratio of the resulting fluorescence profiles were calculated and plotted using Prism (GraphPad) or Excel (Microsoft), transport data from triplicate experiments were normalised to one to allow for comparison. For the pH experiments shown in Supplementary Fig. 6d, the buffer components were as stated above except 5 mM MES was used for pH 6.5 and 5 mM HEPES was used for pH 8.2.

L-Cystine binding assay

DDM-purified wild type and mutated cystinosin were diluted to 10 µM using a binding assay buffer consisting of 20 mM HEPES-NaOH, 150 mM NaCl and 0.03% (w/v) DDM, also containing up to 3.2 mM L-cystine, set to pH 7.2. After a 5 min incubation step at room temperature the solutions were loaded onto a Prometheus NT.48 (NanoTemper) and nanoDSF (differential scanning fluorimetry) experiments were run at 25% intensity using a 0.5 °C min^{-1} increment. We note that the addition of L-cystine did not significantly increase the melting temperature of the protein. Instead, we found that ligand addition led to a reduction in the tryptophan fluorescence emission ratio measured at 350 over 330 nm before the melting temperature was reached. Ten subsequent data points commencing from 25 °C were averaged and subtracted from a control melt without L-cystine. The fluorescence quench observed from each cystinosin variant with 3.2 mM L-cystine present compared to no ligand was finally normalised by dividing it by that of the average of a WT triplicate. All variants were completed in triplicate using a fresh L-cystine stock for each replicate.

Radioactive transport assay

Proteoliposomes were pelleted and resuspended in INSIDE buffer (10 mM MES-NaOH, 120 mM K-acetate, 2 mM $MgSO_4$ at pH 6.2). Four rounds of freeze-thaw were followed by extrusion through a 0.4 µm polycarbonate membrane. To reduce the volume, vesicles were harvested again at 18 °C and resuspended in INSIDE buffer.

Starting each individual assay, vesicles containing 2 µg protein were diluted into 250 µl OUTSIDE buffer (10 mM MES-NaOH, 120 mM NaCl, 2 mM $MgSO_4$ at pH 6.2) also containing 48 µM L-cystine, 2 µM radiocarbon-labelled ^{14}C-L-cystine (specific activity 0.2 Ci mmol^{-1}, Hartmann Analytic) as well as 10 µM valinomycin (Merck). Assays were performed at 20 °C. 45 µl fractions were removed at different timepoints, diluted into 2 ml of OUTSIDE buffer and vesicles were immediately isolated on a 0.22 µm cellulose filter (Merck) using a vacuum manifold. Filters were washed twice with 2 ml OUTSIDE buffer and subsequently transferred into Ultima Gold (PerkinElmer) scintillation liquid. Remaining radioactivity stemming from the inside of the vesicles was measured using a Wallac scintillation counter.

Electrophysiology

Human cystinosin without its C-terminal lysosomal targeting motif (GYDQLN) was subcloned with and without a C-terminal GFP into the pFAW vector for microscopy and electrophysiology experiments respectively. Variants of the protein were generated by site-directed mutagenesis and verified via sequencing. In vitro transcription of wild type and mutant *CTNS* was carried out using AmpliCap-Max T7 high

yield message marker kit (Cellscript). *Xenopus laevis* oocytes were defolliculated by collagenase treatment. They were then injected with 50 nl of nuclease-free water or 75 ng (50 nl of 1.5 µg µl^{-1} RNA) of human cystinosin wild type or mutant mRNA, and were incubated for 2 days at 19 °C in Barth's solution (54 mM NaCl, 30 mM KCl, 2.4 mM $NaHCO_3$, 0.8 mM $MgSO_4(H_2O)_7$, 0.4 mM $CaCl_2$, 0.3 mM $Ca(NO_3)_2(H_2O)_4$, 7.5 mM Tris-HCl, adjusted to pH 7.4) with gentamicin (50 µg ml^{-1})[20]. Two-electrode voltage clamp measurements were carried out on a Roboocyte system (Multi Channel Systems) using 3 M KCl back-filled borosilicate glass pipettes with a resistance of 200–1000 k Ω. Oocytes were voltage-clamped to −40 mV for the measurements. For each oocyte, an initial recording was made with ND-96 solution (96 mM NaCl, 2 mM KCl, 2 mM $MgCl_2$, 1.8 mM $CaCl_2$, 5 mM MES-NaOH, adjusted to pH 5) without cystine, followed by a second recording in ND-96 with 1 mM cystine (pH 5). For the dose-response curves, these measurement pairs were repeated on a single oocyte for each of the tested concentrations (0–1000 µM). Traces were analysed using the Roboocyte software (Multi Channel Systems). Cystine-evoked current values were obtained by subtracting the mean current after the addition of cystine from the mean current before the addition of cystine. Currents were normalised based on the cystine-evoked currents for the wild type human cystinosin injected oocytes of the corresponding oocyte batch. The data obtained for dose-response curves were normalised based on the maximum response measured (i.e., current at 400 µM or 1000 µM) for that particular oocyte and was fit using Prism (GraphPad). All experiments were repeated on at least three different oocyte batches.

Fluorescence Microscopy

Oocytes injected with either water, wild type or mutant human cystinosin-GFP mRNA were washed in 1× PBS, stained with 0.05 mg ml^{-1} of CF®633 wheat germ agglutinin (Biotium) in 1 × PBS for 5 min at RT, and washed with 1 × PBS. Surface expression was imaged using an LSM-780 confocal microscope (10 × lens) with an Argon (488 nm) and He-Ne laser (633 nm).

Reporting summary

Further information on research design is available in the Nature Research Reporting Summary linked to this article.

Data availability

The data that support this study are available from the corresponding authors upon reasonable request. The atomic coordinates have been in the RCSB Protein Data Bank (PDB) under accession code 7ZK1 (no substrate, Syb39 & Nb4), 7ZKZ (no substrate, Nb1 & Nb4), and 7ZKW (cystine bound, Syb39). Source data underlying Figs. 1b, c, 2e, f, 3b, 4a–c, and Supplementary Figs. 3b, 5a, b, 7c, e is provided as a Source Data file. Source data are provided with this paper.

References

1. Liu, G. Y. & Sabatini, D. M. mTOR at the nexus of nutrition, growth, ageing and disease. *Nat. Rev. Mol. Cell Biol.* **21**, 183–203 (2020).
2. Saftig, P. & Puertollano, R. How lysosomes sense, integrate, and cope with stress. *Trends Biochem Sci.* **46**, 97–112 (2021).
3. Hediger, M. A. et al. The ABCs of solute carriers: physiological, pathological and therapeutic implications of human membrane transport proteins. *Pflgers Arch. Eur. J. Physiol.* **447**, 465–468 (2004).
4. Wyant, G. A. et al. mTORC1 activator SLC38A9 is required to efflux essential amino acids from lysosomes and use protein as a nutrient. *Cell* **171**, 642–654.e612 (2017).
5. Talaia, G., Amick, J. & Ferguson, S. M. Receptor-like role for PQLC2 amino acid transporter in the lysosomal sensing of cationic amino acids. *Proc. Natl. Acad. Sci. USA* **118**, https://doi.org/10.1073/pnas.2014941118 (2021).
6. Ballabio, A. & Bonifacino, J. S. Lysosomes as dynamic regulators of cell and organismal homeostasis. *Nat. Rev. Mol. Cell Biol.* **21**, 101–118 (2020).
7. Cesar-Razquin, A. et al. A call for systematic research on solute carriers. *Cell* **162**, 478–487 (2015).
8. Drew, D. & Boudker, O. Shared molecular mechanisms of membrane transporters. *Annu Rev. Biochem* **85**, 543–572 (2016).
9. Zhang, Y., Zhang, Y., Sun, K., Meng, Z. & Chen, L. The SLC transporter in nutrient and metabolic sensing, regulation, and drug development. *J. Mol. Cell Biol.* **11**, 1–13 (2019).
10. Platt, F. M., d'Azzo, A., Davidson, B. L., Neufeld, E. F. & Tifft, C. J. Lysosomal storage diseases. *Nat. Rev. Dis. Prim.* **4**, 27 (2018).
11. Town, M. et al. A novel gene encoding an integral membrane protein is mutated in nephropathic cystinosis. *Nat. Genet* **18**, 319–324 (1998).
12. Attard, M. et al. Severity of phenotype in cystinosis varies with mutations in the CTNS gene: predicted effect on the model of cystinosin. *Hum. Mol. Genet* **8**, 2507–2514 (1999).
13. David, D. et al. Molecular basis of cystinosis: geographic distribution, functional consequences of mutations in the CTNS gene, and potential for repair. *Nephron* **141**, 133–146 (2019).
14. Cherqui, S. & Courtoy, P. J. The renal Fanconi syndrome in cystinosis: pathogenic insights and therapeutic perspectives. *Nat. Rev. Nephrol.* **13**, 115–131 (2017).
15. Castro-Balado, A. et al. Recent research in ocular cystinosis: drug delivery systems, cysteamine detection methods and future perspectives. *Pharmaceutics* **12**, https://doi.org/10.3390/pharmaceutics12121177 (2020).
16. Andrzejewska, Z. et al. Cystinosin is a component of the vacuolar H+-ATPase-Ragulator-Rag complex controlling mammalian target of rapamycin complex 1 signaling. *J. Am. Soc. Nephrol.* **27**, 1678–1688 (2016).
17. Johnson, J. L. et al. Upregulation of the Rab27a-dependent trafficking and secretory mechanisms improves lysosomal transport, alleviates endoplasmic reticulum stress, and reduces lysosome overload in cystinosis. *Mol. Cell Biol.* **33**, 2950–2962 (2013).
18. Jamalpoor, A., Othman, A., Levtchenko, E. N., Masereeuw, R. & Janssen, M. J. Molecular mechanisms and treatment options of nephropathic cystinosis. *Trends Mol. Med* **27**, 673–686 (2021).
19. Kalatzis, V., Cherqui, S., Antignac, C. & Gasnier, B. Cystinosin, the protein defective in cystinosis, is a H(+)-driven lysosomal cystine transporter. *EMBO J.* **20**, 5940–5949 (2001).
20. Ruivo, R. et al. Mechanism of proton/substrate coupling in the heptahelical lysosomal transporter cystinosin. *Proc. Natl Acad. Sci. USA* **109**, E210–E217 (2012).
21. Saudek, V. Cystinosin, MPDU1, SWEETs and KDELR belong to a well-defined protein family with putative function of cargo receptors involved in vesicle trafficking. *PLoS One* **7**, e30876 (2012).
22. Newstead, S. & Barr, F. Molecular basis for KDEL-mediated retrieval of escaped ER-resident proteins - SWEET talking the COPs. *J. Cell Sci.* **133**, https://doi.org/10.1242/jcs.250100 (2020).
23. Brauer, P. et al. Structural basis for pH-dependent retrieval of ER proteins from the Golgi by the KDEL receptor. *Science* **363**, 1103–1107 (2019).
24. Schenk, B. et al. MPDU1 mutations underlie a novel human congenital disorder of glycosylation, designated type If. *J. Clin. Invest* **108**, 1687–1695 (2001).
25. Jezegou, A. et al. Heptahelical protein PQLC2 is a lysosomal cationic amino acid exporter underlying the action of cysteamine in cystinosis therapy. *Proc. Natl Acad. Sci. USA* **109**, E3434–E3443 (2012).
26. Chen, L. Q. et al. Sugar transporters for intercellular exchange and nutrition of pathogens. *Nature* **468**, 527–532 (2010).
27. Latorraca, N. R. et al. Mechanism of substrate translocation in an alternating access transporter. *Cell* **169**, 96–107.e112 (2017).

28. Lee, Y., Nishizawa, T., Yamashita, K., Ishitani, R. & Nureki, O. Structural basis for the facilitative diffusion mechanism by SemiSWEET transporter. *Nat. Commun.* **6**, 6112 (2015).
29. Xu, Y. et al. Structures of bacterial homologues of SWEET transporters in two distinct conformations. *Nature* **515**, 448–452 (2014).
30. Feng, L. & Frommer, W. B. Structure and function of SemiSWEET and SWEET sugar transporters. *Trends Biochem Sci.* **40**, 480–486 (2015).
31. Tao, Y. et al. Structure of a eukaryotic SWEET transporter in a homotrimeric complex. *Nature* **527**, 259–263 (2015).
32. Pardon, E. et al. A general protocol for the generation of Nanobodies for structural biology. *Nat. Protoc.* **9**, 674–693 (2014).
33. Zimmermann, I. et al. Generation of synthetic nanobodies against delicate proteins. *Nat. Protoc.* https://doi.org/10.1038/s41596-020-0304-x (2020).
34. Parker, J. L. & Newstead, S. Method to increase the yield of eukaryotic membrane protein expression in Saccharomyces cerevisiae for structural and functional studies. *Protein Sci.* **23**, 1309–1314 (2014).
35. Parker, J. L., Mindell, J. A. & Newstead, S. Thermodynamic evidence for a dual transport mechanism in a POT peptide transporter. *Elife* **3**, https://doi.org/10.7554/eLife.04273 (2014).
36. Brunner, J. D. & Schenck, S. Production and application of nanobodies for membrane protein structural biology. *Methods Mol. Biol.* **2127**, 167–184 (2020).
37. Parker, J. L. et al. Structural basis of antifolate recognition and transport by PCFT. *Nature*, https://doi.org/10.1038/s41586-021-03579-z (2021).
38. Bannai, S. & Kitamura, E. Role of proton dissociation in the transport of cystine and glutamate in human diploid fibroblasts in culture. *J. Biol. Chem.* **256**, 5770–5772 (1981).
39. Jumper, J. et al. Highly accurate protein structure prediction with AlphaFold. *Nature* **596**, 583–589 (2021).
40. Jardetzky, O. Simple allosteric model for membrane pumps. *Nature* **211**, 969–970 (1966).
41. Shotelersuk, V. et al. CTNS mutations in an American-based population of cystinosis patients. *Am. J. Hum. Genet* **63**, 1352–1362 (1998).
42. Shen, J. et al. Organelle pH in the Arabidopsis endomembrane system. *Mol. Plant* **6**, 1419–1437 (2013).
43. Ohkuma, S. & Poole, B. Fluorescence probe measurement of the intralysosomal pH in living cells and the perturbation of pH by various agents. *Proc. Natl Acad. Sci. USA* **75**, 3327–3331 (1978).
44. Parker, J. L. et al. Proton movement and coupling in the POT family of peptide transporters. *Proc. Natl Acad. Sci. USA* **114**, 13182–13187 (2017).
45. Drew, D. et al. GFP-based optimization scheme for the overexpression and purification of eukaryotic membrane proteins in Saccharomyces cerevisiae. *Nat. Protoc.* **3**, 784–798 (2008).
46. Parker, J. L. et al. Cryo-EM structure of PepT2 reveals structural basis for proton-coupled peptide and prodrug transport in mammals. *Sci. Adv.* **7**, https://doi.org/10.1126/sciadv.abh3355 (2021).
47. Zimmermann, I. et al. Synthetic single domain antibodies for the conformational trapping of membrane proteins. *Elife* **7**, https://doi.org/10.7554/eLife.34317 (2018).
48. Caffrey, M. & Porter, C. Crystallizing membrane proteins for structure determination using lipidic mesophases. *J. Vis. Exp.* https://doi.org/10.3791/1712 (2010).
49. Winter, G., Lobley, C. M. C. & Prince, S. M. Decision making in xia2. *Acta Crystallogr. Sect. D. Biol. Crystallogr.* **69**, 1260–1273 (2013).
50. Winter, G. xia2: an expert system for macromolecular crystallography data reduction. *J. Appl. Crystallogr.* **43**, 186–190 (2009).
51. Waterman, D. G. et al. Diffraction-geometry refinement in the DIALS framework. *Acta Crystallogr D. Struct. Biol.* **72**, 558–575 (2016).
52. Vonrhein, C. et al. Data processing and analysis with the autoPROC toolbox. *Acta Crystallogr. Sect. D., Biol. Crystallogr.* **67**, 293–302 (2011).
53. Evans, P. R. & Murshudov, G. N. How good are my data and what is the resolution? *Acta Crystallogr. Sect. D. Biol. Crystallogr.* **69**, 1204–1214 (2013).
54. Emsley, P., Lohkamp, B., Scott, W. G. & Cowtan, K. Features and development of Coot. *Acta Crystallogr. Sect. D. Biol. Crystallogr.* **66**, 486–501 (2010).
55. Blanc, E. et al. Refinement of severely incomplete structures with maximum likelihood in BUSTER-TNT. *Acta Crystallogr. Sect. D. Biol. Crystallogr.* **60**, 2210–2221 (2004).
56. Winn, M. D., Isupov, M. N. & Murshudov, G. N. Use of TLS parameters to model anisotropic displacements in macromolecular refinement. *Acta Crystallogr. Sect. D. Biol. Crystallogr.* **57**, 122–133 (2001).
57. Chen, V. B. et al. MolProbity: all-atom structure validation for macromolecular crystallography. *Acta Crystallogr. Sect. D. Biol. Crystallogr.* **66**, 12–21 (2010).
58. Schrodinger, L. L. C. *The PyMOL Molecular Graphics System, Version 1.3r1* (2010).
59. Wagner, A., Duman, R., Henderson, K. & Mykhaylyk, V. In-vacuum long-wavelength macromolecular crystallography. *Acta Crystallogr D. Struct. Biol.* **72**, 430–439 (2016).
60. Winter, G. et al. DIALS as a toolkit. *Protein Sci.* **31**, 232–250 (2022).
61. Sheldrick, G. M. Experimental phasing with SHELXC/ D/ E: combining chain tracing with density modification. *Acta Crystallogr. Sect. D. Biol. Crystallogr.* **66**, 479–485 (2010).
62. Thorn, A. & Sheldrick, G. M. ANODE: anomalous and heavy-atom density calculation. *J. Appl Crystallogr* **44**, 1285–1287 (2011).
63. Terwilliger, T. C. et al. Iterative model building, structure refinement and density modification with the PHENIX AutoBuild wizard. *Acta Crystallogr. Sect. D., Biol. Crystallogr.* **64**, 61–69 (2008).

Acknowledgements

The authors would like to thank Dr Alicia Churchill-Angus for help with crystal data analysis and Diamond Light Source for beamtime (proposal mx23459), and the staff of beamlines I24, I04 and I23 for assistance with crystal testing and data collection. Llama immunisation was carried out in collaboration with the Rosalind Franklin Institute under the supervision of Dr Ray Owens and Dr Jiangdong Huo. The synthetic nanobody (sybody) libraries were obtained from Professor Markus Seeger, University of Zurich. This research was supported by Wellcome awards to S.N. (215519;219531), and through BBSRC grants to S.J.T. (BB/T002018/1) and MRC grants to J.L.P. (MR/S021043/1). M.L. is a UKRI MRC DPhil. student and supported by a Clarendon Fund Scholarship in partnership with a Christ Church Clarendon award. S.S. is a UKRI BBSRC DPhil. student supported by a studentship from the Doctoral Training Partnership award (BB/T008784/1).

Author contributions

J.L.P. and S.N. conceived the project. M.L., J.L.P. and S.N. performed protein expression and purification work and analysed the purification and liposome assay data. LCP crystallisation, data collection and structure determination were undertaken by M.L., J.L.P., and supervised by S.N. J.L.P. designed and supervised the in vitro assays conducted and analysed by M.L. M.L. generated and screened the sybodies and identified the nanobodies. S.J.T. supervised and analysed the two electrode voltage experiments conducted and analysed by S.P.S. K.E.O. and A.W. undertook the long wavelength data collection, phasing, and initial model building, aided by M.L. and S.N. M.L., S.P.S., J.L.P., and S.N. wrote the manuscript and prepared the figures, with assistance from all the authors.

Competing interests

The authors declare no competing interests.

Additional information

Supplementary information The online version contains supplementary material available at https://doi.org/10.1038/s41467-022-32589-2.

Correspondence and requests for materials should be addressed to Joanne L. Parker or Simon Newstead.

Peer review information *Nature Communications* thanks Joseph Lyons and Manuel Palacin for their contribution to the peer review of this work.

Bibliography

blx@hook@bibinit

Abramson, J. et al. (2024) “Accurate structure prediction of biomolecular interactions with AlphaFold 3”, *Nature*, **630**(8016), pp. 493–500, DOI: 10.1038/s41586-024-07487-w.

Abu-Remaileh, M. et al. (2017) “Lysosomal metabolomics reveals V-ATPase- and mTOR-dependent regulation of amino acid efflux from lysosomes”, *Science (New York, N.Y.)*, **358**(6364), pp. 807–813, DOI: 10.1126/SCIENCE.AAN6298.

Adelmann, C. H. et al. (2020) “MFSD12 mediates the import of cysteine into melanosomes and lysosomes”, *Nature*, **588**(7839), p. 699, DOI: 10.1038/S41586-020-2937-X.

Afonine, P. V. et al. (2018) “Real-space refinement in PHENIX for cryo-EM and crystallography”, *Acta crystallographica. Section D, Structural biology*, **74**(Pt 6), pp. 531–544, DOI: 10.1107/S2059798318006551.

Aits, S. and M. Jäättelä (2013) “Lysosomal cell death at a glance”, *Journal of cell science*, **126**(Pt 9), pp. 1905–1912, DOI: 10.1242/JCS.091181.

Akgoc, Z. et al. (2015) “Bis(monoacylglycero)phosphate: a secondary storage lipid in the gangliosidoses”, *Journal of lipid research*, **56**(5), pp. 1006–1013, DOI: 10.1194/JLR.M057851.

Akkermans, O. et al. (2022) “GPC3-Unc5 receptor complex structure and role in cell migration”, *Cell*, **185**(21), 3931–3949.e26, DOI: 10.1016/J.CELL.2022.09.025.

Akter, F. et al. (2023) “Multi-Cell Line Analysis of Lysosomal Proteomes Reveals Unique Features and Novel Lysosomal Proteins”, *Molecular and Cellular Proteomics*, **22**(3), p. 100509, DOI: 10.1016/J.MCPRO.2023.100509/ATTACHMENT/4105B6DE-548B-4E8E-8B91-42467DEBAFC3/MMC8.XLSX.

Andrzejewska, Z. et al. (2016) “Cystinosin is a Component of the Vacuolar H+-ATPase-Ragulator-Rag Complex Controlling Mammalian Target of Rapamycin Complex 1 Signaling.”, *Journal of the American Society of Nephrology : JASN*, **27**(6), pp. 1678–1688, DOI: 10.1681/ASN.2014090937.

Anikster, Y. et al. (2000) “Ocular nonnephropathic cystinosis: clinical, biochemical, and molecular correlations”, *Pediatric research*, **47**(1), pp. 17–23, DOI: 10.1203/00006450-200001000-00007.

Antonin, W. et al. (2000) “A SNARE complex mediating fusion of late endosomes defines conserved properties of SNARE structure and function”, *The EMBO Journal*, **19**(23), p. 6453, DOI: 10.1093/EMBOJ/19.23.6453.

Aricescu, A. R. et al. (2006) “A time- and cost-efficient system for high-level protein production in mammalian cells”, *Acta crystallographica. Section D, Biological crystallography*, **62**(Pt 10), pp. 1243–1250, DOI: 10.1107/S0907444906029799.

Armenta, D. A. et al. (2022) “Ferroptosis inhibition by lysosome-dependent catabolism of extracellular protein”, *Cell Chemical Biology*, **29**(11), 1588–1600.e7, DOI: 10.1016/J.CHEMBIOL.2022.10.006/ATTACHMENT/351FCECB-EF56-47A2-883B-E4324FC1CD0D/MMC2.PDF.

Attard, M. et al. (1999) “Severity of phenotype in cystinosis varies with mutations in the CTNS gene: predicted effect on the model of cystinosin”, *Human molecular genetics*, **8**(13), pp. 2507–2514, DOI: 10.1093/HMG/8.13.2507.

Ball, L. J. et al. (2005) "Recognition of proline-rich motifs by protein-protein-interaction domains", *Angewandte Chemie (International ed. in English)*, **44**(19), pp. 2852–2869, DOI: 10.1002/ANIE.200400618.

Ballabio, A. and J. S. Bonifacino (2019) "Lysosomes as dynamic regulators of cell and organismal homeostasis", *Nature Reviews Molecular Cell Biology 2019 21:2*, **21**(2), pp. 101–118, DOI: 10.1038/s41580-019-0185-4.

Bannai, S. (1984) "Transport of cystine and cysteine in mammalian cells", *Biochimica et biophysica acta*, **779**(3), pp. 289–306, DOI: 10.1016/0304-4157(84)90014-5.

Bassi, M. T. et al. (2000) "Cloning of the gene encoding a novel integral membrane protein, mucolipidin-and identification of the two major founder mutations causing mucolipidosis type IV", *American journal of human genetics*, **67**(5), pp. 1110–1120, DOI: 10.1016/S0002-9297(07)62941-3.

Beghein, E. and J. Gettemans (2017) "Nanobody Technology: A Versatile Toolkit for Microscopic Imaging, Protein-Protein Interaction Analysis, and Protein Function Exploration.", *Frontiers in immunology*, **8**, p. 771, DOI: 10.3389/fimmu.2017.00771.

Bepler, T. et al. (2019) "Positive-unlabeled convolutional neural networks for particle picking in cryo-electron micrographs", *Nature Methods 2019 16:11*, **16**(11), pp. 1153–1160, DOI: 10.1038/s41592-019-0575-8.

Berghe, T. V. et al. (2010) "Necroptosis, necrosis and secondary necrosis converge on similar cellular disintegration features", *Cell death and differentiation*, **17**(6), pp. 922–930, DOI: 10.1038/CDD.2009.184.

Berman, E. R. et al. (1974) "Congenital corneal clouding with abnormal systemic storage bodies: A new variant of mucolipidosis", *The Journal of Pediatrics*, **84**(4), pp. 519–526, DOI: 10.1016/S0022-3476(74)80671-2.

Berquez, M. et al. (2023) “Lysosomal cystine export regulates mTORC1 signaling to guide kidney epithelial cell fate specialization”, *Nature Communications*, **14**(1), pp. 1–21, DOI: 10.1038/s41467-023-39261-3.

Berridge, M. J. et al. (2003) “Calcium signalling: dynamics, homeostasis and remodelling”, *Nature reviews. Molecular cell biology*, **4**(7), pp. 517–529, DOI: 10.1038/NRM1155.

Bethuyne, J. et al. (2014) “A nanobody modulates the p53 transcriptional program without perturbing its functional architecture”, *Nucleic Acids Research*, **42**(20), p. 12928, DOI: 10.1093/NAR/GKU962.

Bhardwaj, R. K. et al. (2006) “The functional evaluation of human peptide/histidine transporter 1 (hPHT1) in transiently transfected COS-7 cells”, *European journal of pharmaceutical sciences : official journal of the European Federation for Pharmaceutical Sciences*, **27**(5), pp. 533–542, DOI: 10.1016/J.EJPS.2005.09.014.

Bianchi, G. et al. (2022) “Distribution of Charged Residues Affects the Average Size and Shape of Intrinsically Disordered Proteins”, *Biomolecules*, **12**(4), p. 561, DOI: 10.3390/BIOM12040561/S1.

Bloch, J. S. et al. (2021) “Development of a universal nanobody-binding Fab module for fiducial-assisted cryo-EM studies of membrane proteins”, *Proceedings of the National Academy of Sciences of the United States of America*, **118**(47), e2115435118, DOI: 10.1073/PNAS.2115435118/SUPPL_FILE/PNAS.2115435118.SAPP.PDF.

Bolte, S. and F. P. Cordelières (2006) “A guided tour into subcellular colocalization analysis in light microscopy”, *Journal of Microscopy*, **224**(3), pp. 213–232, DOI: 10.1111/J.1365-2818.2006.01706.X.

Bond, C. et al. (2024) “Multiplexed DNA-PAINT Imaging of the Heterogeneity of Late Endosome/Lysosome Protein Composition”, *bioRxiv*, p. 2024.03.18.585634, DOI: 10.1101/2024.03.18.585634.

Boudewyn, L. C. and S. U. Walkley (2019) “Current concepts in the neuropathogenesis of mucolipidosis type IV”, *Journal of neurochemistry*, **148**(5), pp. 669–689, DOI: 10.1111/JNC.14462.

Boytsov, D. et al. (2024) “Orphan lysosomal solute carrier MFSD1 facilitates highly selective dipeptide transport”, *Proceedings of the National Academy of Sciences of the United States of America*, **121**(13), e2319686121, DOI: 10.1073/PNAS.2319686121/SUPPL_FILE/PNAS.2319686121.SAPP.PDF.

Brams, M. et al. (2020) “Modulation of the erwinia ligand-gated ion channel (ELIC) and the 5-HT3 receptor via a common vestibule site”, *eLife*, **9**, DOI: 10.7554/ELIFE.51511.

Bräuer, P. et al. (2019) “Structural basis for pH-dependent retrieval of ER proteins from the Golgi by the KDEL receptor.”, *Science (New York, N.Y.)*, **363**(6431), pp. 1103–1107, DOI: 10.1126/science.aaw2859.

Brawley, D. N. et al. (2022) “Structural basis for inhibition of the drug efflux pump NorA from Staphylococcus aureus”, *Nature chemical biology*, **18**(7), p. 706, DOI: 10.1038/S41589-022-00994-9.

Bright, N. A. et al. (2005) “Endocytic delivery to lysosomes mediated by concurrent fusion and kissing events in living cells”, *Current biology : CB*, **15**(4), pp. 360–365, DOI: 10.1016/J.CUB.2005.01.049.

Cai, H. et al. (2020) “An improved fluorescent tag and its nanobodies for membrane protein expression, stability assay, and purification”, *Communications Biology*, **3**(1), pp. 1–16, DOI: 10.1038/s42003-020-01478-z.

Calcraft, P. J. et al. (2009) "NAADP mobilizes calcium from acidic organelles through two-pore channels", *Nature*, **459**(7246), pp. 596–600, DOI: 10.1038/NATURE08030.

Campa, C. C. et al. (2018) "Rab11 activity and PtdIns(3)P turnover removes recycling cargo from endosomes", *Nature Chemical Biology*, **14**(8), pp. 801–810, DOI: 10.1038/s41589-018-0086-4.

Cang, C. et al. (2015) "TMEM175 Is an Organelle K(+) Channel Regulating Lysosomal Function", *Cell*, **162**(5), pp. 1101–1112, DOI: 10.1016/J.CELL.2015.08.002.

Cao, M. et al. (2021) "Targeting lysosomes in human disease: from basic research to clinical applications", *Signal Transduction and Targeted Therapy*, **6**(1), p. 379, DOI: 10.1038/s41392-021-00778-y.

Cao, Q. et al. (2015) "BK Channels Alleviate Lysosomal Storage Diseases by Providing Positive Feedback Regulation of Lysosomal Ca2+ Release", *Developmental Cell*, **33**(4), pp. 427–441, DOI: 10.1016/J.DEVCEL.2015.04.010/ATTACHMENT/12A51B3D-2C4A-43BB-B372-C32BBEE50D17/MMC2.PDF.

Cao, Q. et al. (2017) "The lysosomal Ca2+ release channel TRPML1 regulates lysosome size by activating calmodulin", *Journal of Biological Chemistry*, **292**(20), pp. 8424–8435, DOI: 10.1074/JBC.M116.772160/ATTACHMENT/4DBEBB88-4FEF-4ACB-81BD-8B094A2A9959/MMC1.PDF.

Carpenter, E. J. et al. (2022) "GlyNet: a multi-task neural network for predicting proteinâglycan interactions", *Chemical Science*, **13**(22), pp. 6669–6686, DOI: 10.1039/D1SC05681F.

Carvalho-Gontijo, R. D. et al. (2020) "Regulation of neutrophil secretion by the lysosomal amino acid transporter, cystinosin", *The FASEB Journal*, **34**(S1), p. 1, DOI: https://doi.org/10.1096/fasebj.2020.34.s1.07285.

Castellano, B. M. et al. (2017) "Lysosomal cholesterol activates mTORC1 via an SLC38A9-Niemann-Pick C1 signaling complex", *Science (New York, N.Y.)*, **355**(6331), pp. 1306–1311, DOI: 10.1126/SCIENCE.AAG1417.

Castro, M. A. G. de et al. (2016) "Cathepsin B launches an apoptotic exit effort upon cell death-associated disruption of lysosomes", *Cell Death Discovery*, **2**(1), p. 16012, DOI: 10.1038/cddiscovery.2016.12.

Caussinus, E. et al. (2011) "Fluorescent fusion protein knockout mediated by anti-GFP nanobody", *Nature Structural & Molecular Biology 2011 19:1*, **19**(1), pp. 117–121, DOI: 10.1038/nsmb.2180.

Chandra, M. et al. (2011) "A role for the Ca2+ channel TRPML1 in gastric acid secretion, based on analysis of knockout mice", *Gastroenterology*, **140**(3), 857–867.e1, DOI: 10.1053/J.GASTRO.2010.11.040.

Chapel, A. et al. (2013) "An extended proteome map of the lysosomal membrane reveals novel potential transporters.", *Molecular & cellular proteomics : MCP*, **12**(6), pp. 1572–1588, DOI: 10.1074/mcp.M112.021980.

Chattopadhyay, G. and R. Varadarajan (2019) "Facile measurement of protein stability and folding kinetics using a nano differential scanning fluorimeter", *Protein science : a publication of the Protein Society*, **28**(6), pp. 1127–1134, DOI: 10.1002/PRO.3622.

Chauhan, S. et al. (2015) "Pharmaceutical screen identifies novel target processes for activation of autophagy with a broad translational potential", *Nature Communications 2015 6:1*, **6**(1), pp. 1–15, DOI: 10.1038/ncomms9620.

Che, T. et al. (2018) "Structure of the Nanobody-Stabilized Active State of the Kappa Opioid Receptor", *Cell*, **172**(1-2), 55–67.e15, DOI: 10.1016/J.CELL.2017.12.011.

Chen, C. C. et al. (2017) “Patch-clamp technique to characterize ion channels in enlarged individual endolysosomes”, *Nature protocols*, **12**(8), pp. 1639–1658, DOI: 10.1038/NPROT.2017.036.

Chen, C. S. et al. (1998) “Abnormal transport along the lysosomal pathway in Mucolipidosis, type IV disease”, *Proceedings of the National Academy of Sciences of the United States of America*, **95**(11), pp. 6373–6378, DOI: 10.1073/PNAS.95.11.6373/ASSET/F2DB0C1B-FB95-4BAE-8FE2-C2ADA6CFA248/ASSETS/GRAPHIC/PQ1183280005.JPEG.

Cherqui, S et al. (2001) “The targeting of cystinosin to the lysosomal membrane requires a tyrosine-based signal and a novel sorting motif.”, *The Journal of biological chemistry*, **276**(16), pp. 13314–13321, DOI: 10.1074/jbc.M010562200.

Cherqui, S. and P. J. Courtoy (2017) “The renal Fanconi syndrome in cystinosis: pathogenic insights and therapeutic perspectives.”, *Nature reviews. Nephrology*, **13**(2), pp. 115–131, DOI: 10.1038/nrneph.2016.182.

Cherqui, S. et al. (2002) “Intralysosomal cystine accumulation in mice lacking cystinosin, the protein defective in cystinosis”, *Molecular and cellular biology*, **22**(21), pp. 7622–7632, DOI: 10.1128/MCB.22.21.7622-7632.2002.

Christensen, K. A. et al. (2002) “pH-dependent regulation of lysosomal calcium in macrophages.”, *Journal of cell science*, **115**(Pt 3), pp. 599–607, DOI: 10.1242/jcs.115.3.599.

Cui, Z. et al. (2023) “Structure of the lysosomal mTORC1-TFEB-Rag-Ragulator megacomplex”, *Nature*, **614**(7948), pp. 572–579, DOI: 10.1038/s41586-022-05652-7.

Czibener, C. et al. (2006) “Ca2+ and synaptotagmin VII-dependent delivery of lysosomal membrane to nascent phagosomes”, *The Journal of cell biology*, **174**(7), pp. 997–1007, DOI: 10.1083/JCB.200605004.

Dandey, V. P. et al. (2020) “Time-resolved cryo-EM using Spotiton”, *Nature Methods*, **17**(9), pp. 897–900, DOI: 10.1038/s41592-020-0925-6.

David, D. et al. (2019) “Molecular Basis of Cystinosis: Geographic Distribution, Functional Consequences of Mutations in the CTNS Gene, and Potential for Repair.”, *Nephron*, **141**(2), pp. 133–146, DOI: 10.1159/000495270.

Davis, L. C. et al. (2023) “Optical profiling of autonomous Ca2+ nanodomains generated by lysosomal TPC2 and TRPML1”, *Cell Calcium*, **116**, p. 102801, DOI: 10.1016/J.CECA.2023.102801.

Decressac, M. et al. (2013) “TFEB-mediated autophagy rescues midbrain dopamine neurons from α-synuclein toxicity”, *Proceedings of the National Academy of Sciences of the United States of America*, **110**(19), DOI: 10.1073/PNAS.1305623110/-/DCSUPPLEMENTAL/PNAS.201305623SI.PDF.

Deneka, D. et al. (2021) “Allosteric modulation of LRRC8 channels by targeting their cytoplasmic domains”, *Nature Communications 2021 12:1*, **12**(1), pp. 1–14, DOI: 10.1038/s41467-021-25742-w.

Deprey, K. and J. A. Kritzer (2021) “HaloTag Forms an Intramolecular Disulfide”, *Bioconjugate chemistry*, **32**(5), pp. 964–970, DOI: 10.1021/ACS.BIOCONJCHEM.1C00113.

Desmyter, A. et al. (1996) “Crystal structure of a camel single-domain VH antibody fragment in complex with lysozyme”, *Nature Structural Biology 1996 3:9*, **3**(9), pp. 803–811, DOI: 10.1038/nsb0996-803.

Diril, M. K. et al. (2009) “Lysosomal localization of GLUT8 in the testis–the EXXXLL motif of GLUT8 is sufficient for its intracellular sorting via AP1- and AP2-mediated interaction”, *The FEBS journal*, **276**(14), pp. 3729–3743, DOI: 10.1111/J.1742-4658.2009.07089.X.

Dong, J. X. et al. (2019) “A toolbox of nanobodies developed and validated for use as intrabodies and nanoscale immunolabels in mammalian brain neurons”, *eLife*, **8**, DOI: 10.7554/ELIFE.48750.

Dong, X. ping et al. (2010) “PI(3,5)P(2) controls membrane trafficking by direct activation of mucolipin Ca(2+) release channels in the endolysosome.”, *Nature communications*, **1**(4), p. 38, DOI: 10.1038/ncomms1037.

Dong, X.-P. et al. (2008) “The type IV mucolipidosis-associated protein TRPML1 is an endolysosomal iron release channel.”, *Nature*, **455**(7215), pp. 992–996, DOI: 10.1038/nature07311.

Dong, X. P. et al. (2009) “Activating mutations of the TRPML1 channel revealed by proline-scanning mutagenesis”, *Journal of Biological Chemistry*, **284**(46), pp. 32040–32052, DOI: 10.1074/JBC.M109.037184/ATTACHMENT/AEA1AE17-CBCF-492C-8831-B99D6E60F08C/MMC1.PDF.

Drew, D. and O. Boudker (2024) “A toolbox of nanobodies developed and validated for use as intrabodies and nanoscale immunolabels in mammalian brain neurons”, *Nature*, **626**, pp. 963–974, DOI: 10.1038/s41586-024-07062-3.

Driskell, O. J. et al. (2007) “Dynein is required for receptor sorting and the morphogenesis of early endosomes”, *Nature cell biology*, **9**(1), pp. 113–120, DOI: 10.1038/NCB1525.

Du, W. et al. (2021) “Lysosomal Zn2+ release triggers rapid, mitochondria-mediated, non-apoptotic cell death in metastatic melanoma”, *Cell reports*, **37**(3), p. 109848, DOI: 10.1016/J.CELREP.2021.109848.

Elferink, R. P. O. et al. (1983) “The intralysosomal pH in cultured human skin fibroblasts in relation to cystine accumulation in patients with cystinosis.”, *Biochemical and biophysical research communications*, **116**(1), pp. 154–161, DOI: 10.1016/0006-291x(83)90394-7.

Elmonem, M. A. et al. (2016) “Cystinosis: a review”, *Orphanet Journal of Rare Diseases 2016 11:1*, **11**(1), pp. 1–17, DOI: 10.1186/S13023-016-0426-Y.

Emsley, P. and K. Cowtan (2004) “Coot: model-building tools for molecular graphics”, *Acta crystallographica. Section D, Biological crystallography*, **60**(Pt 12 Pt 1), pp. 2126–2132, DOI: 10.1107/S0907444904019158.

Eskelinen, E. L. (2006) “Roles of LAMP-1 and LAMP-2 in lysosome biogenesis and autophagy”, *Molecular aspects of medicine*, **27**(5-6), pp. 495–502, DOI: 10.1016/J.MAM.2006.08.005.

Fan, C. et al. (2024) “Inhibition of lysosomal TRPML1 channel eliminates breast cancer stem cells by triggering ferroptosis”, *Cell Death Discovery*, **10**(1), DOI: 10.1038/S41420-024-02026-Y.

Feng, H. et al. (2013) “Optimizing plant transporter expression in Xenopus oocytes”, *Plant Methods*, **9**(1), pp. 1–6, DOI: 10.1186/1746-4811-9-48/FIGURES/5.

Fernández, B. et al. (2022) “Iron-induced cytotoxicity mediated by endolysosomal TRPML1 channels is reverted by TFEB”, *Cell Death & Disease 2022 13:12*, **13**(12), pp. 1–11, DOI: 10.1038/s41419-022-05504-2.

Festa, B. P. et al. (2018) “Impaired autophagy bridges lysosomal storage disease and epithelial dysfunction in the kidney”, *Nature Communications 2018 9:1*, **9**(1), pp. 1–17, DOI: 10.1038/s41467-017-02536-7.

Festa, M. et al. (2022) “Current Methods to Unravel the Functional Properties of Lysosomal Ion Channels and Transporters”, *Cells*, **11**(6), DOI: 10.3390/CELLS11060921.

Fine, M. et al. (2018) “Structural basis for PtdInsP2-mediated human TRPML1 regulation”, *Nature Communications*, **9**(1), DOI: 10.1038/S41467-018-06493-7.

Flajnik, M. F. et al. (2011) “A Case Of Convergence: Why Did a Simple Alternative to Canonical Antibodies Arise in Sharks and Camels?”, *PLOS Biology*, **9**(8), e1001120, DOI: 10.1371/JOURNAL.PBIO.1001120.

Forsyth, W. R. et al. (2002) “Empirical relationships between protein structure and carboxyl pKa values in proteins”, *Proteins: Structure, Function and Genetics*, **48**(2), pp. 388–403, DOI: 10.1002/PROT.10174.

Frey, N. et al. (2024) “Endolysosomal TRPML1 channel regulates cancer cell migration by altering intracellular trafficking of E-cadherin and β1-integrin”, *Journal of Biological Chemistry*, **300**(1), DOI: 10.1016/J.JBC.2023.105581/ATTACHMENT/F5C1ED4B-847E-4B76-B8E8-AEDA04FEC29B/MMC1.DOCX.

Futter, C. E. et al. (1996) “Multivesicular endosomes containing internalized EGF-EGF receptor complexes mature and then fuse directly with lysosomes.”, *The Journal of cell biology*, **132**(6), pp. 1011–1023, DOI: 10.1083/jcb.132.6.1011.

Gahl, W. A. et al. (1982) “Cystine Transport Is Defective in Isolated Leukocyte Lysosomes from Patients with Cystinosis”, *Science*, **217**(4566), pp. 1263–1265, DOI: 10.1126/SCIENCE.7112129.

Gahl, W. A. et al. (1986) “Course of nephropathic cystinosis after age 10 years”, *The Journal of Pediatrics*, **109**(4), pp. 605–608, DOI: 10.1016/S0022-3476(86)80221-9.

Gahl, W. A. et al. (1987) “Cysteamine therapy for children with nephropathic cystinosis”, *The New England journal of medicine*, **316**(16), pp. 971–977, DOI: 10.1056/NEJM198704163161602.

Gahl, W. A. et al. (2000) “Corneal crystals in nephropathic cystinosis: natural history and treatment with cysteamine eyedrops”, *Molecular genetics and metabolism*, **71**(1-2), pp. 100–120, DOI: 10.1006/MGME.2000.3062.

Gahl, W. A. et al. (2002) “Cystinosis.”, *The New England journal of medicine*, **347**(2), pp. 111–121, DOI: 10.1056/NEJMra020552.

Galarreta, C. I. et al. (2015) “The swan-neck lesion: Proximal tubular adaptation to oxidative stress in nephropathic cystinosis”, *American Journal of Physiology - Renal Physiology*, **308**(10), F1155–F1166, DOI: 10.1152/AJPRENAL.00591.2014/ASSET/IMAGES/LARGE/ZH20081575910010.JPEG.

Galazzo, L. et al. (2020) “Spin-labeled nanobodies as protein conformational reporters for electron paramagnetic resonance in cellular membranes”, *Proceedings of the National Academy of Sciences of the United States of America*, **117**(5), pp. 2441–2448, DOI: 10.1073/PNAS.1913737117/SUPPL_FILE/PNAS.1913737117.SAPP.PDF.

Gan, N. et al. (2022) “Structural mechanism of allosteric activation of TRPML1 by PI(3,5)P2 and rapamycin”, *Proceedings of the National Academy of Sciences of the United States of America*, **119**(7), e2120404119, DOI: 10.1073/PNAS.2120404119/SUPPL_FILE/PNAS.2120404119.SM07.MP4.

Gan, N. et al. (2024) “TRPML1 gating modulation by allosteric mutations and lipids”, *bioRxiv*, DOI: 10.1101/2024.07.04.602033.

García-Ávila, M. et al. (2024) “Permeant cations modulate pore dynamics and gating of TRPV1 ion channels”, *The Journal of general physiology*, **156**(1), DOI: 10.1085/JGP.202313422.

Garrity, A. G. et al. (2016) “The endoplasmic reticulum, not the pH gradient, drives calcium refilling of lysosomes”, *eLife*, **5**, DOI: 10.7554/ELIFE.15887.

Gerndt, S. et al. (2020) “Agonist-mediated switching of ion selectivity in TPC2 differentially promotes lysosomal function”, *eLife*, **9**, DOI: 10.7554/ELIFE.54712.

Goldman, H. et al. (1971) “ADOLESCENT CYSTINOSIS: COMPARISONS WITH INFANTILE AND ADULT FORMS”, *Pediatrics*, **47**(6), pp. 979–988, DOI: 10.1542/PEDS.47.6.979.

Götzke, H. et al. (2019) “The ALFA-tag is a highly versatile tool for nanobody-based bioscience applications”, *Nature Communications 2019 10:1*, **10**(1), pp. 1–12, DOI: 10.1038/s41467-019-12301-7.

Grant, B. D. and J. G. Donaldson (2009) “Pathways and mechanisms of endocytic recycling”, *Nature reviews. Molecular cell biology*, **10**(9), pp. 597–608, DOI: 10.1038/NRM2755.

Graves, A. R. et al. (2008) “The Cl-/H+ antiporter ClC-7 is the primary chloride permeation pathway in lysosomes”, *Nature*, **453**(7196), pp. 788–792, DOI: 10.1038/NATURE06907.

Greenfield, N. J. (2006) “Using circular dichroism spectra to estimate protein secondary structure”, *Nature protocols*, **1**(6), pp. 2876–2890, DOI: 10.1038/NPROT.2006.202.

Griffin, C. S. et al. (2020) “The intracellular Ca2+ release channel TRPML1 regulates lower urinary tract smooth muscle contractility”, *Proceedings of the National Academy of Sciences of the United States of America*, **117**(48), pp. 30775–30786, DOI: 10.1073/PNAS.2016959117/SUPPL_FILE/PNAS.2016959117.SM06.AVI.

Gunshin, H et al. (1997) “Cloning and characterization of a mammalian proton-coupled metal-ion transporter.”, *Nature*, **388**(6641), pp. 482–488, DOI: 10.1038/41343.

Guo, X. et al. (2022) “Structure and mechanism of human cystine exporter cystinosin”, *Cell*, **185**(20), 3739–3752.e18, DOI: 10.1016/J.CELL.2022.08.020.

Gupta, A. et al. (2023) “Mechanism of glycoform specificity and in vivo protection by an anti-afucosylated IgG nanobody”, *Nature Communications 2023 14:1*, **14**(1), pp. 1–11, DOI: 10.1038/s41467-023-38453-1.

Haq, M. R. et al. (2002) “Immunolocalization of cystinosin, the protein defective in cystinosis”, *Journal of the American Society of Nephrology : JASN*, **13**(8), pp. 2046–2051, DOI: 10.1097/01.ASN.0000022012.95680.BA.

Harada, A. et al. (1998) “Golgi Vesiculation and Lysosome Dispersion in Cells Lacking Cytoplasmic Dynein”, *The Journal of Cell Biology*, **141**(1), p. 51, DOI: 10.1083/JCB.141.1.51.

Havelaar, A. C. et al. (1998) “Purification of the Lysosomal Sialic Acid Transporter: FUNCTIONAL CHARACTERISTICS OF A MONOCARBOXYLATE TRANSPORTER”, *Journal of Biological Chemistry*, **273**(51), pp. 34568–34574, DOI: 10.1074/JBC.273.51.34568.

He, L. et al. (2023) “Lysosomal cyst(e)ine storage potentiates tolerance to oxidative stress in cancer cells”, *Molecular Cell*, **83**(19), 3502–3519.e11, DOI: 10.1016/j.molcel.2023.08.032.

Heck, J. et al. (2019) “Transient Confinement of Ca(V)2.1 Ca(2+)-Channel Splice Variants Shapes Synaptic Short-Term Plasticity.”, *Neuron*, **103**(1), 66–79.e12, DOI: 10.1016/j.neuron.2019.04.030.

Hellmeier, J. et al. (2024) “Quantification of absolute labeling efficiency at the single-protein level”, *Nature Methods 2024 21:9*, **21**(9), pp. 1702–1707, DOI: 10.1038/s41592-024-02242-5.

Hesketh, G. G. et al. (2018) “The Lysosome and Intracellular Signalling”, *Progress in molecular and subcellular biology*, **57**, pp. 151–180, DOI: 10.1007/978-3-319-96704-2_6.

Hirschi, M. et al. (2017) “Cryo-EM structure of the lysosomal Ca2+-permeable channel TRPML3”, *Nature*, **550**(7676), p. 411, DOI: 10.1038/NATURE24055.

Hofmann, I. and S. Munro (2006) “An N-terminally acetylated Arf-like GTPase is localised to lysosomes and affects their motility”, *Journal of Cell Science*, **119**(8), pp. 1494–1503, DOI: 10.1242/JCS.02958.

Hollywood, J. A. et al. (2020) “Use of Human Induced Pluripotent Stem Cells and Kidney Organoids To Develop a Cysteamine/mTOR Inhibition Combination Therapy for Cystinosis”, *Journal of the American Society of Nephrology : JASN*, **31**(5), pp. 962–982, DOI: 10.1681/ASN.2019070712.

Hu, M. et al. (2022) “Parkinson’s Disease-risk Protein TMEM175 is a Proton-activated Proton Channel in Lysosomes”, *Cell*, **185**(13), p. 2292, DOI: 10.1016/J.CELL.2022.05.021.

Huang, S. C. C. et al. (2014) “Cell-intrinsic lysosomal lipolysis is essential for alternative activation of macrophages”, *Nature immunology*, **15**(9), pp. 846–855, DOI: 10.1038/NI.2956.

Huffer, K. E. et al. (2020) “Global alignment and assessment of trp channel transmembrane domain structures to explore functional mechanisms”, *eLife*, **9**, pp. 1–33, DOI: 10.7554/ELIFE.58660.

Huizing, M. and W. A. Gahl (2020) “Inherited disorders of lysosomal membrane transporters”, *Biochimica et biophysica acta. Biomembranes*, **1862**(12), DOI: 10.1016/J.BBAMEM.2020.183336.

Huotari, J. and A. Helenius (2011) “Endosome maturation”, *The EMBO journal*, **30**(17), pp. 3481–3500, DOI: 10.1038/EMBOJ.2011.286.

Idevall-Hagren, O. et al. (2015) “Triggered Ca2+ influx is required for extended synaptotagmin 1-induced ER-plasma membrane tethering.”, *The EMBO journal*, **34**(17), pp. 2291–2305, DOI: 10.15252/embj.201591565.

Infante, R. E. et al. (2008) “Purified NPC1 protein. I. Binding of cholesterol and oxysterols to a 1278-amino acid membrane protein.”, *The Journal of biological chemistry*, **283**(2), pp. 1052–1063, DOI: 10.1074/jbc.M707943200.

Ioghen, O. C. et al. (2023) “SH-SY5Y Cell Line In Vitro Models for Parkinson Disease Research-Old Practice for New Trends”, *Journal of integrative neuroscience*, **22**(1), DOI: 10.31083/J.JIN2201020.

Irannejad, R. et al. (2013) “Conformational biosensors reveal GPCR signalling from endosomes”, *Nature 2013 495:7442*, **495**(7442), pp. 534–538, DOI: 10.1038/nature12000.

Ishizuka, Y. et al. (2022) “Development and Validation of Arc Nanobodies: New Tools for Probing Arc Dynamics and Function.”, *Neurochemical research*, DOI: 10.1007/s11064-022-03573-5.

Ivanova, E. A. et al. (2016) “Altered mTOR signalling in nephropathic cystinosis”, *Journal of Inherited Metabolic Disease*, **39**(3), pp. 457–464, DOI: 10.1007/S10545-016-9919-Z/FIGURES/5.

Jamalpoor, A. et al. (2021) “Cysteamine-bicalutamide combination therapy corrects proximal tubule phenotype in cystinosis”, *EMBO molecular medicine*, **13**(7), DOI: 10.15252/EMMM.202013067.

Jardetzky, O. (1966) “Simple Allosteric Model for Membrane Pumps”, *Nature 1966 211:5052*, **211**(5052), pp. 969–970, DOI: 10.1038/211969a0.

Jean, S. et al. (2010) “Extended-synaptotagmin-2 mediates FGF receptor endocytosis and ERK activation in vivo.”, *Developmental cell*, **19**(3), pp. 426–439, DOI: 10.1016/j.devcel.2010.08.007.

Jézégou, A. et al. (2012) “Heptahelical protein PQLC2 is a lysosomal cationic amino acid exporter underlying the action of cysteamine in cystinosis therapy.”, *Proceedings of the National Academy of Sciences of the United States of America*, **109**(50), E3434–43, DOI: 10.1073/pnas.1211198109.

Jin, B. K. et al. (2023) “NANOBODIES: A Review of Generation, Diagnostics and Therapeutics”, *International Journal of Molecular Sciences*, **24**(6), DOI: 10.3390/IJMS24065994.

Johnston, R. J. et al. (2019) “VISTA is an acidic pH-selective ligand for PSGL-1”, *Nature 2019 574:7779*, **574**(7779), pp. 565–570, DOI: 10.1038/s41586-019-1674-5.

Jonas, A. J. et al. (1982) “ATP-dependent lysosomal cystine efflux is defective in cystinosis.”, *Journal of Biological Chemistry*, **257**(22), pp. 13185–13188, DOI: 10.1016/S0021-9258(18)33425-2.

Jouandin, P. et al. (2022) “Lysosomal cystine mobilization shapes the response of TORC1 and tissue growth to fasting.”, *Science (New York, N.Y.)*, **375**(6582), eabc4203, DOI: 10.1126/science.abc4203.

Jumper, J. et al. (2021) “Highly accurate protein structure prediction with AlphaFold”, *Nature 2021 596:7873*, **596**(7873), pp. 583–589, DOI: 10.1038/s41586-021-03819-2.

Jung, J. et al. (2019) “HRAS-driven cancer cells are vulnerable to TRPML1 inhibition”, *EMBO reports*, **20**(4), DOI: 10.15252/EMBR.201846685.

Jungnickel, K. E. et al. (2018) “Structural basis for amino acid transport by the CAT family of SLC7 transporters”, *Nature communications*, **9**(1), DOI: 10.1038/S41467-018-03066-6.

Jungnickel, K. E. J. et al. (2024) “MFSD1 with its accessory subunit GLMP functions as a general dipeptide uniporter in lysosomes”, *Nature Cell Biology 2024 26:7*, **26**(7), pp. 1047–1061, DOI: 10.1038/s41556-024-01436-5.

Kalatzis, V et al. (2001) “Cystinosin, the protein defective in cystinosis, is a H(+)-driven lysosomal cystine transporter.”, *The EMBO journal*, **20**(21), pp. 5940–5949, DOI: 10.1093/emboj/20.21.5940.

Kalatzis, V. et al. (2004) “Molecular pathogenesis of cystinosis: effect of CTNS mutations on the transport activity and subcellular localization of cystinosin.”, *Human molecular genetics*, **13**(13), pp. 1361–1371, DOI: 10.1093/hmg/ddh152.

Kandasamy, P. et al. (2018) “Amino acid transporters revisited: New views in health and disease”, *Trends in Biochemical Sciences*, **43**(10), pp. 752–789, DOI: 10.1016/J.TIBS.2018.05.003/ASSET/7366F237-DBA4-4882-8FDD-6E4556AB7E09/MAIN.ASSETS/GR1.JPG.

Kashiwaya, K. et al. (2009) “Identification of C2orf18, termed ANT2BP (ANT2âbinding protein), as one of the key molecules involved in pancreatic carcinogenesis”, *Cancer Science*, **100**(3), p. 457, DOI: 10.1111/J.1349-7006.2008.01058.X.

Kasitinon, S. Y. et al. (2019) “TRPML1 Promotes Protein Homeostasis in Melanoma Cells by Negatively Regulating MAPK and mTORC1 Signaling.”, *Cell reports*, **28**(9), 2293–2305.e9, DOI: 10.1016/j.celrep.2019.07.086.

Katoh, Y. et al. (2015) “Architectures of multisubunit complexes revealed by a visible immunoprecipitation assay using fluorescent fusion proteins”, *Journal of Cell Science*, **128**(12), pp. 2351–2362, DOI: 10.1242/JCS.168740/260357/AM/MULTISUBUNIT-COMPLEX-ARCHITECTURES-REVEALED-BY.

Ke, N. et al. (2016) “Visualization of Periplasmic and Cytoplasmic Proteins with a Self-Labeling Protein Tag”, *Journal of bacteriology*, **198**(7), pp. 1035–1043, DOI: 10.1128/JB.00864-15.

Kilfeather, P. et al. (2024) “Single-cell spatial transcriptomic and translatomic profiling of dopaminergic neurons in health, aging, and disease”, *Cell reports*, **43**(3), DOI: 10.1016/J.CELREP.2024.113784.

Kim, H. J. et al. (2008) “A novel mode of TRPML3 regulation by extracytosolic pH absent in the varitint-waddler phenotype”, *EMBO Journal*, **27**(8), pp. 1197–1205, DOI: 10.1038/EMBOJ.2008.56/ASSET/24C66078-89F9-4AE4-926D-D9272DFAC343/ASSETS/GRAPHIC/EMBJ200856-FIG-0006-M.JPG.

Kim, J. and K. L. Guan (2011) “Amino acid signaling in TOR Activation”, *Annual Review of Biochemistry*, **80**(Volume 80, 2011), pp. 1001–1032, DOI: 10.1146/ANNUREV-BIOCHEM-062209-094414/CITE/REFWORKS.

Kim, Y. C. and K. L. Guan (2015) “mTOR: a pharmacologic target for autophagy regulation”, *The Journal of Clinical Investigation*, **125**(1), pp. 25–32, DOI: 10.1172/JCI73939.

Kimanius, D. et al. (2021) “New tools for automated cryo-EM single-particle analysis in RELION-4.0”, *The Biochemical journal*, **478**(24), pp. 4169–4185, DOI: 10.1042/BCJ20210708.

Kirchhofer, A. et al. (2010) “Modulation of protein properties in living cells using nanobodies.”, *Nature structural & molecular biology*, **17**(1), pp. 133–138, DOI: 10.1038/nsmb.1727.

Kiselyov, K. et al. (2005) “TRP-ML1 is a lysosomal monovalent cation channel that undergoes proteolytic cleavage”, *Journal of Biological Chemistry*, **280**(52), pp. 43218–43223, DOI: 10.1074/jbc.M508210200.

Kobayashi, T. et al. (1998) “A lipid associated with the antiphospholipid syndrome regulates endosome structure and function”, *Nature*, **392**(6672), pp. 193–197, DOI: 10.1038/32440.

Koenig, P. A. et al. (2021) “Structure-guided multivalent nanobodies block SARS-CoV-2 infection and suppress mutational escape”, *Science*, **371**(6530), DOI: 10.1126/SCIENCE.ABE6230/SUPPL_FILE/ABE6230_S9.MP4.

Koide, S. (2009) “Engineering of recombinant crystallization chaperones”, *Current opinion in structural biology*, **19**(4), p. 449, DOI: 10.1016/J.SBI.2009.04.008.

Kompa, J. et al. (2023) “Exchangeable HaloTag Ligands for Super-Resolution Fluorescence Microscopy”, *Journal of the American Chemical Society*, **145**(5), pp. 3075–3083, DOI: 10.1021/JACS.2C11969/SUPPL_FILE/JA2C11969_SI_002.ZIP.

Kondratskyi, A. et al. (2018) “Ion channels in the regulation of autophagy”, *Autophagy*, **14**(1), p. 3, DOI: 10.1080/15548627.2017.1384887.

Kosicek, M. et al. (2018) “N-glycome of the Lysosomal Glycocalyx is Altered in Niemann-Pick Type C Disease (NPC) Model Cells”, *Molecular & cellular proteomics : MCP*, **17**(4), pp. 631–642, DOI: 10.1074/MCP.RA117.000129.

Krajcovic, M. et al. (2013) “mTOR regulates phagosome and entotic vacuole fission”, *Molecular biology of the cell*, **24**(23), pp. 3736–3745, DOI: 10.1091/MBC.E13-07-0408.

Krishnamurthy, H. and E. Gouaux (2012) “X-ray structures of LeuT in substrate-free outward-open and apo inward-open states.”, *Nature*, **481**(7382), pp. 469–474, DOI: 10.1038/nature10737.

Krogsaeter, E. K. et al. (2019) “The protein interaction networks of mucolipins and two-pore channels.”, *Biochimica et biophysica acta. Molecular cell research*, **1866**(7), pp. 1111–1123, DOI: 10.1016/j.bbamcr.2018.10.020.

Kromann-Hansen, T. et al. (2016) “A Camelid-derived Antibody Fragment Targeting the Active Site of a Serine Protease Balances between Inhibitor and Substrate Behavior”, *The Journal of Biological Chemistry*, **291**(29), p. 15156, DOI: 10.1074/JBC.M116.732503.

Lafourcade, C. et al. (2008) “Regulation of the V-ATPase along the Endocytic Pathway Occurs through Reversible Subunit Association and Membrane Localization”, *PLOS ONE*, **3**(7), e2758–.

Lange, I. et al. (2009) “TRPM2 Functions as a Lysosomal Ca2+-Release Channel in β Cells”, *Science signaling*, **2**(71), ra23, DOI: 10.1126/SCISIGNAL.2000278.

Laqtom, N. N. et al. (2022) “CLN3 is required for the clearance of glycerophosphodiesters from lysosomes”, *Nature 2022 609:7929*, **609**(7929), pp. 1005–1011, DOI: 10.1038/s41586-022-05221-y.

Law, C. J. et al. (2008) “Salt-bridge dynamics control substrate-induced conformational change in the membrane transporter GlpT.”, *Journal of molecular biology*, **378**(4), pp. 828–839, DOI: 10.1016/j.jmb.2008.03.029.

Lee, Y. et al. (2015) “Structural basis for the facilitative diffusion mechanism by SemiSWEET transporter.”, *Nature communications*, **6**, p. 6112, DOI: 10.1038/ncomms7112.

Lees, J. A. et al. (2020) “Insights into Lysosomal PI(3,5)P2 Homeostasis from a Structural-Biochemical Analysis of the PIKfyve Lipid Kinase Complex”, *Molecular cell*, **80**(4), 736–743.e4, DOI: 10.1016/J.MOLCEL.2020.10.003.

Lei, H. T. et al. (2018) “Crystal structure of arginine-bound lysosomal transporter SLC38A9 in the cytosol-open state”, *Nature structural & molecular biology*, **25**(6), p. 522, DOI: 10.1038/S41594-018-0072-2.

Lelek, M. et al. (2021) “Single-molecule localization microscopy.”, *Nature reviews. Methods primers*, **1**, DOI: 10.1038/s43586-021-00038-x.

Leser, C. et al. (2021) “Chemical and pharmacological characterization of the TRPML calcium channel blockers ML-SI1 and ML-SI3”, *European journal of medicinal chemistry*, **210**, DOI: 10.1016/J.EJMECH.2020.112966.

Levy, M. and J. Feingold (2000) “Estimating prevalence in single-gene kidney diseases progressing to renal failure”, *Kidney International*, **58**(3), pp. 925–943, DOI: 10.1046/J.1523-1755.2000.00250.X.

Li, K. et al. (2024) “Drosophila TMEM63 and mouse TMEM63A are lysosomal mechanosensory ion channels”, *Nature Cell Biology 2024 26:3*, **26**(3), pp. 393–403, DOI: 10.1038/s41556-024-01353-7.

Li, M. et al. (2017) “Structural basis of dual Ca2+/pH regulation of the endolysosomal TRPML1 channel”, *Nature structural & molecular biology*, **24**(3), pp. 205–213, DOI: 10.1038/NSMB.3362.

Li, P. et al. (2019) “Lysosomal Ion Channels as Decoders of Cellular Signals”, *Trends in biochemical sciences*, **44**(2), p. 110, DOI: 10.1016/J.TIBS.2018.10.006.

Li, P. et al. (2020) “LRRC8 family proteins within lysosomes regulate cellular osmoregulation and enhance cell survival to multiple physiological stresses”, *Proceedings of the National Academy of Sciences of the United States of America*, **117**(46), pp. 29155–29165, DOI: 10.1073/PNAS.2016539117/-/DCSUPPLEMENTAL.

Li, R.-J. et al. (2016a) “Regulation of mTORC1 by lysosomal calcium and calmodulin.”, *eLife*, **5**, DOI: 10.7554/eLife.19360.

Li, X. et al. (2013) “Regulation of membrane trafficking by signalling on endosomal and lysosomal membranes”, *The Journal of physiology*, **591**(18), pp. 4389–4401, DOI: 10.1113/JPHYSIOL.2013.258301.

Li, X. et al. (2016b) “A molecular mechanism to regulate lysosome motility for lysosome positioning and tubulation.”, *Nature cell biology*, **18**(4), pp. 404–417, DOI: 10.1038/ncb3324.

Lie, P. P. Y. et al. (2021) “Post-Golgi carriers, not lysosomes, confer lysosomal properties to pre-degradative organelles in normal and dystrophic axons”, *Cell Reports*, **35**(4), p. 109034, DOI: https://doi.org/10.1016/j.celrep.2021.109034.

Lie, P. P. et al. (2022) “Axonal transport of late endosomes and amphisomes is selectively modulated by local Ca2+ efflux and disrupted by PSEN1 loss of function”, *Science Advances*, **8**(17), p. 5716, DOI: 10.1126/SCIADV.ABJ5716/SUPPL_FILE/SCIADV.ABJ5716_DATA_S1.ZIP.

Lin-Moshier, Y. et al. (2014) “The Two-pore channel (TPC) interactome unmasks isoform-specific roles for TPCs in endolysosomal morphology and cell pigmentation.”, *Proceedings of the National Academy of Sciences of the United States of America*, **111**(36), pp. 13087–13092, DOI: 10.1073/pnas.1407004111.

Liou, W. et al. (1997) “The Autophagic and Endocytic Pathways Converge at the Nascent Autophagic Vacuoles”, *The Journal of Cell Biology*, **136**(1), p. 61, DOI: 10.1083/JCB.136.1.61.

Liu, B. et al. (2012) “LAAT-1 is the lysosomal lysine/arginine transporter that maintains amino acid homeostasis”, *Science (New York, N.Y.)*, **337**(6092), pp. 351–354, DOI: 10.1126/SCIENCE.1220281.

Liu, B. and D. Yang (2022) “Easily Established and Multifunctional Synthetic Nanobody Libraries as Research Tools”, *International journal of molecular sciences*, **23**(3), DOI: 10.3390/IJMS23031482.

Liu, Y.-T. et al. (2020) “Mesophasic organization of GABA(A) receptors in hippocampal inhibitory synapses.”, *Nature neuroscience*, **23**(12), pp. 1589–1596, DOI: 10.1038/s41593-020-00729-w.

Lloyd, J. B. (1992) *Lysosomal handling of cystine residues: stoichiometry of cysteine involvement.* (1992). DOI: 10.1042/bj2860979.

Lloyd-Evans, E. and H. Waller-Evans (2020) “Lysosomal Ca(2+) Homeostasis and Signaling in Health and Disease.”, *Cold Spring Harbor perspectives in biology*, **12**(6), DOI: 10.1101/cshperspect.a035311.

Lloyd-Evans, E. et al. (2008) “Niemann-Pick disease type C1 is a sphingosine storage disease that causes deregulation of lysosomal calcium.”, *Nature medicine*, **14**(11), pp. 1247–1255, DOI: 10.1038/nm.1876.

Löbel, M. et al. (2022) “Structural basis for proton coupled cystine transport by cystinosin.”, *Nature communications*, **13**(1), p. 4845, DOI: 10.1038/s41467-022-32589-2.

López, D. M. et al. (2020) “Characterization of the complex of the lysosomal membrane transporter MFSD1 and its accessory subunit GLMP”, *FASEB journal : official publication of the Federation of American Societies for Experimental Biology*, **34**(11), pp. 14695–14709, DOI: 10.1096/FJ.202000912RR.

Loreau, V. et al. (2023) “A nanobody toolbox to investigate localisation and dynamics of Drosophila titins and other key sarcomeric proteins”, *eLife*, **12**, DOI: 10.7554/ELIFE.79343.

Los, G. V. et al. (2008) “HaloTag: A novel protein labeling technology for cell imaging and protein analysis”, *ACS Chemical Biology*, **3**(6), pp. 373–382, DOI: 10.1021/CB800025K/SUPPL_FILE/CB800025K-FILE012.PDF.

Luzio, J. P. et al. (2007) “The role of calcium and other ions in sorting and delivery in the late endocytic pathway”, *Biochemical Society transactions*, **35**(Pt 5), pp. 1088–1091, DOI: 10.1042/BST0351088.

Luzio, J. et al. (2009) “The delivery of endocytosed cargo to lysosomes”, *Biochemical Society Transactions*, **37**(5), pp. 1019–1021, DOI: 10.1042/BST0371019.

Mackenzie, B. et al. (2006) “Divalent metal-ion transporter DMT1 mediates both H+ -coupled Fe2+ transport and uncoupled fluxes”, *Pflugers Archiv : European journal of physiology*, **451**(4), pp. 544–558, DOI: 10.1007/S00424-005-1494-3.

Maday, S. et al. (2012) “Autophagosomes initiate distally and mature during transport toward the cell soma in primary neurons”, *The Journal of cell biology*, **196**(4), pp. 407–417, DOI: 10.1083/JCB.201106120.

Mancini, G. M. et al. (2000) “Lysosomal transport disorders.”, *Journal of inherited metabolic disease*, **23**(3), pp. 278–292, DOI: 10.1023/a:1005640214408.

Manglik, A. et al. (2017) “Nanobodies to Study G Protein-Coupled Receptor Structure and Function”, *Annual review of pharmacology and toxicology*, **57**, pp. 19–37, DOI: 10.1146/ANNUREV-PHARMTOX-010716-104710.

Mann, J. B. (1968) “ATOMIC STRUCTURE CALCULATIONS. II. HARTREE-FOCK WAVEFUNCTIONS AND RADIAL EXPECTATION VALUES: HYDROGEN TO LAWRENCIUM.”, DOI: 10.2172/4553157.

Markello, T. C. et al. (1993) “Improved renal function in children with cystinosis treated with cysteamine”, *The New England journal of medicine*, **328**(16), pp. 1157–1162, DOI: 10.1056/NEJM199304223281604.

Martina, J. A. et al. (2012) “MTORC1 functions as a transcriptional regulator of autophagy by preventing nuclear transport of TFEB”, *Autophagy*, **8**(6), pp. 903–914, DOI: 10.4161/AUTO.19653.

Masiulis, S. et al. (2019) “GABAA receptor signalling mechanisms revealed by structural pharmacology”, *Nature*, **565**(7740), pp. 454–459, DOI: 10.1038/S41586-018-0832-5.

Massa, S. et al. (2014) “Site-specific labeling of cysteine-tagged camelid single-domain antibody-fragments for use in molecular imaging”, *Bioconjugate chemistry*, **25**(5), pp. 979–988, DOI: 10.1021/BC500111T.

McMahon, C. et al. (2018) “Yeast surface display platform for rapid discovery of conformationally selective nanobodies”, *Nature Structural & Molecular Biology 2018 25:3*, **25**(3), pp. 289–296, DOI: 10.1038/s41594-018-0028-6.

Medina, D. L. et al. (2011) “Transcriptional activation of lysosomal exocytosis promotes cellular clearance.”, *Developmental cell*, **21**(3), pp. 421–430, DOI: 10.1016/j.devcel.2011.07.016.

Medina, D. L. et al. (2015) “Lysosomal calcium signalling regulates autophagy through calcineurin and âTFEB”, *Nature cell biology*, **17**(3), pp. 288–299, DOI: 10.1038/NCB3114.

Mellman, I (1989) “Organelles observed: lysosomes.”, *Science (New York, N.Y.)*, **244**(4906), pp. 853–854, DOI: 10.1126/science.244.4906.853.

Miao, Y. et al. (2015) “A TRP channel senses lysosome neutralization by pathogens to trigger their expulsion”, *Cell*, **161**(6), pp. 1306–1319, DOI: 10.1016/j.cell.2015.05.009.

Miedel, M. T. et al. (2006) “Posttranslational cleavage and adaptor protein complex-dependent trafficking of mucolipin-1”, *Journal of Biological Chemistry*, **281**(18), pp. 12751–12759, DOI: 10.1074/jbc.M511104200.

Mikhaylova, M. et al. (2015) “Resolving bundled microtubules using anti-tubulin nanobodies”, *Nature Communications 2015 6:1*, **6**(1), pp. 1–7, DOI: 10.1038/ncomms8933.

Minckley, T. F. et al. (2019) “Sub-nanomolar sensitive GZnP3 reveals TRPML1-mediated neuronal Zn2+ signals”, *Nature communications*, **10**(1), DOI: 10.1038/S41467-019-12761-X.

Miyaji, T. et al. (2008) “Identification of a vesicular aspartate transporter.”, *Proceedings of the National Academy of Sciences of the United States of America*, **105**(33), pp. 11720–11724, DOI: 10.1073/pnas.0804015105.

Mizushima, N. et al. (2001) “Dissection of autophagosome formation using Apg5-deficient mouse embryonic stem cells”, *The Journal of cell biology*, **152**(4), pp. 657–667, DOI: 10.1083/JCB.152.4.657.

Molday, L. L. and R. S. Molday (2014) “1D4: a versatile epitope tag for the purification and characterization of expressed membrane and soluble proteins”, *Methods in molecular biology (Clifton, N.J.)*, **1177**, DOI: 10.1007/978-1-4939-1034-2_1.

Morgan, A. J. et al. (2021) “Choreographing endo-lysosomal Ca2+ throughout the life of a phagosome”, *Biochimica et Biophysica Acta (BBA) - Molecular Cell Research*, **1868**(7), p. 119040, DOI: 10.1016/J.BBAMCR.2021.119040.

Morgenstern, T. J. et al. (2019) “A potent voltage-gated calcium channel inhibitor engineered from a nanobody targeted to auxiliary CaVβ subunits”, *eLife*, **8**, DOI: 10.7554/ELIFE.49253.

Morgenstern, T. J. et al. (2022) “Selective posttranslational inhibition of CaVβ1-associated voltage-dependent calcium channels with a functionalized nanobody”, *Nature Communications 2022 13:1*, **13**(1), pp. 1–19, DOI: 10.1038/s41467-022-35025-7.

Moriya, H. (2015) “Quantitative nature of overexpression experiments”, *Molecular Biology of the Cell*, **26**(22), p. 3932, DOI: 10.1091/MBC.E15-07-0512.

Moutel, S. et al. (2016) “NaLi-H1: A universal synthetic library of humanized nanobodies providing highly functional antibodies and intrabodies”, *eLife*, **5**(JULY), DOI: 10.7554/ELIFE.16228.

Mullock, B. M. et al. (1998) “Fusion of lysosomes with late endosomes produces a hybrid organelle of intermediate density and is NSF dependent.”, *The Journal of cell biology*, **140**(3), pp. 591–601, DOI: 10.1083/jcb.140.3.591.

Muyldermans, S. (2013) “Nanobodies: natural single-domain antibodies.”, *Annual review of biochemistry*, **82**, pp. 775–797, DOI: 10.1146/annurev-biochem-063011-092449.

Muyldermans, S. (2021) “Applications of Nanobodies.”, *Annual Review of Animal Biosciences*, **9**, pp. 401–421, DOI: 10.1146/ANNUREV-ANIMAL-021419-083831/CITE/REFWORKS.

Nakamura, S. et al. (2020) “LC3 lipidation is essential for TFEB activation during the lysosomal damage response to kidney injury.”, *Nature cell biology*, **22**(10), pp. 1252–1263, DOI: 10.1038/s41556-020-00583-9.

Napolitano, G. et al. (2015) “Impairment of chaperone-mediated autophagy leads to selective lysosomal degradation defects in the lysosomal storage disease cystinosis.”, *EMBO molecular medicine*, **7**(2), pp. 158–174, DOI: 10.15252/emmm.201404223.

Napolitano, G. et al. (2018) “mTOR-dependent phosphorylation controls TFEB nuclear export”, *Nature communications*, **9**(1), DOI: 10.1038/S41467-018-05862-6.

Nelson, T. et al. (2017) “Lack of specificity of antibodies raised against CLN3, the lysosomal/endosomal transmembrane protein mutated in juvenile Batten disease”, *Bioscience reports*, **37**(6), DOI: 10.1042/BSR20171229.

Nesterova, G. and W. Gahl (2008) “Nephropathic cystinosis: late complications of a multisystemic disease”, *Pediatric nephrology (Berlin, Germany)*, **23**(6), pp. 863–878, DOI: 10.1007/S00467-007-0650-8.

Nevo, N. et al. (2017) “Impact of Cystinosin Glycosylation on Protein Stability by Differential Dynamic Stable Isotope Labeling by Amino Acids in Cell Culture (SILAC).”, *Molecular & cellular proteomics : MCP*, **16**(3), pp. 457–468, DOI: 10.1074/mcp.M116.063867.

Nguyen-Duc, T. et al. (2013) “Nanobody-based chromatin immunoprecipitation/microarray analysis for genome-wide identification of transcription factor DNA binding sites”, *Nucleic Acids Research*, **41**(5), e59–e59, DOI: 10.1093/NAR/GKS1342.

Nishiyama, A. et al. (2020) “Two distinct modes of DNMT1 recruitment ensure stable maintenance DNA methylation”, *Nature Communications*, **11**(1), pp. 1–17, DOI: 10.1038/s41467-020-15006-4.

Nixon, R. A. (2013) “The role of autophagy in neurodegenerative disease”, *Nature medicine*, **19**(8), pp. 983–997, DOI: 10.1038/NM.3232.

Olichon, A. and A. D. Marco (2012) “Preparation of a naïve library of camelid single domain antibodies”, *Methods in molecular biology (Clifton, N.J.)*, **911**, pp. 65–78, DOI: 10.1007/978-1-61779-968-6_5.

Palmieri, M. et al. (2011) “Characterization of the CLEAR network reveals an integrated control of cellular clearance pathways”, *Human molecular genetics*, **20**(19), pp. 3852–3866, DOI: 10.1093/HMG/DDR306.

Paola, S. D. et al. (2018) “TRPML1: The Ca((2+))retaker of the lysosome.”, *Cell calcium*, **69**, pp. 112–121, DOI: 10.1016/j.ceca.2017.06.006.

Pardon, E. et al. (2014) “A general protocol for the generation of Nanobodies for structural biology”, *Nature Protocols 2014 9:3*, **9**(3), pp. 674–693, DOI: 10.1038/nprot.2014.039.

Park, J. G. et al. (2022) “The lysosomal transporter TAPL has a dual role as peptide translocator and phosphatidylserine floppase”, *Nature Communications*, **13**(1), pp. 1–16, DOI: 10.1038/s41467-022-33593-2.

Park, M. et al. (2002) “Lysosomal cystine storage augments apoptosis in cultured human fibroblasts and renal tubular epithelial cells”, *Journal of the American Society of Nephrology : JASN*, **13**(12), pp. 2878–2887, DOI: 10.1097/01.ASN.0000036867.49866.59.

Parker, J. L. et al. (2021a) “Cryo-EM structure of PepT2 reveals structural basis for proton-coupled peptide and prodrug transport in mammals.”, *Science advances*, **7**(35), DOI: 10.1126/sciadv.abh3355.

Parker, J. L. et al. (2021b) “Structural basis of antifolate recognition and transport by PCFT.”, *Nature*, **595**(7865), pp. 130–134, DOI: 10.1038/s41586-021-03579-z.

Pastore, N. et al. (2013) “Gene transfer of master autophagy regulator TFEB results in clearance of toxic protein and correction of hepatic disease in alpha-1-anti-trypsin deficiency”, *EMBO molecular medicine*, **5**(3), pp. 397–412, DOI: 10.1002/EMMM.201202046.

Pechincha, C. et al. (2022) “Lysosomal enzyme trafficking factor LYSET enables nutritional usage of extracellular proteins”, *Science (New York, N.Y.)*, **378**(6615), DOI: 10.1126/SCIENCE.ABN5637.

Pedersen, A. V. et al. (2014) “A conserved salt bridge between transmembrane segments 1 and 10 constitutes an extracellular gate in the dopamine transporter.”, *The Journal of biological chemistry*, **289**(50), pp. 35003–35014, DOI: 10.1074/jbc.M114.586982.

Peng, X. et al. (2024) “Discovery and characterization of novel TRPML1 agonists”, *Bioorganic & Medicinal Chemistry Letters*, **98**, p. 129595, DOI: 10.1016/J.BMCL.2023.129595.

Petit, C. S. et al. (2013) “Recruitment of folliculin to lysosomes supports the amino acid-dependent activation of Rag GTPases”, *The Journal of cell biology*, **202**(7), pp. 1107–1122, DOI: 10.1083/JCB.201307084.

Pettersen, E. F. et al. (2021) “UCSF ChimeraX: Structure visualization for researchers, educators, and developers”, *Protein science : a publication of the Protein Society*, **30**(1), pp. 70–82, DOI: 10.1002/PRO.3943.

Pierzyńska-Mach, A. et al. (2014) “Evaluation of acridine orange, LysoTracker Red, and quinacrine as fluorescent probes for long-term tracking of acidic vesicles”, *Cytometry. Part A : the journal of the International Society for Analytical Cytology*, **85**(8), pp. 729–737, DOI: 10.1002/CYTO.A.22495.

Pillay, C. S. et al. (2002) “Endolysosomal proteolysis and its regulation”, *The Biochemical journal*, **363**(Pt 3), pp. 417–429, DOI: 10.1042/0264-6021:3630417.

Pisoni, R. L. et al. (1985) “THE JOURNAL OF BIOLOGICAL CHEMISTRY Detection and Characterization of Carrier-mediated Cationic Amino Acid Transport in Lysosomes of Normal and Cystinotic Human Fibroblasts ROLE IN THERAPEUTIC CYSTINE REMOVAL?*”, **260**(8), p. 47914798, DOI: 10.1016/S0021-9258(18)89141-4.

Platonova, E. et al. (2015) “Single-molecule microscopy of molecules tagged with GFP or RFP derivatives in mammalian cells using nanobody binders”, *Methods*, **88**, pp. 89–97, DOI: 10.1016/J.YMETH.2015.06.018.

Platt, F. M. et al. (2012) "Lysosomal storage disorders: The cellular impact of lysosomal dysfunction", *Journal of Cell Biology*, **199**(5), pp. 723–734, DOI: 10.1083/jcb.201208152.

Platt, F. M. et al. (2018) "Lysosomal storage diseases", *Nature Reviews Disease Primers 2018 4:1*, **4**(1), pp. 1–25, DOI: 10.1038/s41572-018-0025-4.

Pleiner, T. et al. (2015) "Nanobodies: Site-specific labeling for super-resolution imaging, rapid epitope- mapping and native protein complex isolation", *eLife*, **4**(DECEMBER2015), DOI: 10.7554/ELIFE.11349.

Pleiner, T. et al. (2018) "A toolbox of anti-mouse and anti-rabbit IgG secondary nanobodies", *The Journal of cell biology*, **217**(3), pp. 1143–1154, DOI: 10.1083/JCB.201709115.

Plesch, E. et al. (2018) "Selective agonist of TRPML2 reveals direct role in chemokine release from innate immune cells", *eLife*, **7**, DOI: 10.7554/ELIFE.39720.

Polito, V. A. et al. (2014) "Selective clearance of aberrant tau proteins and rescue of neurotoxicity by transcription factor EB", *EMBO molecular medicine*, **6**(9), pp. 1142–1160, DOI: 10.15252/EMMM.201303671.

Pollmanns, M. R. et al. (2022) "Activated Endolysosomal Cation Channel TRPML1 Facilitates Maturation of α-Synuclein-Containing Autophagosomes", *Frontiers in Cellular Neuroscience*, **16**, p. 861202, DOI: 10.3389/FNCEL.2022.861202/BIBTEX.

Poteryaev, D. et al. (2010) "Identification of the switch in early-to-late endosome transition", *Cell*, **141**(3), pp. 497–508, DOI: 10.1016/J.CELL.2010.03.011.

Pryor, P. R. et al. (2000) "The role of intraorganellar Ca(2+) in late endosome-lysosome heterotypic fusion and in the reformation of lysosomes from hybrid organelles.", *The Journal of cell biology*, **149**(5), pp. 1053–1062, DOI: 10.1083/jcb.149.5.1053.

Pryor, P. R. et al. (2006) "Mucolipin-1 is a lysosomal membrane protein required for intracellular lactosylceramide traffic", *Traffic (Copenhagen, Denmark)*, **7**(10), p. 1388, DOI: 10.1111/J.1600-0854.2006.00475.X.

Pu, J. et al. (2016) "Mechanisms and functions of lysosome positioning", *Journal of Cell Science*, **129**(23), p. 4329, DOI: 10.1242/JCS.196287.

Punjani, A. et al. (2017) "cryoSPARC: algorithms for rapid unsupervised cryo-EM structure determination", *Nature methods*, **14**(3), pp. 290–296, DOI: 10.1038/NMETH.4169.

Qi, X. et al. (2016) "Cathepsin B modulates lysosomal biogenesis and host defense against Francisella novicida infection", *Journal of Experimental Medicine*, **213**(10), pp. 2081–2097, DOI: 10.1084/JEM.20151938.

Racusen, L. C. et al. (1995) "Renal proximal tubular epithelium from patients with nephropathic cystinosis: Immortalized cell lines as in vitro model systems", *Kidney International*, **48**(2), pp. 536–543, DOI: 10.1038/KI.1995.324.

Rajan, S. et al. (2000) "TASK-3, a novel tandem pore domain acid-sensitive K+ channel. An extracellular histidine as pH sensor", *Journal of Biological Chemistry*, **275**(22), pp. 16650–16657, DOI: 10.1074/JBC.M000030200/ASSET/F3BB747B-72D2-4E17-B97C-6F50D87BFB7A/MAIN.ASSETS/GR8.JPG.

Rasmussen, S. G. et al. (2011) "Structure of a nanobody-stabilized active state of the β2 adrenoceptor", *Nature 2011 469:7329*, **469**(7329), pp. 175–180, DOI: 10.1038/nature09648.

Reddy, A. et al. (2001) "Plasma membrane repair is mediated by Ca(2+)-regulated exocytosis of lysosomes", *Cell*, **106**(2), pp. 157–169, DOI: 10.1016/S0092-8674(01)00421-4.

Reed, A. P. et al. (2016) "Dominant-Negative Effect of a Missense Variant in the TASK-2 (KCNK5) K+ Channel Associated with Balkan Endemic Nephropathy", *PLOS ONE*, **11**(5), e0156456, DOI: 10.1371/JOURNAL.PONE.0156456.

Rega, L. R. et al. (2016) "Activation of the transcription factor EB rescues lysosomal abnormalities in cystinotic kidney cells", *Kidney international*, **89**(4), pp. 862–873, DOI: 10.1016/J.KINT.2015.12.045.

Repnik, U. et al. (2012) "Lysosomes and lysosomal cathepsins in cell death", *Biochimica et biophysica acta*, **1824**(1), pp. 22–33, DOI: 10.1016/J.BBAPAP.2011.08.016.

Rice, G. et al. (2023) "TomoTwin: generalized 3D localization of macromolecules in cryo-electron tomograms with structural data mining", *Nature Methods 2023 20:6*, **20**(6), pp. 871–880, DOI: 10.1038/s41592-023-01878-z.

Ries, J. et al. (2012) "A simple, versatile method for GFP-based super-resolution microscopy via nanobodies", *Nature methods*, **9**(6), pp. 582–584, DOI: 10.1038/NMETH.1991.

Rink, J. et al. (2005) "Rab conversion as a mechanism of progression from early to late endosomes.", *Cell*, **122**(5), pp. 735–749, DOI: 10.1016/j.cell.2005.06.043.

Roczniak-Ferguson, A. et al. (2012) "The transcription factor TFEB links mTORC1 signaling to transcriptional control of lysosome homeostasis", *Science signaling*, **5**(228), DOI: 10.1126/SCISIGNAL.2002790.

Rodriguez, C. F. et al. (2021) "Structural basis for substrate specificity of heteromeric transporters of neutral amino acids", *Proceedings of the National Academy of Sciences of the United States of America*, **118**(49), e2113573118, DOI: 10.1073/PNAS.2113573118/SUPPL_FILE/PNAS.2113573118.SAPP.PDF.

Rödström, K. E. et al. (2024) "Extracellular modulation of TREK-2 activity with nanobodies provides insight into the mechanisms of K2P channel regulation", *Nature Communications 2024 15:1*, **15**(1), pp. 1–13, DOI: 10.1038/s41467-024-48536-2.

Rohou, A. and N. Grigorieff (2015) "CTFFIND4: Fast and accurate defocus estimation from electron micrographs", *Journal of structural biology*, **192**(2), p. 216, DOI: 10.1016/J.JSB.2015.08.008.

Rosa-Ferreira, C. and S. Munro (2011) "Arl8 and SKIP act together to link lysosomes to kinesin-1", *Developmental cell*, **21**(6), pp. 1171–1178, DOI: 10.1016/J.DEVCEL.2011.10.007.

Rosato, A et al. (2019) "TRPML1 links lysosomal calcium to autophagosome biogenesis through the activation of the CaMKKβ/VPS34 pathway.", *Nature communications*, **10**(1), p. 5630, DOI: 10.1038/s41467-019-13572-w.

Rothbauer, U. et al. (2006) "Targeting and tracing antigens in live cells with fluorescent nanobodies", *Nature Methods 2006 3:11*, **3**(11), pp. 887–889, DOI: 10.1038/nmeth953.

Rudnik, S. and M. Damme (2021) "The lysosomal membraneâexport of metabolites and beyond", *The FEBS Journal*, **288**(14), pp. 4168–4182, DOI: 10.1111/FEBS.15602.

Rühl, P. et al. (2021) "Estradiol analogs attenuate autophagy, cell migration and invasion by direct and selective inhibition of TRPML1, independent of estrogen receptors.", *Scientific reports*, **11**(1), p. 8313, DOI: 10.1038/s41598-021-87817-4.

Ruivo, R. et al. (2012) "Mechanism of proton/substrate coupling in the heptahelical lysosomal transporter cystinosin.", *Proceedings of the National Academy of Sciences of the United States of America*, **109**(5), E210–7, DOI: 10.1073/pnas.1115581109.

Rust, M. J. et al. (2006) "Sub-diffraction-limit imaging by stochastic optical reconstruction microscopy (STORM)", *Nature Methods 2006 3:10*, **3**(10), pp. 793–796, DOI: 10.1038/nmeth929.

Rutz, S. et al. (2022) "Structure of a volume-regulated heteromeric LRRC8A/C channel", *Nature Structural & Molecular Biology*, **30**(1), pp. 52–61, DOI: 10.1038/s41594-022-00899-0.

Saffi, G. T. and R. J. Botelho (2019) "Lysosome Fission: Planning for an Exit", *Trends in cell biology*, **29**(8), pp. 635–646, DOI: 10.1016/J.TCB.2019.05.003.

Saftig, P. and J. Klumperman (2009) "Lysosome biogenesis and lysosomal membrane proteins: trafficking meets function.", *Nature reviews. Molecular cell biology*, **10**(9), pp. 623–635, DOI: 10.1038/nrm2745.

Saint-Pol, A. et al. (1999) "Cytosol-to-lysosome transport of free polymannose-type oligosaccharides. Kinetic and specificity studies using rat liver lysosomes", *The Journal of biological chemistry*, **274**(19), pp. 13547–13555, DOI: 10.1074/JBC.274.19.13547.

Samie, M. et al. (2013) "A TRP channel in the lysosome regulates large particle phagocytosis via focal exocytosis.", *Developmental cell*, **26**(5), pp. 511–524, DOI: 10.1016/j.devcel.2013.08.003.

Sancak, Y. et al. (2010) "Ragulator-Rag complex targets mTORC1 to the lysosomal surface and is necessary for its activation by amino acids", *Cell*, **141**(2), pp. 290–303, DOI: 10.1016/J.CELL.2010.02.024.

Sandoz, G. et al. (2009) "Extracellular acidification exerts opposite actions on TREK1 and TREK2 potassium channels via a single conserved histidine residue", *Proceedings of the National Academy of Sciences of the United States of America*, **106**(34), pp. 14628–14633, DOI: 10.1073/PNAS.0906267106.

Santoni, G. et al. (2020) “Pathophysiological Role of Transient Receptor Potential Mucolipin Channel 1 in Calcium-Mediated Stress-Induced Neurodegenerative Diseases”, *Frontiers in Physiology*, **11**, DOI: 10.3389/FPHYS.2020.00251.

Sardiello, M. et al. (2009) “A gene network regulating lysosomal biogenesis and function”, *Science (New York, N.Y.)*, **325**(5939), pp. 473–477, DOI: 10.1126/SCIENCE.1174447.

Saudek, V. (2012) “Cystinosin, MPDU1, SWEETs and KDELR belong to a well-defined protein family with putative function of cargo receptors involved in vesicle trafficking.”, *PloS one*, **7**(2), e30876, DOI: 10.1371/journal.pone.0030876.

Saxton, R. A. and D. M. Sabatini (2017) “mTOR Signaling in Growth, Metabolism, and Disease”, *Cell*, **169**(2), pp. 361–371, DOI: 10.1016/J.CELL.2017.03.035.

Scalise, M. et al. (2019) “Insights into the transport side of the human SLC38A9 transceptor”, *Biochimica et Biophysica Acta (BBA) - Biomembranes*, **1861**(9), pp. 1558–1567, DOI: 10.1016/J.BBAMEM.2019.07.006.

Scharenberg, S. G. et al. (2023) “An SPNS1-dependent lysosomal lipid transport pathway that enables cell survival under choline limitation”, *Science Advances*, **9**(16), DOI: 10.1126/SCIADV.ADF8966/SUPPL_FILE/SCIADV.ADF8966_TABLES_S1_TO_S3.ZIP.

Schindelin, J. et al. (2012) “Fiji: an open-source platform for biological-image analysis”, *Nature Methods 2012 9:7*, **9**(7), pp. 676–682, DOI: 10.1038/nmeth.2019.

Schleinitz, A. et al. (2023) “Consecutive functions of small GTPases guide HOPS-mediated tethering of late endosomes and lysosomes”, *Cell Reports*, **42**(1), p. 111969, DOI: 10.1016/J.CELREP.2022.111969.

Schmid, S. L. et al. (2014) “Endocytosis: Past, Present, and Future”, *Cold Spring Harbor Perspectives in Biology*, **6**(12), DOI: 10.1101/CSHPERSPECT.A022509.

Schmiege, P. et al. (2017) “Human TRPML1 channel structures in open and closed conformations.”, *Nature*, **550**(7676), pp. 366–370, DOI: 10.1038/nature24036.

Schmiege, P. et al. (2021) “Atomic insights into ML-SI3 mediated human TRPML1 inhibition”, *Structure*, **29**(11), 1295–1302.e3, DOI: 10.1016/J.STR.2021.06.003.

Schmiege, P. et al. (2024) “Structure and inhibition of the human lysosomal transporter Sialin”, *Nature Communications 2024 15:1*, **15**(1), pp. 1–11, DOI: 10.1038/s41467-024-48535-3.

Schneider, J. A. et al. (1995) “Recent advances in the treatment of cystinosis”, *Journal of inherited metabolic disease*, **18**(4), pp. 387–397, DOI: 10.1007/BF00710051.

Schneider, R. et al. (2015) “Mobility of calcium channels in the presynaptic membrane.”, *Neuron*, **86**(3), pp. 672–679, DOI: 10.1016/j.neuron.2015.03.050.

Schnizler, K. et al. (2003) “The roboocyte: Automated cDNA/mRNA injection and subsequent TEVC recording on xenopus oocytes oin 96-well microtiter plates”, *Receptors and Channels*, **9**(1), pp. 41–48, DOI: 10.1080/10606820308253.

Schoof, M. et al. (2020) “An ultrapotent synthetic nanobody neutralizes SARS-CoV-2 by stabilizing inactive Spike”, *Science*, **370**(6523), pp. 1473–1479, DOI: 10.1126/SCIENCE.ABE3255/SUPPL_FILE/ABE3255_SCHOOF_SM.REV1.PDF.

Schwake, M. et al. (2013) “Lysosomal Membrane Proteins and Their Central Role in Physiology”, *Traffic*, **14**(7), pp. 739–748, DOI: 10.1111/TRA.12056.

Seiferth, D. and P. C. Biggin (2024) “Exploring the influence of pore shape on conductance and permeation”, *Biophysical Journal*, **0**(0), DOI: 10.1016/j.bpj.2024.07.010.

Servais, A. et al. (2008) “Late-onset nephropathic cystinosis: clinical presentation, outcome, and genotyping”, *Clinical journal of the American Society of Nephrology : CJASN*, **3**(1), pp. 27–35, DOI: 10.2215/CJN.01740407.

Settembre, C. et al. (2011) “TFEB links autophagy to lysosomal biogenesis”, *Science (New York, N.Y.)*, **332**(6036), pp. 1429–1433, DOI: 10.1126/SCIENCE.1204592.

Settembre, C. et al. (2012) “A lysosome-to-nucleus signalling mechanism senses and regulates the lysosome via mTOR and TFEB”, *The EMBO journal*, **31**(5), pp. 1095–1108, DOI: 10.1038/EMBOJ.2012.32.

Sevin, C. and K. Deiva (2021) “Clinical Trials for Gene Therapy in Lysosomal Diseases With CNS Involvement”, *Frontiers in Molecular Biosciences*, **8**, p. 624988, DOI: 10.3389/FMOLB.2021.624988/BIBTEX.

Shah, N. B. and T. M. Duncan (2014) “Bio-layer interferometry for measuring kinetics of protein-protein interactions and allosteric ligand effects”, *Journal of visualized experiments : JoVE*(, 84), DOI: 10.3791/51383.

Shang, S. et al. (2016) “Intracellular TRPA1 mediates Ca2+ release from lysosomes in dorsal root ganglion neurons”, *Journal of Cell Biology*, **215**(3), pp. 369–381, DOI: 10.1083/JCB.201603081.

Shen, D. et al. (2012) “Lipid storage disorders block lysosomal trafficking by inhibiting a TRP channel and lysosomal calcium release.”, *Nature communications*, **3**, p. 731, DOI: 10.1038/ncomms1735.

Shotelersuk, V. et al. (1998) “CTNS mutations in an American-based population of cystinosis patients”, *American journal of human genetics*, **63**(5), pp. 1352–1362, DOI: 10.1086/302118.

Skowyra, M. L. et al. (2018) “Triggered recruitment of ESCRT machinery promotes endolysosomal repair”, *Science (New York, N.Y.)*, **360**(6384), DOI: 10.1126/SCIENCE.AAR5078.

Slaugenhaupt, S. A. et al. (1999) “Mapping of the mucolipidosis type IV gene to chromosome 19p and definition of founder haplotypes”, *American Journal of Human Genetics*, **65**(3), pp. 773–778, DOI: 10.1086/302549.

Smits, A. H. and M. Vermeulen (2016) “Characterizing ProteinâProtein Interactions Using Mass Spectrometry: Challenges and Opportunities”, *Trends in Biotechnology*, **34**(10), pp. 825–834, DOI: 10.1016/J.TIBTECH.2016.02.014/ASSET/C86C47BD-2FDC-4251-B6B0-1DEC149D1EE5/MAIN.ASSETS/GR2.JPG.

Sograte-Idrissi, S. et al. (2019) “Nanobody Detection of Standard Fluorescent Proteins Enables Multi-Target DNA-PAINT with High Resolution and Minimal Displacement Errors”, *Cells*, **8**(1), DOI: 10.3390/CELLS8010048.

Solcan, N. et al. (2012) “Alternating access mechanism in the POT family of oligopeptide transporters.”, *The EMBO journal*, **31**(16), pp. 3411–3421, DOI: 10.1038/emboj.2012.157.

Somogyi, A. et al. (2020) “TRPML1: A novel therapeutic target to remediate endolysosomal pathology in Alzheimer’s disease”, *Alzheimer’s & Dementia*, **16**(S2), e043397, DOI: 10.1002/ALZ.043397.

Somogyi, A. et al. (2023) “The synthetic TRPML1 agonist ML-SA1 rescues Alzheimer-related alterations of the endosomal-autophagic-lysosomal system”, *Journal of cell science*, **136**(6), DOI: 10.1242/JCS.259875.

Sönnichsen, B. et al. (2000) “Distinct membrane domains on endosomes in the recycling pathway visualized by multicolor imaging of Rab4, Rab5, and Rab11”, *The Journal of cell biology*, **149**(4), pp. 901–913, DOI: 10.1083/JCB.149.4.901.

Spinelli, S. et al. (1996) “The crystal structure of a llama heavy chain variable domain”, *Nature Structural Biology 1996 3:9*, **3**(9), pp. 752–757, DOI: 10.1038/nsb0996-752.

Spooner, E. et al. (2013) “Systematic screens for proteins that interact with the mucolipidosis type IV protein TRPML1.”, *PloS one*, **8**(2), e56780, DOI: 10.1371/journal.pone.0056780.

Stoorvogel, W et al. (1991) “Late endosomes derive from early endosomes by maturation.”, *Cell*, **65**(3), pp. 417–427, DOI: 10.1016/0092-8674(91)90459-c.

Stortelers, C. et al. (2018) “Modulating ion channel function with antibodies and nanobodies”, *Current Opinion in Immunology*, **52**, pp. 18–26, DOI: 10.1016/J.COI.2018.02.003.

Stralen, K. J. van et al. (2011) “Improvement in the renal prognosis in nephropathic cystinosis”, *Clinical journal of the American Society of Nephrology : CJASN*, **6**(10), pp. 2485–2491, DOI: 10.2215/CJN.02000311.

Su, Q. et al. (2023) “Recent advances of nanobody applications in diagnosis and detection”, *MedComm - Biomaterials and Applications*, **2**(3), e54, DOI: 10.1002/MBA2.54.

Sulea, T. et al. (2020) “Structure-based engineering of pH-dependent antibody binding for selective targeting of solid-tumor microenvironment”, *mAbs*, **12**(1), DOI: 10.1080/19420862.2019.1682866.

Sumayao, R. et al. (2016) "Lysosomal cystine accumulation promotes mitochondrial depolarization and induction of redox-sensitive genes in human kidney proximal tubular cells", *The Journal of Physiology*, **594**(12), p. 3353, DOI: 10.1113/JP271858.

Sumoza-Toledo, A. and R. Penner (2011) "TRPM2: a multifunctional ion channel for calcium signalling", *The Journal of Physiology*, **589**(Pt 7), p. 1515, DOI: 10.1113/JPHYSIOL.2010.201855.

Sun, C. et al. (2023) "Cryo-EM structures reveal native GABAA receptor assemblies and pharmacology", *Nature*, **622**(7981), p. 195, DOI: 10.1038/S41586-023-06556-W.

Sun, J. et al. (2022) "LAMTOR1 inhibition of TRPML1-dependent lysosomal calcium release regulates dendritic lysosome trafficking and hippocampal neuronal function", *The EMBO Journal*, **41**(5), e108119, DOI: https://doi.org/10.15252/embj.2021108119.

Sun, L. et al. (2015) "Novel role of TRPML2 in the regulation of the innate immune response", *Journal of immunology*, **195**(10), p. 4922, DOI: 10.4049/JIMMUNOL.1500163.

Sun, M et al. (2000) "Mucolipidosis type IV is caused by mutations in a gene encoding a novel transient receptor potential channel.", *Human molecular genetics*, **9**(17), pp. 2471–2478, DOI: 10.1093/hmg/9.17.2471.

Swanda, R. V. et al. (2023) "Lysosomal cystine governs ferroptosis sensitivity in cancer via cysteine stress response", *Molecular cell*, **83**(18), 3347–3359.e9, DOI: 10.1016/J.MOLCEL.2023.08.004.

Tang, J. C. et al. (2013) "XA nanobody-based system using fluorescent proteins as scaffolds for cell-specific gene manipulation", *Cell*, **154**(4), pp. 928–939, DOI: 10.1016/

J.CELL.2013.07.021/ATTACHMENT/9FF4AFAF-2F67-4600-899D-2D53431F955B/MMC2.PDF.

Taranta, A. et al. (2008) "Identification and subcellular localization of a new cystinosin isoform", *American journal of physiology. Renal physiology*, **294**(5), DOI: 10.1152/AJPRENAL.00413.2007.

Taranta, A. et al. (2012) "Distribution of cystinosin-LKG in human tissues", *Histochemistry and Cell Biology*, **138**(2), pp. 351–363, DOI: 10.1007/S00418-012-0958-8/FIGURES/8.

Taub, M. and F. Cutuli (2012) "Activation of AMP kinase plays a role in the increased apoptosis in the renal proximal tubule in cystinosis", *Biochemical and Biophysical Research Communications*, **426**(4), pp. 516–521, DOI: 10.1016/J.BBRC.2012.08.115.

Tedeschi, V. et al. (2021) "Lysosomal calcium is modulated by STIM1/TRPML1 interaction which participates to neuronal survival during ischemic preconditioning.", *FASEB journal : official publication of the Federation of American Societies for Experimental Biology*, **35**(2), e21277, DOI: 10.1096/fj.202001886R.

Thakore, P. et al. (2020) "TRPML1 channels initiate Ca 2+ sparks in vascular smooth muscle cells", *Science Signaling*, **13**(637), p. 1015, DOI: 10.1126/SCISIGNAL.ABA1015/SUPPL_FILE/ABA1015_SM.PDF.

Thamotharan, M. et al. (1997) "An active mechanism for completion of the final stage of protein degradation in the liver, lysosomal transport of dipeptides", *The Journal of biological chemistry*, **272**(18), pp. 11786–11790, DOI: 10.1074/JBC.272.18.11786.

Thoene, J. G. et al. (1976) “Cystinosis. Intracellular cystine depletion by aminothiols in vitro and in vivo”, *The Journal of clinical investigation*, **58**(1), pp. 180–189, DOI: 10.1172/JCI108448.

Thoene, J. et al. (1999) “Mutations of CTNS causing intermediate cystinosis”, *Molecular genetics and metabolism*, **67**(4), pp. 283–293, DOI: 10.1006/MGME.1999.2876.

Thoene, J. et al. (2013) “In vitro correction of disorders of lysosomal transport by microvesicles derived from baculovirus-infected Spodoptera cells”, *Molecular Genetics and Metabolism*, **109**(1), pp. 77–85, DOI: 10.1016/J.YMGME.2013.01.014.

Tian, X. et al. (2015) “A Voltage-Gated Calcium Channel Regulates Lysosomal Fusion with Endosomes and Autophagosomes and Is Required for Neuronal Homeostasis”, *PLOS Biology*, **13**(3), e1002103, DOI: 10.1371/JOURNAL.PBIO.1002103.

Town, M et al. (1998) “A novel gene encoding an integral membrane protein is mutated in nephropathic cystinosis.”, *Nature genetics*, **18**(4), pp. 319–324, DOI: 10.1038/ng0498-319.

Tsunemi, T. et al. (2019) “Increased Lysosomal Exocytosis Induced by Lysosomal Ca2+ Channel Agonists Protects Human Dopaminergic Neurons from α-Synuclein Toxicity”, *The Journal of neuroscience : the official journal of the Society for Neuroscience*, **39**(29), pp. 5760–5772, DOI: 10.1523/JNEUROSCI.3085-18.2019.

Tyshchuk, O. et al. (2017) “Detection of a phosphorylated glycine-serine linker in an IgG-based fusion protein”, *mAbs*, **9**(1), p. 94, DOI: 10.1080/19420862.2016.1236165.

Uchański, T. et al. (2020) “Nanobodies to study protein conformational states”, *Current Opinion in Structural Biology*, **60**, pp. 117–123, DOI: 10.1016/J.SBI.2020.01.003.

Uchański, T. et al. (2021) "Megabodies expand the nanobody toolkit for protein structure determination by single-particle cryo-EM", *Nature Methods 2021 18:1*, **18**(1), pp. 60–68, DOI: 10.1038/s41592-020-01001-6.

Udayar, V. et al. (2022) "Lysosomal dysfunction in neurodegeneration: emerging concepts and methods", *Trends in Neurosciences*, **45**(3), pp. 184–199, DOI: 10.1016/J.TINS.2021.12.004.

Uhlén, M. et al. (2015) "Proteomics. Tissue-based map of the human proteome.", *Science (New York, N.Y.)*, **347**(6220), p. 1260419, DOI: 10.1126/science.1260419.

Valm, A. M. et al. (2017) "Applying systems-level spectral imaging and analysis to reveal the organelle interactome.", *Nature*, **546**(7656), pp. 162–167, DOI: 10.1038/nature22369.

Venkatachalam, K. et al. (2015) "The Role of TRPMLs in Endolysosomal Trafficking and Function", *Cell calcium*, **58**(1), p. 48, DOI: 10.1016/J.CECA.2014.10.008.

Venkatarangan, V. et al. (2023) "ER-associated degradation in cystinosis pathogenesis and the prospects of precision medicine", *The Journal of Clinical Investigation*, **133**(19), DOI: 10.1172/JCI169551.

Venugopal, B. et al. (2007) "Neurologic, gastric, and opthalmologic pathologies in a murine model of mucolipidosis type IV", *American Journal of Human Genetics*, **81**(5), pp. 1070–1083, DOI: 10.1086/521954/ASSET/7401BA8A-8239-49EC-B111-DD7A795C07FF/MAIN.ASSETS/GR9.JPG.

Verdon, Q. et al. (2017) "SNAT7 is the primary lysosomal glutamine exporter required for extracellular protein-dependent growth of cancer cells", *Proceedings of the National Academy of Sciences of the United States of America*, **114**(18), E3602–E3611, DOI: 10.1073/PNAS.1617066114.

Vergarajauregui, S. et al. (2008) “Autophagic dysfunction in mucolipidosis type IV patients.”, *Human molecular genetics*, **17**(17), pp. 2723–2737, DOI: 10.1093/hmg/ddn174.

Vergarajauregui, S. et al. (2009) “Identification of the penta-EF-hand protein ALG-2 as a Ca2+-dependent interactor of mucolipin-1”, *The Journal of biological chemistry*, **284**(52), pp. 36357–36366, DOI: 10.1074/JBC.M109.047241.

Vergarajauregui, S. et al. (2011) “LAPTMs regulate lysosomal function and interact with mucolipin 1: new clues for understanding mucolipidosis type IV.”, *Journal of cell science*, **124**(Pt 3), pp. 459–468, DOI: 10.1242/jcs.076240.

Verheijen, F. W. et al. (1999) “A new gene, encoding an anion transporter, is mutated in sialic acid storage diseases.”, *Nature genetics*, **23**(4), pp. 462–465, DOI: 10.1038/70585.

Virant, D. et al. (2018) “A peptide tag-specific nanobody enables high-quality labeling for dSTORM imaging”, *Nature Communications 2018 9:1*, **9**(1), pp. 1–14, DOI: 10.1038/s41467-018-03191-2.

Wakabayashi, K. et al. (2011) “Mucolipidosis Type IV: an Update”, *Molecular genetics and metabolism*, **104**(3), p. 206, DOI: 10.1016/J.YMGME.2011.06.006.

Wallabregue, A. et al. (2016) “Selective Imaging of Late Endosomes with a pH-Sensitive Diazaoxatriangulene Fluorescent Probe”, *Journal of the American Chemical Society*, **138**(6), pp. 1752–1755, DOI: 10.1021/JACS.5B09972/ASSET/IMAGES/LARGE/JA-2015-099723_0004.JPEG.

Wang, H. et al. (2023) “Advances in Drug Discovery Targeting Lysosomal Membrane Proteins”, *Pharmaceuticals 2023, Vol. 16, Page 601*, **16**(4), p. 601, DOI: 10.3390/PH16040601.

Wang, L. and D. I. Yule (2018) “Differential regulation of ion channels function by proteolysis”, *Biochimica et biophysica acta. Molecular cell research*, **1865**(11 Pt B), p. 1698, DOI: 10.1016/J.BBAMCR.2018.07.004.

Wang, W. et al. (2015) “Up-regulation of lysosomal TRPML1 channels is essential for lysosomal adaptation to nutrient starvation.”, *Proceedings of the National Academy of Sciences of the United States of America*, **112**(11), E1373–81, DOI: 10.1073/pnas.1419669112.

Wang, X. et al. (2012) “TPC proteins are phosphoinositide- Activated sodium-selective ion channels in endosomes and lysosomes”, *Cell*, **151**(2), pp. 372–383, DOI: 10.1016/j.cell.2012.08.036.

Waterhouse, A. M. et al. (2009) “Jalview Version 2âa multiple sequence alignment editor and analysis workbench”, *Bioinformatics*, **25**(9), pp. 1189–1191, DOI: 10.1093/BIOINFORMATICS/BTP033.

Wentinck, K. et al. (2022) “Putting on molecular weight: Enabling cryo-EM structure determination of sub-100-kDa proteins”, *Current research in structural biology*, **4**, pp. 332–337, DOI: 10.1016/J.CRSTBI.2022.09.005.

White, P. et al. (2017) “Exploitation of an iron transporter for bacterial protein antibiotic import”, *Proceedings of the National Academy of Sciences of the United States of America*, **114**(45), pp. 12051–12056, DOI: 10.1073/PNAS.1713741114.

Willett, R. et al. (2017) “TFEB regulates lysosomal positioning by modulating TMEM55B expression and JIP4 recruitment to lysosomes”, *Nature communications*, **8**(1), DOI: 10.1038/S41467-017-01871-Z.

Wilmer, M. J. et al. (2011) “Cystinosis: practical tools for diagnosis and treatment”, *Pediatric Nephrology (Berlin, Germany)*, **26**(2), p. 205, DOI: 10.1007/S00467-010-1627-6.

Winkler, M. B. L. et al. (2019) "Structural Insight into Eukaryotic Sterol Transport through Niemann-Pick Type C Proteins.", *Cell*, **179**(2), 485–497.e18, DOI: 10.1016/j.cell.2019.08.038.

Woo, J. S. et al. (2020) "The short isoform of extended synaptotagmin-2 controls Ca(2+) dynamics in T cells via interaction with STIM1.", *Scientific reports*, **10**(1), p. 14433, DOI: 10.1038/s41598-020-71489-7.

Wu, X. and T. A. Rapoport (2021) "Cryo-EM structure determination of small proteins by nanobody-binding scaffolds (Legobodies)", *Proceedings of the National Academy of Sciences of the United States of America*, **118**(41), e2115001118, DOI: 10.1073/PNAS.2115001118/SUPPL_FILE/PNAS.2115001118.SAPP.PDF.

Wyant, G. A. et al. (2018) "Nufip1 is a ribosome receptor for starvation-induced ribophagy", *Science*, **360**(6390), pp. 751–758, DOI: 10.1126/SCIENCE.AAR2663/SUPPL_FILE/AAR2663_WYANT_SM.PDF.

Xiao, Q. et al. (2015) "Neuronal-Targeted TFEB Accelerates Lysosomal Degradation of APP, Reducing Aβ Generation and Amyloid Plaque Pathogenesis", *The Journal of Neuroscience*, **35**(35), p. 12137, DOI: 10.1523/JNEUROSCI.0705-15.2015.

Xu, D. et al. (2019) "Cryo-EM structure of human lysosomal cobalamin exporter ABCD4", *Cell Research 2019 29:12*, **29**(12), pp. 1039–1041, DOI: 10.1038/s41422-019-0222-z.

Xu, H. and D. Ren (2015) "Lysosomal physiology.", *Annual review of physiology*, **77**, pp. 57–80, DOI: 10.1146/annurev-physiol-021014-071649.

Xu, J. et al. (2017) "Stochastic optical reconstruction microscopy (STORM)", *Current protocols in cytometry*, **81**, p. 12.46.1, DOI: 10.1002/CPCY.23.

Yamagata, M. and J. R. Sanes (2018) “Reporter-nanobody fusions (RANbodies) as versatile, small, sensitive immunohistochemical reagents”, *Proceedings of the National Academy of Sciences of the United States of America*, **115**(9), pp. 2126–2131, DOI: 10.1073/PNAS.1722491115.

Yamamoto, A et al. (1998) “Bafilomycin A1 prevents maturation of autophagic vacuoles by inhibiting fusion between autophagosomes and lysosomes in rat hepatoma cell line, H-4-II-E cells.”, *Cell structure and function*, **23**(1), pp. 33–42, DOI: 10.1247/csf.23.33.

Yamashita, T. et al. (1997) “Cloning and functional expression of a brain peptide/histidine transporter”, *The Journal of biological chemistry*, **272**(15), pp. 10205–10211, DOI: 10.1074/JBC.272.15.10205.

Yao, H. et al. (2021) “A high-affinity RBD-targeting nanobody improves fusion partner’s potency against SARS-CoV-2”, *PLOS Pathogens*, **17**(3), e1009328, DOI: 10.1371/JOURNAL.PPAT.1009328.

Yaoid, H. et al. (2021) “A high-affinity RBD-targeting nanobody improves fusion partner’s potency against SARS-CoV-2”, *PLOS Pathogens*, **17**(3), e1009328, DOI: 10.1371/JOURNAL.PPAT.1009328.

Yu, H. et al. (2016) “Extended synaptotagmins are Ca2+-dependent lipid transfer proteins at membrane contact sites.”, *Proceedings of the National Academy of Sciences of the United States of America*, **113**(16), pp. 4362–4367, DOI: 10.1073/pnas.1517259113.

Yu, L. et al. (2010) “Termination of autophagy and reformation of lysosomes regulated by mTOR”, *Nature*, **465**(7300), pp. 942–946, DOI: 10.1038/NATURE09076.

Yu, X. et al. (2020) "Nanobodies derived from Camelids represent versatile biomolecules for biomedical applications", *Biomaterials Science*, **8**(13), pp. 3559–3573, DOI: 10.1039/D0BM00574F.

Yu, Y. et al. (2024) "Organelle proteomic profiling reveals lysosomal heterogeneity in association with longevity", *eLife*, **13**, DOI: 10.7554/ELIFE.85214.

Yuan, Y. et al. (2022) "Segregated cation flux by TPC2 biases Ca2+ signaling through lysosomes", *Nature Communications 2022 13:1*, **13**(1), pp. 1–13, DOI: 10.1038/s41467-022-31959-0.

Zach, G. et al. (2024) "Protein Binder Toolbox for Studies of Solute Carrier Transporters", *J Mol Biol*, **436**(16), DOI: 10.1016/j.jmb.2024.168665.

Zachos, C. et al. (2012) "A critical histidine residue within LIMP-2 mediates pH sensitive binding to its ligand β-glucocerebrosidase", *Traffic (Copenhagen, Denmark)*, **13**(8), pp. 1113–1123, DOI: 10.1111/J.1600-0854.2012.01372.X.

Zajac, M. et al. (2024) "A mechanism of lysosomal calcium entry", *Science Advances*, **10**(7), p. 2317, DOI: 10.1126/SCIADV.ADK2317/SUPPL_FILE/SCIADV.ADK2317_SM.PDF.

Zavrtanik, U. et al. (2018) "Structural Basis of Epitope Recognition by Heavy-Chain Camelid Antibodies", *Journal of molecular biology*, **430**(21), pp. 4369–4386, DOI: 10.1016/J.JMB.2018.09.002.

Zeevi, D. A. et al. (2010) "Heteromultimeric TRPML channel assemblies play a crucial role in the regulation of cell viability models and starvation-induced autophagy", *Journal of Cell Science*, **123**(18), p. 3112, DOI: 10.1242/JCS.067330.

Zerial, M. and H. McBride (2001) "Rab proteins as membrane organizers", *Nature reviews. Molecular cell biology*, **2**(2), pp. 107–117, DOI: 10.1038/35052055.

Zhang, J. et al. (2023) “Lysosomal LAMP proteins regulate lysosomal pH by direct inhibition of the TMEM175 channel”, *Molecular cell*, **83**(14), 2524–2539.e7, DOI: 10.1016/J.MOLCEL.2023.06.004.

Zhang, L. et al. (2022) “Interaction between TRPML1 and p62 in Regulating Autophagosome-Lysosome Fusion and Impeding Neuroaxonal Dystrophy in Alzheimer’s Disease.”, *Oxidative medicine and cellular longevity*, **2022**, p. 8096009, DOI: 10.1155/2022/8096009.

Zhang, S. et al. (2017) “Cryo-EM structures of the mammalian endo-lysosomal TRPML1 channel elucidate the combined regulation mechanism”, *Protein & cell*, **8**(11), pp. 834–847, DOI: 10.1007/S13238-017-0476-5.

Zhang, X. et al. (2012) “Phosphoinositide isoforms determine compartment-specific ion channel activity.”, *Proceedings of the National Academy of Sciences of the United States of America*, **109**(28), pp. 11384–11389, DOI: 10.1073/pnas.1202194109.

Zhang, X. et al. (2016) “MCOLN1 is a ROS sensor in lysosomes that regulates autophagy.”, *Nature communications*, **7**, p. 12109, DOI: 10.1038/ncomms12109.

Zhang, Y. et al. (2021) “mTORC1 couples cyst(e)ine availability with GPX4 protein synthesis and ferroptosis regulation”, *Nature Communications 2021 12:1*, **12**(1), pp. 1–14, DOI: 10.1038/s41467-021-21841-w.

Zhao, Y. G. and H. Zhang (2019) “Autophagosome maturation: An epic journey from the ER to lysosomes”, *The Journal of cell biology*, **218**(3), pp. 757–770, DOI: 10.1083/JCB.201810099.

Zheng, S. Q. et al. (2017) “MotionCor2 - anisotropic correction of beam-induced motion for improved cryo-electron microscopy”, *Nature methods*, **14**(4), p. 331, DOI: 10.1038/NMETH.4193.

Zhou, X. et al. (2000) “Characterization of an oligopeptide transporter in renal lysosomes”, *Biochimica et biophysica acta*, **1466**(1-2), pp. 372–378, DOI: 10.1016/S0005-2736(00)00201-7.

Zhou, X. et al. (2017) “Cryo-EM Structures of the Human Endolysosomal TRPML3 Channel in Three Distinct States”, *Nature structural & molecular biology*, **24**(12), p. 1146, DOI: 10.1038/NSMB.3502.

Zimmermann, I. et al. (2020) “Generation of synthetic nanobodies against delicate proteins.”, *Nature protocols*, **15**(5), pp. 1707–1741, DOI: 10.1038/s41596-020-0304-x.

Zoncu, R. et al. (2011) “mTORC1 senses lysosomal amino acids through an inside-out mechanism that requires the vacuolar H(+)-ATPase”, *Science (New York, N.Y.)*, **334**(6056), pp. 678–683, DOI: 10.1126/SCIENCE.1207056.